

NATIONAL AERONAUTICS AND SPACE ADMINISTRATION

*The Deep Space Network
Progress Report 42-30*

September and October 1975

(NASA-CR-145987) THE DEEP SPACE NETWORK
Progress Report, Sep. - Oct. 1975 (Jet
Propulsion Lab.) 312 p HC \$9.75 CSCL 22D

N76-15190
THRU
N76-15212
Unclass

G3/12 07360



**JET PROPULSION LABORATORY
CALIFORNIA INSTITUTE OF TECHNOLOGY
PASADENA, CALIFORNIA**

December 15, 1975

REPRODUCED BY
NATIONAL TECHNICAL
INFORMATION SERVICE
U.S. DEPARTMENT OF COMMERCE
SPRINGFIELD, VA. 22161

NATIONAL AERONAUTICS AND SPACE ADMINISTRATION

*The Deep Space Network
Progress Report 42-30*

September and October 1975

JET PROPULSION LABORATORY
CALIFORNIA INSTITUTE OF TECHNOLOGY
PASADENA, CALIFORNIA

December 15, 1975

Prepared Under Contract No. NAS 7-100
National Aeronautics and Space Administration

Preface

Beginning with Volume XX, the Deep Space Network Progress Report changed from the Technical Report 32- series to the Progress Report 42- series. The volume number continues the sequence of the preceding issues. Thus, Progress Report 42-20 is the twentieth volume of the Deep Space Network series, and is an uninterrupted follow-on to Technical Report 32-1526, Volume XIX.

This report presents DSN progress in flight project support, tracking and data acquisition (TDA) research and technology, network engineering, hardware and software implementation, and operations. Each issue presents material in some, but not all, of the following categories in the order indicated.

Description of the DSN

Mission Support

- Ongoing Planetary/Interplanetary Flight Projects
- Advanced Flight Projects

Radio Science

Special Projects

Supporting Research and Technology

- Tracking and Ground-Based Navigation
- Communications—Spacecraft/Ground
- Station Control and Operations Technology
- Network Control and Data Processing

Network and Facility Engineering and Implementation

- Network
- Network Operations Control Center
- Ground Communications
- Deep Space Stations

Operations

- Network Operations
- Network Operations Control Center
- Ground Communications
- Deep Space Stations

Program Planning

- TDA Planning
- Quality Assurance

In each issue, the part entitled "Description of the DSN" describes the functions and facilities of the DSN and may report the current configuration of one of the five DSN systems (Tracking, Telemetry, Command, Monitor & Control, and Test & Training).

The work described in this report series is either performed or managed by the Tracking and Data Acquisition organization of JPL for NASA.

Contents

DESCRIPTION OF THE DSN

DSN Functions and Facilities	1 D1
N. A. Renzetti	
DSN Test and Training System	5 D2
H. C. Thorman	
NASA Code 311-03-42-95	

MISSION SUPPORT

Ongoing Planetary/Interplanetary Flight Projects

Summary Report on the Viking 1975 DSN Telecommunications Compatibility Test Program	16 D3
A. I. Bryan	
NASA Code 311-03-22-10	
Viking Mission Support	57 D4
D. J. Mudgway and D. W. Johnston	
NASA Code 311-03-21-70	
Pioneer Mission Support	61 D5
R. B. Miller	
NASA Code 311-03-21-90	
Helios Mission Support	65 D6
P. S. Goodwin, W. G. Meeks, R. E. Morris, and S. E. Reed	
NASA Code 311-03-21-50	

SUPPORTING RESEARCH AND TECHNOLOGY

Tracking and Ground-Based Navigation

A New Global Ionospheric Model	70 D7
K. W. Yip and O. H. von Roos	
NASA Code 310-10-60-46	
Corruption of Radio Metric Doppler Due to Solar Plasma Dynamics: S/X Dual-Frequency Doppler Calibration for These Effects	88 D8
F. B. Winn, S. R. Reinbold, K. W. Yip, R. E. Koch and A. Lubeley	
NASA Code 310-10-60-46	
100-kHz Frequency Divider, Distribution Amplifier	102 D9
G. Lutes	
NASA Code 310-10-61-07	

Communications—Spacecraft/Ground

The X-Band Low-Noise Antenna Measurement Cone 105 *D10*
M. S. Reid, F. E. McCrea, K. B. Wallace, and C. T. Stelzried
NASA Codes 310-20-66-06 and 311-03-42-46

Performance of DSS 13 26-m Antenna at X-Band 113 *D11*
A. J. Freiley
NASA Code 310-20-65-03

DSS 14 X-Band Radar Feedcone 119 *D12*
D. E. Neff and D. A. Bathker
NASA Code 310-20-65-03

A Versatile Data Acquisition System for Goldstone 132 *D13*
M. S. Reid and R. A. Gardner
NASA Codes 310-20-66-06 and 311-03-41-08

Station Control and Operations Technology

Microcontroller for Automation Application 144 *D14*
H. W. Cooper
NASA Code 310-30-68-10

Exciter Switch 148 *D15*
W. L. McPeak
NASA Code 310-30-68-11

Network Control and Data Processing

Priority Repair Schemes in the Deep Space Network 157 *-X*
I. Eisenberger and G. Lorden
NASA Code 310-40-73-01

Variation of GCF Block Error Rate With Block Length 162 *-X*
O. Adeyemi
NASA Code 310-40-70-02

**Effects on Station Productivity of the RF and Antenna
Automation Plans** 166 *-X*
H. L. Kirkbride
NASA Code 310-40-73-01

Remote Automatic Control of DSS 13 174 *-X*
K. I. Moyd
NASA Code 310-40-70-02

NETWORK AND FACILITY ENGINEERING AND IMPLEMENTATION

Network

DSN Telemetry System Performance With Convolutionally Coded Data	184	<i>D16</i>
B. D. L. Mulhall, B. Benjauthrit, C. A. Greenhall, D. M. Kuma, J. K. Lam, J. S. Wong, J. Urech, and L. D. Vit NASA Code 311-03-42-95		

Deep Space Stations

Approximate Mean Time to Loss of Lock for the Symbol Synchronizer Assembly	200	<i>-X</i>
J. I. Molinder NASA Code 311-03-42-95		
Transmitter Fourth-Harmonic Interference at the Mars Station	204	<i>-X</i>
R. C. Coffin NASA Code 311-03-42-95		
Open-Loop Receiver Recording for Telemetry Data Recovery: A Field Demonstration	208	<i>-X</i>
S. S. Kent NASA Code 311-03-42-95		

OPERATIONS

Network Operations

DSN Research and Technology Support	214	<i>D17</i>
E. B. Jackson NASA Code 311-03-14-64		
Symbol Synchronizer Assembly Instability Study: Part II	222	<i>D18</i>
R. C. Bunce NASA Code 311-03-14-52		
Analysis and Prediction of Doppler Noise During Solar Conjunctions	231	<i>D19</i>
A. L. Berman and S. T. Rockwell NASA Code 311-03-13-20		
Correlation of Doppler Noise During Solar Conjunctions With Fluctuations in Solar Activity	264	<i>D20</i>
A. L. Berman and S. T. Rockwell NASA Code 311-03-13-20		

Tracking Operations During the Viking 1 Launch Phase 273 *D21*

A. L. Berman and J. A. Wackley
NASA Code 311-03-13-20

A Relational Data Base Implemented Using MBASIC 291 *D22*

R. M. Smith
NASA Code 311-03-14-64

N76-15191

DSN Functions and Facilities

N. A. Renzetti
Office of Tracking and Data Acquisition

The objectives, functions, and organization of the Deep Space Network are summarized. Deep space station, ground communication, and network operations control capabilities are described.

The Deep Space Network (DSN), established by the National Aeronautics and Space Administration (NASA) Office of Tracking and Data Acquisition (OTDA) under the system management and technical direction of the Jet Propulsion Laboratory (JPL), is designed for two-way communications with unmanned spacecraft traveling approximately 16,000 km (10,000 mi) from Earth to the farthest planets of our solar system. It has provided tracking and data acquisition support for the following NASA deep space exploration projects, for which JPL has been responsible for the project management, development of the spacecraft, and conduct of mission operations:

- (1) Ranger.
- (2) Surveyor.
- (3) Mariner Venus 1962.

- (4) Mariner Mars 1964.
- (5) Mariner Venus 1967.
- (6) Mariner Mars 1969.
- (7) Mariner Mars 1971.
- (8) Mariner Venus/Mercury 1973.

The DSN has also provided tracking and data acquisition support for the following projects:

- (1) Lunar Orbiter, for which the Langley Research Center carried out the project management, spacecraft development, and mission operations functions.

- (2) Pioneer, for which the Ames Research Center carried out the project management, spacecraft development, and mission operations functions.
- (3) Apollo, for which the Lyndon B. Johnson Space Center was the project center and the Deep Space Network supplemented the Spaceflight Tracking and Data Network (STDN), which is managed by the Goddard Space Flight Center (GSFC).
- (4) Helios, a joint United States/West Germany project.
- (5) Viking, for which the Langley Research Center provides the project management and Lander spacecraft, and conducts mission operations, and for which JPL provides the Orbiter spacecraft.

The Deep Space Network is one of two NASA networks. The other, the Spaceflight Tracking and Data Network, is under the system management and technical direction of the Goddard Space Flight Center. Its function is to support manned and unmanned Earth-orbiting and lunar scientific and advanced technology satellites. Although the DSN was concerned with unmanned lunar spacecraft in its early years, its primary objective now and into the future is to continue its support of planetary and interplanetary flight projects.

A development objective has been to keep the network capability at the state of the art of telecommunications and data handling and to support as many flight projects as possible with a minimum of mission-dependent hardware and software. The DSN provides direct support to each flight project through that project's tracking and data systems. This management element is responsible for the design and operation of the hardware and software in the DSN which are required for the conduct of flight operations.

As of July 1972, NASA undertook a change in the interface between the network and the flight projects. Since January 1, 1964, the network, in addition to consisting of the Deep Space Stations and the Ground Communications Facility, had also included the Mission Control and Computing Facility and had provided the equipment in the mission support areas for the conduct of mission operations. The latter facilities were housed in a building at JPL known as the Space Flight Operations Facility (SFOF). The interface change was to accommodate a hardware interface between the network operations control functions and the mission control and computing functions. This resulted in the flight project's picking up

the cognizance of the large general-purpose digital computers, which were used for network processing as well as mission data processing. It also assumed cognizance of all of the equipment in the flight operations facility for display and communications necessary for the conduct of mission operations. The network has already undertaken the development of hardware and computer software necessary to do its network operations control and monitor functions in separate computers. This activity became known as the Network Control System implementation. A characteristic of the new interface is that the network provides direct data flow to and from the stations via appropriate ground communications equipment to Mission Operations Centers, wherever they may be; namely, metric data, science and engineering telemetry, and such network monitor data as are useful to the flight project. It accepts command data from the flight project directly into the ground communications equipment for transmission to the station and thence to the spacecraft in a standardized format.

In carrying out its functions, the network activities can be divided into two general areas. The first includes those functions which are associated with the in-flight support and in tracking the spacecraft; its configuration can be characterized as follows:

- (1) *DSN Tracking System.* Generates radio metric data; i.e., angles, one- and two-way doppler and range, and transmits raw data to mission control.
- (2) *DSN Telemetry System.* Receives, decodes, records, and retransmits engineering and scientific data generated in the spacecraft to Mission Control.
- (3) *DSN Command System.* Accepts coded signals from Mission Control via the Ground Communications Facility (GCF) and transmits them to the spacecraft in order to initiate spacecraft functions in flight.

The second category of activity supports testing, training, and network operations control functions and is configured as follows:

- (1) *DSN Monitor and Control System.* Instruments, transmits, records, and displays those parameters of the DSN necessary to verify configuration and validate the network. Provides operational direction and configuration control of the network and primary interface with flight project mission control personnel.

- (2) *DSN Test and Training System.* Generates and controls simulated data to support development, test, training, and fault isolation within the DSN. Participates in mission simulation with flight projects.

The capabilities needed to carry out the above functions have evolved in three technical areas:

- (1) The Deep Space Stations that are distributed around Earth and which, prior to 1964, formed part of the Deep Space Instrumentation Facility. The technology involved in equipping these stations is strongly related to the state of the art of telecommunications and flight/ground design considerations and is almost completely multimission in character. Table 1 gives a description of the Deep Space Stations and the Deep Space Communications Complexes (DSCCs) they comprise.
- (2) Ground communications. This technology supports the Earth-based point-to-point voice and data communications from the stations to the Network Operations Control Area at JPL, Pasadena, and to the Mission Operations Centers, wherever they may be. It is based largely on the capabilities of the common carriers throughout the world which are engineered into an integrated system by the Goddard Space Flight Center for support of all NASA programs. The term "Ground Communications Facility" is used for the sets of hardware and software needed to carry out the functions.

The Network Operations Control Center is the functional entity for centralized operational control of the network and interfaces with the users. It has two separable functional elements; namely, Network Operations Control and Network Data Processing.

The functions of the Network Operations Control Center are:

- (1) Control and coordination of network support to meet commitments to network users.
- (2) Utilization of the network data processing computing capability to generate all standards and limits required for network operations.
- (3) Utilization of network data processing computing capability to analyze and validate the performance of all network systems.

The personnel who carry out the above functions are on the first floor of Building 230, wherein mission operations functions are carried out by certain flight projects. Network personnel are directed by an Operations Control Chief. The functions of the Network Data Processing are:

- (1) Processing of data used by Network Operations Control for the control and analysis of the network.
- (2) Display in Network Operations Control Area of data processed in Network Data Processing Area.
- (3) Interface with communications circuits for input to and output from Network Data Processing Area.
- (4) Data logging and production of the intermediate data records.

The personnel who carry out these functions are located in Building 202, which is approximately 200 m from Building 230. The equipment consists of minicomputers for real-time data system monitoring, two XDS Sigma 5's, display, magnetic tape recorders, and appropriate interface equipment with the ground data communications.

Table 1. Tracking and data acquisition stations of the DSN

DSCC	Location	DSS	DSS serial designation	Antenna		Year of initial operation
				Diameter, m (ft)	Type of mounting	
Goldstone	California	Pioneer	11	26(85)	Polar	1958
		Echo	12	26(85)	Polar	1962
		(Venus) ^a	13	26(85)	Az-El	1962
		Mars	14	64(210)	Az-El	1966
Tidbinbilla	Australia	Weemala	42	26(85)	Polar	1965
		Ballima	43	64(210)	Az-El	1973
—	Australia	Honeysuckle Creek	44	26(85)	X-Y	1973
Madrid	Spain	Robledo	61	26(85)	Polar	1965
		Cebreros	62	26(85)	Polar	1967
		Robledo	63	64(210)	Az-El	1973

^aA maintenance facility. Besides the 26-m (85-ft) diam Az-El mounted antenna, DSS 13 has a 9-m (30-ft) diam Az-El mounted antenna that is used for interstation time correlation using lunar reflection techniques, for testing the design of new equipment, and for support of ground-based radio science.

DSN Test and Training System

H. C. Thorman
DSN Systems Engineering Office

Key characteristics of the Deep Space Network Test and Training System are presented. Completion of Mark III-75 system implementation is reported. Plans are summarized for upgrading the system to a Mark III-77 configuration to support Deep Space Network preparations for the Mariner Jupiter/Saturn 1977 and Pioneer Venus 1978 missions. A general description of the Deep Space Station, Ground Communications Facility, and Network Operations Control Center functions that comprise the Deep Space Network Test and Training System is also presented.

I. Introduction

A. Key Characteristics

The DSN Test and Training System is a multiple-mission system which provides capabilities to prepare the DSN for mission support. The key characteristics of the system are listed below:

- (1) Supports calibrations, readiness verification, and fault isolation by providing composite signals for input to other DSN systems.
- (2) Supports DSN operational verification tests by providing simulated telemetry, command, and radio metric data patterns.
- (3) Supports performance testing of DSN systems, Deep Space Station (DSS) subsystems, and Network Control subsystems by providing closed-loop validation.
- (4) Supports mission simulations by converting high-speed and wideband blocks of simulated telemetry data into serial streams modulated onto subcarriers and carriers; and by providing Command System operation with dummy load.
- (5) Operates without interfering with normal operation of other DSN systems.

B. Mark III-75 System Implementation

Reference 1 describes the Mark III-75 configuration of the DSN Test and Training System, including incremental upgrade requirements for Viking Mars test and training support. The planned upgrade was completed in early 1975, as scheduled. The upgrade included implementation of a new software program for the Simulation Conversion Assembly (SCA) at all Deep Space Stations and new equipment to provide three-spacecraft telemetry simulation in the 64-m antenna subnet. The upgrade also

provided Network Operations Control Center capability to exercise remote control of the SCA.

C. Mark III-77 System Requirements

Further upgrading of the DSN Test and Training System to a Mark III-77 configuration (Fig. 1) is planned to meet requirements for support of network preparations for the Mariner Jupiter/Saturn 1977 (MJS'77) mission and the Pioneer Venus 1978 (PV'78) mission. The preparations for these missions include extensive implementation of new minicomputers to replace the existing XDS-920 processors in the DSS Telemetry, Command, and Tracking Subsystems.

The Mark III-77 configuration will include the following modifications and additions to the present system:

- (1) Modification of the DSS Simulation Conversion Assembly to provide capability for short-constraint-length convolutional coding of simulated MJS'77 telemetry data and long-constraint-length convolutional coding of simulated PV'78 telemetry data.
- (2) Upgrade of program software for the XDS-910 processor, associated with the SCA, to provide generation of MJS'77 and PV'78 frame-synchronized telemetry test data and control of new SCA equipment.
- (3) Configuring of the DSS Communications Monitor and Formatter backup minicomputer to provide the System Performance Test Assembly functions of on-site closed-loop performance testing and validation of the Tracking, Telemetry, Command, and Monitor and Control Systems.
- (4) Implementation of the Network Control Test and Training Subsystem in the Network Operations Control Center.
- (5) Implementation of the DSN Test and Training System Control Console in the Network Operations Control Center.

Implementation of items (1), (2), and (3) is to begin in early 1976 and is to be completed at all Deep Space Stations by the end of 1977. The station-by-station schedule is such that all DSS Test and Training Subsystem capabilities will be available to support testing of the new data processing subsystems which are to be implemented at each station.

Items (5) and (6) are scheduled for completion in the first half of 1976 as part of the Block III implementation of the Network Control System project (Ref. 2).

II. Deep Space Station Functions

A. DSS Test and Training Subsystem

The functions of the DSS Test and Training Subsystem and the related interfaces are shown in Fig. 2.

1. **Telemetry Simulation and Conversion.** The telemetry simulation and conversion functions are performed by the Simulation Conversion Assembly, which is diagrammed in detail in Fig. 3. The digital and analog capabilities of the SCA are itemized in Tables 1 and 2, respectively.

2. **System Performance Test Functions.** The system performance test functions are performed by the System Performance Test Assembly (SPTA), which is diagrammed in detail in Fig. 4.

B. Receiver-Exciter Subsystem

The Receiver-Exciter Subsystem provides the following test and training functions:

- (1) Generation of simulated S-band and X-band downlink carriers.
- (2) Modulation of telemetry subcarriers from the SCA onto simulated carriers.
- (3) Variable control of simulated downlink carrier frequency to permit simulation of doppler shifts.
- (4) Provision of a transmitter dummy load for Command System test operations.

C. Antenna Microwave Subsystem

The Antenna Microwave Subsystem provides the following test and training functions:

- (1) Variable attenuation of simulated downlink carrier signal level under control of the Simulation Conversion Assembly.
- (2) Routing of simulated downlink carriers to masers and/or receivers.
- (3) Mixing of simulated S-band downlink carriers.

D. Frequency and Timing Subsystem

The Frequency and Timing Subsystem provides the following support functions to the DSS Test and Training Subsystem:

- (1) Reference frequencies inputted to the SCA.
- (2) Time code and reference frequencies inputted to the SPTA.
- (3) Generation and distribution of a simulated time signal which can be substituted for the true GMT

input to the various DSS subsystems. This capability is provided for realistic mission simulations in support of flight project testing and training activities.

III. Ground Communications Facility Functions

The DSN Test and Training System utilizes the Ground Communications Facility Subsystems for communicating data and information between the Network Operations Control Center (NOCC) or any Mission Operations Center (MOC) and the Deep Space Stations.

A. High-Speed Data Subsystem

The High-Speed Data Subsystem provides the following:

- (1) Transmission of text messages, control messages, low-to-medium-rate simulated telemetry data, and simulated command data to any DSS from the Network Operations Control Center or from any Mission Operations Center.
- (2) On-site loop-back of test data for systems performance testing and readiness verifications in the DSS.

B. Wideband Data Subsystem

The Wideband Data Subsystem provides the following:

- (1) Transmission of simulated high-rate telemetry data to the 64-m subnet, the Compatibility Test Area in Pasadena, California, and STDN MIL-71 at Merritt Island, Florida, from the NOCC or from any MOC having wideband capability.
- (2) On-site loop-back of test data for telemetry system performance testing and readiness verification in those stations which have wideband capability.

C. Voice Subsystem

The Voice Subsystem provides operator-to-operator communication of information for purposes of test coordination and monitoring of the DSN Test and Training System status.

IV. Network Operations Control Center Functions

A. Network Control Test and Training Subsystem

Planned functions and interfaces of the Network Control Test and Training Subsystem are shown in Fig. 5. Subsystem data flow details are further diagrammed in Fig. 6.

1. **Present Capabilities.** Test and training capabilities presently operational in the Network Operations Control Center are as follows:

- (1) Selection and output of stored data blocks from the Block I Network Command Subsystem (XDS Sigma-5) to the DSS for system readiness verification.
- (2) Off-line generation of recordings of high-speed data blocks for testing of the Block II real-time monitors in the Network Control Tracking, Telemetry, Command, and Monitor Subsystems.
- (3) Selection and output of prepared Simulation Conversion Assembly text and control messages to the stations from the Block I XDS Sigma-5. This capability provides remote configuration and control of the Simulation Conversion Assembly for support of DSN Operational Verification Tests conducted by the Viking and Helios Network Operations Project engineers.

2. **Future Capabilities.** Test and training functions (Fig. 6) to be implemented in the Network Operations Control Center in 1976 are as follows:

- (1) Real-time generation of data patterns for testing of the Network Control Tracking, Telemetry, Command, Monitor, Support, and Display Subsystems.
- (2) Real-time generation of Simulation Conversion Assembly text and control messages, simulated telemetry data patterns, and simulated project commands for transmission to the Deep Space Stations.

B. DSN Test and Training System Control Console

A DSN Test and Training System Control Console (see Fig. 6) is scheduled for 1976 implementation in the Network Data Processing Area. The console will provide keyboards, a card reader, a magnetic tape unit, volatile displays, and a character printer, so that operation of the Test and Training System will be separate from the operations of the other DSN Systems.

References

1. Thorman, H. C., "DSN Test and Training System," in *The Deep Space Network Progress Report 42-20*, pp. 5-12, Jet Propulsion Laboratory, Pasadena, Calif., Apr. 15, 1974.
2. Friesema, S. E., et al., "Network Control System Project Block III Software," in *The Deep Space Network Progress Report 42-28*, pp. 122-126, Jet Propulsion Laboratory, Pasadena, Calif., Aug. 15, 1975.

Table 1. DSS simulation conversion assembly digital channel requirements

Capability	SCA-I DSS 11, 12, 44, 62, MIL 71	SCA-II DSS 14, 42/43, 61/63, CTA 21
Maximum number of simultaneous data streams	2 channels	Viking prime mission, 6 channels; Viking extended mission, 4 channels; other missions, 3 channels
Bi-orthogonal (32, 6) comma-free block coding	Viking, 2 channels; other missions, none	Viking, 3 channels; other missions, none
Short constraint length convolutional coding ($k = 7$, $r = 1/2$ or $1/3$) ^a	Rate = $1/2$, 2 channels; ^a rate = $1/3$, 1 channel ^a	Rate = $1/2$, 3 channels; ^a rate = $1/3$, 2 channels ^a
Long constraint length convolutional coding ($k = 32$, $r = 1/2$)	Helios, 1 channel; Pioneer 10/11, 1 channel; Pioneer Venus, 2 channels ^a	Helios, 1 channel; Pioneer 10/11, 1 channel; Pioneer Venus, 3 channels ^a
Variable rate control	1 bit/s to 250 kbps on each of 2 channels	1 bit/s to 250 kbps on each of 3 channels
Selection of discrete rates	$8\frac{1}{3}$, $33\frac{1}{3}$ bits/s on each of 2 channels (uncoded)	$8\frac{1}{3}$, $33\frac{1}{3}$ bits/s on each of 3 channels (uncoded)

^aNew requirements to be implemented in DSN Mark III-77 Test and Training System.

Table 2. DSS simulation conversion assembly analog signal capabilities

Capability	SCA-I DSS 11, 12, 44, 62, MIL 71	SCA-II DSS 14, 42/43, 61/63, CTA 21
Data and subcarrier signal conditioning	Biphase modulation, 2 subcarriers	Biphase modulation: Viking prime mission, 6 subcarriers; Viking extended mission, 4 subcarriers; other missions, 3 subcarriers
Subcarrier frequency generation	1 Hz to 10 MHz range	1 Hz to 10 MHz range
Modulation-index angle control	Controllable from 10 to 80 deg on each subcarrier	Controllable from 10 to 80 deg on each subcarrier
Subcarrier mixing and downlink carrier modulation	Single or dual subcarriers onto each of 2 S-band carriers	Single or dual subcarriers onto each of 3 S-band or X-band carriers
Downlink carrier signal level	Attenuation of 0 to 40 dB at output of each test transmitter	Attenuation of 0 to 40 dB at output of each test transmitter

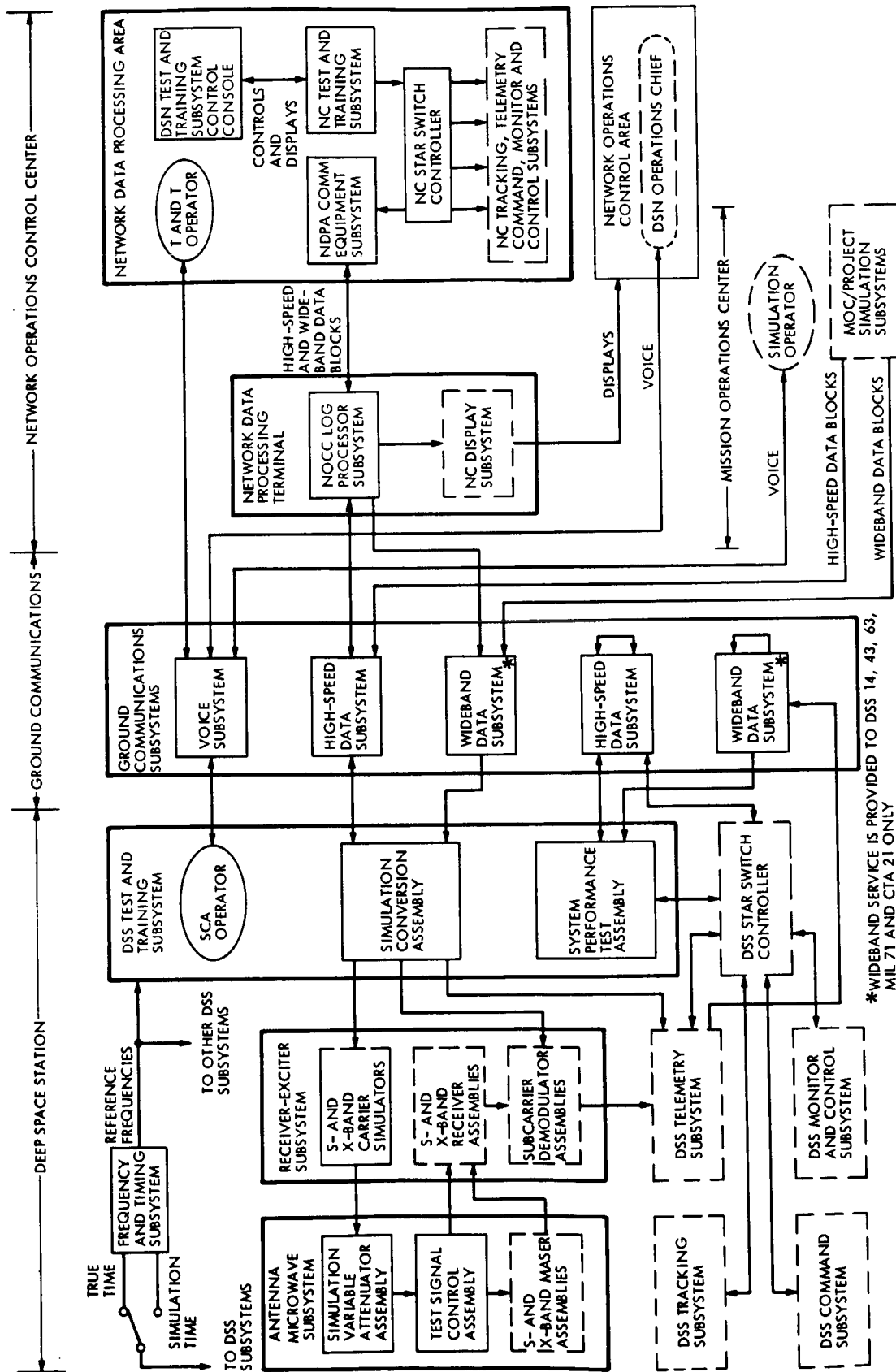


Fig. 1. DSN Mark III-77 Test and Training System block diagram

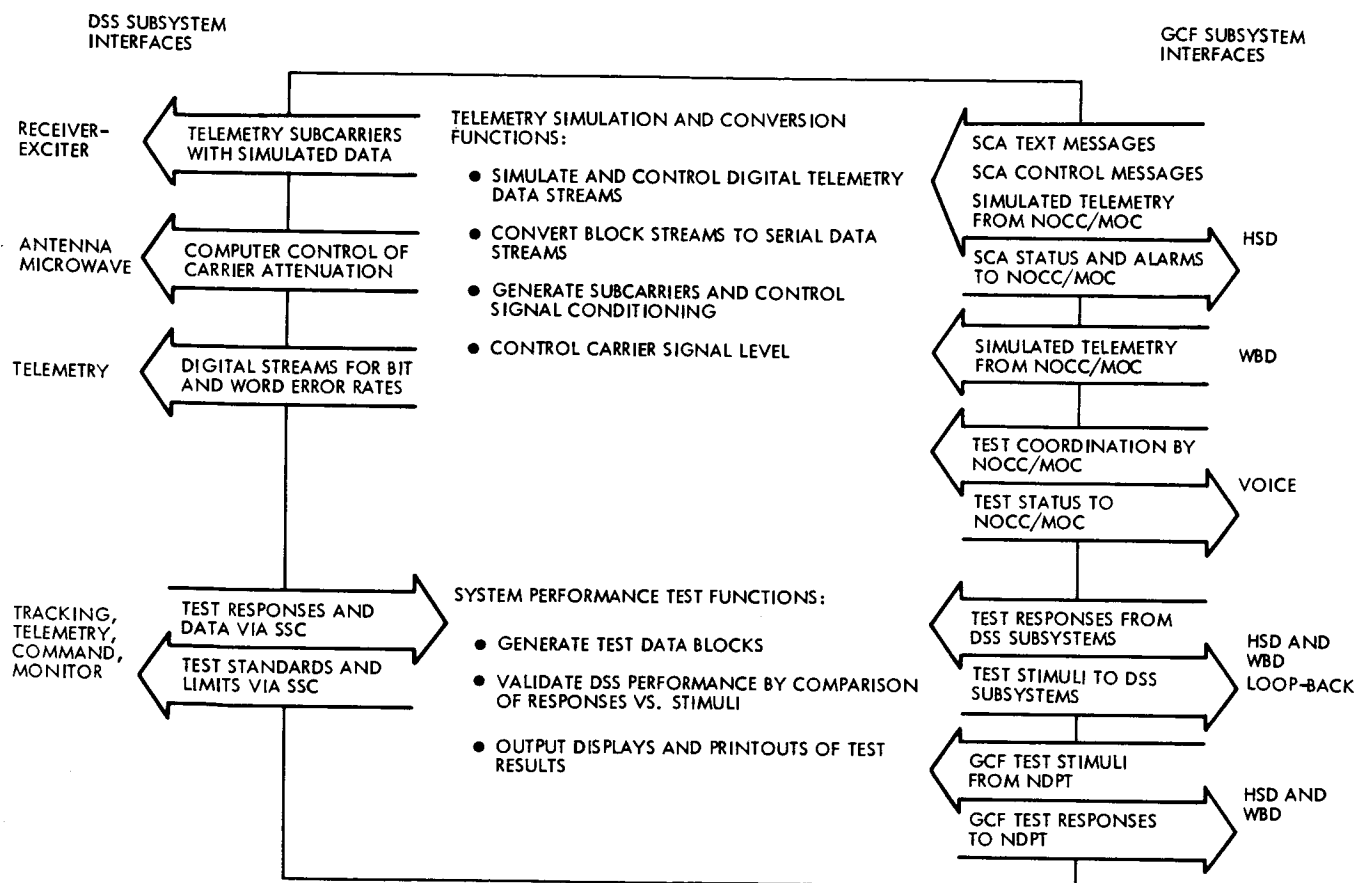


Fig. 2. DSS Test and Training Subsystem functions and interfaces

REPRODUCIBILITY OF THE
ORIGINAL PAGE IS POOR

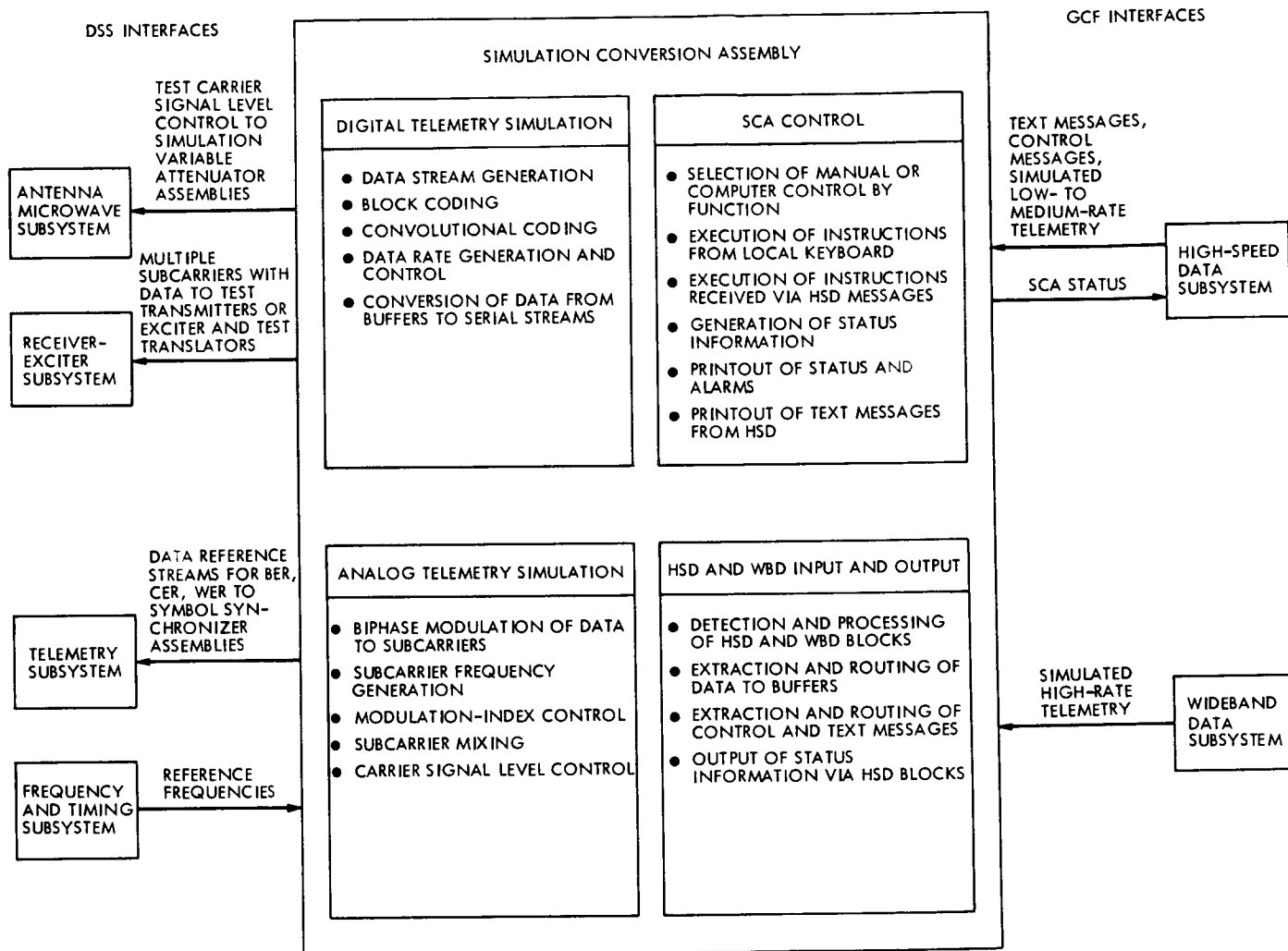


Fig. 3. Simulation conversion assembly functions and data flow

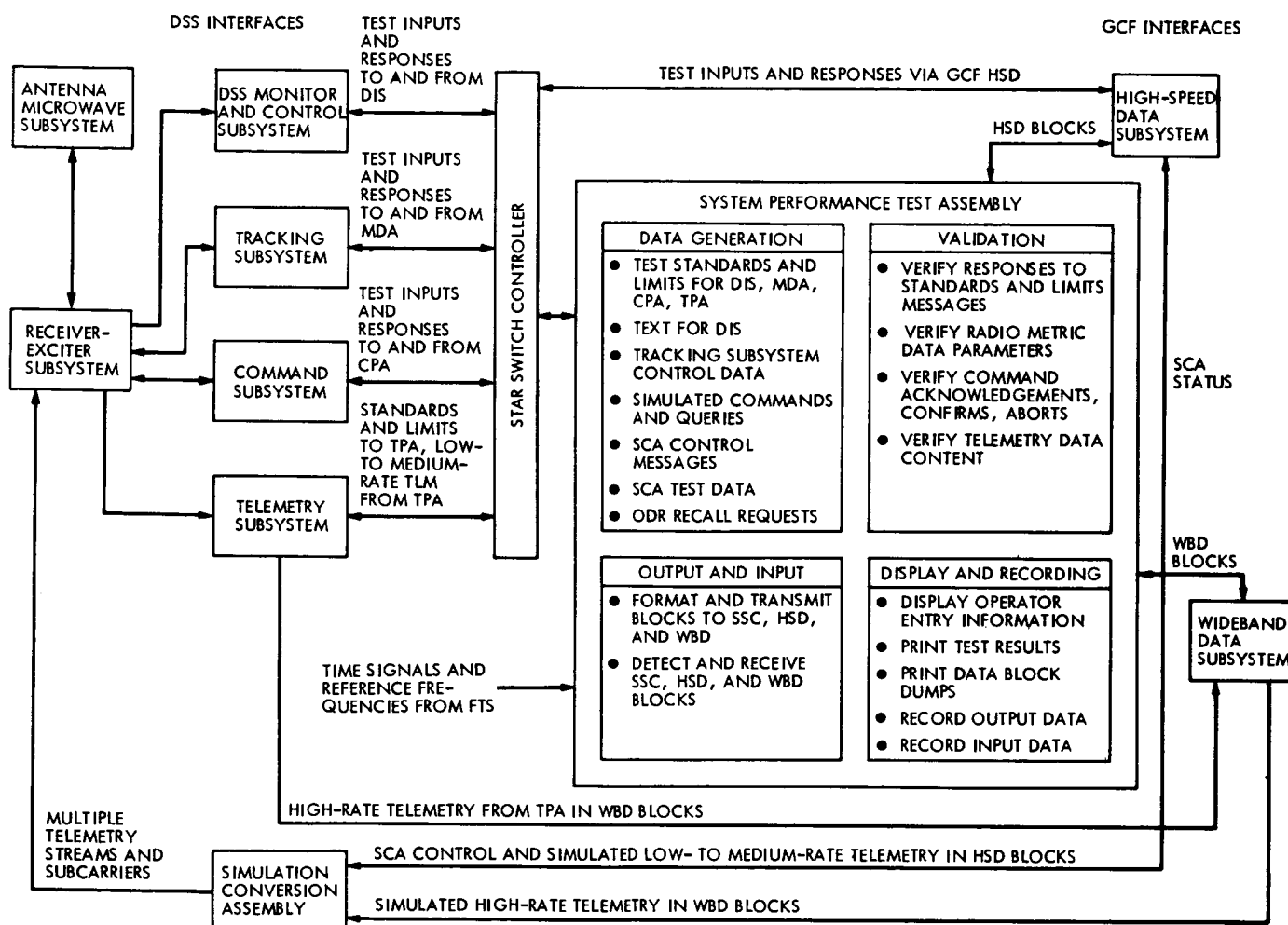


Fig. 4. System performance test assembly functions and data flow

REPRODUCIBILITY OF THE
ORIGINAL PAGE IS POOR

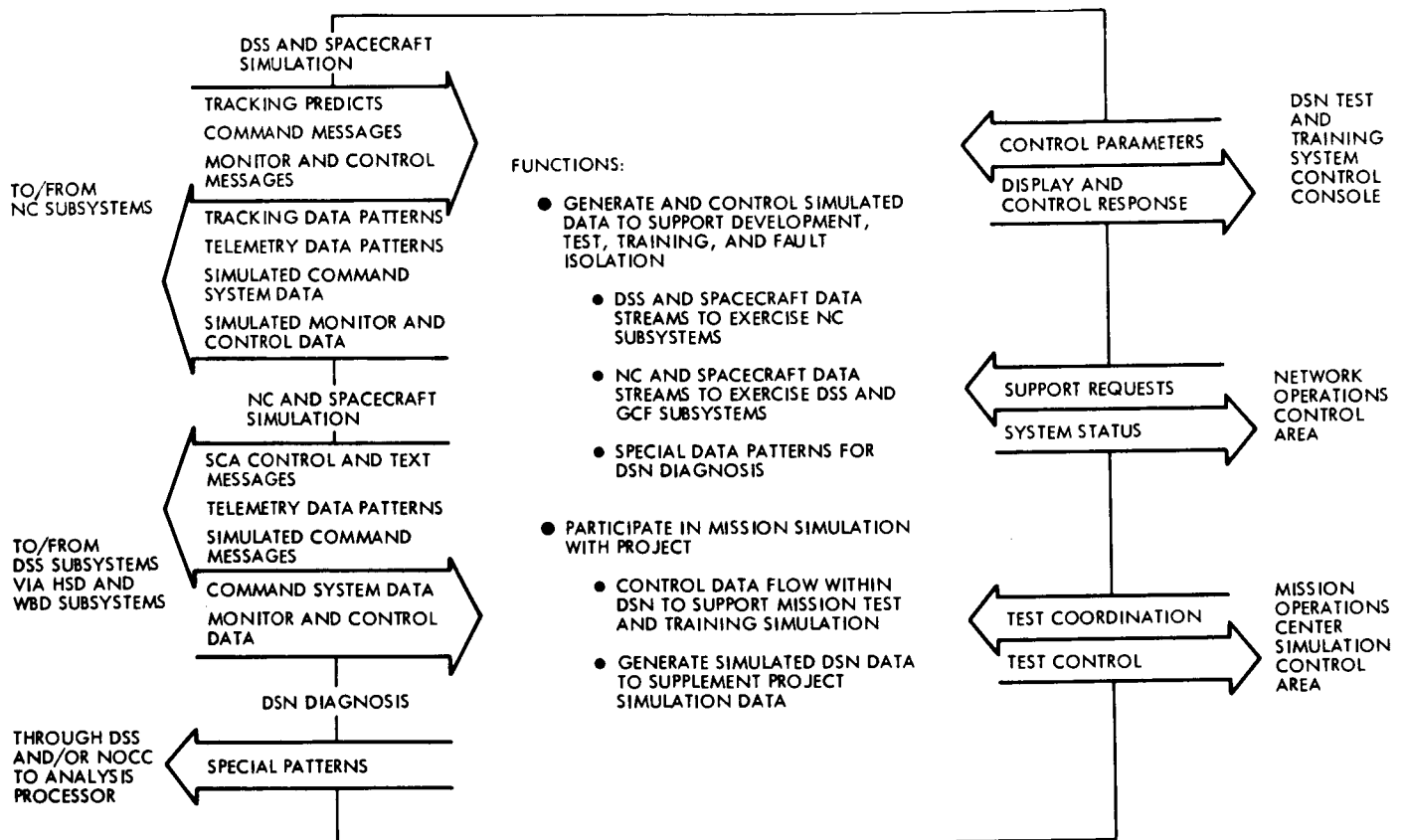


Fig. 5. NC Test and Training Subsystem functions and interfaces

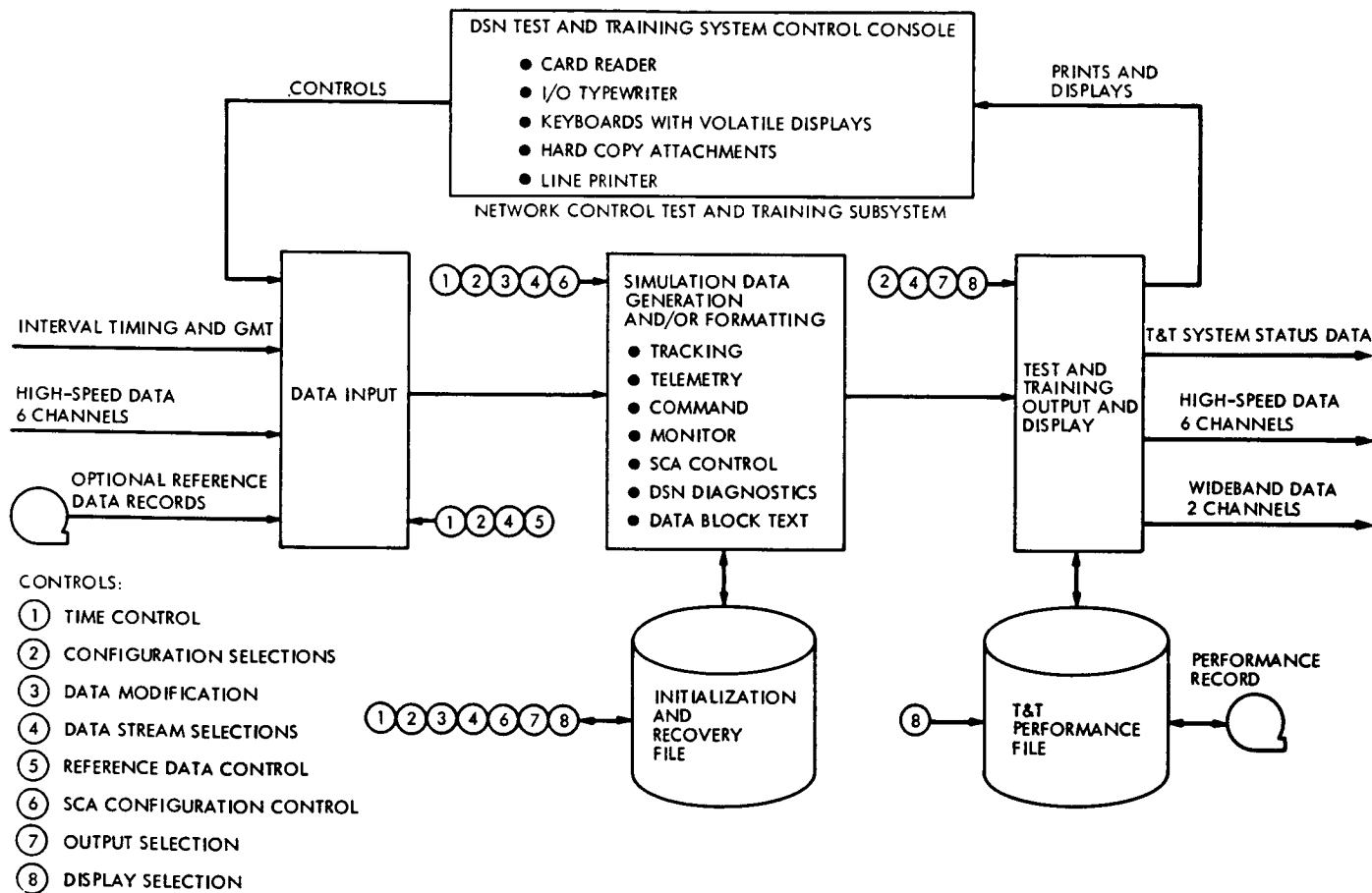


Fig. 6. NC Test and Training Subsystem data flow

N76-15193

Summary Report on the Viking 1975 DSN Telecommunications Compatibility Test Program

A. I. Bryan
DSN Systems Engineering Office

The Viking 1975/DSN Telecommunications Compatibility Test Program consisted of three phases: subsystem design, system design, and system verification tests which were performed at JPL and at the Air Force Eastern Test Range and Kennedy Space Center complexes. Subsystem design tests were performed with the Viking Orbiter (VO) and the Viking Lander (VL) during 1973. System design compatibility tests were performed with the Viking Proof Test Orbiter, Viking Spacecraft Test Lander, and a multiple Viking spacecraft configuration during the summer of 1974. System verification tests were performed with the Viking Orbiter, Viking Lander and Viking spacecraft during the spring and summer of 1975. This article describes the system design tests and test results that provided the basis for establishment of telecommunications design between the DSN and Viking 1975.

I. Introduction

This report summarizes the DSN/Viking Telecommunications Compatibility Test Program covering the period from April 1973 through August 1975. This test program was the most complex and extensive test program ever undertaken by the Deep Space Network. Equipment resources had to be greatly expanded to meet

the challenges and requirements of multiple spacecraft operation. To fulfill the requirements, the Viking Master Integrated Test Plan was developed and agreed to by all major Viking Project systems.

The plan specified that telecommunications design compatibility would be established at the subsystem and system levels and conclude with a final verification at

Cape Canaveral, Florida, prior to launch. Additionally, the DSN and flight project equipment software configurations, requirements, and test objectives in all phases were specified.

Procedures for conducting the tests as well as test design criteria and test parameters for the ground station hardware and software were prepared by network personnel. Spacecraft telecommunications design performance criteria and test parameters to establish flight project nominal and threshold telecommunications conditions were provided by the respective Viking Orbiter and Lander telecommunications teams. The test criteria were included as part of the test procedure to provide real-time assessment of performance. All test procedures were approved by the DSN and flight project representatives.

II. Types of Tests

The test program encompassed three types of tests: (1) DSN/Viking Lander compatibility tests conducted in three phases, (2) DSN/Viking Orbiter compatibility tests conducted in three phases, and (3) DSN/Viking Orbiter and Lander compatibility tests conducted in two phases.

III. Objectives

The objectives of the test program were to demonstrate compatibility between the spacecraft telecommunications subsystems and the Network, to establish system design compatibility between the flight spacecraft and the Network, and to verify continued interface integrity and maintenance of compatibility during prelaunch activities.

IV. Test Results

A. DSN/Viking Lander Compatibility Tests

These three-phase tests were conducted in the major areas of radio frequency acquisition and tracking, command, radio metric data, and telemetry.

1. Phase I: development test model—S-band radio assembly. These tests were conducted at the Compatibility Test Area in Pasadena (CTA 21) with the Lander subsystem components during April 1973. With the exceptions of the Block IV receiver-exciter and the planetary ranging assembly, CTA 21 provided a standard Network configuration for tests with the Lander S-band

radio assembly. The simulation conversion assembly provided simulated spacecraft subcarrier data, and command testing utilized the multimission command compatibility software to investigate interference between S-band channels 13 and 16. Channel 16 downlink was simulated by the CTA 21 test transmitter.

The tests established radio frequency compatibility between the Lander direct communications subsystem and the Network. Command, ranging, and telemetry interference tests revealed no problems with the Lander S-band radio assembly operating on channel 13. However, it should be noted that most of these tests were performed with channel 16 modulated by the Mark 1A ranging subsystem. The planetary ranging assembly was simulated by the simulation conversion assembly in the remaining tests. The question of interference between channels 13 and 16 was not resolved during this phase of testing.

2. Phase II: spacecraft test lander. These tests were conducted at CTA 21 with the Viking Lander in July 1974. The test Lander was configured to represent a flight spacecraft telecommunications system, and CTA 21 was configured to represent a 64-meter-diameter antenna station. The Lander was located in the screen room of the Spacecraft Assembly Facility at JPL. An S-band radio frequency link was established between the Lander and the ground station. The tests were performed at nominal and threshold conditions to prove Network/single spacecraft performance prior to multiple spacecraft telecommunications compatibility testing and to provide prerequisite data bases for performing the data compatibility tests which established data flow system interface compatibility from the spacecraft via the Network to the Viking Mission Control and Computing Center. The results of these tests are documented in *DSN Progress Report 42-24* (Ref. 1).

3. Phase III: Viking Lander capsule. There were two sets of tests in this phase with Viking Lander Capsules 1 and 2. The Network test with Capsule 1 was conducted from January 30 through February 7, 1975, and the test with Capsule 2 from April 7 through April 9, 1975. These tests were conducted with the DSN equipment in the Spacecraft Tracking and Data Network Station (STDN-(MIL 71)) at Merritt Island and the capsules located in the Spacecraft Assembly and Encapsulation Facility at Kennedy Space Center, approximately three miles from MIL 71. Both capsules were configured for mission operations, and MIL 71 was configured to simulate a 64-meter-diameter antenna station. S-band radio frequency links

were utilized between the flight articles and the ground station. Tables 1 and 2 provide a listing of the tests performed; on the basis of these results, continued compatibility between the Network and Viking Lander Capsules 1 and 2 was verified.

B. DSN/Viking Orbiter Compatibility Tests

Phases I and II of these tests were conducted at CTA 21; Phase III was conducted at MIL 71 with the spacecraft located at Cape Canaveral Air Force Station, Florida, which is approximately 7 miles from MIL 71.

1. Phase I: Viking Orbiter subsystem design tests. These tests were conducted with the Orbiter radio frequency subsystem prototype on August 28-29, 1973. The prototype was located in the screen room at the Telemetry Development Laboratory; S-band link was utilized between the prototype and CTA 21. The tests performed were uplink threshold, downlink threshold (one-way and two-way), ranging acquisition and polarity verification, downlink spectrum analysis, and radio frequency acquisition and tracking. The objectives—to establish telecommunications subsystem design compatibility for radio frequency and radio metric data—were met.

2. Phase II: DSN/Viking proof test Orbiter tests. These tests were conducted from June 26 through July 24, 1974. The Orbiter was located in the Space Simulator at JPL. S-band and X-band links were utilized between the Orbiter and CTA 21. The Orbiter was configured to represent a flight spacecraft telecommunication system; CTA 21 was configured to simulate a DSN 64-m-diameter antenna station. The Block IV Receiver-Exciter Subsystem was represented by an engineering model prototype. The tests were performed at nominal and threshold conditions to (1) establish compatibility for telemetry, command, tracking and radio metric data, (2) provide baseline criteria for analysis of the multiple carrier interference effects in the multiple spacecraft radio frequency compatibility tests, and (3) provide prerequisite data bases for performing data compatibility tests. The results of the tests are documented in Ref. 1.

3. Phase III: Viking Orbiter flight model. There were two sets of tests in this phase. Both Orbiters were configured for mission operations, and MIL 71 was configured to simulate a 64-m-diameter antenna station. S-band and X-band links were utilized between the flight articles and the ground station. Tables 3 and 4 provide a listing of the tests performed, and continued compatibility between the Network and the two radio frequency subsystems was verified.

C. DSN/Viking Spacecraft Compatibility Testing

1. Multiple spacecraft testing. These tests were conducted at CTA 21 with the test Lander and the proof test Orbiter located in the Spacecraft Assembly Facility at JPL. A test transmitter to simulate the second Orbiter with an S-band downlink capability only was installed in the screen room of CTA 21. S-band and X-band links were established between the Orbiter and CTA 21. Interface with the test Lander was established via an S-band link between CTA 21 and the Spacecraft Assembly Facility. To support these tests, CTA 21 provided two simultaneous S-band uplink signals and received and processed telemetry data from three simultaneous downlinks.

In general, the tests performed were false uplink acquisition with ranging, false command acquisition with ranging, radio metric degradation with ranging, Viking Lander telemetry degradation by the Viking Orbiter high-rate telemetry, and command and telemetry degradation with ranging. The objectives of the tests were to (1) verify the performance and operational capability of the DSN in a multiple downlink carrier environment, (2) ascertain the performance of the VO and VL under predicted RF interference conditions, and (3) provide baseline criteria as a prerequisite to conducting the multiple spacecraft data compatibility tests. The test descriptions and results are documented in Ref. 1. In general, however, the results established telecommunications system design compatibility between the Viking multiple spacecraft and the DSN.

2. Viking spacecraft testing (flight configuration). These tests were conducted at MIL 71 with the two Viking spacecraft located in the Spacecraft Assembly and Encapsulation Facilities 1 and 2. An S-band link of approximately three miles was utilized between the flight articles and the ground station.

The ground station software utilized in performing these tests was supplied by the DSN and was a subset of software officially released to the station for Viking Project support. The software consisted of the Telemetry and Command Data which provides independent control of the command and telemetry functions. Commands may be controlled manually from the station or automatically from the Mission Control and Computing Center (MCCC). Telemetry may be decoded, formatted, and transmitted to the MCCC for decommutation and display.

In general, the tests performed consisted of a series of command performance tests to verify in the spacecraft

configuration the capability of the Lander to receive commands and reject Orbiter commands, and verify in the spacecraft configuration the capability of the VL to receive commands and reject VO commands.

During the initial attempt to transmit commands to Orbiter 1 on Side 1, it was noted that the Lander command detector 1 toggled in and out of lock. The test conditions under which this anomaly occurred were uplink signal level (total power) set at -99.85 dBm, Orbiter subcarrier frequency of 512.0 Hz, and bit sync acquisition sequence (Idle 2).

Upon detection of this discrepancy, on-line troubleshooting was initiated in real-time. The Command Modulator Assembly (CMA) was returned to Idle 1 (subcarrier only) and the lock status of Lander command detector 1 monitored. Under this condition, a stable out-of-lock condition was detected. The CMA was reconfigured to offset the Orbiter subcarrier to a frequency of 512.1 Hz. Monitoring of the lock status of the Lander command detector 1 while Idle 1 and Idle 2 were transmitted showed that the detector toggled in and out of lock only with Idle 2 present. Photographs of the signal on the interface wires were taken during this on-line investigation with negative results. With these data for off-line investigation and analysis, it was decided to continue with the test in accordance with the procedure and to document test discrepancies in the Martin Marietta Failure Reporting System.

During the test, Lander 1 command detector 1 lock status at no time indicated an in-lock condition when the command waveform to the Orbiter was Subcarrier \oplus Bit Sync \oplus Data. Further, the false in-lock condition of Lander 1 command detector 1 with Idle 2 present occurred at strong uplink signal, as evidenced by the test results at -143 dBm.

The anomalous in-lock conditions identified above were not noted on command detector 2 during the accomplishment of the test. The command detector problem was resolved and documented. The resolution was that the Lander command has four levels of protection and this problem posed no threat to command operations during flight operations.

During the initial attempt to transmit commands to Viking spacecraft no. 2, commands were rejected. It was determined that the cause of this problem was an incorrect spacecraft identifier in the command bit structure. A new set of commands was then transmitted which con-

tained the proper spacecraft identifier. All commands were successfully accepted and executed by the spacecraft. However, two commands (DC-2A, Ranging Channel ON and DC-2AR, Ranging Channel OFF) gave indications of each command containing one bit error, which was corrected by the on-board computer. The octal structures for these two commands were

DC-2A 652050264210257261604

DC-2AR 652050264220257275604

Subsequently, it was learned that these octals were in error and should have been

DC-2A 652050264210257261605

DC-2AR 652050264220257275605

In order for the Command Modulator Assembly (CMA) to function correctly, the command word must contain 63 bits, although only 62 bits are transmitted. Additionally, the 63rd bit of the command structure must always be high. This bit serves as a marker bit to flag the command software that the previous bit (62nd bit of the spacecraft command) is the final bit to be transmitted. To verify that this was a true condition, the proper octals for DC-2A and DC-2AR were successfully transmitted to the spacecraft, accepted and executed and gave no indication of bit errors or corrections.

Detailed results of testing with Viking Spacecraft 1 and 2 are contained in Tables 5 and 6, respectively. Table 7 defines terminology; Table 8 presents RF channels and center frequencies for special RF interference tests.

V. Conclusion

The successful completion of the DSN/Viking Project Telecommunications Compatibility Test Program on schedule and within anticipated cost figures enabled the establishment of telecommunications compatibility as evidenced by the successful launch of the Viking '75 spacecraft on August 21 and September 9, 1975.

The importance of a formal compatibility test program was clearly demonstrated by the problem areas uncovered, verified, and resolved during the testing. Prominent problem areas resolved during the test program were:

- (1) Verification of DSN capability to receive simultaneous multiple downlinks, process and transmit data to the Mission Control and Computing Center.

- (2) Verification of false uplink acquisition by the Viking Orbiter and Lander with S-band rf channels 13 and 20 modulated with command and ranging.
- (3) Ranging modulation polarity inversion by the Block IV exciter.
- (4) Inverted pulse polarity of the Frequency and Timing Subsystem 1 k pulse per second to the Telemetry and Command Processor, which resulted in command symbol period alarm/aborts.
- (5) The Orbiter 1 radio frequency subsystem 202 auxiliary oscillator no. 2 was found to be 800 HZ below design center frequency.
- (6) A transitory increase in spacecraft receiver automatic gain control when discrete ranging modulation is turned on and during a ranging acquisition sequence.
- (7) Viking Orbiter 2 automatic gain control remaining positive during a sweep acquisition until the uplink frequency ramp function is terminated.

These and other problems, undetected and unresolved prior to launch, would have presented serious operational problems to the DSN and Viking Project during the mission.

References

1. Bryan, A. I., "Summary Report On The Deep Space Network/Viking Flight Project Telecommunications Compatibility," in *The Deep Space Network Progress Report 42-24*, pp. 9-34, Jet Propulsion Laboratory, Pasadena, Calif., Dec. 15, 1974.

Test date, 1975	Test title	Test	Deep Space Network								Mode	RM
			BLK IV RCV, dBm	BLK IV EXC, dBm	PRA RNG	CMD	Uplink doppler	Uplink offset	CMA SUBC offset	SDA SUBC offset		
2/3	DL threshold one-way	1A	-145.0	N/A	N/A	N/A	N/A	N/A	N/A	N/A	5B	
2/5		1B	-145.0	N/A	N/A	N/A	N/A	N/A	N/A	N/A	6B	
1/30	UL threshold	2A	-100.0	-140.2	N/A	On	None	None	N/A	N/A	3B	
1/30		2B	-100.0	-140.5	Off	Off	None	None	N/A	N/A	3B	
			-100.0	-140.7	Off	On	None	None	N/A	N/A	3B	
			-100.0	-141.0	On	Off	None	None	N/A	N/A	3B	
			-100.0	-141.5	On	On	None	None	N/A	N/A	3B	
1/30	DL threshold two-way	3A	-145.0	-142.5	On	On	None	None	N/A	N/A	3B	
2/5		3B	-145.0	-120.0	Off	On	None	None	N/A	N/A	6B	
2/4	DL threshold two-way	3C	-145.0	-120.0	On	Off	None	None	N/A	N/A	5AR	
1/30	SC RCV pull-in range and rate RCVR ACQ/ TRK rate	4A	-100.0	-120.0	Off	Off	N/A	-480 Hz	N/A	N/A	3B	
			-100.0	-120.5	Off	Off	N/A	+480 Hz	N/A	N/A	3B	
			-100.0	-142.7	Off	Off	45 Hz/s	+63 kHz	N/A	N/A	3B	
			-100.0	-142.0	Off	Off	45 Hz/s	-63 kHz	N/A	N/A	3B	
			-100.0	-143.2	Off	Off	45 Hz/s	+63 kHz	N/A	N/A	3B	
1/30	SC RCVR pull in range and rate RCVR ACQ/ TRK rate	4A	-100.0	-142.0	Off	Off	45 Hz/s	-63 kHz	N/A	N/A	3B	
		4B	-100.0	-120.9	Off	Off	N/A	-480 Hz	N/A	N/A	5B	
			-100.0	-119.9	Off	Off	N/A	+480 Hz	N/A	N/A	5B	
			-100.0	-141.7	Off	Off	45 Hz/s	+63 kHz	N/A	N/A	5B	
			-100.0	-141.6	Off	Off	45 Hz/s	-63 kHz	N/A	N/A	5B	
			-100.0	-142.0	Off	Off	45 Hz/s	+63 kHz	N/A	N/A	5B	
			-100.0	-141.3	Off	Off	45 Hz/s	-63 kHz	N/A	N/A	5B	
1/30	Carrier residual phase jitter	5A	-100.0	N/A	N/A	N/A	N/A	N/A	N/A	N/A	3B	
			-100.0	-100.0	N/A	N/A	N/A	N/A	N/A	N/A	3B	
2/5		5B	-100.0	N/A	N/A	N/A	N/A	N/A	N/A	N/A	6B	
			-100.0	-100.8	N/A	N/A	N/A	N/A	N/A	N/A	6B	

Table 1. Deep Space Network/Viking Lander Capsule 1 Telecommunications Compatibility Test

Spacecraft								Test data		Test time	Comments
EXC	RCV	PWR	ANT	TWT	RNG	TMU	CDU	Performance	Criteria		
1	2	High		1	Off	A	2	-157.2 dBm	-159.0 ±3 dBm	20 min	DSN RCV signal levels are starting P _c levels.
2	2	High		2	Off	A	2	-157.8 dBm	-159.0 ±3 dBm	21 min	
1	1	High		1	Off	A	1	-149.1 dBm	-150.3 ±2.5 dBm	2 h 32 min	DSN RCV signal levels are starting P _c levels.
1	1	High		1	Off	A	1	-149.2 dBm	-149.2 ±2.5 dBm	2 h 44 min	
1	1	High		1	Off	A	1	-149.0 dBm	-149.2 ±2.5 dBm		
1	1	High		1	Off	A	1	-150.2 dBm	-149.2 ±2.5 dBm		
1	1	High		1	Off	A	1	-151.0 dBm	-149.2 ±2.5 dBm		
1	1	High		1	Off	A	1	-157.2 dBm	-159.0 ±3 dBm	38 min	DSN RCV signal levels are starting P _c levels.
2	2	High		2	Off	A	2	-157.0 dBm	-159.0 ±3 dBm	28 min	
1	2	High		1	On	A	2	-157.3 dBm	-159.0 ±3 dBm	33 min	DSN RCV signal levels are starting P _c levels.
1	1	High		1	Off	A	1	2 sec	SC RCV must lock to UL	5 hr 54 min	
1	1	High		1	Off	A	1	2 sec			
1	1	High		1	Off	A	1	+63.0 kHz	+63.0 kHz		
1	1	High		1	Off	A	1	-63.0 kHz	-63.0 kHz		
1	1	High		1	Off	A	1	ACQ/TRK to +63.0 kHz	ACQ/TRK to +63 kHz		
1	1	High		1	Off	A	1	ACQ/TRK to -61.33 kHz	ACQ/TRK to -63.0 kHz		UL 1 dB weaker than other side. No software problems.
1	2	High		1	Off	A	2	5 s	SC RCV must lock to UL	5 h 01 min	No problems noted.
1	2	High		1	Off	A	2	2 s			
1	2	High		1	Off	A	2	+63.0 kHz	+63.0 kHz		
1	2	High		1	Off	A	2	-63.0 kHz	-63.0 kHz		
1	2	High		1	Off	A	2	ACQ/TRK to +63.0 kHz	ACQ/TRK to +63.0 kHz		
1	2	High		1	Off	A	2	ACQ/TRK to -63.0 kHz	ACQ/TRK to -63.0 kHz		
1	1	High		1	Off	A	1	1.65 deg rms	5.0 deg rms	1 h 27 min	No problems noted.
1	1	High		1	Off	A	1	1.43 deg rms	5.0 deg rms		
2	2	High		2	Off	A	2	4.17 deg rms	5.0 deg rms	1 h 35 min	No problems noted.
2	2	High		2	Off	A	2	1.08 deg rms	5.0 deg rms		

Test date, 1975	Test title	Test	Deep Space Network									Mode	RM
			BLK IV RCV, dBm	BLK IV EXC, dBm	PRA RNG	CMD	Uplink doppler	Uplink offset	CMA SUBC offset	SDA SUBC offset			
1/31	DL spectrum analysis	6A	−85.0	N/A	Off	Off	N/A	N/A	N/A	N/A	3B		
			−85.0	−140.0	Off	Off	N/A	N/A	N/A	N/A	3B		
2/4	DL spectrum analysis	6B	−85.0	N/A	Off	On	N/A	N/A	N/A	N/A	6B		
			−85.0	−120.5	Off	Off	N/A	N/A	N/A	N/A	6B		
			−85.0	−123.0	Off	On	N/A	N/A	N/A	N/A	6B		
2/4	DL spectrum analysis	6C	−85.5	−111.2	On	Off	N/A	N/A	N/A	N/A	5AR		
1/31	Transponder rest frequency	7A	−100.0	−100.0	Off	Off	N/A	N/A	N/A	N/A	3B		
			−100.0	−100.0	Off	Off	N/A	N/A	N/A	N/A	3B		
2/5		7B	−100.0	−120.5	Off	Off	N/A	N/A	N/A	N/A	6B		
			−100.0	−120.5	Off	Off	N/A	N/A	N/A	N/A	6B		
1/4	Auxiliary oscillator frequency	8A	−100.0	N/A	Off	Off	N/A	N/A	N/A	N/A	5B		
2/5		8B	−100.0	N/A	Off	Off	N/A	N/A	N/A	N/A	6B		
1/31	Command capability under doppler conditions	9A	−100.0	−142.5 2.6 db car. sup.	N/A	On	None	+20 kHz	None	N/A	3B		
			−100.0	−142.3 2.3 db car. sup.	N/A	On	None	−20 kHz	None	N/A	3B		
			−100.0	−143.0 2.8 db car. sup.	N/A	On	None	None	384.1 Hz	N/A	3B		
			−100.0	−142.9 2.5 db car. sup.	N/A	On	None	None	383.9 Hz	N/A	3B		
1/4	Command capability under doppler conditions	9B	−100.0	−119.9 2.0 db car. sup.	N/A	On	None	+20 kHz	None	N/A	5B		
			−100.0	−119.9 2.0 db car. sup.	N/A	On	None	−20 kHz	None	N/A	5B		

Table 1 (contd)

Spacecraft								Test data		Test time	Comments
EXC	RCV	PWR	ANT	TWT	RNG	TMU	CDU	Performance	Criteria		
1	1	High		1	Off	A	1	TBD	No spurious components	49 min	Photos taken; no spurs seen. DFT will be performed later.
1	1	High		1	Off	A	1	TBD			
2	2	High		2	Off	A	2	TBD	No spurious components	27 min	Photos taken; no spurs seen. DFT to be performed later.
2	2	High		2	Off	A	2	TBD			
2	2	High		2	Off	A	2	TBD			
1	2	High		1	On	A	2	TBD	No spurious components	17 min	Photos taken; no spurs seen. DFT to be performed later.
1	1	High		1	Off	A	1	VCO freq = 2112.969891 MHz	2112971.451 ± 30 kHz	36 min	SC VCO temp = 30.33° C at start,
1	1	High		1	Off	A	1	SC locked to UL	SC locked to UL		31.18° C at end.
2	2	High		2	Off	A	2	VCO freq = 2112.970760 MHz	2112971.451 ± 30 kHz	39 min	SC VCO temp = 28.94° C at start,
2	2	High		2	Off	A	2	SC locked to UL	SC locked to UL		28.94° C at end.
1	2	High		1	Off	A	2	D/L freq = 2294.634509	2294629.630 ± 30 kHz	50 min	AUX. OSC. temp = 20.21° C at start, 22.26° C at end.
2	2	High		2	Off	A	2	D/L freq = 2294.605568	2294629.630 ± 30 kHz	44 min	AUX. OSC. temp = 28.94° C at start, 28.55° C at end.
1	1	High		1	Off	A	1	All commands successfully detected and executed by SC; 3 aborts with command subcarrier offset ± 0.1 Hz. All CMDS transmitted were successfully detected and executed by SC.	3 segments of 32-word command messages successfully detected and executed by SC for each test condition.	5 h	Uplink varied -141.4 to -142.5 dBm by SC AGC readouts. Internal station check indicated command modulation was stable. 3 command aborts, symbol period 1250 ms instead of 250 ms (see Note 1).
1	1	High		1	Off	A	1				
1	1	High		1	Off	A	1				
1	1	High		1	Off	A	1				
1	2	High		1	Off	A	2	All commands successfully detected and executed by SC.	3 segments of 32 word command messages successfully detected and executed by SC for each test condition.	1 h 17 min	CMA offsets (± 0.1 Hz) not performed because of equipment problems.
1	2	High		1	Off	A	2				

Test date, 1975	Test title	Test	Deep Space Network								Mode	RM
			BLK IV RCV, dBm	BLK IV EXC, dBm	PRA RNG	CMD	Uplink doppler	Uplink offset	CMA SUBC offset	SDA SUBC offset		
2/5	Ranging channel delay threshold and polarity verification	10A	-100.0	-100.8	On	Off	None	None	N/A	N/A	5AR	
			-134.5	-119.9	On	Off	None	None	N/A	N/A	5AR	
2/5	Ranging channel delay threshold and polarity verification	10B	-100.0	-100.8	On	Off	None	None	N/A	N/A	6AR	
			-135.0	-119.9	On	Off	None	None	N/A	N/A	6AR	
1/31	Telemetry performance test	12A	YF = 12.59 -136.0	-140.2	Off	Off	N/A	N/A	N/A	-2.125 Hz -0.350 Hz	3B	
			YF = 12.59 -136.0	-139.6	Off	Off	N/A	+20 kHz	N/A	-2.125 Hz -0.350 Hz	3B	
			YF = 12.59 -136.0	-139.6	Off	Off	N/A	-20 kHz	N/A	-2.125 Hz -0.350 Hz	3B	
2/4	Telemetry performance test	12B	YF = 12.59 -136.0	-120.5	Off	On	N/A	N/A	N/A	-2.125 Hz -0.350 Hz	6B	
			YF = 12.59 -136.0	-120.5	Off	On	N/A	+20 kHz	N/A	-2.125 Hz -0.350 Hz	6B	
			YF = 12.59 -136.0	-121.2	Off	On	N/A	-20 kHz	N/A	-2.125 Hz -0.350 Hz	6B	
2/4		12C	YF = 12.62 -135.5	-120.5	On	Off	N/A	N/A	N/A	-0.35 Hz	5AR	
			YF = 12.62 -135.5	-120.5	On	Off	N/A	+20 kHz	N/A	-0.35 Hz	5AR	
			YF = 12.62 -135.5	-120.5	On	Off	N/A	-20 kHz	N/A	-0.35 Hz	5AR	
2/1	Subcarrier residual phase jitter	13A	-100.0	-101.0	Off	Off	N/A	N/A	N/A	N/A	3B	
			-100.0	-142.2	Off	Off	N/A	N/A	N/A	N/A	3B	
2/5		13B	-100.0	-100.8	Off	Off	N/A	N/A	N/A	N/A	6B	
			-100.0		Off	Off	N/A	N/A	N/A	N/A	6B	

Notes:

1. Corrective action of reversing polarity of 1 K pps in the frequency and time subsystem resolved the command abort problem. Retest of the system at offsets of ± 0.1 Hz and ± 0.2 Hz was successful.

2. Test 10A data not reliable because of ranging inversion problem. Not retested because of time constraint.

REPRODUCIBILITY OF THE
ORIGINAL PAGE IS POOR

Table 1 (contd)

Spacecraft								Test data		Test time	Comments
EXC	RCV	PWR	ANT	TWT	RNG	TMU	CDU	Performance	Criteria		
1	2	High		1	On	A	2	Inconclusive	Range delay	95 min	Discrete spectrum with 15 components, clock acq. time 30, code acq. time 5, DRVID avg. time 30. 2 bad acquisitions (see Note 2).
1	2	High		1	On	A	2		710 ± 75 ns		
2	2	High		2	On	A	2	675.2 ns	Range delay	66 min	Discrete spectrum with 15 components, clock acq. time 30, code acq. time 5, DRVID avg. time 30. 4 bad acquisitions (see Note 3).
2	2	High		2	On	A	2		710 ± 75 ns		
1	1	High		1	Off	A	1	8.05 dB HR 15.83 dB LR	7.9 ± 1.5 dB 14.7 ± 1.5 dB	3 h 49 min	40-s lockup time.
1	1	High		1	Off	A	1	8.05 dB HR 14.95 dB LR	7.9 ± 1.5 dB 14.7 ± 1.5 dB		40-s lockup time.
1	1	High		1	Off	A	1	7.88 dB HR 14.78 dB LR	7.9 ± 1.5 dB 14.7 ± 1.5 dB		40-s lockup time.
2	2	High		2	Off	A	2	7.73 dB HR 15.71 dB LR	7.9 ± 1.5 dB 14.7 ± 1.5 dB	1 h 50 min	40-s lockup time.
2	2	High		2	Off	A	2	8.09 dB HR 15.68 dB LR	7.9 ± 1.5 dB 14.7 ± 1.5 dB		40-s lockup time.
2	2	High		2	Off	A	2	7.54 dB HR 15.65 dB LR	7.9 ± 1.5 dB 14.7 ± 1.5 dB		40-s lockup time.
1	2	High		1	On	A	2	21.01 dB	20.8 ± 1.5 dB	2 h 2 min	40-s lockup time.
1	2	High		1	On	A	2	21.37 dB	20.8 ± 1.5 dB		40-s lockup time.
1	2	High		1	On	A	2	21.07 dB	20.8 ± 1.5 dB		40-s lockup time.
1	1	High		1	Off	A		0.38 deg rms	5.8 deg rms	1 h 11 min	
1	1	High		1	Off	A		0.275 deg rms	5.8 deg rms		
2	2	High		2	Off	A		0.45 deg rms	5.8 deg rms	45 min	
2	2	High		2	Off	A		0.46 deg rms	5.8 deg rms		

3. Original test 10B data not reliable because of ranging code inversion problem. Retest and post-test calibration provided correct data. The block IV exciter inverts the ranging code.

Test date, 1975	Test title	Test	Deep Space Network								Mode	RM
			BLK IV RCV	BLK IV EXC	PRA RNG	CMD	Uplink doppler	Uplink offset	CMA SUBC offset	SDA SUBC offset		
4/8	DL threshold one-way	1A	2294.633680 MHz, RCVR 4	N/A	Off	Off	None	None	None	None	5B	
		1B	2294.649800 MHz, RCVR 4	N/A	Off	Off	None	None	None	None	6B	
4/7	UL threshold	2A	2294.621040 MHz, -100.0 dBm, RCVR 4	2112.963541 MHz, EXC 2	N/A	Off	None	None	N/A	N/A	3B	
					N/A	On	None	None	N/A	N/A	3B	
4/8		2B	2294.630020 MHz, RCVR 4	2112.971810 MHz, EXC 2	Off	Off	None	None	N/A	N/A	5B	
					Off	On	None	None	N/A	N/A	5B	
					On	Off	None	None	N/A	N/A	5B	
					On	On	None	None	None	N/A	5B	
4/7	DL threshold two-way	3A	2294.621040 MHz, RCVR 4	2112.963541 MHz, EXC 2	Off	On	None	None	N/A	N/A	3B	
4/9	DL threshold two-way	3B	2294.628880 MHz, RCVR 4	2112.970704 MHz, EXC 2	Off	On	None	None	N/A	N/A	6B	
4/8		3C	2294.630740 MHz, RCVR 3	2112.972384 MHz, EXC 2	On	Off	None	None	N/A	N/A	5AR	
4/7	SC RCVR pull in range and rate and false lock	4A	-100.0 dBm, RCVR 4	2113.027536 MHz at Offset, EXC 2	Off	Off	250 Hz/s	+63 kHz	N/A	N/A	3B	
				2112.906336 MHz at Offset, EXC 2	Off	Off	250 Hz/s	-63 kHz	N/A	N/A	3B	
		4B	-100.0 dBm, RCVR 4	2113.034736 MHz at Offset, EXC 2	Off	Off	250 Hz/s	+63 kHz	N/A	N/A	5B	
				2112.908736 MHz at Offset, EXC 2	Off	Off	250 Hz/s	-63 kHz	N/A	N/A	5B	
4/8	Carrier residual phase jitter	5A	2294.620660 MHz, -100.0 dBm, RCVR 3 and 4	N/A	Off	Off	None	None	None	None	3B	
4/8	Carrier residual phase jitter		2294.616700 MHz, -100.0 dBm, RCVR 3 and 4	2112.959545 MHz, EXC 2	Off	Off	None	None	None	None	3B	

Table 2. Deep Space Network/Viking Lander Capsule 2 telecommunications compatibility tests

Spacecraft								Test data		Test time	Test Comments
EXC	RCV	PWR	ANT	TWT	RNG	TMU	CDU	Performance	Criteria		
1	2	High	HGA	1	Off	A	2	-157.0 dBm	-159.0 ± 3 dBm	51 min	Avg. of three thresholds.
2	2	High	HGA	2	Off	A	2	-158.7 dBm	-159.0 ± 3 dBm	31 min	Avg. of three thresholds.
1	1	High	LGA	1	Off	A	1	-150.8 dBm	-150.3 ± 2.5 dBm	50 min	Avg. of three thresholds, VCO temp = 26.75°C.
1	1	High	LGA	1	Off	A	1	-150.5 dBm	-150.3 ± 2.5 dBm		Avg. of three thresholds, VCO temp = 27.62°C.
1	2	High	HGA	1	Off	A	2	-150.2 dBm	-149.2 ± 2.5 dBm	1 h 59 min	Avg. of three thresholds, VCO temp = 29.33°C.
1	2	High	HGA	1	Off	A	2	-150.2 dBm	-149.2 ± 2.5 dBm		Avg. of three thresholds, VCO temp = 29.66°C.
1	2	High	HGA	1	Off	A	2	-151.2 dBm	-149.2 ± 2.5 dBm		Avg. of three thresholds, VCO temp = 29.66°C.
1	2	High	HGA	1	Off	A	2	-152.0 dBm	-149.2 ± 2.5 dBm		Avg. of three thresholds, VCO temp = 30.00°C.
1, -147.7 dBm	1	High	LGA	1	Off	A	1	-157.8 dBm	-159.0 ± 3.0 dBm	24 min	Avg. of three thresholds.
2, -119.4 dBm	2	High	HGA	2	Off	A	2	-156.8 dBm	-159.0 ± 3.0 dBm	39 min	Avg. of three thresholds.
1, -120.9 dBm	2	High	HGA	1	Off	A	1	-158.7 dBm	-159.0 ± 3.0 dBm	32 min	Avg. of three thresholds.
1, -120.6 dBm	1	High	LGA	1	Off	A	1	Acquired U/L at 2112.963552 MHz and 5 MHz biased doppler	Acquire/biased doppler = 5 MHz	28 min	DL at acquisition 2294.621100 MHz.
1, -120.6 dBm	1	High	LGA	1	Off	A	1	Acquired U/L at 2112.963120 MHz and 5 MHz biased doppler	Acquire/biased doppler = 5 MHz		DL at acquisition 2294.620660 MHz.
2, -119.4 dBm	2	High	LGA	1	Off	A	2	Acquired U/L at 2112.971904 MHz and 5 MHz biased doppler	Acquire/biased doppler = 5 MHz	40 min	DL at acquisition 2294.630200 MHz.
2, -119.4 dBm	2	High	LGA	1	Off	A	2	Acquired U/L at 2112.971664 MHz and 5 MHz biased doppler	Acquire/biased doppler = 5 MHz		DL at acquisition 2294.630440 MHz.
1	1	High	HGA	1	Off	A	1	1.73 deg rms	5.0 deg rms	59 min	Test performed in one-way.
1, -100.1 dBm	1	High	HGA	1	Off	A	1	0.65 deg rms	5.0 deg rms		Test performed in two-way.

Test date, 1975	Test title	Test	Deep Space Network								Mode	RM
			BLK IV RCV	BLK IV EXC	PRA RNG	CMD	Uplink doppler	Uplink offset	CMA SUBC offset	SDA SUBC offset		
4/9		5B	2294.648180 MHz, - 100.0 dBm, RCVR 3 and 4	N/A	Off	Off	None	None	None	None	6B	
			2294.623740 MHz, - 100.0 dBm, RCVR 3 and 4	2112.966000 MHz, EXC 2	Off	Off	None	None	None	None	6B	
4/8	DL spectrum analysis	6A	2294.630180 MHz, - 85.0 dBm, RCVR 3	N/A	Off	Off	None	None	None	None	3B	
			2294.616460 MHz, - 85.0 dBm, RCVR 3	2112.959232 MHz, EXC 2	Off	Off	None	None	None	None	3B	
			2294.616460 MHz, - 85.0 dBm, RCVR 3	2112.959232 MHz, EXC 2	Off	On	None	None	None	None	3B	
4/9		6B	2294.643680 MHz, - 85.0 dBm, RCVR 4	N/A	Off	Off	None	None	None	None	6B	
			2294.624240 MHz, - 85.0 dBm, RCVR 4	2112.966480 MHz, EXC 2	Off	Off	None	None	None	None	6B	
			2294.624240 MHz, - 85.0 dBm, RCVR 4	2112.966480 MHz, EXC 2	Off	On	None	None	None	None	6B	
4/8		6C	2294.630740 MHz, - 85.0 dBm, RCVR 3	2112.972384 MHz, EXC 2	On	Off	None	None	None	None	5AR	
4/8	Transponder rest frequency	7A	2294.616460 MHz, - 100.0 dBm, BLK III, RCVR 1	N/A	Off	Off	N/A	N/A	N/A	N/A	3B	
			2294.615264 MHz, RCVR 4	2112.958222 MHz, EXC 2	Off	Off	N/A	N/A	N/A	N/A	3B	
4/9		7B	2294.624480 MHz, - 100.0 dBm, BLK III, RCVR 1	N/A	Off	Off	N/A	N/A	N/A	N/A	6B	
			2294.625824 MHz, - 100.0 dBm, RCVR 4	2112.967968 MHz, EXC 2	Off	Off	N/A	N/A	N/A	N/A	6B	

REPRODUCIBILITY OF THE
ORIGINAL PAGE IS POOR

Table 2 (contd)

Spacecraft								Test data		Test time	Test Comments
EXC	RCV	PWR	ANT	TWT	RNG	TMU	CDU	Performance	Criteria		
2	2	High	HGA	2	Off	A	2	1.99 deg rms	5.0 deg rms	48 min	Test performed in one-way.
2	2	High	HGA	2	Off	A	2	1.09 deg rms	5.0 deg rms		Test performed in one-way.
1	1	High	HGA	1	Off	A	1	No spurious components	No spurious components	32 min	Photos taken, no spurs seen; DFT performed off-line.
1	1, -140.8 dBm	High	HGA	1	Off	A	1	No spurious components	No spurious components		Photos taken, no spurs seen; DFT performed off-line.
1	1, -143.3 dBm	High	HGA	1	Off	A	1	No spurious components	No spurious components		Photos taken, no spurs seen; DFT performed off-line.
2	2	High	HGA	2	Off	A	2	No spurious components	No spurious components	54 min	Photos taken, no spurs seen; DFT performed off-line.
2	2, -121.6 dBm	High	HGA	2	Off	A	2	No spurious components	No spurious components		Photos taken, no spurs seen; DFT performed off-line.
2	2, -123.8 dBm	High	HGA	2	Off	A	2	No spurious components	No spurious components		Photos taken, no spurs seen; DFT performed off-line.
1	2, -120.9 dBm	High	HGA	1	On	A	2	No spurious components	No spurious components	14 min	Photos taken, no spurs seen; DFT performed off-line.
1	1	High	HGA	1	Off	A	1	VCO freq = 2112.958222 MHz	2112971.451 ± 30 kHz	35 min	SC VCO temp = 30.25°C at start, 30.54°C at end, 15 min run.
1	1, -120.0 dBm	High	HGA	1	Off	A	1	SC locked to UL	SC locked to UL		SC locked in 1 s.
2	2	High	HGA	2	Off	A	2	VCO freq = 2112.967968 MHz	2112971.451 ± 30 kHz	32 min	SC VCO temp = +32.33°C at start, 15 min run.
2	2, -119.4 dBm	High	HGA	2	Off	A	2	SC locked to UL	SC locked to UL		SC locked in 1 s.

Test date, 1975	Test title	Test	Deep Space Network								Mode	RM
			BLK IV RCV	BLK IV EXC	PRA RNG	CMD	Uplink doppler	Uplink offset	CMA SUBC offset	SDA SUBC offset		
4/8	Auxiliary oscillator frequency	8A	-100.0 dBm, BLK III, RCVR 1	N/A	Off	Off	N/A	N/A	N/A	N/A	5B	
4/9		8B	-100.0 dBm, BLK III, RCVR 1	N/A	Off	Off	N/A	N/A	N/A	N/A	6B	
4/8	Command capability	9A	2294.642474 MHz, -99.5 dBm, RCVR 4	2112.983232 MHz, EXC 2	Off	On	None	+20 kHz	None	None	3B	
			2294.599002 MHz, -99.5 dBm, RCVR 4	2112.943248 MHz, EXC 2	Off	On	None	-20 kHz	None	None	3B	
4/8		9B	2294.652380 MHz, -100.0 dBm, RCVR 4	2112.992400 MHz, EXC 2	Off	On	None	+20 kHz	None	None	5B	
			2294.608906 MHz, -100.0 dBm, RCVR 4	2112.952368 MHz, EXC 2	Off	On	None	-20 kHz	None	None	5B	
4/8	Ranging channel delay, threshold and polarity verification	10A	2294.630740 MHz, -100.0 dBm, RCVR 4	2112.972384 MHz, EXC 2	On	Off	None	None	N/A	N/A	5AR	
4/8			2294.630740 MHz, -135.0 dBm, RCVR 4	2112.972384 MHz, EXC 2	On	Off	None	None	N/A	N/A	5AR	
4/9		10B	2294.631040 MHz, -100.0 dBm, RCVR 4	2112.972672 MHz, EXC 2	On	Off	None	None	N/A	N/A	6AR	
			2294.631040 MHz, -135.0 dBm, RCVR 4	2112.972672 MHz, EXC 2	On	Off	None	None	N/A	N/A	6AR	
4/8	Telemetry performance test	12A	2294.620800 MHz, STb/ No 9.0 dB, -135.0 dBm, RCVR 4	2112.963320 MHz, EXC 2	Off	On	None	None	None	-2.125 Hz -0.35 Hz	3B	
			2294.642424 MHz, STb/ No 9.0 dB, -135.0 dBm, RCVR 4	2112.983232 MHz, EXC 2	Off	On	None	+20 kHz	None	-2.125 Hz -0.35 Hz	3B	
			2294.599002 MHz, STb/ No 9.0 dB, -135.0 dBm, RCVR 4	2112.943248 MHz, EXC 2	Off	On	None	-20 kHz	None	-2.125 Hz -0.35 Hz	3B	

Table 2 (contd)

Spacecraft								Test data		Test time	Test Comments
EXC	RCV	PWR	ANT	TWT	RNG	TMU	CDU	Performance	Criteria		
1	2	High	HGA	1	Off	A	2	Aux. osc. freq = 2294.630672 MHz	2294629.630 ± 30 kHz	46 min	Aux. osc. temp = 30.33°C at start, 30.66°C at end, 30-min run.
2	2	High	HGA	1	Off	A	2	Aux. osc. freq = 2294.647424 MHz	2294629.630 ± 30 kHz	38 min	Aux. osc. temp = 32.33°C at start, 30-min run.
1	1, -142.1 dBm	High	LGA	1	Off	A	1	All commands successfully detected and executed by SC with no errors	3 segments of 32- word command messages suc- cessfully detected and executed by SC for each test condition	1 h 38 min	Center frequencies, UL 2112.963320 DL 2294.620800
1	1, -142.7 dBm	High	LGA	1	Off	A	1				
1	1, -119.4 dBm	High	HGA	1	Off	A	2	All commands successfully detected and executed by SC with no errors	3 segments of 32- word command messages suc- cessfully detected and executed by SC for each test condition	1 h 31 min	Center frequencies, UL 2112.972384 DL 2294.630680
1	1, -120.2 dBm	High	HGA	1	Off	A	2				
1	2, -101.1 dBm	High	HGA	1	On	A	2	683.9 ns	Range delay: 710 ± 75 ns	23 min	No problems noted.
1	2, -120.9 dBm	High	HGA	1	On	A	2	670.3 ns	Range delay: 710 ± 75 ns		
2	2, -99.73 dBm	High	HGA	2	On	A	2	666.8 ns	Range delay: 710 ± 75 ns polarity	44 min	No problems noted.
2	2, -120.2 dBm	High	HGA	2	On	A	2	663.4 ns	Range delay: 710 ± 75 ns		
1	1, -140.5 dBm	High	HGA	1	Off	A	1	8.56 dB HR 15.98 dB LR	7.9 ± 1.5 dB 14.7 ± 1.5 dB	2 h 19 min	LR subcarrier = 11999.725 Hz; HR subcarrier = 71998.325 Hz.
1	1, -140.5 dBm	High	HGA	1	Off	A	1	8.3 dB HR 15.9 dB LR	7.9 ± 1.5 dB 14.7 ± 1.5 dB		
1	1, -140.1 dBm	High	HGA	1	Off	A	1	7.98 dB HR 14.77 dB LR	7.9 ± 1.5 dB 14.7 ± 1.5 dB		

Test date, 1975	Test title	Test	Deep Space Network									Mode	RM
			BLK IV RCV	BLK IV EXC	PRA RNG	CMD	Uplink doppler	Uplink offset	CMA SUBC offset	SDA SUBC offset			
4/9		12B	2294.628640 MHz, STb/ No 9.0 dB, -135.0 dBm, RCVR 4	2112.970512 MHz, EXC 2	Off	On	None	None	None	-2.125 Hz -0.35 Hz	6B		
4/9	DL threshold one-way	12B	2294.650295 MHz, STb/ No 9.0 dB, -135.0 dBm, RCVR 4	2112.990480 MHz, EXC 2	Off	On	None	+20 kHz	None	-2.125 Hz -0.35 Hz	6B		
			2294.606873 MHz, STb/ No 9.0 dB, -135.0 dBm, RCVR 4	2112.950496 MHz, EXC 2	Off	On	None	-20 kHz	None	-2.125 Hz -0.35 Hz	6B		
		12C	2294.630740 MHz, STb/ No 23.8 dB, -134.0 dBm, RCVR 4	2112.972384 MHz, EXC 2	On	Off	None	None	None	-0.35 Hz	5AR		
4/8			2294.652380 MHz, STb/ No 23.8 dB, -134.0 dBm, RCVR 4	2112.992 MHz, EXC 2	On	Off	None	+20 kHz	None	-0.35 Hz	5AR		
			2294.608906 MHz, STb/ No 23.8 dB, -134.0 dBm, RCVR 4	2112.952368 MHz, EXC 2	On	Off	None	-20 kHz	None	-0.35 Hz	5AR		
4/8	Subcarrier residual phase jitter	13A	2294.630400 MHz, -100.0 dBm, RCVR 3 and 4	N/A	Off	Off	None	None	None	None SDA 1 and 2	3B		
4/8		13A	2294.616740 MHz, -100.0 dBm, RCVR 3 and 4	2112.959520 MHz, EXC 2	Off	On	None	None	None	None SDA 1 and 2	3B		
4/9		13B	2294.647800 MHz, -100.0 dBm, RCVR 3 and 4	N/A	Off	On	None	None	None	None SDA 1 and 2	6B		
			2294.620280 MHz, -100.0 dBm, RCVR 3 and 4	2112.962784 MHz, EXC 2	Off	On	None	None	None	None SDA 1 and 2	6B		

Table 2 (contd)

Spacecraft								Test data		Test time	Test Comments
EXC	RCV	PWR	ANT	TWT	RNG	TMU	CDU	Performance	Criteria		
2	2, -120.9 dBm	High	HGA	2	Off	A	2	8.65 dB HR 15.37 dB LR	7.9 ± 1.5 dB 14.7 ± 1.5 dB	1 h 20 min	LR subcarrier = 11999.925 Hz; HR subcarrier = 71999.85 Hz.
2	2, -120.2 dBm	High	HGA	2	Off	A	2	8.51 dB HR 15.66 dB LR	7.9 ± 1.5 dB 14.7 ± 1.5 dB		
2	2, -120.2 dBm	High	HGA	2	Off	A	2	8.52 dB HR 15.59 dB LR	7.9 ± 1.5 dB 14.7 ± 1.5 dB		
1	2, -120.9 dBm	High	HGA	1	Off	A	2	21.06 dB LR	20.8 ± 1.5 dB	1 h	LR subcarrier = 12000.0 Hz.
1	2, -120.9 dBm	High	HGA	1	Off	A	2	20.7 dB LR	20.8 ± 1.5 dB		
1	2, -120.9 dBm	High	HGA	1	Off	A	2	20.95 dB LR	20.8 ± 1.5 dB		
1	1	High	HGA	1	Off	A	1	0.31 deg rms	5.8 deg rms	43 min	Test performed in one-way.
1	1, -142.7 dBm	High	HGA	1	Off	A	1	0.31 deg rms	5.8 deg rms		Test performed in two-way.
2	2	High	HGA	2	Off	A	2	0.33 deg rms	5.8 deg rms	39 min	Test performed in one-way.
2	2, -120.9 dBm	High	HGA	2	Off	A	2	0.34 deg rms	5.8 deg rms		Test performed in two-way.

Test date, 1975	Test title	Test	Deep Space Network									Mode	RM
			RCV	EXC	PRA RNG	CMD	Uplink doppler	Uplink offset	CMA SUBC offset	SDA SUBC offset			
2/27	DL threshold one-way	1A	Blk III, RCV 1	N/A	Off	Off	N/A	N/A	N/A	N/A	1	204	
2/28		1B	Blk IV, RCV 4	N/A	Off	Off	N/A	N/A	N/A	N/A	1	304	
2/27	UL threshold	2A	Blk IV, RCV 4, -114.5 dBm, 23.408637 MHz	Blk IV, 22.035054 MHz	Off	Off	N/A	N/A	N/A	N/A	1	304	
					On	On	N/A	N/A	N/A	N/A	1	304	
2/27	DL threshold two-way	3A	Blk III, RCV 1, 2297.232032 MHz	Blk III, 2115.367872 MHz	Off	Off	N/A	N/A	N/A	N/A	1A	304	
					On	On	N/A	N/A	N/A	N/A	1AR/CMD	305	
2/28	DL threshold two-way	3B	Blk IV, RCV 4, 8423.166325 MHz	Blk IV, 2115.363456 MHz	On	On	N/A	N/A	N/A	N/A	1FR	305	
2/27	SC RCVR pull-in	4A	Blk III, RCV 1, 2297.232032 MHz	Blk IV, 2115.367872 MHz	Off	Off	N/A	-700 Hz	N/A	N/A	1	304	
	SC RCVR range and rate				Off	Off	500 Hz/s	+40 kHz	N/A	N/A	1	304	
	SC RCVR pull-in				-115 dBm	Off	Off	N/A	+700 Hz	N/A	N/A	1	304
	SC RCVR range and rate				Off	Off	500 Hz/s	-40 kHz	N/A	N/A	1	304	
	SC RCVR false lock				4A		Off	Off	500 Hz/s	-10 kHz to +7 kHz	N/A	N/A	1
					Off	Off	500 Hz/s	+10 kHz to -7 kHz	N/A	N/A	1	304	

Table 3. Deep Space Network/Viking Orbiter 1 Telecommunications Compatibility Tests (Radio Frequency Subsystem 203)

Spacecraft								Test data		Test time	Test comments
EXC	RCV	PWR	ANT	TWT	RNG	TMU	CDU	Performance	Criteria		
1	1	High	High	1	Off	A	A	-156.6 dBm	-157.0 \pm 3 dBm	31 min	DL variations \pm 0.25 dB.
1	1	High	High	1	Off	A	A	-151.0 dBm	-153.0 \pm 3 dBm	1 h 8 min	SC in 2-way instead of 1-way mode.
1	1	High	High	1	Off	A	A	-152.5 dBm	-151.5 \pm 2 dBm	47 min	DL variations \pm 0.25 dB. VCO temp = 78.68° F.
1	1	High	High	1	Off	A	A	-153.0 dBm	-151.5 \pm 2 dBm		
1	1, -130.0 dBm	High	High	1	Off	A	A	-157.2 dBm	-157.0 \pm 3 dBm	37 min	\pm 3 dB DL variation.
1	1, -133.7 dBm	High	High	1	On	A	A	-157.7 dBm	-157.0 \pm 3 dBm		
1	1, -129.4 dBm	High	High	1	On	A	A	-155.3 dBm	-153 \pm 3 dBm	47 min	Test run in mode 1 FR not 1 AR, DL variations \pm 1 dB.
1	1, -120.8 dBm	High	High	1	Off	A	A	11-s acquisition time	\leq 60-s acquisition time	2 h 19 min	1st attempt unsuccessful because of ramp cable.
1	1, -120.8 dBm	High	High	1	Off	A	A	Tracked to +40 kHz, no loss of lock	Track to +40 kHz, no loss of lock		During test, DL variations increased from \pm 0.1 dB to \pm 3 dB at 162400Z.
1	1, -120.8 dBm	High	High	1	Off	A	A	31-s acquisition time	\leq 60-s acquisition time		
1	1, -120.8 dBm	High	High	1	Off	A	A	Tracked to -40 kHz, no loss of lock	Track to -40 kHz, no loss of lock		
1	1, -120.8 dBm	High	High	1	Off	A	A	Acquired and tracked to +7 kHz	Acquire near BL and track to +7 kHz		
1	1, -120.8 dBm	High	High	1	Off	A	A	Acquired and tracked to -7 kHz	Acquire near BL and track to -7 kHz		

Test date, 1975	Test title	Test	Deep Space Network									Mode	RM
			RCV	EXC	PRA RNG	CMD	Uplink doppler	Uplink offset	CMA SUBC offset	SDA SUBC offset			
2/27	SC RCVR pull-in	4B	Blk III, RCV 1, 2297.222720 MHz,	Blk III, 2115.359232 MHz	Off	Off	N/A	−700 Hz	N/A	N/A	2	376	
	SC RCVR range and rate				−121 dBm	Off	Off	500 Hz/s	+40 kHz	N/A	N/A	2	376
	SC RCVR pull-in				Off	Off	N/A	+700 Hz	N/A	N/A	2	376	
	SC RCVR range and rate				Off	Off	500 Hz/s	−40 kHz	N/A	N/A	2	376	
	SC RCVR false lock				Off	Off	500 Hz/s	−10 kHz to +7 kHz	N/A	N/A	2	376	
	SC RCVR false lock				Off	Off	500 Hz/s	+10 kHz to −7 kHz	N/A	N/A	2	376	
2/27	Carrier residual phase jitter	5	Blk IV, RCV 3 and 4, 2297.232032 MHz, −106 dBm	N/A	Off	Off	N/A	N/A	N/A	N/A	1A	204	
			Blk IV, RCV 3 and 4, −106 dBm	Blk IV, 2115.367872 MHz	Off	Off	N/A	N/A	N/A	N/A	1A	304	
2/27	Transponder rest frequency best lock and acquisition time	7A	Blk III, RCV 1, 2297.229152 MHz, −114.5 dBm	Blk III, 22.035055 MHz	Off	Off	N/A	N/A	N/A	N/A	1	204	
2/27	Transponder rest frequency best lock and acquisition time	7B	Blk III, RCV 1, 2297.222624 MHz, −120.0 dBm	Blk III, 2115.359232 MHz	Off	Off	N/A	N/A	N/A	N/A	2	376	
2/27	Aux. osc. frequency	8A	Blk III, RCV 1, −114.5 dBm	N/A	Off	Off	N/A	N/A	N/A	N/A	1	204	

Table 3 (contd)

Spacecraft								Test data		Test time	Test comments
EXC	RCV	PWR	ANT	TWT	RNG	TMU	CDU	Performance	Criteria		
2	2, -121.0 dBm	High	Low	2	On	B	B	14-s acquisition time	≤ 60-s acquisition time	87 min	Ranging channel left on in the spacecraft.
2	2, -121.0 dBm	High	Low	2	On	B	B	Tracked to +40 kHz, no loss of lock	Track to +40 kHz, no loss of lock		
2	2, -121.0 dBm	High	Low	2	On	B	B	23-s acquisition time	≤ 60-s acquisition time		
2	2, -121.0 dBm	High	Low	2	On	B	B	Tracked to -40 kHz, no loss of lock	Track to -40 kHz, no loss of lock		
2	2, -121.0 dBm	High	Low	2	On	B	B	Acquired and tracked to +7 kHz	Acquire near BL and track to +7 kHz		
2	2, -121.0 dBm	High	Low	2	On	B	B	Acquired and tracked to -7 kHz	Acquire near BL and track to -7 kHz		
1	1	High	High	1	Off	A	A	2.2 rms	≤ 3.6 rms	46 min	One-way.
1	1, -121.0 dBm	High	High	1	Off	A	A	TBD	≤ 2.8 rms		UL -121 dBm instead of -70 dBm; criteria will be recomputed.
1	1, -120.6 dBm	High	High	1	Off	A	A	31-s acquisition time	60 s max. to regain 2-way lock	34 min	VCO temp = 78.68-79.67°F. During -15 min run DL variations ±0.1 dB.
2	2, -121.0 dBm	High	Low	2	Off	B	B	1-s acquisition time	60 s max. to regain 2-way lock	40 min	DL variations ±1.0 dB. VCO temp = 82.5°F.
1	1	High	High	1	Off	A	A	Avg. DL 2297.222374 MHz	Avg. DL 2297.222400 MHz ±500 Hz	13 min	DL variations ±0.25 dB. Aux. osc. temp = 79.53-80.52°F.

Test date, 1975	Test title	Test	Deep Space Network								Mode	RM
			RCV	EXC	PRA RNG	CMD	Uplink doppler	Uplink offset	CMA SUBC offset	SDA SUBC offset		
2/27	Command capability under doppler conditions	9A	Blk IV, RCV 3, 2297.275517 MHz, -120.0 dBm	Blk IV, 2115.407872 MHz	On	On	N/A	+40.0 kHz	+0.1 Hz	N/A	1R	305
			2297.188639 MHz, -120.0 dBm	2115.327872 MHz	On	On	N/A	-40.0 kHz	-0.1 Hz	N/A	1R	305
		9B	Blk IV, RCV 3, 2297.266112 MHz, -121.0 dBm	Blk IV, 2115.399216 MHz	On	On	N/A	+40.0 kHz	+0.1 Hz	N/A	2R	377
			2297.179328 MHz, -121.0 dBm	2115.319248 MHz	On	On	N/A	-40.0 kHz	-0.1 Hz	N/A	2R	377
2/27	Ranging channel delay, threshold and polarity verification	10A	Blk IV, RCV 3, 2297.232032 MHz, -109.0 dBm	Blk IV, 2115.367872 MHz	On	On	N/A	-40.0 kHz	N/A	N/A	1FR	305
			-132.0 dBm		On	On	N/A	-40.0 kHz	N/A	N/A	1FR	305
		10B	Blk IV, RCV 3, 8423.174145 MHz, -125 dBm	Blk IV, 2115.365280 MHz	On	Off	N/A	N/A	N/A	N/A	1FR	305
2/1	Ranging channel delay, threshold and polarity verification	10C	Blk IV, RCV 3, 2297.222340 MHz, -109.0 dBm	Blk IV, 2115.358848 MHz	On	On	N/A	N/A	N/A	N/A	16FR	375
			-132.0 dBm		On	On	N/A	N/A	N/A	N/A	16FR	375
2/28	Mod. index and spectrum analysis	13A	Blk IV, RCV 4, 2297.229800 MHz, -113 dBm	N/A	Off	Off	N/A	N/A	N/A	N/A	1F	304
			-113 dBm	Blk IV, 2115.365760 MHz	On	On	N/A	N/A	N/A	N/A	1FR	305

Table 3 (contd)

Spacecraft								Test data		Test time	Test comments
EXC	RCV	PWR	ANT	TWT	RNG	TMU	CDU	Performance	Criteria		
1	1, -131.0 dBm	High	High	1	On	A	A	All commands confirmed by SC	SC confirms all commands	1 h 36 min	None
1	1, -131.0 dBm	High	High	1	On	A	A	All commands confirmed by SC	SC confirms all commands		
2	2, -130.0 dBm	High	Low	2	On	B	B	All commands confirmed by SC	SC confirms all commands	34 min	None
2	2, -130.0 dBm	High	Low	2	On	B	B	All commands confirmed by SC	SC confirms all commands		
1	1, -133.0 dBm	High	High	1	On	A	A	942.8 ns	976 ns \pm 100 ns	1 h 38 min	Test run without UL command, mode to increase UL P_c .
1	1, -133.0 dBm	High	High	1	On	A	A	965.4 ns	976 ns \pm 100 ns		
1	1, -129.5 dBm	High	High	1	On	A	A	778.7 ns	844 ns \pm 100 ns	1 h 21 min	DL variations \pm 3 dB. VCO temp = 80.67°F.
2	2, -130.0 dBm	High	High	2	On	B	B	967.6 ns	1012 ns \pm 100 ns	2 h 37 min	60-min DRVID run spread of 4 ns.
2	2, -130.0 dBm	High	High	2	On	B	B	968.6 ns	1012 ns \pm 100 ns		
1	1	High	High	1	Off	A	A	TBS	No spurious com- ponents, verify mod. index	56 min	HR 4k coded, LR 8½ uncoded, no photos taken.
1	1, -120.0 dBm	High	High	1	On	A	A	TBS	No spurious com- ponents, verify mod. index		

Test date, 1975	Test title	Test	Deep Space Network								Mode	RM
			RCV	EXC	PRA RNG	CMD	Uplink doppler	Uplink offset	CMA SUBC offset	SDA SUBC offset		
2/28	Telemetry performance	14A	Blk IV, RCV 3, 2297.229800 MHz, -131 dBm	Blk IV, 44.886517 MHz	On	Off	N/A	N/A	N/A	N/A	1FR	305
2/28	Telemetry performance	14B	Blk IV, RCV 3, 2297.222300 MHz, -147 dBm	Blk IV, 2115.358848 MHz	On	Off	N/A	N/A	N/A	N/A	2AR	377

Table 3 (contd)

Spacecraft								Test data		Test time	Test comments
EXC	RCV	PWR	ANT	TWT	RNG	TMU	CDU	Performance	Criteria		
1	1, -130.0 dBm	High	High	1	On	A	A	LR = 12.29 dB, HR = 7.09 dB	TBD	52 min	DL variance ± 3 dB, 8 $\frac{1}{2}$ k coded, no Y-factor.
2	2, -135.0 dBm	High	Low	2	On	B	B	LR = 8.24 dB	TBD	2 h 15 min	No Y-factor; rest of test scrubbed due to link variations.

Test date, 1975	Test title	Test	Deep Space Network								Mode	RM
			RCV	EXC	PRA RNG	CMD	Uplink doppler	Uplink offset	CMA SUBC offset	SDA SUBC offset		
5/27	DL threshold one-way	1A	BLK 3, RCV 1, 2293.148192 MHz	N/A	Off	Off	N/A	N/A	N/A	N/A	1A	204
		1B	BLK 4, RCV 3, 8408.210320 MHz	N/A	Off	Off	N/A	N/A	N/A	N/A	1A	204
		1C	BLK 4, RCV 4, 2293.148140 MHz	N/A	Off	Off	N/A	N/A	N/A	N/A	16A	374
5/27	UL threshold	2A	BLK 4, RCV 4, 2293.149240 MHz, - 120 dBm	BLK 4, 2111.608224 MHz	Off	Off	N/A	N/A	N/A	N/A	1	304
					On	On	N/A	N/A	N/A	N/A	1	304
5/30		2B	BLK 4, RCV 4, 2293.145820 MHz - 120.0 dBm	BLK 4, 2111.605056 MHz	Off	Off	N/A	N/A	N/A	N/A	16A	374
					On	On	N/A	N/A	N/A	N/A	16A	374
5/27	DL threshold two-way	3A	BLK 4, RCV 4, 2293.149220 MHz	BLK 4, 2111.608224 MHz	Off	Off	N/A	N/A	N/A	N/A	1A	304
					On	On	N/A	N/A	N/A	N/A	1AR	305
5/27		3B	BLK 4, RCV 4, 8408.213805 MHz	BLK 4, 2111.608224 MHz	Off	Off	N/A	N/A	N/A	N/A	1A	304
					On	On	N/A	N/A	N/A	N/A	1AR	305
5/30		3C	BLK 4, RCV 4, 2293.149240 MHz	BLK 4, 2111.605056 MHz	Off	Off	N/A	N/A	N/A	N/A	16A	374
					On	On	N/A	N/A	N/A	N/A	16AR	375
5/27	SC RCVR pull-in	4A	BLK 4, RCV 4, 2293.149240 MHz	BLK 4, 2111.608128 MHz	Off	Off	N/A	-700 Hz	N/A	N/A	1	304
	SC RCVR range and rate		- 120.0 dBm		Off	Off	500 Hz/s	+40 kHz	N/A	N/A	1	304
	SC RCVR pull-in				Off	Off	N/A	+700 Hz	N/A	N/A	1	304
	SC RCVR range and rate				On	Off	500 Hz/s	-40 kHz	N/A	N/A	1	304

Table 4. Deep Space Network/Viking Orbiter 1 Telecommunications Compatibility Tests (Radio Frequency Subsystem 202)

Spacecraft								Test data		Test time	Test comments
EXC	RCV	PWR	ANT	TWT	RNG	TMU	CDU	Performance	Criteria		
1	1	High	High	1	Off	A	A	-158.5 dBm	-157.0 \pm 3 dBm	22 min	DL variations \pm 0.75 dB.
1	1	High	High	1	Off	A	A	-155.7 dBm	-153.0 \pm 3 dBm	41 min	Avg. of three thresholds.
2	2	High	High	2	Off	B	B	-157.5 dBm	-157.0 \pm 3 dBm	20 min	Avg. of three thresholds.
1	1	High	High	1	Off	A	A	-153.0 dBm	-152.0 \pm 2 dBm	19 min	VCO temp = 79.3°F.
1	1	High	High	1	Off	A	A	-152.5 dBm	-152.0 \pm 2 dBm		
2	2	High	High	2	Off	B	B	-154.0 dBm	-152.0 \pm 2 dBm	23 min	VCO temp = 80.36°F.
2	2	High	High	2	Off	B	B	-153.5 dBm	-152.0 \pm 2 dBm		Avg. of three thresholds.
1	1	High	High	1	Off	A	A	-157.7 dBm	-157.0 \pm 3 dBm	1 h 43 min	Avg. of three thresholds.
1	1	High	High	1	On	A	A	-157.5 dBm	-157.0 \pm 3 dBm		
1	1	High	High	1	Off	A	A	-155 dBm	-153.0 \pm 3 dBm	52 min	Avg. of three thresholds.
1	1	High	High	1	On	A	A	-155.2 dBm	-153.0 \pm 3 dBm		Spacecraft ranging channel was on during both thresholds.
2	2, -130.0 dBm	High	High	2	Off	B	B	-157.2 dBm	-157.0 \pm 3 dBm	33 min	Avg. of three thresholds.
2	2	High	High	2	On	B	B	-156.8 dBm	-157.0 \pm 3 dBm		
1	1 -120.0 dBm	High	High	1	Off	A	A	5-s acquisition time	\leq 60-s acquisition time	54 min	No problems noted.
1	1	High	High	1	Off	A	A	Tracked to +40 kHz, no loss of lock	Track to +40 kHz, no loss of lock		
1	1	High	High	1	Off	A	A	44-s acquisition time	\leq 60-s acquisition time		
1	1	High	High	1	Off	A	A	Tracked to -40 kHz, no loss of lock	Track to -40 kHz, no loss of lock		

Test date, 1975	Test title	Test	Deep Space Network									
			RCV	EXC	PRA RNG	CMD	Uplink doppler	Uplink offset	CMA SUBC offset	SDA SUBC offset	Mode	RM
	SC RCVR false lock				Off	Off	500 Hz/s	-10 kHz to +7 kHz	N/A	N/A	1	304
	SC RCVR false lock				Off	Off	500 Hz/s	+10 kHz to -7 kHz	N/A	N/A	1	304
5/29	SC RCVR pull-in	4B	BLK 4, RCV 4, 2293.149240 MHz,	BLK 4, 2111.608224 MHz	Off	Off	N/A	-700 Hz	N/A	N/A	2F	376
	SC RCVR range and rate		-120.0 dBm		Off	Off	500 Hz/s	+40 kHz	N/A	N/A	2F	376
	SC RCVR pull-in				Off	Off	N/A	+700 Hz	N/A	N/A	2F	376
	SC RCVR range and rate				Off	Off	500 Hz/s	-40 kHz	N/A	N/A	2F	376
	SC RCVR false lock				Off	Off	500 Hz/s	-10 kHz to +7 kHz	N/A	N/A	2F	376
	SC RCVR false lock				Off	Off	500 Hz/s	+10 kHz to -7 kHz	N/A	N/A	2F	376
5/28	Carrier residual phase jitter	5A	BLK 4, RCV 3 and 4, 2293.148192 MHz, -110 dBm	N/A	Off	Off	N/A	N/A	N/A	N/A	1A	304
5/30			BLK 4, RCV 3 and 4, 2293.148768 MHz, -110 dBm	BLK 4, 2111.607840 MHz	Off	Off	N/A	N/A	N/A	N/A	1A	304
5/30	Carrier residual phase jitter	5B	BLK 3, RCV 1 and 2, 2293.147328 MHz, -110.0 dBm	N/A	Off	Off	N/A	N/A	N/A	N/A	16A	374
			2293.145888 MHz, -110 dBm	BLK 3, 2111.605152 MHz	Off	Off	N/A	N/A	N/A	N/A	16A	374
5/27	Transponder rest frequency best lock and acquisition time	7A	BLK 3, RCV 1, 2293.149248 MHz, -120 dBm	BLK 3, 2111.608224 MHz	Off	Off	N/A	N/A	N/A	N/A	1	304

Table 4 (contd)

Spacecraft								Test data		Test time	Test comments
EXC	RCV	PWR	ANT	TWT	RNG	TMU	CDU	Performance	Criteria		
1	1	High	High	1	Off	A	A	Acquired and tracked to +7 kHz	Acquire near BL and track to +7 kHz		
1	1	High	High	1	Off	A	A	Acquired and tracked to -7 kHz	Acquire near BL and track to -7 kHz		
2	2, -120.0 dBm	High	Low	2	On	B	B	14-s acquisition time	≤ 60-s acquisition time		No problems noted.
2	2	High	Low	2	On	B	B	Tracked to +40 kHz, no loss of lock	Track to +40 kHz, no loss of lock	32 min	
2	2	High	Low	2	On	B	B	23.5-s acquisition time	≤ 60-s acquisition time		
2	2	High	Low	2	On	B	B	Track to -40 kHz, no loss of lock	Track to -40 kHz, no loss of lock		
2	2	High	Low	2	On	B	B	Acquired and tracked to +7 kHz	Acquire near BL and track to +7 kHz		
2	2	High	Low	2	On	B	B	Acquired and tracked to -7 kHz	Acquire near BL and track to -7 kHz		
1	1	High	High	1	Off	A	A	3.66 deg rms	≤ 3.6 deg rms	21 min	Avg. of three measurements.
1	1, -110 dBm	High	High	1	Off	A	A	2.68 deg rms	≤ 2.8 deg rms		
2	2	High	High	2	Off	B	B	4.56 deg rms	≤ 3.6 deg rms	33 min	Avg. of three measurements.
2	2, -108 dBm	High	High	2	Off	B	B	2.84 deg rms	≤ 2.8 deg rms		
1	1, -119.0 dBm	High	High	1	Off	A	A	1 s acquisition time	60 s max to regain 2-way lock	25 min	VCO temp = 79.3°F.

Test date, 1975	Test title	Test	Deep Space Network								Mode	RM
			RCV	EXC	PRA RNG	CMD	Uplink doppler	Uplink offset	CMA SUBC offset	SDA SUBC offset		
5/29		7B	BLK 3, RCV 1, 2293.149152 MHz, -120.0 dBm	BLK 3, 2111.608224 MHz	Off	Off	N/A	N/A	N/A	N/A	2	376
5/27	Aux. osc. frequency	8A	BLK 3, RCV 1, -120.0 dBm	N/A	Off	Off	N/A	N/A	N/A	N/A	1	304
5/29 5/30	Aux. osc. frequency	8B	BLK 3, RCV 1, -120.0 dBm	N/A	Off	Off	N/A	N/A	N/A	N/A	16	274
5/28	Command capability under doppler conditions	9A	BLK 4, RCV 4, 2293.193354 MHz, -120.0 dBm	BLK 4, 2111.648880 MHz	On	On	N/A	+40.0 kHz	+0.1 Hz	N/A	1R	305
			2293.106459 MHz, -120.0 dBm	2111.568864 MHz	On	On	N/A	-40.0 kHz	-0.1 Hz	N/A	1R	305
5/29		9B	BLK 4, RCV 4, 2293.193354 MHz, -120.0 dBm	BLK 4, 2111.648880 MHz	On	On	N/A	+40.0 kHz	+0.1 Hz	N/A	2R	377
			2293.106459 MHz, -120.0 dBm	2111.568864 MHz	On	On	N/A	-40.0 kHz	-0.1 Hz	N/A	2R	377
5/28	Ranging channel delay, threshold and polarity verification	10A	BLK 4, RCV 4, 2293.106459 MHz, -109.0 dBm	BLK 4, 2111.568864 MHz	On	On	N/A	-40.0 kHz	N/A	N/A	1FR	305
			-132.0 dBm		On	On	N/A	-40.0 kHz	N/A	N/A	1FR	305
5/28		10B	BLK 4, RCV 3, 8408.213975 MHz, -139 dBm	BLK 4, 2111.608128 MHz	On	Off	N/A	N/A	N/A	N/A	1FR	305
5/30	Ranging channel delay, threshold and polarity verification	10C	BLK 4, RCV 4, 2293.145800 MHz, -109.0 dBm	BLK 4, 2111.605056 MHz	On	On	N/A	N/A	N/A	N/A	1FR	375
					On	On	N/A	N/A	N/A	N/A	1FR	375

Table 4 (contd)

Spacecraft								Test data		Test time	Test comments
EXC	RCV	PWR	ANT	TWT	RNG	TMU	CDU	Performance	Criteria		
2	2, -120.0 dBm	High	Low	2	Off	B	B	1 s acquisition time	60 s max to regain 2-way lock	29 min	VCO temp = 78.4°F.
1	1	High	High	1	Off	A	A	Avg DL 2293.148192 MHz	Avg. DL 2293.148148 MHz ±500 MHz	16 min	Aux. osc. temp = 81.9–82.9°F.
2	2	High	High	2	Off	B	B	Avg DL 2293.147328 MHz	Avg. DL 2293.148148 MHz ±500 MHz	14 min	Aux. osc. temp = 87.65–87.6°F.
1	1, -118.0 dBm	High	High	1	On	A	A	All commands confirmed by SC	SC confirms all commands	1 h 12 min	No problems noted.
1	1, -118.0 dBm	High	High	1	On	A	A	All commands confirmed by SC	SC confirms all commands		
2	2, -119.5 dBm	High	Low	2	On	B	B	All commands confirmed by SC	SC confirms all commands	29 min	No problems noted.
2	2, -119.5 dBm	High	Low	2	On	B	B	All commands confirmed by SC	SC confirms all commands		
1	1, -129.0 dBm	High	High	1	On	A	A	1018, ns	976 ±100 ns	1 h 29 min	Exciter freq at -40.0 kHz offset, 43.991018 MHz.
1	1, -129.0 dBm	High	High	1	On	A	A	1017, ns	976 ±100 ns		
1	1, -129.0 dBm	High	High	1	On	A	A	834 ns	844 ±100 ns		
2	2, -129.0 dBm	High	High	2	On	B	B	1001 ns	1012 ±100 ns	1 h 55 min	
2	2, -129.0 dBm	High	High	2	On	B	B	1002 ns	1012 ±100 ns		80.36°F VCO temp.

Test date, 1975	Test title	Test	Deep Space Network									Mode	RM
			RCV	EXC	PRA RNG	CMD	Uplink doppler	Uplink offset	CMA SUBC offset	SDA SUBC offset			
5/30	Ranging channel delay, simultaneous S/X-band	10D	BLK 4, RCV 3, 8408.212445 MHz, -130.4 dBm, BLK 4, RCV 4, 2293.148820 MHz, -113.5 dBm	BLK 4, 2111.607840 MHz	On	On	N/A	N/A	N/A	N/A	1FR	305	
5/28	Mod. index and spectrum analysis	13A	BLK 4, RCV 4, 2293.148260 MHz, -96.5 dBm	N/A	Off	Off	N/A	N/A	N/A	N/A	1FR	304	
			2293.149980 MHz, -96.5 dBm	BLK 4, 2111.608896 MHz	On	On	N/A	N/A	N/A	N/A	1FR	305	
5/29		13B	BLK 4, RCV 4, 2293.147380 MHz, -91.0 dBm	N/A	Off	Off	N/A	N/A	N/A	N/A	2A	376	
			2293.148300 MHz, -91.0 dBm	BLK 4, 2111.607360 MHz	On	On	N/A	N/A	N/A	N/A	2AR	377	
5/28	Telemetry performance	14A	BLK 4, RCV 4, 2293.149980 MHz, -133.5 dBm, 5 dB STB/No	BLK 4, 2111.608896 MHz	On	Off	N/A	N/A	N/A	N/A	1FR	304/ 305	
5/28- 29		14B	BLK 4, RCV 4, 2293.149160 MHz, -150.0 dBm 8.6 dB STB/No	BLK 4, 2111.608224 MHz	On	Off	N/A	N/A	N/A	N/A	2AR	376/ 377	
			2293.189132 MHz, -139.5 dBm, 18.8 dBm, STB/No	2111.644992 MHz	On	Off	26 Hz/s	+36.8 kHz	N/A	-0.22 Hz	2AR	377	
			2293.189132 MHz, -139.5 dBm, 18.8 dB, STB/No	2111.644992 MHz	On	Off	N/A	+36.8	N/A	-0.22 Hz	2AR	377	

Table 4 (contd)

Spacecraft								Test data		Test time	Test comments
EXC	RCV	PWR	ANT	TWT	RNG	TMU	CDU	Performance	Criteria		
1	1, -128.8 dBm	High	High	1	On	A	A	848 ns 1015 ns	$844 \pm 100 \times$ delay 976 ± 100 S delay	47 min	79.3°F VCO temp.
1	1	High	High	1	Off	A	A	TBS	No spurious components, verify mod. index	51 min	No problems noted.
1	1, -113.0 dBm	High	High	1	On	A	A	TBS			
2	2	High	Low	2	Off	B	B	TBS	No spurious components, verify mod. index	29 min	No problems noted.
2	2, -111.0 dBm	High	Low	2	On	B	B	TBS			
1	1, -127.0 dBm	High	High	1	On	A	A	LR = 8.26 dB HR = 3.07 dB	10.3 ± 1.9 dB 3.1 ± 1.1 dB	1 h 10 min	
2	2, -128.2 dBm	High	Low	2	On	B	B	LR = 5.1 dB	4.8 ± 1.4 dB	2 h 13 min	
2	2, -137.0 dBm	High	Low	2	On	B	B	LR = 16.9 dB	16.2 ± 1.7 dB		
2	2, -137.5 dBm	High	Low	2	On	B	B	LR = 17.32 dB	17.5 ± 1.7 dB		

Test date, 1975	Test title	Test	Deep Space Network									
			RCV	EXC	PRA RNG	CMD	Uplink doppler	Uplink offset	CMA SUBC offset	SDA SUBC offset	Mode	RM
3/22	Orbiter/ Lander command discrimination	3A	BLK IV, RCV 4, 2295.739338 MHz, -100.0 dBm	BLK IV, 2113.993344 MHz	Off	CMA 1 on, CMA 2 off	N/A	N/A	CMA 1 = VL 0.0 Hz, CMA 2 = VO 0.0 Hz	N/A	N/A	306 VO
					Off	CMA 1 off, CMA 2 on						
					On	CMA 1 on, CMA 2 off	N/A	+40.0 kHz	CMA 1 = VL +0.1 Hz, CMA 2 = VO +0.1 Hz	N/A	N/A	307 VO
					On	CMA 1 off, CMA 2 on						
					Off	CMA 1 on, CMA 2 off	N/A	+40.0 kHz	CMA 1 = VL +0.1 Hz, CMA 2 = VO +0.1 Hz	N/A	N/A	306 VO
					Off	CMA 1 off, CMA 2 on						
		3B	BLK IV, RCV 4, 2295.743780 MHz, -100.0 dBm	BLK IV, 2113.997376 MHz	Off	CMA 1 on, CMA 2 off	N/A	N/A	CMA 1 = VL 0.0 Hz, CMA 2 = VO 0.0 Hz	N/A	N/A	316
					Off	CMA 1 off, CMA 2 on,						
					On	CMA 1 on, CMA 2 off	N/A	+40.0 kHz	CMA 1 = VL +0.1 Hz, CMA 2 = VO +0.1 Hz	N/A	N/A	317
					On	CMA 1 off, CMA 2 on						
					Off	CMA 1 on, CMA 2 off	N/A	+40.0 kHz	CMA 1 = VL +0.1 Hz, CMA 2 = VO +0.1 Hz	N/A	N/A	316
					Off	CMA 1 off, CMA 2 on						

Table 5. Deep Space Network/Viking Spacecraft 1 Telecommunications Compatibility Test

Spacecraft								Test data		Test time	Test comments
EXC	RCV	PWR	ANT	TWT	RNG	TMU	CDU	Performance	Criteria		
N/A	1 -99.85 dBm	N/A	N/A	N/A	Off	N/A	1	Met criteria	All commands successfully detected by Lander (step 7)	3 h 39 min	None.
								Met criteria	All commands successfully detected by Orbiter (step 11)		VL indicated sporadic in/out-of-lock with VO subcarrier plus bit sync present.
N/A	1 -112.0 dBm	N/A	N/A	N/A	On	N/A	1	Met criteria	All commands successfully detected by Lander (step 18)		None.
								Met criteria	All commands successfully detected by Orbiter (step 23)		VL indicated sporadic in/out-of-lock with VO subcarrier plus bit sync present.
N/A	1 -143.2 dBm	N/A	N/A	N/A	Off	N/A	1	Met criteria	All commands successfully detected by Lander (step 29)		None.
								Met criteria	All commands successfully detected by Orbiter (step 34)		VL indicated no lock at -143.2 dBm UL P _c .
N/A	1 -111.0 dBm	N/A	N/A	N/A	On	N/A	1	Met criteria	All commands successfully detected by Lander (step 42)		None.
								Met criteria	All commands successfully detected by Orbiter (step 48)		VL indicated sporadic in/out-of-lock with VO subcarrier plus bit sync present.
N/A	2 -98.5 dBm	N/A	N/A	N/A	Off	N/A	2	Met criteria	All commands successfully detected by Lander (step 7)	1 h 40 min	None.
								Met criteria	All commands successfully detected by Orbiter (step 11)		None.
N/A	2 -113.6 dBm	N/A	N/A	N/A	On	N/A	2	Met criteria	All commands successfully detected by Lander (step 18)		None.
								Met criteria	All commands successfully detected by Orbiter (step 23)		None.
N/A	2 -142.9 dBm	N/A	N/A	N/A	Off	N/A	2	Met criteria	All commands successfully detected by Lander (step 29)		None.
								Met criteria	All commands successfully detected by Orbiter (step 34)		None.

Test date, 1975	Test title	Test	Deep Space Network									
			RCV	EXC	PRA RNC	CMD	Uplink doppler	Uplink offset	CMA SUBC offset	SDA SUBC offset	Mode	RM
7/7	Orbiter/ Lander command discrimination	3A	BLK IV, RCV 4, 2297.225380 MHz, -99.5 dBm	BLK IV, 2115.366912 MHz	Off	CMA 1 on, CMA 2 off	N/A	N/A	CMA 1 = VL 0.0 Hz, CMA 2 = VO 0.0 Hz	N/A	N/A	306 VO
					Off	CMA 1 off, CMA 2 on						
					On	CMA 1 on, CMA 2 off	N/A	+40.0 kHz	CMA 1 = VL +0.1 Hz, CMA 2 = VO +0.1 Hz	N/A	N/A	307 VO
					On	CMA 1 off, CMA 2 on						
					Off	CMA 1 on, CMA 2 off	N/A	+40.0 kHz	CMA 1 = VL +0.1 Hz, CMA 2 = VO +0.1 Hz	N/A	N/A	306 VO
					Off	CMA 1 off, CMA 2 on						
					Off	CMA 1 on, CMA 2 off	N/A	-40.0 kHz	CMA 1 = VL -0.1 Hz, CMA 2 = VO -0.1 Hz	N/A	N/A	307 VO
					Off	CMA 1 off, CMA 2 on						
		3B	BLK IV, RCV 4, 2297.223040 MHz, -100.0 dBm	BLK IV, 2115.359520 MHz	Off	CMA 1 on, CMA 2 off	N/A	N/A	CMA 1 = VL 0.0 Hz, CMA 2 = VO 0.0 Hz	N/A	N/A	316
					Off	CMA 1 off, CMA 2 on						
					On	CMA 1 on, CMA 2 off	N/A	+40.0 kHz	CMA 1 = VL +0.1 Hz, CMA 2 = VO +0.1 Hz	N/A	N/A	317
					On	CMA 1 off, CMA 2 on						
					Off	CMA 1 on, CMA 2 off	N/A	+40.0 kHz	CMA 1 = VL +0.1 Hz, CMA 2 = VO +0.1 Hz	N/A	N/A	316
					Off	CMA 1 off, CMA 2 on						

Table 6. Deep Space Network/Viking Spacecraft 2 Telecommunications Compatibility Test

Spacecraft								Test data		Test time	Test comments
EXC	RCV	PWR	ANT	TWT	RNG	TMU	CDU	Performance	Criteria		
N/A	1 -101.0 dBm	N/A	N/A	N/A	Off	N/A	1	Met criteria	All commands successfully detected by Lander (step 7)	6 h 33 min	See paragraph 3.1.2.1 of test report.
								Met criteria	All commands successfully detected by Orbiter (step 11)		
N/A	1 -112.7 dBm	N/A	N/A	N/A	On	N/A	1	Met criteria	All commands successfully detected by Lander (step 18)		
								Met criteria	All commands successfully detected by Orbiter (step 23)		
N/A	1 -143.0 dBm	N/A	N/A	N/A	Off	N/A	1	Met criteria	All commands successfully detected by Lander (step 28)		
								Met criteria	All commands successfully detected by Orbiter (step 33)		
N/A	1 -112.0 dBm	N/A	N/A	N/A	On	N/A	1	Met criteria	All commands successfully detected by Lander (step 41)		
								Met criteria	All commands successfully detected by Orbiter (step 46)		
N/A	2 -99.6 dBm	N/A	N/A	N/A	Off	N/A	2	Met criteria	All commands successfully detected by Lander (step 7)	1 h 40 min	See paragraph 3.1.2.1 of test report.
								Met criteria	All commands successfully detected by Orbiter (step 11)		
N/A	2 -113.0 dBm	N/A	N/A	N/A	On	N/A	2	Met criteria	All commands successfully detected by Lander (step 18)		
								Met criteria	All commands successfully detected by Orbiter (step 23)		
N/A	2 -143.0 dBm	N/A	N/A	N/A	Off	N/A	2	Met criteria	All commands successfully detected by Lander (step 28)		
								Met criteria	All commands successfully detected by Orbiter (step 33)		

Table 7. Definition of terms

Term	Definition
Bit rate	clock frequency of the telemetry bit information
Car. sup.	downlink carrier suppression due to telemetry modulation
CMA SUBC offset	command modulation assembly subcarrier frequency offset relative to nominal
DL	S-band RF downlink
DSN CMD	telemetry and command data handling command modulation
DRVID	differenced range vs integrated doppler
DSN EXC	the standard DSN Block III/Block IV exciter equipment
DSN RCVR	the standard DSN Block III/Block IV receiving equipment
HR	high rate
LR	low rate
P_c	power in carrier
DSN RNG	planetary ranging assembly modulation
SC ant	spacecraft antenna
SC CDU	spacecraft command detector unit
SC EXC	spacecraft S-band exciter equipment
SC mode	spacecraft telemetry mode
SC PWR	spacecraft transmitter power mode
SC RCV	spacecraft S-band receiving equipment
SC RNG	spacecraft ranging channel—ON/OFF
SC RM	spacecraft radio mode
SC TMU	spacecraft telemetry modulation unit
SC TWT	spacecraft traveling wave tube amplifier
SDA SUBC offset	subcarrier demodulator assembly subcarrier frequency offset relative to nominal
TBD	to be determined
TLM	telemetry
UL	S-band RF uplink
Uplink doppler	ramp rate of the uplink carrier frequency
Uplink offset	uplink carrier frequency offset relative to the spacecraft receiver rest frequency

Table 8. RF channels and center frequencies for special RF interference tests

	Orbiter Channel 9, MHz	Lander Channel 13, MHz	Test transmitter Channel 20, MHz
DSN receive	2293.148148	2294.629630	2297.222222
DSN transmit	2111.607253	2112.971451	Not Applicable

N76-15194

Viking Mission Support

D. J. Mudgway
DSN Systems Engineering Office

D. W. Johnston
DSN Operations Office

This article describes the launches of Vikings 1 and 2 and the circumstances surrounding each launch, followed by early cruise coverage of both spacecraft. The article also includes the planetary testing effort being carried out by the DSN to prepare for planetary operations.

I. Introduction

The previous article in this series describes the compatibility testing with the Viking 2 spacecraft. These tests marked the end of formal radio frequency telecommunications compatibility testing between the DSN and the Viking spacecraft. Also described are the prelaunch Operational Verification Tests, Configuration Verification Tests, and Mission Configuration Tests. This article describes additional testing necessitated by launch delays, launch and cruise activities of both Viking spacecraft, and the planetary testing planned for the 64-meter subnet and the conjoint 26-meter subnet.

II. DSN Launch and Cruise Support

The launches and initial acquisitions of Viking 1 on August 20, 1975 and of Viking 2 on September 9, 1975 were flawless and according to plan. The first midcourse maneuvers (trajectory corrections) of both spacecraft occurred as predicted with no problems of any kind and to

this writing both spacecraft are being supported by the DSN with no problems or concerns.

A. Viking 1 Initial Acquisition and Cruise Support

As described elsewhere in this issue ("Tracking Operations During the Viking 1 Launch Phase," by A. L. Berman and J. A. Wackley), the initial acquisition of Viking 1 by DSS 42 was according to plan (Ref. 1). This success confirmed the value of the prelaunch initial acquisition testing effort. Following launch and initial acquisition, the DSN provided normal cruise coverage.

A first midcourse maneuver for Viking 1 was supported on August 27, 1975. This maneuver was needed to bring the spacecraft trajectory into closer proximity to the planet Mars following the initial launch "safe" (no impact) trajectory. A change in spacecraft velocity of 16.9 km/h (10.5 mph) was also made, which targeted Viking 1 to arrive at Mars on June 19, 1976. The performance of the DSN throughout the maneuver was without incident.

B. Viking 2 Initial Acquisition and Cruise Support

As a result of the change in the Viking 1 launch date, the Viking 2 launch date had slipped to September 3, 1975. During routine prelaunch checks, a degradation of 3 dB in the spacecraft receiver threshold was detected when switched to the high-gain antenna. In order to investigate this anomaly, the spacecraft was demated from the launch vehicle and the shroud was removed. The problem was cleared after a complete set of new hardware (high-gain antenna, cables, joints, etc.) was installed forward of the diplexer. The spacecraft was then rechecked and mated to the launch vehicle. The revised launch date was now September 9, 1975, and all systems were green. To insure optimum performance additional prelaunch initial acquisition testing was performed with DSSs 42 and 44 (Australia). These stations again entered a configuration freeze condition prior to launch. As was the case with Viking 1, the initial acquisition of Viking 2 was as predicted, and again the testing effort and preparation of the DSN were proved effective.

On September 19, 1975 the DSN provided support for the first midcourse maneuver of Viking 2. All went as planned, and this maneuver has targeted Viking 2 to arrive at Mars on August 7, 1976.

III. DSN Planetary Test and Training

In order to prepare for Viking lander planetary operations, a DSN program of planetary test and training was begun in October 1975. This test series comprises Mission Configuration Tests (MCTs) and Operational Verification Test (OVTs) as shown in Fig. 1. Of primary concern is the training of the 64-meter subnet (DSSs 14, 43, and 63) and the conjoint 26-meter subnet (DSSs 11, 61, and 42). Later another series of tests will be conducted in order to check the Network Operations Control Center (NOCC) Block III system, which will be operational in February 1976. These tests will involve the 64-meter and conjoint 26-meter subnets and the Network Operations Control Center. These tests will be conducted primarily for the training of the network operations control team. During April 1976 a short series of OVTs will be conducted with the 64-meter DSSs to check the operation of the new station monitor consoles, validate added enhancement equipment, and maintain DSN operational proficiency in the planetary mode. Upon completion of this final test phase, the DSN will be qualified to support planetary operations. Figure 1 shows the scheduled phases of test activity.

A. Mission Configuration Test and System Performance Test Status

Mission Configuration Tests and System Performance Tests with DSS 14, which were begun in October, required 96 hours of testing to complete on approximately November 1, 1975. The test series at DSSs 43 and 63 was begun in mid-October and requires 233 hours; these are scheduled to be completed by December 1, 1975. The 26-meter subnet (DSSs 11, 42, and 61) requires 16 hours of testing to be concluded by mid-November. All Deep Space Stations will support an additional 20 hours of DSS Monitor and Control MCTs during February 1976.

B. Operational Verification Test Status

Viking planetary testing was begun October 21, 1975 by an Operational Verification Test (OVT) conducted with DSS 14 located at Goldstone, California. The first phase of the planetary testing will comprise eight OVTs with the Goldstone complex—the first four involving only DSS 14 and the remaining four involving DSS 14 and DSS 11, the conjoint 26-meter station. In November a similar testing program will commence with the overseas stations DSSs 63 and 61 in Spain and DSSs 43 and 42 in Australia. Ten OVTs are scheduled for each of the overseas facilities. These will be divided, as was the series with DSSs 14 and 11, so that the first five will be with the 64-meter stations and the remaining five with both the 64-meter and the respective 26-meter conjoint stations. The first half of the tests have the purpose of training 64-meter-station personnel for planetary operations involving the processing of telemetry data from three spacecraft (two orbiters and one lander, six simultaneous data streams); commanding of orbiters and landers individually (no dual commanding is planned at this time); and tracking of the spacecraft, processing doppler and radio metric data of only one spacecraft at any one time. The second half of the tests involves both the 64-meter and the respective 26-meter conjoint stations, and will be primarily concerned with practicing the Viking planetary failure strategies. This will involve rerouting of telemetry data through the 26-meter conjoint station. The practice of these backup configurations is essential, because during full planetary operations all of a 64-meter station's equipment is fully committed, with no backup equipment existing at the facility. Upon completion of this first phase of testing, the DSN will be prepared to support the scheduled Viking flight-team training tests. The two additional phases of OVTs will be discussed in greater detail in future articles.

IV. DSN Support of Additional Viking Testing

Soon after the internal DSN planetary testing begins, the DSN will be required to extend support to other Viking test programs. These include Viking Mission Control and Computing Center (VMCCC) System Integration Tests (SITs) and the Ground Data System (GDS) testing similar to the cruise tests conducted prior to Launch. The schedule for these tests is depicted in Fig. 1.

A. VMCCC System Integration Test

The first SIT is scheduled for November 12, 1975 with DSS 14. Time has also been scheduled for retests, if required, on November 21 and November 28, 1975. Following the system integration testing with DSS 14, these same tests will be conducted with DSS 43 on January 5, 1976 with a retest scheduled for January 13, 1976, and with DSS 63 on January 8, 1976 with a retest scheduled for January 16, 1976. Upon completion of these tests, the DSN and VMCCC will be prepared to support the Viking Project planetary testing effort.

B. Viking Project Ground Data System Tests

The first Viking Ground Data System (GDS) test scheduled for December 6, 1975, will be GDS 5.1, and will be a combined station test involving the 64-meter station, DSS 14, and the 26-meter conjoint station, DSS 11. The next GDS test 5.31 will be conducted with DSSs 14 and 11 and is scheduled for December 16, 1975 with a possible retest on December 29, 1975.

The overseas stations, DSSs 43 and 42 in Australia and DSSs 63 and 61 in Spain, are scheduled to begin GDS testing in January 1976. Ground Data System 5.32 is scheduled first with the Australian stations scheduled for January 21, 1976 with a possible retest on January 29;

GDS 5.32 test is scheduled with the Spanish stations on January 24, 1976 with a possible retest on February 1, 1976. The GDS 6.0 combined station test will be conducted following GDS 5.32. Ground Data System 6.0 will have an 18-hour test involving DSSs 14 and 11 at Goldstone and DSSs 43 and 42 in Australia. Ground Data System 6.0 test will conclude the GDS planetary series.

C. Flight Operations Personnel Test and Training

Following the GDS testing, the flight operations personnel test and training exercises will be conducted. These will involve the DSN and are scheduled for late February and March of 1976. Detailed discussions of these will be reserved for future articles in this series.

V. Summary

Now that the Viking mission is in its long cruise phase the DSN has a dual function to perform. First, it is responsible for real-time flight operations of the two Viking spacecraft, and, secondly, it must embark on an extensive planetary test and training program. The testing program described herein is directed toward providing proper and timely support for all areas of the Viking mission. During planetary operations the Viking mission will utilize virtually all of the resources of the DSN; therefore, it is imperative that all functions be tested to insure success.

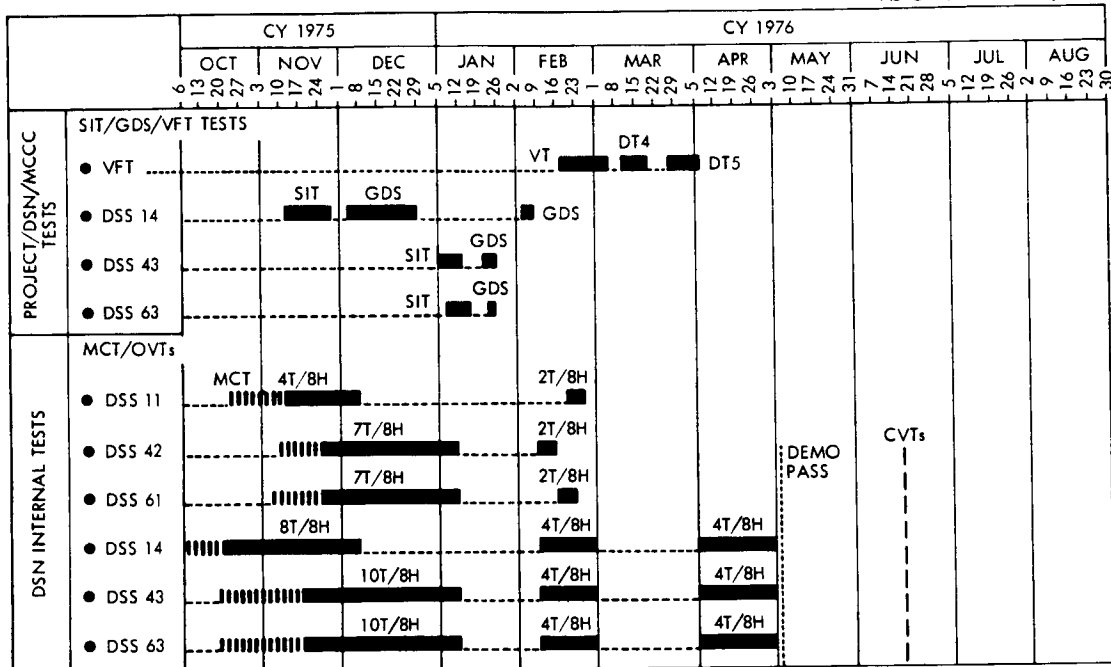
VI. Conclusions

It is felt that the planetary testing effort as planned will bring the DSN to the same high level of proficiency as was attained by launch and cruise testing effort. The progress of the DSN's endeavors toward this goal will be reported in future articles.

Reference

1. Mudgway, D. J., Bryan, A. I., and Johnston, D. W., "Viking Mission Support," in *The Deep Space Network Progress Report 42-29*, pp. 10-14, Jet Propulsion Laboratory, Pasadena, Calif., Oct. 15, 1975.

AS OF OCTOBER 22, 1975



SIT = VMCCC/DSN SYSTEM INTEGRATION TESTS
 GDS = GROUND DATA SYSTEM TESTS
 VFT = VIKING FLIGHT TEAM
 MCT = MISSION CONFIGURATION TESTS

VT = VERIFICATION TEST
 DT = DEMONSTRATION TEST
 OVT = OPERATIONAL VERIFICATION TESTS
 NT x NH = TESTS x HOURS EACH

Fig. 1. Viking operations test schedule

N76-15195

Pioneer Mission Support

R. B. Miller
DSN Systems Engineering Office

Current status of the Pioneer 10 and 11 missions and Pioneer Venus 1978 mission is described.

I. Pioneer 10 and 11

The Pioneer 10 spacecraft is continuing to return data on new regions of the solar system never before explored by a man-made object. Pioneer 10 is continuing to be tracked daily by stations of the Deep Space Network (DSN).

In an effort to experimentally increase the range by which a DSN 26-m antenna can receive useful data from Pioneer 10, an R&D low-noise cone was installed at the Pioneer Station (DSS 11) at Goldstone. The result was an improvement of approximately 0.7 dB in performance. On October 4, 1975, an experimental 3-Hz loop was added to a receiver at the same station and has resulted in an additional (approximately 1-dB) improvement in performance. This configuration at DSS 11 will add several months of 26-m antenna coverage capability for Pioneer 10.

Starting in May 1975, an unexplained drifting of the spin axis of Pioneer 10 was observed. Several different theories were proposed, after a gas leak was eliminated as a possible cause, to explain this drift by unusual forces or radiation pressures in the region of the solar system the spacecraft had entered. It was finally discovered in July that, during a routine spacecraft orientation maneuver, the

Pioneer 10 star sensor had shifted from the star Betelgeuse to Sirius, and therefore a twisting of the reference frame had caused an apparent drift northward instead of the natural east-west drift due to the relative Earth motion.

Pioneer 11 had experienced several occurrences of spurious commanding since its encounter with the planet Jupiter. Several of these incidences resulted in extensive analysis by the DSN to ensure that the spurious commands had not been transmitted by a Deep Space Station due to some kind of failure on the ground. A turn-off of all the science instruments with a staged turn-on seems to have isolated spurious commanding problems to some kind of failure associated with the asteroid-meteoroid detector. Pioneer 11 is now operating with that instrument turned off. The plasma analyzer has also apparently failed, although efforts are continuing to periodically activate the instrument. All other aspects of the Pioneer 11 spacecraft seem to be functioning normally.

A trajectory correction for the purpose of the Saturn encounter targeting is planned for December 17, 1975. Several Saturn encounter alternatives are still being debated, which include going inside or outside the rings, and a possible approach to the moon Titan.

Figure 1 is a plot of the received carrier power and bit rate for Pioneer 10 and 11 through 1979. This chart is an update by Network Operations Planning of a chart which was published in a previous Progress Report article.

II. Pioneer Venus

The Pioneer Venus program was threatened when FY-76 funds were cut by the House of Representatives. However, after two months, a Joint Congressional Committee restored essentially all funding, and the program is on course and schedule.

The Pioneer Venus multiprobe entry includes a differenced long baseline interferometry (DLBI) experiment which will attempt to measure the wind velocity on Venus as the four probes descend through the atmosphere. This experiment has been described in previous Progress Report articles (see in particular Ref. 1). Basically, the experiment will be using interferometry techniques to measure components of the velocity across the line-of-sight (Earth-spacecraft direction) and established doppler techniques to measure the velocity components along the line-of-sight. The interferometry technique involves receiving each probe signal simultaneously with the signal from the bus at several ground stations. As described in previous articles, the bus is retarded by a trajectory correction after it releases the probes, so that it enters the Venusian atmosphere after all four probes have reached the surface of the planet. In this way, the bus serves as a reference signal, undisturbed by the Venusian atmosphere. A corrected difference is taken between the bus signal and each of the probe signals at a particular station to eliminate ionospheric and interplanetary effects, and a second difference is taken between two stations which produces a measure of the angle subtended by the two stations and a probe, and the rate of change of that angle is the measure of the velocity of the probe perpendicular to the line-of-sight.

Each pair of stations resolves only one dimension of the velocity. The two 64-m DSN stations at Goldstone,

California, and Canberra, Australia, are the primary stations for the multiprobe entry. However, if they were used alone, only one component of the wind perpendicular to the line-of-sight would be resolved. It was therefore necessary to locate at least one other station with an appropriate long baseline in or adjacent to the Pacific Basin in order to resolve all components of the wind. The experimenter had proposed a 26-m station in Kishima, Japan, which belongs to the Radio Research Laboratories branch of the Ministry of Posts and Telecommunications of Japan, and the 9-m station located near Santiago, Chile, which is a part of the Spaceflight Tracking and Data Network (STDN). When the Pioneer Project Office appealed to the Office of Space Science for guidance as to how to proceed in obtaining two non-DSN stations to support the DLBI experiment, the Office of Tracking and Data Acquisition (OTDA) recommended that only stations which were part of the NASA inventory should be considered for cost and reliability considerations. In particular, OTDA recommended the use of the STDN stations at Guam and at Santiago, Chile, and assigned the TDA office at JPL the responsibility of coordinating the Santiago and Guam support for the project. The resulting network for the DLBI is shown geographically in Fig. 2. Note that a fourth station is included for redundancy and closure.

Upon receipt of the direction from OTDA, negotiations were initiated between the DSN and STDN for the purpose of establishing the engineering and operational interfaces necessary for coordinating the engineering, implementation, and operation of the Santiago and Guam stations. A first meeting for coordination purposes was held at Goddard on June 3, 1975. Tentative agreement reached is that the STDN stations will utilize STDN low-noise amplifiers, receivers, and timing subsystems and that the STDN will provide the required down-converters to interface with the STDN receivers, as well as the method of calibrating the STDN stations. The DSN will provide the high-rate digital recorders and associated A to D converters and electronics for the STDN stations.

Reference

1. Miller, R. B., "Pioneer Venus 1978 Mission Support," in *The Deep Space Network Progress Report 42-27*, pp. 28-35, Jet Propulsion Laboratory, Pasadena, Calif., June 15, 1975.

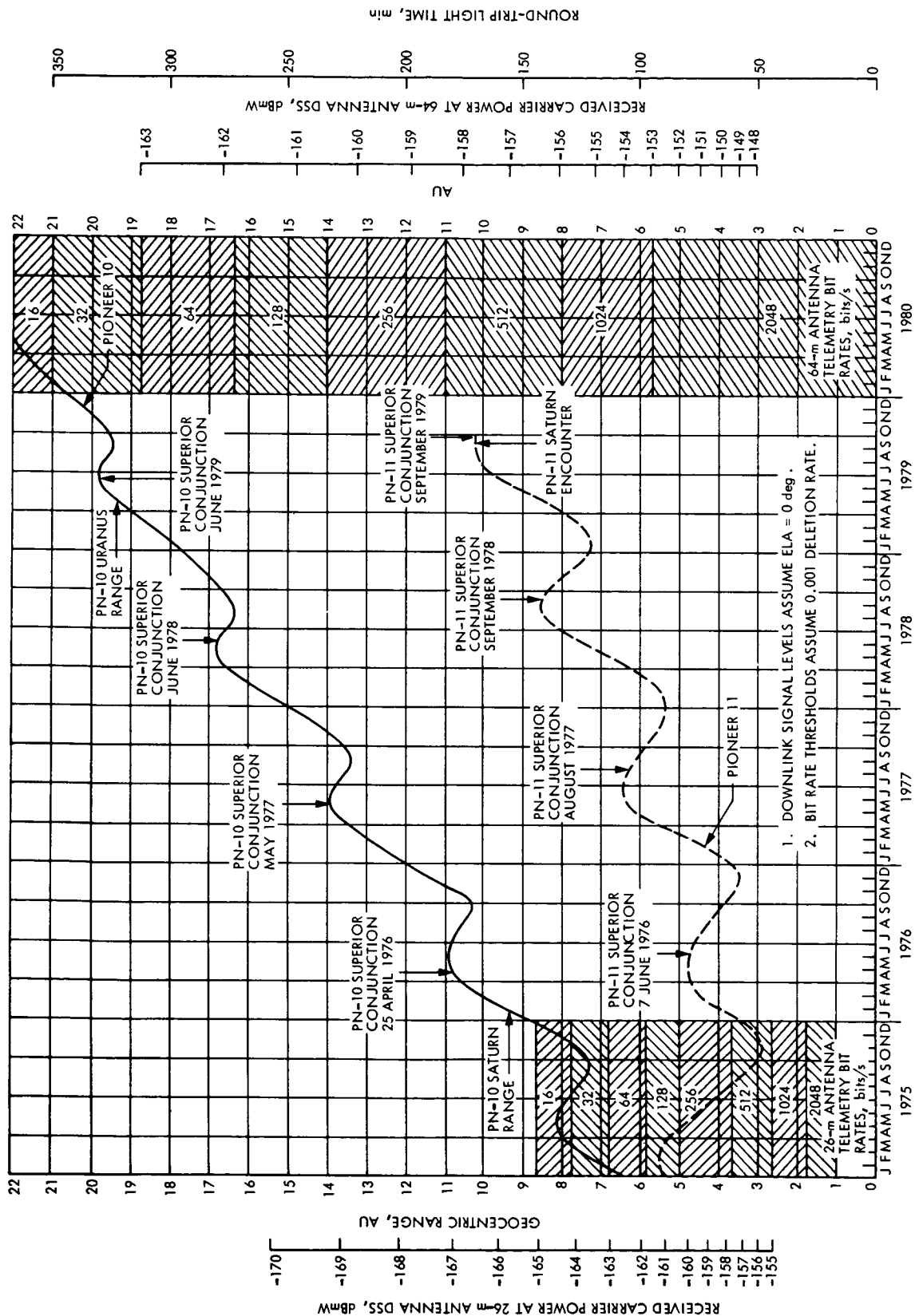


Fig. 1. Downlink performance estimates for Pioneers 10 and 11

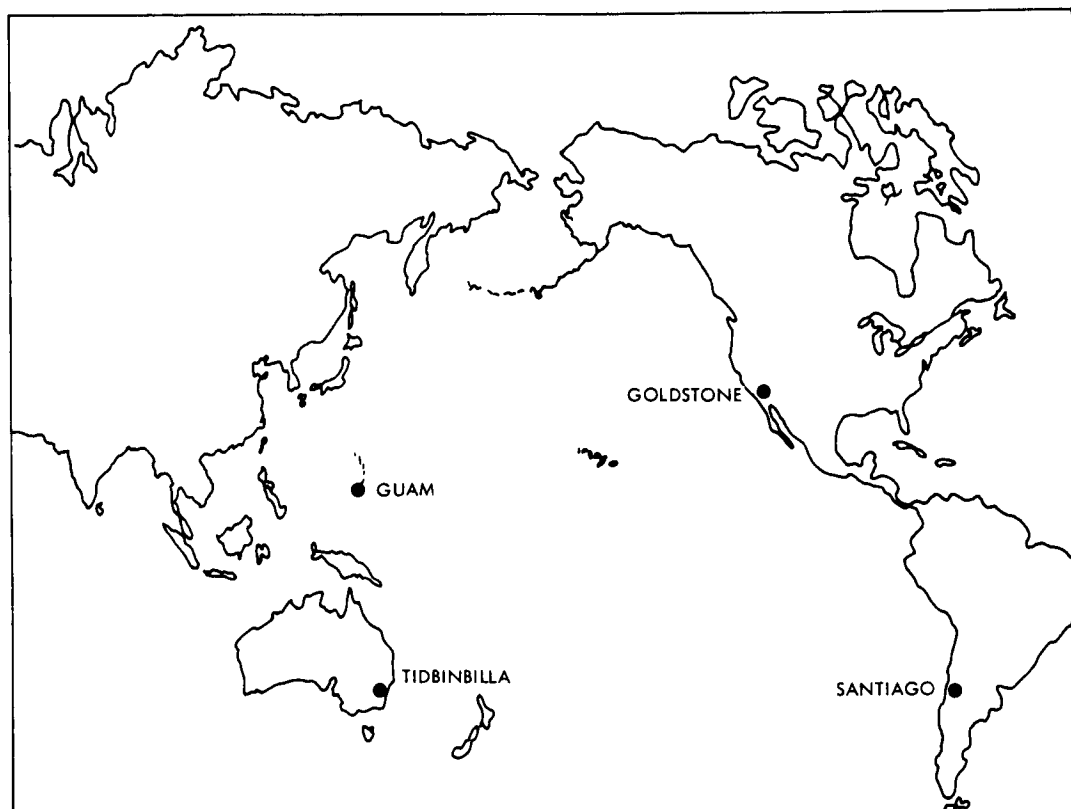


Fig. 2. Tracking stations supporting the Pioneer Venus DLBI experiment

4 N76-15196

Helios Mission Support

P. S. Goodwin

DSN Systems Engineering Office

W. G. Meeks, R. E. Morris, and S. E. Reed

Network Operations Office

The Helios-1 spacecraft has completed its dual superior conjunctions and second perihelion passage of the Sun and is rapidly approaching its second aphelion, near the Earth's heliocentric trajectory. Valuable scientific data were obtained during these two important events. Helios-B testing activities are proceeding according to schedule, with test results reported in this article.

I. Introduction

This is the sixth article in a series that discusses the Helios-1 flight support provided by the DSN. The previous article (Ref. 1) reported on that mission period between the first and second superior conjunctions of the Helios-1 spacecraft and initial Helios-B test and training results. This article covers the Helios-1 second superior conjunction and second perihelion operations. Additionally, DSN tracking coverage and systems performance are discussed, as well as the Helios-B test and training activity.

II. Mission Status and Operations

A. Helios-1 Second Superior Conjunction

The second Helios-1 superior conjunction occurred on August 31, 1975, and lasted for only 16 days. The superior conjunction period is determined by the amount of time which is necessary for the spacecraft trajectory to cross from occultation entry minus 3 degrees, through solar

conjunction to exit plus 3 degrees, within the ecliptic plane. The second superior conjunction was relatively short as compared to the first, which took 56 days to traverse this "blackout" region. The second blackout period started on August 22 and extended through September 6, 1975. The spacecraft was configured for blackout two days earlier than planned when unexpected solar interference was encountered at a Sun-Earth-probe (SEP) angle of 3.65 degrees. A detailed spacecraft analysis was initiated by the German Control Center (GCC) when the spacecraft's downlink signal-to-noise ratio was unexpectedly degraded by 2 dB. The analysis revealed that the degraded performance could be attributed only to solar interference, which was much more intense than anticipated. During the time in which the spacecraft was configured for blackout operation, the Goldstone 64-meter station (DSS 14) was denoted the prime station for support of radio metric and polarimetry data. In addition to project requirements, the DSN Tracking and Telemetry Analysis Groups continued their own parallel studies of

the observed radio metric and spectral broadening effects resulting from the varied solar phenomena.

B. Helios-1 Second Perihelion

The second perihelion phase started four days after the termination of the second superior conjunction. The second Helios-1 perihelion occurred at 12:16 GMT (05:16 PDT) on September 21, 1975. The perihelion phase includes perihelion plus and minus 12 days while the probe gathers its objective data within the environs of our solar sphere. DSN support provided during the second perihelion was not continuous, as during the first perihelion, but the tracking coverage was substantial. The Goldstone 64-meter station did provide daily coverage during September; the Madrid 64-meter station, which was scheduled for the first time for Helios-1 support, covered six tracking passes at their longitude during the September portion of the second perihelion phase. DSN 26-meter station support was scheduled to complete the coverage requirements when their services were not committed to flight projects with higher priority than Helios 1.

The overall performance of the spacecraft's subsystems and science instruments during perihelion was excellent. At second perihelion the minimum distance to the Sun was 0.309 AU (46.2885 million km), and the distance to the Earth was 1.01 AU. As expected, the probe encountered slightly higher temperatures during the second perihelion. The increased temperatures were caused by the gradual degradation of the spacecraft skin due to the high-radiation environment.

C. Post-Perihelion Performance and Operations

A problem was observed on October 10, 1975, within the spacecraft's ranging subsystem. The anomaly occurred during a ranging pass over DSS 14 and was subsequently verified by the Australian and Madrid 64-meter stations. The anomaly is manifested by an apparent absence of ranging modulation on the downlink carrier when all other correlated spacecraft ranging functions appear normal. Subsequent to the Network verification, a special ranging test was conducted on October 18, 1975 at DSS 14. The uplink was modulated with a 500-kHz signal while a downlink spectrum analysis was performed to determine if the 500-kHz modulation was detectable. This test revealed that the modulation and a harmonic at a 1.5-MHz interval was present but markedly degraded. The ranging anomaly analysis continues under project and DSN investigation.

D. Tracking Coverage

The DSN is investigating the possibility of obtaining support for the Helios Mission from the Spaceflight

Tracking and Data Network (STDN). This cross support is desirable for all parties: the DSN is committed to an exceedingly demanding flight support program; STDN has available resources to provide support through the projected Helios mission lifetime; and the Helios project would receive data that would otherwise be lost. The present prospects for STDN cross support for Helios tracking coverage rose substantially with the completion of two STDN Helios data acquisition tests. The tests were conducted at Goldstone utilizing DSS 12 and the STDN-Apollo 26-meter station to determine the respective performance differences between an STDN 26-meter station and a standard 26-meter DSN station. Analysis of the real-time telemetry performance, coupled with non-real-time data retrieval from STDN analog tapes at the Merritt Island Compatibility Test Area (STDN (MIL 71)) will then provide long-range cross-support projection for Helios coverages. STDN (MIL 71), the only location where STDN-DSN systems are co-located, will become the focal point of the cross-support system. The STDN analog recordings will be converted to DSN digital recordings and merged into the Master Data Record at JPL via the high-speed data lines from STDN (MIL 71). While confidence of success remains high, a functional cost-effective operational system has yet to be completely demonstrated. Test completion is expected in mid-November 1975.

E. Actual Tracking Coverage Versus Scheduled Coverage

This report covers Helios-1 tracking coverage provided by the DSN from August 15 through October 16, 1975. Spacecraft operations during this time period included both the second superior conjunction and second perihelion.

The revised DSN long-range Helios-1 forecast had requested 101 tracking passes within this time frame. This requested coverage had projected continuous coverage throughout the second perihelion period. Due to higher priority commitments to other flight projects, continuous coverage for Helios 1 was not available. Nevertheless, DSN operations supported 122 Helios-1 tracking passes during this reporting period of 62 days, in which a total of 186 tracks were available. The total requested support equalled 54% of the available tracks with 66% actually supported, for a total of 927.2 hours of coverage. Total support during this period had a slight drop from the last period, but there was a 16-day blackout period where only DSS 14 was required to provide 14 days of coverage. The average pass duration changed little and was 7.6 hours long. Support during perihelion increased from 61 to 71%

of available tracks, excluding any mission support provided by the German network during perihelion. The DSN 64-meter stations supported for 626.1 hours out of the total 927.2 hours of coverage. In summary, the total Helios-1 DSN tracking coverage provided to the project continues to fulfill the total requested project tracking coverage requirements.

III. Helios-B Test and Training Status

The Helios-B mission has been delayed from its December 8, 1975 launch to a date between January 15 and February 7, 1976. The delay resulted from fire damage to the launch pad ground support equipment during launch of the Viking 2 spacecraft.

The test and training activities in preparation for Helios-B launch and flight support have been progressing according to schedule. Simulation System, Ground Data System, and Operations Verification tests were completed in September. Initial Acquisition and Step II Maneuver tests are scheduled for late October and early November. The Mission Operations System Tests began in mid-October.

A. Simulation System Tests

Simulation System testing was conducted with all 26-meter stations scheduled to support Helios B. These tests verified correct long-loop operation of the Helios system while also providing operator training. This system was used to support the Mission Operations System tests.

B. Ground Data System Tests

Two Ground Data System (GDS) tests were conducted during September, prior to joining the German network in the U.S.-German Performance Demonstration Test on September 28, 1975. The objectives of the latter test were to verify the performance of the Helios GDS Telemetry, Command, and Monitor System functions and to verify the system interfaces between the Jet Propulsion Laboratory and the German Control Center (GCC), while the respective Control Centers were operating in their normal multimission environments. All test objectives were met; therefore, the U.S.-German Combined System Test, which had similar objectives, was cancelled. The Ground Data System was declared ready to support the Mission Operations System tests.

C. DSN Test and Training

The 26-meter stations completed their Operation's Verification tests for Helios B in early September with the last three tests being performed with DSS 42, 61, and 62.

These tests were conducted during Helios-1 spacecraft tracks and were designed to test only those operational requirements infrequently used in day-to-day operations, such as manual mode commanding and analog tape playback. All three tests were successfully completed, reinforcing the Helios-B test and training philosophy of minimizing redundant testing and concentrating on Helios-B unique operational requirements.

Special DSN tests, concerning critical portions of the mission (Initial Acquisition and Step II Maneuver), were begun in mid-October, and will continue through mid-November. Approximately six each of these tests are planned, four in October with the remaining in November. As of this writing three Initial Acquisition tests have been conducted with DSS 42/44. All have been completed satisfactorily with only minor discrepancies. The two recent Viking launches have added a measure of confidence and experience to the operational crews.

Step II Maneuver Tests are planned for the first half of November with DSSs 11 and 12. Each station is scheduled to perform three Step II Maneuver Tests.

In the interest of reducing the number of test conflicts between Helios B and various flight projects, and because of the excellent results of testing thus far, the DSN Helios-B Performance Demonstration Tests were cancelled. DSN Configuration Verification Tests have been scheduled for late December. The Helios-B Spacecraft End-to-End Test (spacecraft-STDN (MIL 71)-JPL-German Control Center) is now due to be performed the first week of November.

D. Mission Operations System Test and Training

Mission Operations System (MOS) tests and training began on October 21 with a Helios-B launch exercise. This test, conducted from the German Control Center, was successfully completed while simulating the Initial Acquisition at DSS 42. The backup Spacecraft Operations Team and Attitude Control Team, located at JPL, also participated in these tests. Two other MOS tests, Step II Maneuver, and Post Step II Maneuver plus Experiment Turn-On, were scheduled during the month of October. Both tests employed computer simulation of the Deep Space Stations. Actual DSN support of MOS testing is scheduled to begin in mid-November and continue until launch.

IV. DSN System Performance for Helios

A. Command System

The DSN command activity for Helios 1 sharply increased over the last period because of increased command requirements during the perihelion period. During August and September 1975, the DSN transmitted 3349 commands to Helios 1; in the prior period only 1803 commands were transmitted. The DSN cumulative total now stands at 18,632 commands transmitted with an attendant abort total of 11. The DSN Command System experienced one abort for a cumulative total of 3 aborts. Project aborts also increased by 1, to a total of 8 project aborts.

The DSN abort occurred at DSS 42 in Australia and was caused by a GMT timing problem in the Telemetry and Command Processor. The correction for this anomaly was to reseal the logic cards within the time display buffer of the computer.

The command capability lost throughout the DSN decreased in proportion to total support and was 5.85 hours. The 64-meter and 26-meter station contributions were also representative of their respective support. Additionally, 57 minutes of command capability were lost due to overseas high-speed data line outages. In total, 11 incidents resulted in 6.8 hours of lost command capability to the Helios Project, with the longest outage being 70 minutes and the average outage equal to 37 minutes.

B. Tracking System

The performance of the DSN Tracking System during superior conjunction and perihelion continued to more than satisfactorily fulfill all DSN and Helios Project requirements. One significant Discrepancy Report was submitted on a DSS 42/43 planetary ranging subsystem problem. Fortunately, it was a timing interface problem, and it has been determined that the ranging data will eventually be recoverable when an appropriate timing bias is applied to the data reduction process.

Superior conjunctions always reflect the importance of radio metric data, and extensive analysis of these data was performed by both the Project Scientists and the DSN Tracking Analysis Group. Following considerable work, the DSN Tracking Analysis Group has developed an improved model of the effects of Sun-Earth-spacecraft geometry upon doppler noise. This model is now being used and was compared to an extensive set of historical values of doppler noise. Very good correlation has been obtained using this model, and its results will be reported

in greater detail in a separate report initiated by the DSN Tracking Analysis Group.

A special 2-MHz doppler bias capability was implemented to insure quality doppler data during the second Helios-1 perihelion. Due to the Sun-Earth-probe geometry during this perihelion, the Earth-received doppler is shifted in a negative direction outside the normal operating range of the Tracking System. Selected DSN stations received the modified doppler configuration for operational support from September 11 to October 11, 1975. Additionally, the stations had to compensate for the excessive doppler effects in the uplink and downlink communication signal by switching from the standard S-band channel 21 frequency. The doppler effect resulted in a receive frequency within the channel 22 range, while the transmitter frequency dropped to a channel 20 frequency. This operational mode existed from September 3 to October 24, 1975. These special modes operated flawlessly during this important stage of the mission.

C. Telemetry System

The analysis of the Telemetry System performance during August and September was accomplished in two parts. All solar conjunction data analysis is viewed as extraordinary data and is outside the normal range of performance analysis. Therefore, a special data analysis and report was undertaken by the DSN Telemetry Analysis Group.

All other Helios-1 telecommunication link performance data during this period revealed the following trends. Preceding entry into superior conjunction, both the downlink signal level and the signal-to-noise ratio departed from established trends and had degraded performance curves earlier than expected. Following superior conjunction, the degradations returned to their normal trends. The average signal level differential for actual-versus-predicted performance is near zero dB, while the actual-versus-predicted signal-to-noise ratio average is -0.5 dB. There were no significant discrepancy reports during this period. A problem area which has been corrected concerned numerous Discrepancy Reports on erroneous signal level calibration curves; most of the errors were operator procedural errors. The DSN Telemetry Analysis Group is also supporting the on-going analysis of the aforementioned spacecraft ranging problem.

V. Conclusions

The Helios-1 spacecraft has now completed its second superior conjunction and second perihelion of the Sun. As

the spacecraft enters its second aphelion, making its closest approach to the Earth, all experiments except spacecraft ranging remain active. During the second superior conjunction and second perihelion, data from both passive and active spacecraft subsystems and ground experiment instruments again contributed to an increased and much-valued second opportunity for the Helios Project scientists to collect collaborating solar data.

The preparations for Helios-B launch and flight support (now scheduled for late January 1976) have increased

during this report period and are presently progressing smoothly. Special tests conducted between the DSN and the Spaceflight Tracking and Data Network seem promising as a possible alternative for providing future Helios telemetry coverage.

As other flight project support activities increase, DSN coverage of the Helios-1 spacecraft is likely to decrease from previous levels.

Acknowledgment

The authors wish to thank the following persons from the Network Operations Analyst Group, for their contribution of Periodic Network Performance Reports: Command—R. Frampton, B. Hoffman, and W. Tucker; Telemetry—J. Henricks and C. Lunde; Tracking—R. Schlaifer.

Reference

1. Goodwin, P. S., et al., "Helios Mission Support," in *The Deep Space Network Progress Report 42-29*, pp. 15-19, Jet Propulsion Laboratory, Pasadena, Calif., Oct. 15, 1975.

N76-15197

A New Global Ionospheric Model

K. W. Yip and O. H. von Roos
Tracking and Orbit Determination Section

A new global ionospheric model has been successfully implemented. The daytime portion of this model provides one-way ionospheric range corrections that compare favorably with those derived from the Mariner Venus/Mercury (MVM'73) S- and X-band dual frequency doppler data. For elevation angles, γ , higher than 30 deg and solar zenith angle, X , less than 80 deg, this model provides calibrations accurate to a few centimeters. The calibrations provided by the nighttime model are also very reasonable. These, however, will have to be compared with the S/X data from Viking '75 for final confirmation.

It is interesting to note that the daytime ionospheric calibrations derived from the current calibration scheme, DIEN/TIEN, are fairly close to those given by the new global model, especially in the temporal variations and thus the doppler effects. In the daytime and for $\gamma \geq 30$ deg and $X < 80$ deg, the calibrations from the two models agree almost exactly. However, for situations when γ is below 30 deg and X is larger than 80 deg simultaneously, as much as 12% (~ 70 cm, typically) improvement of the new model over DIEN/TIEN results.

The comparison between the nighttime model and DIEN/TIEN has been based on the one-way ionospheric range corrections for three passes near the Mariner 9 encounter with Mars in 1971 tracked at Goldstone. It is found that they can differ by over 30% (typically 20 cm). As mentioned, the confirmation of these nighttime calibrations awaits the availability of the Viking S/X dual frequency doppler data.

Finally, the ionospheric calibration effects on orbit determination provided by DIEN/TIEN, the global model, and the S/X data will be intercompared during the Viking Mission.

I. Introduction

It has been shown (Ref. 1) that the Chapman ionospheric electron content distribution (Ref. 2), which the ionospheric calibration model DIEN/TIEN (Ref. 3) uses for deep space probe tracking, is an inadequate representation of Earth's ionosphere for low elevation angles and large solar zenith angles. Moreover, this electronic distribution, which is used in the daytime model, may not be a good description for the nighttime ionosphere. To improve the DSN spacecraft tracking capability, a global ionosphere model (Ref. 1) has been developed. This model consists of three distinct parts: the daytime model, the nighttime model, and the dawn model. Physically, the daytime model consists of the situation when electron production in the ionosphere due to solar ultraviolet predominates. This differs from the Chapman model in that the curvature of Earth has been taken into account, thus avoiding the singularity in the Chapman model when the solar zenith angle, X , is close to 90 deg. The nighttime model encompasses the situation when recombination and diffusion of the ionospheric electrons dominate. Finally, the dawn model considers the transition from the nighttime model to the daytime model. This article reports on the implementation and application of the daytime and nighttime ionospheric models. It has also been shown that the duration of dawn in the ionosphere is so short (~ 5 min) that the implementation of this part of the model is not necessary.

sphere is so short (~ 5 min) that the implementation of this part of the model is not necessary.

II. Mathematical Background of the Daytime Ionospheric Model

Several assumptions are involved in the development of the daytime model:

- (1) N , the number density of the ionospheric neutral species obey an exponential law, i.e.,

$$N = N_0 \exp \left[- \left(\frac{r - R_e}{H} \right) \right]$$

where

N_0 = number density at Earth's surface

R_e = radius of Earth

H = scale height of neutral species

- (2) Macroscopic charge neutrality, i.e., $N_i = N_e$ where the subscripts i and e represent ions and electrons, respectively.

- (3) Stationary condition, i.e., $(d/dt) N_e = 0$

With these assumptions, the electronic distribution as a function of geocentric distance, r , is

$$N_e(r) = k_1 \exp \left\{ \frac{1}{2} \left[- \frac{r - R_e}{H} + k_2 \int_{\infty}^r \exp \left(- \frac{x - R}{H} \right) \left(1 - \frac{y_0^2 + z_0^2}{x^2} \right)^{-1/2} dx \right] \right\} \quad (1)$$

where k_1 and k_2 are constants involving the ultraviolet absorption cross sections, recombination coefficients, and other physical parameters of the air molecules and solar radiation, and y_0 and z_0 are the Cartesian coordinates in a Sun-fixed coordinate system (Fig. 1).

The first principle quantities (k_1 , k_2) in Eq. 1 are then linked to the Chapman parameters of a Chapman ionosphere, which is given by

$$N_e^{\text{Chap}}(Z) = N_{e_{\max}} \exp \left\{ \frac{1}{2} [1 - Z - \sec X \exp(-Z)] \right\} \quad (2)$$

where

$$Z = \frac{r - R_e - h_{\max}}{H}$$

X = solar zenith angle, angle between the direction of the Sun's rays and the observer's zenith,

$N_{e_{\max}}$ = maximum electron concentration at altitude $h = h_{\max}$ and for $X = 0$

H = scale height of the ionosphere.

In other words, $X = 0$ in Eq. (2) corresponds to $y_0 = z_0 = 0$ in Eq. (1). Thus

$$N_e(\gamma) = N_{e_{\max}} \exp \left\{ \frac{1}{2} \left[1 - Z + \int_{\infty}^Z \frac{\exp(-x)}{\left(1 - \frac{y_0^2 + z_0^2}{(Hx + R_e + h_{\max})^2} \right)^{1/2}} dx \right] \right\} \quad (3)$$

where

$$y_0 = (HZ + R_e + h_{max}) \sin \theta_0 \sin \phi_0$$

$$z_0 = (HZ + R_e + h_{max}) \cos \theta_0$$

with ϕ_0 and θ_0 the longitude and colatitude in the Sun-fixed coordinate system (Fig. 1).

It has been shown (Ref. 4) that the range correction due to a tenuous plasma is given by

$$\Delta \rho = \frac{2\pi e^2}{m \omega^2} \int_{R_e} dr \left(1 - \frac{R_e^2 \cos^2 \gamma}{r^2} \right)^{-1/2} N_e(s(r)) \quad (4)$$

The additional symbols in Eq. (4) are defined as: $s(r)$, the unperturbed (straight) ray path between the Earth-bound station and the distant spacecraft expressed as a function of r , which is the distance from the center of Earth; and γ , the elevation angle. In principle, therefore, Eq. (3) and Eq. (4) combined yield the ionospheric range change along any tracking station (location θ_0 , ϕ_0)—spacecraft line of sight.

Now the Sun-fixed coordinates y_0 , z_0 can be related to the Sun-fixed geographic locations θ_0 , ϕ_0 and the elevation and azimuth angles γ and α . All these in turn can be transformed back into the usual Earth-fixed coordinate system. The details of this are outlined in Ref. 1 and are not repeated here. Only a summary of the relevant equations is displayed below:

$$S = -R_e \sin \gamma + \sqrt{r^2 - R_e^2 \cos^2 \gamma} \quad (5)$$

$$y_0 = S(\sin \gamma \sin \theta_0 \sin \phi_0 - \cos \gamma \cos \alpha \cos \theta_0 \sin \phi_0 + \cos \gamma \sin \alpha \cos \phi_0) + R_e \sin \theta_0 \sin \phi_0 \quad (6)$$

$$z_0 = S(\sin \gamma \cos \theta_0 + \cos \gamma \cos \alpha \sin \theta_0) + R \cos \theta_0 \quad (7)$$

$$\cos \theta_0 = \sin \delta_0 \sin \theta_0 \cos \phi_0 + \cos \delta_0 \cos \theta_0 \quad (8)$$

$$\begin{aligned} \sin \theta_0 \cos \phi_0 = & -\cos T \sin \delta_0 \cos \theta_0 \\ & + \cos T \cos \delta_0 \sin \theta_0 \cos \phi_0 \\ & - \sin T \sin \theta_0 \sin \phi_0 \end{aligned} \quad (9)$$

$$\begin{aligned} \sin \gamma \cos \theta_0 + \cos \gamma \cos \alpha \sin \theta_0 = & \sin \delta (\sin \gamma \sin \theta_0 \cos \phi_0 \\ & - \cos \gamma \cos \alpha \cos \theta_0 \cos \phi_0 - \cos \gamma \sin \alpha \sin \theta_0 \\ & + \cos \delta (\sin \gamma \cos \theta_0 + \cos \gamma \cos \alpha \sin \theta_0)) \end{aligned} \quad (10)$$

For these equations, the subscript 0 refers to quantities in the Sun-fixed coordinate system whereas the subscript

G refers to quantities in the Earth-fixed coordinate system. γ , the elevation angle, is the same in both systems while the azimuth is transformed from α to α_0 . δ_0 is the declination of the Sun and $T \equiv 12^h - UT$ is the time coordinate.

III. Implementation of the Daytime Ionospheric Model

The daytime ionospheric model has been used to map the ionospheric total electron contents from a station-geostationary satellite ray path to the station-spacecraft ray path. As is the case with the old ionospheric model DIEN/TIEN, the input Faraday rotation data are space-time translated and then mapped to the desired elevation angle, γ . This elevation angle mapping is accomplished by the multiplication of the ratio of the range change at γ to that at $\gamma = 90$ deg. However, the elevation angle mapping of the new model does not involve the ray-trace solutions through a Chapman ionosphere. This avoids the inadequacies of the Chapman ionospheric representation at large solar zenith angles and low elevation angles of the old model. The magnetic latitude adjustments are again applied in a similar manner.

A computer program has been coded for the implementation of the daytime ionospheric model. The boundary of the "daytime" ionosphere is defined conservatively. Figure 2 shows a schematic Earth in the Sun-fixed coordinate system. A tracking station S is considered to be tracking in the daytime only if $|\phi_0| \leq 90$ deg. This is conservative since for the situation illustrated in the figure, no calibration will be provided even though the tracking is still done in the daytime ionosphere. This conservative "cut-off" does not affect the following comparisons.

IV. Validity of the Daytime Ionospheric Model

During the MVM'73 mission, both S- and X-band doppler data were available. Thus the station-spacecraft line-of-sight charged particle contents (i.e., both of ionospheric and space plasma origin) were readily deduced (Ref. 5). The three earliest S/X dual-frequency passes in the mission have been chosen in the comparison with the calibrations provided by the daytime ionospheric model.

Due to the proximity of the spacecraft to Earth for these three passes, the significance of solar plasma contribution to the line-of-sight charged particle content is probably minimal. Moreover, the calibrations provided by these three passes have been compared in detail with those

provided by the old ionospheric calibration program DIEN/TIEN (Ref. 6). Thus, the improvement, if any, of the new daytime model over the old one can be deduced as well.

Figures 3, 4, and 5 show the comparisons of the charged particle calibrations provided by the S/X dual-frequency doppler data and the new daytime ionospheric model. The calibrations given for DIEN/TIEN are also plotted on the same figures for comparison. Except for the beginning and end portions of the second pass (Dec. 30, 1973), the old and new models yield almost identical one-way ionospheric range changes.

1. Pass 1: December 15, 1973. The first S/X data of suitable quality were obtained at DSS 14 on December 15, 1973 (Fig. 3). The data spans ~ 6 h. They reveal a long term decrease in the line-of-sight electron content: a 1-m decrease over the 6-h interval. In addition to the long-term signature, there is also a repetitive short-term structure (~ 40 min from one local maximum to the next). These short-term structures have been found to be correlated with the roll limit cycle of the spacecraft by B. W. Dysart and W. L. Martin. Modification of the experimental dual frequency receivers at the Mars Station, Goldstone, corrected this problem. Subsequent S/X data passes do not show this repetitive structure.

Table 1 shows the prevalent elevation angle, γ , and solar zenith angle, X , for the beginning and end portions of the three passes. It can be seen that for this first pass, when the elevation angle is fairly low ($\lesssim 30$ deg), the solar zenith angle is not excessively high ($\lesssim 60$ deg). Thus reasonable ionospheric modeling should result (Ref. 1) and, as expected, the agreement between the S/X and the new ionospheric calibrations is good to ~ 10 cm throughout the entire pass.

Table 2 shows the values of the Chapman parameters on this day obtained by means of ionosonde data from Point Arguello, California, and White Sands, New Mexico. Figure 6 displays the variations of the ionospheric reference points (Ref. 3) between the station-spacecraft ray path on this day and the two ionosonde data sources. Since rather significant uncertainties could be involved in ionosonde measurements (Ref. 7), constant values of 250 km and 39 km have been used, respectively, for the Chapman parameters h_{max} and H in the computation of one-way range effects from the daytime model on this day (Eq. 3 and 4). Moreover, these numbers are approximate averages of those observed at the two ionosonde sites.

The mapped Faraday rotation data assess only the total electron content of the ionosphere along the station-spacecraft line of sight, while the S/X dual doppler data assess the variation of the electron content of the ionosphere and the space plasma collectively. Since the S/X and Faraday data yield electron contents that do not drift relative to each other by more than 0.2 m, the plasma must not exceed this level during the 6-h period of this pass.

Since the Faraday data have to be mapped over a distance of more than 1500 km (~ 13 deg in angular separation at the ionospheric reference points) in the beginning of the pass, and more than 350 km (~ 3 deg in angular separation) at the end of the pass, the fine structure variations along the station-spacecraft ray paths are not expected to be accounted for by the "mapped" Faraday data. As seen in Fig. 3, the short-term variations of the Faraday and S/X data do not correlate, and the maximum difference is < 0.2 m.

2. Pass 2: December 30, 1973. Again, the relevant elevation and solar zenith angles for this pass are shown in Table 1. Towards the end of the pass, low elevation angles ($\lesssim 30$ deg) are accompanied by large solar zenith angles ($\gtrsim 90$ deg). As expected, the new and old ionospheric models diverge the most ($\lesssim 10$ cm) towards the end of the pass, with the new model in better agreement with the S/X data. Since the old model is based on a Chapman ionospheric profile, which is known to be inadequate for $X \gtrsim 85$ deg (Ref. 2), the disagreement between the old model and the S/X data is not too surprising. The new model, however, should be valid for the entire daytime ionosphere. Thus, it is likely that the S/X data are detecting space plasma variations as well as those of the ionosphere. Figure 4 reveals that the S/X electron content is higher than the Faraday electron content in the beginning of the pass while the reverse is true for the end of the pass. Recalling that the S/X data measure only the time rate of change of the line-of-sight electron content, while the Faraday data measures the absolute line of sight total electron content, the disagreement can be explained by having a plasma cloud entering the station-spacecraft ray path in the beginning of the pass and leaving it towards the end.¹ Since the motion of the cloud relative to Earth is not known, the size of the cloud cannot be ascertained. The existence of a plasma

¹This explanation is plausible because the Earth-spacecraft distance has been 15×10^6 km on this day. Typical plasma cloud dimensions are of the order of 10^6 km. Therefore, a plasma cloud may well have entered the ray path without engulfing Earth and affecting the ionosphere.

cloud drifting across the station-spacecraft ray path however, can explain the disagreements between the Faraday and S/X calibrations observed during this pass.

It should be noted that constant values of 250 km and 39 km have been adopted again for the parameters h_{max} and H (Table 3). Attempts made to account for the disagreements between the Faraday and S/X data by varying these parameter values have not succeeded. It has been found that the sensitivity of the one-way range change on the parameter H is very small. Moreover, an increase of h_{max} from 250 km to 350 km decreases the range change at UT $\approx 24^h 70$ ($\gamma \approx 36$ deg) by only $\lesssim 1\%$, for example. Thus, uncertainties in the parameter values cannot cause the discrepancies. The existence of space plasma seems to be a very plausible explanation.

3. Pass 3: January 3, 1974. Table 1 shows the relevant angular information for this pass and Fig. 5 displays the three calibrations. The agreements between these calibrations are excellent. This stems from two developments: DSS 14 S/X hardware had been modified and the data were taken at a more favorable geometry, i.e., elevation angles were higher ($\gtrsim 40$ deg) and the Faraday data had to be mapped over a shorter distance ($\lesssim 6$ deg in angular separation of the ray paths). The maximum difference between the mapped Faraday and the S/X measurements is < 0.05 m.

V. Mathematical Background of the Nighttime Ionospheric Model

In Ref. 1, the electron density approximately applicable at high altitudes ($\gtrsim 300$ km) as a function of time and height is given by

$$\frac{\partial N}{\partial t} = \alpha \exp(z) \left(\frac{\partial^2 N}{\partial z^2} + \frac{3}{2} \frac{\partial N}{\partial z} + \frac{1}{2} N \right) - \beta \exp(-z) N \quad (11)$$

where the first term on the right-hand side of the equation is responsible for the diffusion and the second term for attachment (α and β are the diffusion and recombination coefficients respectively). These are the only processes assumed to be occurring in the ionosphere at nighttime. Solving this linear differential equation, the solution is found to be the summation of a series of Laguerre polynomials, with the constants determined by matching the boundary conditions with the daytime ionospheric electron distribution at dusk. It has been found, however, that for most cases, this sum converges slowly. It is therefore not suitable for analytic applications. However, this

series can be summed in closed form. Thus, the nighttime ionospheric electron profile is then given by:

$$N(z, t) = \left(\frac{\beta}{\alpha} \right)^{1/4} N_{max} \exp \frac{1}{2} \left\{ \left(1 + \frac{h_{max}}{H} \right) \right\} (1 - X)^{-1/2} \\ \times \left(A + \frac{X}{1 - X} \right)^{-1/2} \exp \left\{ -z - \frac{1}{2} Y \right\} (XY)^{-1/2} \\ \times \exp \left\{ -\frac{3}{2} \sqrt{\alpha \beta} t + Z - XY/(1 - X) \right\} \\ \times \{ 2 \operatorname{erf}(\sqrt{Z}) \} \quad (12)$$

where

$$z = \frac{r - R}{H}$$

$$Z = XY / \{ (1 - X)^2 A + X(1 - X) \}$$

$$X = \exp \{ -2 \sqrt{\alpha \beta} t \}$$

$$Y = 2 \sqrt{\beta / \alpha} \exp(-z)$$

$$A = \frac{1}{2} \left(1 + \sqrt{\frac{\pi R \alpha}{2 H \beta}} \exp \left(\frac{h_{max}}{H} \right) \right)$$

and

R = radius of Earth

H = ionospheric scale height

α = diffusion coefficient of electrons in s^{-1} (see Ref. 1)

β = attachment coefficient of electrons in s^{-1} (see Ref. 1)

t = time in seconds from dusk

h_{max} = height above ground where electron density distribution is maximum

N_{max} = maximum electron concentration at altitude $h = h_{max}$ and for solar zenith angle, X , = 0.

Note that the parameters H , h_{max} , N_{max} appear due to the matching of boundary conditions between the daytime and nighttime ionospheres at dusk. In terms of the geocentric distance, r , this electronic distribution can be written as

$$N(r, t) = N_{max} \exp \left[\frac{1}{2} \left(1 + \frac{h_{max}}{H} \right) \right] [AX(1 - X) + X^2]^{-1/2} \\ \times \exp \left[-\frac{3}{2} \sqrt{\alpha \beta} t \right] \exp \left\{ -\frac{1}{2} \left(\frac{r - R}{H} \right) \right\} \\ + \sqrt{\frac{\beta}{\alpha}} \left[\frac{X - A(1 + X)}{X + A(1 - X)} \right] \exp \left(\frac{r - R}{H} \right) \operatorname{erf}(\sqrt{Z}) \quad (13)$$

Thus, the range change, $\Delta\rho$, due to this nighttime ionospheric electron distribution is

$$\begin{aligned} \Delta\rho(t) = & \frac{2\pi e^2}{m\omega^2} N_{max} \exp\left[\frac{1}{2}\left(1 + \frac{h_{max}}{H}\right)\right] \{AX(1-X) + X^2\}^{-1/2} \\ & \times \exp\left[-\frac{3}{2}\sqrt{\alpha\beta}(UT - T_{90})\right] \\ & \times \int_R^\infty d\tau \left(1 - \frac{R^2 \cos^2 \gamma}{\tau^2}\right)^{-1/2} \exp\left\{-\frac{1}{2}\left(\frac{\tau - R}{H}\right)\right. \\ & \left. + \frac{\beta}{\alpha}\left[\frac{X - A(1+X)}{X + A(1-X)}\right] \exp\left(-\frac{\tau - R}{H}\right)\right\} \operatorname{erf}(\sqrt{Z}) \end{aligned} \quad (14)$$

where $T_{90} = \cos^{-1}(\tan \delta_\odot \cot \theta_G) - \phi_G + \pi$ is the universal time when the tracking station in question has a "Sun-fixed" station longitude equal to $\pi/2$ (see Section III). In other words, nighttime ionospheric condition prevails from this time on.

Furthermore,

δ_\odot = declination of the Sun.

θ_G = geographic tracking station co-latitude

ϕ_G = geographic tracking station longitude

Incidentally, Eq. (14) is, in appearance at least, very much different from the range change given by a Chapman-like electronic distribution. Thus, the ionospheric range changes resulting from the new nighttime model may be quite different from those given by DIEN/TIEN.

VI. The Diffusion and Recombination Coefficients

The implementation of the nighttime ionospheric model depends on obtaining reasonable values for the diffusion and recombination coefficients α and β . Unfortunately, as mentioned in Ref. 8, these values are quite uncertain. They not only depend on the exact knowledge of the composition in the upper ionosphere, but also on the knowledge of the exact diffusion and recombination rates. At a 300-km altitude they are given as $1.95 \times 10^{-4} \text{s}^{-1}$, $2.6 \times 10^9 \text{cm}^2/\text{s}$, and $4 \times 10^{-4} \text{s}^{-1}$, $2 \times 10^{10} \text{cm}^2/\text{s}$ respectively for moderate levels of solar activity. Although attempts (Ref. 11) to explain the order of magnitude difference between the experimental value of α by Quinn, et al. (Ref. 9), and the theoretical value by Risbeth, et al. (Ref. 10), have been made, the situation is still very uncertain due to the lack of the exact knowledges men-

tioned above. Moreover, since these conditions are quite variable from region to region, it would only seem reasonable to use the α and β values that are determined locally. As a matter of fact, as will be shown below, the evaluation of the ionospheric one-way range changes using the "best" values of α and β from Quinn, et al., yields unacceptable results.

The following procedure illustrates how the values of α and β can be determined for Goldstone using the zenith total electron content (TEC) data measured at Goldstone, and Eq. (13).

The time dependence of the zenith TEC as given by Eq. (13) is fairly complex. Note that the time dependence is contained in the parameters X and Z and thus in the terms $\{AX(1-X) + X^2\}^{-1/2} \operatorname{erf}(\sqrt{Z})$, $\exp -(3\sqrt{\alpha\beta}t)/2$ and $\exp \sqrt{\beta/\alpha} [X - A(1+X)]/[X + A(1-X)]$. Fortunately, it can be shown that for the nighttime ionosphere, i.e., $0 \leq t \lesssim 12$ h, the first and third terms vary fairly slowly in comparison to the second one, $\exp -(3\sqrt{\alpha\beta}t)/2$. This is confirmed by the actual zenith TEC measurements. Figures 7 and 8 show four days (November 11, 12, 13, and 14, 1971) of zenith TEC observed in Goldstone. These TECs are plotted on semi-log scales. Except for November 12 (more discussion on this day later), an exponential decay in the zenith TEC is clearly indicated after T_{90} (footnote 2), confirming that $\exp -(3\sqrt{\alpha\beta}t)/2$ is the dominating factor. Moreover, it can also be shown that while the first and third terms vary by factors of two or three over the whole night, the exponential decaying factor varies by two to three orders of magnitude. Thus it can be concluded that the decay has the slope roughly equal to $1.5\sqrt{\alpha\beta}$.

It is obvious that a constant set of α and β cannot be used for the entire night. If this were the case, changes in range of two to three orders of magnitude would be expected, and this would not agree with the observations. As can be deduced from Figs. 7 and 8, the first set is applicable only for a few hours after dusk. A second (or maybe even third set) will have to be applied later during the night.

Before discussing the second and/or third set of values for α and β , investigation will now be made on the values for the first set, i.e., the set applicable from around dusk on. Since only the product $\alpha\beta$ (Table 4) can be determined from the measured zenith TEC data, another independent determination has to be available. The clue

²The beginning of night.

to this determination comes from the observation that the value of β seems to be more consistent from different sources (e.g., Refs. 9 and 10). Thus, the approach here is to adopt a published value for β and then determine the value of α from the derived product of α and β . Moreover, to justify the validity of the above approach and to obtain an idea for the uncertainty of the resultant range change, computations for other values of β (variations over a decade, 0.5 s^{-1} to 5 s^{-1}) and their corresponding values of α have been used in the determination of $\Delta\rho$. Table 5 shows the range corrections for the different α and β values for the three nights under investigation. The daytime range changes have also been computed (Section III) for comparison. It is seen that the variation in $\Delta\rho$ due to the different α and β values is reasonably small ($\lesssim 15\%$, $\sim 12 \text{ cm}$). Besides, the variation in β is usually much less than an order of magnitude anyway.

β and α in Eq. (13) can also be obtained from published values by the multiplication of the factor $\exp \pm(300/H)$ (footnote 3). Note that different signs apply to α and β since recombination decreases with increases of altitude (from $\sim 300 \text{ km}$ upward) while the reverse is true for diffusion. It should also be noted that, following Quinn, et al. (Ref. 9), the scale height H is taken to be 33 km for the recombination process and 66 km for the diffusion process.⁴ Table 6 shows the α and β values thus derived. As mentioned, the corresponding range corrections are unacceptably large.

Table 4 also shows decaying exponents for other parts of the night for November 11, 13, and 14. Note that within the framework of the present nighttime model, an increase in zenith TEC cannot be accounted for. This is the reason why the evaluation for the nighttime ionospheric range change for November 12 has been omitted.⁵

Now, the knowledge of the values for α and β during the so-called 'night-stationary' conditions (Ref. 10) are even less understood. However, as will be shown later, when the product of α and β takes on such small values, it does not matter much what the exact values of α and β

³The reason for the factor $\exp \pm(300/H)$ is the fact that both α and β have been given for $h = 300 \text{ km}$ and have to be scaled accordingly for any other altitude.

⁴Diffusion scale height for electrons = two times scale height for neutrals (Ref. 12).

⁵The reason for the increase in TEC later during the night on November 12 can be explained only by lateral motion of the upper atmospheric gas masses or cosmic ray bursts. Such effects have not been incorporated into the present model.

are. Table 7 shows the range changes for the other parts of the nights with α and β taking on arbitrary values but keeping their products fixed. For the November 14 pass, the second slope is so close to zero that the product α and β is several orders of magnitude smaller than the values obtained for the other two nights. Incidentally, it is interesting to note that when the values of α and β are small enough, as in the case of November 14, further decrease in their product values causes no variation in the one-way range changes. It should be noted, however, that although no major variations have been obtained using these arbitrary values of α and β , this lack of an exact knowledge and the resulting differences in $\Delta\rho$ ($\gtrsim 0.1 \text{ m}$) set a limit to the accuracy of range change evaluation for the second and subsequent portions of the nighttime ionosphere.

VII. Nighttime Ionospheric One-Way Range Changes

Figures 9, 10, and 11 show the one-way range changes due to the nighttime ionosphere on November 11, 13, and 14 in 1971 for the spacecraft Mariner 9 tracked by DSS 14 at Goldstone. The daytime portion of the ionospheric range changes have been computed using the new daytime model (Section III). Note that due to the unfavorable elevation angle ($\lesssim 35 \text{ deg}$) and solar zenith angle ($\gtrsim 90 \text{ deg}$) geometry, the improvement of the daytime model over DIEN/TIEN ($\lesssim 70 \text{ cm}$) is more apparent. Different values of α and β are also indicated. It is seen that the values of α and β can vary by factors of two and still yield reasonable one-way range changes. It seems that this uncertainty can be resolved only when S/X dual-frequency doppler data from the spacecraft become available in the nighttime. The gap between the day and night range changes is due to the loss of precision of the computer when the integration of the daytime model gets to be too close to dusk. Attempts will be made to improve on this. Incidentally, when this gap gets to be sufficiently small, it may be possible to select out the nighttime curve for the proper values of α and β . Note also that one-way range points from the current ionospheric calibration technique DIEN/TIEN have also been plotted. Although magnitude-wise, the difference between the new nighttime model curve and the DIEN/TIEN curve may be fairly small ($\sim 22 \text{ cm}$), the fractional difference is quite large ($\gtrsim 30\%$) due to the smaller range changes in the nighttime ionosphere.

It should be pointed out that a preliminary study in the improvement of the tracking doppler residuals by

means of the ionospheric calibrations from these three passes are rather inconclusive. More passes of calibration with the new global ionospheric model will be evaluated and the results will be published in a future article.

VIII. Ionospheric Model at Dawn

As was pointed out earlier, the duration of twilight (Fig. 12) in the upper ionosphere at midlatitudes either north or south from the equator is rather short. This means that the transition from complete darkness to complete daylight in the *F* layer of the ionosphere may be neglected as far as range correction computations are concerned, thus saving considerable time and effort.

It has been shown (Ref. 1) that the duration of twilight is given by the expression:

$$\tau_t = \dot{\theta}^{-1} \sin^{-1} \left\{ \frac{\cos \delta_\odot}{\sin \theta_G} \left[\left(2 \frac{h_{max} + H}{R} \right)^{1/2} - \left(2 \frac{h_{max}}{R} \right)^{1/2} \right] \right\} \quad (15)$$

Here τ_t is the duration of twilight, δ_\odot is the declination of the sun, θ_G the geographical colatitude, h_{max} the altitude of maximum electron density, H the scale height of the *F* layer, R is the radius of Earth, and $\dot{\theta} = 7.3 \times 10^{-5}$ rad/s, Earth's spin rate. Taking nominal values for h_{max} , H , and R (i.e., $H = 39$ km, $h_{max} = 250$ km, $R = 6370$ km) we find:

$$\tau_t = 1.4 \times 10^4 \sin^{-1} \left\{ 0.021 \frac{\cos \delta_\odot}{\sin \theta_G} \right\} [s] \quad (16)$$

Table 8 shows a list of the twilight durations τ_t for $\theta_G = 60$ deg, the approximate colatitude of the DSN stations as a function of δ_\odot .

We therefore see that the transition time between night and day is rather short. The reason for this is the

fact that only geometrical factors enter the derivation of Eq. (15), since light scattering is negligible because of the low density of matter ($\ll 10^{14}$ atoms/cm³). In other words, shadows are sharp.

IX. Conclusion

On the basis of the comparisons with the S/X dual-frequency doppler data from MVM73, it can be concluded that as the old model DIEN/TIEN, the new daytime ionospheric model is capable of calibrating the station-spacecraft ray-path ionospheric total electron content to a few centimeters for elevation angles $\gtrsim 30$ deg and solar zenith angles $\lesssim 80$ deg. However, for elevation angles below 30 deg and solar zenith angles larger than 80 deg simultaneously, the new model can improve the ionospheric calibration by as much as 12% over the old model. Nevertheless, the doppler calibrations provided by both models are quite similar. As mentioned, both models usually cannot account for fine structure variations along the tracking station-spacecraft ray path.

As for the nighttime ionospheric model, although there are slight uncertainties in the exact values for the diffusion and recombination constants α and β , the nighttime range changes join smoothly to the range changes generated from the new daytime ionospheric model. Moreover, the range corrections computed by the new nighttime model may differ by over 30% (~ 20 cm) from the currently used calibration technique DIEN/TIEN.

The one-way range changes from the nighttime model will be compared with those deduced from the Viking S/X dual-frequency doppler data when the latter become available. Also, the effects of the entire new global ionospheric model on the doppler tracking data and orbit determination will be checked out and published in a future article.

References

1. von Roos, O. H., Yip, K. W., Escobal, P. R., "A Global Model of the Earth's Ionosphere for Use in Space Applications," *Astronautica Acta*, Vol. 18 (Supp.), p. 215, 1974.
2. Chapman, S., "The Absorption and Dissociative or Ionizing Effect of Monochromatic Radiation in an Atmosphere on a Rotating Earth," *Proc. Phys. Soc. (London)*, Vol. 43, p. 25, 1931.
3. Yip, K. W., Winn, F. B., Reid, M. S., Stelzried, C. T., "Decimeter Modeling of Ionospheric Columnar Electron Content at S-Band Frequencies," paper presented at the Ionospheric Effects Symposium, Jan. 20-22, 1975, sponsored by the Naval Research Laboratory, Washington, D. C.
4. von Roos, O. H., "Tropospheric and Ionospheric Range Corrections for an Arbitrary Inhomogeneous Atmosphere (First Order Theory)," *The Deep Space Network Progress Report*, Technical Report 32-1526, Vol. VI, p. 99. Jet Propulsion Laboratory, Pasadena, Calif., Dec. 1971.
5. Madrid, G. A., "The Measurement of Dispersive Effects Using the Mariner 10 S- and X-Band Spacecraft to Station Link," *The Deep Space Network Progress Report* 42-22, p. 22. Jet Propulsion Laboratory, Pasadena, Calif., May 1974.
6. Winn, F. B., Yip, K. W., Reinbold, S. J., "DSN-MVM73 S/X Dual Frequency Doppler Demonstration," *The Deep Space Network Progress Report* 42-22, p. 28. Jet Propulsion Laboratory, Pasadena, Calif., May 1974.
7. Wright, J. W., Smith, G. H., "Review of Current Methods for Obtaining Electron-Density Profiles from Ionograms," *Radio Science*, Vol. 2, p. 1119, Oct. 1967.
8. Rishbeth, H., "A Review of Ionospheric F Region Theory," *Proc. of IEEE*, Vol. 55, p. 16, January 1967.
9. Quinn, T. P., Nisbet, J. S., "Recombination and Transport in the Nighttime F Layer of the Ionosphere," *J. Geophys. Res.*, Vol. 70, p. 113, Jan. 1965.
10. Rishbeth, H., Garriott, O. K., *Introduction to Ionospheric Physics*, Academic Press, New York and London, 1969.
11. Shimazaki, T., "Nighttime Variations of F-Region Electron Density Profiles at Puerto Rico, 2. An Attempt to Separate the Effects of Temperature Variation and Drift Velocity," *J. Geophys. Res.*, Vol. 71, p. 3177, July 1966.
12. Ferraro, V. C. A., "Diffusion of Ions in the Ionosphere," *Terr. Magn. Atmos. Elect.*, Vol. 50, p. 215, 1945.

Table 1. Elevation and solar zenith angles for the first three S/X passes

Date	Time (UT), h	Elevation angle γ , deg	Solar zenith angle X , deg
12/15/73	18.30	16.79	58.55
	18.78	22.62	58.65
	19.21	27.63	58.90
	:	:	:
	23.30	57.70	78.85
	23.47	57.39	80.20
	23.65	56.86	81.65
	:	:	:
12/30/73	19.13	39.21	58.3
	19.50	42.81	58.5
	:	:	:
	24.70	35.96	87.65
	25.08	31.79	90.50
	25.48	27.31	93.35
	25.92	22.24	96.15
1/3/74	19.36	43.80	58.05
	19.54	45.38	58.15
	:	:	:
	22.08	52.44	67.45
	23.82	40.27	79.70

Table 2. Chapman parameters h_{max} and H for Dec. 15, 1973

Ionosonde site	Time (UT), h	H_{max} , km	H , km
Point Arguello, Calif.	17:00	231	34
	17:30	218	39
	18:00	229	31
	18:30	239	46
	19:00	241	43
	19:30	255	36
	20:00	241	50
	20:30	238	34
	21:00	228	42
	21:30	239	53
	22:00	245	40
	22:30	251	57
	23:00	219	23
	23:30	233	40
	24:00	272	52
	0:30	256	52
	1:00	247	31
White Sands, New Mexico	17:00	219	43
	17:30	259	45
	18:00	230	32
	18:30	219	37
	19:00	254	43
	19:30	221	20
	20:00	226	43
	20:30	231	
	21:00	221	27
	21:30	233	30
	22:00	234	33
	22:30	227	36
	23:00	235	33
	23:30	238	40
	24:00	250	35
	0:30	245	38
	1:00	241	36

Table 3. Chapman parameters h_{max} and H for Dec. 30, 1973

Ionosonde site	Time (UT), h	h_{max} , km	H , km
Point Arguello, Calif.	18:00	252	39
	18:30	267	47
	19:00	253	39
	19:30	251	38
	20:00	266	49
	20:30	248	46
	21:00	262	59
	21:30	232	28
	22:00	228	34
	22:30	227	30
	23:00	221	35
	23:30	224	45
	24:00	243	43
	0:30	230	35
	0:45	226	39
	2:00	274	45
White Sands, New Mexico	18:00	250	41
	18:30	249	39
	19:00	274	46
	19:30	250	31
	20:00	232	33
	20:30	244	42
	21:00	245	33
	21:30	231	30
	22:00	220	41
	22:30	223	28
	23:00	226	33
	23:30	237	46
	24:00	264	54
	0:30	244	36
	1:00	264	41
	1:30	295	43
	2:30	303	34

Table 4. Summary of $\alpha\beta$ values

Date	Time span, h	$\alpha\beta$, s^{-2}
11/11/71	26.70-28.3	$\sim 1.18 \times 10^{-8}$
	28.3 -29.35	$\sim 2.02 \times 10^{-10}$
	29.35 on	undefined
11/13/71	26.71-29.4	$\sim 1.97 \times 10^{-9}$
	29.4 on	$\sim 2.70 \times 10^{-12}$
11/14/71	26.71-29.0	$\sim 4.92 \times 10^{-10}$
	29.0 -31.0	~ 0

Table 5. Ionospheric one-way range changes

Date	UT	Elevation, deg	$\Delta\rho$, m				DIEN/TIEN	
			New daytime model	Nighttime model				
11/11/71	21.99	7.06	5.23					4.63
	22.87	16.86	3.61					3.21
	23.53	23.72	2.66					2.99
	24.14	29.41	1.99					1.64
	24.72	34.15	1.50					1.14
	25.28	37.96	1.11					0.73
	⋮			$\beta = 0.5$	$\beta = 1$	$\beta = 2$	$\beta = 5$	⋮
	⋮			$\alpha = 2.36 \times 10^{-8}$	$\alpha = 1.18 \times 10^{-8}$	$\alpha = 5.91 \times 10^{-9}$	$\alpha = 2.36 \times 10^{-9}$	⋮
	⋮							
	26.93	42.68		0.66	0.65	0.66	0.72	0.44
	27.48	41.77		0.60	0.60	0.61	0.63	0.44
	28.03	39.64		0.59	0.59	0.59	0.60	0.46
	28.58	36.41		0.59 ^a	0.59 ^a	0.59 ^a	0.59 ^a	0.53
	29.15	32.19		0.60 ^a	0.59 ^a	0.59 ^a	0.59 ^a	0.49
	29.74	27.04		0.61 ^a	0.60 ^a	0.60 ^a	0.59 ^a	0.60
30.36	20.90		0.62 ^a	0.61 ^a	0.60 ^a	0.59 ^a	0.71	
31.08	13.20		0.60 ^a	0.59 ^a	0.57 ^a	0.56 ^a	0.88	
11/13/71	22.10	9.30	4.86					4.40
	22.90	18.24	3.44					3.09
	23.55	24.92	2.56					2.23
	24.15	30.47	1.93					1.60
	24.73	35.11	1.45					1.12
	25.29	38.80	1.07					0.71
	⋮			$\beta = 0.5$	$\beta = 1$	$\beta = 2$	$\beta = 5$	⋮
	⋮			$\alpha = 3.95 \times 10^{-9}$	$\alpha = 1.97 \times 10^{-9}$	$\alpha = 9.86 \times 10^{-10}$	$\alpha = 3.95 \times 10^{-10}$	⋮
	⋮							
	26.93	43.06		0.52	0.53	0.55	0.63	0.44
	27.48	41.97		0.50	0.51	0.52	0.55	0.44
	28.03	39.67		0.51	0.51	0.52	0.53	0.46
	28.59	36.28		0.52	0.52	0.53	0.53	0.49
	29.16	31.91		0.55	0.55	0.55	0.55	0.54
	29.75	26.62		0.59 ^a	0.59 ^a	0.58 ^a	0.58 ^a	0.61
30.38	20.31		0.65 ^a	0.64 ^a	0.63 ^a	0.62 ^a	0.72	
31.12	12.32		0.72 ^a	0.70 ^a	0.68 ^a	0.66 ^a	0.90	
11/14/71	21.48	2.72	5.88					5.19
	22.56	15.02	3.93					3.59
	23.25	22.38	2.90					2.57
	23.87	28.36	2.18					1.87
	24.45	33.41	1.65					1.33
	25.01	37.52	1.24					0.90
	⋮			$\beta = 0.5$	$\beta = 1$	$\beta = 2$	$\beta = 5$	⋮
	⋮			$\alpha = 9.83 \times 10^{-10}$	$\alpha = 4.92 \times 10^{-10}$	$\alpha = 2.46 \times 10^{-10}$	$\alpha = 9.83 \times 10^{-11}$	⋮
	⋮							
	26.94	43.24		0.48	0.49	0.52	0.60	0.43
	27.49	42.06		0.47	0.48	0.50	0.53	0.44
	28.04	39.68		0.48	0.49	0.50	0.51	0.46
	28.60	36.20		0.50	0.51	0.51	0.52	0.49
	29.16	31.76		0.54 ^a	0.54 ^a	0.54 ^a	0.54 ^a	0.54
	29.76	26.41		0.59 ^a	0.58 ^a	0.64 ^a	0.58 ^a	0.61
30.39	20.01		0.66 ^a	0.65 ^a	0.64 ^a	0.63 ^a	0.72	
31.14	11.85		0.76 ^a	0.74 ^a	0.72 ^a	0.70 ^a	0.91	

*Second (or third) set of α and β values should have been used.

Table 6. Values of α and β from Refs. 7 and 8

Source	α (s^{-1})	β (s^{-1})	Comment
Quinn, et al. (Ref. 10)	2.53×10^{-6}	1.73	Summer, moderate solar activity
Quinn, et al. (Ref. 10)	2.53×10^{-6}	0.80	Winter, moderate solar activity
Rishbeth, et al. (Ref. 11)	1.37×10^{-4}	0.05	Sunspot minimum
	1.95×10^{-5}	3.55	Sunspot maximum

Table 7. Ionospheric one-way range changes

Date	UT, h	Elevation, deg	$\Delta\rho$, m		DIEN/TIEN
			$\beta = 1$ $\alpha = 2.02 \times 10^{-10}$	$\beta = 10^{-4}$ $\alpha = 2.02 \times 10^{-6}$	
11/11/71	28.58	36.41	0.50	0.61	0.49
	29.15	32.19	0.53	0.61	0.53
	29.74	27.04	0.58 ^a	0.64 ^a	0.60
	30.36	20.90	0.65 ^a	0.70 ^a	0.71
	31.08	13.20	0.74 ^a	0.80 ^a	0.88
11/13/71			$\beta = 1$ $\alpha = 2.7 \times 10^{-12}$	$\beta = 10^{-6}$ $\alpha = 2.7 \times 10^{-6}$	
	29.75	26.62	0.58	0.64	0.61
	30.38	20.31	0.65	0.70	0.72
	31.12	12.32	0.76	0.81	0.90
11/14/71			$\beta = 5$ $\alpha = 9.83 \times 10^{-15,17}$	$\beta = 8.2 \times 10^{-7,9}$ $\alpha = 6 \times 10^{-8}$	
	29.16	31.76	0.53	0.56	0.54
	29.76	26.41	0.57	0.61	0.61
	30.39	20.01	0.63	0.71	0.72
	31.14	11.85	0.72	0.86	0.91

^aPositive slope indicated in Fig. 1.

**Table 8. Duration of twilight for DSS located at
| 30 deg | latitude**

τ_t , [min]	δ_s , deg
5.7	0
5.6	10
5.3	20

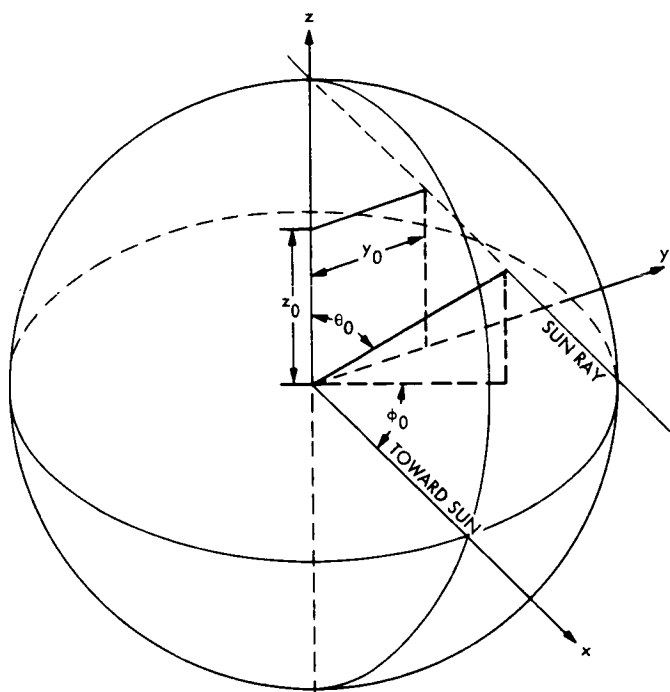


Fig. 1. Geometry of the system

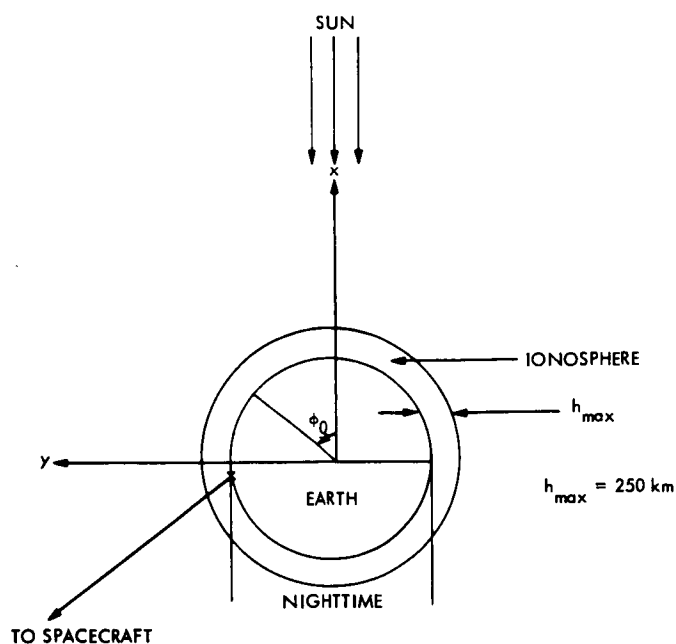


Fig. 2. Schematic of daytime and nighttime ionosphere

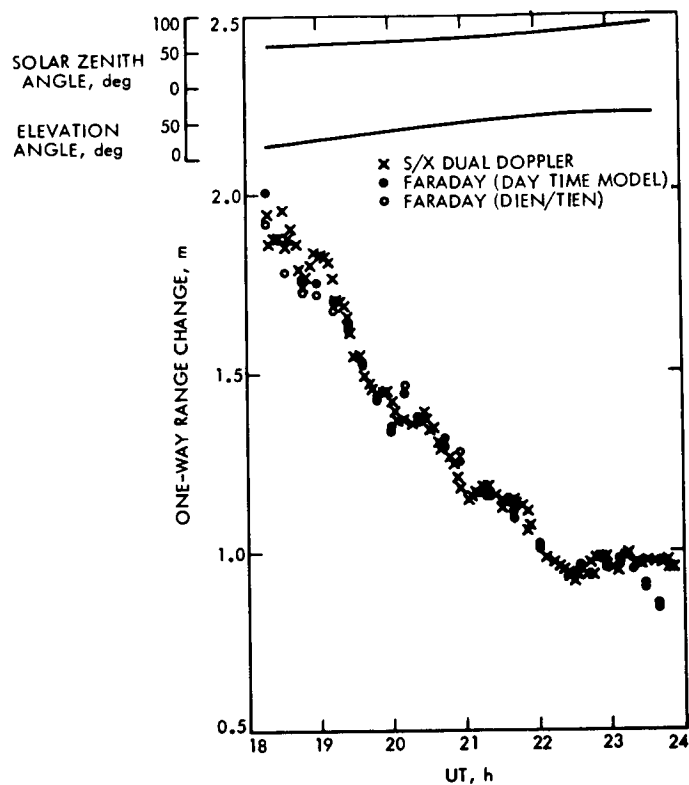


Fig. 3. Comparison of daytime ionospheric one-way range changes on Dec. 15, 1973

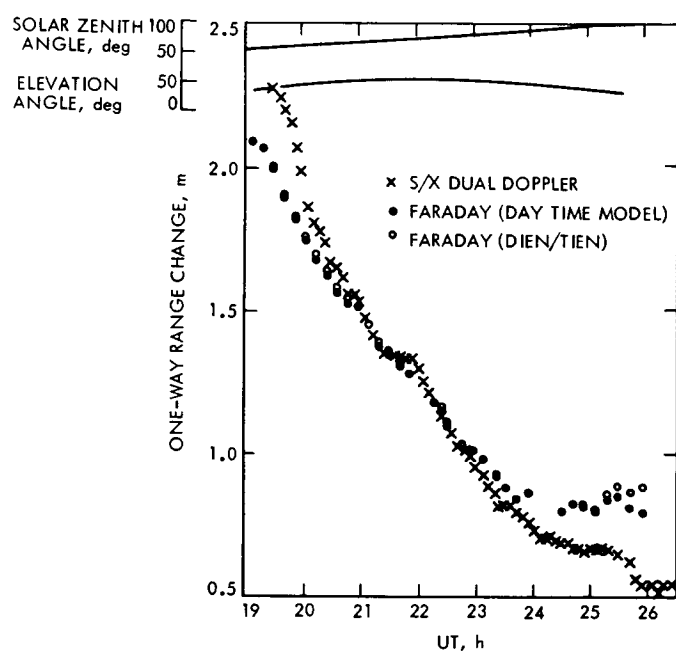


Fig. 4. Comparison of daytime ionospheric one-way range changes on Dec. 30, 1973

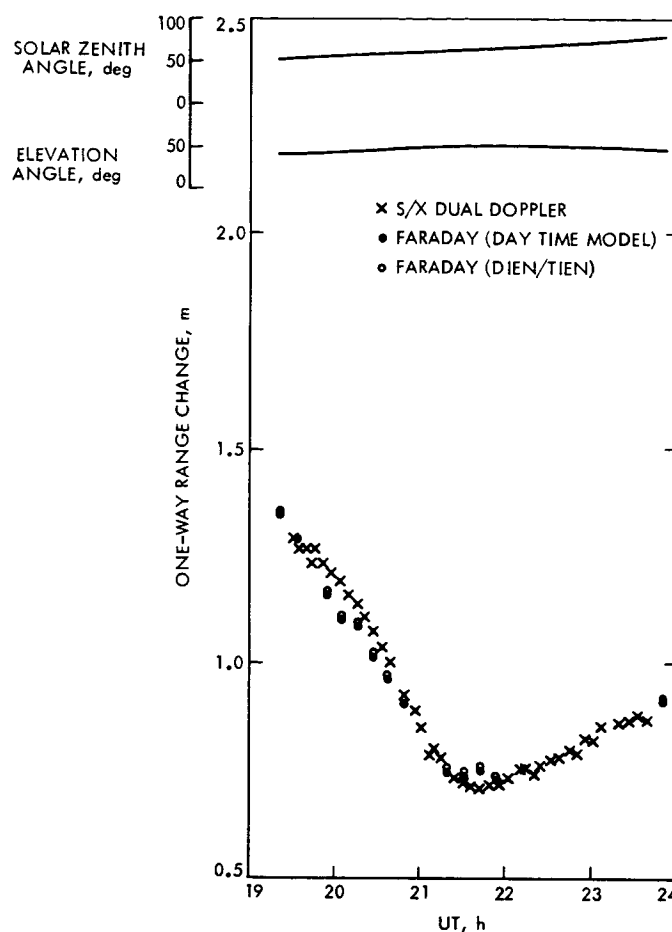


Fig. 5. Comparison of daytime ionospheric one-way range changes on Jan. 3, 1974

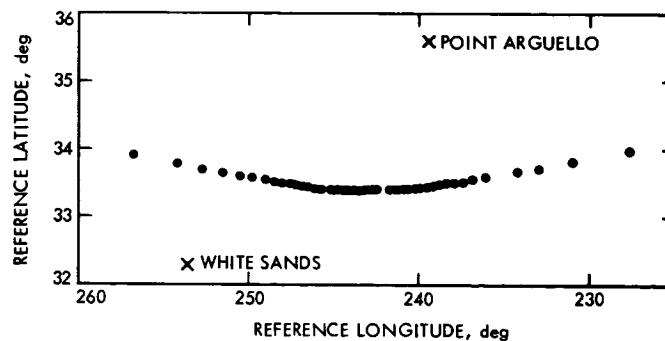


Fig. 6. Variation of ionospheric reference coordinates on Dec. 15, 1973

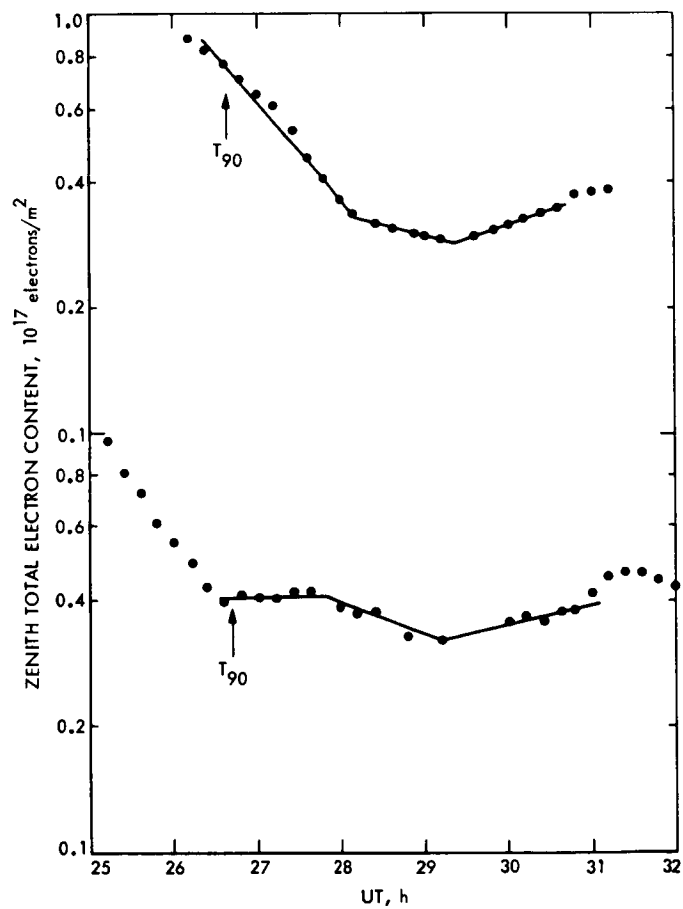


Fig. 7. Nighttime zenith total electron content at Goldstone, Calif., on Nov. 11 and 12, 1971

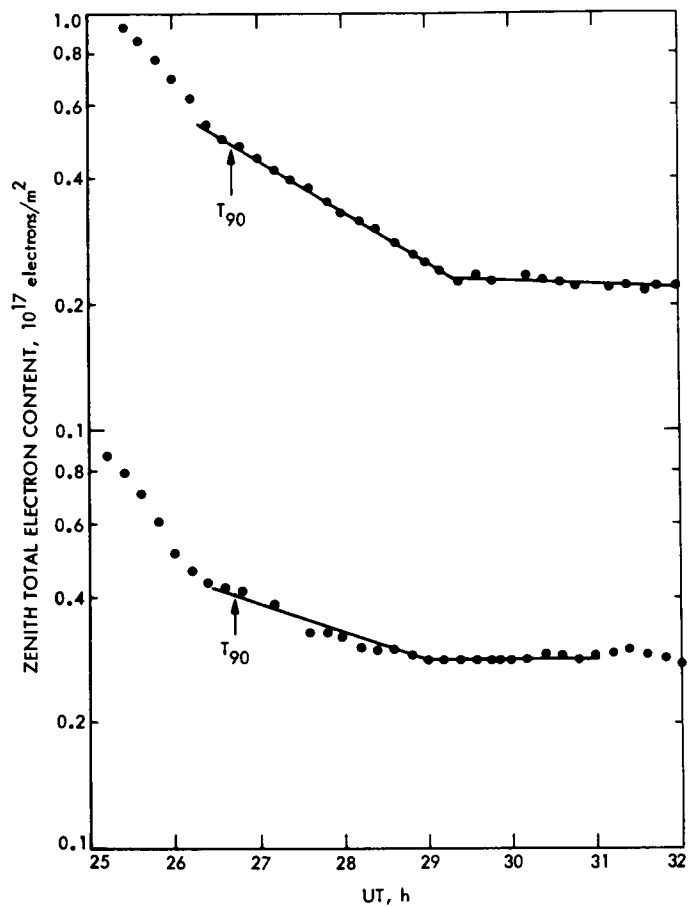


Fig. 8. Nighttime zenith total electron content at Goldstone, Calif., on Nov. 13 and 14, 1971

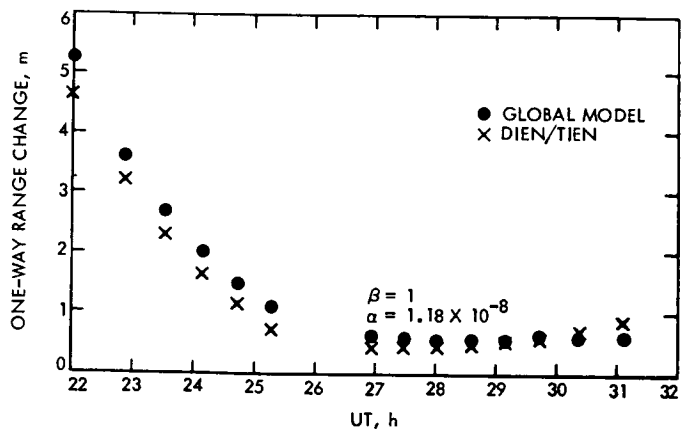


Fig. 9. Comparison of ionospheric one-way range changes on Nov. 11, 1971

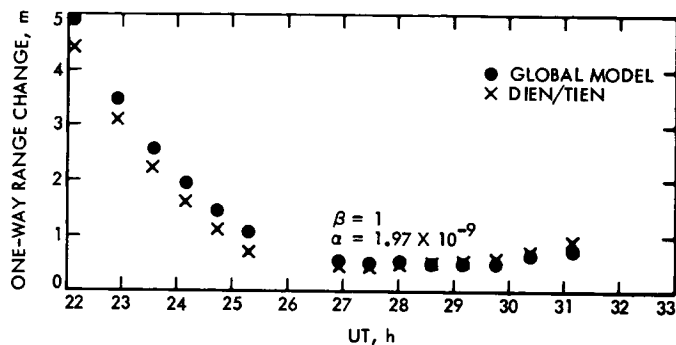


Fig. 10. Comparison of ionospheric one-way range changes on Nov. 13, 1971

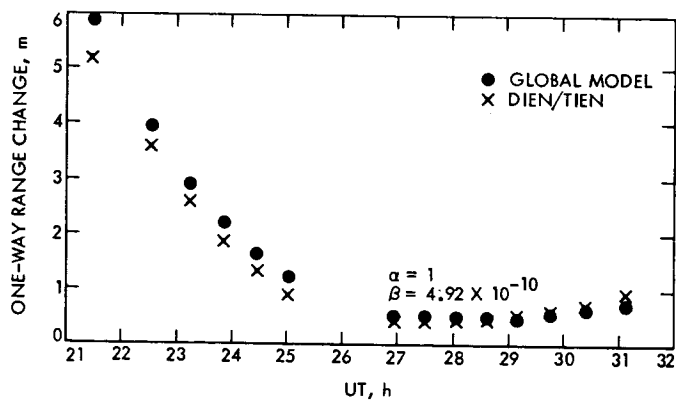


Fig. 11. Comparison of ionospheric one-way range changes on Nov. 14, 1971

N76-15198

Corruption of Radio Metric Doppler Due to Solar Plasma Dynamics: S/X Dual-Frequency Doppler Calibration for These Effects

F. B. Winn, S. R. Reinbold, K. W. Yip, and R. E. Koch
Tracking and Orbit Determination Section
A. Lubeley
Mission Computing Section

The quality of DSN radio metric doppler, for spacecraft beyond a distance of 1 AU from Earth, is a strong function of the Sun-Earth-probe angle. The rms noise levels of both S- and X-band doppler for Sun-Earth-probe angle < 20 deg are observed to be orders of magnitude greater than nominal. Mariner 6, 7, 9, and 10 and Pioneer 10 and 11 doppler data are discussed and the rms noise level for various Sun-Earth-probe angles are shown. Such solar plasma-related doppler degradation reduced the Mariner 10-Mercury II encounter navigation accuracy by nearly a factor of 10. Furthermore, this degradation is shown to be indirectly related to plasma dynamics and not a direct measure of the dynamics.

I. Doppler RMS Noise Dependence on Sun-Earth-Probe angle

For spacecraft beyond 1 AU from Earth, radio metric doppler rms noise is observed to be a predominant function of the angular separation of the probe and the Sun as seen from Earth.

The positions and velocities of a spacecraft in the solar system are estimated usually by a least squares, differential correction technique (Orbit Determination Program, Ref. 1). The doppler shift experienced by round-trip radio trans-

mission from Earth to the spacecraft and back is the prime observable used in the least squares technique. A part of the procedure computes the difference between the observed doppler shift and the doppler shift computed from numerical integrations of the equations of motion of all the significant solar system bodies.

The rms noise for each deep space station-spacecraft view period is computed:

$$\frac{1}{N} \left\{ \sum (O - C)^2 - \left(\sum (O - C) \right)^2 \right\}^{1/2} \quad (1)$$

where

N \equiv number of observations that exist for a given tracking pass after the obvious "blunder observations" have been removed from consideration.

O \equiv observed doppler shift

C \equiv computed doppler shift

Figure 1 shows Mariner 9 and 10 and Pioneer 10 and 11 rms doppler noise levels (for each pass) for a range of Sun-Earth-probe (SEP) angles.

The Orbit Determination Program (ODP) does not utilize any model to account for the plasma corruptions of doppler. No model of sufficient accuracy exists at this time. Typically, empirical measurements (differenced range versus integrated doppler (DRVID), Ref. 2) are used to provide information concerning the long-term fluctuations of the plasma. Plasma dynamics of short time durations (< 1 second) are not recorded by DRVID. Yet, it is these high-frequency dynamics which yield the phase jitter, the rms doppler noise shown in Fig. 1.

Muhleman (Ref. 3) notes that the rms phase jitter is dependent on the observing wavelength and the line-of-sight electron content fluctuation. He further notes that for space regions beyond 5 solar radii the electron density fluctuation is approximately proportional to the mean plasma density. Assuming these observations hold for all solar distances, he predicted rms doppler noise levels for $|SEP| < 90$ deg (Fig. 1).

Although, in general, the maximum rms noise occurs at $SEP = 0$ deg and diminishes rapidly with increased SEP angle, there are localized fluctuations which change the noise levels of 2 to 10 times in many cases. They are most clearly resolved in the Mariner Venus-Mercury (MVM73) noise plot.

Additionally, as one might expect, the amplitude and temporal variations of the rms phase jitter are different for each mission: This long-term variability is most likely tied to the amount of solar activity. Indeed, studies by MacDoran (Ref. 2) and Berman (Ref. 4) have shown that a relationship between the two does exist. Although these studies are encouraging, there is no way to predict the amount of doppler phase jitter that will result at a particular point in space and at an instant in time.

II. Doppler Noise Characteristics

Plasma-corrupted doppler differs from nominal doppler in two ways: (1) increased phase jitter or high-frequency noise, and (2) occasional to frequent doppler phase discontinuities (cycle slips).

Increased rms noise of plasma-influenced doppler is apparent in Fig. 2. Esposito (Ref. 5) originally presented this figure. There are occasions of plasma-corrupted data shown here at SEP angles > 20 deg. And all doppler acquired at $|SEP| < 10$ deg has been so affected. These doppler sets were acquired from the Mariner 6 and 7 spacecraft in 1969, a year in which the Sun activity was at minimum.

With an increased resolution in time, Fig. 3 shows nominal and plasma-corrupted doppler residuals. A doppler residual is defined as the difference between the doppler shift observed (O in Eq. 1) and the doppler shift computed using the ODP mathematical model (C in Eq. 1). Figures 3a through e show doppler residuals for the Pioneer spacecraft. The lower a frame appears in the sequence, the smaller the associated SEP angle. All of the Pioneer doppler have been averaged over a 60-s count time.

Figures 3a and b are good examples of nominal doppler residuals and corrupted residuals. During the first two hours of those passes of tracking data, nominal doppler noise is apparent. Each of these nominal periods is followed by time periods in which the doppler residual noise increases 5 to 10 times. In addition, short-term temporal variations appear in the doppler residuals that are not present in the nominal doppler residuals.

There is no assurance that these signatures and/or the phase jitter (high-frequency variation) are due to solar plasma concentrations, especially for such large SEP angles: $SEP \approx 130$ deg for Fig. 3a and $SEP \approx 100$ deg for Fig. 3b. However, note the similarity between the Pioneer doppler residuals acquired at $SEP \approx 130$ and 12 deg. The residuals in Fig. 3a show monotonic frequency changes over time scales of tens of minutes. There is a series of them during the fifth and seventh hours of this tracking period. A very similar behavior is evident in Fig. 3d, which shows residuals associated with an SEP angle of 12 deg. And, of course, there is the excessive phase jitter noise.

III. Correlated Noise Events of Different Spacecraft

These doppler residual noise patterns are thought to be the result of plasma fluctuations. This contention is supported by observations that both the noise (Fig. 1) and the time duration of the disturbances (Fig. 4) decrease as the SEP angle increases. Additionally, it is interesting to note that P. S. Callahan, A. J. Anderson, and G. W. Null, and the authors have succeeded in correlating doppler "noise bursts" believed to be plasma-related seen along the Pioneer 10 line-of-sight with those seen along the Pioneer 11 line-of-sight a day later. Figure 5 shows one such correlated event/set discovered by Null.

IV. The Dispersive Nature of Charged-Particle Dynamics

If, indeed, the doppler noise dependence on SEP angle and time stems from plasma dynamics only, then dual-frequency doppler observations can be used to compute the plasma fluctuations which occur along the raypath during any continuous observation period. Theory and observations (Ref. 6) show

$$\Delta l = - \frac{e^2}{2\epsilon_0 m \omega^2} \int N(l) dl \quad (2)$$

where

e = electron charge

m = electron mass

ϵ = electric permittivity of free space

ω = frequency of propagation

N = electron density at l

V. Dual-Frequency Charged-Particle Calibration Experience

The Mariner Venus-Mercury 1973 mission was the first to use both S- and X-band frequency doppler to derive charged-particle calibrations in a navigation application. Basically, the system functioned in the following manner:

- (1) An S-band frequency (~ 2100 MHz) was transmitted from a DSN station to the Mariner 10 spacecraft.

- (2) The spacecraft in turn retransmitted the received S-band frequency after multiplication of the received signal by 40/221.
- (3) The spacecraft simultaneously multiplied the received signal by 880/221 (a factor of 11/3 greater than 240/221) and retransmitted the signal to the ground station.

Thus, on the spacecraft-to-ground station downleg path, dual S/X frequency radio propagations were transmitted.

This dual-frequency system was possible because the spacecraft had both S- and X-band transmitters and G. Levy and others equipped the Mars Station (DSS 14) at Goldstone, California with an experimental X-band receiver. DSS 14 was the only deep space station so equipped.

In practice, the time histories of the DSS 14 S- and X-band phase over a tracking interval were differenced as follows:

$$\Delta\phi = 1.02 \left(\phi_s - \frac{3}{11} \phi_x \right) \quad (3)$$

where ϕ_s , ϕ_x are the accumulated phase changes of the S- and X-band carriers from the start of the tracking interval. Both phase time histories show the radial velocity of spacecraft relative to the station, but this will be differenced out in Eq. (3), leaving the charged-particle dynamics information.

The factor 1.02 accounts for the fact that the X-band phase delay due to charged-particle dynamics is not zero, but $(3/11)^2$ of the S-band phase delay resulting from charged-particle dynamics.

The S/X dual-frequency doppler technique appears to have functioned as expected for the approach navigation of Mariner 10 for the first encounter with Mercury (Ref. 7).

In the 13 days just before the encounter (March 16 to March 29, 1974), the doppler tracking data on 6 of these days (Fig. 6) showed abnormally high-frequency noise (10–20 MHz peak-to-peak amplitude) and over periods of hours. During this time period the SEP angle was ≈ 34 deg.

S/X dual-frequency doppler data were used (near-real-time) to identify solar plasma dynamics as the source of

the increased doppler noise: later, as a demonstration, the calibrations were applied to the affected doppler (for which calibrations existed) to show that the calibrations:

- (1) Improved the accuracy of the navigation by 80%, reducing the navigation error at Mercury by almost 500 km.
- (2) Improved the quality of the data "fit," removing much of the plasma signatures from the residuals as shown in Figs. 7 and 8.

When radio waves propagate through fluctuating charged-particle mediums, the amplitude and phase of the wave will fluctuate. If the rapid phase changes of a radio wave can be tracked and recorded, then the fluctuations of the total electron content along a raypath can be determined.

After the first Mercury encounter, once the SEP angle became less than 27 deg, there was strong evidence that the S-band doppler radio transmission was being phase-scintillated by plasma fluctuations. The S-band rms noise was now typically ~ 0.04 Hz (10 times nominal). Superimposed on the 0.04-Hz rms noise background were frequent noise increases where in some instances the rms noise doubled (Fig. 1).

The X-band doppler rms noise was 6 to 20 times higher than the S-band doppler noise at $SEP \approx 27$ deg. If the X- and S-band radio waves were phase-scintillated as a result of charged-particle fluctuations, the X-band noise should be $(3/11)^2$ of the S-band noise except for the multiplication of $(11/3)$ before scintillation. Thus, either the S- and X-band propagations, or both, were exhibiting noise that was not a direct measure of charged-particle dynamics.

Spacecraft radio tracking systems employ second-order phase-lock-loop electronics (Ref. 8). Both ground and spacecraft receivers do. Such loops require less than $\pi/2$ radians of phase coherence over time scales of a second. $\pi/2$ radians of phase scintillation translates to ~ 3.5 cm of S-band doppler phase jitter or electron content fluctuations of 5×10^{15} electrons/m² along the raypath. When such plasma fluctuations do occur, then the S-band phase jitter may exceed the performance limitations of second-order phase-lock-loop receivers. Thus, cycle slips may be introduced into the doppler data stream.

However, it will be remembered that the X-band propagation was obtained at the spacecraft by multiplying the received uplink S-band carrier by 880/221. Thus, the

phase jitter of the S-band uplink radio wave is also multiplied by 880/221. The X-band radio wave transmitted from the spacecraft has ~ 4 times more phase jitter than did the spacecraft S-band signal.

D. L. Brunn of JPL has shown that if the spacecraft-received S-band carrier has an rms phase jitter of $\sim \pi/6$ radians, the resultant X-band signal transmitted from the spacecraft will appear non-coherent to the DSS second-order phase-lock-loop receiver. This conclusion was based on laboratory measurements.

Mariner 10 telemetry data indicate that the rms phase jitter of the spacecraft-received S-band carrier was $\pi/12$ radians or less for the range of SEP angle of 30 deg down to 10 deg. And, undoubtedly, the statistical properties of the plasma dynamics as a doppler noise generator differ appreciably from those used in the laboratory. Thus, the X-band phase jitter being greater than the S-band phase jitter means

- (1) Four times the phase jitter of the spacecraft-received S-band carrier exceeds the round-trip S-band carrier phase jitter, and, perhaps that
- (2) Four times the phase jitter of the spacecraft-received S-band carrier is beyond the ability of second-order phase loops to track coherently.

Assume that the plasma dynamics encountered by the DSS-to-spacecraft uplink S-band transmission is also encountered on the downlink S-band transmission. Then the round-trip phase jitter on the S-band carrier is 2 or $\sqrt{2}$ times the one-way phase jitter, depending if statistical independence is assumed or not. The phase jitter of the X-band carrier is 4 times the one-way S-band phase jitter. Thus, the ratio X-band phase jitter to S-band phase jitter cannot exceed 4 if plasma dynamics constitute the sole source of the jitter. A relative noise pattern of S- and X-band, 60-s doppler is shown in Fig. 9.

When S/X dual-frequency doppler calibrations are computed using Eq. (3), the calibrations exhibit noise similar to the X-band doppler noise, the relationship being

$$\sigma_c \approx \sqrt{\sigma_x^2 + \sigma_s^2}$$

When S-band doppler is calibrated for plasma effects, the calibrated S-band doppler then exhibits noise similar to the X-band doppler noise (Fig. 10). If the calibrations are averaged over 20 minutes, the phase jitter is reduced an order of magnitude (Fig. 11), but the resultant time history of the plasma fluctuation over the view period is

not consistent with the S-band doppler structures assumed to the result of plasma dynamics (Fig. 10). When S/X dual-frequency calibrations are applied to the orbit determination process, the estimate of the Mariner 10-Mercury II encounter position is in error by $\sim 10,000$ km. When uncalibrated doppler is used in the ODP, the position estimate for the second Mercury encounter has only a 170-km error. Obviously, these calibrations are erroneous for these high plasma dynamics.

Root mean square doppler noise, as indicated in Fig. 1, represents a major problem to deep space navigation. The Mariner Venus-Mercury 1973 Orbit Determination Team used such "noisy" doppler to predict the second Mercury encounter, target-plane encounter coordinates of the Mariner 10 spacecraft. Tracking data arcs (of extremely edited doppler) from 3 days to months in length were "fit" to the probe state. Although the scatter of these predictions was 800 km (σ) in the Mercury target plane, the "mean adopted" prediction was only 170 km removed from the *a posteriori* encounter position. The large scatter stems, in the main, from the continuous high and variable intensity of the "unmodeled" plasma dynamics. Using tracking data arcs of the same time duration prior to the third Mercury encounter when the doppler revealed little evidence of plasma effects, the spread in the third encounter target plane coordinate estimates was < 70 km (σ), an order of magnitude less.

VI. Viking 1975 S/X Dual-Frequency Plans

The next opportunity to evaluate S/X dual-frequency calibrations for the influence of charged particles on S-band doppler will be during the Viking 1975 mission. During the cruise and Mars orbital phases of that mission, S/X dual-doppler, S/X dual-range, differenced range versus integrated doppler, and S-band doppler integrated phase will be compared. The time histories of the plasma dynamics will be compared to ascertain at what level of plasma dynamics inconsistencies, if any, occur.

The S- and X-band doppler will be tracked by second-order phase-lock-loop receivers during the Viking mission. Additionally, the Viking Radio Science Team plans to record S- and X-band signals following the last mixers

(before the signals enter the second-order phase-lock loops). The recorded bandwidths are tenths of kilohertz wide. Digital computer programs will then reduce two data streams to differential measurements of dispersive doppler shifts. This information will be compared to the differential measurements derived from the phase-lock-loop circuitry for consistency. It is hoped that these comparisons can be made over a spread of Sun-Earth-probe angle and plasma dynamics to determine under what plasma conditions the conventional tracking system yields valid S/X dual-frequency charged-particle calibrations.

The Radio Science Team has plans to develop power spectra for the phase and amplitude variations that are computed by the team's computer programs. As often as practical, S- and X-band doppler will be acquired at high sample rates (10 points/second) and autocorrelation processes will be used to develop a power spectra of the second phase-lock-loop differential measurements. The relative consistencies of the periodic natures and power distributions of the two will be examined.

VII. Conclusion

Doppler rms noise increases orders of magnitude as the Sun-Earth-probe angle changes from 30 to 3 deg for spacecraft at a distance greater than 1 AU from Earth.

S/X dual-frequency doppler data can yield valid charged-particle calibrations if the plasma fluctuations do produce S-band phase jitter near $\pi/12$ radians. At phase jitter levels higher than $\pi/12$ radians, valid calibrations may perhaps still be derived from S- and X-band doppler. However, for Mariner 10, once the angular separation between the probe and Sun as seen from Earth became less than 27 deg, S/X dual-frequency doppler did not yield valid charged-particle calibrations. The rms noise and signatures seen in the S- and X-band doppler are *not* a direct measure of plasma dynamics but the detection of them.

Although Mariner 10 long trajectory arcs of doppler were sufficiently stable to permit adequate navigation, order of magnitude uncertainties were introduced into the navigation for the second encounter with Mercury.

References

1. Moyer, T. D., *Mathematical Formulation of the Double-Precision Orbit Determination Program (DPODP)*, Technical Report 32-1527, Jet Propulsion Laboratory, Pasadena, Calif., May 15, 1971.
2. MacDoran, P. F., Callahan, P. S., and Zygielbaum, A. I., "Probing the Solar Plasma With Mariner Radio Metric Data, Preliminary Results," in *The Deep Space Network Progress Report*, Technical Report 32-1526, Vol. I, pp. 14-21, Jet Propulsion Laboratory, Pasadena, Calif., Feb. 15, 1971.
3. Muhleman, D. W., "A Measurement of the General Relativistic Time Delay with Data from Mariner 6 and 7," edited by R. W. Davies, *Proceedings of the Conference on Experimental Tests of Gravitation Theories*, California Institute of Technology, Pasadena, Calif., Nov. 11-13, 1970.
4. Berman, A. L., and Rockwell, S. T., "Correlation of Doppler Noise During Solar Conjunctions With Fluctuations in Solar Activity," in *The Deep Space Network Progress Report 42-30* (this volume), Jet Propulsion Laboratory, Pasadena, Calif., Dec. 15, 1975.
5. Esposito, P. B., *Helios—Investigation of Solar Corona and Relativistic Time Delays During Superior Conjunction*, EM 391-478, Aug. 22, 1973 (JPL internal document).
6. Laurence, R. S., et al., "A Survey of Ionospheric Effects Upon Earth-Space Radio Propagation," *Proc. IEEE*, Jan. 1964.
7. Winn, F. B., et al., *S/X Dual-Frequency Demonstration*, EM 391-582, July 11, 1974 (JPL internal document). Also available in AIAA Paper 74-832, presented at the AIAA Mechanics and Control of Flight Conference, Anaheim, Calif., Aug. 5-9, 1974.
8. Gardner, F. M., *Phaselock Techniques*, John Wiley & Sons, Inc., New York, 1966.

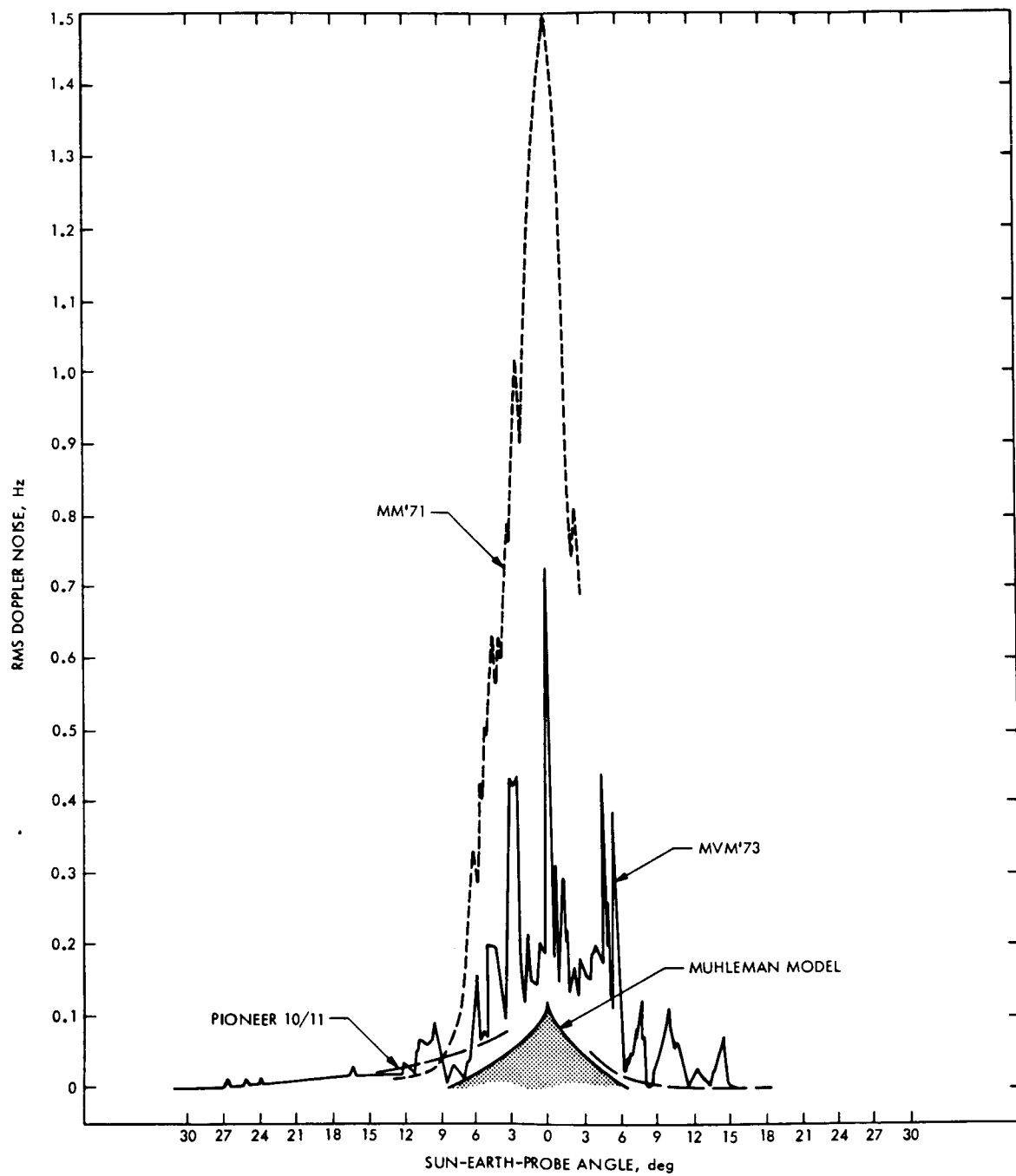


Fig. 1. RMS doppler noise vs Sun-Earth-probe angle

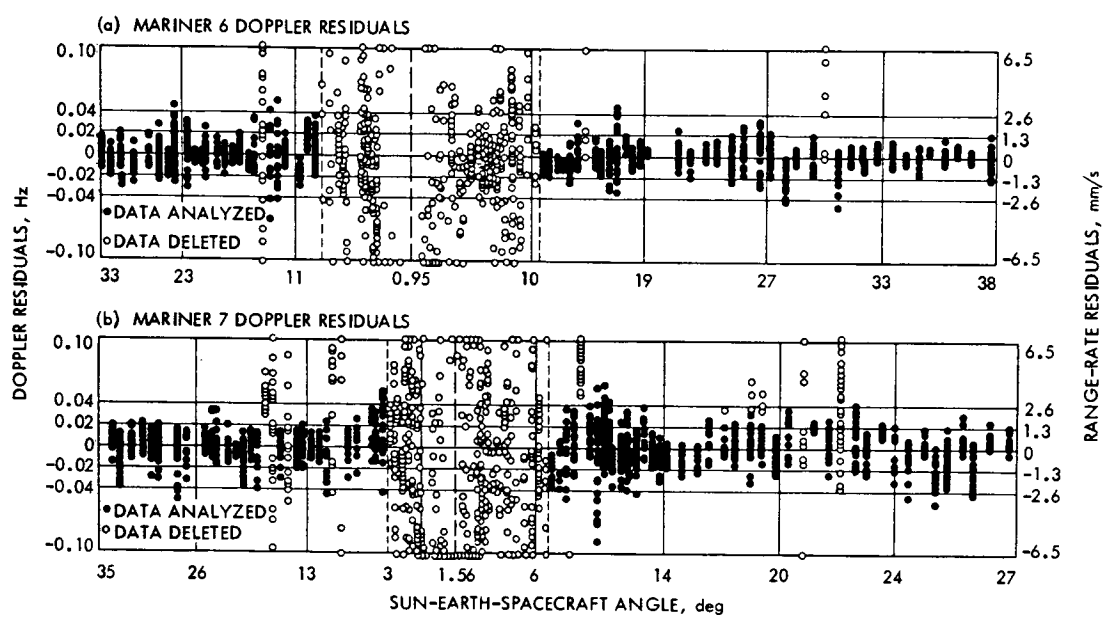


Fig. 2. Mariner 6 and 7 doppler residuals

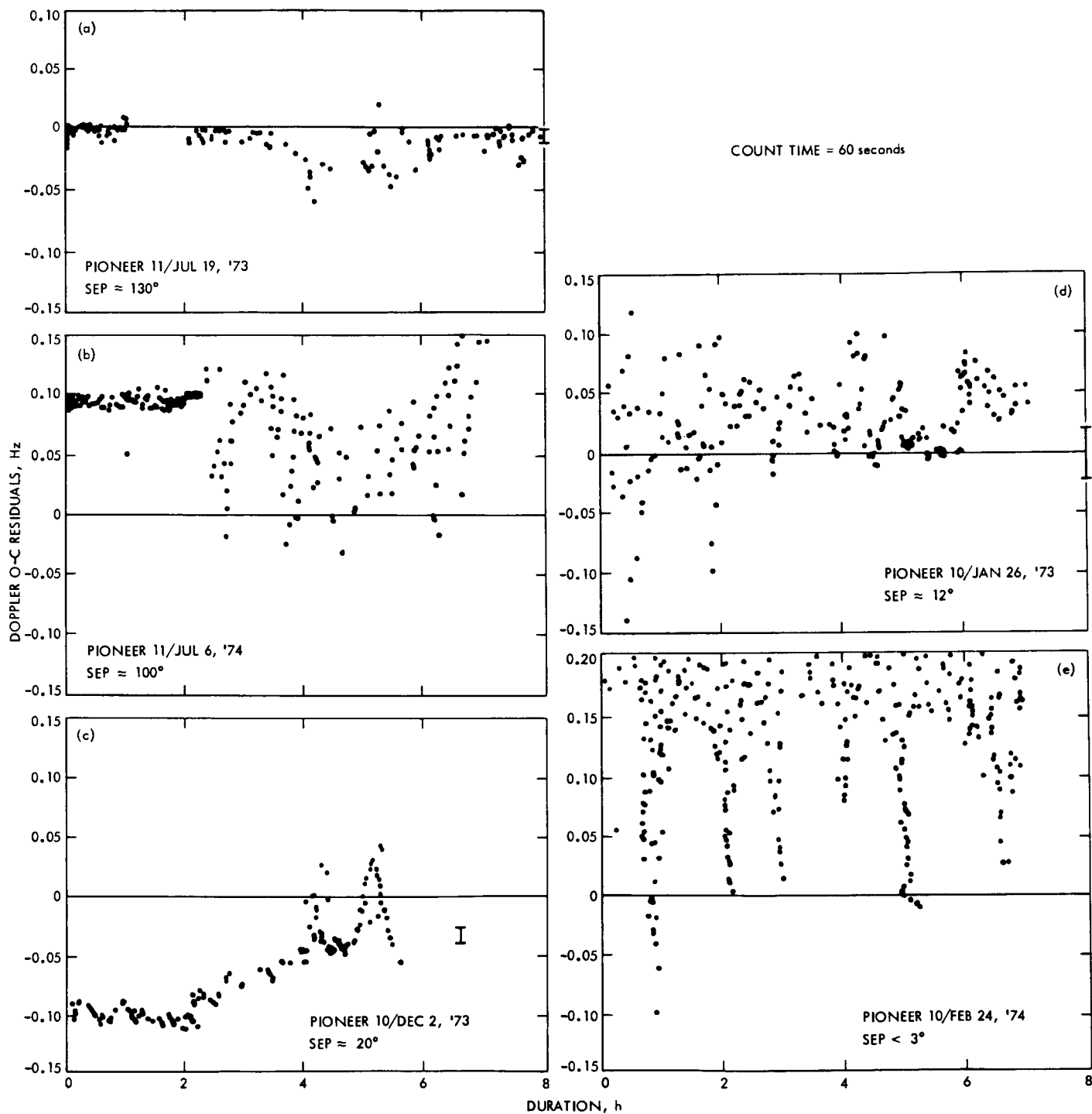


Fig. 3. Pictorials of Pioneer 10 and 11 doppler residuals

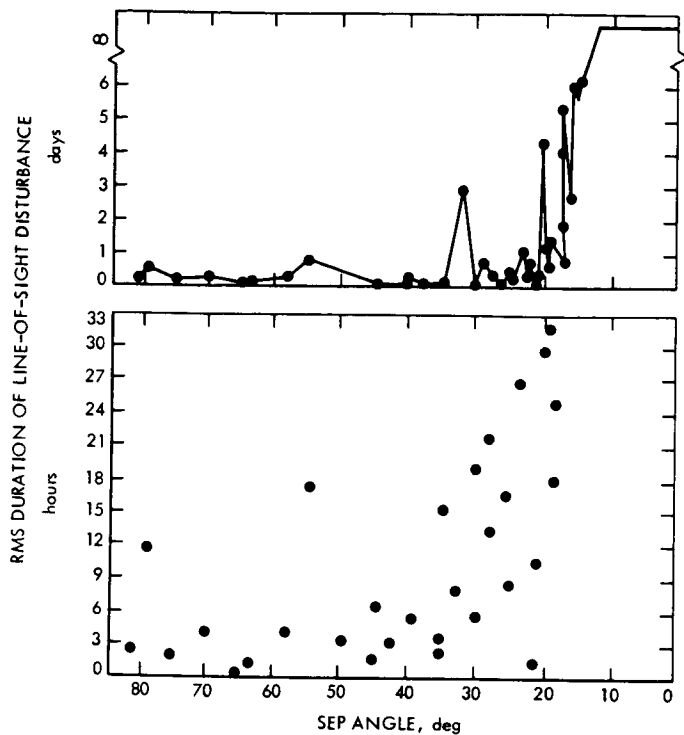


Fig. 4. Time duration of doppler degradation for Mariners 6, 7, and 10 and Pioneers 10 and 11

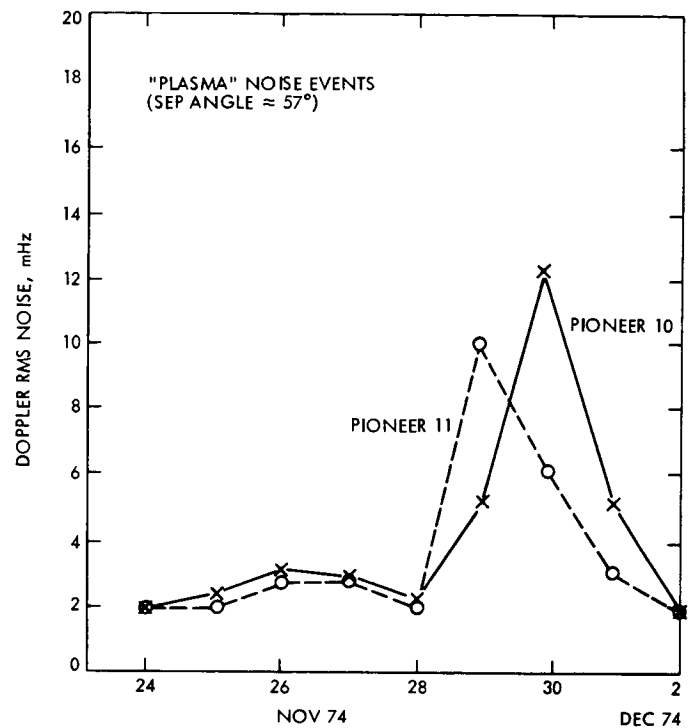


Fig. 5. Pioneer 10/11 time-correlated doppler degradations

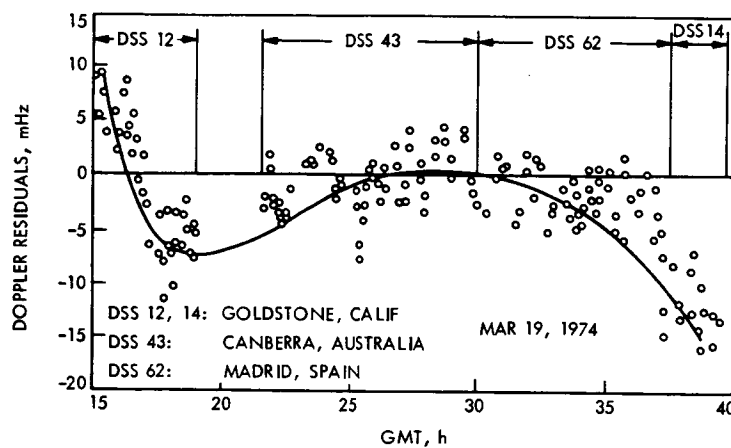


Fig. 6. Mercury I approach doppler noise patterns

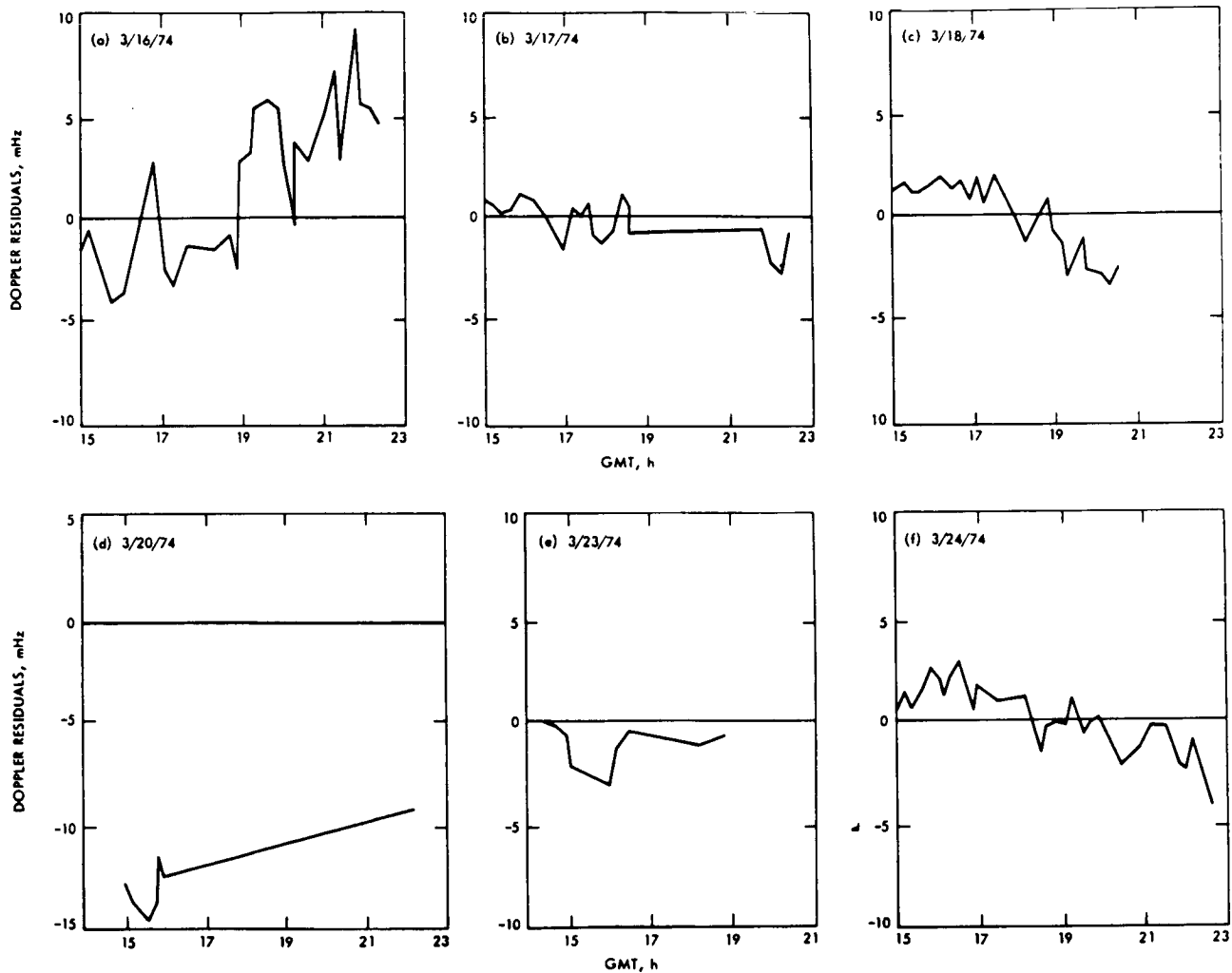


Fig. 7. S-band doppler residuals (600-s count time; no charged-particle calibrations) for Mariner 10-Mercury I encounter (residuals joined by line segments to aid viewing)

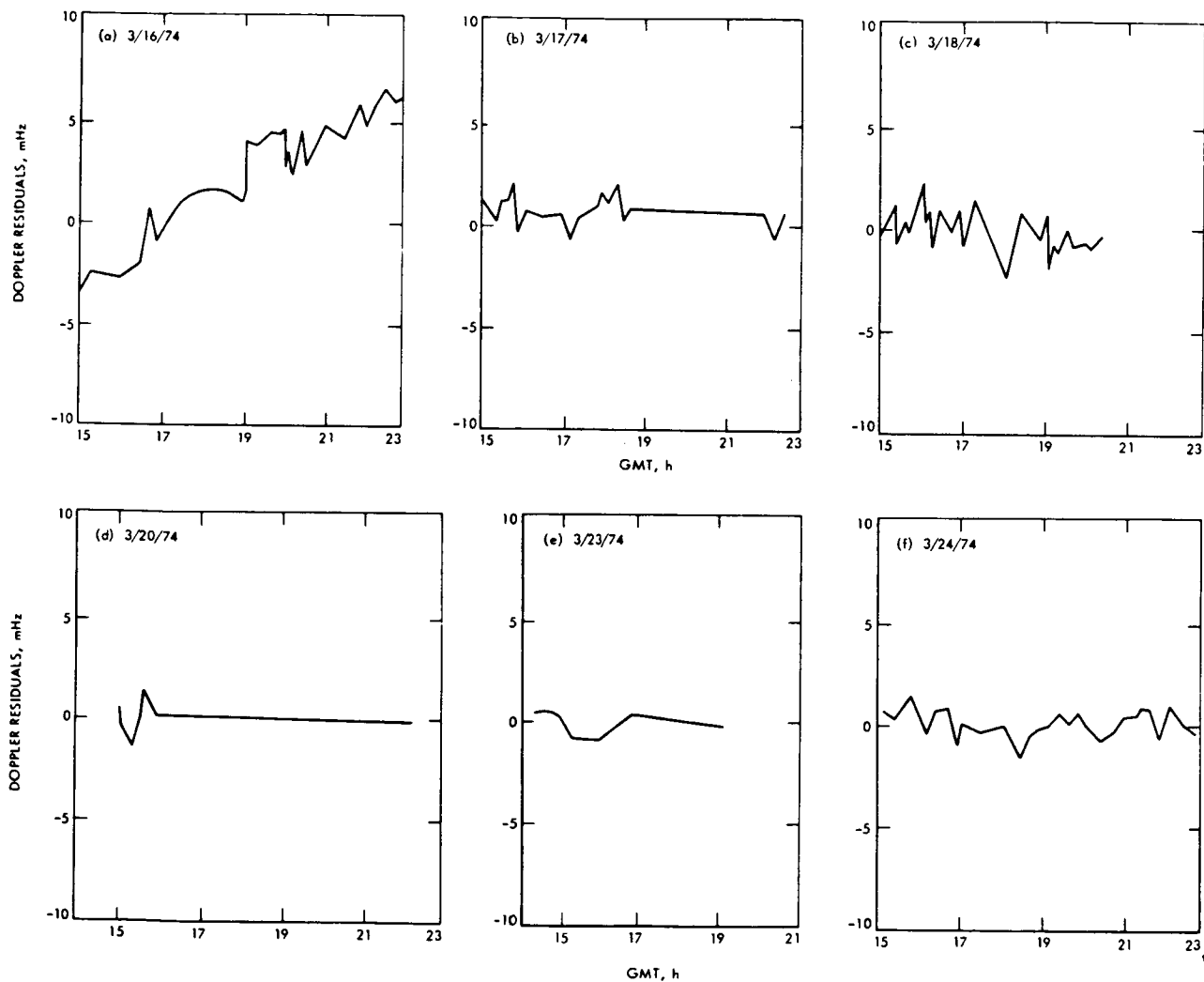


Fig. 8. Calibrated doppler residuals for Mariner 10-Mercury I encounter

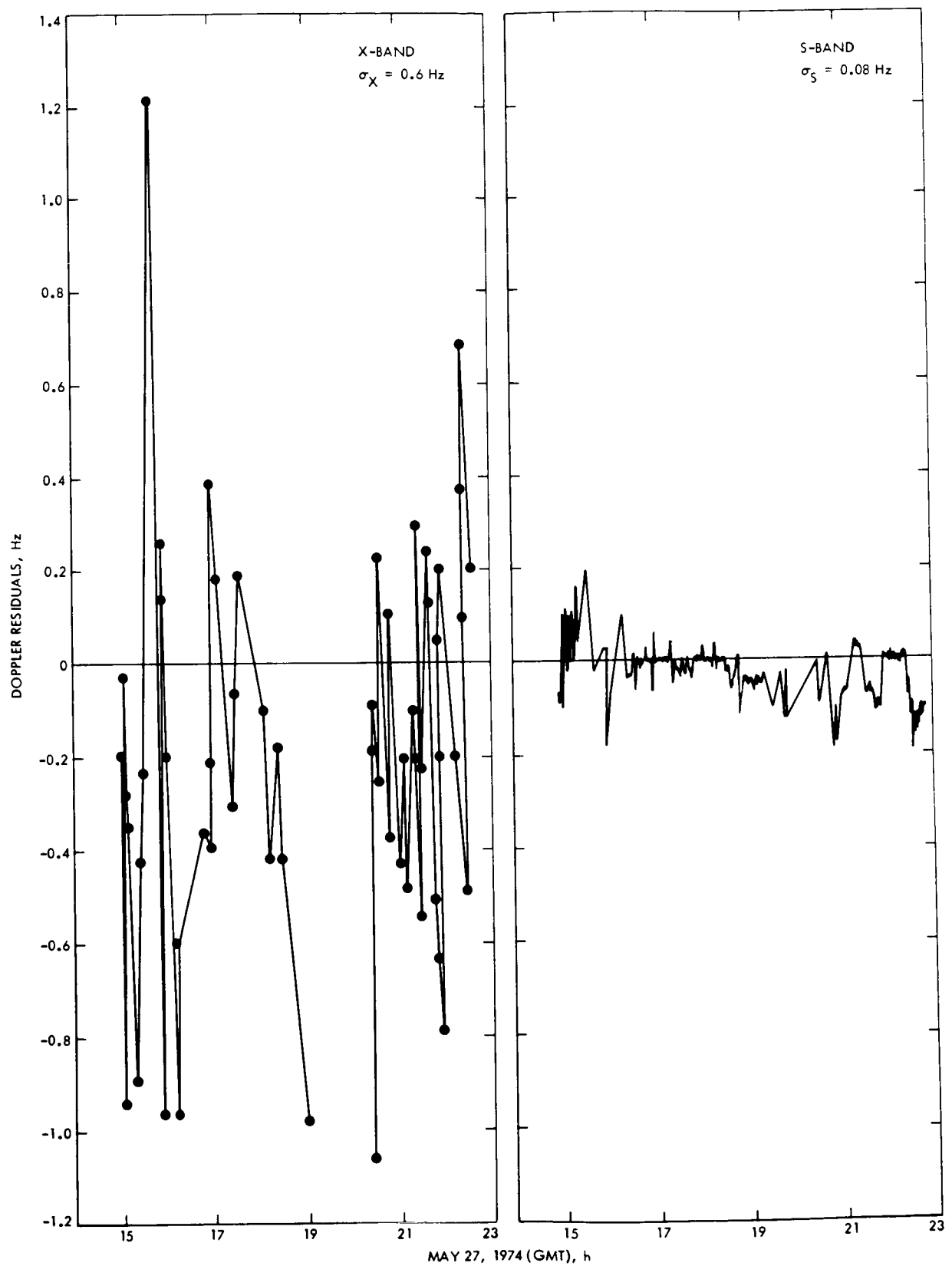


Fig. 9. Relative noise of X- and S-band doppler residuals

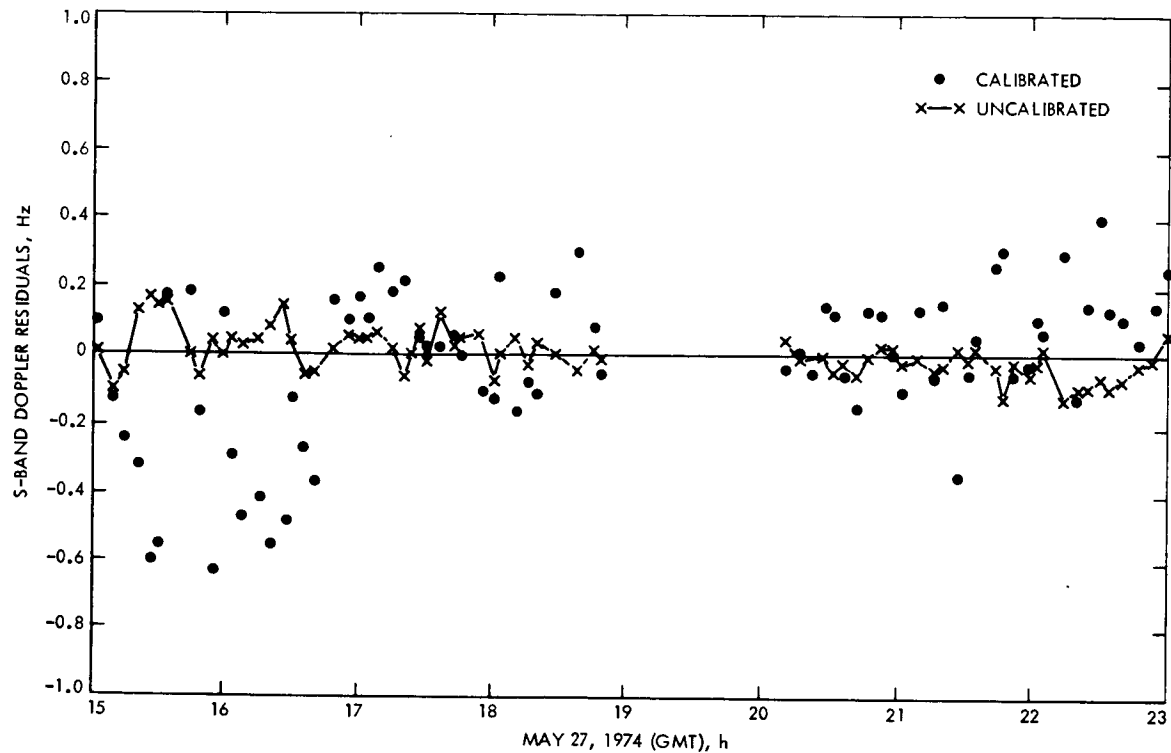


Fig. 10. Calibrated and uncalibrated S-band tracking doppler residuals

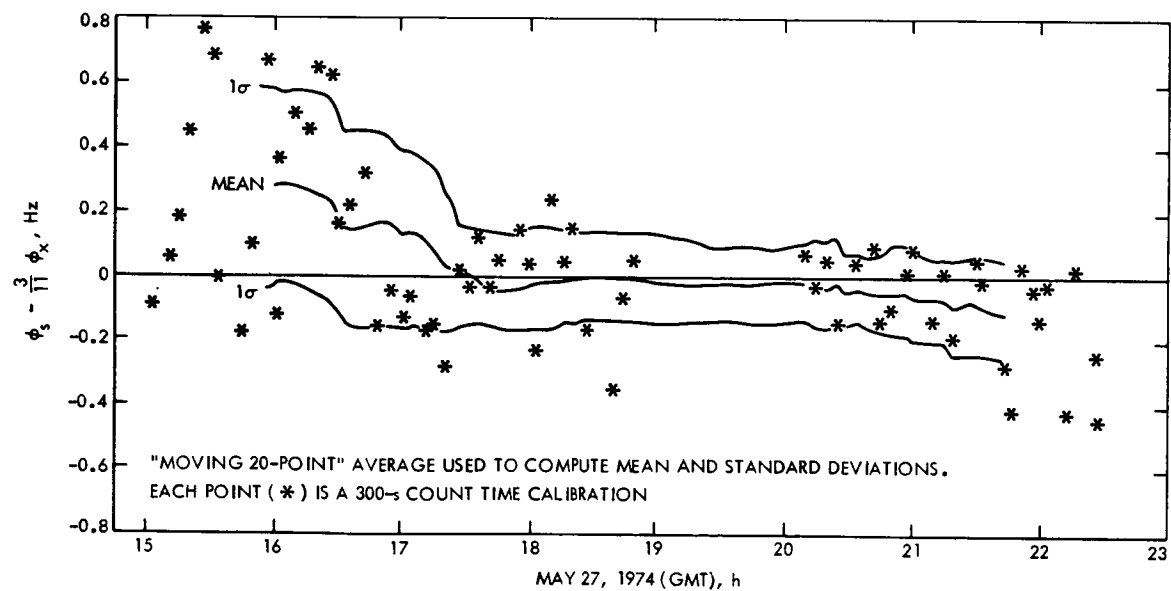


Fig. 11. S/X dual-doppler charged-particle calibration

N76-15199

100-kHz Frequency Divider, Distribution Amplifier

G. Lutes

Communications Systems Research Section

A 1-MHz to 100-kHz frequency divider, distribution amplifier module having low phase noise and low phase drift with temperature and high isolation between outputs has been developed for use in the hydrogen maser frequency standard, where it divides 1 MHz from the previous frequency divider down to 100 kHz and provides four transistor-transistor logic (TTL) outputs.

One-hundred-kilohertz divider, distribution amplifier modules have been developed for use in the hydrogen maser frequency standard. These modules develop a 100-kHz TTL-level signal by dividing the 1-MHz emitter-coupled logic (ECL) level signal from the previous frequency divider by 10 and then translating it to TTL-level signals which are distributed to the four outputs through line driver isolation amplifiers.

If the digital signal at 100 kHz were to be converted to a sine wave, another module would be required, which would increase the cost of the system. This conversion would also degrade the signal, and the degradation could become much greater if the sine waves were converted back to TTL levels by the user. Since this frequency is most often used as a clock, we thought it best to condition the signal for this use.

These frequency dividers are optimized for low phase noise and low phase drift with temperature. Low phase

noise is achieved by the use of ECL circuitry in the digital frequency divider and by using amplifiers having a large amount of negative feedback.

As seen in the block diagram (Fig. 1), the input circuit is an ECL digital frequency divider, which divides the input from 1 MHz to 100 kHz. This divider circuit is nearly identical to the 100- to 10-MHz divider circuit used in the 100-MHz frequency divider module. The only difference is that no comparator is used at the input to the divider since it receives a 1-MHz ECL-level signal from the previous module.

The 100-kHz, ECL-level signal goes through a translator having four TTL-level outputs which drive the four inverting field effect transistor (FET) input line driver isolation amplifiers. The signal from these amplifiers has the inverse polarity due to the amplifier. This inversion is corrected by a level shifting circuit at the output. Table 1 shows the test results of a typical 100-kHz divider, distribution amplifier module.

**Table 1. Test results of typical 100-kHz divider,
distribution amplifier module**

Input impedance (50 Ω nominal)	1.1:1 VSWR
Output impedance (50 Ω nominal)	1.1:1 VSWR
Output signal level	-0.6 to +2.7 V square wave into 50 Ω
Phase noise	-150 dB below carrier (100 kHz) in a 1-Hz bandwidth 10 Hz from carrier
Power supply requirements	+5 V, 52 mA -5 V, 290 mA +15 V, 180 mA -15 V, 195 mA

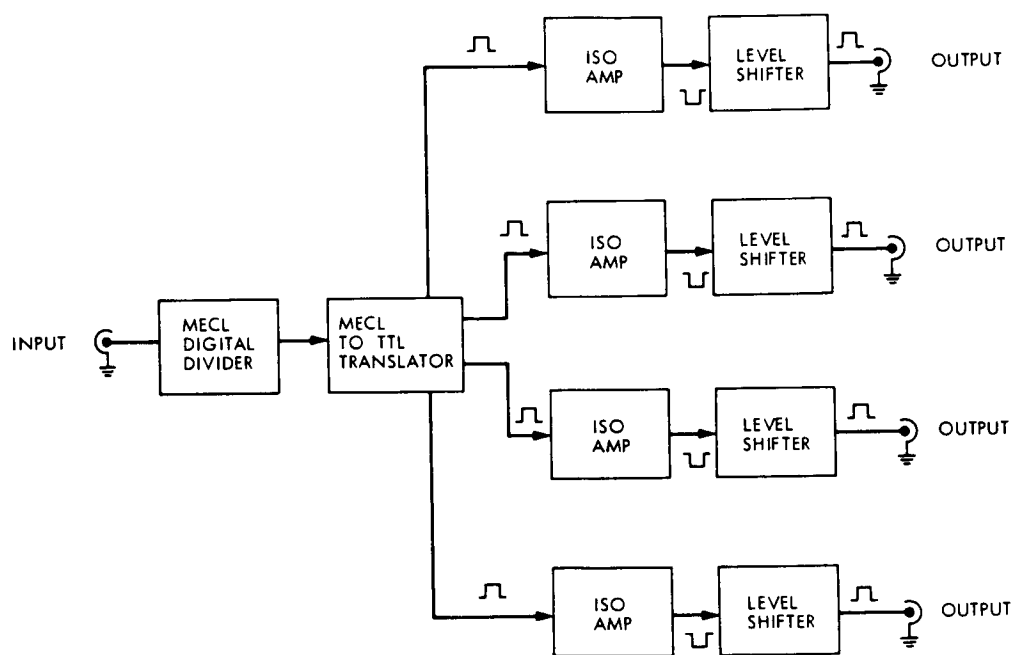


Fig. 1. 100-kHz frequency divider, distribution amplifier block diagram

N76-15200

The X-Band Low-Noise Antenna Measurement Cone

M. S. Reid, F. E. McCrea, K. B. Wallace, and C. T. Stelzried
Communications Elements Research Section

An X-band low-noise receiving cone with 17-MHz instantaneous bandwidth has been built to evaluate the 26-m antenna at the Venus Station (DSS 13), Goldstone, California, at X-band frequencies, and also to provide a means for precise radio source calibrations in this frequency range. These measurements are necessary to provide more accurate antenna gain performance calibrations for the 64-m antenna subnet. The zenith system temperatures with the cone on the ground and on the antenna are 17.5 and 20.8 K, respectively.

The X-band low-noise antenna (XLA) measurement cone has been built to evaluate the 26-m antenna at the Venus Station (DSS 13, Goldstone, California) at X-band frequencies, and also to provide a means for precise radio source calibrations in this frequency range. These measurements will provide the means to improve the calibration accuracy of the gain performance of the three antennas in the 64-m subnet.

The block diagram of the XLA cone is shown in Fig. 1. The X-band traveling wave maser (TWM) described in Ref. 1 has been modified, with a superconducting magnet in place of the permanent magnet and push-push pumping at 19 and 24 GHz. This modified maser, which has 45-dB gain and 17-MHz instantaneous bandwidth, has been installed in the XLA cone. As there is no waveguide switch between the horn and the input to the TWM, all Y-factor system temperature measurements are made with

an aperture load. The 33-dB coupler provides an access port which is normally terminated in a load, as shown in Fig. 1. This port allows the injection of test signals to the input of the maser.

Three noise diodes, ND1, ND2, and ND3 in the diagram, have been provided which, when activated, inject approximately 90, 6.5, and 190 K, respectively, into the system. The diagram also shows that a switch and 10-dB coupler have been built into the ND2 path to provide an optional reduction in ND2's equivalent noise temperature to approximately 0.6 K. The concept of a low-level noise diode is to provide a capability for a noise-adding radiometer (NAR) (Ref. 2) during spacecraft tracking with minimum system performance degradation. A requirement for on-line system temperature measurement in the network during spacecraft tracking could be satisfied by a NAR, provided the noise diode injected level was

sufficiently low. The switched 10-dB coupler potentially provides the required noise diode calibration under high-level operation.

Figure 2 shows a block diagram of the cone receiver. There are four input ports and two output ports. A 5-MHz reference signal, derived from a frequency synthesizer, drives a times 20 multiplier, and thence a phase-locked multiplier, to provide a local oscillator signal for the mixer module, as shown in the diagram. The mechanical tuning range of the phase-locked multiplier is 1.5 GHz. The high stability of this local oscillator signal chain provides a very long baseline interferometry capability for the cone. The radio frequency (RF) input is fed from the receiver port shown in Fig. 1, and the output from the mixer module is the intermediate frequency (IF) signal, which is processed in a convenient manner determined by each experimenter. The signal generator module provides two separate methods of generating the beacon signal from a 50-MHz source. The beacon signal is fed into the system, as shown in Fig. 1.

Figure 3 shows the upper section of the cone feed. The gears and drive motor assembly are not used and not connected. They form part of the right and left circular polarization change equipment that was used in the multifrequency X- and K-band (MXK) cone which was removed from DSS 14 earlier this year. The upper feed

section shown in the photograph was taken from the MXK cone and used in the building of the XLA cone without modification in order to keep the construction costs down.

Figure 4 shows the lower section of the XLA cone feed. The 33-dB coupler is shown on the input to the maser.

Figure 5 is a photograph of the maser showing both input and output sections. Figure 6 is a photograph of the noise box, which is also shown in the block diagram (Fig. 1).

The system temperature, measured at zenith with the cone on the ground at 8.45 GHz, was 17.5 K. The reference point for system temperature measurements is the maser input reference flange, which is shown in Figs. 1, 4, and 5. The follow-up contribution was 0.5 K, with a maser gain of 41 dB. The noise temperature of the maser is 7.5 K. When the cone was mounted on the 26-m antenna at DSS 13, the zenith system temperature was 20.8 K, with a follow-up contribution of 0.16 K. This results in an effective differential temperature between the cone on the ground and the cone on the antenna of 3.6 K.

When the XLA cone is not being used on the 26-m antenna, it will be operated on the ground at DSS 13. These ground measurements will verify and back up the X-band atmospheric noise temperature statistics program (described in Ref. 3).

References

1. Clauss, R. C., and Quinn, R. B., "Low Noise Receivers; Microwave Maser Development," in *JPL Space Programs Summary 37-61*, Vol. 2, pp. 86-88, Jet Propulsion Laboratory, Pasadena, Calif., Jan. 31, 1970.
2. Batelaan, P. D., Goldstein, R. M., and Stelzried, C. T., "A Noise Adding Radiometer for Use in the DSN," in *JPL Space Programs Summary 37-65*, Vol. 2, pp. 66-69, Jet Propulsion Laboratory, Pasadena, Calif., September 1970.
3. Reid, M. S., Parham, O. B., and Gardner, R. A., "An X-band Radiometer for the Microwave Weather Project," in *The Deep Space Network Progress Report 42-29*, pp. 54-59, Jet Propulsion Laboratory, Pasadena, Calif., Oct. 15, 1975.

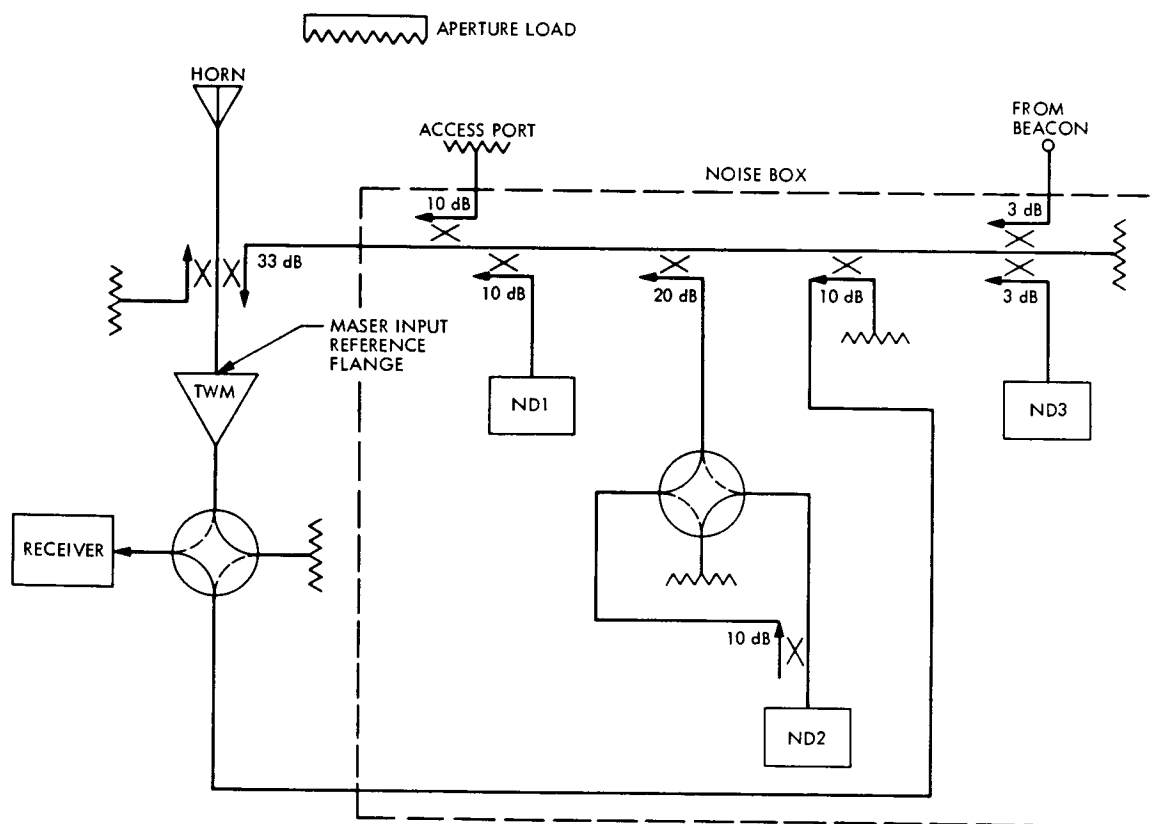


Fig. 1. Block diagram of the XLA cone

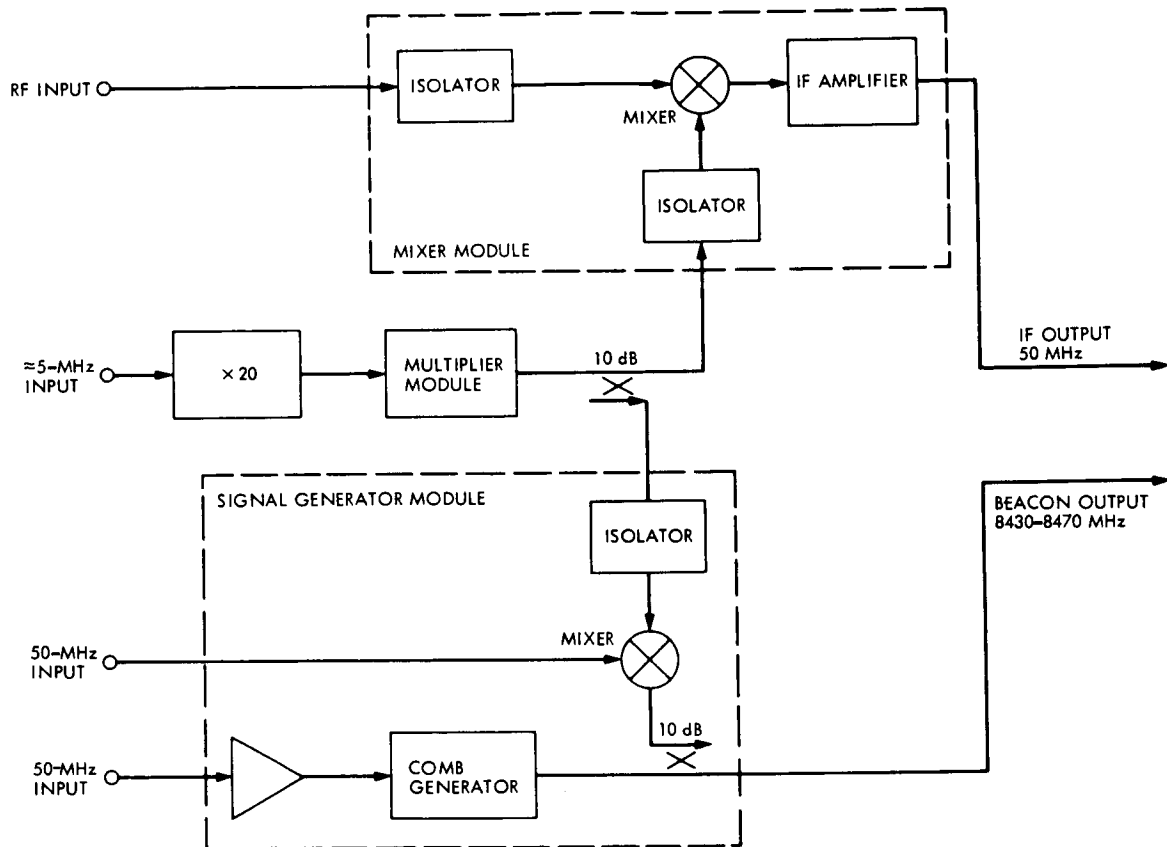


Fig. 2. The XLA cone receiver

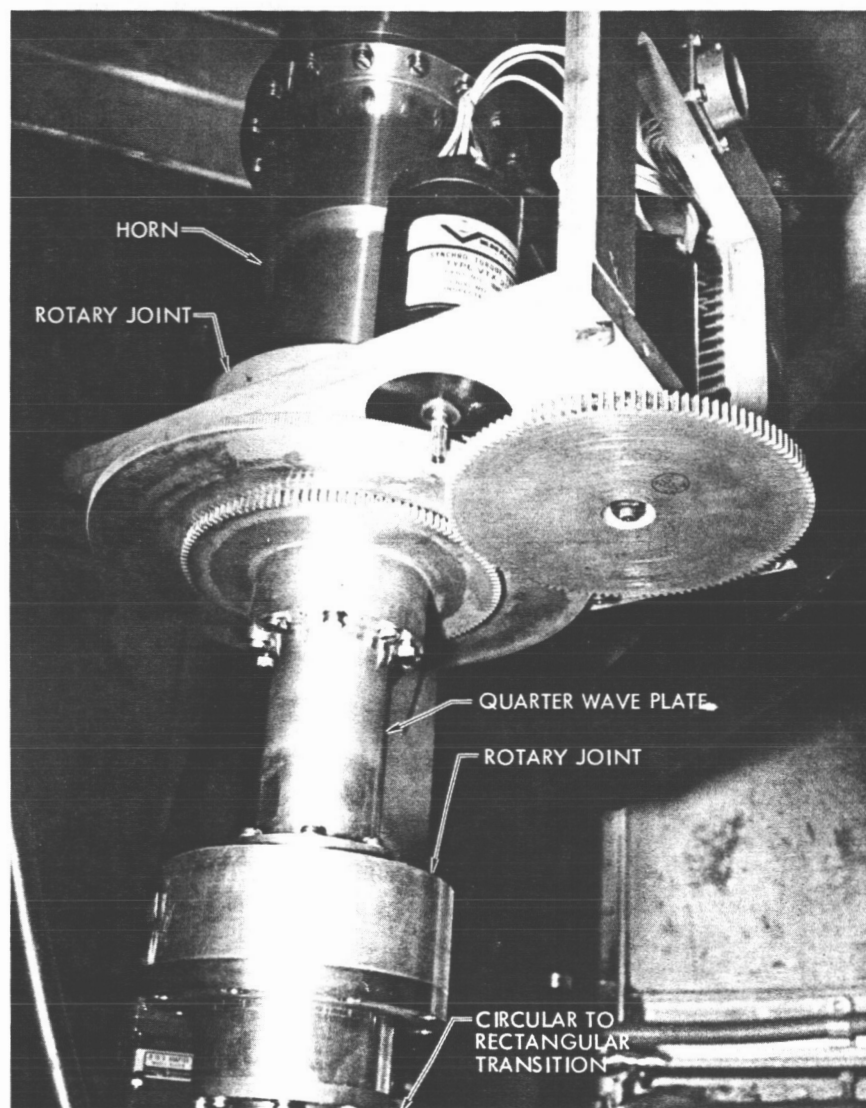


Fig. 3. Upper section of the XLA cone feed

REPRODUCIBILITY OF THE
ORIGINAL PAGE IS POOR

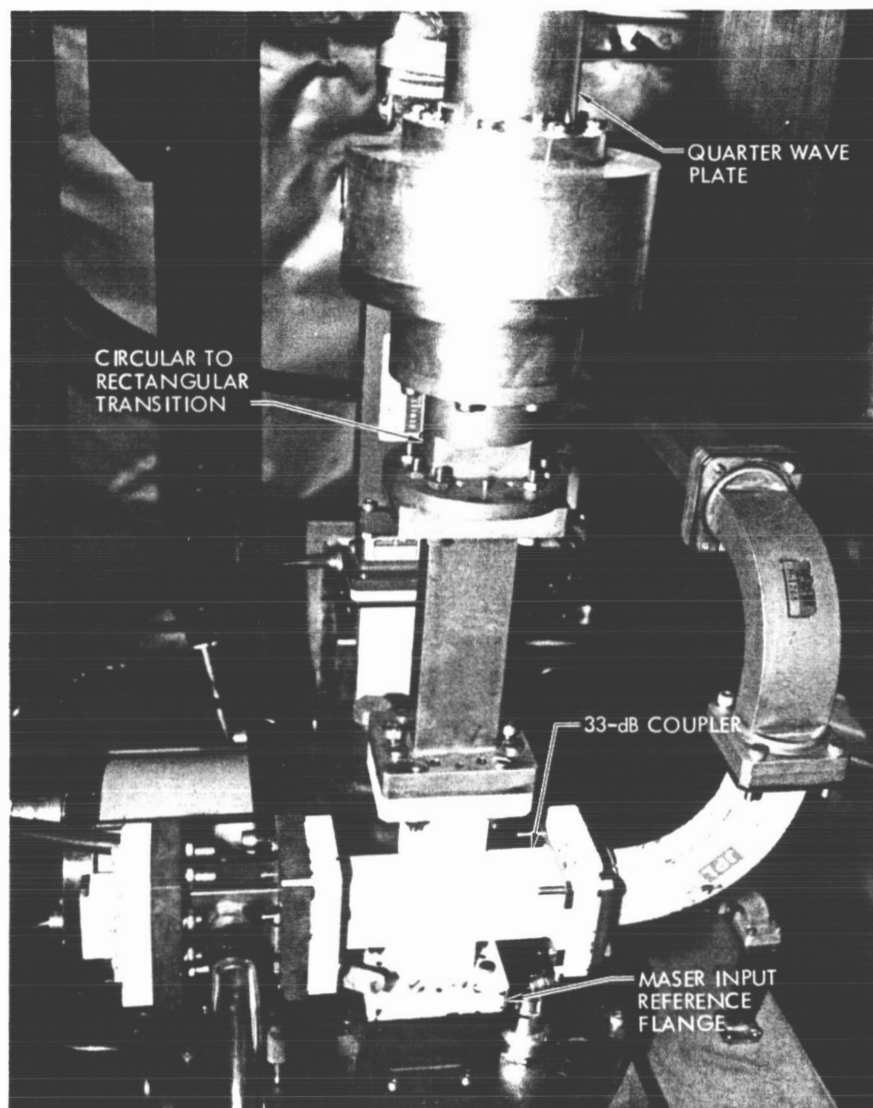


Fig. 4. Lower section of the XLA cone feed

REPRODUCIBILITY OF THE
ORIGINAL PAGE IS POOR

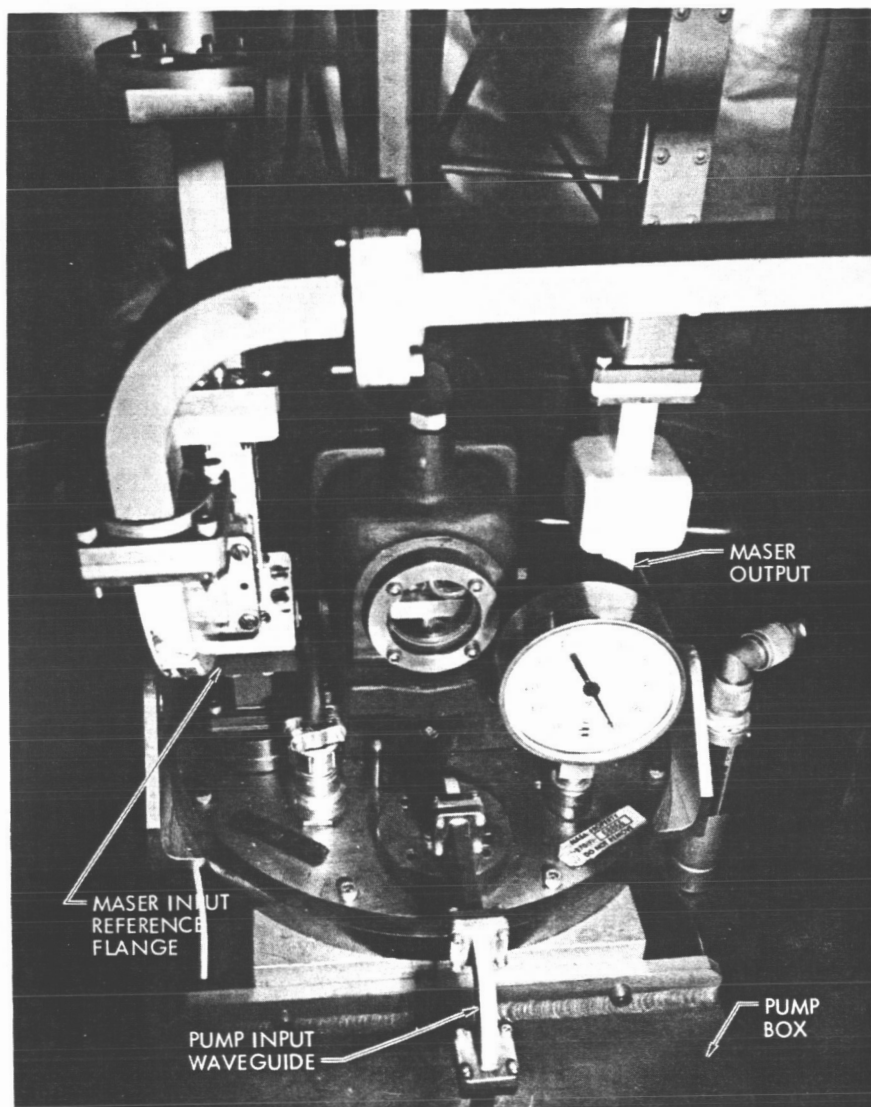


Fig. 5. XLA cone maser

REPRODUCIBILITY OF THE
ORIGINAL PAGE IS POOR

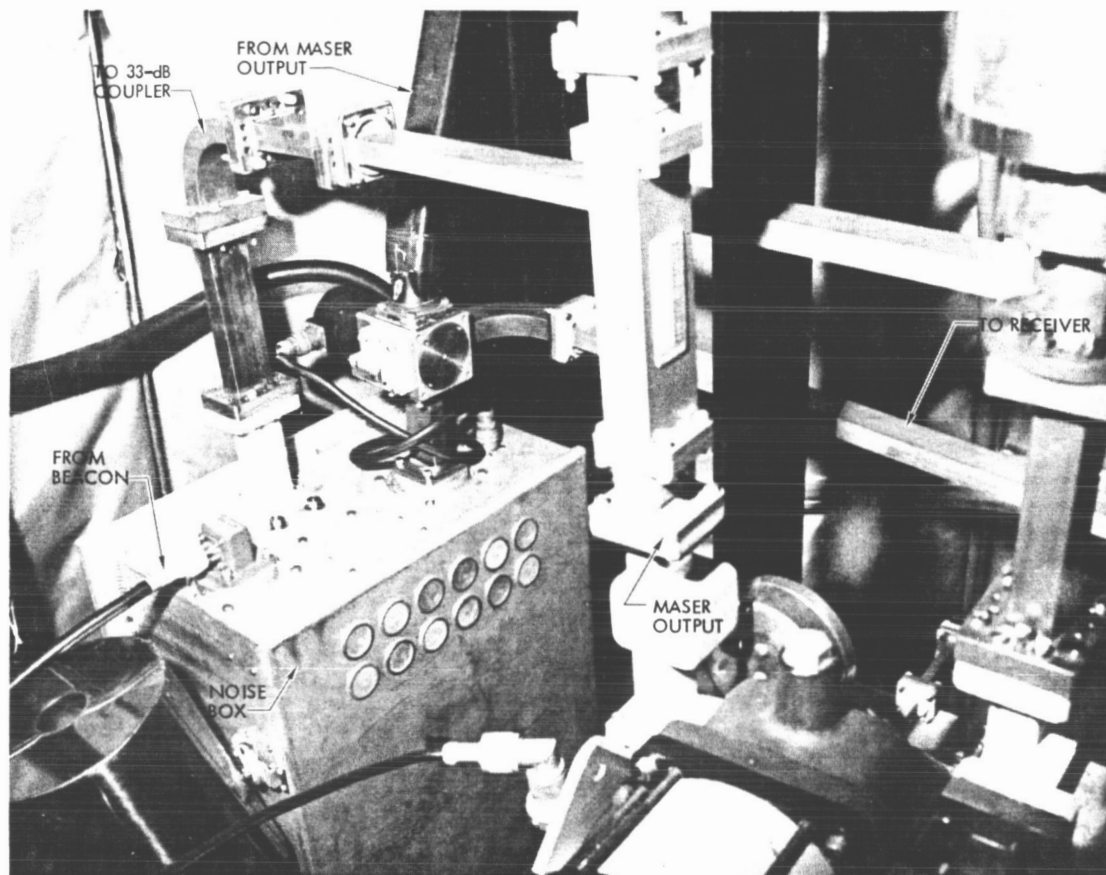


Fig. 6. XLA cone noise box

REPRODUCIBILITY OF THE
ORIGINAL PAGE IS POOR

N76-15201

Performance of DSS 13 26-m Antenna at X-Band

A. J. Freiley

Communications Elements Research Section

The X-band low-noise antenna (XLA) measurement feedcone was operated on the DSS 13 26-m antenna at Goldstone, California, during June 1975 to evaluate, primarily, the overall system efficiency. Radio sources were selected, commonly accepted values of flux density established, and measurements completed, and some conclusions are drawn. The antenna system presently suffers from poor pointing stability. On the other hand, the previously welded and rebolted main reflector has remained quite stable over a period of approximately 5 years.

I. Introduction

The DSS 13 26-m antenna was operated at 8450 MHz during June 1975 for the purpose of overall antenna system evaluation. The antenna reflector portion had previously been operated at X-band during June 1967 and October 1968 with an early feedcone system (Refs. 1,2). During the intervening time, the antenna structure has undergone many changes, necessitating the current set of measurements. To evaluate the antenna performance, the X-band low-noise antenna (XLA) measurement feedcone was installed, and radio metric observations of selected radio sources were performed using a noise-adding radiometer. The antenna parameters evaluated were axial focus of the subreflector, beam pointing characteristics, beamwidth, operating system temperatures, and overall system efficiency.

II. Selected Radio Sources

The performance characteristics of the antenna system were evaluated using 3C123, 3C273, 3C274 (Virgo A), DR 21, and the planets Venus and Jupiter. The important radio source characteristics assumed are listed in Table 1. The primary factors affecting the selection of a radio source to be used for antenna calibrations are accuracy of flux density, distribution of flux, source angular size, and source positions. The source 3C274 (Virgo A) was used to evaluate the gain of the system to be consistent with and comparable to previous work. The sources 3C123, DR 21, Venus, and Jupiter were used for both efficiency and pointing evaluations. The source 3C273 was also used for pointing evaluation, but the variability of its flux density makes it a poor standard for efficiency measurements. The use of more than one source for antenna performance

evaluation gives a more complete and consistent calibration of the performance.

III. Antenna Performance

A. Antenna Feed System

The antenna feed system with the XLA feedcone is a low-noise system. The overall operating system temperature at zenith (T_{op}) was approximately 21 K. The operating system temperature as a function of elevation angle, including atmospheric loss and antenna spillover, is presented in Fig. 1. The antenna polarization was set to right circular. By using the drift curve technique, the half-power beamwidth was measured to be 0.1 deg or about 6 arc minutes, as expected.

B. Pointing

The pointing characteristics of the antenna were evaluated using the technique of boresighting about the half-power points of the main beam. The measured elevation offsets as a function of elevation angle are presented in Fig. 2. The mean elevation offset is ($+0.014 \pm 0.013$) deg (1σ). Assuming the main beam shape is gaussian, the ± 0.013 -deg uncertainty results in approximately 0.2 dB (1σ) gain loss. The corresponding measured azimuth offsets as a function of azimuth angle are presented in Fig. 3. The mean azimuth offset is ($+0.122 \pm 0.019$) deg (1σ). Again assuming the gaussian beam shape, the ± 0.019 -deg uncertainty results in approximately 0.4 dB (1σ) gain loss. As an example of the effect of this level of poor pointing, assume the boresight errors were, in each axis, at the 1σ levels of $+0.013$ and $+0.019$ deg previously mentioned. The resulting error would be 0.023 deg, and the corresponding gain loss is approximately 0.6 dB. Random pointing errors of ± 0.020 deg would result in 0.5 dB of gain loss and are common, as seen in Fig. 2 and 3. This performance is considered unacceptable in the context of a high-performance X-band reflector antenna. During a windy period of 50–80 km/h (30–50 mph) gusts, observations of the planet Venus were attempted. The antenna-mounted television camera enabled the visual observations of the antenna pointing performance. Momentary pointing errors of ± 0.050 -deg peaks (~ 3 dB loss excursions) were observed during large wind gusts, implying that the entire antenna framework was being moved.

C. Axial Focus

To examine the main reflector focal length as a function of elevation angle, the antenna is set to track a radio source while the subreflector is slewed in the axial direction. The optimum position is displayed by the

analog output of the noise-adding radiometer at a particular elevation angle. Performing this test at various elevation angles during a track, the function can be determined. After performing this procedure for the DSS 13 26-m antenna, the optimum indicated control room position was determined not to be elevation-dependent. The indicated control room position of 320 deg is valid for all elevations. The measured data are presented in Fig. 4. This result indicates that the focal length stability of the antenna is excellent. The bolting and welding of the main reflector backup structure and other improvements done previously are apparently still tight. Previous measurements, described in Ref. 3, have indicated large changes in the axial focus which are a clear symptom of very flexible antenna radial ribs. Fortunately, this effect has been completely corrected.

D. System Efficiency

System efficiency is defined as the antenna efficiency including the atmosphere loss as measured at the input flange of the maser amplifier. To examine the system efficiency, the technique of ON/OFF source system temperature measurements was utilized. This technique measures system temperature with and without the noise contribution from the radio source. By calculating the change in system temperature (ΔT_a) caused by the radio source and by knowing the flux density of the radio source, the system efficiency can be determined. The system efficiency vs. elevation angle data are presented in Fig. 5, with a second-order curve fitted to the data. From the fitted curve, the peak efficiency is 43% at 44-deg elevation angle. The poor pointing of the antenna is the primary cause of the large scatter in the efficiency. A change to the antenna system which could contribute to the decrease in mean efficiency is the fully welded subreflector, including the S-band vertex plate. This vertex plate was removed from the antenna for the measurements described in Ref. 2 but could not be removed for this series of tests. Some combination of the welding distortion and the effect of the vertex plate which modifies the aperture illumination has reduced the system efficiency from 50.3% (October 1968) to 43% (this reporting). This decrease in efficiency corresponds to 0.7 dB of gain loss.

IV. Conclusion

In the period between the measurements of October 1968 to the measurements of June 1975, the system efficiency has decreased from 50.3 to 43%. The axial focal length stability of the antenna remains unchanged; that is, the antenna need not be refocused as a function of elevation angle. The most serious problem of operating

the DSS 13 26-m antenna at the shorter wavelength is clearly the overall pointing stability of the system. Such changes in the antenna pointing as described by Figs. 2 and 3 degrade the total performance of the antenna system. This degraded performance would be operation-

nally experienced for many missions where boresighting is infrequently done, if at all. As was stated in Ref. 2, there remains a problem in pointing ability of the 26-m antenna which seriously hampers future work at the shorter wavelengths.

References

1. Bathker, D. A., "Efficient Antenna Systems: X-Band Gain Measurements," in *The Deep Space Network*, Space Programs Summary 37-49, Vol. II, pp. 65-67, Jan. 31, 1968.
2. Norman, R. A., "Efficient Antenna Systems: X-Band Gain Measurements, 85 ft Antenna," in *The Deep Space Network*, JPL Space Programs Summary 37-55, Vol. II, pp. 47-49, Jan. 31, 1969.
3. Bathker, D. A., "Efficient Antenna Systems: X-Band Gain Measurements," in *The Deep Space Network*, JPL Space Programs Summary 37-47, Vol. II, pp. 77-80, Sept. 30, 1967.
4. Dent, W. A., "A Flux-Density Scale for Microwave Frequencies," *Ap. J.*, Vol. 177, pp. 93-99, Oct. 1972.

Table 1. Radio source characteristics

Source	S 8450 MHz	Source size	Source structure	Size correction factor	Spectral index at 8450 MHz
3C123	10 f.u.	Two points	Close double sep. 13 arc sec	1.017	-0.94
3C273	21 f.u. Variable	Point	—	1.00	—
3C274 (Virgo A)	42 f.u.	40 × 20 arc sec	Core halo	1.13	-0.85
DR 21	20 f.u.	20 arc sec	Gaussian	1.00	-0.13 (Ref. 4)
Venus	18 f.u.	Semi diam 11.43 arc sec	Planet (disk at 660 K)	1.00	—
Jupiter	13 f.u.	Semi diam 17.30 × 18.51 arc sec	Planet (disk at 230 K)	1.00	

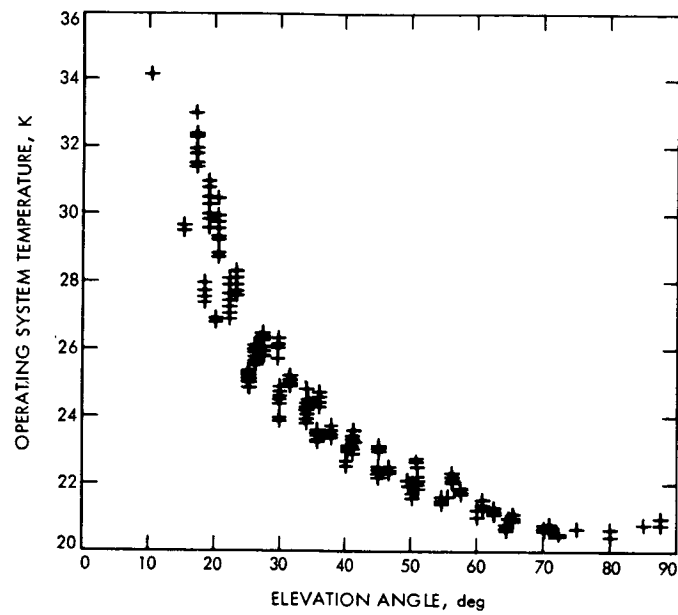


Fig. 1. Operating system temperature as a function of elevation angle, XLA feedcone, DSS 13

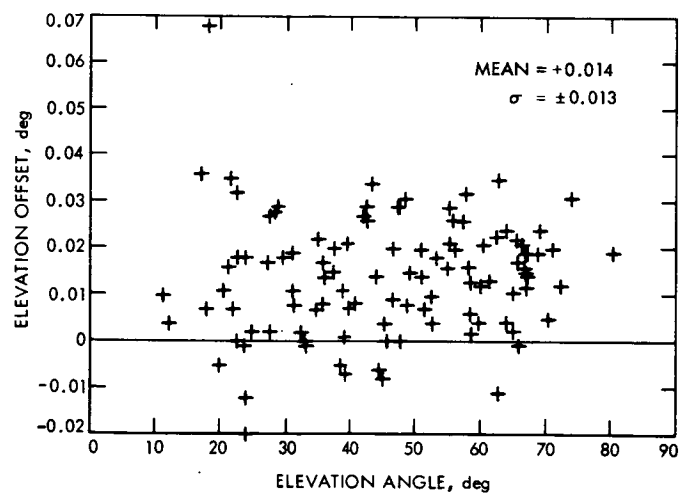


Fig. 2. Elevation offsets as a function of elevation angle, XLA feedcone, DSS 13

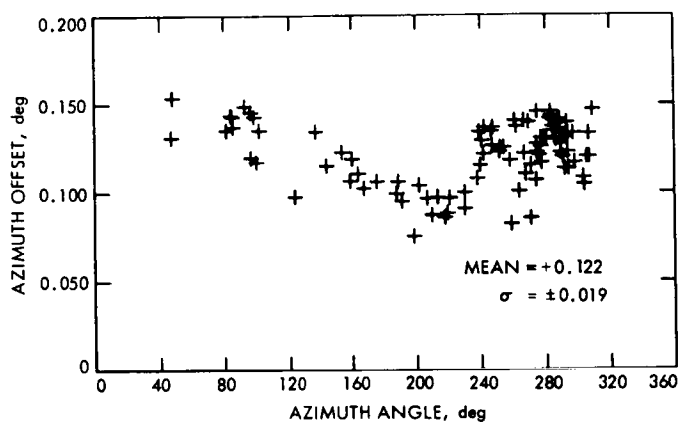


Fig. 3. Azimuth offsets as a function of azimuth, XLA feedcone, DSS 13

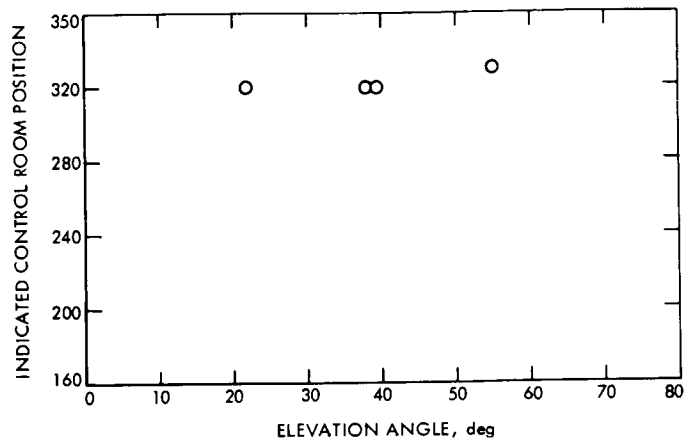


Fig. 4. Axial focus as a function of elevation angle, XLA feedcone, DSS 13

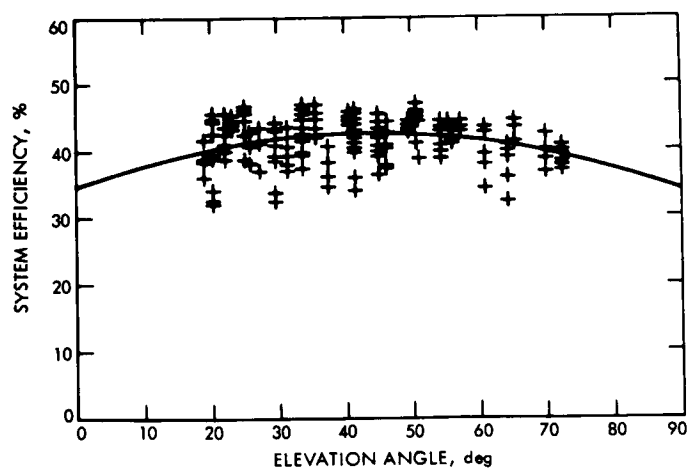


Fig. 5. System efficiency as a function of elevation angle, XLA feedcone, DSS 13

N76-15202

DSS 14 X-Band Radar Feedcone

D. E. Neff and D. A. Bathker
Communications Elements Research Section

A high-power 400-kW continuous-wave (CW) X-band radar feed system is described for use with the Goldstone, California, 64-m DSS 14 antenna system. Design considerations, their solutions, and final system testing are discussed. The radar system, unique in terms of antenna size, radiated power, and efficiency, became operational in December 1974.

I. Introduction

There were two aspects to the feed development for the DSS 14 400-kW X-band radar: the radar feed system and hardware design and the integration of all elements within a new antenna feedcone. At the start of this project, an existing research feedcone then in use at DSS 14 (MXK for multiple X-band, K-band) contained wide-band X-band and separate K-band receiving systems. Both front end systems performed with high feed efficiency and very low noise levels (Refs. 1, 2, 3, and 4).

II. Radar Feed System Design

A new feedcone was planned, based on retention of all existing research capabilities, the addition of a high-power radar feed, and integration of the transmitter within. The new feedcone (XKR for X-band, K-band, radar) would occupy the 64-m-diameter antenna Bay 1 research and development position on the DSS 14 tricone. As shown in Figs. 1 and 2, the tricone structure consists of three bays, or feedcone locations. The upper two feedcone locations

are reserved for the network operational S/X-band radio system. Each of the upper feed cone locations includes one subreflector stop or focal position, providing perfect overall antenna system (axial) pointing. The lower feedcone location includes three subreflector stops, 1R, 1, and 1L, each providing perfect antenna system pointing when the subreflector is so positioned. Of course, only one focal position may be used at a given time (with the exception of the operational position of the S/X-band reflex dichroic feed system on the upper two feedcones, Fig. 2). Each of the three available research focal positions is occupied in the new feedcone design, as shown in Fig. 1.

The major consideration in the X-band radar feed system design was the polarization selection technique. Right-hand or left-hand circular polarization (RCP or LCP) was required for transmission, with the opposite polarization required for "matched" reception (accounting for signal phase reversal after reflection) and the same polarization desired (but not mandatory) for "crossed" reception experiments. Several common waveguide

devices (turnstile junction, orthomode transducer, quarter-wave plate between rotary joints) have provided switchable polarization in high-CW-power planetary radars. In the case of the X-band 400-kW radar, it was necessary to commit to acceptable performance by a firmly established date: the Saturn ring opportunity of January 1975. The high risk of waveguide breakdown failures in the candidate waveguide devices indicated that a more reliable polarization selection technique was needed.

The plan evolved was as follows: One of the waveguide devices would be selected for further development, with a goal of providing an operationally simple yet reliable conventional switched feed polarizing system. In parallel, a nonswitched (fixed polarization) feed would be developed for the high-power transmit function. The tricone subreflector focus position would be the switch element, alternating between transmit and receive feedhorns (1L to 1 in Fig. 1) during the transmit/receive changeovers. Even though questions of 64-m antenna system quadripod dynamic behavior (damping time) and subreflector motor/gearing wearout arose, this proposed mode remained the primary backup to assure a functional X-band radar by January 1975.

Once the above system planning, with backup provision, was established, the X-band portion of the complete XKR feedcone block diagram was completed (Fig. 3). The preferred radar operation would be as follows: transmission and reception would both occur through the radar feed, with the subreflector fix-focused in the 1L position; switching from radar-transmit to radar-receive would be accomplished by rotating the high-power polarization switch and changing the transmit/receive switch. The wideband receive feed would serve as the backup receive system for the radar as well as continue in use for the normal radio science and DSN development activities.

III. Radar Feed Component Design

As mentioned above, the major system and component consideration for the radar feed was the polarization selection technique. Use of a waveguide orthomode coupler, together with a fixed circular polarizing device, was considered, but no acceptable low-power design was available for modification to serve at high power. Further, breakdown risk exists due to complex fields within orthomode couplers. Rotary joints, in TE₁₁ mode cylindrical waveguide, have given reliable 400-kW service in DSN operational and planetary radar systems at S-band (with obvious larger-size waveguide and attendant lower internal field strengths). At X-band, the scaled diameter of the rotary joint cylindrical waveguide, 34.77 mm (1.369

in.), provides a theoretical breakdown level (based on 30×10^5 V/m) of 4.4 megawatts (MW). The 34.77-mm cylindrical waveguide (WC137), compared with the other system waveguide (WR125), which has a theoretical breakdown level of 2.5 MW, appears acceptable. This is further enhanced when derating factors are introduced (Ref. 5). For WR125, practical considerations lead to a derating factor of 0.28, or 0.70 MW maximum rating. For WC137, the derating factor is estimated at 0.40, or 1.8 MW maximum rating. Thus, the cylindrical WC137 waveguide is stressed a factor of 2.5 less (in power) than the rectangular WR125 waveguide.

Despite relatively unknown electric field conditions present within the choke assemblies of such TE₁₁ mode rotary joints, the risk vs. payoff of adopting this approach for further development appeared acceptable. Similar choke assemblies used in rectangular waveguide switches had previously given good service at 100 kW CW in WR112 at 7150 MHz, an earlier JPL lunar radar. It is interesting to note that in this previous experience, 100-kW operations were conducted within a waveguide having a derated maximum power ability of 400 kW, or a 4:1 power safety margin. In the new radar, the WR125 rectangular waveguide provides only a 1.75:1 power safety margin (0.70/0.40). The WC137 provides a 4.5:1 power margin (1.8/0.40). Clearly, careful attention to details such as waveguide internal cleanliness, surface finish, and avoidance of hot spots was recognized necessary for successful operation of the new radar with such a slim safety margin, particularly in the WR125 rectangular waveguide portion.

The radar feed assembly consists of three major parts; the hybrid mode (TE- and TM-component) corrugated waveguide horn, the quarterwave plate polarizer, and the transition from cylindrical to rectangular waveguide. The parts are constructed principally of OFHC copper, with reduced microwave path lengths and nonflanged waveguide joints where possible to minimize dissipation loss and resultant heating. One primary difference between the radar feed assembly and the older existing low-power wideband receive feed assembly is in a feedhorn matching device. As will be described in the performance section, the low-power receive feedhorn is matched in such a way (with a dual iris section) as to provide good polarization axial ratio (or ellipticity) at two frequencies: the DSN receive band at 8.4 GHz and the cooperative Goldstack radar (and radio science very long baseline interferometry (VLBI)) frequency near 7.8 GHz. For the high-power radar, the matching device was too risky from a breakdown viewpoint; it was eliminated in the high-power design.

Figure 4 presents a cross section of the radar feed assembly, showing the three major parts:

- (1) Hybrid mode feedhorn. The low-power design of the corrugated waveguide horn has been discussed elsewhere (Ref. 6). The high-power horn assembly utilizes the internal structure of the low-power design, differing only in the added water cooling and round waveguide connections. The high-power horn is divided into four sections, each approximately 150 mm long. The feedcone roof is used to provide a heat sink for the larger-diameter (lower dissipation loss) aluminum sections (see Fig. 8) at the connection between the aperture and third sections. The smaller-diameter (higher dissipation loss) first and second sections are made of OFHC copper, with water cooling jackets. Three flanges are used in the larger sections of the horn; bolts are placed on approximately 15-mm centers. The small-diameter end of the horn is an integral part of one rotary joint, as shown in Fig. 4.
- (2) Polarizer section. The polarizer section converts a linearly polarized TE_{11}^0 mode into a circularly polarized (RCP or LCP) TE_{11}^0 mode through quarterwave plate action. No flanges are used in this section; the breakpoints are designed as integral parts of the rotary joints, as shown in Fig. 4. OFHC copper construction is used with water cooling jackets. In this section, water cooling not only inhibits elevated surface (and possible particulate debris) temperatures; it also limits thermal expansion of the critical rotary joint bearings and choke details. The theoretical loss of cylindrical copper WC137 waveguide used in the polarizer section is approximately 0.040 dB/m (0.012 dB/ft); 4.6 kW/m (1.4 kW/ft) is dissipated. Thermal expansion is worrisome since clearances between rotating surfaces are only 0.125 to 0.250 mm (0.005 to 0.010 in.). Pressurization gas seals are used to minimize leakage of the 0.22 N/cm² (5-oz/in.²) nitrogen used in the waveguide system. As mentioned, relatively unknown electric field conditions in the choke details remains a minor risk with this section.
- (3) Waveguide transition. A smooth, tapered transition from cylindrical WC137 to rectangular WR125 waveguide was available from a previous program. With the exception of water jacket and integral rotary joint details, no design was required. While this transition is relatively long, as seen in Fig. 4 (with resultant dissipation loss), use of a shorter four-section stepped transition (as in the wideband receive feed assembly) was discarded on the basis of

complex field conditions within, particularly in this case of an unfiltered transmitter output, with possible resultant harmonic fields in the output transmission lines.

IV. Radar Feed Component Testing

Early development tests consisting of feedhorn pattern and polarizer ellipticity (July 1973–March 1974) were conducted using the 20-m anechoic chamber at the JPL Mesa Antenna Range. Medium-power tests (March 1974–September 1974) were conducted at the DSS 13 transmitter building. High-power testing was started at DSS 14 (November 1974) on the antenna and continues as time permits.

A. Antenna Range Tests

The antenna range tests consisted of selecting the proper cylindrical waveguide phasing sections and exact quarterwave plate length for the 8495-MHz radar frequency. The development phase was extended due to the fact that an OFHC copper materials shortage developed and fabrication was delayed. Also, the final polarizer and transition sections required fabrication using the electric discharge machine process and required additional time. Final assembly and testing was done in a relatively short period during March 1974.

The radar feed system ellipticity is shown in Fig. 5. The voltage standing wave ratio (VSWR) at 8495 MHz is less than 1.05. Performance below 8450 MHz is a natural function of the quarterwave plate; from 8450 to 8550 MHz, phasing of minor internal mismatches produced a very-high-quality polarization performance.

The low-power wideband receive feed for the XKR feed cone was further developed at this time. Again, cylindrical waveguide phasing sections and exact quarterwave plate length, and (as mentioned) a feedhorn matching device were the development parameters. The feedhorn matching device is a suitably spaced iris pair, weakly resonant (and well matched) at the 8.4-GHz band; simultaneously, the iris pair provides a desired reflection coefficient (magnitude and phase) at the 7.8-GHz band. As seen in Fig. 5, the natural behavior of 8.4-GHz design quarterwave plate of the type used here is to provide approximately 3 dB of ellipticity at 7.8 GHz. This level of cross polarization is considered unacceptable; use of the matching device reflects a specified portion of an outgoing (test) wave. Due to two passes of the reflected wave through the quarterwave plate (and cross-polarized reflection at the input end), the reflected wave exits the

feed primarily at the feedhorn aperture end rather than at the input end. By proper overall phasing, the total outgoing wave can then be corrected in ellipticity, since it then consists of three components: Component A, the desired polarization; Component B, the undesired polarization (these components are output on the first "pass"); and finally, Component C, the twice reflected specified portion, phased to largely cancel Component B. That this technique works is seen in Fig. 6. High-quality polarization performance is obtained in both the 7.8- and 8.4-GHz bands for the wideband receive feed, as is needed for the multi-purpose functions provided by this equipment.

B. DSS 13 Medium-Power Testing

The first medium-power testing was done in a special modified klystron test fixture, mounted on one of the feedcone elevators at the DSS 13 transmitter building. The feedhorn and transmitter were raised as an assembly to allow transmission through a small hole in the roof of the building (Fig. 7). Over a 2-3 month period, both the fixed (backup) and rotary joint feed assemblies were tested. A final test at 170 kW (May 1974) with a single klystron was made on the rotary joint feed for 2-1/2 h. The successful sustained test at 170 kW represented 65% of the expected field strength at 400 kW; with this encouragement, a firm decision was made to install the rotary feed in the new feedcone, in anticipation of full-power dual-klystron tests. Feedcone testing at DSS 13 was later limited to 250 kW due to various problems.

The full assembly of the radar feed unit is shown in Fig. 8. The feedcone roof interface provides a nonrotatable reference; the rectangular waveguide end provides the second reference. The polarization switch drive acts to rotate the quarterwave plate between two stable (and highly repeatable) positions 90 mechanical degrees apart, for LCP or RCP transmission or reception. A closeup of the polarization switch drive is seen in Fig. 9. This rugged mechanism has a built-in dwell feature to permit ring, worm, and motor overtravel during motor coast-down. The cycle time of the mechanism is 6 s; this relatively long switch cycle was considered adequate for the intended initial purpose of the radar.

Figure 10 shows the non-water-jacketed low-power wideband receive feed, ready for feedcone installation. Finally, Fig. 11 shows the top of the completed XKR feedcone. The two X-band horns are seen, as well as the K-band (14-17 GHz) horn. Three future feedhorn mounting locations are visible. Space for a K-band off-axis (reference) horn, as well as the two intermediate locations, is provided. Internal space is, however, another matter. The XKR feedcone, as completed with the dual-klystron

400-kW transmitter in the lower section and three feeds and two traveling wave masers (TWMs) for X- and K-band in the upper section, is very crowded.

C. DSS 14 Antenna High-Power Tests

Early in the initial high-power tests (November 21, 1974), a Kapton 0.075-mm (0.003-in.) horn window was destroyed when a large hole was burned in the surface. Replacement of the horn window with a thinner 0.025-mm (0.001-in.) sheet and cleaning of the connecting waveguide corrected the problem.

The X-band radar feed and feed cone system became operational in December 1974 for the planned Saturn ring experiment and successfully continued transmitting at power levels up to 400 kW into February 1975. No high-power failures of any consequence occurred with the feed during this period.

V. Radar Feedcone RF Performance

After installation at DSS 14, the XKR feedcone was checked at X-band (November 9, 1974) for overall system efficiency (η) and operating system noise temperature (T_{op}), as functions of elevation angle. Both possible receive paths, as shown in the block diagram (Fig. 3), were checked (subreflector 1 and 1L positions in Fig. 1). As expected, overall antenna system pointing was the same on either receive path, verifying the excellent subreflector positioning (and feedhorn placement accuracy within the feedcone) previously observed with the DSS 14 antenna mechanical system.

Figures 12 and 13 show the measured performance. As is normal for DSN 64-m antenna systems operated at X-band, subreflector z-axis focussing, as a function of elevation angle, is necessary, and the effects of proper focussing are included in the data. The term "receiving conditions only" in Fig. 11 refers to the fact that the measurements are done with a radio star. It is possible (although unlikely) that some performance degradation might occur under transmitting conditions. In Fig. 12, overall system efficiency includes effects of the normally clear Earth atmosphere (as is usually encountered in operations). Also, it should be noted in Fig. 12 that the two efficiencies given are both for receiving conditions referenced to the TWM input. (More on transmitting conditions later.) Overall efficiencies of 46 and 45% are indicated for the two receive systems, or approximately 0.10 dB difference. This unexpectedly high difference was thought, at the time, to arise in either the transmit/receive switch or WR125/WR112 waveguide intercon-

necting piece (Fig. 3). Figure 13, which shows the operating noise level, basically confirms the radio star data; at zenith, the radar feed exhibited a 26-K noise level, while the wideband receive feed exhibited 21 K; the 5-K difference, at ambient temperature, represents 0.075 dB of dissipation loss. This unexpected condition continued during initial radar operations (December 1974 through February 1975).

In April 1975, the suspect transmit/receive switch was replaced with a spare unit in an attempt to reduce the 5-K difference in receive system noise temperatures. This was a worthwhile activity, since use of the radar in its intended mode (transmit and receive using the subreflector 1L position, as shown in Fig. 1) necessitated acceptance of significant receive system performance degradation ($-10 \log 26/21$ or 0.9 dB) at zenith. The results were essentially as expected: the radar feed receive system noise temperature was reduced 2.5 to 23.5 K at zenith. Upon careful testing (for insertion loss), however, the original transmit/receive waveguide switch was found entirely acceptable, with 0.010 dB of dissipative loss (the value of the replacement switch). It is concluded that the noise temperature reduction of 2.5 K (about 0.04 dB) is due to the careful cleaning of the radar feed accomplished at this time. Presumably, some contamination was responsible for the added insertion loss. This hypothesis is not completely acceptable, however, since such a high loss (nearly 1% absolute) would lead to extremely hot particulate temperatures within the waveguide, with resultant breakdown failures. In general, high reflections are ruled out as the cause for the anomalous behavior since noise temperature is a sensitive detector of dissipation, not reflection loss.

Table 1 is a collection of available XKR feedcone data as of June 1975. The later value of total operating noise temperature for the radar feed at zenith is given (23.5 K). The overall system efficiencies are, however, unchanged in Table 1. With consideration for the data scatter (Fig. 12) and the estimated absolute accuracies, the small difference (0.04 dB or 0.5% efficiency at approximately 50% efficiency) goes unnoticed in the gain term. As seen in Table 1, the K-band system has not been fully checked out.

VI. Conclusions

The 400-kW X-band radar transmit feed and separate receive feed systems in the XKR feedcone system have been successfully completed in time for the initial requirements of the radar program. The major consideration in system and component design was the method used

to achieve reliable switchable polarization between transmit and receive functions. The selected approach of a cylindrical waveguide rotary joint polarization switch was entirely successful despite (1) the relatively unknown electric field conditions within the rotary joint choke regions and (2) the relatively unknown harmonic output content of the unfiltered klystron (and resultant complex fields with increased breakdown risk). A totally reliable backup approach of a fixed-polarized feed, which was to have depended on subreflector switching to provide the necessary reversed transmit/receive polarizations, was built and tested but not used. Except for an initial horn aperture window failure, no erratic behavior has been experienced with the feed. It is unlikely that any arcs have occurred in the total feed assembly.

Despite the success of the key feed component (polarization switch), the actual operating mode of the radar at this time makes use of the subreflector switching mode. This is due to the operating noise levels of the two available receive paths which, at zenith, are 23.5 K (26.5 K during December 1974 to March 1975) for the radar receive and 21.5 K for the wideband receive systems. This difference in signal-to-noise performance (formerly 0.9 dB, now 0.4 dB) remains sufficiently great for experimenters to favor the lower-noise system. The difference is due to two additional components in the radar receive path (compared with the wideband receive path); a transmit/receive waveguide switch and an approximately 500-mm WR125 waveguide. The insertion loss of the additional components (0.01 dB for the switch and 0.03 dB for the waveguide) exactly account for 2.5 K of additional noise when looking out the radar receive path (see block diagram, Fig. 2). Future work towards eliminating this aspect of the system design would be useful.

Although the high-power radar feed system has been successful to date, rather minimal operating time has accumulated. The equipment must be recognized for what it is: quite new in R&D terms and extremely highly stressed in power-level terms. Lack of attention to proper servicing (nicked or broken waveguide flange, admittance of debris into the waveguide or horn, nitrogen pressurization failure) will provide a virtual guarantee of erratic (and possibly dangerous) operations. It is advised that above average attention be devoted to the care of this equipment.

Finally, mention of possible future work is made. The use of a recently developed dual-hybrid-mode feedhorn (Ref. 7) was considered at the outset of the radar project. The R&D nature of the improved feedhorn at the time and the total lack of use experience weighed against its

adoption for the time-constrained radar development. An important element of any future radar upgrade should be the new horn, which provides 0.3 dB one-way (0.6 dB radar system) advantage. The basic XKR feedcone roof structure is built to accommodate the above option. It should be recognized, however, that major internal

waveguide rearrangements would be needed, both to the radar itself and the wideband radio science and DSN development front end equipments. Such a future upgrade could be doubly advantageous if combined with a decision to relocate the existing X-band maser or add an unshared X-band maser fully dedicated to the radar.

References

1. Reid, M. S., Clauss, R. C., et al., "Low-Noise Microwave Receiving Systems in a Worldwide Network of Large Antennas," *Proc. IEEE*, Vol. 61, No. 9, September, 1973, pp. 1330-1335.
2. Batelaan, P. D., and Reid, M. S., "Improved RF Calibration Techniques: MXK Cone (Mod 0) Waveguide and Noise Temperature Calibrations," in *The Deep Space Network*, Space Programs Summary 37-62, Vol. II, pp. 78-81, Jet Propulsion Laboratory, Pasadena, Calif., March 31, 1970.
3. Freiley, A. J., "Radio Frequency Performance of DSS-14 64-m Antenna at 3.56- and 1.96-cm Wavelengths," in *The Deep Space Network Progress Report*, Technical Report 32-1526, Vol. XIX, pp. 110-115, Jet Propulsion Laboratory, Pasadena, Calif., February 15, 1974.
4. Batelaan, P. D., "Waveguide Voltage Reflection Calibrations of the MXK Cone (Mod 1)," in *The Deep Space Network Progress Report*, Technical Report 32-1526, Vol. VI, pp. 123-129, Jet Propulsion Laboratory, Pasadena, Calif., December 15, 1971.
5. Buchanan, H. R., "X-Band Uplink Microwave Components," in *The Deep Space Network Progress Report*, Technical Report 32-1526, Vol. XII, pp. 22-25, Jet Propulsion Laboratory, Pasadena, Calif., December 15, 1972.
6. Brunstein, S. A., "A New Wideband Feed Horn with Equal E- and H-Plane Beamwidths and Suppressed Sidelobes," in *The Deep Space Network*, Space Programs Summary 37-58, Vol. II, pp. 61-64, Jet Propulsion Laboratory, Pasadena, Calif., July 31, 1969.
7. Thomas, R. F., and Bathker, D. A., "A Dual Hybrid Mode Feedhorn for DSN Antenna Performance Enhancement," in *The Deep Space Network Progress Report* 42-22, pp. 101-108, Jet Propulsion Laboratory, Pasadena, Calif., August 15, 1974.

Table 1. XKR feedcone characteristics

XKR feedcone system	Overall system efficiency, gain tolerance, and T_{op} at 8495 MHz			Estimated system gain tolerance (3σ) absolute, dB	Total operating system noise temperature at zenith (T_{op}), K	Primary frequency range, MHz	Usable frequency range, MHz
	η , % 20-deg EL	η , % 45-deg EL	η , % 70-deg EL ^a				
Radar transmit feed ^b	40	43	42	+0.3 -0.8	N/A ^c	8495 \pm 10	8400-8700
Wideband receive feed ^d	43	46	45	+0.2 -0.7	21.0	7800-7900 8400-8500	7750-8800
Radar receive feed ^d (Use of TX horn for both functions)	42	45	44	+0.2 -0.7	23.5	8495 \pm 10	8400-8700
K-band receive feed	N/A	N/A	N/A	N/A	N/A	15,000-16,000	14,500-16,500

^aValues determined from curve fit through data but extended beyond the range of measured data.

^bFrom power combiner output, including losses; estimated efficiencies.

^cN/A = not available.

^dReferenced to the TWM input; measured efficiencies.

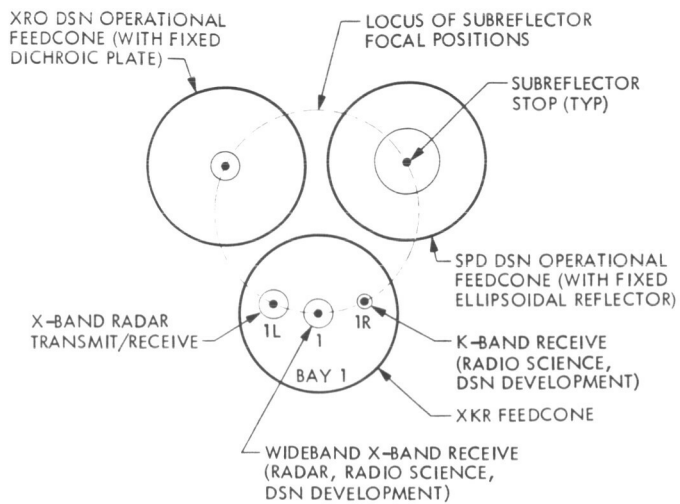


Fig. 1. Face view of DSS 14 tricone

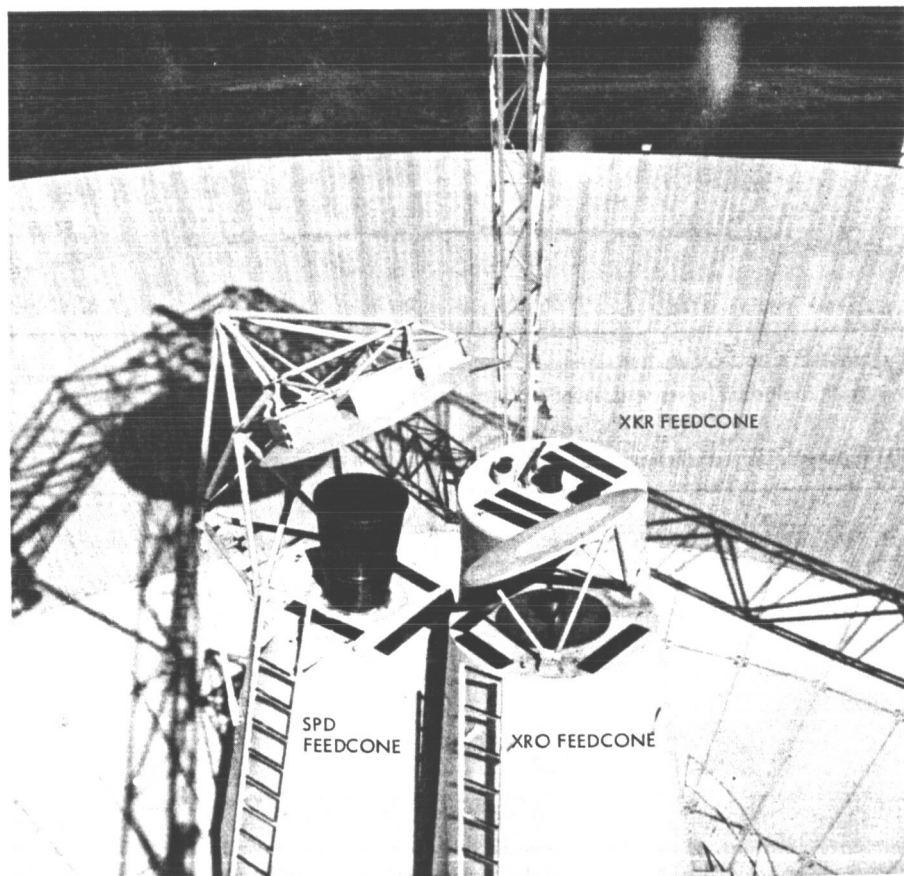


Fig. 2. Tricone feed system at DSS 14

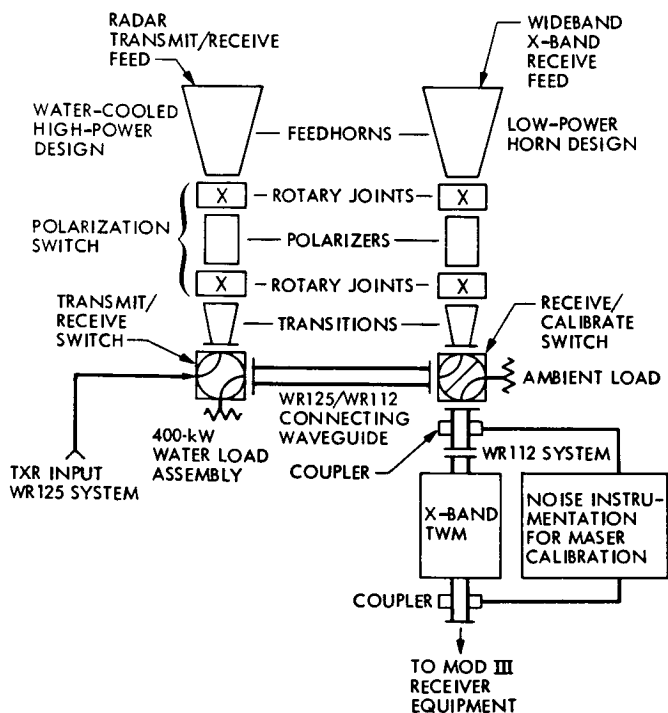


Fig. 3. XKR feed cone, X-band block diagram

REPRODUCIBILITY OF THE
ORIGINAL PAGE IS POOR

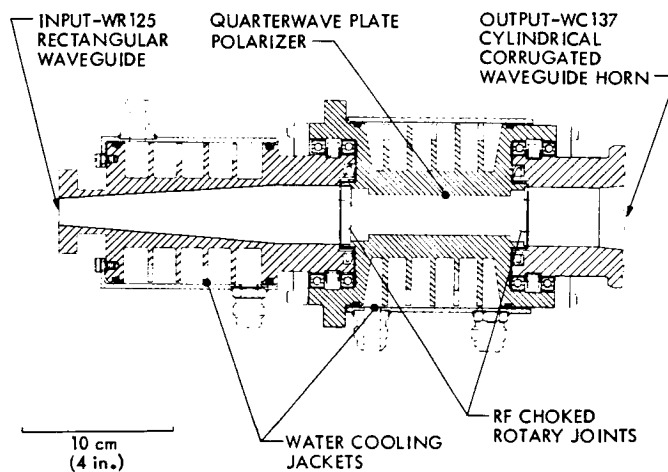


Fig. 4. Radar feed assembly

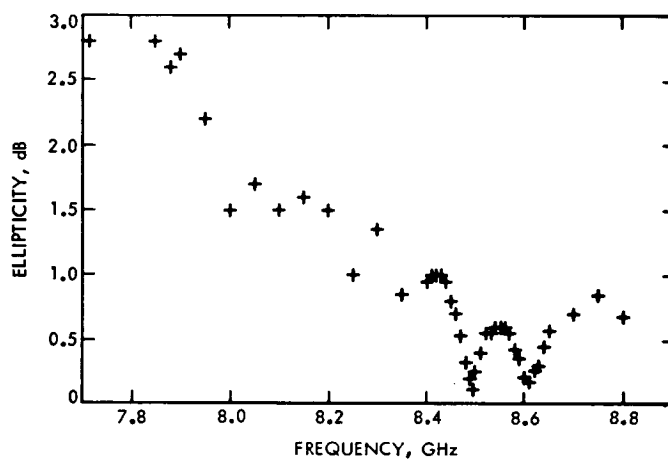


Fig. 5. Radar feed system ellipticity

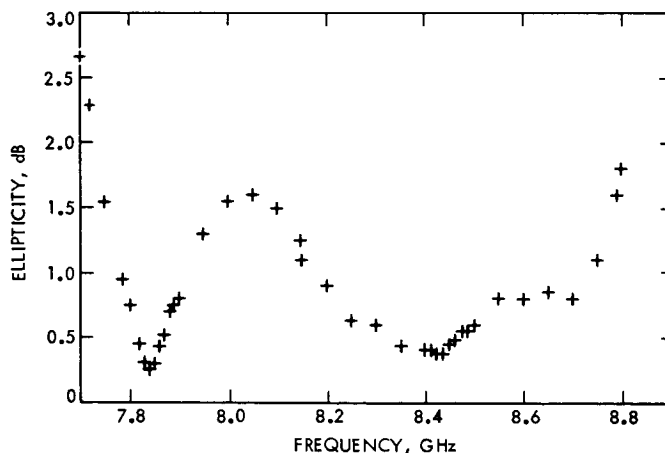


Fig. 6. Wideband receive feed sytem ellipticity

REPRODUCIBILITY OF THE
ORIGINAL PAGE IS POOR



Fig. 7. Radar feed assembly power tests

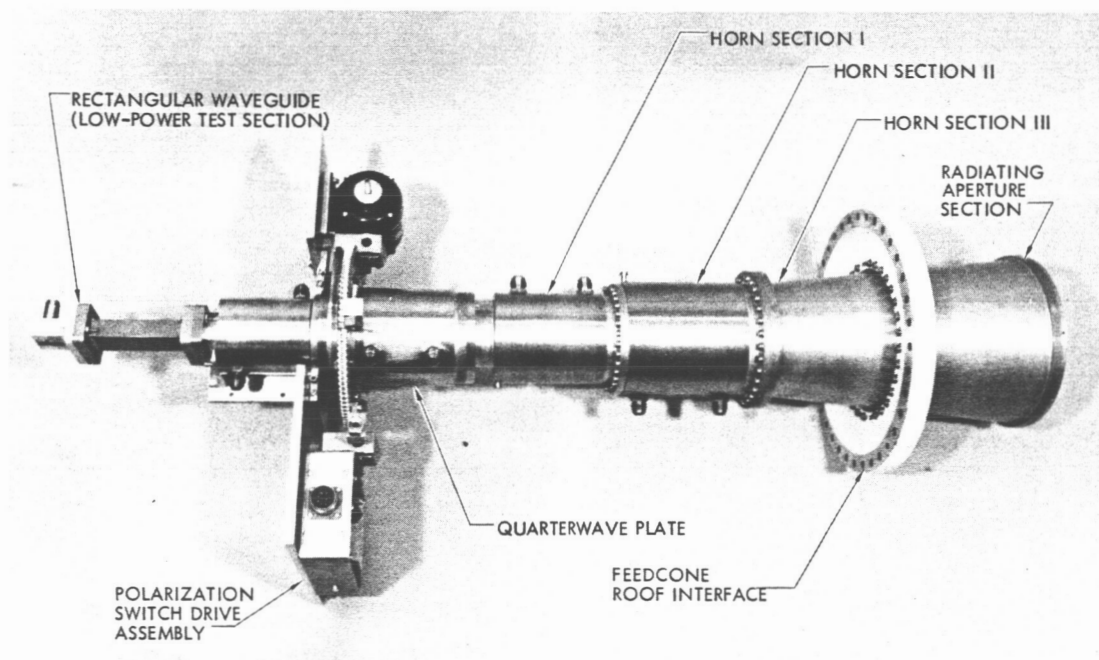


Fig. 8. X-band radar feed assembly

REPRODUCIBILITY OF THE
ORIGINAL PAGE IS POOR

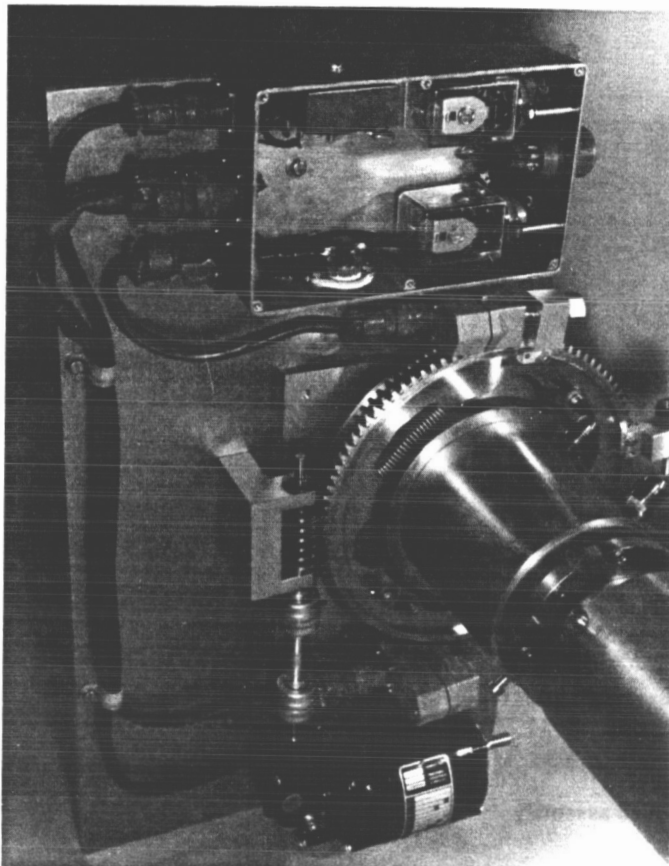


Fig. 9. Polarization switch drive

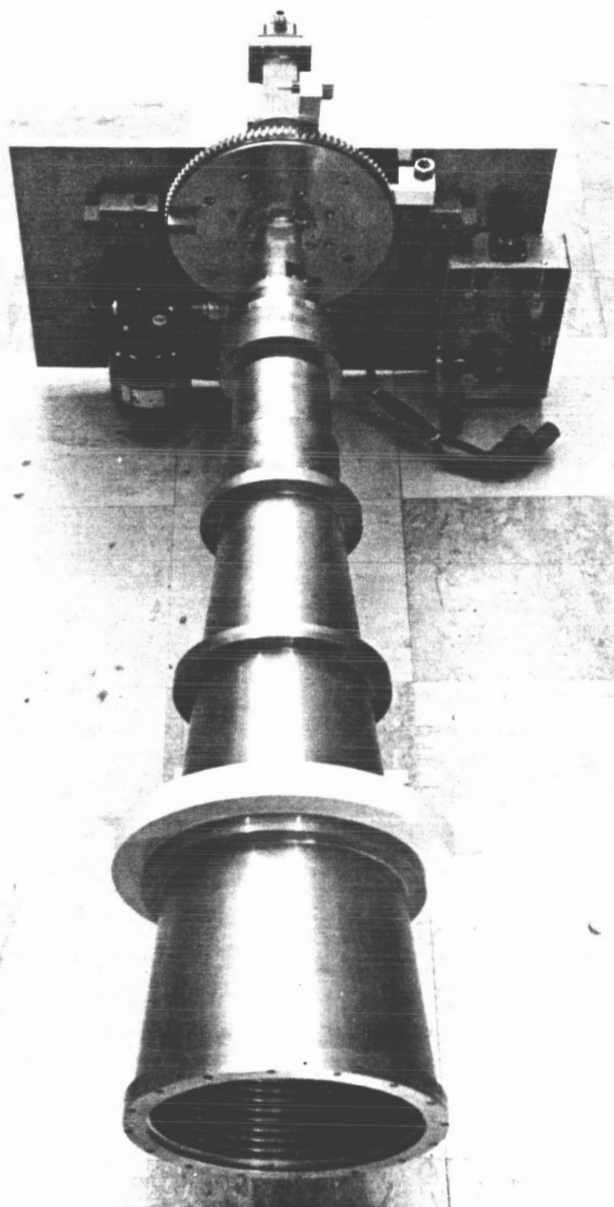


Fig. 10. Wideband receive feed

REPRODUCIBILITY OF THE
ORIGINAL PAGE IS POOR

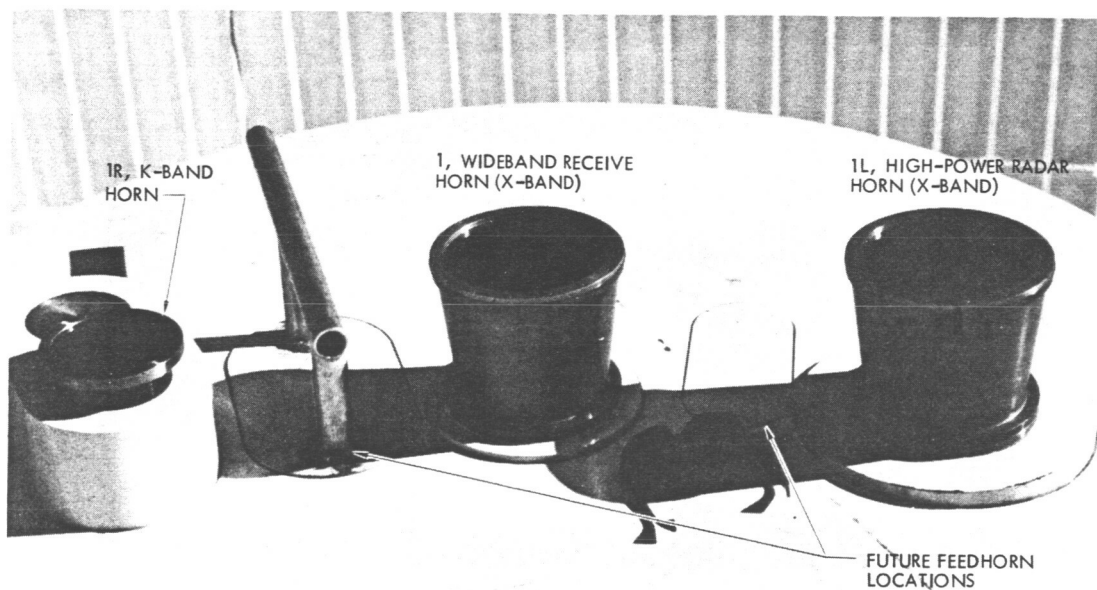


Fig. 11. XKR feedcone roof

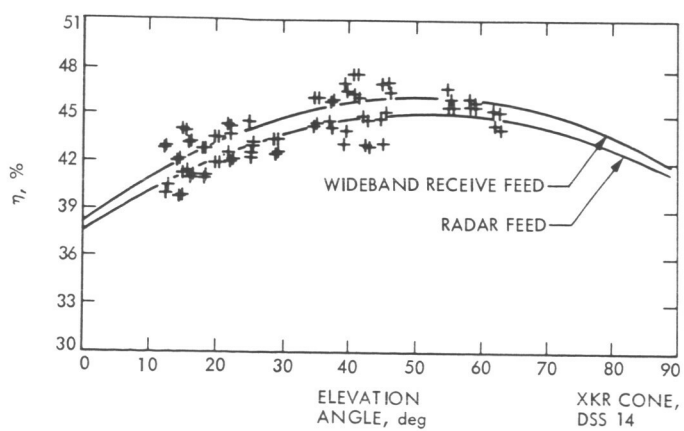


Fig. 12. Overall system efficiency vs. elevation angle

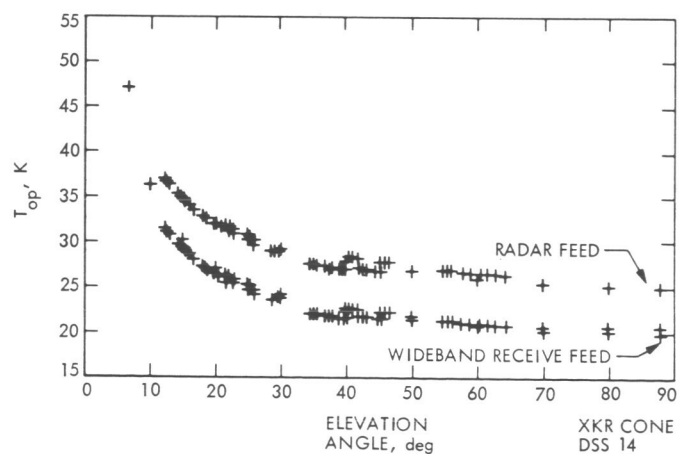


Fig. 13. Operating system noise temperature vs. elevation angle

N76-15203

A Versatile Data Acquisition System for Goldstone

M. S. Reid and R. A. Gardner
Communications Elements Research Section

A versatile data acquisition system has been provided at Goldstone. It is capable of recording a wide variety of parameters from widely separated geographical locations with varying integration times and recording speeds. It is fast, accurate, and modular in form so that it can be readily expanded. This article describes the data system, discusses accuracies, and gives examples of data recorded with the system's capability of operation with preprocessing.

I. Introduction

A data acquisition system designated Solar and Microwave Data Acquisition System (SMDAS) has been designed, built, and implemented at the Venus Station (DSS 13) at Goldstone. This system is used for the acquisition of microwave data for the atmospheric radio propagation program (Refs. 1 and 2), solar energy data for the solar energy instrumentation program (Ref. 3), and meteorological data for the use of both of these projects. The data system has been designed for maximum flexibility in type of data, number of channels, location of sensors and speed of recording. Maximum flexibility of operation has also been a design consideration so that the response time for the inclusion of new or additional experimental data is minimal. This article describes the SMDAS, discusses accuracy of recording, and gives examples of recorded data.

II. System Description

The system consists of a central station, housed in a standard electronics rack, and up to ten remote stations. The remote stations are housed in environmental enclosures which can withstand extremes of ambient weather conditions. The remote stations can be 500 m from the central station or greater distances with line amplifiers. All power to the remote stations is supplied by the central station. The remote stations interface with transducers which generate the data to be recorded.

A remote station is connected to the central station via a cable containing three shielded twisted pairs. The remote station is addressed by a self-clocking 10-bit serial binary word generated by the central station. The remote station then senses the addressed channel and generates a 33-bit serial word which is transmitted to the central

station. Several types of data can be accepted by the remote station:

Analog, up to 160 channels per remote station, in any combination of high- or low-level signals (± 10 mV to ± 10 V full scale) in 8-channel increments, each

Digital, up to 16 channels of eight-digit 1248 binary-coded decimal (BCD) and up to 4 channels of eight-digit 1224 BCD, making a total of 20 channels per remote station.

Frequency, up to 10 channels per remote station in any combination of 1 Hz to 1 MHz or 100 Hz to 2 MHz, each range having an input sensitivity of 100 mV rms.

Contact Closure, up to 112 per remote station in groups of 8 per address.

The central station provides random access and flexibility in output format, automatically and manually interrogates the remote station, formats the data into 2048 character records, and writes the records on magnetic tape. The magnetic tape unit has the capability of read-after-write for checking that the data are being recorded correctly. The central station includes a real-time clock (days, hours, minutes, seconds) with crystal time base, as well as the capability of using an externally generated time code. The scan cycle rate is adjustable from 1 minute (or less if the total channel capacity is not fully used) to 24 hours.

Ten thumb wheels are provided on the front panel of the central station for reference data which are recorded in every record. A slow-speed paper printer allows operators to check the data being recorded on the magnetic tape. This printer is used for temporary, intermittent paper record of time selected data only, and is independent of the magnetic record. A visual display of time and any manually selected channel is provided in digital form on the central station. This display is independent of the operation of both the paper and magnetic records.

Each record written on the magnetic tape consists of as many data words as there are channels in operation plus header words. The header words are: (1) reference data selected by the thumb wheels on the central station, number of remote stations in operation, etc., and (2) the time code. Each data word is tagged with the remote station identification number and channel number.

All input channel signal conditioning is modularized so that a remote station has minimum configuration without excessive unused channels. Expansion of a remote station to maximum input channel configuration is by the addition of plug-in modules with no wiring changes required.

An uninterruptible power source maintains the system in full operation during momentary line power failures. A fully implemented system (ten remote stations) will operate for at least ten minutes without regular line power.

III. Recording Accuracy

One objective in the design of the data acquisition system was to make the errors in data transmission and recording insignificant in comparison with the inherent uncertainty in a wide variety of measuring sensors. A typical hemispherical pyranometer has an accuracy of about $\pm 3\%$. The tracking heliometers, described below, have a specified accuracy of $\pm 2\%$. The overall accuracy of the data system is of the order of 0.1%.

Figure 1 shows a block diagram of the data system.¹ The sensors detect a variety of physical parameters and convert the measurements to electrical signals which appear at the sensor's output terminals. Certain key parameters are recorded in analog form on strip chart recorders for immediate visual checking and comparisons. The diagram shows that some parameters are recorded in digital form, some as a frequency, and the remainder in analog form. The digital recording chain is the most precise, the standard method is the direct analog chain, and the frequency technique is intermediate between these two. The voltage-to-frequency converters are used for precise integration and accuracy in recording. If resistance-capacitance (RC) time constants are used for integration, then components with high stability and high precision must be used. Furthermore, integration times are limited to about 10 seconds with RC circuits because of the large values of the components. The voltage-to-frequency (V/F) conversion is a convenient method of providing accurate and flexible integration times. The input impedance for the V/F converters is of the order of 50 to 100 megohms and these devices will over-range to 2.5 times. The output from the V/F converters is 0 to 100 kHz for an input of 0 to 10 mV. Internal noise was measured as about 20 Hz in 100 kHz. The temperature coefficient is $\pm 0.005\%$ per $^{\circ}\text{C}$ (0 to 55°C).

¹The multiplexer and data recording system were supplied by Instrumentation Technology Corporation of California.

Data which enter the SMDAS in frequency form allow integration by plug-in counter boards in the data system. Integration times of 0.1, 1, 10, 100, 1000 seconds are available in the system as well as 1, 2, 4, and 8 minutes.

Variable integration times are available in the high-precision chain shown in Fig. 1. The V/F output is fed into a computing counter and programmer pair, and the digital output is recorded directly in the SMDAS. The output from the programmer is digital BCD data in 5 significant figures. The computing counter is the Hewlett-Packard Model 5360A, whose frequency measurement accuracy is given by

$$\frac{10^{-9}}{\text{Count start/stop time}} \pm \text{trigger error} \pm \text{time base error}$$

The trigger error is inversely proportional to signal amplitude and is negligible except for very noisy or very-low-frequency signals, conditions which do not apply in this application. The built-in time base has a specification of 5 parts in 10^{11} for a 1-second averaging time. The overall accuracy of the frequency count is better than 0.01% for all possible conditions. In addition to providing variable integration times, the programmer is capable of inserting scaling factors, unit conversions or data calibrations, as required. Preprocessing of certain high data volume parameters can also be carried out by the computing counter-programmer combination, as described below.

Special attention has been paid to the accuracy of the transfer of signals from the various sensors to the input terminals of the data system. Typical output signals from the sensors are dc voltages in the range of 0 to 10 mV. The Spectrolab hemispherical pyranometer, for example, has an output of 7 mV per kW/m² insolation input. If the sensors are located more than a meter or two from the data system input, then the transmission line is subject to interference, line noise, ground loops, attenuation errors, etc. If amplifiers are used to boost the sensors' output to a level where these problems are suppressed, then the amplifiers are subject to temperature changes with the ambient environment. The Jet Propulsion Laboratory's experience over many years of building highly stabilized amplifiers has been used in designing and constructing suitable amplifiers and enclosures. Amplifiers with a gain of approximately 1000 are in use at Goldstone with accuracies of 0.5% (output) over an ambient temperature change of 100°C, and with accuracies of 0.01% (output) over the same ambient temperature range for oven-stabilized designs.

IV. Calibration

Calibration procedures depend on the parameter under investigation and on the type of sensor and measurement method. The calibration of microwave parameters has been discussed in the open literature (Refs. 4, 5, and 6) and in JPL reports (Refs. 7 and 8). In this report the calibration of two solar energy instruments will be discussed.

A typical pyranometer in the JPL solar measurement program is the Spectrolab Hemispherical Pyranometer, Model SR-75. Figure 2 shows the traceability of the calibration of this instrument to the World Radiation Center in Davos, Switzerland.

In addition to pyranometers, the JPL solar measurement program operates tracking heliometers. The heliometer is the Mark 3 Kendall Solar Radiometer System. This radiometer is almost identical with the primary absolute cavity radiometer, designed and built at JPL, and which has been described in the technical literature (Refs. 9 and 10). The only differences between the Mark 3 radiometer system and the primary absolute cavity radiometer (known as PACRAD) is the view angle which is 15 degrees instead of 5 degrees, and the flat quartz lens covering the aperture for all weather operation. The quartz lens contributes an attenuation of approximately 5%, which is not present in the PACRAD. The Mark 3 radiometers at Goldstone, both with and without the quartz lens, have been extensively calibrated against the PACRAD, which has itself undergone intercomparisons at the World Radiation Center at Davos, Switzerland (Ref. 10).

The Mark 3 radiometer system is a cavity-type radiometer with provisions for self-calibration. Figure 3 is a photograph of the system. The radiometer is designed for tracking and measuring solar irradiance. It is intended for use in outdoor environments in the Mojave area. It is compensated for changes in ambient temperature and is relatively insensitive to wind and rain. It has been designed to operate unattended over long periods of time (one or two months) in remote locations. In addition to the original calibration of the Mark 3 radiometer against the Kendall Mark 6 PACRAD absolute standard, it is also calibrated by correlating its output with an internally heated cavity. This allows subsequent calibrations to be made using a known applied voltage and current. These calibrations are checked periodically and program plans call for an annual recalibration against the PACRAD standard.

V. Examples of Computed Results

In order to demonstrate the flexibility and recording capability of the programmer chain in Fig. 1, some examples of wind data will be presented. Wind speed is measured at DSS 13 by a cup anemometer located at the top of a 30-m tower. The output from the anemometer was fed through a V/F converter and into the data system via a computing counter and programmer as shown in Fig. 1.

Two parameters of wind velocity are of interest to investigators of wind energy systems. These two parameters are: (1) the ratio of the mean of the cubes of wind velocity to the cube of the means of wind velocity over short periods of time, such as 2 minutes, as a function of wind velocity, and (2) the standard deviation of wind velocity over the same short periods as a function of wind velocity.

Wind speed was sampled and digitized at a 1-ms rate for a period of two minutes, less computation time and time taken to write a record on the magnetic tape. If the wind speed measurements in the 2-minute period are denoted V_i , then the following computations were performed by the computing counter-programmer combination:

$$\bar{V} = \frac{1}{N} \sum V_i \quad (1)$$

$$\overline{V^3} = \frac{1}{N} \sum (V_i)^3 \quad (2)$$

where N is the number of wind speed samples in the 2-minute period. In addition to these two computations, the standard deviation σ_V of the set of V_i measurements was calculated, and the peak value of V_i , \hat{V} was found.

The following data were recorded on magnetic tape for each 2-minute period: Mean velocity \bar{V} , mean of the cubes $\overline{V^3}$, standard deviation of wind velocity σ_V , and

peak wind velocity \hat{V} . From these recorded data it was possible to plot the ratio $\overline{V^3}/(\bar{V})^3$ as a function of \bar{V} , or any other combination of parameters of interest. Two 24-hour periods were chosen as representative examples. The first period was 2130 (PST) August 16 to 2200 (PST) August 17, 1975, when wind speeds of up to 16 m/s (about 35 mph) were experienced, and the second period was 0000 to 2400 (PST) September 13, 1975, which was a relatively calm period. Figure 4 shows a plot of the ratio of the mean of the cubes to the cube of the means of wind velocity ($\overline{V^3}/(\bar{V})^3$) as a function of mean wind velocity in each 2-minute period for August 16/17. There are as many data points plotted as there are 2-minute periods in this time range. A third-order curve has been fitted to the data to show the trend. Figure 5 shows a similar plot (to the same scales as Fig. 4) for the calm period, September 13, also with a third-order curve fitted to the data. Figure 6 is the same as Fig. 5, except the abscissa has been expanded. Figure 7 is a graph of the standard deviation of wind velocity in each 2-minute period against mean wind velocity in the same 2-minute periods for August 16/17, 1975. Here, again, there are as many data points plotted as there are 2-minute periods in this time span. A straight line has been fitted to the data to show the trend. Figure 8 is a similar plot for September 13, 1975.

VI. Conclusion

A flexible and versatile data acquisition system has been provided at Goldstone. It is capable of recording a wide variety of parameters from widely separated geographical locations with varying integration times and recording speeds. It is fast, accurate, and expandable to a maximum of 1600 analog channels plus 200 digital channels, plus 100 frequency channels, plus 1120 contact closures. It has demonstrated satisfactory operation by recording meteorological, microwave, solar energy, wind, and ionospheric data. Satisfactory operation in conjunction with preprocessing equipment or microprocessors has also been demonstrated.

References

1. Reid, M. S., and Lockhart, T. J., "The Variation of Atmospheric Temperatures at Microwave Frequencies," Conference Record of *Conference on the Propagation of Radio Waves at Frequencies about 10 GHz*, London, England, Apr. 1973.
2. Reid, M. S., "Tracking and Ground Based Navigation: A Description of the Weather Project," in *The Deep Space Network Progress Report*, Technical Report 32-1526, Vol. X, pp. 116-122, Jet Propulsion Laboratory, Pasadena, Calif., Aug. 15, 1972.
3. Reid, M. S., Gardner, R. A., and Parham, O. B., "Goldstone Solar Energy Instrumentation Project: Description, Instrumentation, and Preliminary Results," in *The Deep Space Network Progress Report* 42-26, pp. 133-144, Jet Propulsion Laboratory, Pasadena, Calif., Apr. 15, 1975.
4. Stelzried, C. T., and Reid, M. S., "Precision Power Measurements of Spacecraft CW Signal Level with Microwave Noise Standards," *Trans. IEEE, Instrumentation and Measurement*, Vol. IM-15, No. 4, pp. 318-324, Dec. 1966.
5. Stelzried, C. T., "A Liquid Helium Cooled Coaxial Termination," *Proc. IRE*, Vol. 49, No. 7, p. 1224, July 1961.
6. Stelzried, C. T., "Temperature Calibration of Microwave Thermal Noise Sources," *Trans. IEEE, Microwave Theory and Techniques*, Vol. MTT-13, No. 1, p. 128, Jan. 1965.
7. Reid, M. S., and Stelzried, C. T., "Error Analysis of CW Signal Power Calibration with Thermal Noise Standards," in *Supporting Research and Advanced Development*, Space Programs Summary 37-36, Vol. IV, pp. 268-277, Jet Propulsion Laboratory, Pasadena, Calif., Dec. 31, 1965.
8. Reid, M. S., "Improved RF Calibration Techniques: System Operating Noise Temperature Calibrations of Low Noise Cones," in *The Deep Space Network*, Space Programs Summary 37-66, Vol. II, pp. 57-61, Jet Propulsion Laboratory, Pasadena, Calif., Nov. 30, 1970.
9. Kendall, J. M., Sr., *Primary Absolute Cavity Radiometer*, Technical Report 32-1396, Jet Propulsion Laboratory, Pasadena, Calif., July 15, 1969.
10. Frohlich, C., "The Third International Comparisons of Pyrheliometers and a Comparison of Radiometric Scales," *Solar Energy*, Vol. 14, No. 2, pp. 157-166, 1973.

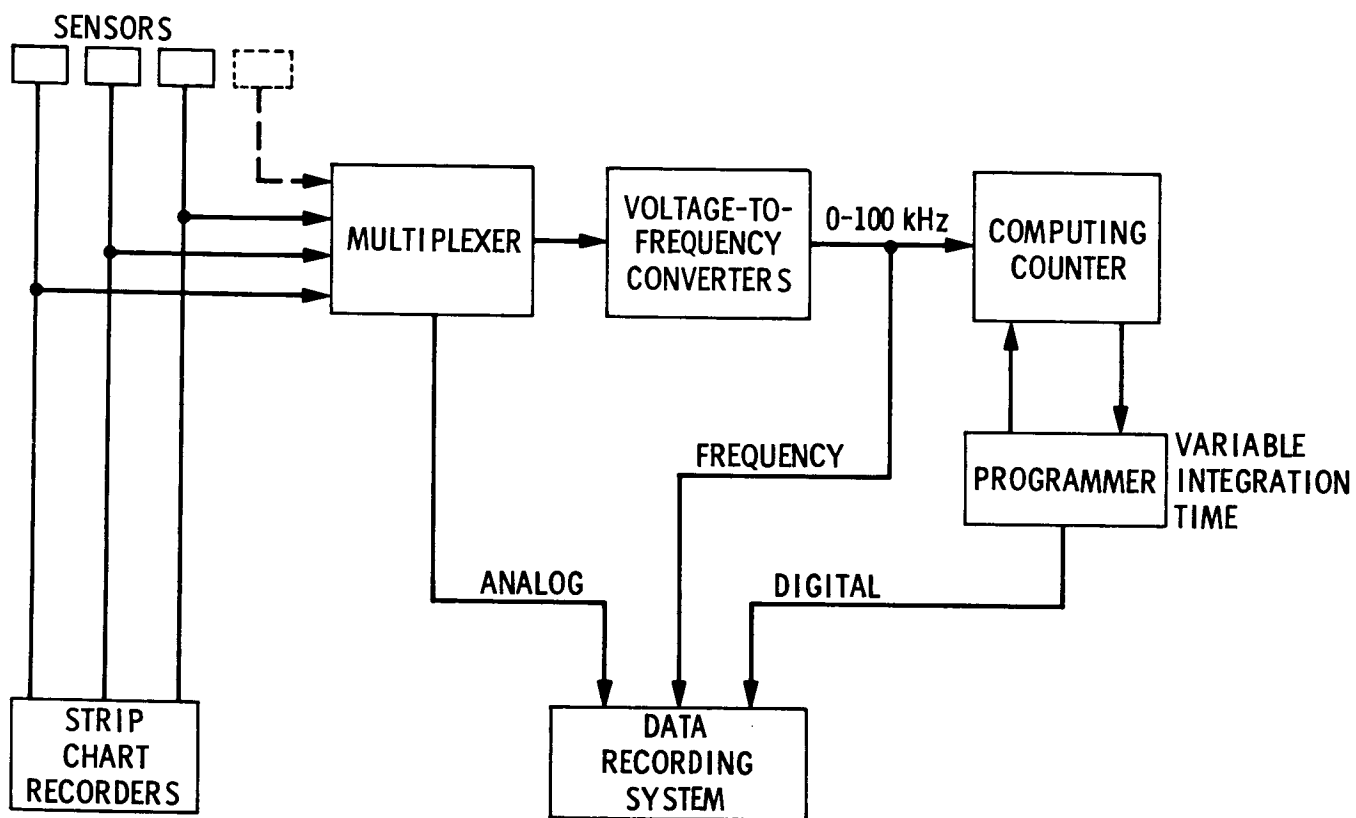


Fig. 1. Block diagram of the data acquisition system

REPRODUCIBILITY OF THE
ORIGINAL PAGE IS POOR

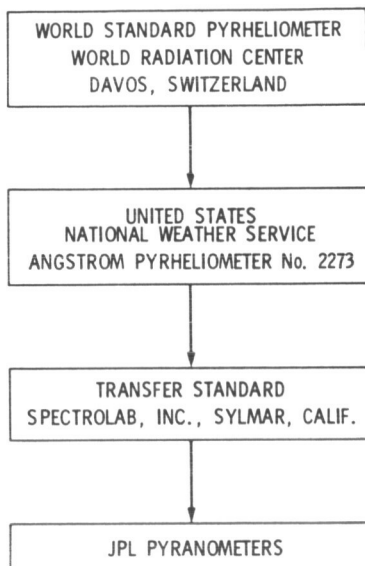


Fig. 2. Traceability of the calibration
of JPL pyranometers

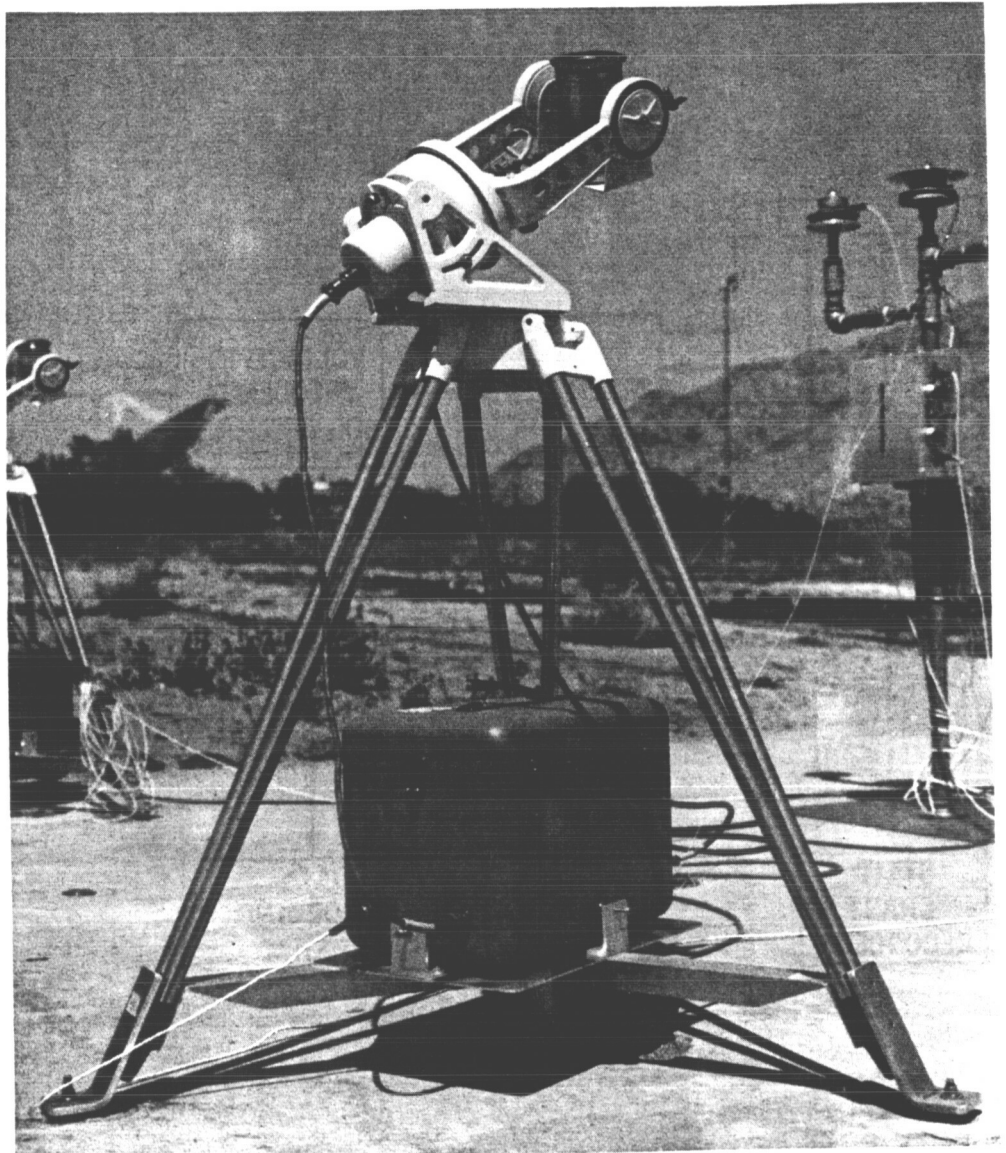


Fig. 3. The Mark 3 Kendall Solar Radiometer System

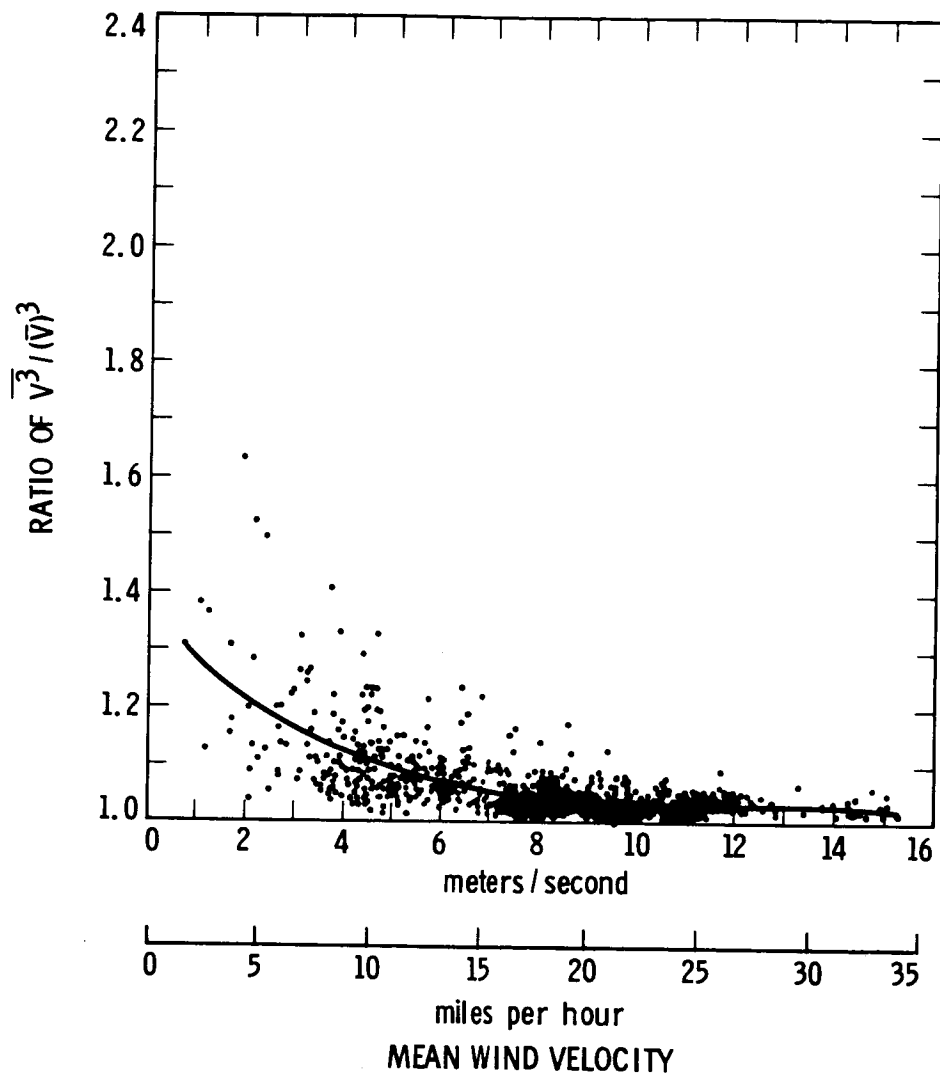


Fig. 4. Ratio of $\overline{V^3} / (\overline{V})^3$ as a function of mean wind velocity for August 16/17, 1975 measured at Goldstone

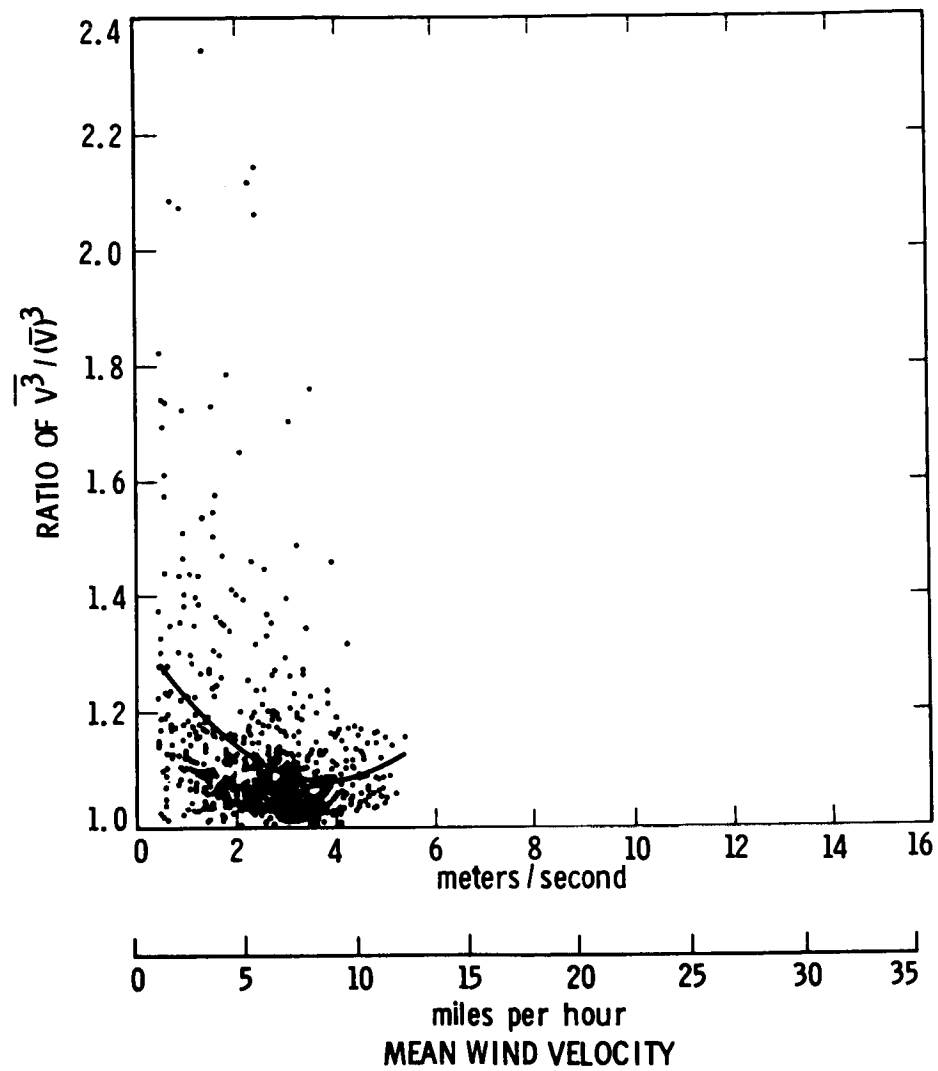


Fig. 5. Ratio of $\overline{V^3} / (\overline{V})^3$ as a function of mean wind velocity for September 13, 1975 measured at Goldstone

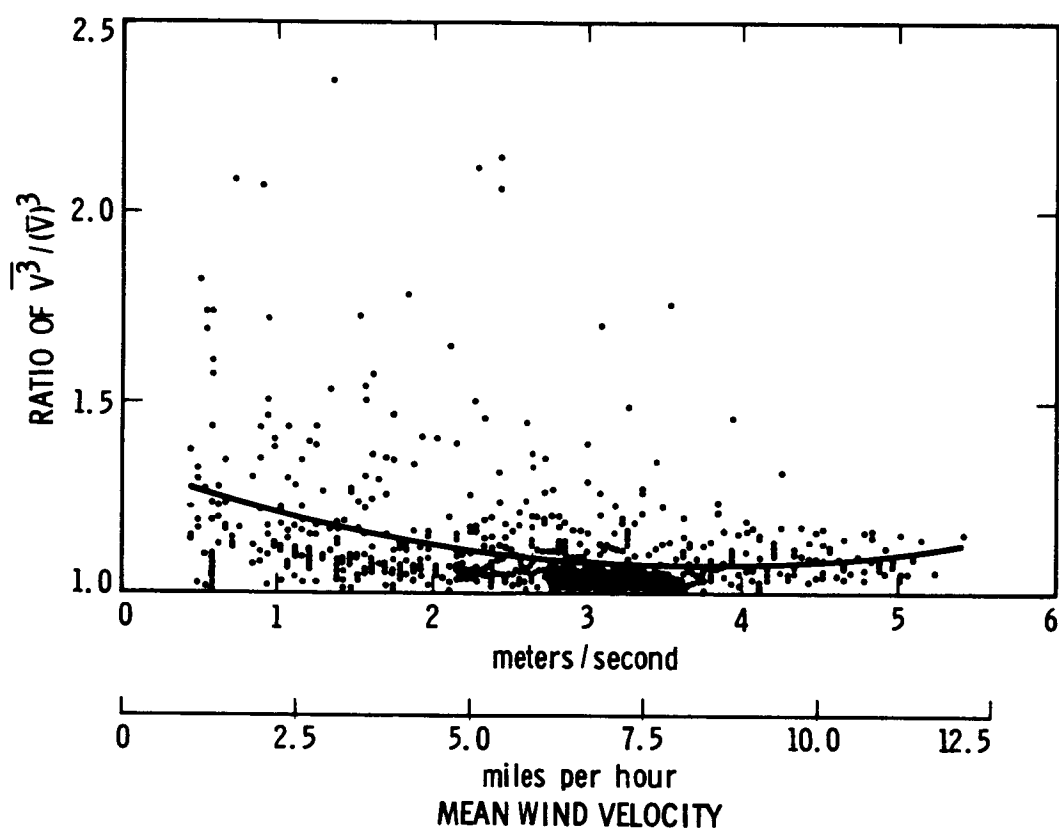


Fig. 6. Ratio of $\overline{V^3} / (\overline{V})^3$ as a function of mean wind velocity for September 13, 1975 on an expanded scale

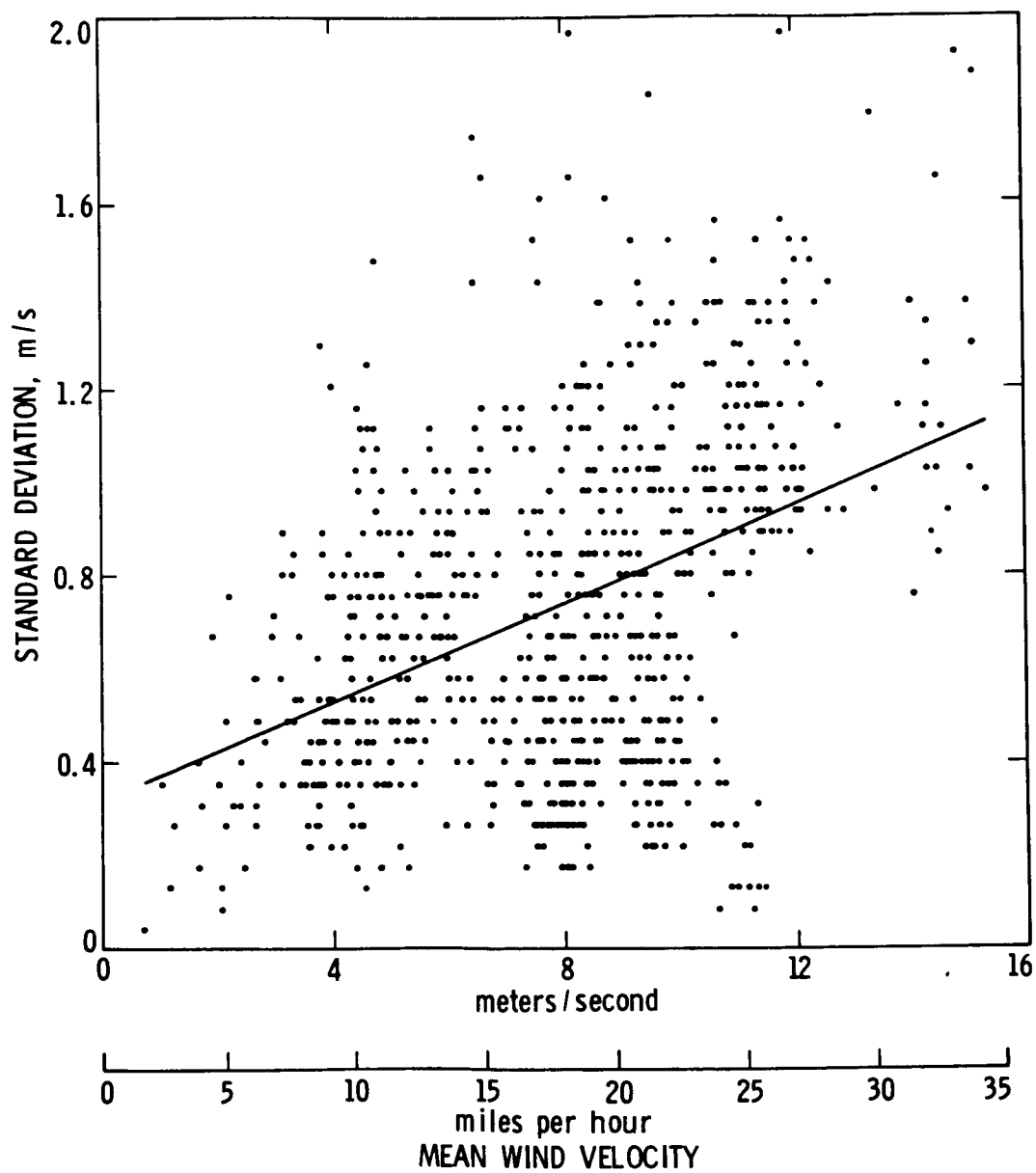


Fig. 7. Standard deviation of wind velocity as a function of mean wind velocity for August 16/17, 1975

REPRODUCIBILITY OF THE
ORIGINAL PAGE IS POOR

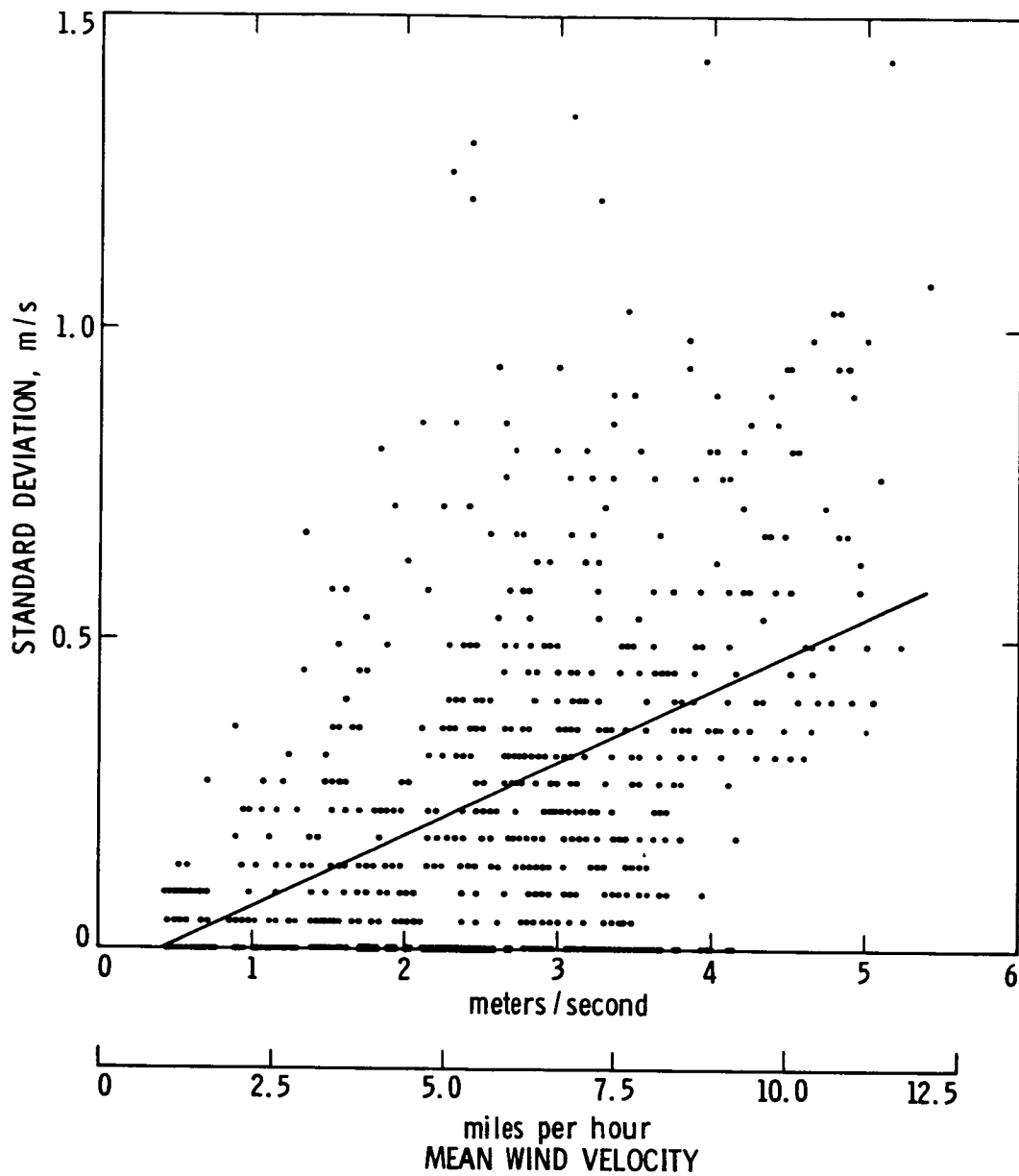


Fig. 8. Standard deviation of wind velocity as a function of mean wind velocity for September 13, 1975

N76-15204

Microcontroller for Automation Application

H. W. Cooper
R. F. Systems Development Section

A microcontroller for automation application is currently being developed. It is basically an 8-bit microcomputer with a 40K byte random access memory/read only memory, and can control a maximum of 12 devices through standard 15-line interface ports.

I. Introduction

A breadboard microprocessor controller was used in an RF automation demonstration held in June 1975 at the Mars Station, DSS 14. The controller was used to control two Subcarrier Demodulator Assemblies (SDAs) upon receiving macro commands from a master PDP-11 computer. The controller that configured, calibrated, monitored, and provided failure backup for the SDAs performed flawlessly throughout the demonstration. It was then decided to repack the controller in a more suitable form for future applications.

II. Description

The microcontroller shown in Fig. 1 is actually a small computer designed around the Intel 8080 microprocessor chip. Many of the various modules that comprise the computer portion of the microcontroller have been purchased from Intel Corp. These include the central processor unit (CPU), random access memory (RAM), read only memory (ROM), and input/output (I/O) modules. Other modules such as the 4-port, 15-line interface

module, and the hardware bootstrap module are built at JPL. All modules plug into a chassis containing a module cage, power supplies, and various connectors and switches. The microcontroller fits into a standard 48-cm (19-in.) RETMA rack. It is 22 cm (8-3/4 in.) high and 48 cm (19 in.) deep.

The primary function of the microcontroller is to control various subassemblies that have a standard 15-line interface port. The microcontroller can communicate with a maximum of 12 ports. Although the microcontroller is intended to be a stand-alone controller, peripheral equipment is required during program development. The microcontroller will interface with a teletype (TTY), a video display terminal, a high-speed paper tape reader, and a high-speed paper tape punch.

The microcontroller module cage contains a modified Intel Intellec 8/mod 80 motherboard. Modifications were made to provide a larger memory capability, which consists of up to ten 4K RAM or ROM memory modules (see Fig. 2). The module cage also holds three I/O modules that interface with the TTY, video display

terminal, and the high-speed paper tape punches and readers. one of the I/O modules drives three 15-line interface modules, each of which controls four 15-line interface ports. The hardware bootstrap module contains a number of special circuits that include (1) a selectable address hardware bootstrap loader, (2) a status lamp display driver, and (3) a power supply monitor to determine if all required voltages are present.

Programming can be accomplished using either assembly language or PL/M high-level language. In either case, several software aids are available to the user. Residing in the JPL Univac 1108 computer, there are three programs helpful to the user. They are: (1) a PL/M Compiler, (2) a MAC 80 Assembler, and (3) an 8080 Simulator. The use of these programs along with the 1108's text editor and permanent file system makes programming relatively easy.

The user may also elect to develop his program using the resident (paper tape) assembler and text editor. While this is satisfactory for short assembly language programs, larger programs are developed more efficiently on the 1108, since paper tape handling is not required.

A system monitor program is supplied on ROMs with every microcontroller. This resident program performs many housekeeping functions; the most important are tape loading and punching, and modifying and displaying on a CRT or TTY, the contents of various registers and memory locations. Other software currently being developed consists of memory diagnostic routines, I/O diagnostic routines, CPU diagnostic routines, string

manipulation routines, 15-line interface drivers, and mathematical functions.

Controls and indicators on the microcontroller are minimal and are located behind a door on the front panel. There is an ADDRESS SELECT switch. The address corresponding to each switch position is listed on a card on the rear of the door. When the BOOT switch is depressed, a GO TO instruction is issued into the CPU causing the program to jump to the designated address. This feature allows the user to immediately jump to specific routines such as the System Monitor, I/O diagnostic, memory diagnostic, or the user program. The PWR lamp indicates that all required voltages are present, i.e., +5 Vdc, +12 Vdc, and -9 Vdc. The eight status lamps are under user software control. Normally, they are used to indicate the condition of various flags in the user's program. Initial application of power automatically starts the microcontroller at the selected address.

III. Summary

The microcontroller with its power supply monitor and memory, I/O, and CPU diagnostics has been designed to provide a very reliable unit. All modules with the exception of the power supplies are plug-in modules. With the help of the resident diagnostics, a defective module can be isolated and replaced in minutes. Program development cost and time should be minimal through the use of common software routines and other program development aids. The cost of the microcontroller will be \$5,000 to \$10,000, depending on the memory and I/O requirements. Programming and operation manuals are also available.

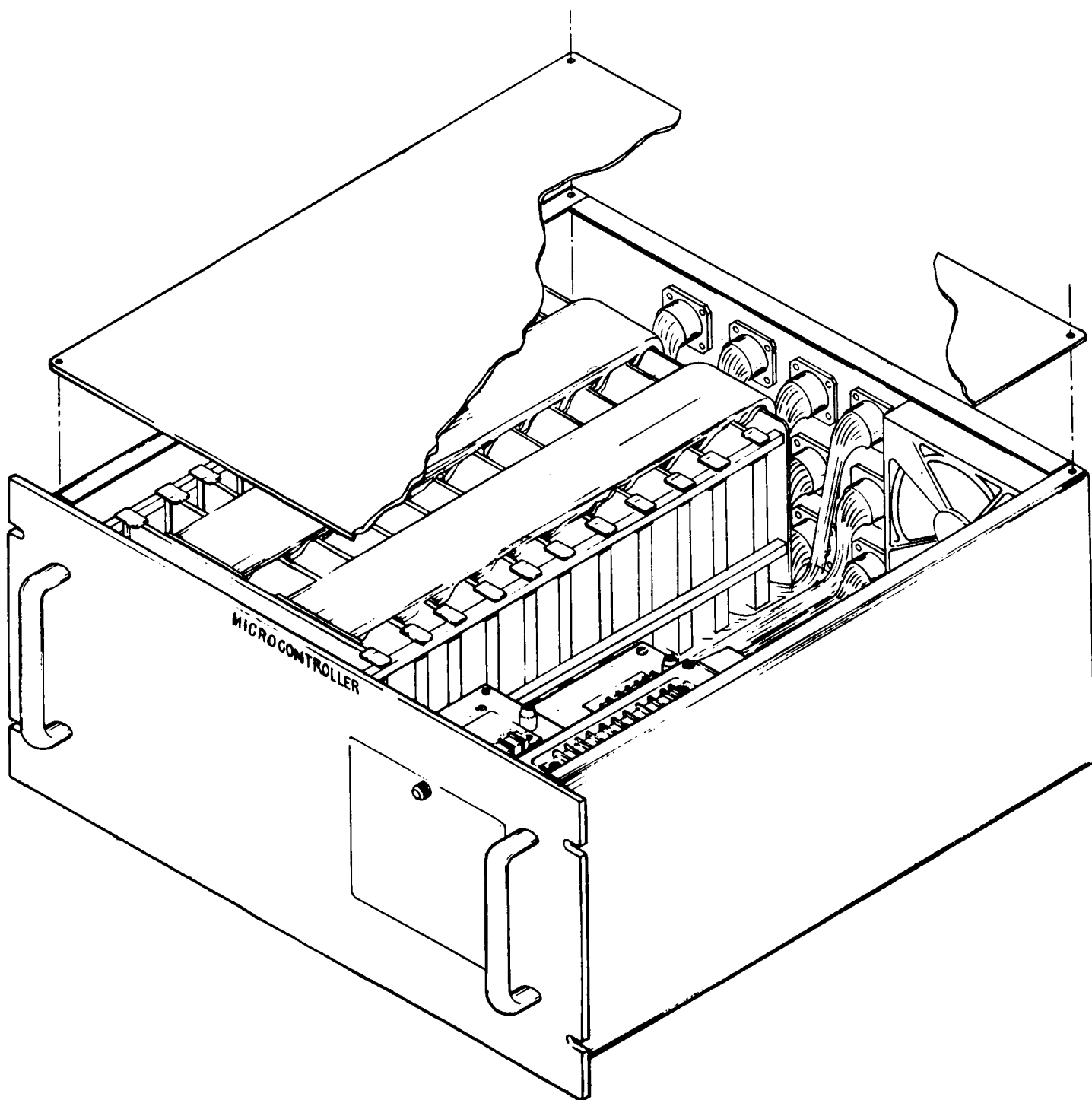


Fig. 1. Microcontroller

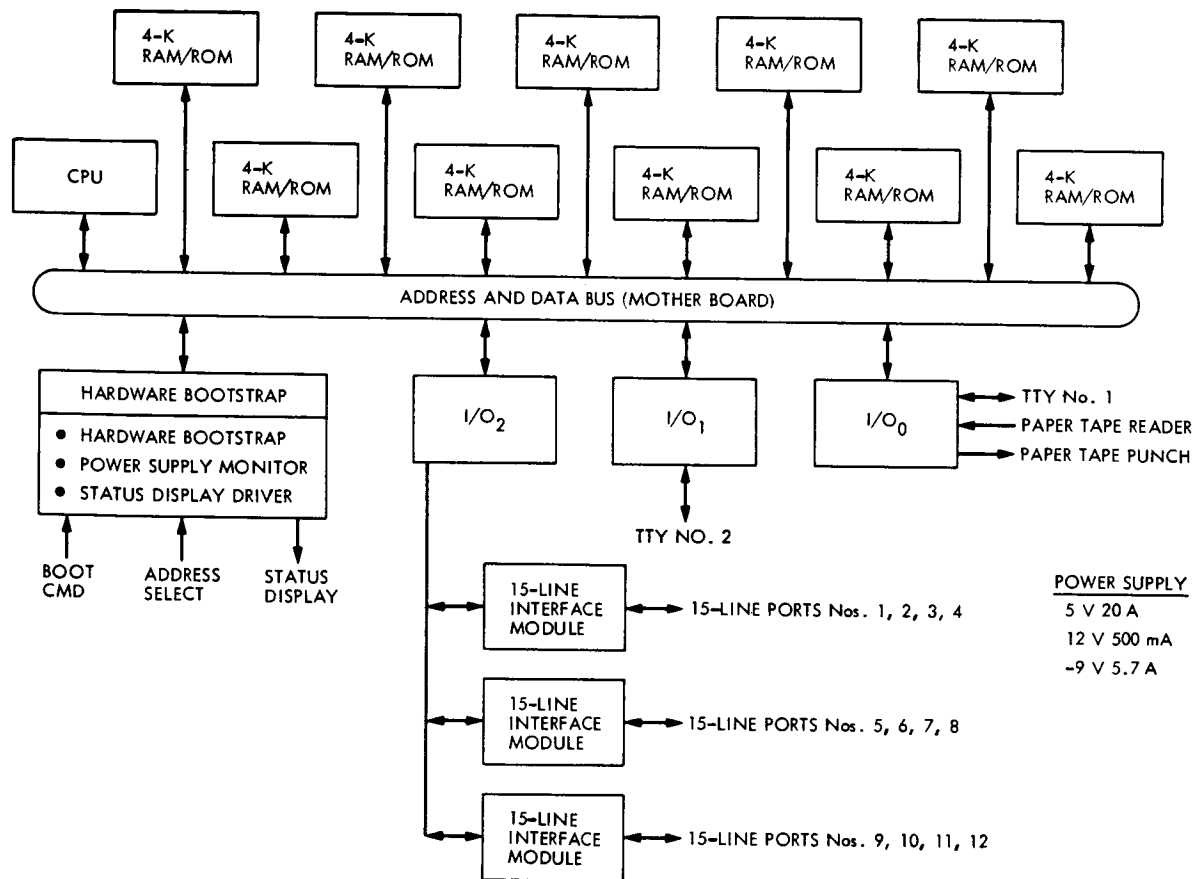


Fig. 2. Block diagram, microcontroller

N76-15205

Exciter Switch

W. L. McPeak

R. F. Systems Development Section

A new exciter switch assembly has been installed at the three DSN 64-m deep space stations. This assembly provides for switching Block III and Block IV exciters to either the high-power or 20-kW transmitters in either dual-carrier or single-carrier mode. In the dual-carrier mode, it provides for balancing the two drive signals from a single control panel located in the transmitter local control and remote control consoles. In addition to the improved switching capabilities, extensive monitoring of both the exciter switch assembly and Transmitter Subsystem is provided by the exciter switch monitor and display assemblies.

I. Summary

A prototype exciter switch was installed and tested at Goldstone (DSS 14) in November 1972. Subsequently, three new exciter switches were procured to replace the prototype and for installation in Australia at DSS 43 and in Madrid at DSS 63. The new assembly provides an excellent example of combining RF hybrid stripline techniques with digital control and monitoring circuits.

The exciter switch consists of four separate assemblies. The first, (Fig. 1) contains the RF package and control logic. The second (Fig. 2) contains multichannel data collection, conditioning, and serial transmission logic. The last two are the dual-carrier and diagnostic display and control panels. One (Fig. 3) displays RF switching configuration and RF level monitoring. In dual-carrier

mode, klystron output levels are controlled from this panel. The other (Fig. 4) displays compute transmitter operating parameters. Both displays provide thumbwheel switches for selecting any of the 416 status channels sampled by the exciter switch monitor.

The four assemblies thus provide necessary RF switching between the two exciters and the 20-kW and high-power transmitters in single-carrier and dual-carrier mode. This RF switching within the exciter switch is controlled from the Antenna Microwave Subsystem. In the dual-carrier mode, dual receivers are used to provide a simple and accurate method for monitoring and adjusting the relative carrier outputs of the klystron. Through the digital scanning of the exciter switch and transmitter operating parameters, the assemblies provide extensive operation and diagnostic information.

II. Exciter Switch Assembly

A. New Design

The exciter switch assembly provides the interface of the Block III and Block IV exciters with the 20-kW and high-power transmitters (Fig. 5). A new exciter switch assembly has been installed at the three DSN 64-m sites. This assembly replaced a similar prototype exciter switch design installed at DSS 14 for testing purposes (Ref. 1).

The new assembly provides for switching of Block III and Block IV exciters into the 20-kW or high-power transmitter in either the single- or dual-carrier mode, and remote balancing of the exciter drive levels. Some functions not found in the prototype were added to the new assembly:

- (1) Dual receivers were added to the exciter switch assembly to extract the relative output carrier levels being transmitted and to display these levels on the control panel. The control panels also contain the controls for balancing the two output carriers in the dual-carrier mode. This eliminates the need for a monitoring spectrum analyzer with operator interpretation to perform the needed calibration.
- (2) The multi-channel data collection and serial transmission portion of the original prototype (Ref. 2) is now packaged in a separate J-box (Fig. 2), and additional capabilities have been added, such as
 - (a) Expanded channels: Using monolithic analog multiplexers, 208 (0 to 5 V) analog channels are multiplexed into a (12-bit) analog-to-digital converter, and 208 corresponding digital channels are multiplexed into one bit for serial transmission to the control areas.
 - (b) Ten 61-pin connectors: These connectors are available for interfacing the monitoring assembly to other assemblies within the Transmitter Subsystem. Six 61-pin connectors are available for future monitoring requirements.
 - (c) A programmable calculator: This calculator performs digital scaling and computation on the analog inputs. Such parameters as calorimeter power measurements can be calculated from the water flow and temperature changes within the klystron. All collected as well as calculated information is available at the display panels in the control areas.

B. RF Drive Signal Flow (Fig. 6)

Block III and Block IV drive signals, channel A and channel B, respectively, are received from the exciter assembly through semi-rigid cable at their respective S-band frequencies (2114 ± 4 MHz). The two drive signals are first sampled with an RF power head, and then the drive signals are amplified to 10 W through a solid-state buffer amplifier (Ref. 3). The drive signals then pass into a dual-channel RF hybrid combiner. Each channel of the hybrid consists of couplers for RF-level monitoring, a diode switch, and a diode attenuator. The couplers provide RF-level indications prior to entering the diode switch and after passing through the diode attenuator.

The dual-carrier display panels (Fig. 3) provide direct readout of the RF levels after leaving the attenuator. Other power readings may be accessed using the thumbwheel switch on the lower portion of the panels. On the dual-carrier display panels, other controls adjust bias levels on the diode attenuators for carrier balancing in dual-carrier mode. The diode switches (Fig. 6) are used to select dual-carrier or single-carrier mode. In single-carrier mode, the outputs from the diode switches go directly to a pair of coaxial switches (Fig. 3), where the drive is either terminated or switched into the selected transmitter. In dual-carrier mode (Fig. 6), the two channels are combined and fed through the coaxial switches to the selected transmitter. The microwave switch panel in the control room provides controls for the pin diode and coaxial switches.

C. Dual-Carrier Transmission

The dual-carrier mode provided by the exciter switch allows two separate RF signals to be transmitted through a single transmitter. However, difficulties arise in trying to adjust the two carriers to provide specified carrier levels. Power meter measurements are unusable due to the close spacing of the two S-band carriers (nominally 300 kHz) and the resulting intermodulation due to the klystron nonlinearity (Fig. 7). The close spacing of the carrier prohibits the use of S-band filters.

Previous methods of balancing the output carriers required sampling of the transmitter output with a spectrum analyzer. The spectrum analyzer was used to monitor carrier levels while adjusting drive levels from controls in the control room (Ref. 1). Although straightforward, it required reconfiguration and interpretation of test equipment which, at best, provided only a coarse indication of the carrier level with poor repeatability and resetability. A new technique for recovering the relative RF output levels was then developed (Fig. 8) that allows

accurate monitoring of the output carrier levels and accurate adjusting of these levels from a single display panel. Two similar receiver circuits are used to detect each carrier. Channel A receiver's local oscillator (LO) frequency is derived from multiplying the Block III exciter LO (66-MHz) frequency to 66 MHz above Block III carrier frequency. The receiver LO frequency is then mixed with a sample of the transmitter output. The resulting complex signal is passed through a narrow bandpass filter. The resulting signal represents the relative Block III carrier level. Channel B uses a similar receiver with local oscillator frequency 44 MHz above Block IV carrier frequency and a 44-MHz filter to provide Block IV carrier level indications.

The output of each filter is connected to a power meter, which is converted to a three-digit BCD number in the exciter switch monitor. It is then transmitted (as described in Section IV) for display at the two dual-carrier display panels (Fig. 3) as channel A and channel B. The same display contains "raise" and "lower" controls for the two carriers, greatly simplifying calibration. Also, each channel can be checked against the transmitter waterload calorimeter reading displayed on the same panel.

III. Exciter Switch Monitor Assembly (Fig. 2)

The control and monitoring capabilities of the exciter switch are contained in the exciter switch monitor J-box, which is mounted in close proximity to the exciter switch, and two display panels located in the control areas. Serial interface between the exciter switch monitor and the display panel is used to minimize cabling, and optical isolators are used as line receivers to reduce ground loop problems and provide a 27-kHz bit rate over 610 m (2000 ft) of cable.

The interface between the exciter switch (Fig. 5) and exciter switch monitor is provided through a 61-pin connector carrying parallel and digital signals. The parallel analog signals represent power meter readings and power supply voltages. The parallel digital signals represent exciter switch switching configuration.

In addition to monitoring functions in the exciter switch, the monitor samples status and level indications from the high-power transmitter and provides both operational and diagnostic information, which is available on the dual-carrier and diagnostic display panels located in the control areas.

IV. Exciter Switch Monitor Circuit Description

The exciter switch monitor accepts 208 (0 to 5 V) analog signals and 208 (0 V = logic "0," +5 volts = logic "1") digital signals, and multiplexes these parallel lines into 208 channels, 24 bits wide. Each 24-bit channel contains 11 bits of address information, 12 bits (3 BCD digits) corresponding to the analog input signal, and 1 bit representing the logic state of the digital input line. The 24-bit word is latched into a shift register and shifted into the accumulator register of a programmable calculator, where it can be used for input to the calculator or replaced with the calculator output. It is then serially shifted out of the exciter switch monitor and into the display panels in the control areas. The synchronous transmission technique requires that a clock and latching pulse accompany the data over a three-pair cable.

The data are shifted serially through the display panels, with each display panel acting as a driver for the next. Within the display panel, decoding logic is enabled during occurrence of the latch pulse, allowing data to be stored by the addressed display and ignored by all other displays.

References

1. Smith, R. H., "Dual Carrier," in *The Deep Space Network Progress Report*, Technical Report 32-1526, Vol. XII, pp. 200-203, Jet Propulsion Laboratory, Pasadena, Calif., Dec. 15, 1973.
2. Smith, R. H., "Data Collection System for the Dual-Carrier Exciter," in *The Deep Space Network Progress Report*, Technical Report 32-1526, Vol. XV, pp. 63-65, Jet Propulsion Laboratory, Pasadena, Calif., June 15, 1973.
3. Smith, R. H., "10-W S-Band Amplifier," in *The Deep Space Network Progress Report*, Technical Report 32-1526, Vol. IX, pp. 196-200, Jet Propulsion Laboratory, Pasadena, Calif., June 15, 1972.

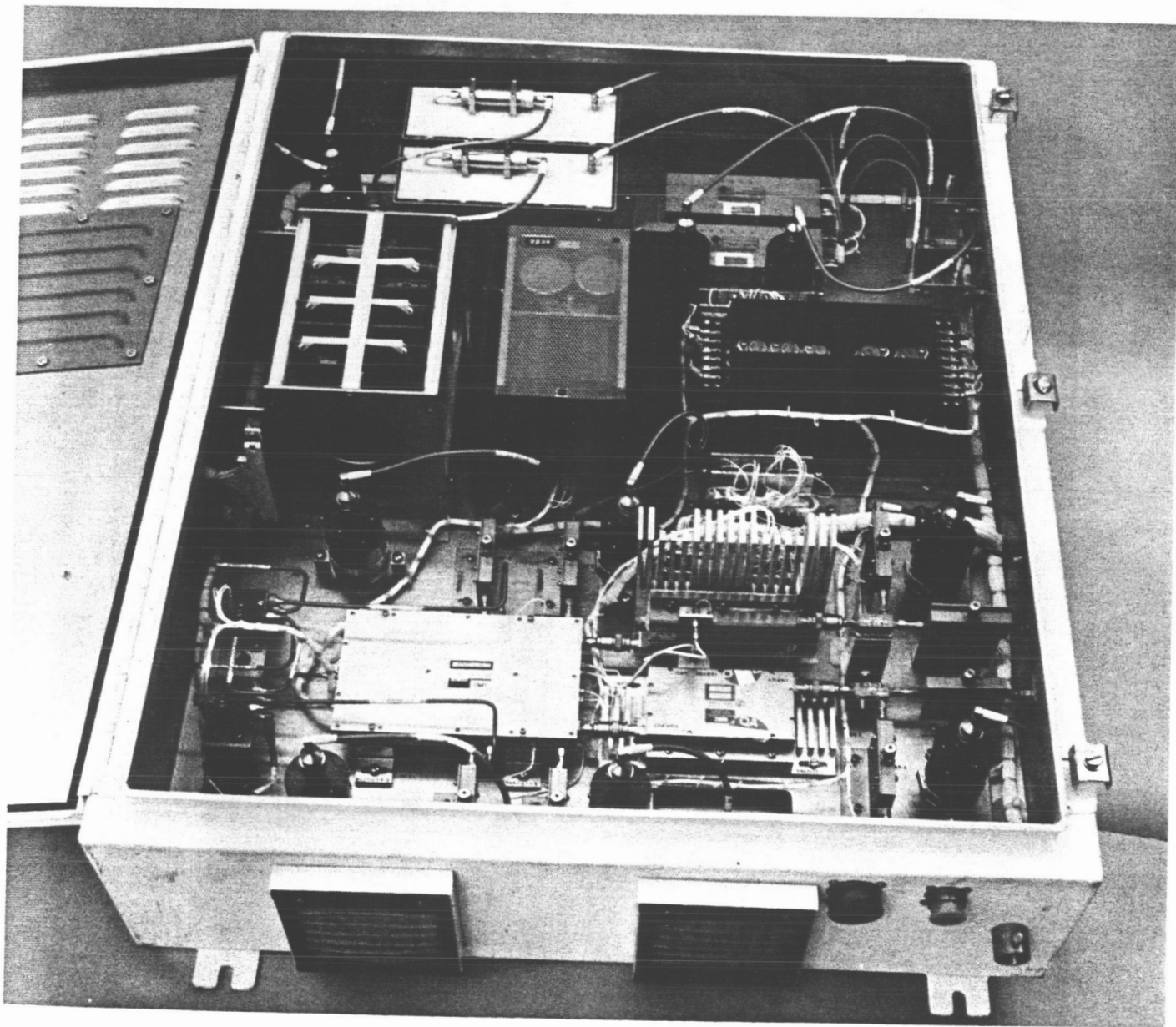


Fig. 1. Exciter switch assembly

REPRODUCIBILITY OF THE
ORIGINAL PAGE IS POOR

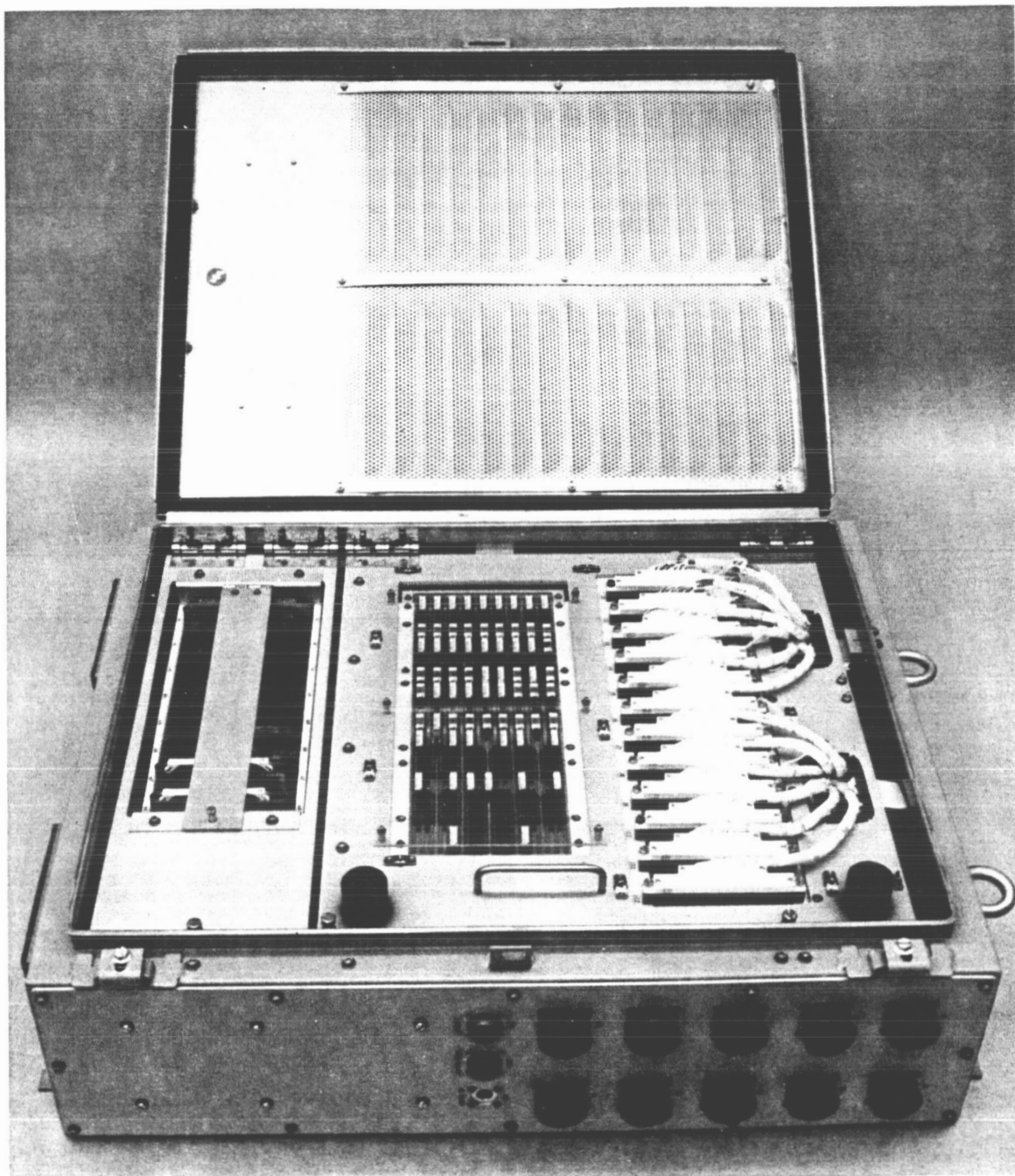


Fig. 2. Exciter switch monitor assembly

REPRODUCIBILITY OF THE
ORIGINAL PAGE IS POOR

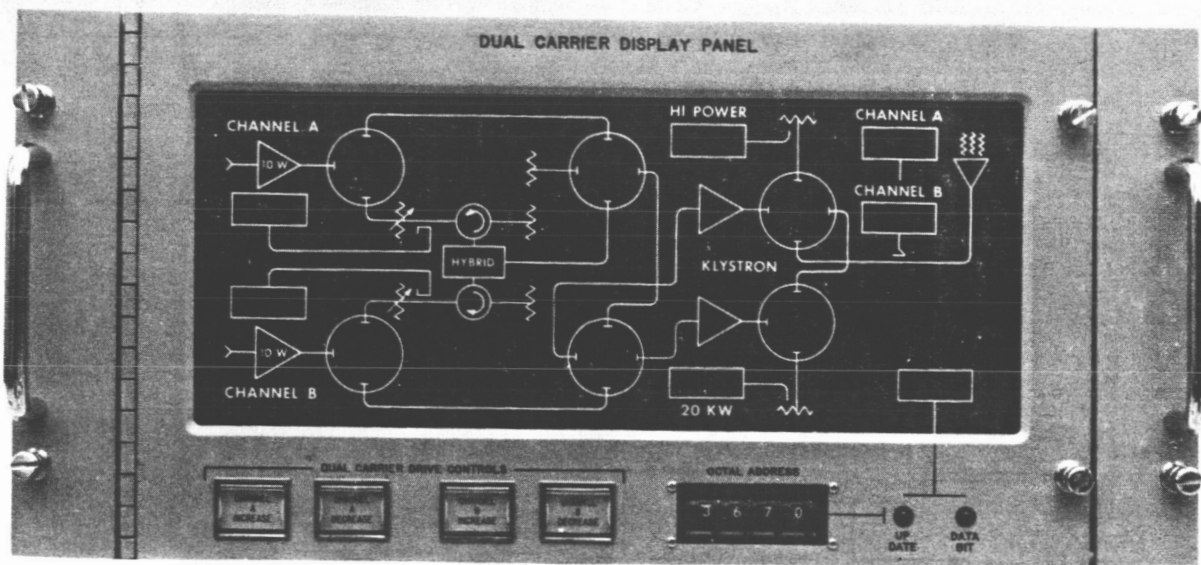


Fig. 3. Dual-carrier display assembly

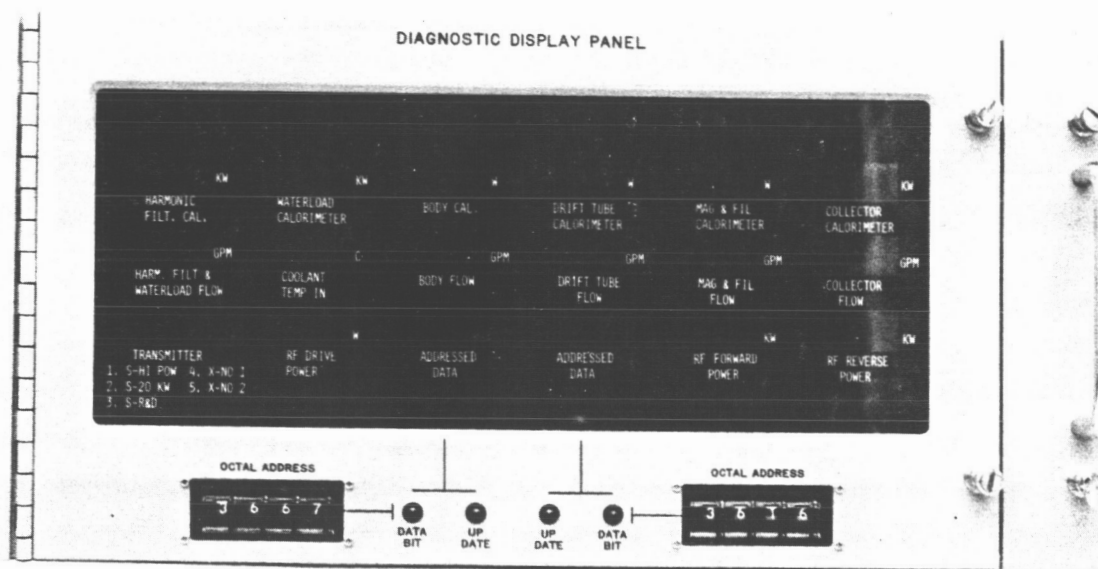


Fig. 4. Diagnostic display panel

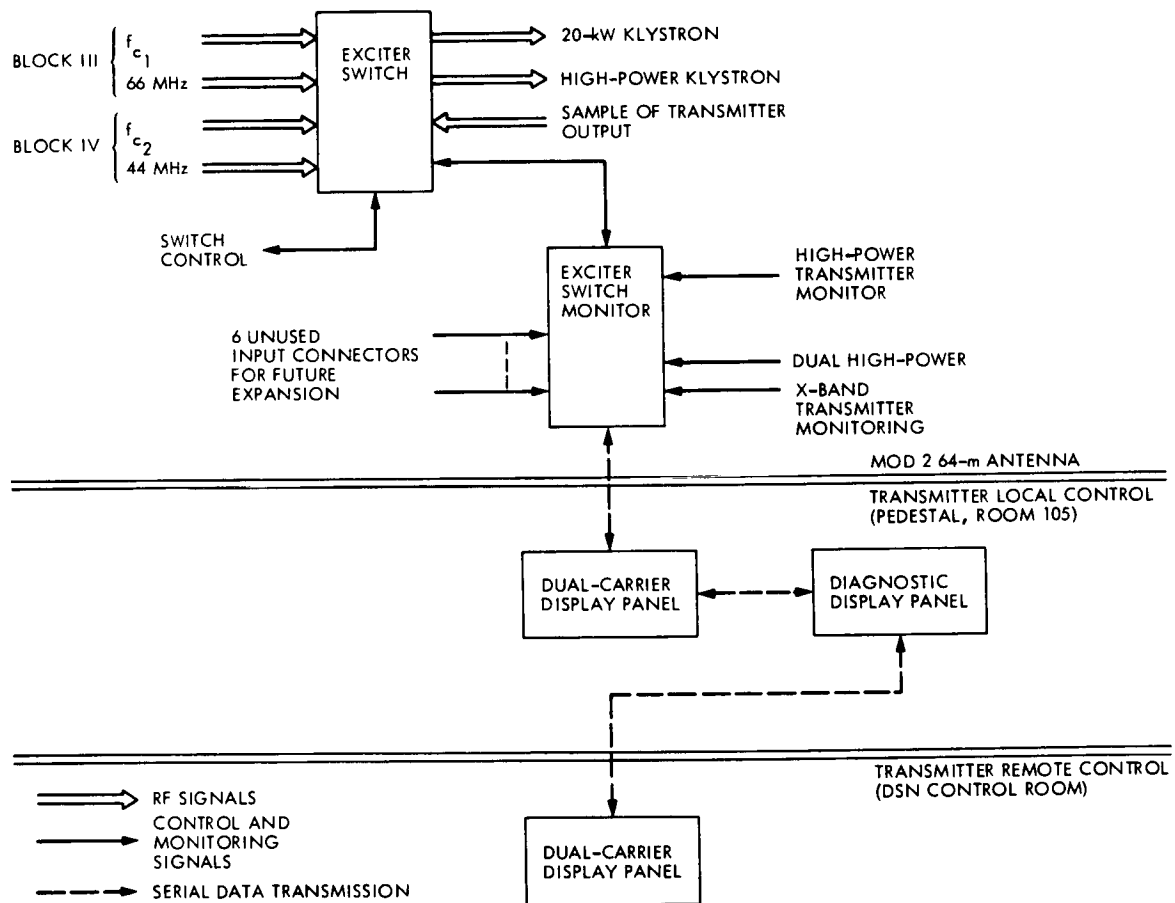


Fig. 5. Exciter switch interconnect

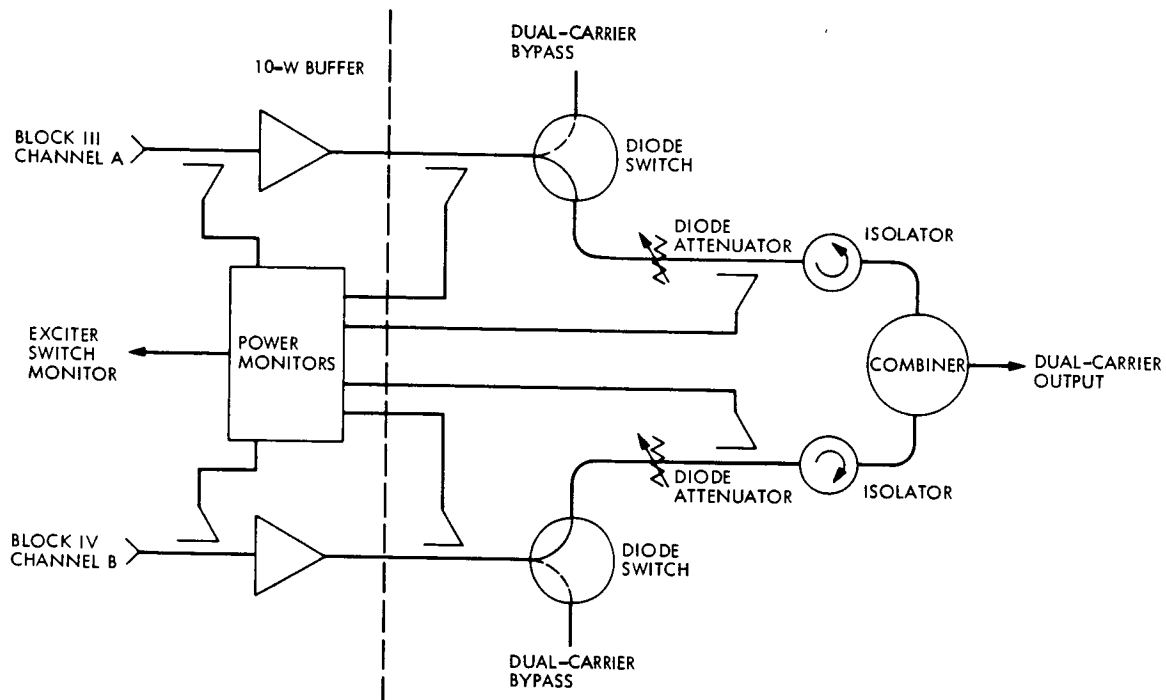


Fig. 6. Hybrid combiner

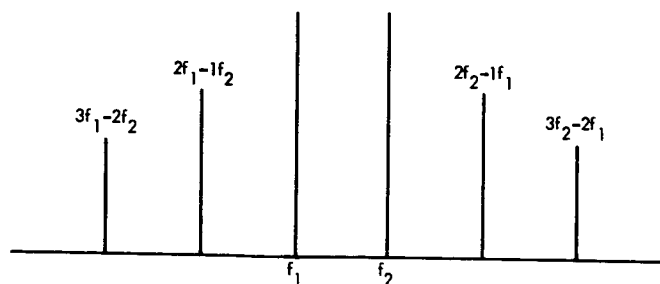


Fig. 7. Transmitter output spectrum

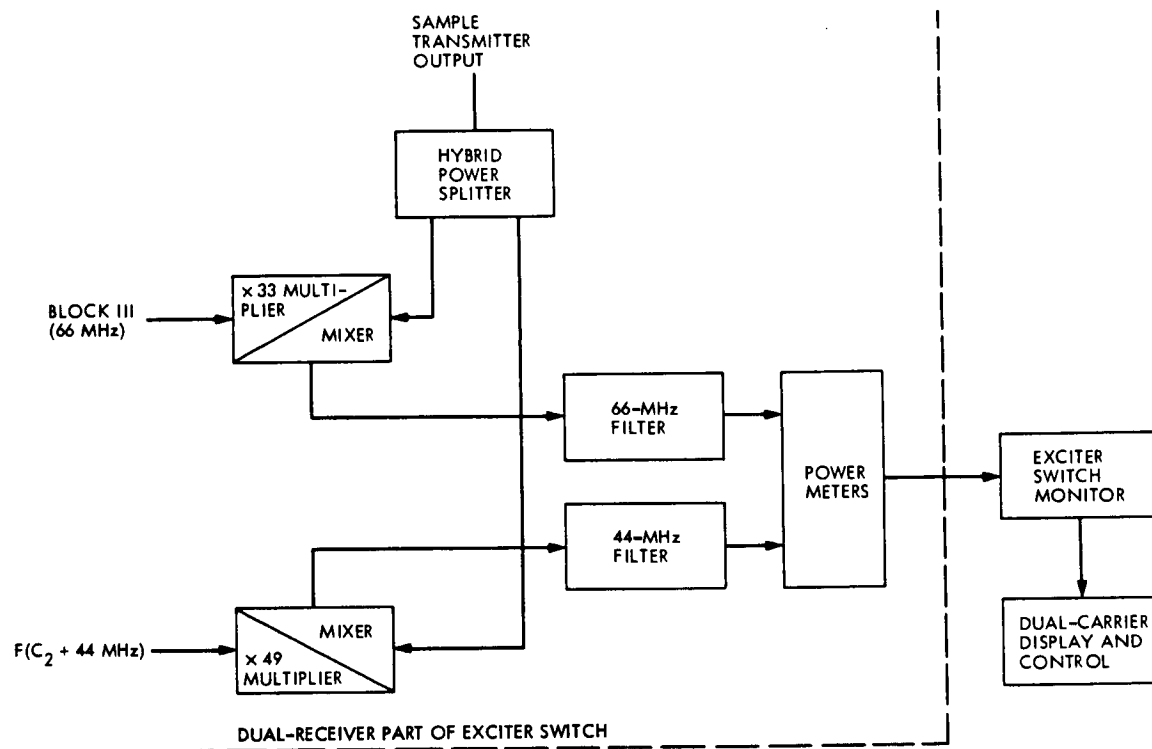


Fig. 8. Dual-carrier calibration receivers

Priority Repair Schemes in the Deep Space Network

I. Eisenberger

Communications Systems Research Section

G. Lorden

California Institute of Technology

A method is given to increase the cost-effectiveness of spares pools by performing repairs of each type of module on a priority basis whenever the number of available spares falls below a critical level. For a system already operating with established spares pools, the problem of choosing the critical levels is solved by an algorithm which attains the largest possible uptime ratio (UTR) for any specified total amount of priority repairing. Provisioning of new spares in conjunction with priority repairing is also optimized so as to achieve any UTR goal with minimum cost. Examples are given to show that even a small amount of priority repairing can yield a substantial reduction of sparing costs.

I. Introduction

The idea of a priority scheme for repair facilities in the Deep Space Network (DSN) is based on simple considerations. Experience has shown that the average time for repair of failed modules is about two weeks, assuming that the repair is performed locally at the complex. Most of that time is spent waiting for the actual repair. So long as an adequate number of spares is available, the two-week turnaround time is not critical. But when spares are temporarily unavailable because they have been used for recent replacements of failed modules, the two-week wait incurs a substantial risk of downtime. If these critical situations are treated on a priority basis and the turnaround time is shortened, say, to one week, then there is a dramatic improvement in the system uptime

ratio (UTR), the fraction of time the entire system is operable. For example, if only 5 to 10% of all repairs are performed on a priority basis, the improvement in UTR is nearly as large as if all repairs had a turnaround time of one week. This is illustrated by the examples in Section III.

In Section IV, the idea of priority repairing is considered in the context of cost-effective spares provisioning (Ref. 1), the problem of providing a spares package for a system. A method of combining the choice of a priority scheme and a spares package is given which optimizes the trade-offs between total cost, uptime ratio, and total priority workload, i.e., the frequency of priority repairs. An example in Section V illustrates the fact that substantial savings in the cost of spares needed to meet uptime

ratio goals are realizable through the introduction of priority schemes, even when the priority workload is held at less than 10%.

II. Description of Optimal Priority Schemes

The crucial thing to determine is when to give priority to repairs of a particular type of module. Our method chooses a critical level r for the number of available spares, depending upon the type of module and the spares complement. Whenever the number of spares available falls below r , priority is given to that type. Priority status ends when there are once again at least r spares. At any time, several module types may have priority status. It is assumed that these are repaired in the order that they went into priority.

The different choices of r for different types of modules are based on a trade-off between the priority workload, i.e., frequency of priority repairs, and the system uptime ratio. Let $i = 1, \dots, k$ denote the types of modules in the system n_i the number of type i operating in the system, N_i the number of spares, and r_i the critical level to be chosen. Assume given the mean time between failures (MTBFs) for the k types, the mean time to repair without priority μ (same for all types), and the mean time to repair under priority μR (an $R < 1$ is specified). The Markov method of Ref. 2 can be used to calculate for each $i = 1, \dots, k$ the uptime ratio UTR_i of the i th type and the frequency of priority repairs F_i (e.g., 4.2 priority repairs per year). The system uptime ratio is defined by

$$UTR = (UTR_1) \times (UTR_2) \times \dots \times (UTR_k) \quad (1)$$

and the system frequency of priority repairs is

$$F = F_1 + \dots + F_k \quad (2)$$

The trade-off is made by choosing a value of $d > 0$ and maximizing

$$\log(UTR) - d \cdot F = \sum_{i=1}^k (\log UTR_i - d \cdot F_i) \quad (3)$$

over all priority schemes, i.e., sets of critical levels $\{r_1, \dots, r_k\}$. This is done by maximizing the right-hand side of Eq. (3) termwise, i.e., for each i , the value of r_i is chosen among the possible values $0, 1, \dots, N_i + 1$ to maximize $\log UTR_i - d \cdot F_i$. It should be noted that as d gets larger, the r_i 's get smaller and so do the F_i 's and UTR_i 's.

Every priority scheme $\{r_1, \dots, r_k\}$ obtained in this way for some d is optimal in the sense that neither its UTR nor its F can be improved upon without sacrificing the other. To see this, suppose that for a particular $d = d^*$, the values UTR^* and F^* are obtained by the algorithm described above. Let UTR^{**} and F^{**} denote the values for some other priority scheme. Since Eq. (3) was maximized for $d = d^*$ by using the algorithm, it is clear that

$$UTR^* - d^* \cdot F^* \geq UTR^{**} - d^* \cdot F^{**} \quad (4)$$

By Inequality (4), if $F^{**} < F^*$, then $UTR^{**} < UTR^*$, i.e., the UTR is sacrificed. Similarly, if $UTR^{**} > UTR^*$, then $F^{**} > F^*$, i.e., F is sacrificed.

It can also be shown that every optimal priority scheme is obtainable by using the algorithm for some $d > 0$; in other words, if a priority scheme is not obtainable by the algorithm for some d , then either its UTR and F can both be improved upon simultaneously or one of them can be improved without sacrificing the other.

III. Priority Schemes for Existing Spares Packages

A variety of examples were computed to determine the kind of uptime ratio improvement one can expect from the use of optimal priority schemes as described in Section II. For these examples, it was assumed that the numbers of spares N_1, N_2, \dots , of each module type are given, along with the numbers operating, n_1, n_2, \dots , and the failure rates and repair rate. In each example, several choices of the parameter d of Section II were made, and in each case the uptime ratio and a total rate of priority repairs were computed. The latter rate was used to determine the fraction of all repairs performed under priority. This fraction seems more meaningful intuitively than the rate of priority repairs itself.

These results yielded plots of uptime ratio against the priority repair fraction, such as the one in Fig. 1, which is typical. The value $R = 0.5$ was used for Fig. 1, whereas $R = 0.25$ (quadruple rate for priority repairs) was used for the same package in Fig. 2. This package consisted of a total of 55 spares for 30 module types.

Notice that in both Figs. 1 and 2 the improvement in uptime ratio is dramatic, even with a small fraction of priority repairs. The improvement levels off rapidly once the priority fraction reaches 10–15%. In other words, 10–15% priority fraction yields very nearly as high an UTR as 100%, the latter amounting to performing all repairs at the high priority repair rate.

The examples computed revealed that the steep improvement in UTR for small priority fractions is even more pronounced when the existing system uptime ratio is high and also when R is low. For example, a larger spares package for the same system as in Figs. 1 and 2 showed an initial UTR of 0.955, which improved to 0.998 with a 4% priority fraction and $R = 0.25$.

IV. Method of Spares Provisioning Using Priority

The problem is to choose the number of spares N_i and the priority level r_i for each module type i so that the overall package achieves the greatest UTR for the lowest total cost and total priority fraction. To formulate this mathematically, use relations (1) and (2) defining the system uptime ratio and system frequency of priority repair, together with the relation

$$C = C_1 + \dots + C_k \quad (5)$$

where C denotes the total cost of spares, and the C_i 's are the cost of spares for the different types of modules. The determination of optimal trade-offs is made by extending the method of Section II. Replacing the fundamental relation, (3) of that section is the relation

$$\log(UTR) - d \cdot F - e \cdot C = \sum_{i=1}^k (\log UTR_i - d \cdot F_i - e \cdot C_i) \quad (6)$$

which expresses the quantity to be maximized for given d and $e > 0$. The reason for seeking to maximize Eq. (6) is the same as in Section II: A total package of N_i 's and r_i 's maximizing Eq. (6) for some d and $e > 0$ is optimal in the sense that neither its UTR, nor its F , nor its C can be improved without sacrificing one or both of the others. As in Section II, the fact that the quantity to be maximized, in this case Eq. (6), is expressed as a sum over i means that it can be maximized term-wise. So, for each i , it is necessary to choose an N_i and an r_i to maximize

$$\begin{aligned} \log UTR_i - d \cdot F_i - e \cdot C_i &= \log UTR_i(N_i, r_i) \\ &\quad - d \cdot F_i(N_i, r_i) - e \cdot C_i(N_i) \end{aligned} \quad (7)$$

where the right-hand side shows the dependence on N_i and r_i . Since the cost of spares C_i depends only on N_i and not on r_i , the problem is immediately solved by fixing N_i and choosing the r_i which maximizes

$$\log UTR_i(N_i, r_i) - d \cdot F_i(N_i, r_i)$$

among the possible values of $r_i = 0, 1, \dots, N_i + 1$.

Once the optimal choice of r_i for each N_i has been determined in this way, the dependence on r_i in Eq. (7) is removed, and one has to choose N_i to maximize

$$\log UTR_i(N_i) - d \cdot F_i(N_i) - C_i(N_i) = V(N_i) - PN_i$$

using a briefer notation, where P denotes e times the unit cost of spares of type i . The expression $V(N_i) - PN_i$ is exactly of the form considered in Ref. 1 (the value-cost lemma) in connection with the optimal choice of spares packages without consideration of priority. The algorithm given in that paper for recursively generating *all* optimal packages applies in this case because the required monotonicity condition has been found to be satisfied over the range of interest. In the present context, this means that for a given $d > 0$ the algorithm generates all the optimal packages obtainable over an arbitrary interval of e values.

In practice, one wants a listing of the specifications (uptime ratio, cost, and priority fraction) for a variety of optimal packages, keeping the specifications within prescribed ranges. This is most effectively accomplished by fixing a d value, listing the specifications of all optimal packages whose cost (or uptime ratio) is less than a prescribed limit, and then repeating the process for other d values (higher d values give lower priority fractions). Because of the discrete nature of the packages, small changes in d will often produce the same (or many of the same) sets of specifications. It is not difficult, however, by judicious choices of d , to keep this repetition to a minimum and still obtain virtually all the optimal packages over the range of interest.

V. A Spares Provisioning Example

The spares provisioning algorithm described in Section IV was applied to several examples of system configurations in an attempt to determine the range of typical cost reductions achievable using priority schemes. These cost reductions are measured from the cost of optimal spares provisioning for the same system uptime ratio without priority (based on Ref. 1).

The example illustrated below was chosen with the stipulation that the fraction of priority repairs be 9-10%, which was felt to be within the range of reasonable levels. Figure 3 shows the cost in thousands of dollars of the spares packages as a function of the system uptime ratio.

The bottom curve does this for the no-priority case with mean repair time of one week, half the normal two-week time. The middle curve shows the case of 9–10% priority repairing, with one-week repair time under priority, two weeks otherwise. The top curve depicts the case where no priority is used and the repair time is 1.82 weeks—a little less than two weeks, this value being chosen to yield the same *average* rate of repair as the 9–10% priority scheme, namely, 0.55 per week. This value is used for the top curve to provide a truer comparison with the middle curve representing the priority schemes: the difference between the two is not due to any improvement in average repair time, but is only due to the effectiveness

of the priority schemes in allocating repair work according to immediate needs.

Note that the cost reduction of the middle (priority) curve over the top curve is about 20% in the range of uptime ratios from 0.9 to 0.995. Even if the high-priority repair time were always in effect, so that the bottom curve would apply, the additional cost reduction would be only about 8% in the uptime ratio range below 0.95, dropping steadily to about 3% at the 0.99 level. Thus, the priority approach achieves nearly all of the cost reduction possible through speedier repairs, even though the speedier repairs are required less than 10% of the time.

References

1. Eisenberger, I., Lorden, G., and Maiocco, F., "Cost Effective Spares Provisioning for the Deep Space Network," in *The Deep Space Network Progress Report 42-20*, pp. 128–134, Jet Propulsion Laboratory, Pasadena, Calif., Apr. 15, 1974.
2. Eisenberger, I., Lorden, G., and Maiocco, F., "A Preliminary Study of Spares Provisioning for the Deep Space Network," in *The Deep Space Network Progress Report*, Technical Report 32-1526, Vol. XVIII, pp. 102–110, Jet Propulsion Laboratory, Pasadena, Calif., Dec. 15, 1973.

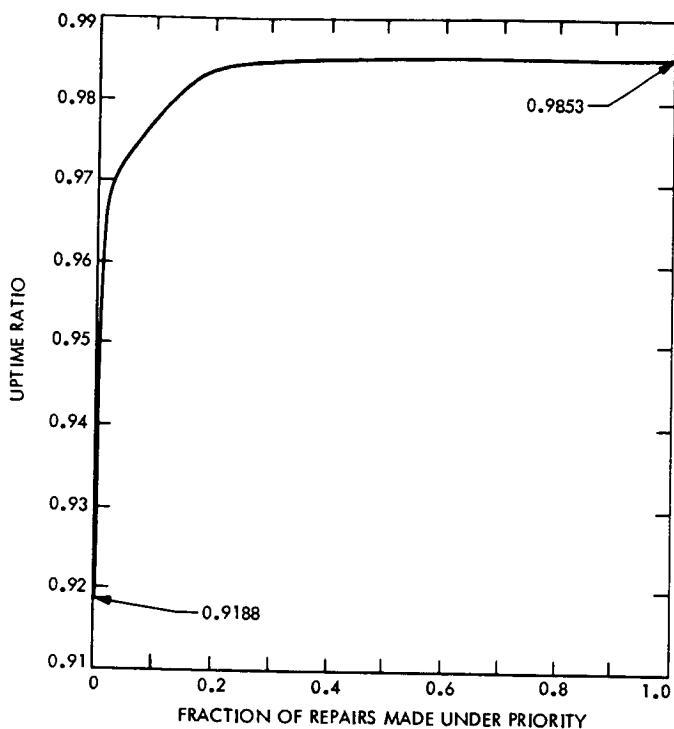


Fig. 1. Improvement in system UTR as the fraction of repairs made under priority increases, $\mu = 336$ h, $R = 0.5$

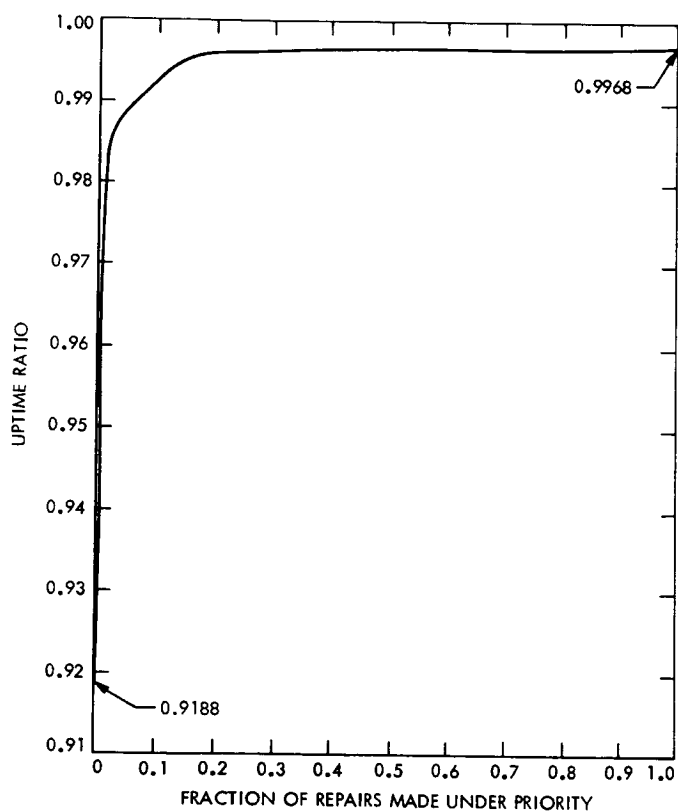


Fig. 2. Improvement in system UTR as the fraction of repairs made under priority increases, $\mu = 336$ h, $R = 0.25$

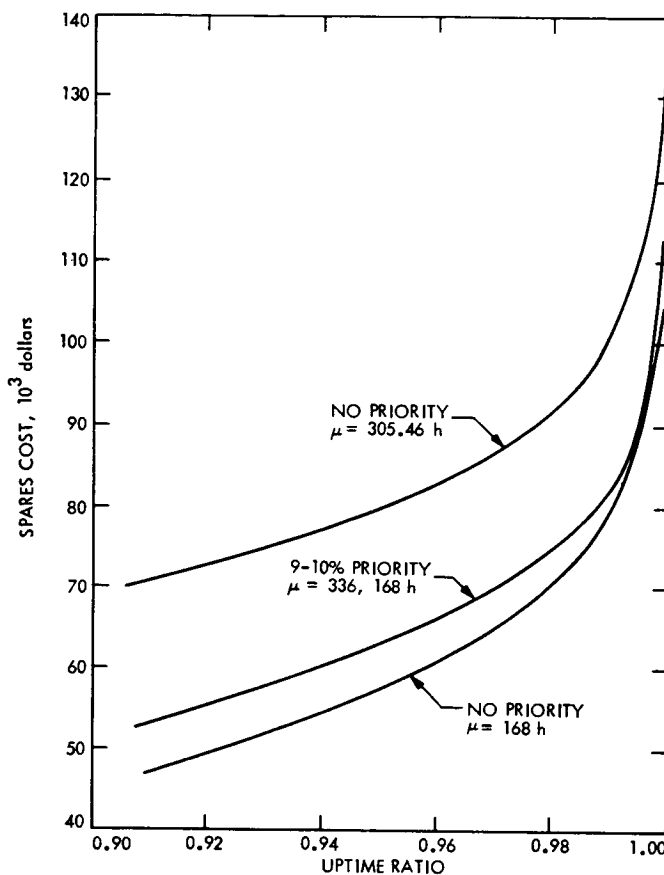


Fig. 3. Cost of spares vs UTR for repairs with no priority and 9-10% repairs made under priority

Variation of GCF Block Error Rate With Block Length

O. Adeyemi

Communications Systems Research Section

Increasing the Ground Communications Facility (GCF) block length to 4800 bits from the present 1200 bits will no more than triple the error rate.

In the Error Control Study (Ref. 1) of the GCF, all numerical calculations were based on the current NASA-standard block length of 1200 bits for the GCF. Now that it is being contemplated to standardize all of NASA Communications system (NASCOM) for a block length of 4800 bits, it is important to know how much this change would affect the GCF error rate. This question will be answered here for both the 4800-bit/s high-speed and 50-kbit/s wideband data lines.

If the GCF errors were random instead of occurring in bursts, a percentage increase in block length would be accompanied by approximately the same percentage increase in the block error rate. So, for example, going from a block length of $n = 1200$ bits to a longer block of length $N = 4800$ bits would make the error rate approximately four times as great. It is not so with burst noise channels; while it is true that the block error rate still increases with block size, the error is no longer a linear function of the block length (see Ref. 1, pp. 166 and 173). For the same bit error rate (BER), the random error channel has a higher block rate, although the error blocks

on a bursty channel contain a higher density of bit errors. This is why forward error correction coding alone (capable of correcting only a few bit errors or short bursts) is not effective in the GCF, thus making error correction by feedback retransmission method a must.

Table 1 shows the predicted block error rates for block sizes up to 6000 bits. For the 4800-bit/s data line, the expected block rate for 4800-bit blocks varies from twice (at the highest RED error mode) to (just) less than four times (at the GREEN mode) the present GCF error rate for the 1200-bit blocks. This means that changing to 4800-bit blocks would increase the block error rate to about 4×10^{-2} from the current 2 percent. The average rate would increase from 2.2×10^{-3} to about 7×10^{-3} . The increases are not as sharp in the 50-kbit/s data line, where the highest error rate is not expected to rise above 8×10^{-3} .

For comparison, these variations in rates are graphed for both the high-speed and wideband data lines. Table 2 contains the average performances in the RED, AMBER, and GREEN error modes.

Reference

1. Adeyemi, O., *Error Control in the GCF: An Information-Theoretic Model for Error Analysis and Coding*, Technical Memorandum 33-699, Jet Propulsion Laboratory, Pasadena, Calif., October 1974.

Table 1. Error probability ($\times 10^{-4}$)

Block length, bits	Highest error (RED mode) $BER = 5.06 \times 10^{-4}$	Overall average performance $BER = 4.38 \times 10^{-5}$	GREEN mode $BER = 1.89 \times 10^{-6}$
4800-bit/s data line			
1200	179.0	21.9	2.1
1800	208.0	29.3	3.0
2400	255.1	36.0	3.9
3000	262.1	42.5	4.8
3600	289.0	48.8	5.6
4200	315.7	55.0	6.5
4800	342.4	61.1	7.4
5400	369.1	67.3	8.2
6000	395.7	73.4	9.1
	$BER = 2.42 \times 10^{-4}$	$BER = 3.54 \times 10^{-5}$	
50-kbit/s data line			
1200	41.6	6.8	
1800	48.4	8.1	
2400	54.2	9.5	
3000	59.2	10.8	
3600	63.5	12.1	
4200	67.3	13.4	
4800	70.6	14.7	
5400	73.5	16.1	
6000	76.1	17.4	

Table 2. Error probability ($\times 10^{-4}$)

Block length, bits	Averaged RED group $BER = 2.45 \times 10^{-4}$	Averaged AMBER group $BER = 2.93 \times 10^{-5}$	Averaged GREEN group $BER = 3.32 \times 10^{-6}$
48-bit/s data line			
1200	65.0	21.2	3.7
1800	76.8	30.7	5.6
2400	87.3	39.9	7.4
3000	97.6	48.8	9.2
3600	107.7	57.5	11.0
4200	117.8	65.9	12.9
4800	128.0	74.1	14.7
5400	138.1	82.0	16.5
6000	148.2	89.8	18.3

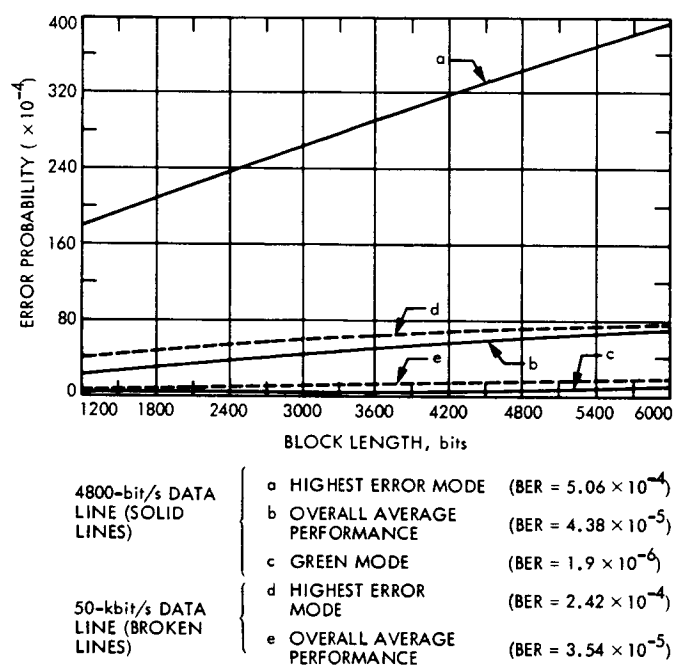


Fig. 1. Variation of block error rate with block size

Effects on Station Productivity of the RF and Antenna Automation Plans

H. L. Kirkbride

Communications Systems Research Section

In May 1975, a demonstration of the RF automation plan was held at the Mars Station (DSS 14). This automation design used a central computer to calibrate and configure the RF subsystem automatically. In August 1975, a demonstration was held at the Venus Station (DSS 13) to show the operation of a remote automatic pulsar data acquisition program. This article attempts to identify the effects of implementation of either of these plans at the deep space stations on network operations, especially in the areas of increasing available tracking time and reducing the level of effort required in the maintenance of network equipment. The percentage of station time spent in calibration can be reduced significantly by automatic calibration and configuration. The amount of scheduled maintenance time spent in corrective maintenance can be reduced due to the capability of automated equipment for self-diagnosis. Station downtime during scheduled tracking time will be reduced to the extent that operator errors will be minimized.

I. Introduction

The goal of the first RF automation demonstration performed in May 1975 was to configure and calibrate automatically the DSS 14 RF subsystem, consisting of two Block IV receivers and one exciter, two Block IV subcarrier demodulator assemblies (SDAs), the Microwave Subsystem, the noise-adding radiometer, and the high-power S-band transmitter—and then automatically acquire the carrier and subcarrier. A central computer accepted configuration messages from the demonstration operator

and distributed them to the appropriate subassembly controllers. Diagnostic messages from the subassemblies were printed on a teletype for the demonstration operator's use. In areas where hardware redundancy existed, detection of a failed module within a hardware assembly caused a backup assembly to be automatically switched in and the hardware string to be reconfigured to accommodate the new equipment. Several changes are planned for the next demonstration in November 1976, including replacing the PDP-11 minicomputers used in the previous demonstration with Intel 8080 microcomputers,

eliminating the polling scheme adopted in the software by developing the new software on an interrupt-driven basis, and using the high-level programming language PL/M instead of RT-11 Basic. The demonstration operator will be provided with more powerful software tools for handling unexpected events.

The plan to automate antenna operation at DSS 14 began with the development and demonstration in August 1975 of the remote automatic pulsar data acquisition program at DSS 13. After initial configuration by station personnel, the operator in this demonstration, who was located at JPL, typed in position information and caused the antenna to be pointed at a pulsar and then begin sidereal rate tracking. At the same time, the data collection hardware was automatically initialized to begin recording pulsar data on magnetic tape. At DSS 13, one XDS 930 and two XDS 910 computers were used in the pulsar observing project. In adapting the antenna pointing portion of the program for use at DSS 14, a Modcomp II/25 will replace the antenna pointing system's XDS 910.

This article is not an analysis of the technology used in either of the two automation projects. Rather it is an attempt to identify the effects of implementing either of these plans at the deep space stations on network operations, especially in the areas of increasing available tracking time and reducing the level of effort required in the maintenance of network equipment.

II. Station Productivity

Evaluation of the effect of automation on network productivity, which can be defined as

$$\text{network productivity} = \frac{\text{delivered tracking hours}}{\text{manhours expended in DSN}}$$

reduces to examining the changes in delivered tracking hours due to implementation of the automation plans when the manpower required for operation of the stations can be expected to remain constant. The antenna automation plan will reduce the workload of the two crew members stationed in the 64-m antennas by introducing hydraulics monitoring hardware inside the antenna. However, since these crew members also perform duties other than monitoring hydraulics systems, the need for operators in the antenna will remain. In connection with increasing available tracking hours at the deep space stations, three areas in particular are interesting to consider; these are the reduction of precal time, the reduction of maintenance time required to repair failed equipment, and the reduction of downtime due to equipment failure or operator error. There is, of course,

no guarantee that increasing available tracking hours will necessarily increase actual tracking hours by an equivalent amount; however, radio science can profitably occupy available tracking time not required for spacecraft tracking.

III. Calibration Time

Table 1 depicts the estimated decrease in the total number of hours required per year in completing countdowns at the deep space stations. These data were collected from the DSN weekly schedules for CY 1974. There are certain exceptions to the claim that a level-two countdown can be completed in 45 min. This is true only if certain other functions which were not under computer control during the first RF automation demonstration and are not planned to be during the second are, in fact, brought under the control of the RF automation central computer. Several operations in the precalibration of the high-power transmitter require manual operation of equipment in the antenna; valve positions for the heat exchangers must be set for the appropriate transmitter, a number of high-current switches must also be configured for the transmitter to be used in the track, and the main motor generator, if not already running, must be started. None of these operations is time-critical, and they could be accomplished at a time prior to the start of the precal procedure in the control room.

The Y-factor chart cannot at present be generated automatically, and the test signal control panel which serves to route the test signal is still operated from the front panel. In the first RF automation demonstration, the test translator was used in place of the test transmitter, which is not under computer control, to run automatic gain control (AGC) curves. Finally, the carrier suppression calibration requires manual installation and removal of attenuators in the receivers. If, in fact, interface hardware is added to allow computer control of these functions, then implementation of the RF automation plan can be expected to reduce total precal time about 77% over a period of a year. At present, the two crew members charged with monitoring the hydraulics equipment in the antenna perform the manual part of the transmitter precalibration procedure.

A level-one precalibration will be reduced in length only slightly because this procedure requires complete calibration of the Block III as well as the Block IV RF hardware, and there is no capability for computer control now installed in the Block III equipment. A level-two countdown treats only one string as being prime and the other as backup. Under the RF automation scheme, the

Block IV equipment comprises the prime string, and the Block III equipment need only be calibrated to level-three countdown conditions; this requires only a brief check for malfunctions and a three-point AGC curve instead of a full curve, but it must be done manually, since no capability exists for computer control of Block III equipment. The RF subsystem calibration is the major contributor to the length of the station precalibration procedure. The existing antenna precal procedure is still shorter than the 45-min estimate for the automated RF precal; therefore, antenna automation will have no effect on overall precal time.

IV. Station Maintenance Time

A reduction in the number of precal hours required at the stations yields an increase in the number of hours available for other activities. Table 2 and Fig. 1 show the present distribution of station hours per year in the Deep Space Network listed in DSN time utilization reports, as well as the resultant distribution if all available hours gained from the reduction in precal time were devoted to tracking, and the distribution if the additional hours were divided among various activities according to their present fraction of non-precal or maintenance time. These data also take into account the reduction due to the automation plans of the 20.2% of station time scheduled for maintenance; 3.2% of station time is scheduled for minor modification, during which time engineering change orders are implemented that require only 2 to 3 h for completion. Table 3 shows the distribution of maintenance time by activity estimated by maintenance personnel at DSS 14. It indicates that of this combined 23.4% of station time, 30% is spent in corrective maintenance, isolating the faults which have occurred during a track causing a hardware system to fail and necessitating switching to the backup string to minimize data loss. Since no repair of hardware occurs at the station, all of the 30% corrective maintenance time is spent actually isolating the fault to the circuit card or blue board chassis level.

Development of hardware which incorporates efficient fault isolation capabilities would lead to a reduction in corrective maintenance time at the stations. Maintenance time is distributed among the major hardware systems as shown in Table 4; 33% of all maintenance time is spent either on the antenna or receiver systems, with approximately 30% spent on the RF subsystem and 3% on the antenna.¹ The savings in station hours per year if

¹I. Eisenberger, *Estimated Manpower Costs for Operating and Maintaining Three Major Subsystems at DSS-11, DSS-12 and DSS-14*, IOM 331-75-30, Jet Propulsion Laboratory, Pasadena, Calif., April 15, 1975, p. 2.

automatic fault location techniques, which could be expected to reduce failure location time by 75%, were incorporated into the RF and antenna hardware only would be about 1200 h or a total of 2% of all station hours.

Another benefit which can be derived from the use of error-finding hardware is the automatic logging of failure information. If the failure of a module not only initiated a fault-locating routine in the controlling hardware but also caused a failure report to be recorded with information concerning the time and location of the fault, as closely as can be automatically determined, histories of particular pieces of hardware concerning failure rates and failure-prone areas could be easily accumulated.

V. Mission Changeover Time

Mission changeover time will not be affected significantly by the RF automation program due to the fact that most of the present 30 to 60 min of changeover time is spent loading programs in the digital and antenna systems, as well as waiting for the antenna to move. The time needed to reconfigure the antenna could not, of course, be reduced below the 15 min required to move the antenna from horizon to horizon.

VI. Station Downtime

Scheduled track time and delivered track hours differ by the amount of time that data flow is interrupted due to equipment failure or operator error. Table 5 shows the number of hours per year lost in the DSN during tracking time as recorded in discrepancy reports. The reductions in downtime credited to the two automation plans are derived from an estimation of the reduction in the number of operator errors producing data loss, the improvement in hardware assembly replacement and reconfiguration time with automatic failure backup, and the capability to constantly monitor conditions in the subsystem which are not now detectable to the operator. In addition, in the antenna automation scheme, a change in the procedure for reloading programs makes it possible to correct errors faster and thus save downtime.

Implementation of both RF and antenna automation plans would yield approximately a 20% decrease in the downtime recorded for 1 year of operation at all nine stations, the RF automation contributing about 18% and the antenna automation about 2% of the reduction. As can be seen in Table 6, the lost time listed in discrepancy reports as being associated with the antenna or the antenna pointing system would be reduced by 30% by the

antenna automation plan as designed at present. The time lost over all deep space stations due to failures or errors in the RF subsystem alone would be reduced by about 50%.

In almost all cases, as soon as a fault is detected in the primary data string, the station switches to the backup string to minimize lost data time. The exceptions to this rule, where there is no backup, are in the microwave hardware (excluding the masers), the antenna servo system, the high-power transmitter, and the Block IV exciter. In the last case, only the ranging capability is lost, since the Block III exciter would still be able to support command capability and a two-way doppler link. The 20-kW transmitter can often be used to replace the failed 400-kW transmitter. In all systems where redundancy does exist, therefore, no reduction in downtime is likely due to added fault location capability. The length of time necessary to accomplish the switch to the backup string depends on how thoroughly the second string was calibrated during the countdown procedure and whether equipment merely needs initializing or programs must be loaded to continue the track. Reductions in the time required to locate the fault in a failed assembly after the track is completed are probable, however, if additional fault diagnosis is possible with the automation hardware. In systems such as the antenna controller, where no backup equipment exists, controlling hardware can also be programmed to monitor changes in a system's condition and diagnose a problem with a list of most-probable causes. This would serve to narrow down the list of possibilities the station personnel would have to investigate in order to locate the problem.

Generating a complete automatic gain control curve, -176 to -90 dB at 5-dB intervals, requires about 40 min to set up the test transmitter and run the calibration. Accuracy is limited due to the instability of the readout near threshold. The AGC calibration is run again after the track, and the expected value during track is found by interpolation. The RF automation plan will reduce setup and run time for the AGC calibration to 15 min; variations in amplifier gain will be calculated frequently from measurements of system noise temperature change during the track to minimize errors induced by an incorrect AGC curve estimate. Errors concerning the AGC curve account for a number of data losses, each of which entails the loss of a significant portion of a spacecraft track. For example, a discrepancy report shows 495 min of outage when the station reported not having time to run an AGC curve.

Operator errors take many forms, some of which go unexplained in the discrepancy reports. Operator errors will not be eliminated by RF and antenna automation,

since there will still be operators at the station; however, as the number of repetitive tasks are reduced, so are the opportunities for operator error. In some systems, operator errors can cause the loss of a whole track, as in the case where the wrong AGC curve was loaded in the Digital Instrumentation Subsystem. However, in the antenna or RF systems, they more often take the form of incorrect predict data being entered, causing an inability to lock onto the spacecraft signal. A discrepancy report shows 32 min of outage due to an incorrect receiver bandwidth setting. An automatic failure backup capability will reduce the amount of time now required to detect a failed module within a hardware assembly and reconfigure the subsystem to include a backup assembly. If the number of scheduled hours of track remains at the present value, the implementation of the antenna and RF automation plans would cause an increase of 0.4% (from 98.2 to 98.6%) in the percentage of scheduled tracking hours in which data are actually delivered.

Both automation plans will result in a change in equipment at the station. The RF automation plan will add interface hardware plus six microcomputers with 40K of memory each, all of which, with the exception of a teletype, a cathode ray tube, and a transmitter microcomputer controller which will be located in the antenna, will fit into existing equipment racks in the control room. Except for the standard microcomputer controllers, all of the equipment will be built at JPL. The Intel 8080 microcomputers appear to have a very low failure rate; in the 13 months since the microcomputers have been delivered, the manufacturer has recorded failures in only 1% of the existing units. The antenna automation plan will replace the XDS 910 in the antenna pointing system with a Modcomp II/25.

Failures in the controlled hardware in the RF automation plan should be detected and compensated for by the controlling microcomputer. Failures in the controlling hardware itself present a different problem. If the central computer fails, then, of course, each individual hardware assembly could be calibrated as is now done. However, when a level-two countdown is scheduled and only 45 min are allowed, approximately 4 h of track time will be lost due to the extended precal procedure. If, in fact, any of the individual standard controllers fails, the associated hardware assembly will have to be manually calibrated, and any functions that the manually run hardware performs in conjunction with other hardware assemblies will have to be performed in a manual mode. It seems likely, then, that the failure of any of the six standard controllers could cause a significant delay in completing a countdown. In such a case, fault location capability in the

standard controllers would be very valuable. A failure in the controlling computers in the antenna automation scheme is likely to cause loss of the ability to point the antenna and then track unless the problem can be solved by reloading the XDS 910 or 930 programs. Otherwise, it will be impossible to operate the antenna until the malfunctioning hardware is repaired.

VII. Conclusion

Implementation of the RF and antenna automation plans will probably not affect the number of operators required at the stations. Since no backup equipment exists in the antenna pointing system, the use of self-diagnostic techniques in the design of automated equipment can

reduce the amount of downtime due to failures in the antenna controller. Calibration time will probably not be affected by antenna automation, but the RF automation scheme will cause a significant decrease. The capacity for automatic failure backup in the RF automation plan will permit a decrease in the amount of downtime during scheduled tracking time spent switching to a backup string and recalibrating. While the use of self-diagnostic hardware will save downtime only in isolated parts of the RF subsystem, scheduled maintenance time will be reduced by automatic error-locating techniques. An overall increase of approximately 25% in available tracking time as well as a reduction in the number of station personnel required at the 64-m stations can be expected if both the RF and antenna automation plans are implemented.

Table 1. Distribution of countdowns performed in DSN, CY 1974^a

	Level 1 countdown	Level 2 countdown	Level 3 countdown	All countdowns
Number per year	106	750	2322	3178
Percent of all countdowns	3.3	23.6	73.1	100
Present average duration, h	9.52	4.80	1.87	2.81
Estimated average duration, h	8.5	0.75	0.25	0.64
Total time/year at present, h	1009.1	3600.0	4342.1	8951.2
Estimated total time/year, h	901.0	562.5	580.5	2044.0

^aFrom data collected over a 26-week period.

Table 2. Station utilization for all stations in DSN, CY 1975^a

	Hours spent/year at all stations and percent of total station hours		Estimated hours/year and percent of total if all additional hours spent tracking		Estimated hours/year and percent of total if additional time allocated proportionally among all activities	
	h	%	h	%	h	%
Track time	19580.3	28.7	24513.6	35.9	21558.8	31.6
Precal	4843.9	7.1	1106.1	1.6	1124.0	1.6
Postcal	886.9	1.3	886.9	1.3	922.7	1.4
Radio science	750.5	1.1	750.5	1.1	818.7	1.2
Training	2319.6	3.4	2319.6	3.4	2592.5	3.8
Maintenance	13781.2	20.2	12585.7	18.5	12485.0	18.3
Project-related support	6208.4	9.1	6208.4	9.1	6822.4	10.0
DSN operational prep	1842.0	2.7	1842.0	2.7	2046.7	3.0
DSN development	272.9	0.4	272.9	0.4	272.9	0.4
Minor modifications	2183.2	3.2	2183.2	3.2	2456.1	3.6
Reconfiguration and implementation	5867.3	8.6	5867.3	8.6	6481.3	9.5
Other	9687.8	14.2	9687.8	14.2	10642.9	15.6
Total			68224.0			

^aFrom data collected over a 23-week period.

**Table 3. Scheduled maintenance: Estimated distribution
by activity**

Scheduled activity	Percent of maintenance time allocated
Preventive	20
Corrective	30
ECO implementation	50

**Table 4. Scheduled maintenance: Distribution by
hardware system, CY 74**

Hardware system	Percent of maintenance time spent
TCD	60
RCV	30
ANT	3

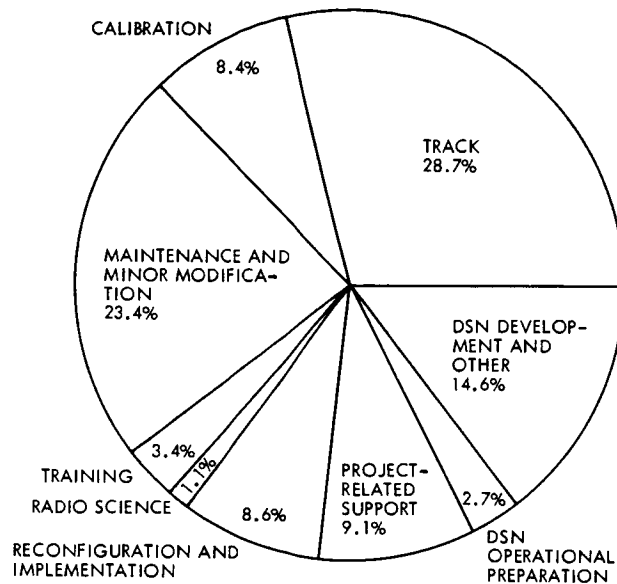
Table 5. Downtime in hours/year at all stations

	No automation	RF automation only	Antenna automation only	RF and antenna automation
Hours/year	343.8	280.9	336.9	274.0
Percent of present downtime/year	100	81.7	98.0	79.7
Percent of scheduled track time during which data are delivered, assuming 19580.3 h scheduled	98.2	98.6	98.3	98.6

Table 6. Summary of discrepancy reports written 1/1/74 to 7/13/75

Sub-system	Number of DRs written	Uncorrectable		Correctable			Total minutes of outage		Percent difference
		Number	Minutes of outage	Number	Minutes of outage	Estimated minutes of outage with automation	Present	Estimated with automation	
SDA	3	1	1	2	300	75	301	76	
TXR	90	62	2620	28	557	140	3177	2760	
UWV	17	6	419	11	1900	85	2319	504	
R/E	55	23	1330	32	3473	190	4803	1520	(RF) -54
ANT	88	51	1012	37	1148	505	2160	1517	(Ant) -30
Whole station							31,425	25,043	-20

PRESENT DISTRIBUTION
OF STATION HOURS
BY ACTIVITY



ESTIMATED DISTRIBUTION OF
STATION HOURS BY ACTIVITY
WITH RF AND ANTENNA AUTO-
MATION, IF ALL ADDITIONAL
HOURS SPENT TRACKING

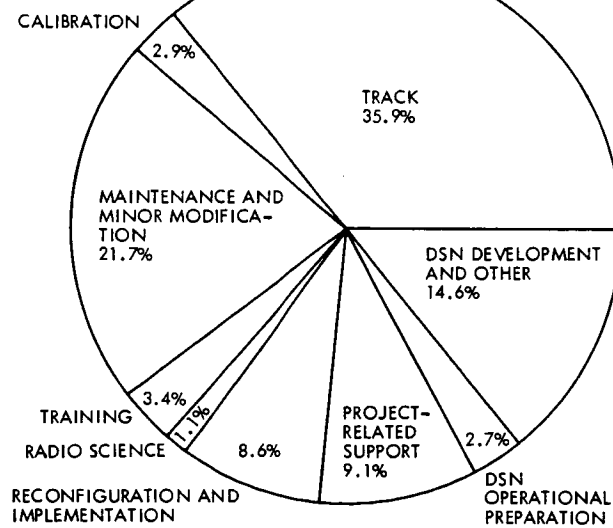


Fig. 1. Station utilization

Remote Automatic Control of DSS 13

K. I. Moyd

Communications Systems Research Section

The control of pulsar observing at the Venus station (DSS 13) by an operator at JPL is described. The emphasis is on the JPL end of the system and the communication between JPL and DSS 13. A six-hour observing run on August 14, 1975, is described.

I. Introduction

The remote automatic pulsar data acquisition system at DSS 13 is now operational. Once the station is put into a specified initial configuration, no further action is required of the station personnel until the end of the observing run. The pulsar observing is controlled by an operator located at JPL. Status messages and data are sent to JPL. On August 14, 1975, the system was used for a six-hour observing run. This system is an extension of the locally controlled automatic system described in Ref. 1.

Section II describes the DSS 13 end of the system and Section III the JPL end. In Section IV the communication between DSS 13 and JPL is described. In Section V the details of the observing run on August 14, 1975, are presented, and in Section VI plans for future use and development of the system are given.

II. DSS 13

Three SDS computers at DSS 13 are involved in the control. The 16-kiloword memory SDS 930 is the station control computer. It generates commands for the other two computers, initiates collection of pulsar data, plots and records the data, and communicates with JPL. The 8-kiloword SDS 910A controls a programmable oscillator; the 8-kiloword SDS 910B controls the 26-meter antenna. Each of the 910's is connected to the 930 by a twin coaxial cable communication link.

The 930 is programmed in real-time FORTRAN; the 910's are programmed in assembly language. All of the programs are interrupt driven. That is, most actions are done in response to externally generated interrupts rather than in a specified sequential manner.

The station configuration is the same as that for the locally controlled automatic pulsar data acquisition system except that there are two additional interrupts into the 930, associated with the JPL communication.

III. JPL

Two computers at JPL are involved in the control. The 8-kiloword memory SDS 920 acts as a communications buffer; the 32-kiloword XDS Sigma 5 is the control computer. The Sigma is a time-shared computer with the ability to have programs run simultaneously from the batch entry (card reader) and from a remote terminal. The pulsar data acquisition system is controlled through the terminal. The Sigma program is written in FORTRAN. Features in the Sigma FORTRAN allowed the Sigma program to be written as a structured program.

The Sigma program was written so that incoming status information and data would be handled automatically without JPL operator intervention. Therefore, status messages are displayed on the terminal when received, and are also stored on the random-access device (RAD) for later retrieval. A message is displayed when a data block is received, and the data and parameters for the observation are stored on the RAD. At any time the operator may request the display of the status messages or observation parameters received during a specific time period or he may request that one or more data blocks be plotted. The plotter uses only single sheets of paper, so continuous plotting is not practical.

The only output devices accessible to terminal programs are the terminal cathode-ray tube (CRT) display, the plotter and the RAD. During an observing run, there is no way to get hard-copy output at the Sigma computer. Once the observing run is finished, the contents of the files stored on the RAD can be recorded on magnetic tape or listed on the printer using programs from the batch entry.

Sending commands to DSS 13 is done at the request of the operator. Once observing on a pulsar has been started, observations will continue to be taken until commanded otherwise. As with the locally controlled automatic system, the remote controlled system is controlled by Tutorial Input. The command entry is from the Sigma terminal keyboard, and the responses and error indications are displayed on the terminal. The Tutorial Input

communication is also typed out on the 930 typewriter at DSS 13. The message "DONE" is displayed on the terminal each time a complete set of commands has been received by the 930. By waiting for this message, the JPL operator insures that the 930 program is not hung up in the Tutorial Input routine because of insufficient parameters or an error in the input. The Tutorial Input commands are the same as those used for the locally controlled system and are given in Appendix A.

The Sigma program is also controlled by Tutorial Input. The commands and parameters are listed in Appendix B. There is no overlap in names between the Sigma Tutorial Input commands and the 930 Tutorial Input commands, so an "UNRECOGNIZED COMMAND" message will be given if a command is entered for the wrong mode.

IV. Communication Between DSS 13 and JPL

Communication between DSS 13 and JPL is conducted by means of dedicated teletype lines between the SDS 930 at DSS 13 and the SDS 920 at JPL. The 920 is connected to the Sigma 5 by a twin coaxial cable communication link.

The development of the software handling the communication between the 930 and the Sigma through the 920 was separated from the development of the rest of the software. An interface between the non-communication or background software and the communication software was specified in the form of a set of FORTRAN subroutine calls along with the function of each of the subroutines. The implementation of these subroutines in both the Sigma and the 930 and the 920 program will be described separately.

As far as the background programs are concerned, the Sigma communicates directly with the 930. The communication is divided into two logical channels. The background programs can treat them as two physically separate, full-duplex (allowing simultaneous communication in both directions) channels. There is actually only a single physical channel which, at least for the 920-Sigma link, is half-duplex (one direction at a time). The communication software takes care of merging and separating the messages.

The Tutorial Input communication is carried in both directions on one channel; the status messages and data are carried from the 930 to the Sigma on the other

channel. The status messages are listed in Appendix C. The OBSR message alerts the Sigma program that the next message is a data block. Because the transmission rate of the teletype lines is very low (ten 5-bit characters per second), the data block contains 250 averaged points rather than the 5000 original data points. This is sufficient to determine the quality of the data.

V. Details of Observing Run

On August 14, 1975, the remote automatic pulsar data acquisition system was used for a six-hour observing run. Seven different pulsars were observed. The observing schedule was supplied by one of the scientists of the pulsar observing project. The station personnel were not notified by phone in advance of changes in the antenna position, although they could look at the Tutorial Input typeouts. Much of the time the JPL end was left unattended. The Sigma was used by others in batch mode during the observing run. The observations are tabulated in Table 1.

VI. Future Developments

One major change in the system will be the addition of scheduling. This will allow the JPL operator to enter the entire observing schedule at one time. He will later be able to change the schedule, based on the results of the observing. If he wished, he could leave the system unattended.

Some other changes are being considered. One is the use of high-speed data lines instead of the teletype lines so that the primary data record will be at JPL rather than at DSS 13. Another is the inclusion of sufficient controls and monitors for the station to be left unattended. This will necessitate including a wind monitor so the system will stow the antenna in case of high wind.

It is intended that the system be used on a regular basis to collect pulsar data and to study its reliability. Additional status tests and messages may be added to increase the failure detection, and some failure isolation and correction may be included.

Reference

1. Moyd, K. I., "Automatic Control of DSS 13," in *The Deep Space Network Progress Report 42-29*, pp. 107-114, Jet Propulsion Laboratory, Pasadena, Calif., Oct. 15, 1975.

Table 1. Pulsar observations on August 14, 1975

ID number	Start time, UT	Number of observations ^a
0329	16 14 10	4
0355	16 43 14	15
0833	17 38 23	15
0525	18 27 29	3
0823	20 05 03	13
1133	21 17 21	4
1642	22 02 22	3

^aThe time per observation depends on the pulsar period and ranges from 3 minutes for 0833 to about 30 minutes for 0525.

Appendix A

930 Tutorial Input Commands

I. Basic Parameter Entry

<i>Command</i>	<i>Parameter</i>	<i>Description</i>
OFFD		Change default offsets. New values will be used immediately.
	AZDF	Default azimuth offset in degrees. Initially: .145.
	ELDF	Default elevation offset in degrees. Initially: 0.
DIST		Change pointing parameters. The new values will not be used until a new antenna command is given. Values are to be entered in millidegrees (i.e., 10 degrees is entered as 10000).
	HSPD	Minimum azimuth pointing error for which high speed is to be used. Elevation value is half of azimuth value. Initially: 12000.
	DECL	Azimuth pointing error at which high-speed deceleration is started. Elevation value is half of azimuth value. Initially: 10000. (It is required that DECL < HSPD.)
	TRKD	Maximum pointing error (in each axis separately) for on-target condition to be satisfied. Initially: 50.
	TRKV	Maximum velocity (in each axis separately) for on-target condition to be satisfied. Initially: 25.
PDCL		Change default pulsar data collector parameters. The new values will be used the next time parameters are sent to the data collector (i.e., following an OBJ, GO, TSYN, ENDO or EXP command).
	XDEF	Number of synthesizer pulses between observations. Initially: 200.
	YDEF	Number of observations per period. Initially: 5000.
DATE		Enter date. (Date is based on UT, not local time.)
	MON	Month—up to 4 numbers or letters.
	DAY	Day of the month.
	YEAR	Year—4 digits.

II. Antenna Commands

A. New Position

These are acted upon immediately if the previous antenna command was STOP, AZEL, or STOW; if the antenna was stopped by the computer for another reason (breakpoint 4 set and then reset, elevation too low); or when the program is first started. Otherwise they will be acted on after the current observation is finished and the data processed.

<i>Command</i>	<i>Parameter</i>	<i>Description</i>
AZEL		Move the antenna to the specified azimuth and elevation and hold it there.. Do not collect data.
	AZ	Azimuth between 0 and 360 degrees with up to three decimal places. The decimal point must be typed.
	EL	Elevation in degrees with up to three decimal places. The decimal point must be typed.
	REGN	Wrap-up region. 'R' for right, 'L' for left. Anything else will be interpreted as center.

<i>Command</i>	<i>Parameter</i>	<i>Description</i>
STOW		Move the antenna to the stow position (AZ = 180 degrees, EL = 85 degrees, center region) and hold it there.
OBJ		Move the antenna to the specified right ascension (RA) and declination (DEC) and track. When the antenna is on-target, initiate data collection with a start-next-second.
	ID	Pulsar identification number—up to 4 digits.
	RA	Hours of RA.
	RAM	Minutes of RA.
	RAS	Tenths of seconds of RA (i.e., 34.5 seconds is put in as 345).
	DEC	Degrees of DEC. Include sign if negative.
	DECM	Minutes of DEC, no sign.
	DECS	Seconds of DEC (2 digits), no sign.
	TMCN	Time constant setting for the pulsar receiver.

B. Other Control Commands

STOP	Stop the antenna (decelerate safely, put on the brakes, change to low speed). Ignore any data being taken. Acted upon immediately. To resume operation, one of the other antenna commands must be given.
GO	Resume observation of the object entered by the previous OBJ command. Used after the antenna has been stopped. Acted upon immediately unless breakpoint 4 is set.

III. Data Collection Commands

All of the commands except ENDO are acted upon only after the data from the current observation has been processed.

<i>Command</i>	<i>Parameter</i>	<i>Description</i>
LINK		Enable the 930–910A link.
NLNK		Disable the 930–910A link. (This is the initial condition).
PLO		Entry of oscillator frequency. If the 930–910A link is enabled, the frequency will be sent to the local oscillator and the setting will be confirmed. The next observation will be a start-next-second.
	FREQ	Oscillator frequency in hertz. Up to 10 characters including the decimal point.
WAIT		Do not start the next observation until another command has been received. This allows the operator to see the data before specifying a new observation.
CONT		Initiate a start-in-phase-add after a WAIT command has been given.
TSYN		Initiate a start-next-second. (This is done automatically for the first observation after an OBJ, GO, PLO or ENDO command.)

<i>Command</i>	<i>Parameter</i>	<i>Description</i>
ENDO		Abort the current observation and ignore the data. It is acted upon immediately if an observation is in progress. Otherwise it has no effect. If no other command is received, the next observation will be a start-next-second.
EXP		Subsequent observations are to be expanded. The parameters are based on the data taken as the result of the previous start-next-second command. These expansion parameters will be used until an antenna command, PLO, TSYN, ENDO or another EXP command is given.
DEL		The original data point (between 0 and YDEF-1) corresponding to the 0th observation (i.e., origin) for the expanded observations. If DEL = 0, the origin is in phase with the second at which the original observation was taken.
IINT		The number of <i>original</i> data points to be included in the expanded observations.
IEXP		The expansion factor (number of observation points for each original observation). IEXP must be a factor of XDEF. $IEXP \times IINT \leq 5000$.

Appendix B

Sigma Tutorial Input Commands

<i>Command</i>	<i>Parameter</i>	<i>Description</i>
STAT		Display status messages or data parameters.
	UTB	UT of earliest message to be displayed.
	UTE	UT of latest message to be displayed.
	TYPE	"STAT" for status messages. "PULS" for data parameters.
PLOT		Plot one or more data records.
	REC B	Record number of first record to be plotted (obtained from DATA message or data parameter display).
	NREC	Number of records to be plotted.
GTS		Send commands to DSS 13. All subsequent keyboard entries will be sent to DSS 13 until "ENDT" is typed.

Appendix C

Status Messages

I. Introduction

Status messages may indicate normal operation or they may indicate error conditions. Normal operation messages are used to keep the remote operator aware of the progress of the observing and to notify him when a new data block has been received. The error messages are in response to failures occurring in the antenna system, the teletype link, the program timing, and the local oscillator setting. In general, they do not require any response from the remote operator to protect the system; however, response may be necessary to resume operation. Certain of the messages may occur in response to a command given by the operator. For example, an ENDO command will generate a STOP OBS message; a STOP command will generate a STOP ANT message. These will be listed as error messages since they will not be expected to occur under normal operating conditions. Some messages are generated within the Sigma 5 rather than being received from DSS 13. These will not be stored on the disk for later retrieval and will not be displayed if they occur during plotting. This fact will be noted in the message description.

II. Normal Operation Messages

<i>Message</i>	<i>Type</i>	<i>Description</i>
ON	TARG	Antenna is on-target, i.e., the position error in each axis is less than TRKD (see Tutorial Input commands) and the velocity error in each axis (based on the source tracking velocity) is less than TRKV. An observation has been started.
OBSR		An observation has been completed and data are being sent. The parameter is the pulsar ID number.
	1	Observation was a start-next-second.
	2	Observation was a start-in-phase-add.
	3	Observation was a start-in-phase-clear.
DATA		Data have been received and can be plotted. The parameter is the pulsar ID number. The record number is that corresponding to the data record. This message is not stored on the disk. The STAT command can be used to retrieve the complete observation message later.

III. Error Messages

<i>Message</i>	<i>Type</i>	<i>Description</i>
FRER		The local oscillator setting does not agree with that commanded. The command to the local oscillator will be repeated. No parameter.
ANTE		The antenna cannot be controlled by the computer. The parameter gives the specific reason: <ol style="list-style-type: none"> 1 Hydraulic pressure too low. 2 Antenna in azimuth prelimit zone. 4 Antenna in elevation prelimit zone. 8 Computer not given control. <p>The parameter is the sum of all the applicable codes; e.g., a parameter of 9 indicates hydraulics off and manual control. This message is repeated once a minute as long as one of the conditions applies.</p>

<i>Message</i>	<i>Type</i>	<i>Description</i>
ATO1		A command to change one of the antenna functions has not been obeyed. This message occurs one minute after the command was given.
	AZBR	The command was for azimuth brakes. The parameter = -1 for commanded set; 1 for commanded release.
	ELBR	The command was for elevation brakes. The parameter = -1 for commanded set; 1 for commanded release.
	AZSP	The command was for azimuth speed. The parameter = -1 for commanded low speed; 1 for commanded high speed.
	ELSP	The command was for elevation speed. The parameter = -1 for commanded low speed; 1 for commanded high speed.
ATO2		A command to change one of the antenna functions has not been obeyed. This message occurs two minutes after the command was given (one minute after the corresponding ATO1). No further messages are sent. The types and parameters are the same as for ATO1.
POSN	EL	The elevation is out of range. This message is always given if the source has elevation < 0 degrees. If the source has elevation between 0 and 8 degrees, the message is given if the source is setting (elevation decreasing). The antenna will be stopped until a new antenna command is given.
PP50		There were not fifty 50-pulse-per-second interrupts during one second. The parameter specifies how many did occur. This condition may occur while data are being written on the magnetic tape; it will not affect tracking or data collection in this case.
STOP	ANT	The antenna has been stopped by the computer in response to a STOP command from JPL or the setting of breakpoint 4 at DSS 13. In the latter case, the antenna cannot be moved until breakpoint 4 is reset. In either case, it will not be moved until an antenna command is given.
	OBS	The current observation has been aborted by an ENDO command. Unless an antenna or data collection command has been given, a start-next-second observation has been initiated.
TTY		An unrecovered error has occurred on the link between JPL and DSS 13.
	SEND	The error was in sending from DSS 13 to JPL. The parameter gives the channel: <ul style="list-style-type: none"> 1 Data and message channel. 2 Tutorial Input channel.
	REC	The error was in sending from JPL to DSS 13 on the Tutorial Input channel. The parameter gives the number of attempts. After the second attempt, the Tutorial Input will be terminated under the assumption that the link is down. (The 930 may be hung up waiting for the input.) This message is not stored on the disk.

N76-15206

DSN Telemetry System Performance With Convolutionally Coded Data

B. D. L. Mulhall, B. Benjauthrit, C. A. Greenhall,
D. M. Kuma, J. K. Lam, and J. S. Wong

DSN Systems Engineering

J. Urech

Station Director, Cebreros, Spain

L. D. Vit

Operations Manager for the Robledo Station

DSN Telemetry System performance in decoding convolutionally coded data by both sequential and maximum likelihood techniques is being determined by testing at various Deep Space Stations. The evaluation of performance models is also an objective of this activity. This article reports the results obtained to date and the plans for future experiments.

I. Introduction

The Deep Space Network currently performs sequential decoding of Pioneer and Helios spacecraft convolutionally coded telemetry data using the Fano algorithm. The Network is implementing maximum likelihood decoding using the Viterbi algorithm for outer-planet Mariner spacecraft such as the Mariner Jupiter-Saturn. For the telecommunication system design the characteristics of these decoders must be known. This report describes the test activities presently in progress, the results obtained to date, and the plans for the near future to complete the specification of Network performance in sequential and maximum likelihood decoding.

II. Sequential Decoding

The objectives of these tests are to determine DSN Telemetry System performance. Specifically, frame deletion rate, probability of undetected bit errors, and optimum modulation index as a function of carrier power, data power, and data rate are the performance parameters being sought.

Sequential decoding performance has been investigated for some time since the effects of the noisy carrier reference on the decoder were first appreciated (Ref. 1). Tests were performed at various stations by both JPL and Ames Research Center personnel to develop empirical models

and to verify the theoretical models described in Refs. 2 and 3. These tests were the basis for the performance specification published in the current Deep Space Network/Flight Project Interface Design Handbook, 810-5, Revision D. However, the specification has not been completed for data rates below 512 bps.

Both Pioneer and Helios spacecraft use data rates down to 8 bps. The difficulty in obtaining results for low data rates arises when a long telemetry frame is used together with a small frame deletion rate (FDR). For example, past tests were run to obtain frame deletion rates of 10^{-4} with a frame length of 1152 bits, the Helios frame length.

The tests described in this report attempt to overcome this problem by performing two types of tests. The first type employs the sequential decoder implemented in the Data Decoder Assembly (DDA) (Fig. 1). These tests are called on-line decoding since the decoding is performed in real-time. Only the computations per frame are recorded. These data are subsequently processed and the plots shown in Figs. 2-9. The on-line tests are run with a relatively short frame length of 192 bits to obtain results rapidly.

The second type of tests are referred to as off-line tests. The results of the analog-to-digital conversion of each symbol are recorded. The data are later decoded in a sequential decoding program written for the Univac 1108.¹ The off-line decoding can be performed for various frame lengths and the effect of frame length on performance determined. By this means, the results obtained from the on-line test can be related to other frame lengths.

Four other advantages of the off-line tests are that undetected bit errors produced by the decoder can be monitored, the effect of the resolution of the A-D conversion on performance can be studied, the computational cutoff can be extended, and sequential decoding can be compared to maximum likelihood decoding.

The test plan employed a pattern which can be decoded by both the sequential decoder used for Pioneer and the maximum likelihood decoder planned for Mariner Jupiter-Saturn (MJS). Thus the identical off-line data can be decoded by both decoders and the results compared.

¹Based on a program supplied by L. Hofman of the NASA Ames Research Center.

III. Maximum Likelihood Decoding

The objectives of the maximum likelihood decoding tests are to establish the DSN Telemetry System performance in this mode of operation. For this purpose a Univac 1108 computer program² was developed (Ref. 4). This program uses the Viterbi algorithm to determine the characteristic of the decoder—specifically, bit error rate (BER), best branch metric decision vs majority vote, burst error length and density, length of error-free runs, decoder synchronization time, and optimum modulation index as a function of carrier and data power.

Tests currently under way in Spain at DSS 62 are being performed using a commercial Viterbi decoder (Ref. 5). In addition to the objectives listed, these tests will determine the relation between the performance monitor (normalization rate) provided by the decoder and signal-to-noise ratio (SNR).

IV. Test Procedures

One difficulty in performing tests in a Deep Space Station or in the Compatibility Test Area (CTA 21) is establishing the signal-to-noise ratio exactly. To avoid this uncertainty, errors in the coded symbols are monitored by both the Viterbi and the sequential decoding programs, and the symbol error rate is computed. The symbol error rate is used as the independent variable of the observation. This rate can be converted to a signal-to-noise ratio (energy per bit over noise spectral density) by using the complementary error function to obtain the ST_b/N_0 (E_b/N_0) presented to the decoder. Modeling of the receiver, demodulator, and symbol synchronizer losses is required to calculate the ST_b/N_0 presented to the front end of the DSN telemetry system.

Figure 1 shows the test setup for both the on-line and off-line tests. The simulation Conversion Assembly (SCA) generates a symbol stream which simulates both a Pioneer 32:1/2 and the MJS 7:1/2 codes. The data stream is modulated on the subcarrier and passed to the test transmitter, where the carrier is modulated. A Y-factor is used to measure signal-to-noise ratio (Ref. 6). The data passes through the microwave equipment (UWV) to the receiver and demodulator. At the output of the Subcarrier Demodulator Assembly (SDA) the stream is split into two branches. In one branch, the on-line test, the symbols

²Based on a program supplied by B. Baston of the NASA Johnson Space Center.

are synchronized, the data are decoded sequentially, and the computations per frame are recorded.

The second branch, the off-line test, is processed normally only up through the Symbol Synchronizer Assembly (SSA). The eight-bit A-D conversion of each symbol is recorded on magnetic tape for subsequent decoding and analysis.

Table 1 lists the test conditions used for medium-to-low-rate sequential and maximum likelihood decoding tests. Modulation indices in these tests were selected near theoretical optimum to determine the actual optimum. The test conditions A through F listed in Table 1 are primarily oriented to Pioneer and Helios. Later tests are MJS-oriented and are also intended to determine the effect of Block III vs Block IV receiver performance on both types of decoding.

V. Test Anomalies

Significant difficulty was experienced in reading magnetic tapes written by the XDS-920 into the Univac 1108. A special tape reading program³ was used to overcome numerous parity errors on the test data tapes. Checks were performed by preprocessing programs to eliminate bad records so that results would not be contaminated.

The importance of balancing the SDA-SSA interface became apparent when the distribution of symbol errors was monitored. In cases where SDA balance was off, the frequency of ones in error far outweighed the zeros in error. Consequently, SDA balance calibrations were performed before each test.

One anomaly, which has not been explained, was the occurrence of a more frequent symbol error in one symbol position. A six-symbol pattern was generated by the six binary-coded fixed toggle switches on the Simulation Conversion Assembly front panel. In one test, the first symbol accounted for 80% of the errors in the entire file. This anomaly has never reappeared. The test data were not used.

VI. Sequential Decoding

This section presents an account of some of the sequential decoding tests.

³Written by R. B. Hartley, TDA Planning Section.

A. Decoding Program

The U1108 sequential decoding program is a straightforward implementation of the basic Fano algorithm described in Ref. 7. Following are some properties of the program:

- (1) *Computation count* increases by 1 each time the decoder looks forward one step or backward one step in the code tree.
- (2) *Frame length* must be a multiple of 36. Since, for these tests, the on-line decoder frame length was set to 192 bits (384 symbols), we used a frame length of 180 for most runs. One file was run with a range of frame lengths from 180 to 1152 to test dependence of results of this parameter.
- (3) The *tail sequence* is just the last 32 bits of each frame. Thus, for a 180-bit frame, only the first 148 decoded bits are checked against the known pattern for "undetected" bit errors.
- (4) If the computation count for a frame exceeds the preset *computational cutoff*, that frame is declared erased. For on-line decoding, the cutoff is inversely proportional to data rate. For off-line decoding, it was often not economical to use the on-line value of cutoff, because erased frames cost much central processing unit (CPU) time. For most tests, a default value of 100 computations per bit was used.
- (5) A running tabulation of hard-decision *symbol error rate* (SER) is printed by the program.

B. Format of Performance Measures

The tests are identified by data rate in bits per second (bps), modulation index (MI), and signal-to-noise ratio (SNR) $E_b/N_0 = ST_b/N_0$ as seen by the decoder. SNR at the input of the receiver is difficult to determine accurately, but hard decision SER was directly observed. Thus we chose to estimate decoder E_b/N_0 from observed probability P_E of symbol errors by inverting the usual complementary error function formula

$$P_E = \operatorname{erfc}(\sqrt{2E_b/N_0}) = \operatorname{erfc}(\sqrt{E_b/N_0})$$

where

$$\operatorname{erfc}(x) = (2\pi)^{-1/2} \int_x^\infty \exp\left(-\frac{1}{2}t^2\right) dt$$

Graphical display of decoding performance is achieved by a log-log plot of the sample distribution function of the number of computations per bit for all frames decoded

or erased. The horizontal coordinate is the number of computations L per bit (number of computations divided by frame length), and the vertical coordinate is the fraction of frames such that the number of computations equals or exceeds L .

We have also plotted some linear-scale histograms of the above sample distribution, normalized so that the total area under the histogram is 1. They give a closer look at the distributions near the point of maximum density.

Other performance parameters shown are mean number of computations per bit (CPB) and undetected bit error rate (BER). Some of the sample distributions have rather long, heavy tails. This causes mean CPB to depend strongly on computational cutoff. Therefore, in calculating mean CPB, each distribution was truncated at 100 CPB; that is, any datum greater than 100 was set equal to 100.

C. Comparison of 64-bps Tests

Figure 2 and Table 2 compare six tests at this data rate. Mean CPB and the distribution function values increase as E_b/N_0 decreases, except for test D6. This test has a relatively high modulation index, and the Telemetry Analysis Program of G. Dunn shows a receiver SNR degradation of 2.4 dB. The symbol errors, although scanty, appear to occur in bursts; this forces the decoder to make long searches.

The "undetected" bit errors invariably occur in bursts near the end of the 148-bit data portion of the 180-bit frame. Apparently, if a burst of bad symbols occurs at about this point, it is sometimes possible for the decoder to reach the end of the frame before these errors have been corrected or the computational cutoff has been reached.

D. Comparison of CTA 21 and DSS 62 Results

As previously described, on-line and off-line tests were performed at CTA 21. To investigate station-to-station variation in performance, on-line tests at 8 bps were performed at Madrid, DSS 62. The Madrid station used a pseudorandom data source, encoded with the 32:1/2 code. On the other hand, the CTA 21 tests used a short repetitive pattern since these tests had the dual purposes of sequential and maximum likelihood decoding performance.

The DSS 62 data were reduced, analyzed, and compiled on site by station personnel.

Figure 3 and Table 3 contain results from the two stations. At CTA 21, only tests F1, F2, and F3 have been reduced. The distribution functions from DSS 62 are encased by 90% confidence intervals for the whole 32-h test (lightweight solid curves), and by 1σ intervals for a 2-h subtest (dashed curves). These are shown here for tests F4 and F5. We have omitted them from the F1, F2, and F3 plots to avoid overcrowding these figures, which also contain the CTA 21 curves.

The main difference between the DSS 62 and CTA 21 results is the shape of the distributions near $L = 1$. Each CTA 21 distribution function has a knee there, but the DSS 62 functions have none. This means that the CTA 21 tests yielded fewer "very good" frames. The histograms of the CTA 21 tests (Fig. 4) show that the most likely number of computations per bit is about 1.6 for F1-3, 1.3 for F2, and 1.1 for F3. At DSS 62 the most likely value appears to be 1 for these tests.

E. Comparison with Lesh's Model

Figure 5 compares two of our off-line 64-bps tests with J. R. Lesh's theoretical model, which Lesh has implemented on the 1108 (Ref. 3). The slope of the model agrees well with the slope of the experimental curve for more than 10 computations per bit. The frame length is 180 bits; Ref. 3 reported that the model fits long-frame-length data better than short. In the future, we will compare Lesh's model to off-line decoding at frame lengths up to 1152.

F. Different Frame Lengths

We decoded the same symbol stream with frame lengths of 180, 216, 504, and 1152. Figure 6 shows the distribution functions, and Figure 7 shows the histograms. The data rate is 128 bps and SER is 2.32%, from which decoder E_b/N_0 is deduced to be 5.98 dB. There were no bit errors. Mean computations per bit are 1.146, 1.145, 1.148, 1.148, respectively.

The distributions keep the same mean, but as the frame length increases, they tend to become more symmetric. This behavior resembles that of a model in which the number of computations for a frame is the sum of a collection of identically distributed, independent, random variables with finite variance. The longer the frame, the more of these variables are summed, and the more the distribution of the sum approaches a Gaussian. It would be desirable to repeat this experiment with (1) a longer symbol stream, to get better statistics on the longer frame

lengths, and (2) a test in which the distributions have such long, heavy tails that, when extrapolated indefinitely far, they have infinite variance or mean.

Looking at the results for 180-bit and 216-bit frames, we conclude that either is an acceptable substitute for the 192-bit frame.

VII. Maximum Likelihood Convolutional Decoding

In addition to the sequential decoding tests, the off-line test data have been used to investigate maximum likelihood decoding. These tests collect Symbol Synchronizer Assembly (SSA) output data as shown in Fig. 1. The data are read into the Univac 1108, where a program (Ref. 4) decodes the data, measures symbol and bit error rate, error burst statistics, and the distribution of error-free runs. A user's guide to the program is given in Ref. 8.

To verify the correctness of the implementation of the Viterbi algorithm in the Univac 1108 program as a simulation of the maximum likelihood convolutional decoder (MCD) being implemented in the Network, a series of simulation cases were run. A Univac 1108 program (CODER, Ref. 8) was used to produce simulated output data corrupted by additive white Gaussian noise (AWGN). These data were decoded and the results are compared (see Table 4 and Fig. 8) to the prototype MCD acceptance test results. Since the prototype decoder acceptance tests were performed presumably with AWGN, this type of noise was applied to the simulated data to establish the correctness of the simulated decoder.

The Univac 1108 Viterbi decoding program has the capability of using two different criteria to choose the most likely branch and, hence, decode each bit correctly. First, all surviving branches can be polled and a majority vote taken. Second, the surviving branch with the best state metric can be selected. Figure 8 and Table 4 compare these criteria when AWGN is applied.

It is interesting to note that when the best metric criteria are used, ties frequently occur even with 3-bit quantized symbols. An early implementation of the Univac 1108 Viterbi decoding program would select the first of the tying branches encountered. This resulted in the best metric criterion performing more poorly than the majority vote criterion. When the program was modified to select the last of the tying branches, the best

metric criterion performed better than the majority vote criterion and compared very well to the prototype decoder acceptance test results.

It is believed that this sensitivity of the best metric criterion to resolving ties is due to the data pattern. A nonrandom data pattern was used which causes the correct branches to be a certain few in one part of the trellis. If the trellis is always searched from the top down and if the first tying best-state metric is always selected, then the performance of the decoder can be biased, depending on whether the true branches are near the top or the bottom of the trellis. Consequently, ties in best-best metrics should be resolved randomly if the data are not random.

Figure 9 provides a comparison of an 1108 simulation curve using the receiver quantization threshold spacing $0.5\sqrt{N_0/2}$, the functional requirements, and the prototype decoder acceptance test results. The threshold spacing of the data obtained from CTA 21 has been calculated to be in the neighborhood of $0.5\sqrt{N_0/2}$.

To investigate decoder performance in the DSN Telemetry System and, in particular, the effect of correlated noise produced by the receiver phase error, test data from CTA 21 were decoded and the results to date listed in Table 5. These tests show that DSN telemetry system functional requirements are being met. As in the case of sequential decoding performed on the U1108, the symbol error rate was monitored and used as the independent variable of the observation. Symbol error rate was converted to E_b/N_0 at the input to the decoder by the complementary error function.

VIII. Future Activities

Major future testing activities include:

- (1) Determining the effect on performance of sequential and maximum likelihood decoders of Block III receivers and demodulators vs Block IV.
- (2) Determining performance of the decoders for S- vs X-band.
- (3) Determining MJS '77 encounter data rates using X-band performance with maximum likelihood decoding.
- (4) Completion of MJS '77 cruise data rates currently under way at DSS 62.

References

1. Layland, J. W., "A Sequential Decoding Medium Rate Performance Model," in *The Deep Space Network*, Technical Report 32-1526, Vol. XVIII, pp. 29-40, Jet Propulsion Laboratory, Pasadena, Calif., Dec. 15, 1973.
2. Layland, J. W., "DSS Tests of Sequential Decoding Performance," in *The Deep Space Network Progress Report 42-20*, pp. 69-77, Jet Propulsion Laboratory, Pasadena, Calif., Apr. 15, 1974.
3. Lesh, J. R., "Sequential Decoding in the Presence of a Noisy Carrier Reference," in *The Deep Space Network Progress Report 42-23*, pp. 111-124, Jet Propulsion Laboratory, Pasadena, Calif., Oct. 15, 1974.
4. Benjauthrit, B., Mulhall, B. D. L., and Wong, J. S., "A Viterbi Decoding Program for DSN Telemetry System Analysis," in *The Deep Space Network Progress Report 42-28*, pp. 5-10, Jet Propulsion Laboratory, Pasadena, Calif., Aug. 15, 1975.
5. *The LV7015 Reference Manual*, LINKABIT Corp., San Diego, Calif. 1972.
6. Baumgartner, W. S., et al., "Multiple-Mission Telemetry System Project," in *The Deep Space Network*, Space Program Summary 37-60, Vol. II, pp. 152-169, Jet Propulsion Laboratory, Pasadena, Calif., Nov. 30, 1969.
7. Wozencraft, Z. M., and Jacobs, I. M., *Principles of Communication Engineering*, John Wiley and Sons, Inc., New York, 1965.
8. Benjauthrit, B., Mulhall, B. D. L., and Wong, J. S., "A Viterbi Decoding Program for Telemetry System Analysis (User's Guide)," IOM AE-75-21, Jet Propulsion Laboratory, Pasadena, Calif., Sept. 3, 1975 (an internal document).

Table 1. Convolutional decoding test plan

Test	Data rate (SPS)	Modulation index, (deg)	P_T/N_0 , dB sec ⁻¹	E_s/N_0 , dB	Degraded E_s/N_0 , dB	SSA estimate, dB	SER, %
A1	4096	55.0	39.0	1.14	0.95	1.96	5.74
A2	4096	55.0	39.5	1.64	1.46	2.28	4.71
A3	4096	55.0	40.0	2.14	1.98	2.62	3.79
A4	4096	55.0	40.5	2.64	2.49	2.98	2.98
A6	4096	67.6	39.5	2.69	2.42	2.94	3.07
A7	4096	75.0	39.5	3.08	2.64	3.09	2.77
B1	2048	55.0	36.0	1.15	0.85	1.91	5.95
B2	2048	55.0	36.5	1.65	1.37	2.22	4.88
B3	2048	55.0	37.0	2.15	1.89	2.57	3.93
B4	2048	55.0	37.5	2.65	2.41	2.93	3.09
B6	2048	67.6	36.5	2.71	2.27	2.83	3.31
B7	2048	75.0	36.5	3.09	2.34	2.87	3.21
C1	256	55.0	29.2	2.56	1.59	2.37	4.46
C2	256	55.0	29.2	3.38	2.52	3.00	2.94
C3	256	55.0	30.0	4.18	3.40	3.67	1.82
C4	256	42.0	29.2	1.63	1.00	1.99	5.63
C5	256	67.6	29.2	4.44	2.67	3.12	2.72
D1	128	55.0	26.4	3.60	2.21	2.78	3.41
D2	128	55.0	27.2	4.40	3.14	3.47	2.11
D3	128	55.0	28.0	5.20	4.06	4.19	1.20
D4	128	42.0	27.2	2.64	1.80	2.50	4.10
D5	128	58.4	27.2	4.73	3.24	3.54	2.00
D6	128	66.5	27.2	5.38	2.79	3.20	2.56
E1	32	42.0	21.4	2.86	0.72	1.86	6.22
E2	32	42.0	22.2	3.66	1.78	2.52	4.12
E3	32	42.0	23.0	4.46	2.80	3.23	2.54
E4	32	37.2	22.7	3.31	1.77	2.51	4.15
E5	32	45.0	22.2	4.14	2.09	2.72	3.61
F1	16	42.0	19.4	3.87	0.78	1.89	6.08
F2	16	42.0	20.0	4.47	1.72	2.48	4.23
F3	16	42.0	20.6	5.07	2.61	3.09	2.81
F4	16	37.2	20.5	4.12	1.92	2.61	3.88
F5	16	45.0	20.0	4.95	1.92	2.61	3.88

Table 2. Off-line sequential decoding of 64-bps tests

Test identi- fication	Modu- lation index, deg	SER, %	E_b/N_0 ^a , dB	Mean CPB	BER
D1	55.0	3.70	5.04	1.602	0
D2	55.0	2.98	5.50	1.437	6×10^{-6}
D3	55.0	1.61	6.61	1.078	0
D4	42.0	6.62	3.55	8.98	1.6×10^{-4}
D5	58.4	2.06	6.20	1.240	6×10^{-6}
D6	66.5	2.52	5.83	5.26	1.3×10^{-4}

^aDecoder SNR deduced from observed SER.

Table 3. Off-line sequential decoding of 8-bps tests at CTA 21 and DSS 62

Test identi- fication (station)	Modu- lation index, deg	SER, %	E_b/N_0 ^a , dB	Mean CPB	BER
F1-1 (21)	42.0	7.28	3.26	10.4	1.6×10^{-3}
F1-3 (21)	42.0	6.32	3.68	2.96	2.5×10^{-5}
F1 (62)	42.0	6.43	3.64		0 ^b
F2 (21)	42.0	4.98	4.34	1.888	0
F2 (62)	42.0	4.14	4.79		0
F3 (21)	42.0	3.91	4.92	1.327	0
F3 (62)	42.0	2.69	5.71		0
F4 (62)	37.2	3.73	5.02		0
F5 (62)	45.0	3.10	5.42		0

^aDecoder SNR deduced from observed SER.

^bOne blunder run excluded.

Table 4. Summary of program performance

Description	Threshold spacing	E_b/N_0 , dB	Errors (best metric)	Errors maj. vote.	Error rate			Total			Average, bits		
					BER, $\times 10^{-4}$	BER, maj, $\times 10^{-4}$	SER, %	Bits, $\times 10^5$	Bursts	Gaps	Errors/burst	Burst length	Gap length
MCD prototype	-	3.0	3039	-	7.410	9.000 ^a	5.75	40.96	-	-	4.3 ^b	7.6 ^b	-
	-	4.0	1621	-	0.396	0.600 ^a	4.00	409.6	-	-	3.8 ^b	6.2 ^b	-
	-	5.0	89	-	0.0136	0.025 ^a	2.50	655.3	-	-	-	-	-
1108 simulation based on selection of tied best metric states from last one encountered	0.5	2.0	169	213	188.3	237.4	10.45	0.08974	14	156	10.6	17.6	48.5
	0.5	3.0	187	366	8.659	16.947	7.92	4.31928	35	188	5.2	8.4	1147.8
	0.5	4.0	9	20	0.417	0.926	5.69	2.15964	2	10	4.5	6.5	21595.5
	0.5	4.3	2	4	0.062	0.123	5.06	3.24000	1	3	2.0	2.0	61999.0
	0.6	2.0	131	168	145.99	187.23	10.44	0.08973	17	132	7.7	12.8	67.0
	0.6	3.0	125	230	11.58	21.30	7.93	1.07964	23	126	5.4	9.8	855.9
	0.6	4.0	5	6	0.463	0.556	5.72	1.07964	1	6	5.0	7.0	17993.2
1108 simulation based on selection of tied best metric states from first one encountered	0.6	2.0	142	168	158.3	187.2	10.44	0.08973	21	143	6.2	9.8	61.8
	0.6	3.0	9	29	8.361	26.942	7.86	0.10764	2	10	3.5	6.0	1075.5
	0.6	4.0	13	6	1.204	0.556	5.72	1.07964	1	14	5.0	7.0	7710.8

^aFunctional requirement BER.^bFrom Ref. 7.

Table 5. Preliminary results

Test	E_b/N_0 , dB	Errors	Errors, maj	Error rate			Total			Average, bits		
				BER, $\times 10^{-4}$	BER, maj, $\times 10^{-4}$	SER, %	Bits	Bursts	Gaps	Errors/ burst	Burst length	Gap length
E1	3.28	16	78	5.079	8.938	6.8	155520	16	78	4.7	8.5	1688.6
F1	3.69	19	41	1.290	2.790	6.3	147132	5	20	3.4	5.4	7355.7
F2	4.34	22	22	1.370	1.370	5.0	160236	5	23	4.4	6.2	6965.8
A2	4.57	3	7	0.043	0.100	4.5	699840	1	4	3.0	3.0	99918.5
E5	4.73	10	12	0.429	0.514	4.5	233280	2	11	3.0	4.0	21206.4
A3	4.89	5	5	0.058	0.058	4.2	855360	1	6	5.0	7.0	66538.0

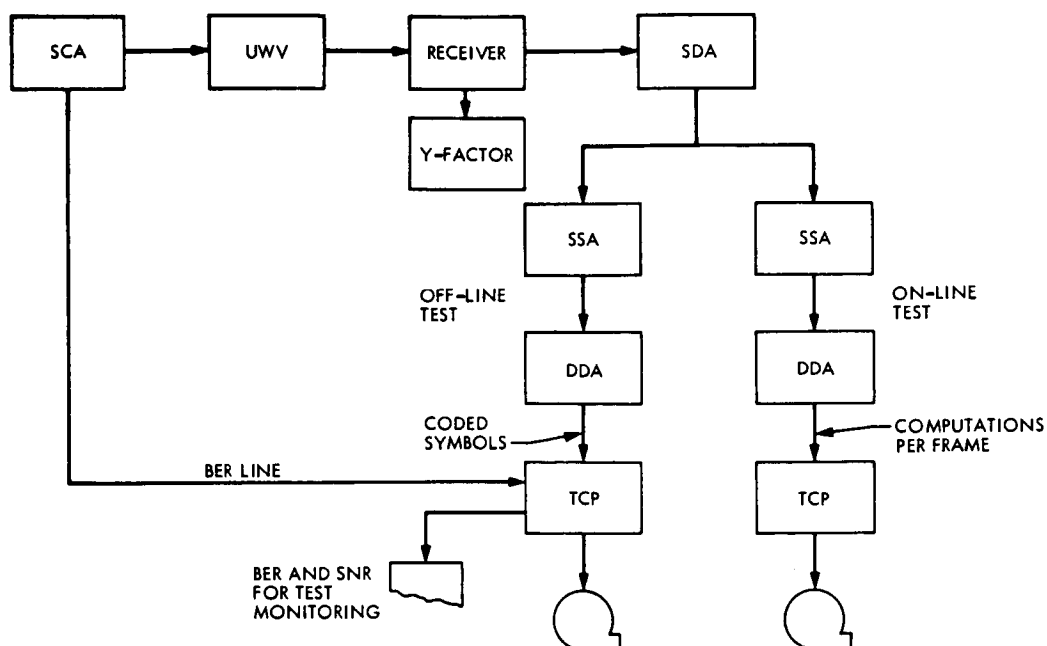


Fig. 1. Test configuration for DSN Telemetry System performance with convolutional codes

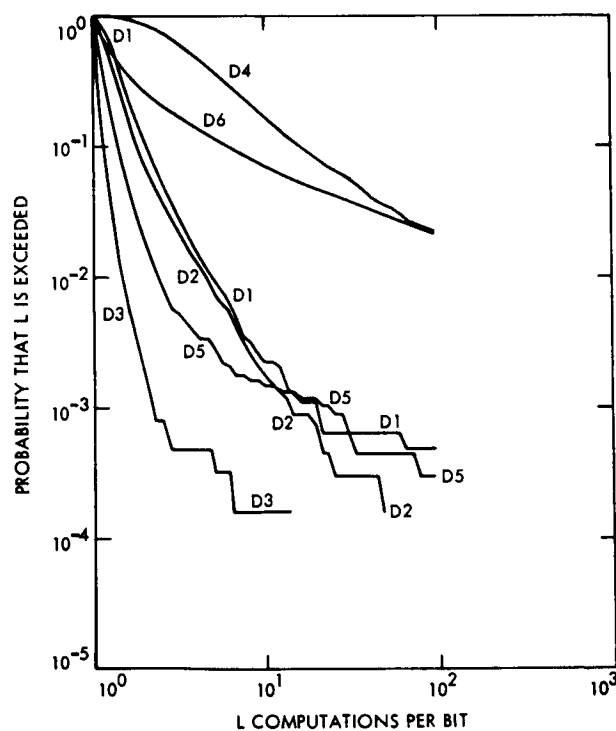


Fig. 2. Off-line sequential coding of 64-bps tests

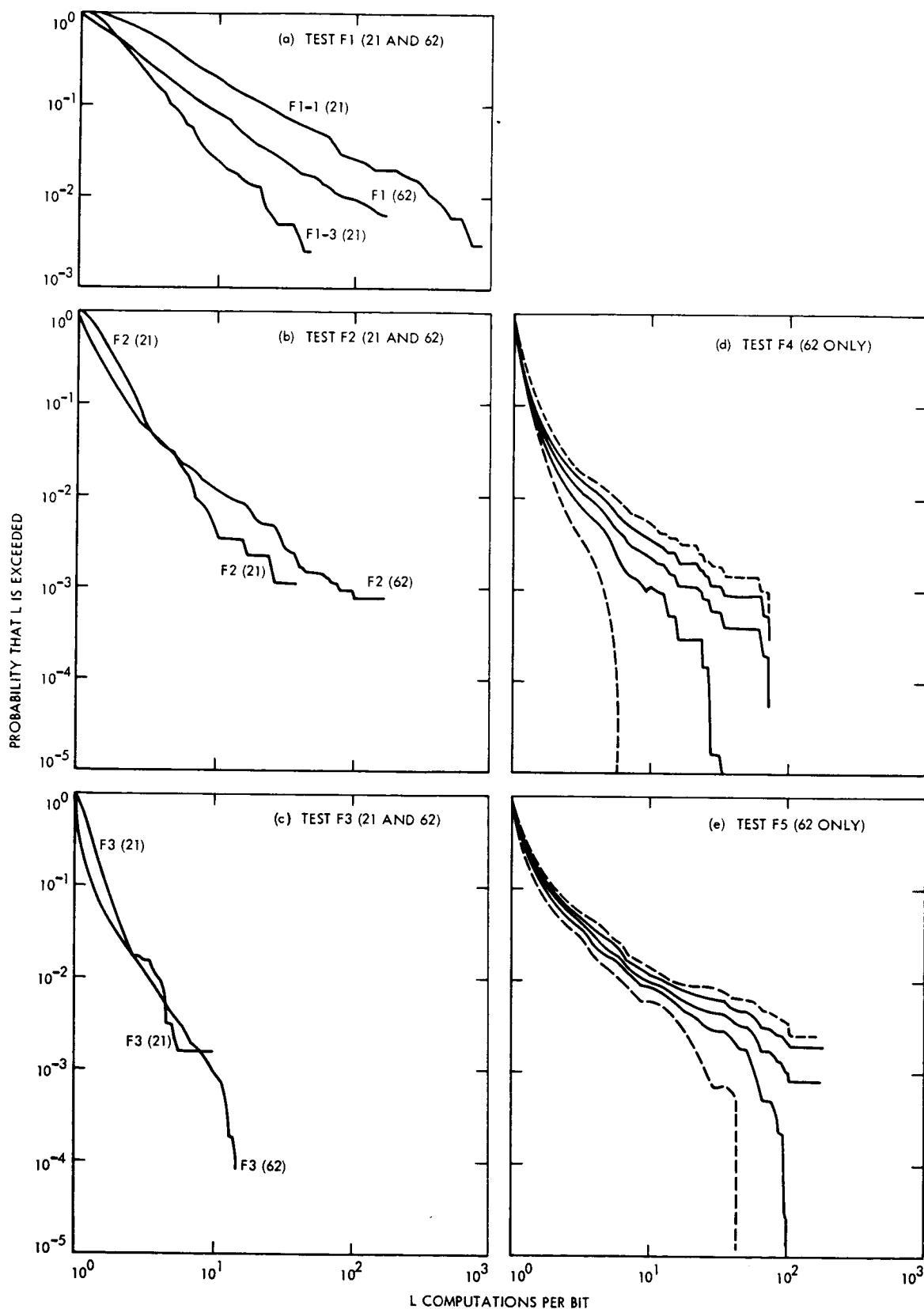


Fig. 3. The 8-bps tests at CTA 21 and DSS 62

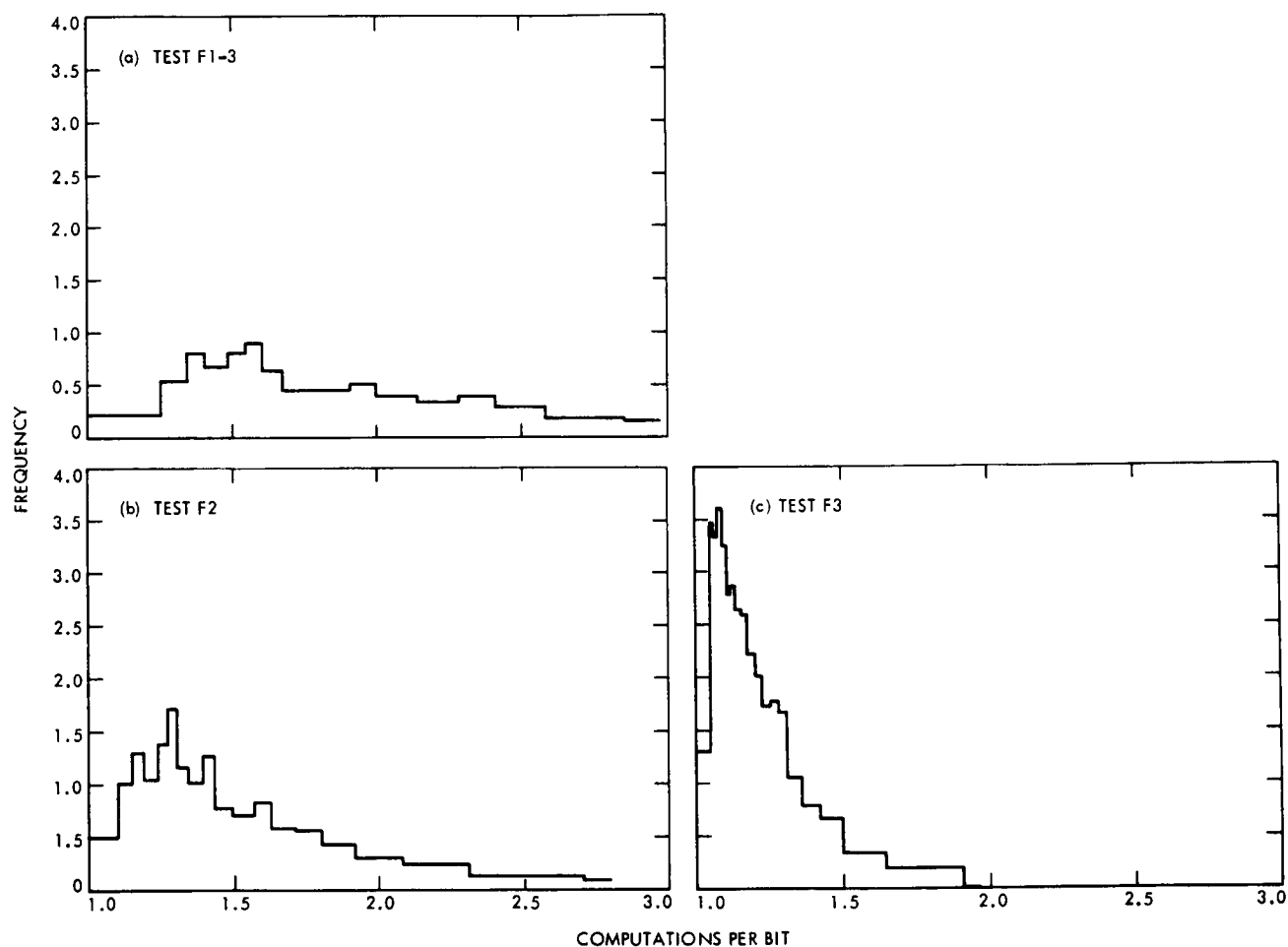


Fig. 4. Histograms of sequential decoding of 8-bps tests from CTA 21

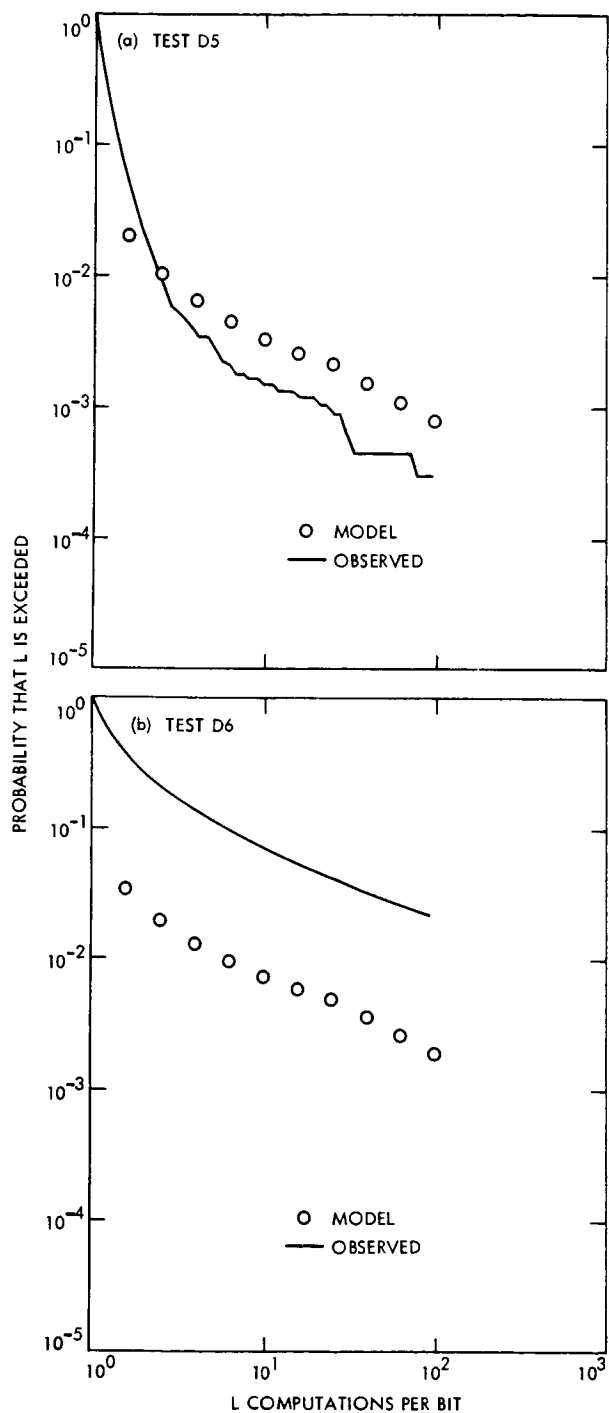


Fig. 5. Comparison of 64-bps tests with Lesh's model

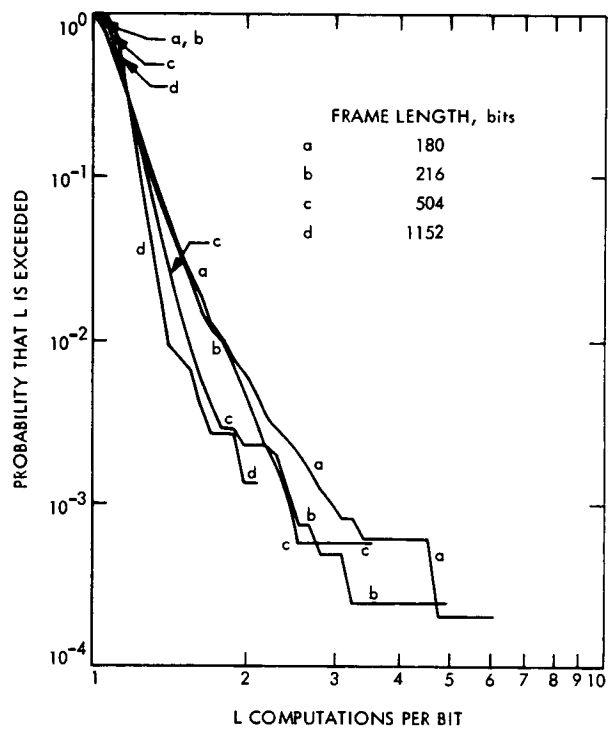


Fig. 6. Sequential decoding with different frame lengths: distribution functions

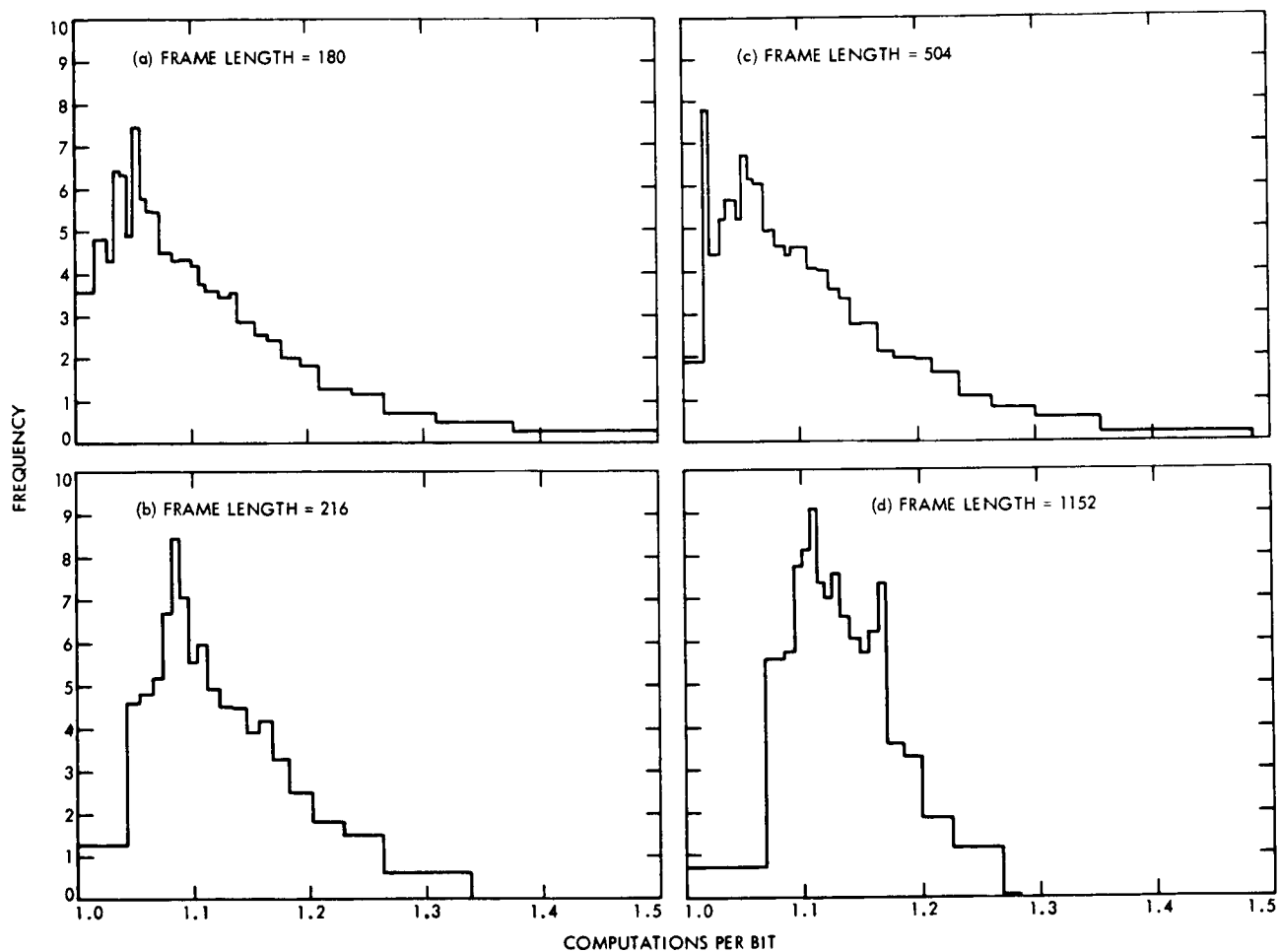


Fig. 7. Sequential decoding with different frame lengths: histograms

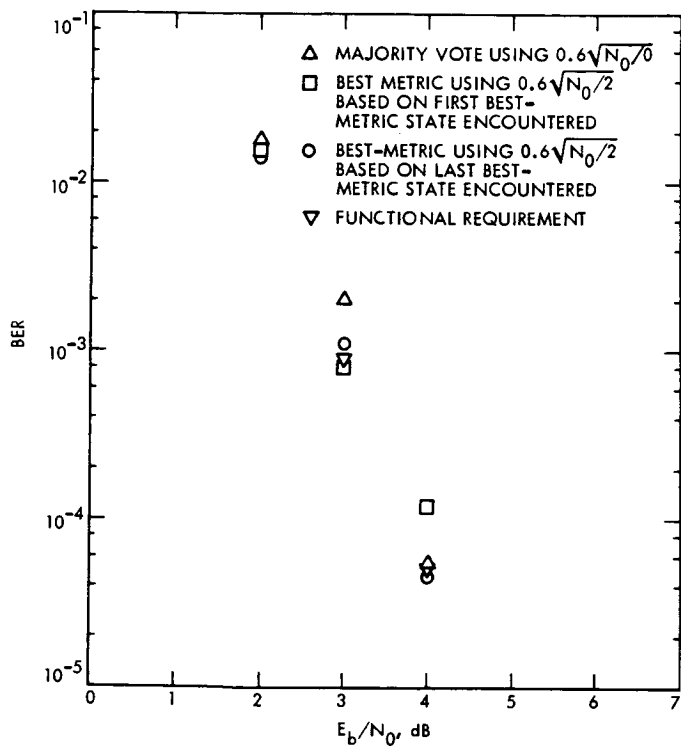


Fig. 8. Viterbi decoding program performance

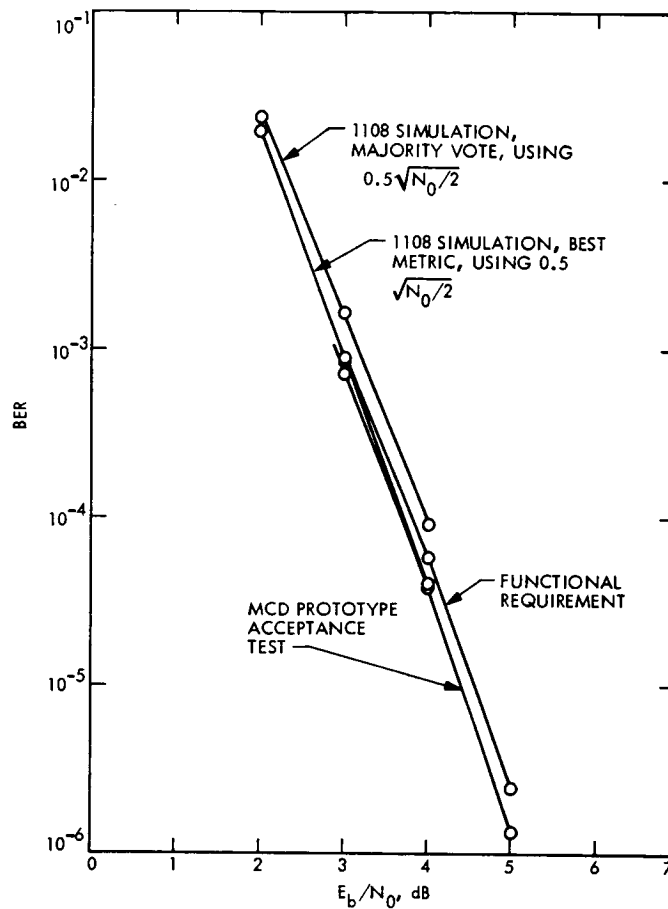


Fig. 9. Comparison of program performance, functional requirement E_b/N_0 (dB), and MCD prototype acceptance results

Approximate Mean Time to Loss of Lock for the Symbol Synchronizer Assembly

J. I. Molinder

DSN Systems Engineering Office/Harvey Mudd College

An approximate analysis of the mean time to loss of lock for the Symbol Synchronizer Assembly (SSA) is given. The results are used to determine the minimum required SSA input signal-to-noise ratio when the SSA is constrained to operate in the wide-wide or wide-medium bandwidth because of instabilities in the symbol stream time reference.

I. Introduction

The Symbol Synchronizer Assembly (SSA) is capable of operating at symbol signal-to-noise ratios as low as -5 dB (Ref. 1). This requires that the input symbol stream have a highly stable time reference so that after acquisition the SSA loop bandwidth can be narrowed for tracking. If the symbol stream time reference is less stable (for example, during playback of recorded Subcarrier Demodulator Assembly output) a wider SSA loop bandwidth must be used. This results in performance degradation due to the lower loop signal-to-noise ratio.

To determine the effect of bandwidth on Symbol Synchronizer Assembly lock, performance tests were performed at Goldstone (DSS 12) by R. Bartolett and R. Caswell. An input symbol stream with stable time reference was applied from the Subcarrier Demodulator Assembly and the Symbol Synchronizer Assembly constrained to operate with a fixed bandwidth setting. The results indicate that for 2-kbps (32,6) block coded data a signal-to-noise ratio $ST_b/N_0 \geq 8$ dB is required to hold lock in the wide-wide bandwidth ($\omega_L T_s = 0.02$) and $ST_b/N_0 \geq 4$ dB is required in the wide-medium bandwidth ($\omega_L T_s = 0.005$). In this article an approximate

analysis of the mean time to loss of lock is developed. The results compare favorably with the experimental data.

II. Analysis

The rms phase error for an in-lock linear phase-lock loop is given by

$$\sigma = \frac{1}{\sqrt{SNR_L}} \quad (1)$$

where SNR_L is the loop signal-to-noise ratio. For the SSA this is related to the symbol signal-to-noise ratio $R = ST_s/N_0$ by (Ref. 2)

$$SNR_L = \frac{R \left[\operatorname{erf} \left(R \frac{1}{2} \right) \right]^2}{\pi^2 W \omega_L T_s} \quad (2)$$

where

W = fractional window width = 0.25

ω_L = two-sided loop noise bandwidth

T_s = symbol duration

and

$$\operatorname{erf}(x) = \frac{1}{\sqrt{2\pi}} \int_0^x e^{-t^2} dt$$

Certainly the loop will be in lock as long as the phase error is such that symbol transitions remain within the fractional window width (i.e., $|\phi| < \pi/4$ for $W = 0.25$). This is a conservative lock definition since the loop applies restoring force for transitions outside the fractional window width. Thus the loop probably has a longer average time to loss of lock than that predicted by this analysis.

Let q be the probability that the phase error is within the fractional window width on a particular transition. Then

$$\begin{aligned} q &= P(|\phi| < \pi/4) \\ &= 2 \int_0^{\pi/4} \frac{1}{\sqrt{2\pi}\sigma} \exp[-\phi^2/2\sigma^2] d\phi \\ &= 2 \int_0^{\pi/4\sigma} \frac{1}{\sqrt{2\pi}} \exp[-x^2/2] dx \end{aligned}$$

$$= 2 \left\{ 0.5 - \int_{\pi/4\sigma}^{\infty} \frac{1}{\sqrt{2\pi}} \exp[-x^2/2] dx \right\} \quad (3)$$

Thus

$$q = 1 - 2Q(\alpha)$$

where

$$\begin{aligned} Q(\alpha) &= \int_{\alpha}^{\infty} \frac{1}{\sqrt{2\pi}} \exp[-x^2/2] dx \\ &\cong \frac{1}{\sqrt{2\pi}\alpha} \exp[-\alpha^2/2] \end{aligned} \quad (4)$$

for $\alpha = \pi/4\sigma > 2$ (Ref. 3).

Consider a series of transitions separated by a time interval T long enough so that the phase error at one transition may be considered independent of that at the previous transition. Roughly, this requires $T \geq 1/\omega_L$, where ω_L is the two-sided loop noise bandwidth. The average number of transitions separated by T for which the phase error is within the fractional window width is then

$$\bar{n} = \sum_{n=1}^{\infty} n q^n = \frac{q}{1-q^2} \quad (5)$$

Substituting $q = 1 - 2Q(\alpha)$ yields

$$\bar{n} = \frac{1 - 2Q(\alpha)}{4Q^2(\alpha)} \cong \frac{1}{4Q^2(\alpha)}, \quad Q(\alpha) \ll 1 \quad (6)$$

This corresponds to an average time interval

$$T_{\text{ave}} = \bar{n}T = \frac{\bar{n}}{\omega_L} = \frac{\bar{n}T_s}{\omega_L T_s} \quad (7)$$

where T_s is the symbol duration.

III. Example

For 2-kbps (32,6) block coded data,

$$T_s = \left(\frac{6}{32} \right) \left(\frac{1}{2 \times 10^3} \right) \cong 94 \mu\text{s}$$

The values of α , $Q(\alpha)$, and \bar{n} as a function of loop signal-to-noise ratio are given in Table 1 as well as T_{ave} for relative loop bandwidths of 0.02 and 0.005.

From Table 1 it appears that a reasonable threshold is a loop signal-to-noise ratio of about 12 dB. Using Eq. (2), it can be shown that this corresponds to $ST_s/N_0 \cong 0$ dB for $w_L T_s = 0.02$ and $ST_s/N_0 \cong -3$ dB for $w_L T_s = 0.005$.

For a (32,6) block code, $ST_b/N_0 = ST_s/N_0 + 7.3$ dB. Thus, the threshold corresponds to $ST_b/N_0 = 7.3$ and 4.3 dB for $w_L T_s = 0.02$ and 0.005, respectively, which agrees very well with the experimental results.

Acknowledgment

The author is indebted to W. Hurd for pointing out the necessity of considering transitions spaced by intervals of $T = 1/w_L$ to insure independence, and to J. Layland for an informative discussion.

References

1. Frey, W., Petrie, R., and Greenberg, R., "Multiple-Mission Telemetry System Project," in *The Deep Space Network*, Space Programs Summary 37-61, Vol. II, p. 122, Jet Propulsion Laboratory, Pasadena, Calif., Jan. 31, 1970.
2. Anderson, T. O., and Hurd, W. J., "Symbol Synchronizer for Low Signal-to-Noise Ratio Coded Systems," in *The Deep Space Network*, Space Programs Summary 37-53, Vol. II, pp. 51-63, Jet Propulsion Laboratory, Pasadena, Calif., Sept. 30, 1968.
3. Wozencraft, J. M., and Jacobs, I. M., *Principles of Communication Engineering*, p. 83, John Wiley & Sons, Inc., New York, 1965.

Table 1. T_{ave} versus SNR_L

SNR_L , dB	$a = \frac{\pi}{4\sigma}$	$Q(a)$	\bar{n}	T_{ave}	
				$w_L T_s = 0.02$	$w_L T_s = 0.005$
11	2.79	2.92×10^{-3}	2.94×10^4	2.3 min	9.2 min.
12	3.13	9.51×10^{-4}	2.76×10^5	21.6 min	86.4 min
13	3.51	2.40×10^{-4}	4.34×10^6	5.7 h	22.8 h
14	3.94	4.31×10^{-5}	1.35×10^8	7.3 days	29.2 days

Transmitter Fourth-Harmonic Interference at the Mars Station

R. C. Coffin
R. F. Systems Development Section

Measurements made at the Goldstone Mars Station (DSS 14) by various experimenters have indicated the presence of a relatively strong X-band fourth-harmonic level in the X-band receiver. Results of measurements on typical transmitters support this possibility. An X-band fourth-harmonic filter has now been installed in the microwave system at DSS 14 to reduce the radiated interference. This article reports on measurements of the effectiveness of the X-band fourth-harmonic filter.

I. Introduction

Observations have been reported of interference signals in the X-band receiver which are at the appropriate frequency to be attributable to the fourth harmonic of S-band. Recognizing that transmitters are usually operated in saturation, and considering the power levels involved, it is not surprising that fourth-harmonic signals are present in the waveguide system.

In the system design phase of development of the Block IV receiver, the possibility of fourth-harmonic interference was recognized because the 880/221 transponder ratio is very nearly harmonically related. There was no reliable information on the harmonic output of the klystrons at that time. Furthermore, the subnet was not equipped with X-band receiving capability, nor was there a suitable far-field receiving location. Consequently, the existing transmitter harmonic filters were designed using

best engineering judgment unconfirmed by experimental data. These filters are low-pass absorptive-type units with approximately 50 dB attenuation at X-band.

Recently a device for measuring the X-band fourth-harmonic content of signals in a waveguide system has been developed with supporting research and technology (SR&T) funds (Refs. 1 and 2). Some preliminary measurements have been made using this device which will provide further insight into the spectral content of klystron signals.

The Mariner Venus Mercury 1973 (MVM'73) mission employed an X-band maser having a narrow bandwidth (15 MHz), centered well away from the fourth-harmonic of the uplink. However, researchers still reported the existence of a potentially interfering X-band fourth harmonic. An X-band fourth-harmonic filter was therefore

procured and installed at DSS 14 to enhance MVM'73 data. The X-band receive only cone having a maser bandwidth of nominally 50 MHz has recently been installed, re-emphasizing the X-band fourth-harmonic interference problem. This article reports on the effectiveness of the X-band fourth-harmonic filter at DSS 14.

There are two factors that could create problems. The first is ranging sideband power. When the S-band uplink is modulated by ranging code, 500-kHz sidebands are generated. These sidebands will also appear on the fourth harmonic. The potential problem here is that these sidebands could be of significant amplitude, 38 MHz below the fourth harmonic, and therefore create interference in the X-band downlink. Careful selection of frequencies could not protect against this form of interference because of the effect of doppler.

The second concern is that fourth-harmonic carrier level in the X-band receiver could be of sufficient level, when radiating at high power, to create saturation conditions. Several researchers have reported levels that were approaching the upper limit of the receiver and maser.

II. Measurements

The basic philosophy was to establish a set of baseline measurements with the X-band fourth-harmonic filter installed. These measurements were then repeated for the system operating without the X-band fourth-harmonic filter. Areas of consideration were receiver saturation, maser saturation, inband interference from ranging sidebands, interference with telemetry data, and location of the source of the fourth harmonic. The following measurements were made to develop a baseline:

Fourth-harmonic leakage

Fourth-harmonic vs. transmitter level

Ranging sideband levels

Maser gain with/without transmitter on

Maser operating temperature with/without transmitter on

AGC level with/without transmitter on

These measurements were made using the 20-kW transmitter with the X-band fourth-harmonic filter installed and then repeated with the filter removed for both the 20-kW transmitter and the high-power transmitter operating at 300 kW. All measurements were made at

channel 9 (2111.6 MHz) uplink, since this frequency would produce a fourth harmonic (8446.4 MHz) slightly above X-band channel 33, which is on the edge of the passband of the X-band receive only maser. Figure 1 indicates the relative location of channels 9 and 33 downlink as well as the location of the channel 9 uplink fourth harmonic in the XRO maser passband.

The measurement of fourth-harmonic leakage consisted of a series of measurements designed to identify leakage paths other than the primary transmitter feedhorn-to-antenna-to-receiver feedhorn path. A number of paths were identified. The composite effect of these leakage signals is of the same order of magnitude as the primary path when the X-band fourth-harmonic filter is installed. Any improvements in X-band fourth-harmonic leakage over the levels obtained with the X-band fourth-harmonic filter installed will have to involve abatement of leakage via these paths.

Fourth-harmonic level vs. transmitter level consisted of measurements directed toward determining the effect of transmitter saturation on the X-band fourth-harmonic level. Figure 2 shows the relative strength of the X-band fourth harmonic in the receiver as a function of transmitter power. It is apparent that the level is a nonlinear function of transmitter power. This is to be expected at high transmitter levels, since the transmitter operates in a saturated mode at high power levels. The measurements of Fig. 2 were made with the klystron power supply level fixed at that required for the 20-kW saturated mode. The drive power was used to adjust power output level. The nonlinear characteristic at 1 kW was not expected, but it demonstrates the uncertainty of extrapolating measured data to other conditions. Furthermore, power level is not the only parameter of concern. Measurements by other experimenters have shown that fourth-harmonic levels generated by the 100-kW transmitters are frequency-dependent. X-band fourth-harmonic levels from the high-power transmitter were not measured until after removal of the X-band fourth-harmonic filter. Fourth-harmonic level due to the high-power transmitter operating at 300 kW was approximately -80 dBm, whereas the 20-kW transmitter generated about -87 dBm. The uncertainty of the levels is approximately ± 6 dB. That is, the results for identical conditions were found to vary from day to day or week to week by ± 6 dB. This is typical of leakage signals.

Ranging sideband measurements consisted of tuning the receiver to the selected sideband and recording the received signal level. Upper sidebands were not measured, since these are attenuated by the passband of the maser.

Three groups of sidebands were identified for investigation. Close-in sidebands (1st-9th) indicate the shape of the modulation envelope. Sidebands about 12 MHz below the fourth harmonic (23rd-25th) are in the channel 20 downlink passband. The third group of sidebands investigated were those appearing in the channel 9 downlink. These sidebands were found to be below receiver threshold even when radiating at 300 kW. More recent investigation has shown that low-pass filters in the ranging coders and in the receiver modulator attenuate the high-order components of the range code sufficiently to prevent same-channel downlink interference.

Figure 3 shows the X-band fourth harmonic and two groups of ranging sidebands, as observed while radiating at 13 kW. Each spectral line is drawn with two arrowheads, indicating the signal level with and without the X-band fourth-harmonic filter installed. It is evident that the X-band fourth-harmonic filter is effective in reducing the level of fourth-harmonic and fourth-harmonic ranging sideband levels in the receiver. The close-in sidebands are reduced almost to receiver threshold. However, the level of ranging sidebands in the channel 20 downlink (~8423 MHz) produced by the modulation on the channel 9 uplink are not reduced to insignificance. These sidebands, with the presence of doppler on the downlink, would definitely create interference in channel 20. The channel 9 uplink/channel 20 downlink investigation was selected from among the possible Viking channel allotments because it places the fourth harmonic closest to the downlink, thereby constituting the worst case. Other projects may have different channel assignments and therefore require more data if S-band ranging and X-band telemetry are to be scheduled simultaneously. It is safe to say, however, that same-channel uplink/downlink will not experience ranging sideband interference.

The last three entries in the list of baseline measurements pertain to receiver saturation caused by X-band

fourth-harmonic interference. Maser gain and receiver gain (as indicated by AGC voltage), at channel 9, were measured with and without the X-band fourth-harmonic filter installed. However, no discernible effect was found. Maser operating temperature at channel 9 in the presence of the fourth-harmonic interference while radiating at 300 kW without an X-band fourth-harmonic filter did show a small increase (0.1 dB). The receiver and maser cognizant design engineers agree that X-band fourth-harmonic interference signals of the magnitude reported here are very close to that required to produce saturation. The slight observed rise of system temperature may signal the beginning of saturation.

III. Conclusion

At DSS 14 it is evident that an X-band fourth-harmonic filter is required. This conclusion is predicated on the magnitude of the fourth-harmonic interference in relation to the saturation characteristics of the maser and receiver and the fact that our tests were limited to 300 kW, whereas the planned capability is for 400 kW. Furthermore, these test results were found to be highly variable, as is the nature of leakage signals.

Extrapolating these results to other deep space stations which have different transmitters is tenuous at best. Results of tests at DSS 63 in Madrid indicate that the X-band fourth-harmonic level is below receiver saturation by about 10 dB. The S-band ranging with X-band telemetry restriction probably holds at all stations. With a 10-dB margin between measured interference and receiver saturation, further tests should be conducted to insure that different conditions will not cause saturation. Evidence at DSS 14 indicates that different frequencies, transmitter saturation conditions, and perhaps antenna configuration affect X-band fourth-harmonic level.

References

1. Smith, R. H., "Fourth Harmonic Analyzer," in *The Deep Space Network Progress Report 42-20*, pp. 121-123, Jet Propulsion Laboratory, Pasadena, Calif., April 15, 1974.
2. Grigsby, Y. L., "Automation of Data Gathering and Analysis for the Fourth Harmonic Analyzer" in *The Deep Space Network Progress Report 42-26*, Jet Propulsion Laboratory, Pasadena, Calif., April 15, 1974.

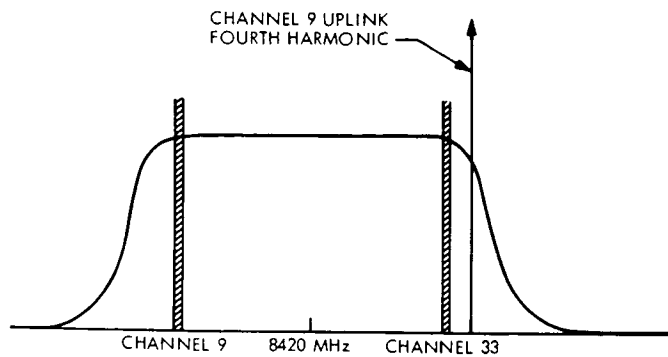


Fig. 1. XRO maser passband

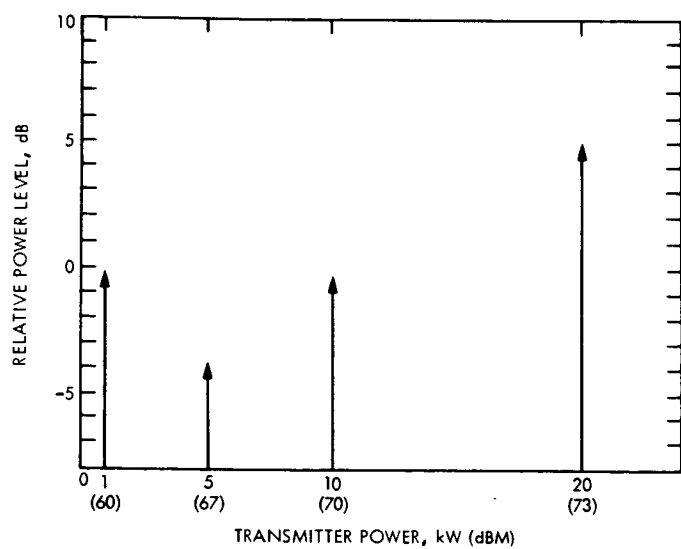


Fig. 2. Relative level of fourth-harmonic leakage vs. transmitter power

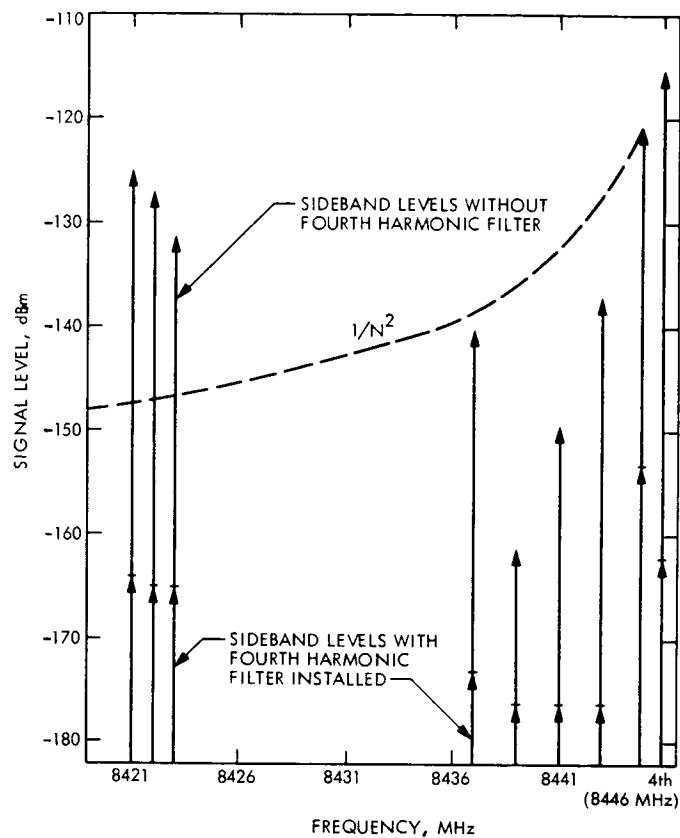


Fig. 3. Low-side ranging sidebands

Open-Loop Receiver Recording for Telemetry Data Recovery: A Field Demonstration

S. S. Kent
R. F. Systems Development Section

During a normal scheduled track of Pioneer 11 at DSS 12, open-loop receiver analog recordings were made of the spacecraft signal. These recordings were later played back at the Compatibility Test Area using an up-converter to provide an S-band input signal to the normal telemetry string. The results of this demonstration show a telemetry loss of 0.9 dB based on average symbol error rate values.

I. Introduction

During a normal scheduled track of Pioneer 11 on May 22, 1975 at DSS 12, open-loop receiver analog recordings were made of the spacecraft signal on a non-interference basis to real-time telemetry reception. A Block III receiver, configured as an open-loop receiver (OLR), heterodyned the S-band carrier down to 174 kHz for recording on an Ampex FR-2000A recorder operating at 76 cm/s (30 in./s). Two recordings, each approximately one hour long, were made of the Pioneer 11 signal. During the recording period, the real-time telemetry string (represented by the other Block III receiver, subcarrier demodulator assembly, symbol synchronizer assembly and data decoder assembly configured as a 32-bit constraint length, rate 1/2, convolutional decoder) provided symbol error rate (SER) statistics on decoded bits (256 bps) and frame erasure data to the digital instrumentation

subsystem (DIS), which provided a printout of the SER and frame erasures.

In early June the two recordings were played back at the Compatibility Test Area (CTA 21) using an up-converter to provide an S-band input signal to the telemetry string. The digital instrumentation subsystem provided SER statistics on decoded bits and frame erasures during the playback. Playback was accomplished on an Ampex FR-2000A recorder operating at 76 cm/s (30 in./s).

II. Configuration

Figure 1 is a block diagram showing the telemetry string configuration for the demonstration. Receiver 2 was used as the open-loop receiver on a non-interfering

basis to real-time telemetry reception in receiver 1. The digital instrumentation subsystem was loaded with Monitor III Program software.

Figure 2 is a partial diagram of the Block III-C receiver showing how the telemetry B string channel was configured to provide a low-frequency IF output to the analog recorder. To operate as an open-loop receiver, the phase-locked loop was disabled by "shorting out" the output of the loop filter. The voltage-controlled oscillator, then, was capable of being preset to any desired frequency by means of the manual frequency control voltage. The two blocks in Fig. 2 shown in dashed lines are not a part of the normal receiver. Since the selectable band-pass filter has four preset bandwidths, the variable band-pass filter was employed to minimize the noise bandwidth so as to maximize the signal-to-noise ratio in order to assure sufficient signal level for up-conversion without fear of noise limiting in the playback process.

The single-sideband (SSB) mixer (Ref. 1) is necessary to reject the image noise occurring below 10 MHz. The output frequency response of the SSB mixer is from 100 Hz to greater than 2.0 MHz, with the unwanted image noise reduced by more than 20 dB.

Figure 3 is a block diagram of the up-converter used to convert the low-frequency signal up to S-band for processing through the normal telemetry string for data recovery.

Figure 4 is a simplified diagram showing the configuration employed at CTA 21 during the playback of the tapes recorded at DSS 12 (Goldstone).

III. Recording/Playback Technique

The basic technique described herein was originally reported in DSN Progress Report 42-20 (Ref. 2), which presented results of tests performed at CTA 21. For those particular tests, an Ampex FR-1400 analog recorder was used to record the signal, and an Ampex FR-2000 analog recorder was employed during playback. Because of the poor instantaneous stability of the FR-1400, a time jitter compensator was used to limit the data degradation to an acceptable level.

With the advent of the newer generation analog tape recorders, such as the Ampex FR-2000A, it was determined that time jitter compensation was not necessary to achieve data degradation less than 1.5 dB due to the recording and playback process.

Thus, without the need for compensation, the recording technique reduces to one of offsetting the signal in the open-loop receiver such that its spectrum falls within the recording range of the analog recorder, adjusting the total power level (signal plus noise) so saturation does not occur, and then simply recording at the proper tape speed.

Playback, then, is a matter of up-converting the signal to S-band and injecting it into the normal telemetry string for data reduction. There are two main concerns: (1) sufficient signal gain without noise saturation, and (2) signal frequency knowledge to insure receiver acquisition.

IV. Recording Bandwidth Requirements

The Pioneer 11 spacecraft was transmitting a long constraint length rate 1/2 convolutional coded signal at 256 bps biphasic-modulated on a square wave subcarrier with a frequency of 32.768 kHz, which was, in turn, phase-modulated on a sine wave carrier with a frequency of 2292.407407 MHz. Due to doppler effects, the actual carrier and subcarrier frequencies received were 2292.210656 MHz and 32.770 kHz.

With square wave modulation, the total data power contained in the received RF signal can be expressed as

$$P_D = P_T \sin^2 \theta \quad (1)$$

where

P_D = total data power

P_T = total RF power

θ = modulation index

and the power contained in the n th harmonic (P_n) of the square wave frequency is

$$P_n = P_D \left[\frac{2 \sin \theta}{n\pi} \right]^2 \quad (n = \text{odd numbers}) \quad (2)$$

Since, from Eq. (2), the relative power contained in the n th sideband is proportional to $1/n^2$, the theoretical total relative power (P_R) is dependent upon the number of sidebands received, or

$$P_R = \sum_{n=1}^{\infty} \frac{1}{n^2} \rightarrow \frac{\pi^2}{8} = 1.2337 \quad (n = \text{odd}) \quad (3)$$

If only the first three components are received, the power loss is

$$P_L = 10 \log \frac{1.1511}{1.2337} = -0.301 \text{ dB} \quad (4)$$

Assuming the additional bandwidth requirement due to the low data rate is negligible compared to that required for the square wave subcarrier, the minimum recording bandwidth (for 0.3-dB loss) then is approximately 328 kHz.

The FR-2000A recorder, in the direct record mode, has a lower frequency response (-3 dB) of 400 Hz at all tape speeds and on upper response (-3 dB), as shown in Table 1.

In addition to its amplitude limitations the phase response of the recorder is linear only to about 60% of its upper response limit. Based on Table 1 and the recorder phase response, a tape speed of 76 cm/s (30 in./s) was selected for this demonstration. Thus, the anticipated

data degradation due to sideband losses alone were on the order of 0.3 dB.

V. Data Summary

The monitor program provided a printout of the number of frames decoded, the number of frames erased, and the number of detected symbol errors in the Data Decoder Assembly. Table 2 is a summary of the data collected during the recording of the real-time telemetry at DSS 12 and the playing back of the tapes at CTA 21 on May 30 and June 3. The symbol signal-to-noise ratio (SSNR) tabulated in Table 2 is based on the average symbol error rate.

The average SSNR during recording was 1.85 dB, thus the average SSNR of the playback of 0.94 dB represents a telemetry loss of 0.91 dB.

Frame erasure statistics are deemed insufficient, on such a small data sample, to be used as a good measure of telemetry loss.

Acknowledgments

The author wishes to thank E. S. Burke, Jr., for making all necessary arrangements to conduct the demonstration at DSS 12 as well as suggesting the use of the monitor software program for data reduction. Appreciation is also expressed to J. R. McAllaster and W. Snow for their expertise and assistance with the analog recorder, to the crews of DSS 12 and CTA 21 for their efforts in gathering and playing back the data, and to M. H. Brockman for technical guidance in this effort.

References

1. Rogers, A. E. E., "Broad-Band Passive 90° RC Hybrid with Low Component Sensitivity for Use in the Video Range of Frequencies," *Proceedings of the IEEE, Proceedings Letters*, pp. 1617-1718, Nov. 1971.
2. Kent, S. S., and Sleky, A. G., "Open-Loop Receiver/Predetection Recording System for the DSN," in *The Deep Space Network Progress Report 42-20*, pp. 139-148, Jet Propulsion Laboratory, Pasadena, Calif., Apr. 15, 1974.

Table 1. FR-2000A upper frequency response (-3 dB)

Tape speed		Response, MHz
cm/s	in./s	
305	120	2.0
152	60	1.0
76	30	0.50
38	15	0.25

Table 2. Summary of data accumulated during record and playback

Tape	Frames accumulated	SER average	SSNR, dB	Erased frames
Record				
1	5307	0.041	1.80	7
2	2500	0.039	1.90	0
Playback				
5/30				
1	4400	0.060	0.80	—
2	4534	0.055	1.05	34
6/3				
1	4547	0.061	0.80	47
2	4222	0.054	1.10	22

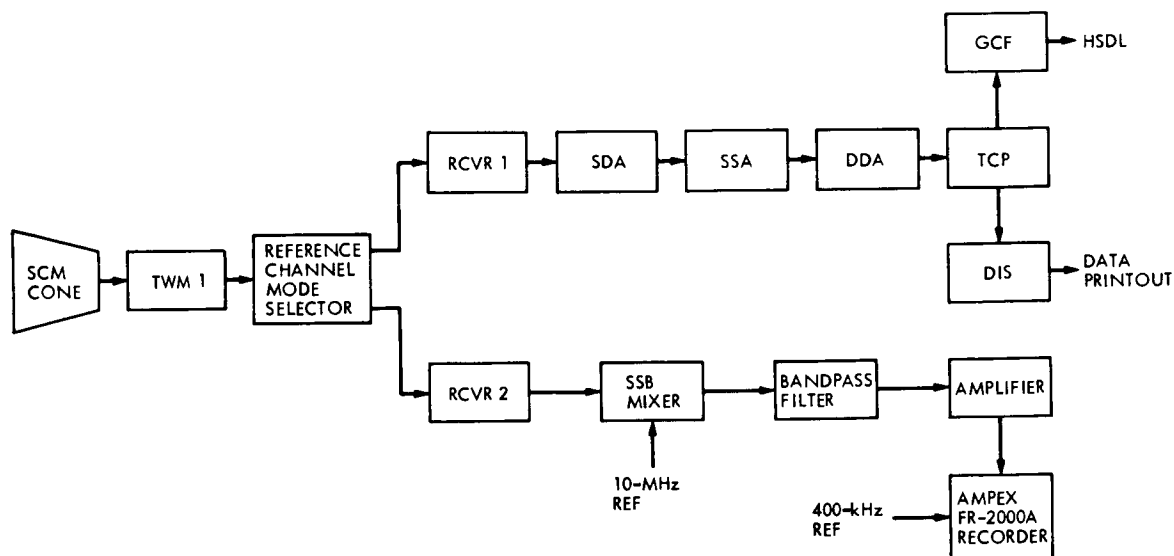


Fig. 1. Telemetry configuration

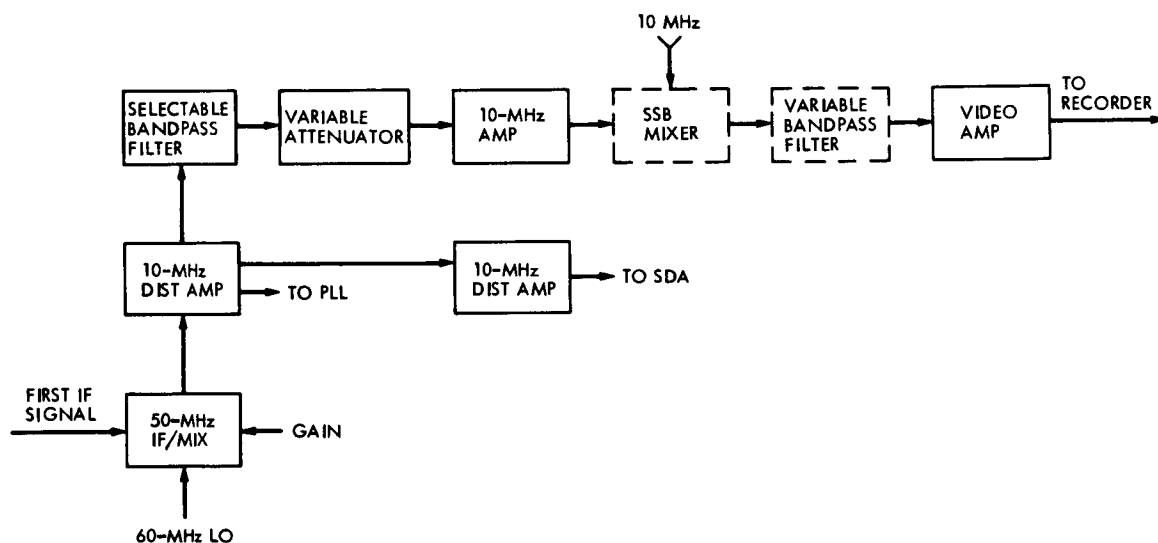


Fig. 2. Partial diagram of the Block III-C receiver showing open-loop configuration

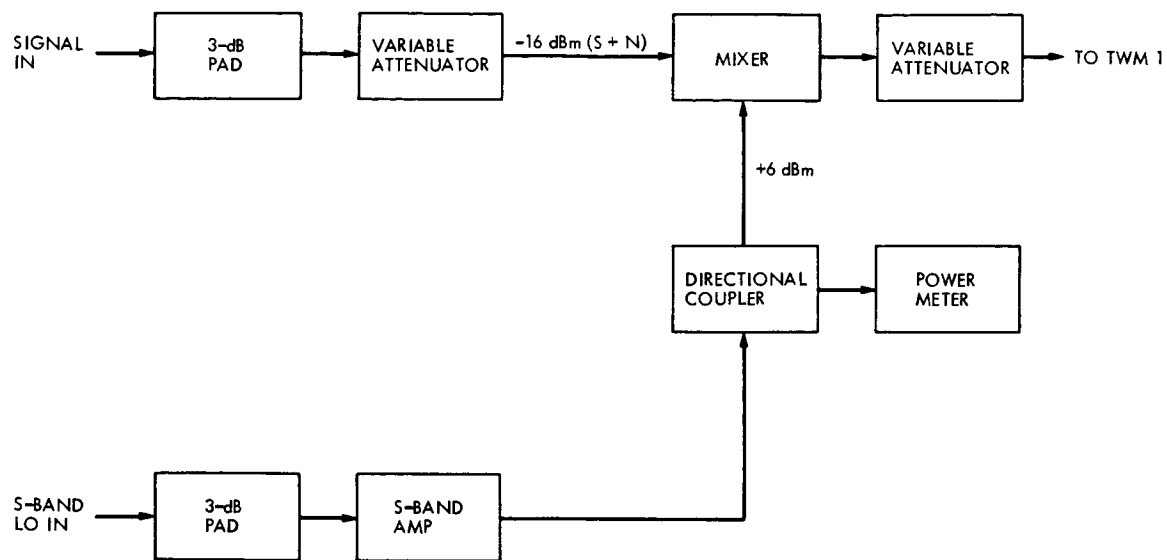


Fig. 3. Block diagram of up-converter

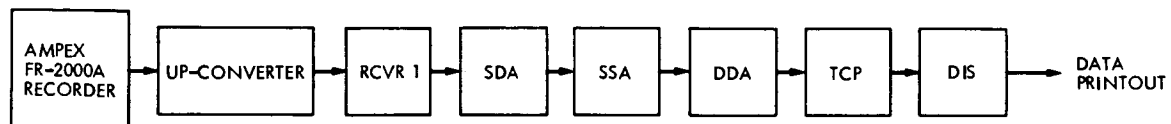


Fig. 4. Block diagram of CTA 21 configuration

N76-15207

DSN Research and Technology Support

E. B. Jackson

RF Systems Development Section

The activities at the Venus Station (DSS 13) and the Microwave Test Facility, both operated by the Development Support Group, during the 6-month period ending October 15, 1975, are discussed and progress is noted.

Successful remote operation of the Venus Station from Pasadena during a pulsar observing track is described, along with significant tracking of the planet Venus in an interferometric planetary radar mode. Completion of the first phase of the demonstration of long-distance (1.6-km) transmission of microwave power is reported, with an RF-to-dc conversion efficiency of better than 80% and 30 kW of dc recovered. Extensive support to the X-band radar and the Block IV receiver-exciter at the Mars Station (DSS 14) is reported, along with support to noise-adding radiometer (NAR) reliability experiments, antenna gain standardization, planetary radio astronomy, platform parameters very long baseline interferometry (VLBI), interstellar microwave spectroscopy, Venus/Ovro VLBI, and differential phase VLBI. Routine transmission of clock synchronization signals to the overseas complexes with 64-m antenna stations is also discussed, and extensive analysis of a reported problem with the DSS 14 HV dc power supply which resulted in excessive ripple voltage interfering with transmitter operation is described.

During the 6-month period ending October 15, 1975, the Development Support Group, in operating the Venus Station (DSS 13) and the Microwave Test Facility (MTF), supported various programs as discussed below.

I. Station Automation

In support of Network Monitor, Control and Operations Technology, a demonstration of a remotely operated,

automated station is planned, using DSS 13 as the test station. Working toward this goal, hardware and software testing continued (Ref. 1). Communications between the Sigma-5 computer at JPL and the XDS-930 computer at DSS 13 proved to be a stumbling block (timing problems), and in an effort to resolve these problems, 570 h of intercomputer communications testing was performed. As the timing problems, data dropout, and other hindrances were resolved, testing of the rest of the system was also

performed. In culmination of 83 h of system testing, an automated station under local (DSS 13) control was successfully demonstrated on March 20, 1975. The station was placed into a preconfiguration condition and antenna movement, system temperature measurement, and data collection from 7 pulsars were accomplished using only local input into the XDS-930 typewriter input.

Building on this base, full remote control of the station using a Sigma-5 computer at JPL was demonstrated in August 1975, with two separate observing periods of 6 h each, during which control was completely exercised from JPL without prior notification of changes in the antenna position being given to DSS 13 personnel. Testing to obtain reliability data is continuing.

II. Pulsar Observations

In support of the Radio Science experiment Pulsar Rotation Constancy, we provided 135 h of observations, during which data on the pulsars, tabulated in Table 1, were recorded. These data, from observations made at 2388 MHz, left-circular polarization, are used to determine precise pulse-to-pulse spacing, pulse shape, and pulse power content of the signals emitted by these pulsars.

III. Interferometric Planetary Radar

Continuing mapping of the planet Venus, 86 h of support were provided, during which 61 h of actual observing produced 207 data runs. (A run varies in length, being the round-trip light time to the target, the planet Venus.) In this experiment, the 64-m antenna at DSS 14 illuminates the target with a suitably coded signal, and after a round-trip light time has elapsed, both the 64-m antenna at DSS 14 and the 26-m antenna at DSS 13 receive the reflected signal. The signals are combined at DSS 14 and converted into power spectra by means of the discrete Fourier transform. The cycle is then repeated, with alternate transmit and receive periods. Approximately 1000 min of data have thus been received and transformed into power spectra during this reporting period. These observations are conducted at 2388 MHz using the 400-kW transmitter at DSS 14 as the illuminator.

IV. Noise-Adding Radiometer Reliability Testing

Using the DSS 13 26-m antenna, station receiver, and the noise-adding radiometer (NAR), total receive system temperature is automatically recorded during the night

and weekend periods when the station is nonoperational. This continuous operation provides reliability data and, in addition, produces a radio brightness temperature sky map as Earth's rotation sweeps the fixed antenna beam across the sky. The antenna is positioned at a fixed azimuth and progressively different elevations to produce, in time, a complete sky map. During this period, 1075 h of data were gathered with the antenna positioned at an azimuth of 0 deg and at progressive elevations of 55 through 53.3 deg in 0.1-deg increments. Measurements are made at a frequency of 2295 MHz using right-circular polarization.

V. Antenna Gain Standardization

To check the gain of the network antennas, transfer gain standards are needed. To provide such standards, the 26-m antenna at DSS 13, whose gain is known, is used to determine the flux density of suitable radio calibration sources. During this period, measurements were made of radio sources Cassiopeia A, 3C123, and Virgo A (3C274), at a frequency of 2278.5 MHz, using right-circular polarization on the 26-m antenna. These data, taken semi-automatically using the NAR, were collected for a total of 20 h during this period.

VI. Microwave Power Transmission

The operational desk/console, consisting of an Interdata 7/16 minicomputer, teletype I/O, cathode ray tube display terminal, non-impact printer, and a control keyboard with a cassette tape system, was installed in the Operations and Data Processing building at DSS 13. The rectenna subarrays were installed on the collimation tower, and testing was performed. After measurement of energy distribution within the antenna beam, rectenna efficiency, reflected power, etc., a successful demonstration was performed during which 30.1 kW of dc power were recovered by the rectenna array, with an average RF-to-dc efficiency of better than 80%. (RF-to-dc efficiency, in this case, is defined as the ratio between the RF energy incident upon the rectenna array and the dc output from the array.) The system was subsequently demonstrated to the Satellite Power Team and various members of NASA, universities, and private industry. Inclement weather is awaited for further testing of the system.

VII. X-Band Radar

The production version of the buffer amplifier was installed and suffered a failure of one of the Logimetrics power supplies. The system was then removed for further testing and evaluation. Meanwhile, the transmit-receive

waveguide switch was replaced, and the receive system temperature was improved 2.5 K. During subsequent testing, one of the klystrons failed. A spare klystron was installed, and the buffer amplifier was reinstalled and again suffered problems. Difficulties were encountered with body current monitoring, arc detector functioning, and interconnections within the buffer amplifier. The problems were solved, the system was made operational and, during subsequent full system testing, both klystrons failed, with cracked output waveguide windows.

Analysis of the failure indicated possible malfunctioning of one of the TWTAs in the buffer amplifier, and a crowbar circuit was added to the system to prevent drive to the final klystron in the event of oscillation in the buffer amplifier. The system was again made operational with one klystron installed, and a planetary radar track was successfully run with one klystron, 130 kW output power. Subsequent scheduled tracks were canceled because of problems with the computer data collection system.

VIII. Block IV Receiver-Exciter, DSS 14

Continued support was provided for a total of 222 manhours to the subsystem testing of the Block IV receiver-exciter at DSS 14. Problems with the X-band doppler chain were solved by cable and module replacement. The exciter configuration control and status assembly was installed, and additional problems were encountered with the doppler extractor modules and noise on the cabling. Cable replacement and careful work on the ground returns, along with relay and module replacements, aided in making the system operational and effecting transfer to operations.

IX. 100-kW Transmitter Installation in Australia and Spain

The support for the 100-kW transmitter installation was completed by shipment of the spare X-3060 klystrons to their stations. Special matched sets of shims, adapters, magnets, and socket tanks were also shipped. (The shim and adapters were necessary to compensate for varying lengths of the klystrons, along with irregularities in the mounting plates.)

X. Fourth-Harmonic Testing, DSN Klystrons

In anticipation of X-band operation with the Viking spacecraft, the level of the fourth harmonic of the S-band transmitter klystrons was measured. A specially designed and built (by Varian Associates) filter/analyzer was used to

measure the harmonic output of the X-3060 klystrons operating at 100-kW output power. Measurements were also made on the X-3075 klystrons at 400-kW output power. Measurements, made before and after the standard harmonic filter, indicated that it was desirable to add additional filtering to assure that the fourth harmonic of the S-band transmitter output did not interfere with operation at X-band with the Viking spacecraft.

XI. Excess Property Disposal and Storage Area Screening

The recent series of personnel reductions and resulting reduction in the operating hours of the Venus Station, coupled with a change in the emphasis of the station's mission, indicated the desirability of reducing the property inventory. All portable test equipment within the Development Support Group has been reviewed, and all items which have no foreseeable usage in its revised mission have been placed with the Property Department for disposal through the usual channels. Additionally, temporary personnel have been hired to aid in screening the storage areas to separate and arrange all material held therein. A significant amount of surplus and scrap material has been produced as a result of these activities.

XII. Mars Station HV (90-kV) dc Power Supply

Reported excessive ripple voltage on the output of the 2-MW, 90-kV dc high-voltage transmitter power supply at DSS 14 prompted an intensive investigation. After ascertaining that none of the phases was missing on the input 400-Hz three-phase line, and observing that the input 400-Hz voltages and currents were balanced on the three phases, a decision was made to open up the power supply and check the rectifier diodes.

Upon opening the rectifier section of the power supply, it was observed that the insulating oil was clear with no undue coloring. The rectifier diodes are arranged in series, with voltage and current balancing resistors and capacitors, into a stack. The stacks, which contain 78 diodes each, are again arranged in series to provide the necessary peak inverse voltage rating. Twelve of these stacks are thus arranged into an assembly, with one assembly per phase. Figure 1 shows how the assemblies are fitted between wooden rails and electrical contact is made with copper tubing. On the right in the photograph can be seen a diode assembly, with one stack visible at the top. The assembly in the center is an array of peak clipping selenium rectifiers designed to prevent excessive peak

alternating current voltages from being applied across the diode stacks whenever transient disturbances occur on the alternating current line.

It was decided to test the stacks in a manner similar to that originally used by the manufacturer. Two tests were used, a forward voltage drop test and an inverse voltage current test. In the forward voltage test, direct current voltage was applied in the forward direction across the stack and adjusted so that the forward current was 10 A. The voltage drop across the stack was then measured. In the inverse current test, 20,000 V direct current was applied across the stack in the inverse direction, and the resulting current was measured. Exploratory measurement on a spare stack indicated that repeatable measurements could be made in the reverse direction by using a General Radio high-voltage ohmmeter set for 500 V output voltage. Measurements taken with this instrument and with the 20-kV test voltage indicated the same resistance within 4%, so measurements were continued using the high-voltage ohmmeter. A Hewlett-Packard Model 6483C current-regulated power supply was used for the forward voltage drop measurements and, to ensure minimization of heating effects, the voltage drop was measured with a Hewlett-Packard Model 3430 digital voltmeter 5 s after the 10-A forward current was established by turning on the power supply. Figure 2 shows the interconnection of the equipment. Examination of the test data indicated that no diodes were open but one stack most likely had one diode shorted. Each stack has a nominal reverse voltage rating of 49,200 V, while maximum peak inverse voltage across each stack at 90 kV dc output voltage is only 7875 V; one failed diode therefore introduces minimal additional stress.

Inasmuch as the rectifier stacks were good, transformer secondary voltage balance was checked. Temporary reconnection of the HV supply was made with the top off for access. Using a test lead made of a high-voltage stick with a large fuse clip connected to an electrostatic voltmeter, secondary transformer voltages were measured at a dc output voltage of 40 kV and an output current of 7.4 A. The secondary phase to neutral voltages were all balanced within 0.6%, so transformer problems were ruled out. With no apparent fault in the transformer/rectifier, the wave shape of the input 400-Hz line on the primary of the transformer was then examined. Since this transformer is connected in a balanced delta on the primary, waveform measurements were made using two Tektronix HV probes connected to a differential input oscilloscope. Figure 3 shows that the waveform is distorted, with what appears to be a strong sixth harmonic component. Waveform measurement of the ripple voltage appearing at the input

to the filter choke also reveals a strong 2400-Hz component which is strongly sinusoidal, as indicated by Fig. 4. Measurements of the inductance of the filter choke revealed that it had decreased from a nominal nameplate value of 1.0 H to a measured 16 mH, while the spare choke measured 1.35 H. The spare choke was placed into service, and measurements of the ripple voltage indicated that, at 20 kV dc output voltage, the ripple on the choke input was 16 kV peak-to-peak, while the ripple on the output of the filter choke was 46 V peak-to-peak. It is believed that, in the absence of any faults found with the transformer/rectifier, the high value of ripple on the filter choke input is caused by the strong 2400-Hz component on the 400-Hz input to the primary of the transformer/rectifier. The most likely cause of this 2400-Hz component is a high impedance in the frequency converter at this frequency, as evidenced by a no-load waveform check, which revealed that the frequency converter output waveshape is a near-perfect sinusoid when not furnishing power to the transformer/rectifier.

Experimentation with an unbalanced pi ripple filter indicates that the ripple voltage on the choke input can be reduced substantially by connection of a relatively small value capacitor to bypass the ripple back to the power supply. Figure 5 illustrates that, at 20 kV dc output voltage, the peak-to-peak ripple voltage is reduced from 16 to 1 kV by connection of a capacitor having a nominal value of 0.15 μ F to bypass the ripple back to the power supply return line.

Further testing is under way to determine the optimum size capacitor that will reduce the ripple to an acceptable level while limiting capacitor charging current to a safe level which will not harm the rectifier diodes.

XIII. Planetary Radio Astronomy

In support of the Planetary Radio Astronomy experiment, observations are made of the planet Jupiter and various radio calibration sources. Total receiving system temperature, both on- and off-source, is measured. Received flux density of the source can then be calculated. The measurements are made at 2295 MHz, both left-circular polarization and right-circular polarization, and utilize the 26-m antenna, the station receiving system, and the NAR. Observations, in addition to those of Jupiter, were made of the sources shown in Table 2, while the data were collected semi-automatically under the control of the NAR. A total of 177 h of data were thus collected.

XIV. Platform Parameters VLBI

The objective of this activity is the refinement of the application of the VLBI technique to measurements of navigation platform parameters, specifically UT1, polar motion, and relative station locations. The support given by the Venus Station (DSS 13), a total of 11 h of observing, is to aid in the development of a position catalog of 50-100 compact extragalactic radio sources for use as navigation sources. During the 11 h, 65 sources were observed, with DSS 63 (Madrid) as the other VLBI station operating at 2290 MHz.

XV. Interstellar Microwave Spectroscopy

The objective of this activity is the measurement of the location and abundance of complex interstellar molecules, involving recombination line study in various regions. DSS 13 provided 15-1/2 h of observing, during which time the regions Orion A and MON-R2 were studied at 2272.62 MHz. These measurements utilize the 26-m antenna, the station receiving system, and the NAR.

XVI. Venus/Ovro VLBI

The objective of this experiment is to make high-resolution observations of the strongest 100 radio sources in the complete 3C catalog. DSS 13 provided 123 h of

observing, during which 159 source observations were made in the VLBI mode, with the Owens Valley Radio Observatory as the other station. Observations were made at 2310 MHz and utilized the 26-m antenna, a special mixer, and a special video tape recorder for data recording.

XVII. Differential Phase VLBI

The objective of this experiment is to investigate and demonstrate a technique of obtaining accurate phase measurements by VLBI observations. In conjunction with the Owens Valley Radio Observatory, 32 h of observations were made at 2290 MHz using the DSS 13 26-m antenna, the station receiver, and a special video recorder for recording data.

XVIII. Clock Synchronization Transmissions

Routine transmissions, typically 1 h in duration each, have been made as scheduled. Additionally, required testing to assure operability has been performed. With the completion of the overseas 64-m antenna stations, timing signals are distributed to the 26-m stations by the 64-m stations. Therefore, transmissions are made only to the 64-m antenna stations in Spain and Australia. Fifteen transmissions were made to DSS 42/43 in Australia, while 14 transmissions were made to DSS 61/63 in Spain.

Reference

1. Jackson, E. B., and Price, A. L., "DSN Research and Technology Support," in *The Deep Space Network Progress Report 42-27*, pp. 107-111, Jet Propulsion Laboratory, Pasadena, Calif., June 15, 1975.

Table 1. Pulsars observed at DSS 13 (April 16 through October 15, 1975)

0031 - 07	0628 - 28	1133 + 16	1911 - 04	2045 - 16
0329 + 54	0736 - 40	1237 + 25	1929 + 10	2111 + 46
0355 + 54	0823 + 26	1604 - 00	1933 + 16	2218 + 47
0525 + 21	0833 - 45	1642 - 03	2021 + 51	

Table 2. Radio calibration sources observed at DSS 13 (April 16 through October 15, 1975)

3C17	3C123	3C218	NGC 7252	Virgo A
3C48	3C138	3C348	PKS 0237-23	
3C58	3C147	3C353	PKS 2134	

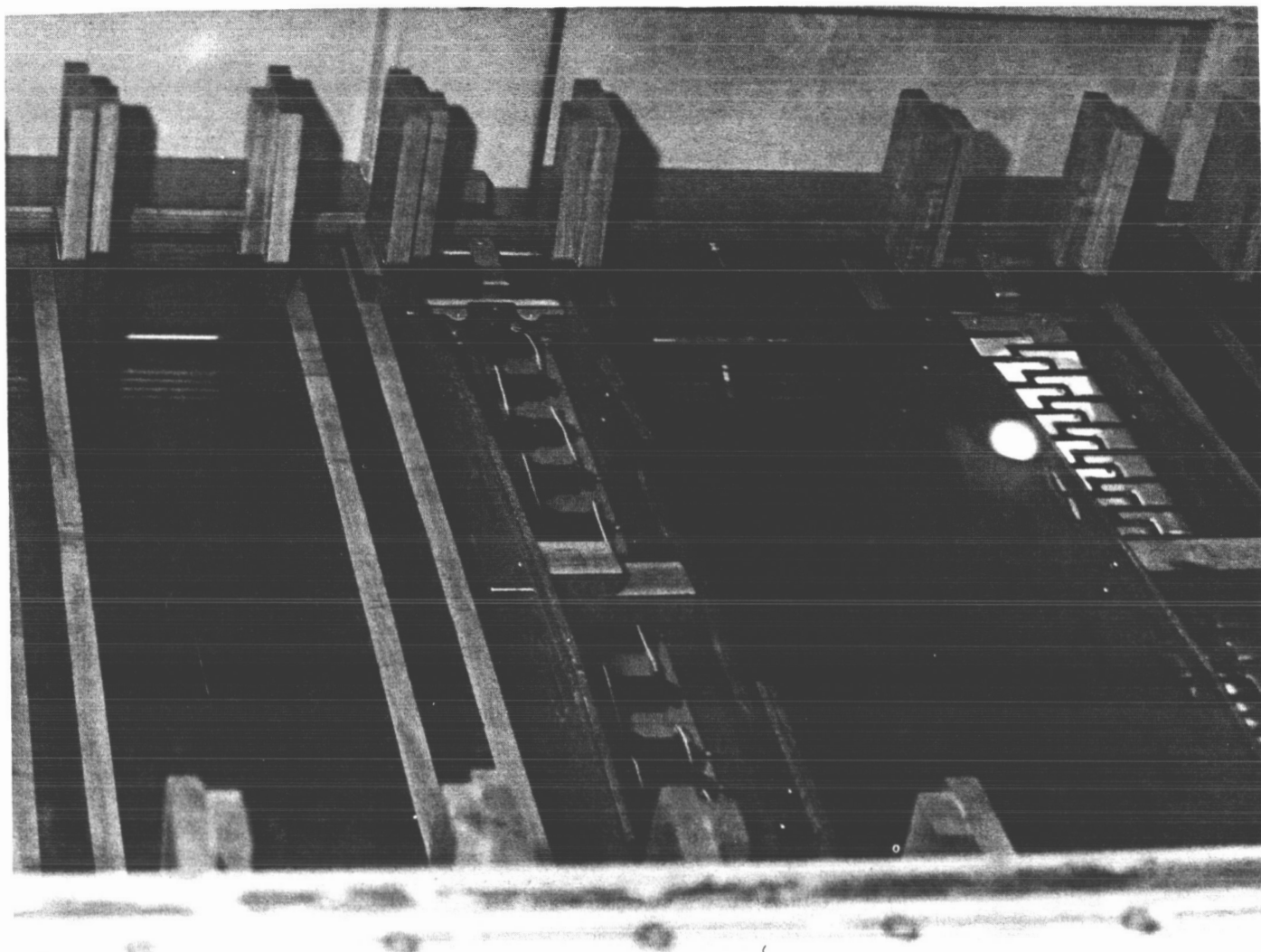


Fig. 1. Interior construction of rectifier side of HV dc power supply

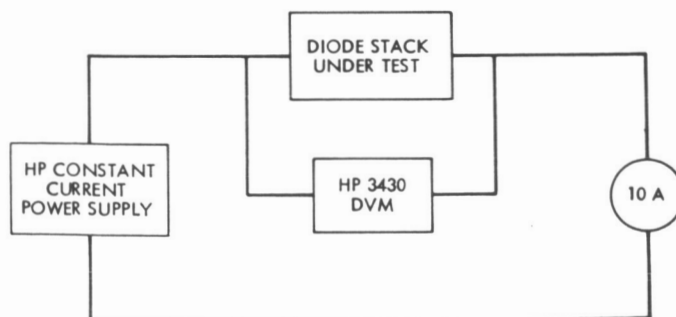


Fig. 2. Forward voltage drop test configuration

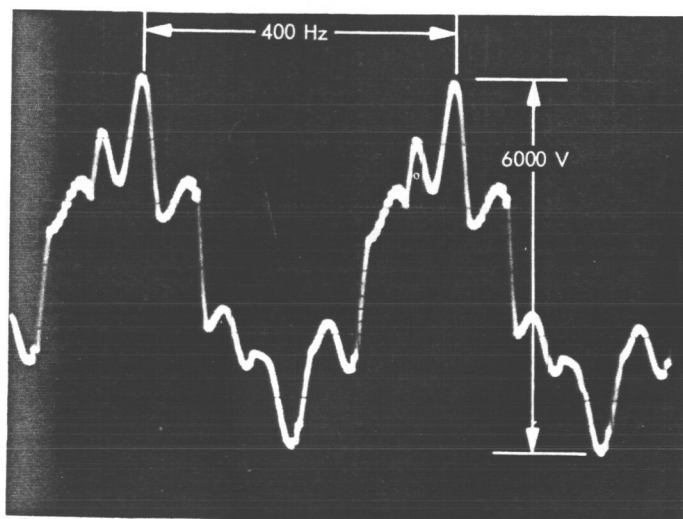


Fig. 3. Voltage at 400 Hz input to transformer, DSS 14 HV dc power supply

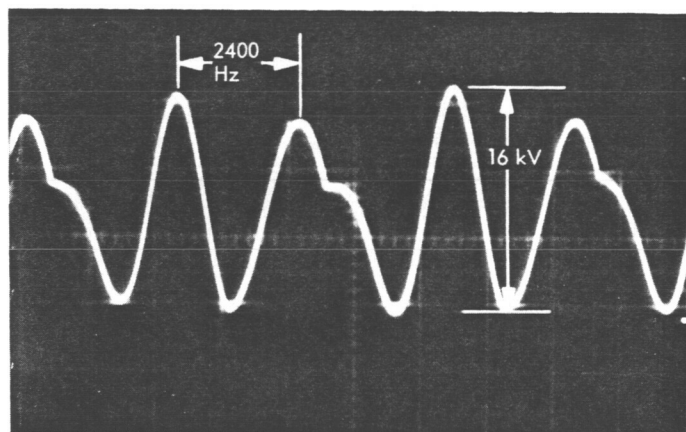


Fig. 4. Voltage at filter choke input, DSS 14 HV dc power supply

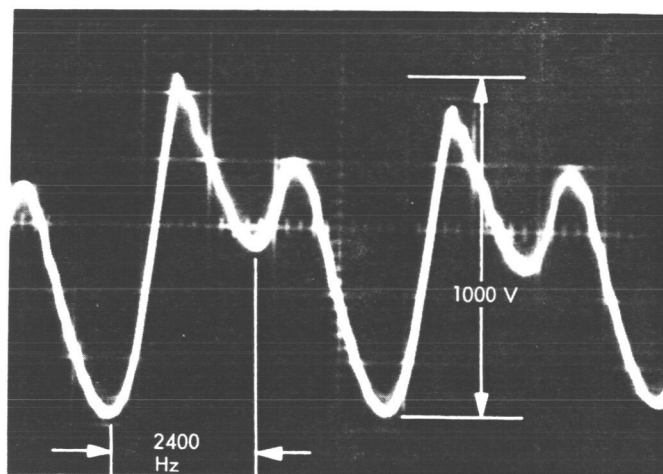


Fig. 5. Voltage at filter choke input, DSS 14 HV dc power supply, with added $0.15\text{-}\mu\text{F}$ filter capacitor

N76-15208

Symbol Synchronizer Assembly Instability Study: Part II

R. C. Bunce
Network Operations Office

Part I (Ref. 1) developed a simple frequency ramp model to initiate understanding of the Symbol Synchronizer Assembly (SSA) instability at low bit rates in narrow bandwidths. Part II, presented here, describes extensive data processing to develop a third-order phase model and then to translate all such processed data to the frequency realm for further analysis. The frequency study yields a long frequency modulation (FM) drift sinusoid (1600-s period), an impressed secondary drift wave with a period of about 116 s, and a set of even harmonics of twice the ramp period—the latter arising from, and used to modify, the phase detector model. The result is applied secondarily to estimate the strong-signal SSA phase detector response "out-of-lock." Finally, the main drift components are verified against all available data, and the result is used to estimate minimum lock conditions and the SSA drift effect under normal operating modes. The instability problem appears marginally resolvable if the acquisition technique is modified.

I. Spurious Drift Model Phase Reduction

An SSA simplified block diagram is shown in Fig. 1, with several parameters of the study noted. The loop phase error, point ①, affects the time pulses at point ②. The integrator varies in synchronization with the input symbol stream by this error. The output, absolved and combined with additive system noise, is then sampled over 30-s periods. The samples are appropriately combined in a common algorithm to yield sequential estimates of S/N in dB (point ③).

The S/N data in this study varied widely, indicating that the phase error was passing through all possible

values, and the loop was continually going "in- and out-of-lock," if the idea of "lock" applies at all under such conditions.

In order to study the phase error at point ①, from the data at point ③, and finally isolate the spurious phase behavior at the VCO output, point ②, it was necessary to perform several data reduction steps (see Table 1):

- (1) The effect of absolving the S/N computation input, and the addition of system noise at this point, must be removed. A very complicated algorithm due to Lesh (Ref. 1) yielded a curve that was empirically fit over the lower region after sys-

tem noise was removed by simple variance subtraction. The system noise, designated DBY, was estimated from the maximum S/N seen (+26 dB) during very-strong-signal runs.

- (2) The modified S/N, now approximately linear with signal, was reduced to phase equivalent and fit with a third-order polynomial across a subject out-of-lock ("ramp") data region. This fit gave an approximate function for use in the S/N computation model.
- (3) Since the phase varied across the sampling period, the phase equivalent and the true "central" phase during S/N computation differed.

Also, phase jitter and the phase variance across the sampling period appeared as additional noise, when the loop had no phase control. After some trial, the jitter effect was removed by simply dropping the input S/N (from 18 to 17.3 dB) and computing, then simply adding, the variance of the deterministic phase function within the period.

After all of the above effects were enacted, the resulting S/N was reduced to central phase estimates and compared with the original phase at (2) above. The differences were fit to a third-order curve designed to cancel the summation displacement effect, and the difference rms was evaluated. The process was iterated until the rms was below 1 deg. The final modified phase data (10 points) were considered to estimate the actual phase at central time of the S/N sampling period.

In order to find spurious drift accurately, it was necessary to remove loop "internal" effects due to phase detector response in the out-of-lock region. This response was simply modeled as a cosine wave with half-period of the ramp duration; the model was a rough approximation to common strong-signal analysis curves (see Table 2). The modified phase data were (again) fit to a third-order function, and this function became the argument for the phase detector model. The model was singly numerically integrated for the first-order filter effect and doubly numerically integrated for the second-order filter effect. The resulting sum phase was subtracted from the data phase and the process iterated until parameters stabilized. This yielded phase data substantially free of internal effects and a deterministic function expressing the residual model. This was the same point reached in Part I (Ref. 1), except that the data were "clean" and the spurious drift model was third-order. The process would not have been fully valid, except that the S/N sampling

period vastly increases S/N; the residual rms is less than 1.0 deg.

Investigation of the model immediately showed the value of the third-order term. In all trials, the second- and third-order term signs *opposed* one another, indicating a peak frequency near the center of the ramp period. Also, the second-order term was much smaller (0.8×10^{-6} vs. 4.4×10^{-6} Hz/s) than in Part I. These effects led to the conclusion that the data should be investigated in the frequency realm; the function was being masked by phase consideration only.

II. Spurious Drift Frequency Analysis

The final phase data from above, roughly free of all expected effects, were differenced analytically to obtain a frequency data set. They consisted of an obviously complicated waveform (about 0.5×10^{-3} Hz P-P) with a large offset (1.5×10^{-3} Hz) and a small negative ramp, as above. A program was established to process a "growing" FM model and compute differences and rms at each stage; semiautomated variation of parameter techniques were used (see Table 3):

- (1) The offset and ramp were estimated and removed. A predominant apparent sinusoid with a period of 116 s was the residual.
- (2) The sinusoid was estimated (amplitude and phase) and added.
- (3) Residuals with periods of about 240 and 60 s appeared, roughly 20 dB down. They were estimated and added.
- (4) The "raw" frequency of all available data (23 points) covering 1100 s was plotted. It showed a predominant "1 + cosine" waveform with a period of 1600 s and an amplitude of 1.56×10^{-3} Hz P-P. The "fine" data above were just beyond the "peak"; the zero was a long lock period about 15 min earlier. This was obviously the SSA "in-lock" start point. The original "ramp" was this drift near its small-slope maximum.
- (5) The main drift waveform was added, and a final component, with a period of about 480 s appeared. Also, a sharp triangle pattern of small amplitude was obvious.
- (6) When all the above components were combined and parameters "trimmed," the final rms was less than 0.001×10^{-3} Hz. This is meaningless, for it lies

beyond the data resolution. The final result is shown in Fig. 2. Except for the large waveform with a 116-s period, all components other than main drift form an even harmonic series, with the fundamental that of the cosine wave phase detector model. Such a series invariably describes some combination of half-wave rectification, with a "dead area." Thus, the harmonics, with some possible contribution from an indiscernible 120-s (fourth harmonic) wave, were attributed to the phase detector frequency function, the small "triangle" being the rate function residual. These were combined to yield an estimate of the phase detector function at strong signal, as shown in Fig. 3 after a single smoothing. Note the "dead area" at central period when the S/N is very small. This is possibly due to system noise effects during S/N reduction rather than being a phase detector characteristic.

Finally, it was confirmed from wideband data that the majority of the 116-s sine wave is *not* a phase detector phenomenon but rather is present as part of the drift—a secondary waveform of frequency so close to the fourth harmonic of the detector function (120-s period) that they cannot be distinguished. A check of wider-band data placed the period at the quoted 116 s.

The main ramp with this secondary component impressed is shown in Fig. 4, as noted. This result leads to the main conclusion of the analysis, that narrowband operation is limited by internal frequency drifts of the SSA. Note that all contributions in the loop except the main drift waveform lead to an rms of only 2 deg and are thus important only to describe the phase detector function.

III. Stability Criteria

The SSA stability is thus affected severely only by the main drift wave. In Part I, this was taken to be a simple frequency ramp; in this part, it has become evident as a sine wave with long period. It has a maximum rate of

$$\frac{0.76 \times 10^{-3} \pi}{800} = 3.0 \times 10^{-6} \text{ Hz/s} \quad (1)$$

This is some 15 times what can be simply tracked in the SSA narrow-narrow bandwidth at a data rate of 8½ bits/s.

However, since the disturbing drift appears to be sinusoidal FM, the "ramp" is of finite duration, following a

sine wave pattern. Its effect can be expressed, by integration, as a phase function:

$$\begin{aligned} \phi(t) &= 0.762 \int \left[1 + \cos \left(\frac{\pi}{800} t + \alpha \right) \right] dt + \phi_0 \\ &= 0.762t + \frac{0.762 \times 800}{\pi} \sin \left(\frac{\pi}{800} t + \alpha \right) + \phi_0 \\ \phi(t) \text{ deg} &= 0.762 \times 360 \times 10^{-3} t + \frac{0.762 \times 800}{\pi} \\ &\quad \times 360 \times 10^{-3} \sin \left(\frac{\pi}{800} t + \alpha \right) + \phi_0 \end{aligned}$$

or

$$\begin{aligned} \phi(t) \text{ deg} &= 0.273t + 69.3 \sin \left(\frac{2\pi}{1600} t + \alpha \right) + \phi_0 \\ &\approx 7.0 \times 10^{-7} t^3 \text{ at acquisition} \end{aligned} \quad (2)$$

This expression is quite significant. The frequency of the second term (1/1600 Hz) is below any tracking bandwidth in the SSA, and will be attenuated, or "tracked out," at least partially, under all operating conditions. In the narrow-bandwidth and 8½-bit/s condition, it is attenuated to an amplitude of only 19.5 deg rms, or marginally *within tracking range*; even the transient overshoot can possibly be handled. However, the leading term is present because acquisition takes place (zero frequency) at the negative extreme of the wave. This term, like a frequency step, cannot be "zeroed," or tracked with the sine wave present. A change in acquisition technique could possibly relieve this. Note the cubic approximation at present acquisition.

If acquisition "zero" took place at the wave midpoint, overshoot would only be to about 27 deg, and the frequency offset would be missing. Automated acquisition at the low-frequency extreme of the wave is the final basis for the instability behavior.

The secondary term leads to

$$\begin{aligned} \phi(t) &= 0.279 \int \cos \left[\frac{\pi}{58} t + \alpha_1 \right] + \phi_1 \\ \phi(t) \text{ deg} &= \frac{0.279 \times 58 \times 360 \times 10^{-3}}{\pi} \sin \left(\frac{\pi}{58} t + \alpha_1 \right) + \phi_1 \text{ deg} \\ &= 1.90 \text{ deg} \sin \left(\frac{\pi}{58} t + \alpha_1 \right) + \phi_1 \text{ deg} \end{aligned}$$

The frequency of this term is 0.0083 Hz, indicating prominence in the narrow-medium bandwidth, 8½-bit/s

configuration. The term is small but leads to variations of about 0.5 dB. Such variations were observed at a frequency with a period of about 116 s. As noted, this confirmed that the "fourth harmonic" was a true spurious component and not a phase detector harmonic.

Both the above components are small—"tracked-out"—in larger bandwidths. The larger component is less than 1.0 deg peak (0.13 dB) when the bandwidth is increased 4:1, to 0.00668 Hz. The secondary component becomes indistinguishable at all bandwidths above this.

The analytical expressions used in all the above descriptions are summarized, as noted, in Tables 1 through 3.

IV. Summary

Part I (Ref. 1) indicated the presence of a phase ramp rate (frequency drift) beyond narrowband tracking capability, but data only marginally conclusive. Part II investigated the S/N ratio data from the SSA for a number of phase and frequency effects: pre-absoluting, summation-period phase displacement, loop internal contributions, and finally, spurious frequency drift. The data were adjusted to remove all but the spurious products by data processing of out-of-lock points, translated to frequency using several iteration procedures. Both the strong-signal phase detector function and the drift process were mod-

eled, and the phase detector function was determined and sketched.

The spurious frequency drift model showed that the "ramp" of Part I was actually part of an FM sinusoid pair consisting of two components, a large one with a period of 1600 s and a secondary one with a period of about 116 s. Both presumably arose from the SSA search oscillator. The magnitude was compatible with manufacturers' specifications.

Phase functions of the frequency sinusoids were determined and analyzed. They have little effect above a bandwidth of 0.01 Hz but are important below this point. An approximate 0.5-dB jitter occurs at narrow-medium 8½ mode due to the secondary component, and lock is not possible in narrow-narrow 8½ mode, under present conditions, due to the major drift component offset.

Thus, the major conclusion of the entire study, Part I and Part II, is that a large FM internal drift is present (about 25-min period), together with a secondary FM drift (about 116-s period), and these drifts cannot presently be tracked in SSA bandwidths narrower than 0.01 Hz. Such bandwidths occur only in the narrowband SSA configuration. Even in this configuration, it appears that lock could be marginally held with the present drift if "in-lock" and oscillator-stop were declared in the "middle" of the drift cycle, when the oscillator ramp was greatest. This is not, however, the present mechanization.

References

1. Bunce, R. C., "Symbol Synchronization Assembly Instability Study: Part I," in *The Deep Space Network Progress Report 42-28*, pp. 95-105, Jet Propulsion Laboratory, Pasadena, Calif., Aug. 15, 1975.
2. Lesh, J. R., "Accuracy of the Signal-to-Noise Ratio Estimator," in *The Deep Space Network Progress Report*, Technical Report 32-1526, Vol. 10, pp. 217-235, Jet Propulsion Laboratory, Pasadena, Calif., Aug. 15, 1972.

Table 1. SSA S/N conversion to linear phase data

Step	Expressions	Definitions and notes
System noise removal	$DB_{1i} = -10 \log [10^{-(DBS_i/10)} - 10^{-(DBY/10)}]$	DBS_i = S/N data at T_i DBY = system S/N = 26 dB
Absolute correction (empirical fit)	$DBL_i = \begin{cases} DB_{1i} & DB_{1i} > 5 \\ DB_{1i} + \left[1 - \frac{6}{DB_{1i} + 1} \right] & DB_{1i} < 5 \end{cases}$	DBX = signal S/N = 17.3 dB in ramp
Initial phase estimate	$\hat{\phi}_{1i} = \frac{K}{2} \pm \frac{1}{4} \{1 - 10[(DBL_i - DBX)/20]\}$, cycles	$K = 0 \left\{ \begin{array}{l} \hat{\phi}_{1i} < 1/4 \\ \text{SIGN} = + \end{array} \right\}$ $K = 1 \left\{ \begin{array}{l} \hat{\phi}_{1i} > 1/4 \\ \text{SIGN} = - \end{array} \right\}$ } single ramp only
Correction for S/N central phase offset	$\hat{\phi}_{N_i} = a_{0N} + a_{1N}(\hat{\phi}_{1i}) + a_{2N}(\hat{\phi}_{1i})^2 + a_{3N}(\hat{\phi}_{1i})^3$	
Continuous phase function estimate	$\hat{\phi}_N(t) = b_{0N} + b_{1N} \cdot t + b_{2N} \cdot t^2 + b_{3N} \cdot t^3$	N = iteration index S = normalized signal level
S/N algorithm model (linearized by above reduction steps)	$\hat{R}_{N_i} = \frac{\bar{S}^2}{2\sigma_S^2} \quad \bar{S} = \frac{1}{31} \sum_{n=-15}^{15} [1 - 4\hat{\phi}_N(T_i)]$ $\sigma_S^2 = \frac{1}{R^*} = \frac{1}{31} \sum_{n=-15}^{15} [1 - 4\hat{\phi}_N(T_i) - \bar{S}]^2$	R^* = DBX converted to power ratio $a_{0N}, a_{1N}, a_{2N}, a_{3N}$ yielded by least-squares fit of set $\phi_{1i}, \hat{\phi}_{N_i}'$ $b_{0N}, b_{1N}, b_{2N}, b_{3N}$ yielded by least-squares fit of set $T_i, \hat{\phi}_{N_i}$
Phase differential computation and iteration	$\hat{\phi}_{N_i}' = \frac{K}{2} \pm \frac{1}{4} \left[1 - \frac{\hat{R}_{N_i}}{R^*} \right]$ yields the a_n with ϕ_{1i} set $\phi_{E_i} = (\hat{\phi}_{N_i} - \phi_{1i})$ if $\sigma_{\phi_E} < 1$ deg, iteration stopped	

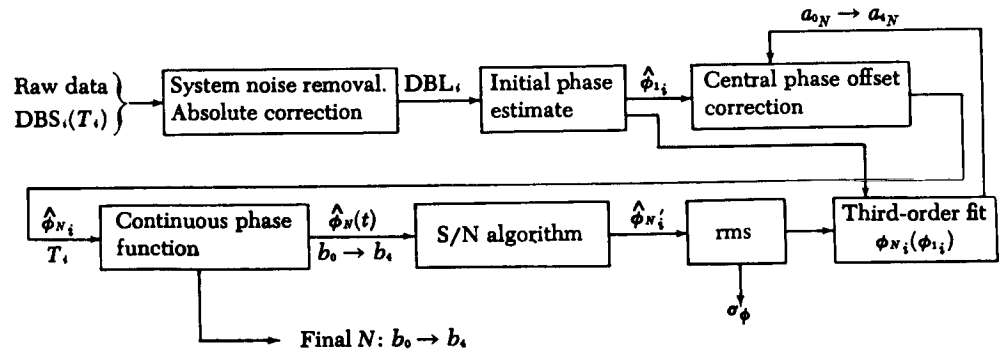


Table 2. Out-of-lock phase detector initial model

Step	Expressions	Definitions and notes
Initial empirical phase detector model	$\hat{V}(\phi) = V_{\max} \cos \left[2\pi \cdot \frac{4}{3} \cdot \left(\phi - \frac{1}{16} \right) \right]$	V = phase detector output voltage $\frac{4}{3}$ and $-\frac{1}{16}$
First-order phase term	$\dot{\phi}(V_{\max}) = -2W\Delta\phi_{\max} = -\frac{W}{8}$ $\hat{\phi}_{1i} = -\frac{W}{8} \int_0^{T_i} \cos \left\{ \frac{8\pi}{3} \left[\hat{\phi}_N(t) - \frac{1}{16} \right] \right\} dt$	Confine $\frac{1}{2}$ -cycle to ramp period W = loop bandwidth at $G \approx 2G_0; \quad \zeta = 1$
Second-order phase term	$\ddot{\phi}(V_{\max}) = -W^2\Delta\phi_{\max} = -\frac{W^2}{16}$ $\hat{\phi}_{2i} = -\frac{W^2}{16} \int_0^{T_i} \int_0^{\tau} \cos \left\{ \frac{8\pi}{3} \left[\hat{\phi}_N(t) - \frac{1}{16} \right] \right\} dt d\tau$	Integration numerically by machine $W = 0.00129 \text{ Hz}$ $W \cdot TS = 0.000155$
Phase correction	$\hat{\phi}_{1N_i}(t_i) = \hat{\phi}_{1i} + \hat{\phi}_{2i}$ $\hat{\phi}_{N_i} = (\hat{\phi}_{N-1i} - \hat{\phi}_{1N_i})$ $\hat{\phi}_N(t) = b_{0N} + b_{1N}t + b_{2N}t^2 + b_{3N}t^3$	$TS = \frac{1}{8\frac{1}{3}} = 0.120$ (strong signal)
Iteration stopped when parameters stabilize to 1×10^{-4} .		
Final parameter values for out-of-lock set chosen	$b_0 = 0.06252 \text{ cycles} = 22.51 \text{ deg}$ $b_1(0) = 0.94862 \text{ mHz}$ $2b_2(0) = 8.065 \text{ } \mu\text{Hz/s}$ $6b_3(0) = -0.0559806 \text{ } \mu\text{Hz/s}^2$	

Table 3. Frequency conversion and analysis

Step	Expressions	Definitions and notes
Phase to frequency conversion estimate	$F_i(T_i) = \frac{1}{2} \left[\frac{\phi_i - \phi_{i-1}}{T_i - T_{i-1}} + \frac{\phi_{i+1} - \phi_i}{T_{i+1} - T_i} \right]$	$F_R(t)$ = residual after estimating $F_N(t)$
Component analysis	$F_{N_i}(T_i) = \sum_{n=1}^{N-1} F_N(T_i) - F_i(T_i)$ $E_{N_i} = A_N \left\{ \begin{array}{l} \sin \\ \cos \end{array} \right\} (2\pi f_N T_i + a_N) - F_{N_i}(T_i)$ <p>σ_{E_N} minimized by variation of parameters A_N, f_N, a_N after observational estimates.</p>	One small component showed a triangular, rather than sinusoidal, form. It was apparently the phase detector model F residual, as noted.
Final equation ($\sigma_{E_N} < 10^{-4}F$) F , mHz $F_0 = 0.00209059$ Hz (period = 478.334 s)	$F(t) = 0.761658 \left[1 + \cos \left(\frac{2\pi}{1600} t + 0.12 \right) \right]$ $+ 0.003$ $- 0.2788 \cos \left[\frac{2\pi}{117.2} t + 0.133603 \right]$ <p style="text-align: center;">(secondary drift)</p> $+ 0.064 \sin (2\pi \cdot F_0 t + 0.1956)$ $- 0.052 \sin (2\pi \cdot 2F_0 t + 0.24886)$ $+ F(4F_0 t) \left\{ \begin{array}{l} \text{could not be distinguished} \\ \text{from secondary drift} \end{array} \right\}$ $+ 0.038665 \cos (2\pi \cdot 8F_0 t + 0.0)$ $- \left\{ \begin{array}{lll} 0.002 & - 0.000123t & t < 100 \\ 0.04216 + 0.000273t & & t > 100 \end{array} \right\}$	<p>phase detector model components (see text)</p> <p>model \dot{f} residual</p>

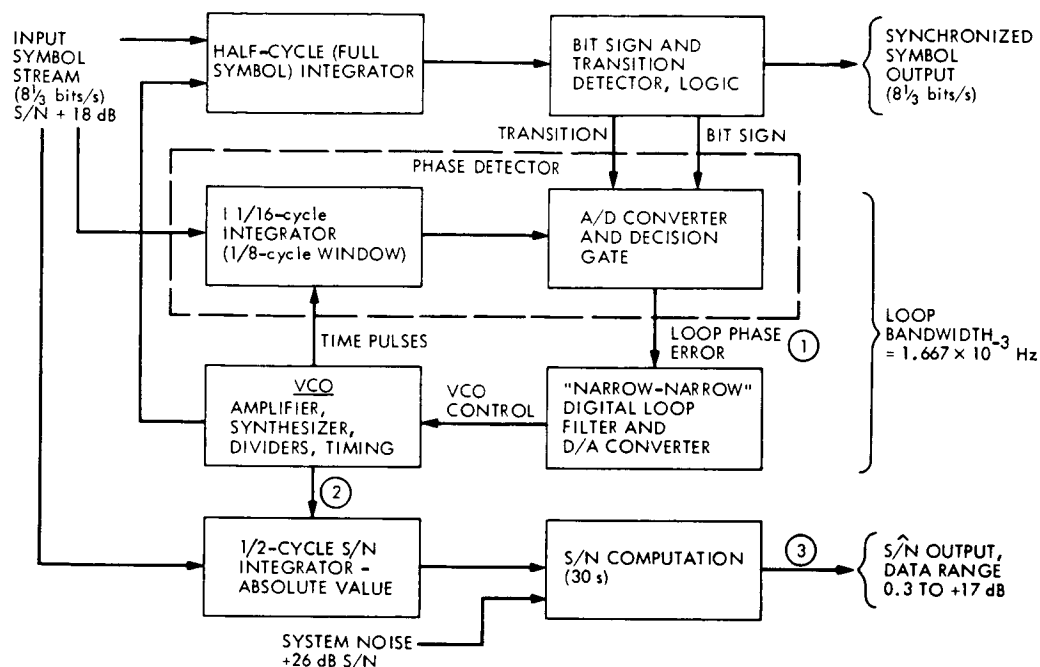


Fig. 1. SSA simplified block diagram with values noted while data were taken

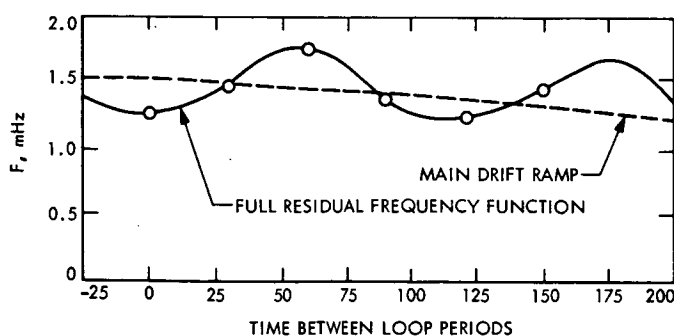


Fig. 2. SSA phase detector mean strong-signal characteristic (+18 dB S/N), as reconstructed from harmonic analysis of frequency data

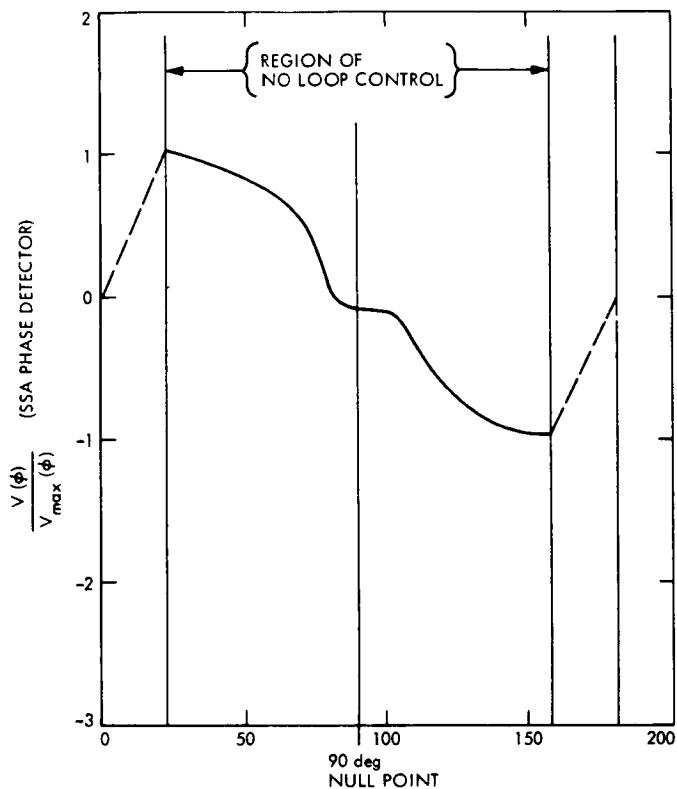


Fig. 3. Main drift and secondary wave adjusted for estimated fit to extended "raw" data

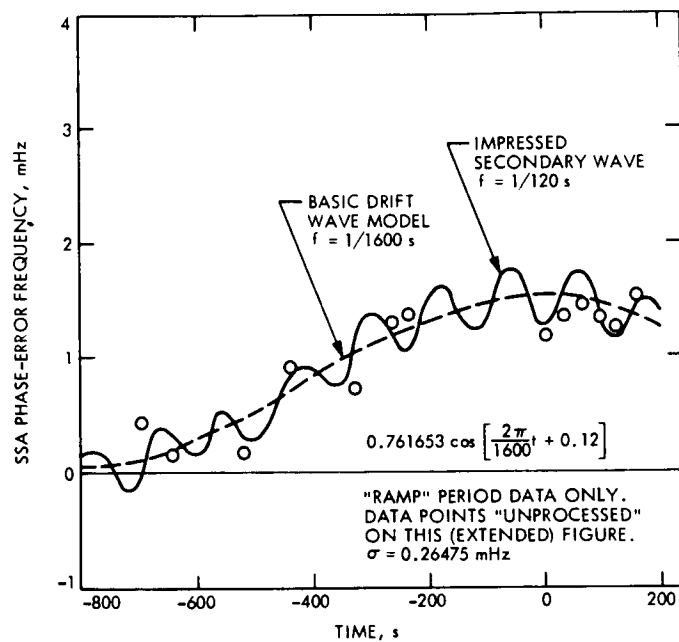


Fig. 4. Residual frequency function obtained by processing pre-adjusted phase data from SSA S/N output, narrow-narrow 8 1/3-bit/s mode

N76-15209

Analysis and Prediction of Doppler Noise During Solar Conjunctions

A. L. Berman and S. T. Rockwell
Network Operations Office

This report presents the results of a study of doppler data noise during solar conjunctions. During the first half of 1975, a sizeable data base of doppler data noise (estimates) for the Pioneer 10, Pioneer 11, and Helios 1 solar conjunctions was accumulated. To analyze these data, certain physical assumptions are made, leading to the development of a geometric parameter ("ISI") which correlates strongly with doppler data noise under varying Sun-Earth-spacecraft geometries. Doppler noise models are then constructed from this parameter, resulting in the newfound ability to predict doppler data noise during solar conjunctions, and hence to additionally be in a position to validate doppler data acquired during solar conjunctions.

I. Introduction

During past solar conjunctions, a large increase (sometimes greater than two orders of magnitude) in doppler data noise has invariably occurred. Other than the basic observation and noting of the phenomenon, little is known about the mechanisms which result in the noise or how to predict the phenomenon for future solar conjunctions. From the standpoint of the Deep Space Network (DSN), two very cogent requirements exist which deeply underscore the need for additional study in this area, to wit:

- (1) Prediction of doppler noise so that the generation of doppler data by the tracking system during solar conjunctions can be validated.
- (2) Prediction of doppler noise for future planning of critical mission phases. As a prime example, the Pioneer 11 Saturn encounter occurs during solar conjunction, and it would be extremely useful to know the expected quality of the doppler data during the encounter.

In the past, it has frequently been assumed that high doppler noise during solar conjunctions could be accounted for by some combination of the following possible effects:

- (1) Solar radiation and/or charged particles affecting the signal during transit.
- (2) Increase in system noise temperature or other possible solar/antenna effects.

It was the authors' surmise that (1), above, was far more likely to be the predominant effect, so this was initially chosen as the direction in which this investigation of solar conjunction doppler noise would proceed.

II. Accumulation of a Solar Conjunction Doppler Noise Data Base

In early 1975, it was decided to accumulate a solar conjunction doppler noise data base for subsequent study. The first half of 1975 was a fortuitous period for collection of such data as it was during this period that Pioneers 10 and 11 underwent superior solar conjunctions, while Helios 1 underwent both inferior and superior solar conjunctions. The minimum angular separations and dates of occurrence for these events are:

- (1) Pioneer 10 superior conjunction
Date of occurrence = April 4, 1975 (DOY 094)
Minimum angular separation = 1.9 deg
- (2) Pioneer 11 superior conjunction
Date of occurrence = March 25, 1975 (DOY 084)
Minimum angular separation = 2.0 deg
- (3) Helios 1 inferior conjunction
Date of occurrence = February 19, 1975 (DOY 050)
Minimum angular separation = 0.5 deg
- (4) Helios 1 superior conjunction
Date of occurrence = May 6, 1975 (DOY 126)
Minimum angular separation = 0.4 deg

The doppler noise data were accumulated over the following intervals:

Mission	Start (DOY)	End (DOY)
Pioneer 10	064	166
Pioneer 11	061	163
Helios 1	063	166

and consist of an "average doppler noise" value for each pass (tracked) during the preceding periods. Obviously, then, each "average doppler noise" value is completely specified by three parameters:

- (1) Spacecraft
- (2) Deep Space Station (DSS)
- (3) Pass (actually date of pass)

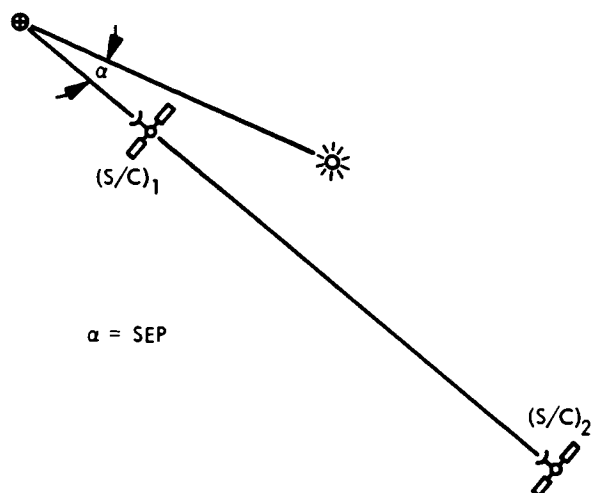
The "average doppler noise" values were obtained by manually scanning the Network Operations Control Center (NOCC) pseudoresidual output for each pass and selecting the three best (in the sense of smallest) groups of 10 to 20 values of running standard deviation (noise). The data considered were restricted to good, two-way, 60-second-sample-rate doppler data. An average value for each of the three groups was estimated and recorded, and, finally, the three group estimates were averaged to produce the "pass average." It is immediately obvious that the results obtained are the "best" (smallest noise) possible, and that one should consider that these data define the lower boundary of a band of possible noise which might be obtained on the dates the data were taken. This process was chosen because it was felt that the same process could easily be duplicated day after day, whereas any other more general averaging technique would be more difficult and less useful, because during these high noise periods, the pseudoresidual output frequently oscillates to almost meaninglessly high values.

The accumulated data comprise Tables 1, 2, and 3. Additionally, the data are plotted versus Sun-Earth-probe (SEP) angle and Earth-Sun-probe (ESP) angle in Figs. 1 through 6. The data were plotted as a function of both SEP and ESP because doppler noise is obviously a very strong function of either angle, and yet the angles, under varying Sun-Earth-spacecraft geometries, can behave (as, say, a function of time) in quite dissimilar fashions. Finally, the data in Figs. 1 through 6 are presented so that one can easily distinguish between station complexes and between 64-meter and 26-meter stations.

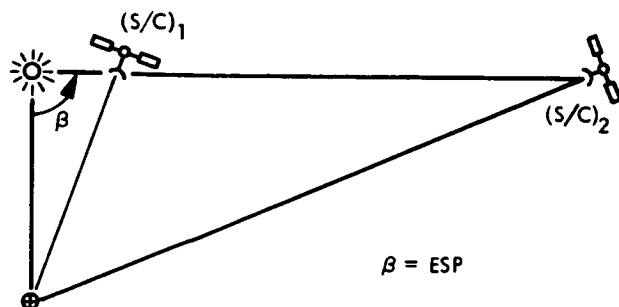
III. Consideration of Solar Effects During Signal Transit

It was originally intended to accomplish a strictly empirical fit of the collected noise data to the SEP angle or, perhaps, the ESP angle. However, it immediately strikes one that neither seems to be uniquely qualified to serve

as an independent variable. For instance, if one considers the SEP angle:



Obviously, in the above sketch, solar effects on the (S/C)₂ signal will be far higher than on the (S/C)₁ signal, and yet the spacecraft have identical SEP angles. In a similar vein, consider the ESP angle:



Equally obvious, the solar effects on the (S/C)₁ signal will be far higher than on the (S/C)₂ signal, and yet the spacecraft have identical ESP angles. It is an inescapable conclusion that neither of these angles alone, although both showing a strong functional relationship to doppler noise, is capable of serving as a reasonable independent variable for an empirical representation of doppler noise. At this point, it was felt that perhaps an elementary consideration of solar effects might shed some clues as to a more beneficial approach to the evaluation and prediction of doppler noise during solar conjunctions.

It would seem that one might expect the signal at any point to be corrupted by the solar emitted electromag-

netic field energy (flux) and/or the density of solar emitted charged particles. These two possible sources of signal corruption will be considered very briefly below, as will the conclusion to be drawn from their consideration.

A. Solar Electromagnetic Energy Flux

One can start by writing the expression for the rate of production of energy within an arbitrary finite volume:

$$\int_V \mathbf{J} \cdot \mathbf{E} dV$$

where

\mathbf{J} = current density

\mathbf{E} = electric field intensity

Now, using the Ampère/Maxwell law,

$$\nabla \times \mathbf{H} = \frac{4\pi}{c} \mathbf{J} + \frac{1}{c} \frac{\partial \mathbf{D}}{\partial t}$$

where

\mathbf{H} = magnetic field intensity

c = speed of light

\mathbf{D} = electric displacement

one obtains

$$\int_V \mathbf{J} \cdot \mathbf{E} dV = \int_V \frac{c}{4\pi} \left\{ \nabla \times \mathbf{H} - \frac{1}{c} \frac{\partial \mathbf{D}}{\partial t} \right\} \cdot \mathbf{E} dV$$

using the vector identity

$$\nabla \cdot (\mathbf{F} \times \mathbf{G}) = \mathbf{G} \cdot (\nabla \times \mathbf{F}) - \mathbf{F} \cdot (\nabla \times \mathbf{G})$$

so that

$$\nabla \cdot (\mathbf{E} \times \mathbf{H}) = \mathbf{H} \cdot (\nabla \times \mathbf{E}) - \mathbf{E} \cdot (\nabla \times \mathbf{H})$$

one would have

$$\int_V \mathbf{J} \cdot \mathbf{E} dV = \int_V \frac{c}{4\pi} \left\{ \mathbf{H} \cdot (\nabla \times \mathbf{E}) - \nabla \cdot (\mathbf{E} \times \mathbf{H}) - \frac{1}{c} \frac{\partial \mathbf{D}}{\partial t} \cdot \mathbf{E} \right\} dV$$

By applying Faraday's law

$$\nabla \times \mathbf{E} = -\frac{1}{c} \frac{\partial \mathbf{B}}{\partial t}$$

where \mathbf{B} is the magnetic induction, one obtains

$$\begin{aligned} \int_V \mathbf{J} \cdot \mathbf{E} dV &= \int_V \frac{c}{4\pi} \left\{ -\mathbf{H} \cdot \frac{1}{c} \frac{\partial \mathbf{B}}{\partial t} \right. \\ &\quad \left. - \nabla \cdot (\mathbf{E} \times \mathbf{H}) - \frac{1}{c} \frac{\partial \mathbf{D}}{\partial t} \cdot \mathbf{E} \right\} dV \\ &= - \int_V \frac{c}{4\pi} \{ \nabla \cdot (\mathbf{E} \times \mathbf{H}) \} dV \\ &\quad + \int_V -\frac{1}{4\pi} \left\{ \mathbf{H} \cdot \frac{\partial \mathbf{B}}{\partial t} + \frac{\partial \mathbf{D}}{\partial t} \cdot \mathbf{E} \right\} dV \end{aligned}$$

since

$$\mathbf{B} = \mu \mathbf{H}$$

and

$$\mathbf{D} = \epsilon \mathbf{E}$$

where

ϵ = dielectric constant

μ = permeability constant

combined with differentiation of a vector dot product

$$\frac{\partial}{\partial t} (\mathbf{F} \cdot \mathbf{G}) = \mathbf{F} \cdot \frac{\partial \mathbf{G}}{\partial t} + \frac{\partial \mathbf{F}}{\partial t} \cdot \mathbf{G}$$

yields

$$\mathbf{H} \cdot \frac{\partial \mathbf{B}}{\partial t} + \mathbf{E} \cdot \frac{\partial \mathbf{D}}{\partial t} = \frac{1}{2} \left\{ \frac{\partial}{\partial t} [\mathbf{H} \cdot \mathbf{B} + \mathbf{E} \cdot \mathbf{D}] \right\}$$

Finally, utilizing the divergence theorem

$$\int_V \nabla \cdot \mathbf{F} dV = \oint_A \mathbf{F} \cdot d\mathbf{A}$$

or

$$\int_V \frac{c}{4\pi} \nabla \cdot (\mathbf{E} \times \mathbf{H}) dV = \oint_A \frac{c}{4\pi} (\mathbf{E} \times \mathbf{H}) \cdot d\mathbf{A}$$

one arrives at the Poynting theorem:

$$\begin{aligned} \int_V \mathbf{J} \cdot \mathbf{E} dV &= - \oint_A \frac{c}{4\pi} (\mathbf{E} \times \mathbf{H}) \cdot d\mathbf{A} \\ &\quad - \frac{\partial}{\partial t} \int_V \frac{1}{8\pi} \{ \mathbf{H} \cdot \mathbf{B} + \mathbf{E} \cdot \mathbf{D} \} dV \end{aligned}$$

The theorem basically states that the production of energy within a volume equals the time rate of change of the density of energy within a volume plus the amount of energy flux through the closed surface of the volume. The quantity of interest here is the Poynting vector (\mathbf{S}),

$$\mathbf{S} = \frac{c}{4\pi} (\mathbf{E} \times \mathbf{H}), \quad \text{in watts/meter}^2$$

where \mathbf{S} represents the energy flux at a given point. The Poynting theorem then becomes

$$\begin{aligned} \int_V \mathbf{J} \cdot \mathbf{E} dV &= - \oint_A \mathbf{S} \cdot d\mathbf{A} \\ &\quad - \frac{\partial}{\partial t} \int_V \frac{1}{8\pi} \{ \mathbf{H} \cdot \mathbf{B} + \mathbf{E} \cdot \mathbf{D} \} dV \end{aligned}$$

One can now make some assumptions which greatly simplify the expression:

- (1) *Solar Steady State.* It is assumed that solar radiation is in approximate equilibrium; hence

$$\frac{\partial}{\partial t} \int_V \frac{1}{8\pi} \{ \mathbf{H} \cdot \mathbf{B} + \mathbf{E} \cdot \mathbf{D} \} dV \approx 0$$

- (2) *Constant Production of Solar Energy.* It is assumed that the production of solar energy is approximately constant; hence

$$\int_V \mathbf{E} \cdot \mathbf{J} dV \approx -K_0$$

with the result that

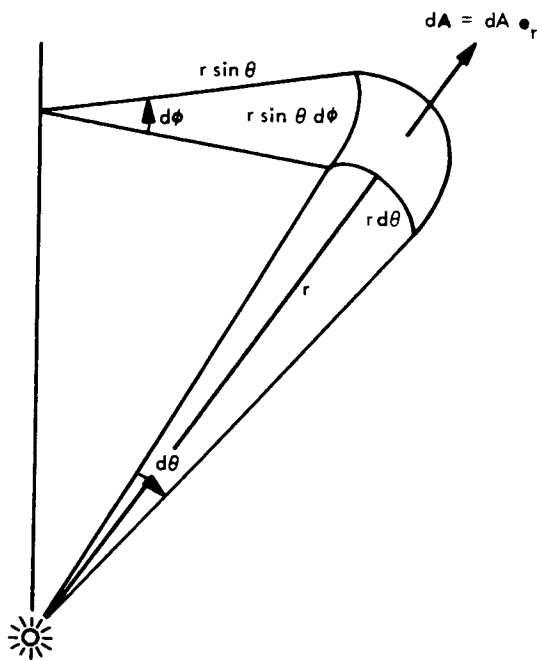
$$\oint_A \mathbf{S} \cdot d\mathbf{A} \approx K_0$$

- (3) *Spherical Uniformity of Solar Radiation.* It is assumed that solar radiation is spherically uniform, so that \mathbf{S} can only depend on the r coordinate and

can only have a component in the \mathbf{e}_r direction, i.e.,

$$\mathbf{S} = S(r) \mathbf{e}_r$$

considering a small element of surface dA



or

$$\begin{aligned} dA &= (r d\theta) (r \sin \theta d\phi) \mathbf{e}_r \\ &= r^2 \sin \theta d\theta d\phi \mathbf{e}_r \end{aligned}$$

so that

$$\begin{aligned} \oint_A \mathbf{S} \cdot d\mathbf{A} &= \int_0^{2\pi} \int_0^\pi S(r) \mathbf{e}_r \cdot r^2 \sin \theta d\theta d\phi \mathbf{e}_r \\ &= S(r) r^2 (\mathbf{e}_r \cdot \mathbf{e}_r) \int_0^{2\pi} \left[\int_0^\pi \sin \theta d\theta \right] d\phi \\ &= 2\pi S(r) r^2 \int_0^\pi \sin \theta d\theta \\ &= 4\pi S(r) r^2 \end{aligned}$$

or, finally,

$$S(r) \approx \frac{K_0}{4\pi r^2}$$

or, essentially, that solar electromagnetic radiation is proportional to $(r)^{-2}$

$$S(r) \propto \frac{1}{r^2}$$

B. Solar Emission of Charged Particles

If one could assume that charged particles are emitted spherically uniform and at a constant rate, one would define:

N = number of charged particles/second emitted by the Sun perpendicular to the surface

v_N = (uniform) particle velocity

Then, at any subsequent radius r , there will be contained in a spherical shell of volume ΔV

$$\Delta V = v_N \{4\pi r^2\} \Delta t$$

$N\Delta t$ particles, or a particle density ρ_N of

$$\rho_N \approx \frac{N\Delta t}{v_N 4\pi r^2 \Delta t} \approx \frac{N}{v_N 4\pi r^2}$$

which is just to say in a very rough sense that

$$\text{charged-particle density} \propto \frac{1}{r^2}$$

C. Final Premise for Investigation of Solar Conjunction Doppler Noise

Subsections A and B, above, indicate that the types of solar effects which might figure in the corruption of signals in transit all seem to be at least (roughly) proportional to $(r)^{-2}$. This motivates the following assumptions, which can then (possibly) be combined to construct an independent variable for correlation and prediction of solar induced doppler noise:

- (1) Assume signal corruption proportional to total length of time exposed to electromagnetic energy flux and charged particles.
- (2) Assume signal corruption proportional to intensity of electromagnetic energy flux and charged particles at any given instant.

Combining the above, let R be the path length between spacecraft and DSS. It is then hypothesized that

$$\begin{aligned} \text{Signal corruption} &\propto \int_{\text{DSS}}^{\text{S/C}} [\text{intensity}] dt \\ &= \int_0^R \left[\frac{1}{r^2} \right] \left\{ \frac{dR}{c} \right\} \end{aligned}$$

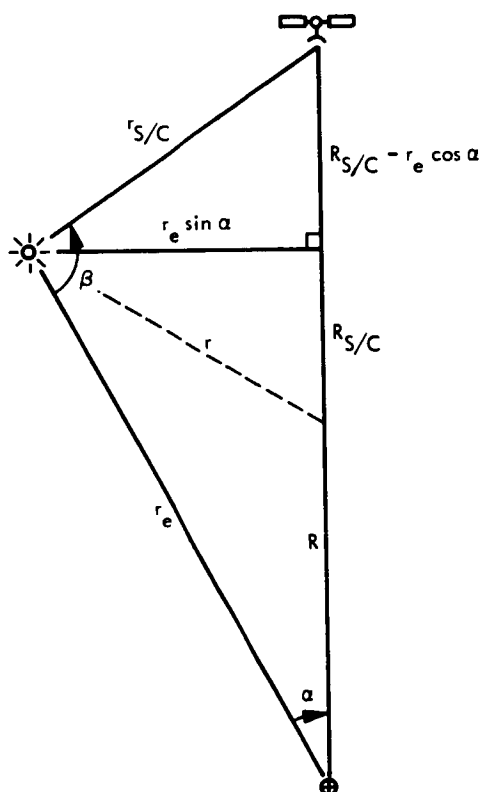
Thus a quantity *ISI* (integrated solar intensity) is formulated here to be

$$ISI = K \int_0^R \left(\frac{1}{r^2} \right) dR$$

where r is the distance to the Sun from any point on the signal path. If the hypothesis has any validity, then the quantity *ISI* might indeed be a reasonable candidate for a parametric representation of solar induced noise. The closed form solution of *ISI* is presented in the following section.

IV. Determination of the Parameter ISI

The Sun-Earth-spacecraft geometry can be seen in the accompanying sketch.



By the law of cosines

$$r^2 = R^2 + r_e^2 - 2Rr_e \cos \alpha$$

where

$r_{S/C}$ = spacecraft-Sun distance

r = distance from Sun to signal

R = distance along Earth-spacecraft line of sight

r_e = Earth-Sun distance

$R_{S/C}$ = Earth-spacecraft distance

α = Sun-Earth-probe angle

β = Earth-Sun-probe angle

so that

$$\begin{aligned} ISI &= K \int_0^{R_{S/C}} \frac{dR}{r^2} \\ &= K \int_0^{R_{S/C}} \frac{dR}{R^2 + r_e^2 - 2Rr_e \cos \alpha} \\ &= K \int_0^{R_{S/C}} \frac{dR}{(R^2 - 2Rr_e \cos \alpha + r_e^2 \cos^2 \alpha) + r_e^2 - r_e^2 \cos^2 \alpha} \\ &= K \int_0^{R_{S/C}} \frac{dR}{(R - r_e \cos \alpha)^2 + r_e^2 (1 - \cos^2 \alpha)} \\ &= K \int_0^{R_{S/C}} \frac{dR}{(R - r_e \cos \alpha)^2 + r_e^2 \sin^2 \alpha} \end{aligned}$$

Let

$$x = R - r_e \cos \alpha$$

$$dx = dR$$

$$a = r_e \sin \alpha$$

so that

$$\begin{aligned} ISI &= K \int_{-r_e \cos \alpha}^{R_{S/C} - r_e \cos \alpha} \frac{dx}{x^2 + a^2} \\ &= \frac{K}{a^2} \int_{-r_e \cos \alpha}^{R_{S/C} - r_e \cos \alpha} \frac{dx}{\left(\frac{x^2}{a^2} + 1 \right)} \end{aligned}$$

Now let

$$\frac{x}{a} = \tan w$$

$$dx = a \sec^2 w dw$$

so that

$$ISI = \frac{K}{a^2} \int_{\tan^{-1} \left(\frac{-r_e \cos \alpha}{a} \right)}^{\tan^{-1} \left(\frac{R_{S/C} - r_e \cos \alpha}{a} \right)} \frac{a \sec^2 w dw}{\tan^2 w + 1}$$

$$= \frac{K}{a} \int_{\tan^{-1}\left(\frac{-r_e \cos \alpha}{a}\right)}^{\tan^{-1}\left(\frac{R_{s/c} - r_e \cos \alpha}{a}\right)} dw$$

$$= \frac{K}{a} \left\{ \tan^{-1}\left(\frac{R_{s/c} - r_e \cos \alpha}{a}\right) - \tan^{-1}\left(\frac{-r_e \cos \alpha}{a}\right) \right\}$$

Since $a = r_e \sin \alpha$,

$$ISI = \frac{K}{r_e \sin \alpha} \left\{ \tan^{-1}\left(\frac{R_{s/c} - r_e \cos \alpha}{r_e \sin \alpha}\right) - \tan^{-1}(-\cot \alpha) \right\}$$

and from the sketch

$$R_{s/c} - r_e \cos \alpha = r_e \sin \alpha \left[\tan \left(\beta - \left\{ \frac{\pi}{2} - \alpha \right\} \right) \right]$$

combined with

$$\cot \alpha = \tan \left(\frac{\pi}{2} - \alpha \right)$$

yield

$$ISI = \frac{K}{r_e \sin \alpha} \left\{ \tan^{-1} \left[\tan \left(\beta - \frac{\pi}{2} + \alpha \right) \right] - \tan^{-1} \left[-\tan \left(\frac{\pi}{2} - \alpha \right) \right] \right\}$$

$$= \frac{K}{r_e \sin \alpha} \left\{ \beta - \frac{\pi}{2} + \alpha - \left(\alpha - \frac{\pi}{2} \right) \right\}$$

$$= \frac{K}{r_e \sin \alpha} \{\beta\} = \frac{K\beta}{r_e \sin \alpha}$$

K will be chosen to be

$$K = r_e \{1/\text{degrees}\}$$

so that ISI will be a unitless number when $\beta = \beta$ (degrees)

$$ISI = ISI(\alpha, \beta) = \frac{\beta}{\sin \alpha}$$

V. Correlation of ISI Versus Doppler Noise

All doppler noise data accumulated in the data base were plotted against the corresponding ISI number and can be seen in Fig. 7. It is obvious that there exists a strong correlation between observed doppler noise and ISI on a

multimission basis, and hence tends to confirm the hypothesis that ISI might represent an attractive independent variable for a doppler noise model. The hypothesis was of the form:

$$NOISE_L = C_1 \{ISI\} + C_2$$

The nominal noise (i.e., when not in solar conjunction) is considered to be approximately 0.003 Hz. Furthermore, since the correlation of doppler noise versus ISI displays a fair scatter, a reasonable set of C_1 and C_2 can be selected without the necessity of resorting to rigorous methods. The following were chosen:

$$C_1 = 3.1277 \times 10^{-5}$$

$$C_2 = -6.3831 \times 10^{-3}$$

so that the noise model $NOISE_L$ (for "linear") is defined as:

$$NOISE_L (\text{Hz}) = \begin{cases} 0.003, & ISI \leq 300 \\ C_1 \{ISI\} + C_2, & ISI > 300 \end{cases}$$

This model can be seen as plotted in Fig. 7. However, from mere observation of Fig. 7, it can be seen that a more reasonable fit to the data would be a slightly "stronger" function of ISI , say, in the form of:

$$NOISE_P = K_1 (ISI)^{1+K_2}$$

K_1 and K_2 were selected to be:

$$K_1 = 2.8 \times 10^{-6}$$

$$K_2 = 2.9 \times 10^{-1}$$

so that a noise model $NOISE_P$ (for "power") is defined as follows:

$$NOISE_P (\text{Hz}) = \begin{cases} 0.003, & ISI \leq 223 \\ K_1 (ISI)^{1+K_2}, & ISI > 223 \end{cases}$$

This model is also seen in Fig. 7.

In Figs. 8, 9, and 10, the observed doppler noise data have been plotted against ISI , and, additionally, the $NOISE_L$ and $NOISE_P$ models are included, for Pioneer 10, Pioneer 11, and Helios 1, respectively. As can be seen, the models are more reasonable for the composite doppler noise data set than they are for any of the individual

mission doppler noise data sets. These differences can be categorized as follows:

- (1) The Helios 1 observed noise data are considerably higher than the models for moderate and high *ISI*.
- (2) The Pioneer 11 observed noise data are considerably lower than the models for moderate and high *ISI*.
- (3) The Pioneer 10 observed noise data are slightly higher than the models at high *ISI*.

These differences are analyzed in detail in the following article (Ref. 1) in this Progress Report.

Tables 1, 2, and 3 present the complete data base and related *ISI* information for Pioneer 10, Pioneer 11, and Helios 1. Indicated in the tables are the following parameters:

- (1) Station (DSS)
- (2) DOY (day of year of pass)
- (3) Noise (Hz)
- (4) α (deg)
- (5) β (deg)
- (6) *ISI* (unitless)

VI. Behavior of the Quantity *ISI* for Differing Sun-Earth-Spacecraft Geometries

It is now reasonable to briefly examine the behavior of the quantity *ISI* under varying circumstances and perhaps adduce some generalities in regard to dominant characteristics displayed by *ISI* for differing Sun-Earth-spacecraft geometries.

A. Superior Conjunctions

Obviously, the major functional nature of the quantity *ISI* is almost completely determined by the quantity $(\sin \alpha)^{-1}$ as β is practically constant (~ 180 deg) when α becomes very small; hence for superior conjunctions

$$\text{Doppler noise} \propto \frac{1}{\sin \alpha}$$

B. Inferior Conjunctions

At inferior conjunctions, the *ISI* is extremely small. For instance, assume a spacecraft at 0.5 AU so that for small

α , one has

$$\alpha \approx \beta$$

and

$$ISI = \frac{\beta(\text{deg})}{\sin \alpha} = \left(\frac{180}{\pi} \right) \frac{\beta(\text{radians})}{\sin \alpha}$$

and since

$$\sin \alpha \approx \alpha \approx \beta$$

then

$$ISI \approx \frac{180}{\pi}$$

One would therefore expect no appreciable increase in doppler noise during inferior conjunctions. Helios 1 underwent inferior conjunction on February 18, 1975 and no increase in doppler noise during the period immediately surrounding February 18 was noted.

C. Helios 1 Perihelion

On March 15, 1975, Helios 1 underwent its first perihelion passage, and this represents a unique geometrical configuration to test the hypothesis from which the quantity *ISI* was generated. Over a small matter of days, while α was nearly constant ($16 \text{ deg} \lesssim \alpha \lesssim 18 \text{ deg}$), β swung from approximately 30 to 110 deg. During this interval, *ISI* became appreciable (i.e., ~ 300) when β reached approximately 85 deg. At this point, doppler noise should have begun to increase according to the proposed models, but mostly due to changing β , in sharp contrast to the more frequent superior conjunctions when almost the entire increase in doppler noise is due to changing α . Figure 11 shows the region described above, and, as predicted, the noise at *ISI* ~ 300 begins to increase, thereby lending additional confirmation to the original hypothesis from which *ISI* was derived.

D. Maximum Doppler Noise

If one considers the below conditions as lending to the maximum possible solar induced doppler noise (i.e., just prior to solar occultation),

$$\alpha \approx 0.25 \text{ deg}$$

$$\beta \approx 180 \text{ deg}$$

so that

$$ISI \approx 41,300$$

yielding

$$NOISE_L \approx 1.3 \text{ Hz}$$

$$NOISE_P \approx 2.5 \text{ Hz}$$

As a way of comparison, the highest noise recorded in this study was for Helios 1 superior conjunction:

$$\text{Doppler noise} \approx 1.7 \text{ Hz}$$

and Yip et. al., in Fig. 13 of Ref. 2, indicate a maximum obtained noise for Mariner Mars 1971 of

$$\text{Doppler noise} \approx 1.5 \text{ Hz}$$

E. Comparison to Theory

In 1970, D. O. Muhleman et. al. (Ref. 3) computed (the equivalent of) doppler noise from scintillation theory; his theoretical model is compared to $NOISE_P$ in Fig. 12. The theoretical model for all but the smallest α is far below the $NOISE_P$ model and, of course, the observed noise; however, this is not surprising as Yip et. al. (Ref. 2) made a similar observation in 1974.

In summation, the functional behavior of the quantity ISI matches the observed doppler noise at superior conjunctions, inferior conjunctions, and Helios 1 perihelion and, hence, tends to strengthen confidence in the original hypothesis and the derivative models.

VII. Summary

During early 1975, a large data base of doppler noise data was accumulated for the solar conjunctions of Pioneer 10, Pioneer 11, and Helios 1. In analyzing these

data, certain elementary physical assumptions about the nature of solar-induced corruption of doppler data were made, with the result being the development of a parameter " ISI " which is solely dependent on a given Sun-Earth-spacecraft geometry, viz:

$$ISI(\alpha, \beta) = \frac{\beta}{\sin \alpha}$$

where

α = Sun-Earth-probe angle

β = Earth-Sun-probe angle

This parameter is shown to correlate strongly with observed doppler noise on a multimission basis, and, additionally, functionally matches observed doppler noise for three radically different types of Earth-Sun-spacecraft geometries:

- (1) Superior solar conjunctions
- (2) Inferior solar conjunctions
- (3) Helios 1 perihelion

Using the parameter ISI , a noise model ($NOISE_P$) is presented for operations usage:

$$NOISE_P(\text{Hz}) = \begin{cases} 0.003, & ISI \leq 223 \\ K_1 (ISI)^{1+K_2}, & ISI > 223 \end{cases}$$

where

$$K_1 = 2.8 \times 10^{-6}$$

$$K_2 = 2.9 \times 10^{-1}$$

The above model should allow for preplanning of critical mission phases which intersect solar conjunctions and also for routine validation of doppler data quality and tracking system performance during solar conjunctions.

Acknowledgment

The authors would like to acknowledge Larry E. Bright for technical consultation, M. Leung for collection of the data, and M. F. Cates for the very fine graphical illustrations.

References

1. Berman, A. L., and Rockwell, S. T., "Correlation of Doppler Noise During Solar Conjunctions With Fluctuations in Solar Activity," in *The Deep Space Network Progress Report 42-30* (this volume), Jet Propulsion Laboratory, Pasadena, Calif., Dec. 15, 1975.
2. Yip, K. W., Winn, F. B., and Reinbold, S. J., "DSN-MVM'73 S/X Dual-Frequency Doppler Demonstration During Superior Conjunction," in *The Deep Space Network Progress Report 42-25*, pp. 47-55, Jet Propulsion Laboratory, Pasadena, Calif., Feb. 15, 1975.
3. Muhleman, D. O., Anderson, J. D., Esposito, P. B., and Martin, W. L., "Radio Propagation Measurements of the Solar Corona and Gravitational Field; Applications to Mariner 6 and 7," in *Proceedings of the Conference on Experimental Tests of Gravitational Theories*, California Institute of Technology, Pasadena, Calif., Nov. 1970.

Table 1. Pioneer 10 solar conjunction, 1975

Deep Space Station (DSS)	Day of year (DOY)	Average doppler noise, Hz	Sun-Earth-probe angle α , deg	Earth-Sun-probe angle β , deg	Integrated solar intensity (ISI)
11	65	0.0076	23.18	153.58	390
11	66	0.0078	22.34	154.50	406
11	67	0.0102	21.52	155.42	424
11	70	0.0121	19.11	158.17	483
11	72	0.0173	17.50	160.00	532
11	74	0.0120	15.90	161.83	591
11	77	0.0115	13.51	164.56	705
11	78	0.0139	12.71	165.47	752
11	79	0.0147	11.92	166.38	806
11	80	0.0151	11.13	167.28	867
11	82	0.0221	9.55	169.08	1019
11	83	0.0407	8.77	169.98	1115
11	109	0.0213	12.28	166.00	781
11	110	0.0173	13.07	165.11	730
12	76	0.0139	14.30	163.65	662
14	88	0.1240	4.94	174.35	2025
14	89	0.1900	4.21	175.19	2386
14	90	0.1173	3.51	175.98	2874
14	91	0.0950	2.87	176.72	3529
14	117	0.0054	18.59	158.84	498
14	128	0.0117	27.34	148.98	324
14	130	0.0073	28.94	147.20	304
14	131	0.0045	29.74	146.30	295
14	138	0.0069	35.35	140.05	242
14	140	0.0034	36.97	138.26	230
14	142	0.0056	38.58	136.48	219
14	144	0.0041	40.20	134.70	209
14	145	0.0037	41.01	133.81	204
14	146	0.0029	41.82	132.91	199
14	149	0.0038	44.25	130.24	187
14	150	0.0040	45.07	129.35	183
14	151	0.0032	45.88	128.46	179
14	161	0.0036	54.11	119.56	148
42	64	0.0051	23.94	152.66	376
42	65	0.0122	23.18	153.58	390
42	68	0.0081	20.72	156.34	442
42	70	0.0138	19.11	158.17	483
42	71	0.0128	18.30	159.09	507
42	136	0.0174	33.75	141.83	255
42	137	0.0075	34.55	140.94	249
42	139	0.0112	36.16	139.15	236
43	84	0.0385	7.99	170.87	1229
43	85	0.0345	7.21	171.75	1368
43	89	0.1167	4.21	175.19	2386

Table 1 (contd)

Deep Space Station (DSS)	Day of year (DOY)	Average doppler noise, Hz	Sun-Earth-probe angle α , deg	Earth-Sun-probe angle β , deg	Integrated solar intensity (ISI)
43	98	0.0647	3.87	175.58	2602
43	99	0.0545	4.58	174.77	2189
43	100	0.0393	5.38	173.93	1856
43	104	0.0343	8.37	170.45	1171
43	106	0.0208	9.93	168.67	978
43	108	0.0297	11.49	166.89	838
43	109	0.0163	12.28	166.00	781
43	111	0.0132	13.85	164.21	686
43	112	0.0096	14.64	163.32	646
43	113	0.0059	15.43	162.42	610
43	114	0.0049	16.22	161.53	578
43	115	0.0050	17.01	160.63	549
43	118	0.0052	19.38	157.94	476
43	120	0.0042	20.97	156.15	436
43	121	0.0097	21.77	155.25	419
43	122	0.0053	22.56	154.36	402
43	124	0.0066	24.15	152.57	373
43	159	0.0032	52.45	121.34	153
43	160	0.0034	53.28	120.45	150
43	161	0.0039	54.11	119.56	148
43	162	0.0038	54.93	118.67	145
44	74	0.0183	15.90	161.83	591
44	77	0.0147	13.51	164.56	705
44	80	0.0298	11.13	167.28	867
44	81	0.0157	10.34	168.18	937
44	120	0.0118	20.97	156.15	436
61	64	0.0083	23.94	152.66	376
61	66	0.0055	22.34	154.50	406
61	72	0.0160	17.50	160.00	532
61	83	0.0323	8.77	169.98	1115
61	135	0.0120	32.94	142.73	262
61	149	0.0110	44.25	130.24	187
62	147	0.0032	42.63	132.02	195
63	70	0.0082	19.11	158.17	483
63	74	0.0108	15.90	161.83	591
63	81	0.0089	10.34	168.18	937
63	85	0.0291	7.21	171.75	1368
63	86	0.0670	6.45	172.63	1538
63	87	0.0813	5.69	173.50	1751
63	88	0.0950	4.94	174.35	2025
63	89	0.0950	4.21	175.19	2386
63	90	0.0960	3.51	175.98	2874
63	91	0.1490	2.87	176.72	3529

Table 1 (contd)

Deep Space Station (DSS)	Day of year (DOY)	Average doppler noise, Hz	Sun-Earth-probe angle α , deg	Earth-Sun-probe angle β , deg	Integrated solar intensity (ISI)
63	92	0.1570	2.33	177.34	4362
63	94	0.1703	1.90	177.83	5364
63	99	0.0615	4.58	174.77	2189
63	100	0.0487	5.38	173.93	1856
63	101	0.0413	6.09	173.07	1632
63	102	0.0391	6.83	172.20	1448
63	105	0.0232	9.15	169.56	1067
63	106	0.0236	9.93	168.67	978
63	107	0.0236	10.71	167.78	903
63	108	0.0214	11.49	166.89	838
63	109	0.0225	12.28	166.00	781
63	110	0.0159	13.07	165.11	730
63	111	0.0099	13.85	164.21	686
63	112	0.0082	14.64	163.32	646
63	113	0.0061	15.43	162.42	610
63	115	0.0048	17.01	160.63	549
63	116	0.0046	17.80	159.73	523
63	117	0.0043	18.59	158.84	498
63	118	0.0046	19.38	157.94	476
63	120	0.0033	20.97	156.15	436
63	121	0.0099	21.77	155.25	419
63	122	0.0066	22.56	154.36	402
63	123	0.0049	23.35	153.46	387
63	124	0.0046	24.15	152.57	373
63	125	0.0091	24.95	151.67	360
63	126	0.0063	25.74	150.78	347
63	127	0.0096	26.54	149.88	335
63	128	0.0076	27.34	148.98	324
63	130	0.0096	28.94	147.20	304
63	131	0.0079	29.74	146.30	295
63	132	0.0072	30.54	145.41	286
63	133	0.0046	31.34	144.51	278
63	134	0.0103	32.14	143.62	270
63	136	0.0154	33.75	141.83	255
63	137	0.0065	34.55	140.94	249
63	138	0.0054	35.35	140.05	242
63	139	0.0049	36.16	139.15	236
63	140	0.0030	36.97	138.26	230
63	141	0.0030	37.77	137.37	224
63	143	0.0031	39.39	135.59	214
63	144	0.0028	40.20	134.70	209
63	145	0.0027	41.01	133.81	204
63	148	0.0031	43.44	131.13	191
63	150	0.0032	45.07	129.35	183
63	151	0.0025	45.88	128.46	179
63	152	0.0031	46.70	127.57	175
63	153	0.0037	47.52	126.68	172

Table 1 (contd)

Deep Space Station (DSS)	Day of year (DOY)	Average doppler noise, Hz	Sun-Earth-probe angle α , deg	Earth-Sun-probe angle β , deg	Integrated solar intensity (ISI)
63	154	0.0030	48.34	125.79	168
63	156	0.0027	49.98	124.01	162
63	157	0.0024	50.80	123.12	159
63	158	0.0028	51.63	122.23	156
63	159	0.0025	52.45	121.34	153
63	161	0.0027	54.11	119.56	148
63	162	0.0031	54.93	118.67	145
63	163	0.0040	55.76	117.79	142
63	164	0.0033	56.60	116.90	140
63	165	0.0029	57.43	116.01	138

Table 2. Pioneer 11 solar conjunction, 1975

Deep Space Station (DSS)	Day of year (DOY)	Average doppler noise, Hz	Sun-Earth probe angle α , deg	Earth-Sun-probe angle β , deg	Integrated solar intensity (ISI)
11	76	0.0235	5.22	173.63	1905
11	87	0.0350	3.56	175.64	2829
11	89	0.0227	4.80	174.12	2081
11	90	0.0203	5.45	173.33	1825
11	91	0.0255	6.11	172.51	1621
11	92	0.0230	6.78	171.69	1454
11	93	0.0211	7.45	170.87	1318
11	94	0.0200	8.13	170.03	1203
11	95	0.0139	8.81	169.20	1105
11	98	0.0196	10.86	166.68	885
11	103	0.0116	14.29	162.46	658
12	61	0.0170	15.84	160.75	589
12	64	0.0111	13.66	163.38	692
12	66	0.0187	12.22	165.12	780
12	67	0.0172	11.50	165.99	833
12	69	0.0223	10.07	167.72	959
12	70	0.0216	9.36	168.58	1037
12	71	0.0218	8.66	169.44	1125
12	72	0.0473	7.95	170.29	1231
12	74	0.0307	6.57	171.98	1503
12	100	0.0165	12.23	164.99	779
12	104	0.0122	14.98	161.62	625
12	108	0.0112	17.73	158.25	520
12	109	0.0172	18.41	157.40	498
12	110	0.0088	19.10	156.56	478
12	111	0.0078	19.79	155.72	460
12	112	0.0119	20.47	154.88	443
12	113	0.0043	21.16	154.04	427
12	114	0.0033	21.84	153.20	412
12	115	0.0034	22.53	152.36	398
12	116	0.0037	23.21	151.53	384
12	117	0.0033	23.90	150.69	372
12	119	0.0038	25.27	149.01	349
12	122	0.0040	27.32	146.51	319
12	123	0.0046	28.00	145.67	310
12	124	0.0041	28.69	144.84	302
12	125	0.0071	29.37	144.01	294
12	126	0.0051	30.05	143.17	286
12	127	0.0080	30.74	142.34	278
12	129	0.0056	32.11	140.68	265
12	130	0.0039	32.89	139.85	258
12	131	0.0057	33.48	139.02	252
12	132	0.0069	34.16	138.19	246
12	135	0.0033	36.22	135.71	230
12	136	0.0077	36.90	134.89	225
12	137	0.0032	37.59	134.06	220

Table 2 (contd)

Deep Space Station (DSS)	Day of year (DOY)	Average doppler noise, Hz	Sun-Earth probe angle α , deg	Earth-Sun-probe angle β , deg	Integrated solar intensity (ISI)
12	138	0.0044	38.27	133.24	215
12	139	0.0047	38.96	132.41	211
12	140	0.0053	39.64	131.59	206
12	144	0.0025	42.39	128.30	190
12	145	0.0033	43.07	127.49	187
12	146	0.0029	43.76	126.67	183
12	147	0.0035	44.45	125.85	180
12	148	0.0034	45.14	125.03	176
12	149	0.0029	45.83	124.21	173
12	150	0.0030	46.52	123.40	170
12	151	0.0026	47.21	122.58	167
12	152	0.0054	47.90	121.76	164
12	153	0.0031	48.59	120.95	161
12	154	0.0044	49.28	120.13	159
12	155	0.0028	49.98	119.32	156
12	156	0.0027	50.67	118.51	153
12	158	0.0026	52.06	116.88	148
12	159	0.0025	52.76	116.07	146
12	160	0.0026	53.45	115.25	143
12	161	0.0024	54.15	114.44	141
12	162	0.0044	54.85	113.63	139
12	163	0.0051	55.55	112.82	137
14	82	0.1217	2.04	177.50	4986
14	83	0.0973	1.97	177.58	5166
14	85	0.0573	2.51	176.93	4040
14	129	0.0053	32.11	140.68	265
14	157	0.0025	51.36	117.69	151
42	82	0.1583	2.04	177.50	4986
42	135	0.0050	36.22	135.71	230
42	140	0.0032	39.64	131.59	206
42	148	0.0031	45.14	125.03	176
42	158	0.0023	52.06	116.88	148
43	88	0.0343	4.17	174.90	2405
43	102	0.0143	13.61	163.31	694
43	103	0.0125	14.29	162.46	658
43	107	0.0127	17.04	159.09	543
43	120	0.0037	25.95	148.18	339
44	65	0.0175	12.94	164.25	733
44	66	0.0145	12.22	165.12	780
44	67	0.0206	11.50	165.99	833
44	69	0.0225	10.07	167.72	959
44	70	0.0252	9.36	168.58	1037
44	73	0.0338	7.26	171.14	1354

Table 2 (contd)

Deep Space Station (DSS)	Day of year (DOY)	Average doppler noise, Hz	Sun-Earth probe angle α , deg	Earth-Sun-probe angle β , deg	Integrated solar intensity (ISI)
44	75	0.0285	5.89	172.81	1684
44	89	0.0403	4.80	174.12	2081
44	90	0.0230	5.45	173.33	1825
44	96	0.0152	9.49	168.36	1021
44	98	0.0150	10.86	166.68	885
44	99	0.0148	11.55	165.84	828
44	100	0.0258	12.23	164.99	779
44	104	0.0139	14.98	161.62	625
44	105	0.0111	15.67	160.78	595
44	106	0.0136	16.35	159.93	568
44	108	0.0132	17.73	158.25	520
44	109	0.0153	18.41	157.40	498
44	110	0.0097	19.10	156.56	478
44	111	0.0063	19.79	155.72	460
44	112	0.0075	20.47	154.88	443
44	113	0.0041	21.16	154.04	427
44	114	0.0053	21.84	153.20	412
44	115	0.0050	22.53	152.36	398
44	116	0.0049	23.21	151.53	384
44	117	0.0048	23.90	150.69	372
44	118	0.0045	24.58	149.85	360
44	119	0.0052	25.27	149.01	349
44	121	0.0064	26.63	147.34	329
44	122	0.0058	27.32	146.51	319
44	123	0.0049	28.00	145.67	310
44	136	0.0084	36.90	134.89	225
44	137	0.0045	37.59	134.06	220
44	138	0.0040	38.27	133.24	215
44	139	0.0055	38.96	132.41	211
44	141	0.0037	40.33	130.77	202
44	143	0.0036	41.70	129.12	194
44	144	0.0034	42.39	128.30	190
44	145	0.0040	43.07	127.49	187
44	146	0.0037	43.76	126.67	183
44	147	0.0041	44.45	125.85	180
44	149	0.0043	45.83	124.21	173
44	150	0.0046	46.52	123.40	170
44	151	0.0038	47.21	122.58	167
44	152	0.0047	47.90	121.76	164
44	153	0.0052	48.59	120.95	161
44	154	0.0059	49.28	120.13	159
44	155	0.0053	49.98	119.32	156
44	156	0.0044	50.67	118.51	153
44	157	0.0049	51.36	117.69	151
44	159	0.0042	52.76	116.07	146
44	160	0.0032	53.45	115.25	143
44	161	0.0044	54.15	114.44	141
44	162	0.0044	54.85	113.63	139

Table 2 (contd)

Deep Space Station (DSS)	Day of year (DOY)	Average doppler noise, Hz	Sun-Earth probe angle α , deg	Earth-Sun-probe angle β , deg	Integrated solar intensity (ISI)
61	63	0.0075	14.38	162.51	654
61	64	0.0124	13.66	163.38	692
61	65	0.0142	12.94	164.25	733
61	68	0.0215	10.78	166.86	892
61	70	0.0280	9.36	168.58	1037
61	72	0.0333	7.95	170.29	1231
61	73	0.0275	7.26	171.14	1354
61	74	0.0278	6.57	171.98	1503
61	75	0.0467	5.89	172.81	1684
61	88	0.0340	4.17	174.90	2405
61	89	0.0207	4.80	174.12	2081
61	90	0.0243	5.45	173.33	1825
61	91	0.0208	6.11	172.51	1621
61	92	0.0237	6.78	171.69	1454
61	94	0.0260	8.13	170.03	1203
61	95	0.0155	8.81	169.20	1105
61	97	0.0163	10.17	167.52	949
61	98	0.0177	10.86	166.68	885
61	99	0.0201	11.55	165.84	828
61	100	0.0136	12.23	164.99	779
61	101	0.0129	12.92	164.15	734
61	102	0.0164	13.61	163.31	694
61	104	0.0125	14.98	161.62	625
61	105	0.0129	15.67	160.78	595
61	106	0.0107	16.35	159.93	568
61	107	0.0088	17.04	159.09	543
61	108	0.0125	17.73	158.25	520
61	109	0.0117	18.41	157.40	498
61	110	0.0124	19.10	156.56	478
61	111	0.0080	19.79	155.72	460
61	112	0.0065	20.47	154.88	443
61	113	0.0048	21.16	154.04	427
61	114	0.0035	21.84	153.20	412
61	118	0.0041	24.58	149.85	360
61	119	0.0036	25.27	149.01	349
61	120	0.0038	25.95	148.18	339
61	129	0.0053	32.11	140.68	265
61	130	0.0052	32.89	139.85	258
61	132	0.0062	34.16	138.19	246
61	133	0.0033	34.85	137.37	240
61	137	0.0064	37.59	134.06	220
61	138	0.0038	38.27	133.24	215
61	139	0.0040	38.96	132.41	211
61	140	0.0032	39.64	131.59	206
61	141	0.0032	40.33	130.77	202
61	145	0.0026	43.07	127.49	187
61	151	0.0032	47.21	122.58	167

Table 2 (contd)

Deep Space Station (DSS)	Day of year (DOY)	Average doppler noise, Hz	Sun-Earth probe angle α , deg	Earth-Sun-probe angle β , deg	Integrated solar intensity (ISI)
61	152	0.0028	47.90	121.76	164
61	153	0.0034	48.59	120.95	161
61	158	0.0025	52.06	116.88	148
61	162	0.0029	54.85	113.63	139
61	163	0.0035	55.55	112.82	137
62	117	0.0051	23.90	150.69	372
62	121	0.0044	26.63	147.34	329
62	122	0.0077	27.32	146.51	319
62	123	0.0046	28.00	145.67	310
62	124	0.0045	28.69	144.84	302
62	125	0.0051	29.37	144.01	294
62	126	0.0071	30.05	143.17	286
62	127	0.0078	30.74	142.34	278
62	128	0.0067	31.42	141.51	271
62	131	0.0059	33.48	139.02	252
62	133	0.0087	34.85	137.37	240
62	135	0.0041	36.22	135.71	230
62	136	0.0123	36.90	134.89	225
62	142	0.0032	41.01	129.95	198
62	143	0.0036	41.70	129.12	194
62	146	0.0032	43.76	126.67	183
62	147	0.0034	44.45	125.85	180
62	148	0.0032	45.14	125.03	176
62	149	0.0037	45.83	124.21	173
62	150	0.0036	46.52	123.40	170
62	154	0.0038	49.28	120.13	159
62	155	0.0037	49.98	119.32	156
62	156	0.0031	50.67	118.51	153
62	159	0.0029	52.76	116.07	146
62	160	0.0032	53.45	115.25	143
62	161	0.0031	54.15	114.44	141
63	77	0.0326	4.56	174.43	2194
63	78	0.0587	3.93	175.20	2556
63	79	0.0550	3.33	175.93	3029
63	80	0.0540	2.78	176.60	3641
63	82	0.0850	2.04	177.50	4986
63	83	0.1060	1.97	177.58	5166
63	84	0.0613	2.14	177.38	4750
63	85	0.0737	2.51	176.93	4040
63	86	0.0490	3.00	176.33	3369
63	155	0.0028	49.98	119.32	156

Table 3. Helios 1 solar conjunction, 1975

Deep Space Station (DSS)	Day of year (DOY)	Average doppler noise, Hz	Sun-Earth probe angle α , deg	Earth-Sun-probe angle β , deg	Integrated solar intensity (ISI)
12	63	0.0041	16.21	29.90	107
12	75	0.0050	17.17	91.94	311
12	79	0.0197	14.89	114.51	446
12	88	0.0109	9.18	149.12	935
12	89	0.0099	8.61	151.68	1013
12	90	0.0112	8.07	154.03	1097
12	91	0.0198	7.56	156.19	1187
12	92	0.0253	7.06	158.19	1287
12	93	0.0255	6.59	160.03	1394
12	94	0.0727	6.14	161.73	1512
12	95	0.0527	5.71	163.29	1641
12	98	0.1293	4.55	167.28	2109
12	99	0.0790	3.57	170.41	2737
12	101	0.1153	4.21	168.41	2294
12	102	0.2017	3.28	171.30	2994
14	64	0.0044	16.84	33.62	116
14	65	0.0033	17.37	37.64	126
14	66	0.0054	17.80	41.96	137
14	67	0.0031	18.14	46.59	150
14	69	0.0057	18.49	56.74	179
14	70	0.0063	18.51	62.23	196
14	73	0.0037	17.97	79.85	259
14	74	0.0053	17.61	85.91	284
14	76	0.0074	16.67	97.87	341
14	77	0.0118	16.11	103.64	374
14	78	0.0132	15.52	109.20	408
14	81	0.0164	13.59	124.24	529
14	83	0.0211	12.27	132.76	625
14	84	0.0190	11.62	136.57	678
14	85	0.0177	10.98	140.09	736
14	86	0.0103	10.36	143.35	797
14	96	0.0631	5.30	164.73	1783
14	97	0.1460	4.92	166.06	1936
14	100	0.1210	3.88	169.45	2504
14	103	0.2000	3.01	172.11	3278
14	104	0.2783	2.76	172.86	3590
14	109	0.5433	1.72	175.76	5856
14	110	0.7050	1.56	176.20	6472
14	111	0.4893	1.41	176.60	7177
14	112	0.5500	1.27	176.96	7984
14	113	0.5133	1.14	177.28	8911
14	114	0.8800	1.03	177.57	9878
14	115	0.8367	0.92	177.83	11075
14	117	1.7333	0.75	178.26	13618
14	138	1.5933	0.91	178.09	11213
14	150	0.3583	2.01	175.86	5014
14	166	0.1267	3.96	171.96	2490

Table 3 (contd)

Deep Space Station (DSS)	Day of year (DOY)	Average doppler noise, Hz	Sun-Earth probe angle α , deg	Earth-Sun-probe angle β , deg	Integrated solar intensity (ISI)
42	84	0.0252	11.62	136.57	678
42	88	0.0133	9.18	149.12	935
42	89	0.0108	8.61	151.68	1013
42	90	0.0127	8.07	154.03	1097
42	98	0.0793	4.55	167.28	2109
42	99	0.0823	4.21	168.41	2294
42	100	0.0790	3.88	169.45	2504
42	101	0.1150	3.57	170.41	2737
42	150	0.4283	2.01	175.86	5014
42	154	0.2300	2.47	174.94	4059
43	63	0.0049	16.21	29.90	107
43	65	0.0048	17.37	37.64	126
43	66	0.0052	17.80	41.96	137
43	67	0.0033	18.14	46.59	150
43	69	0.0046	18.49	56.74	179
43	70	0.0051	18.51	62.23	196
43	73	0.0039	17.97	79.85	259
43	80	0.0134	14.24	119.52	486
43	81	0.0148	13.59	124.24	529
43	83	0.0248	12.27	132.76	625
43	84	0.0161	11.62	136.57	678
43	85	0.0157	10.98	140.09	736
43	86	0.0129	10.36	143.35	797
43	96	0.0385	5.30	164.73	1783
44	92	0.0313	7.06	158.19	1287
44	93	0.0387	6.59	160.03	1394
44	94	0.0565	6.14	161.73	1512
44	95	0.0451	5.71	163.29	1641
44	97	0.0893	4.92	166.06	1936
44	103	0.2083	3.01	172.11	3278
62	64	0.0072	16.84	33.62	116
62	65	0.0036	17.37	37.64	126
62	72	0.0032	18.25	73.84	236
62	73	0.0068	17.97	79.85	259
62	76	0.0081	16.67	97.87	341
62	79	0.0230	14.89	114.51	446
62	86	0.0137	10.36	143.35	797
62	93	0.0723	6.59	160.03	1394
62	100	0.0707	3.88	169.45	2504

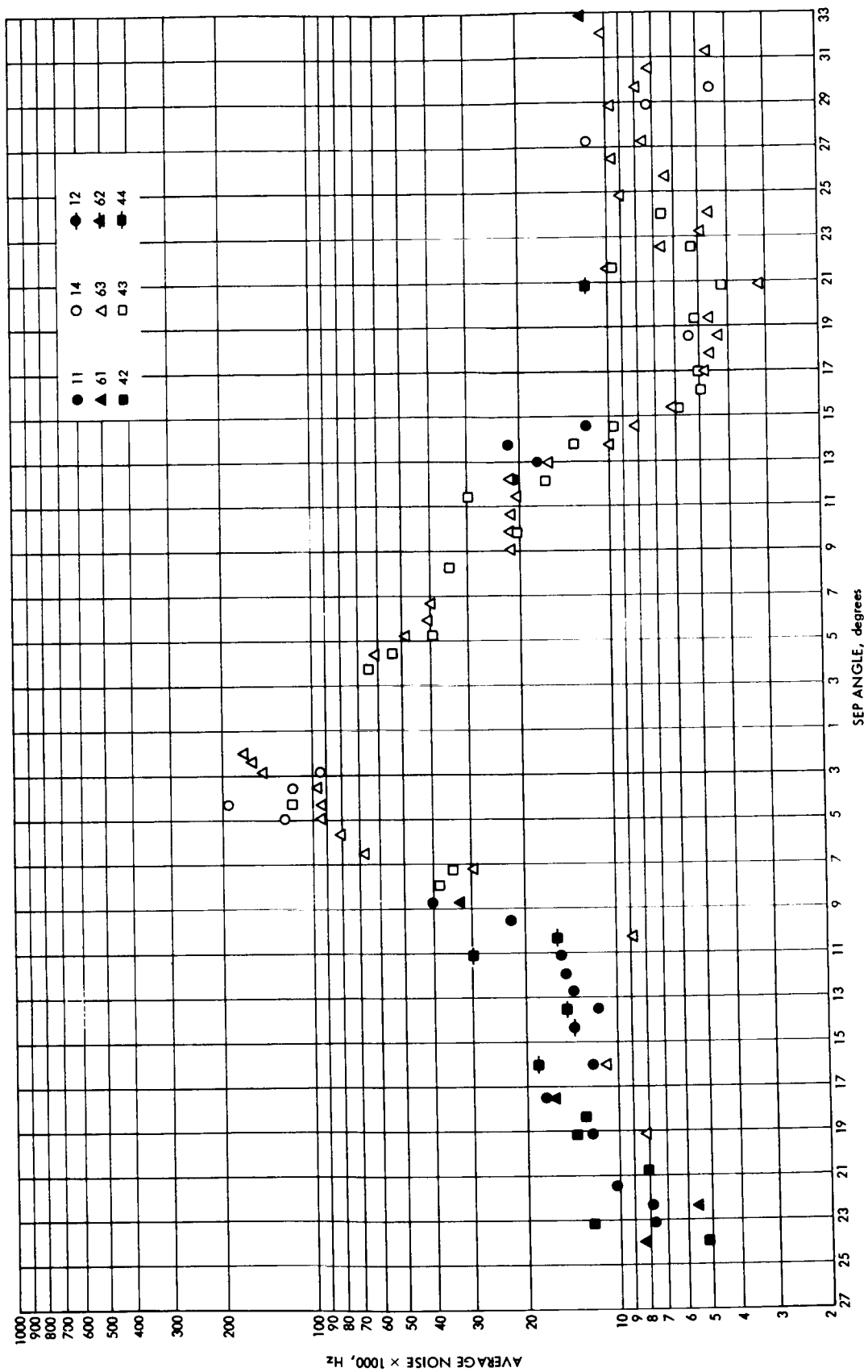


Fig. 1. Pioneer 10 average noise vs SEP angle

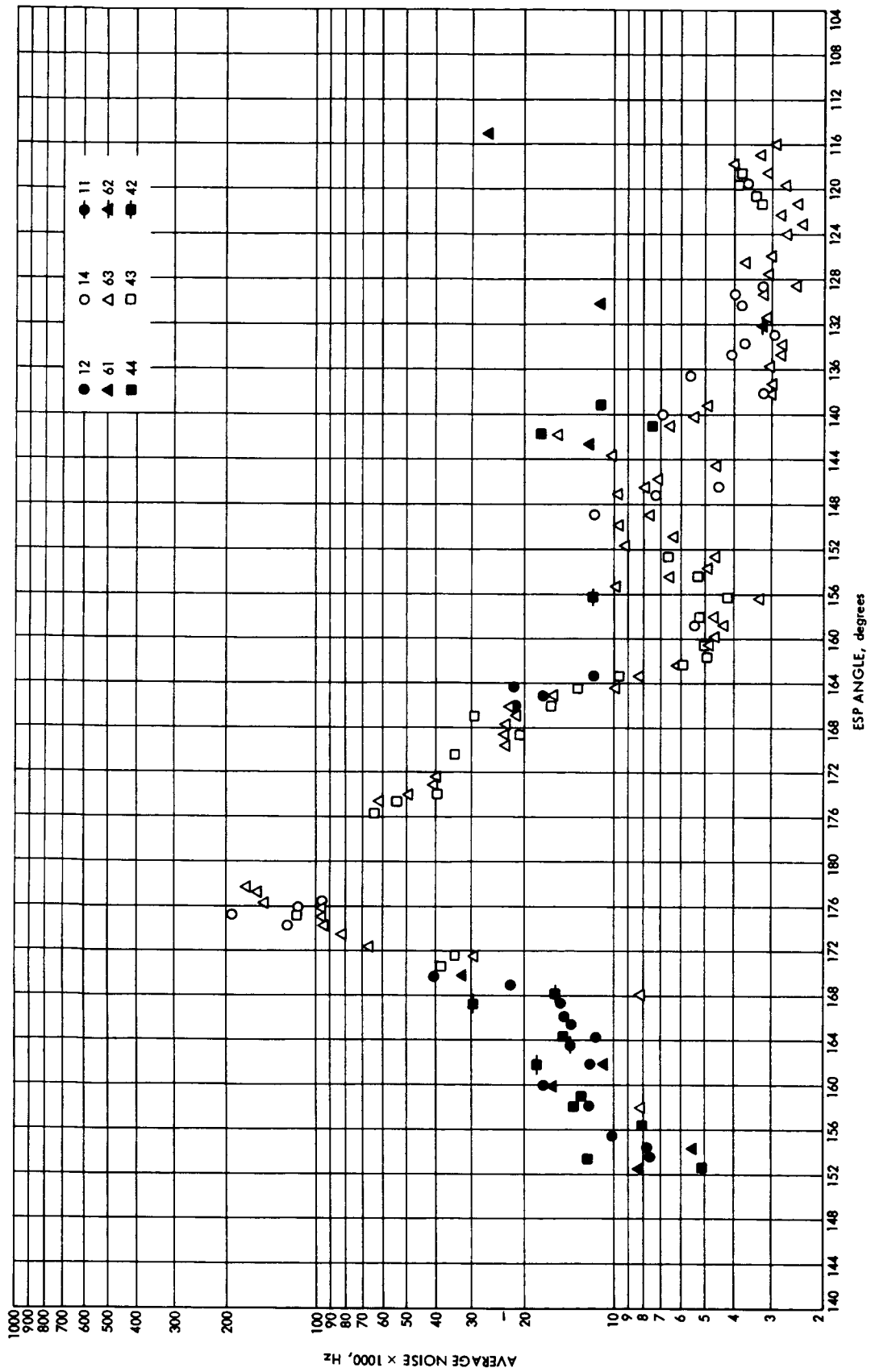


Fig. 2. Pioneer 10 average noise vs ESP angle

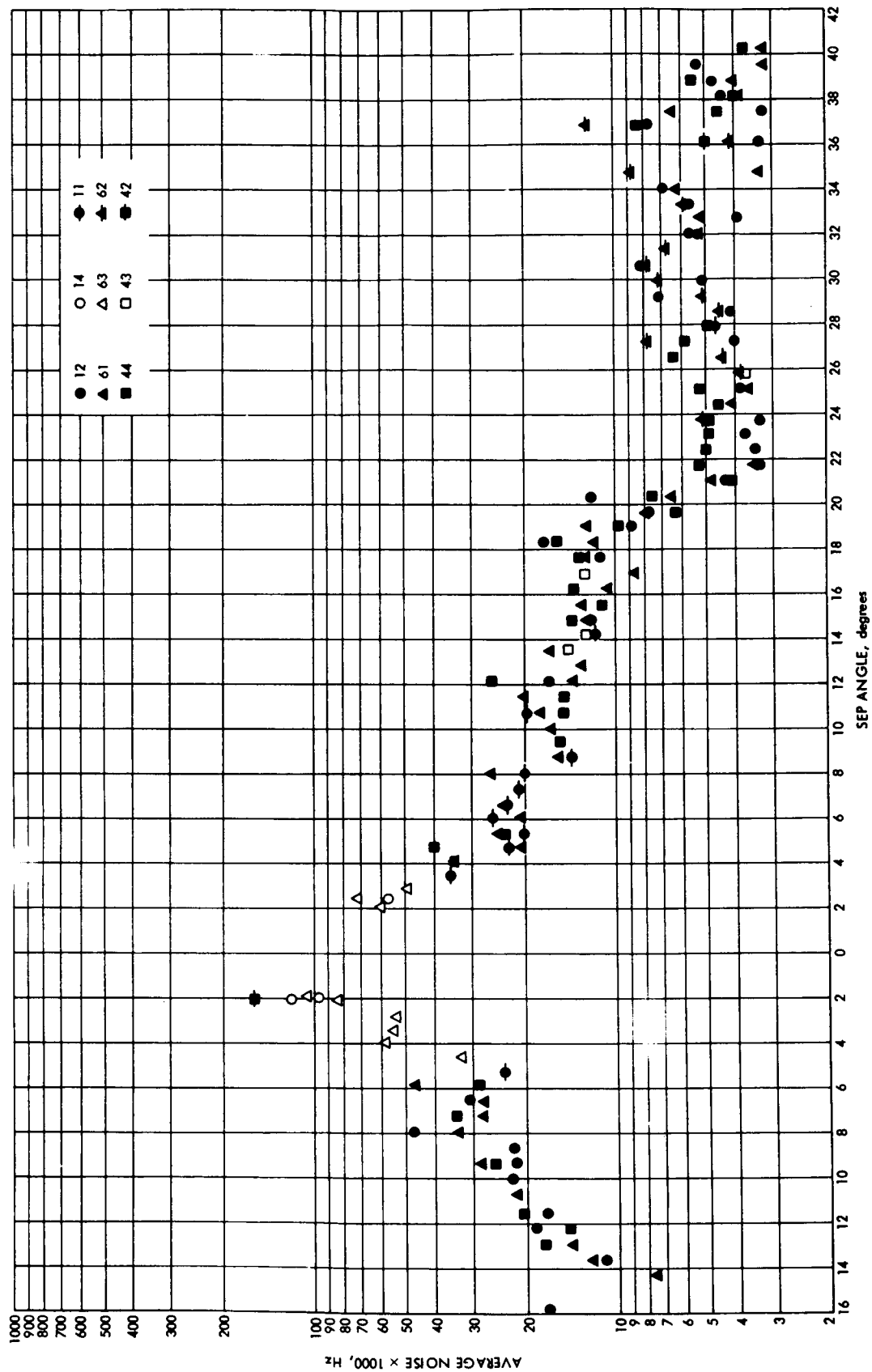


Fig. 3. Pioneer 11 average noise vs SEP angle

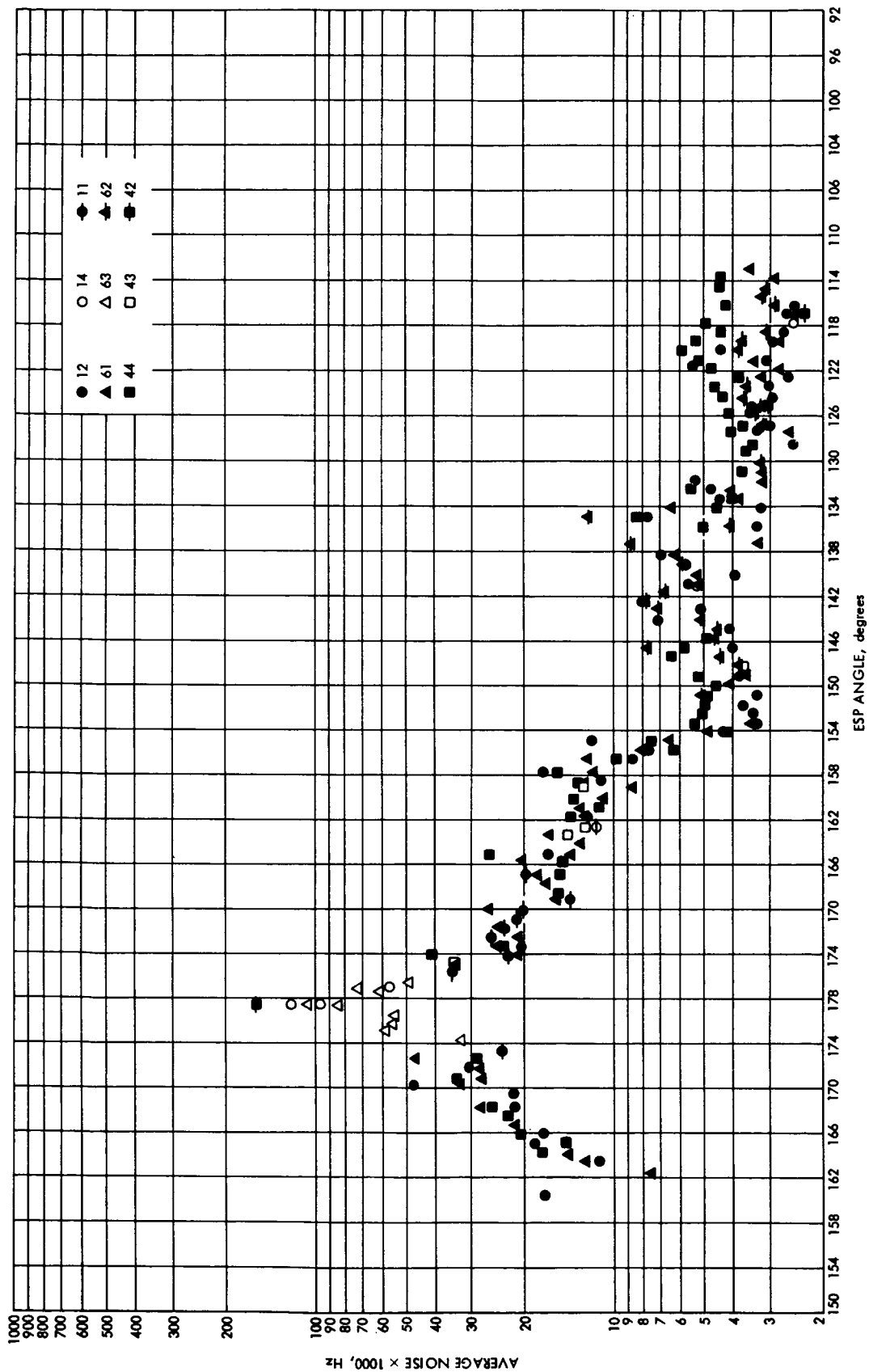
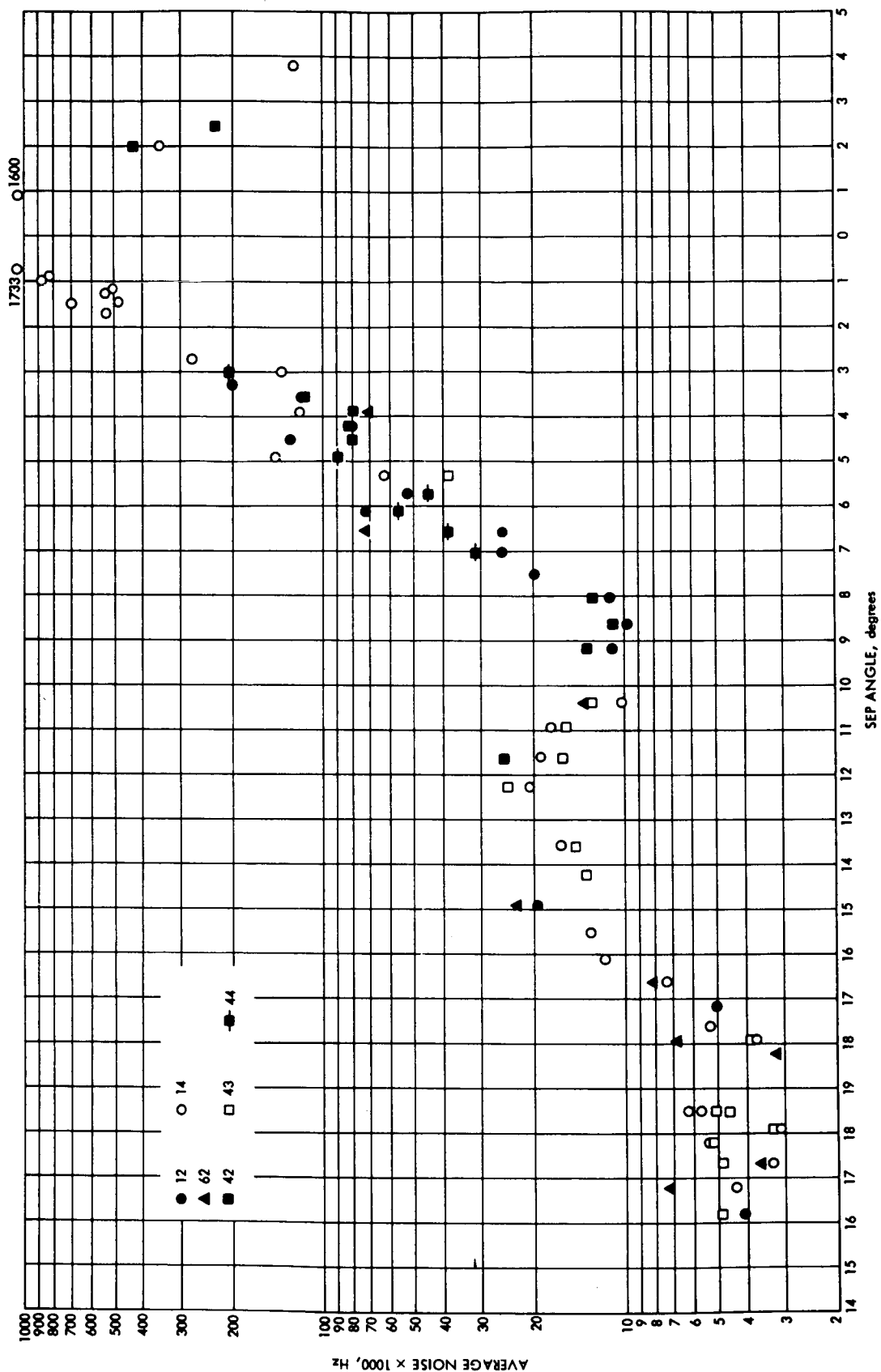


Fig. 4. Pioneer 11 average noise vs ESP angle



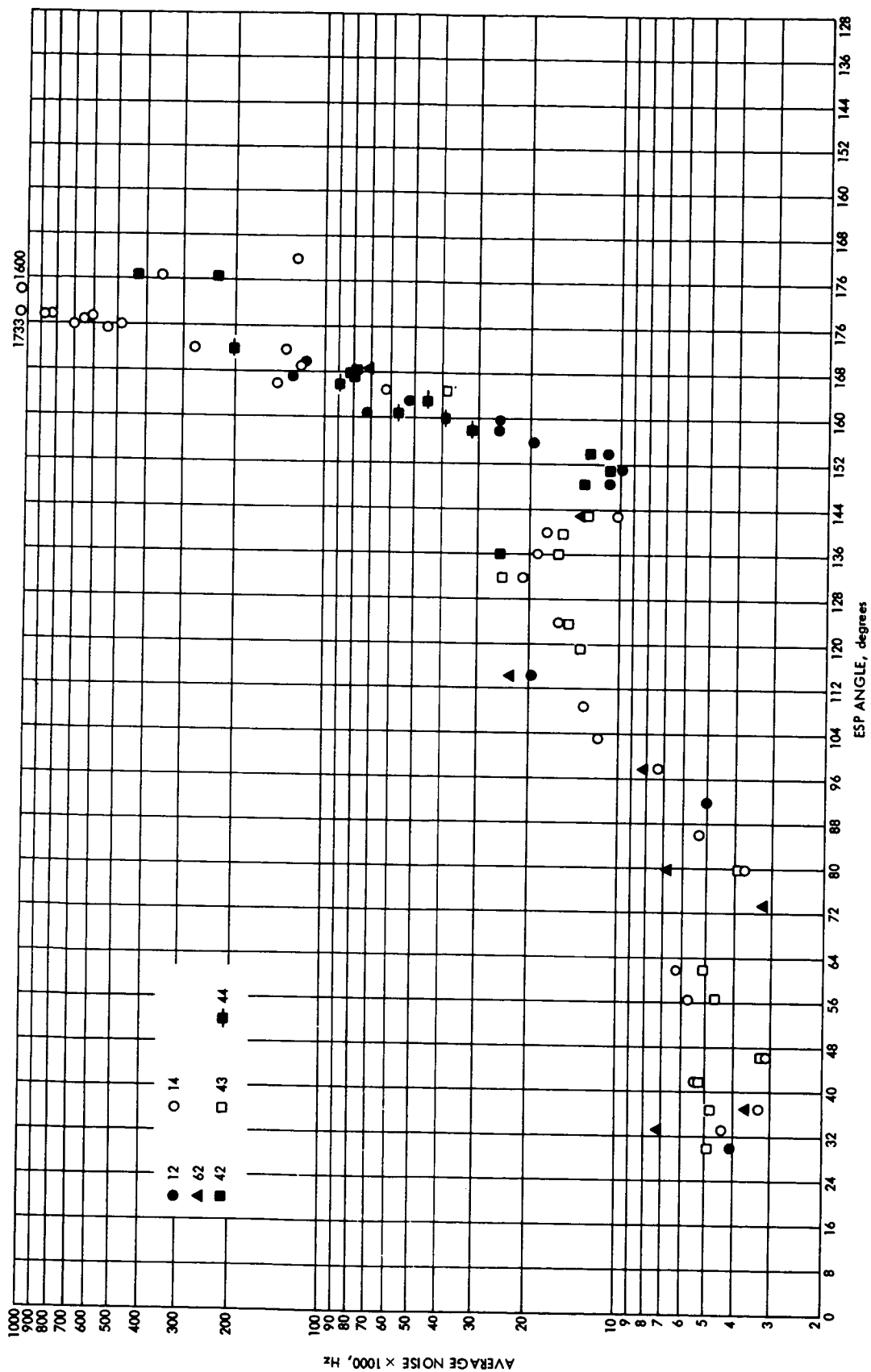


Fig. 6. Helios 1 average noise vs ESP angle

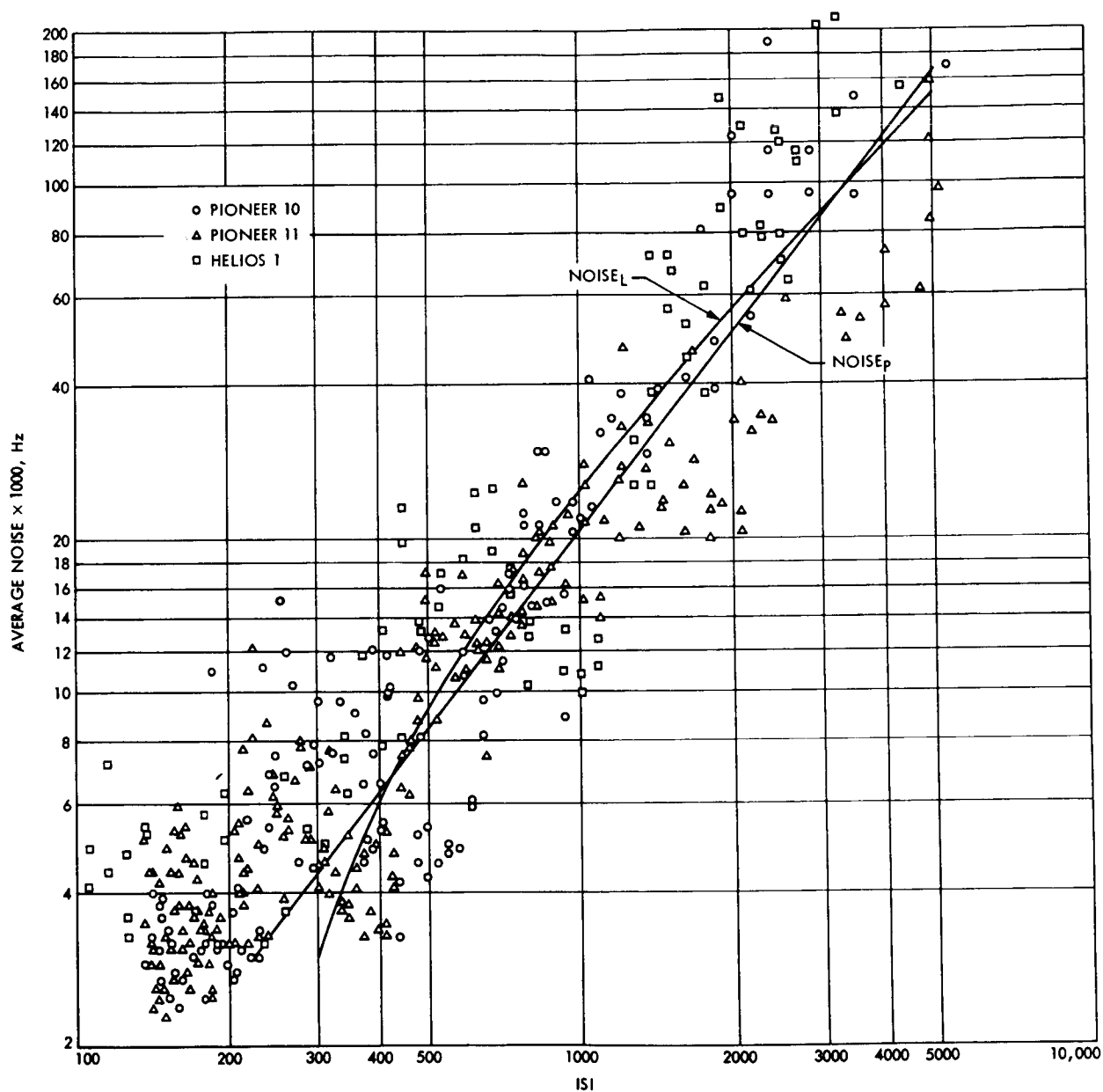


Fig. 7. Average noise vs ISI (mission composite)

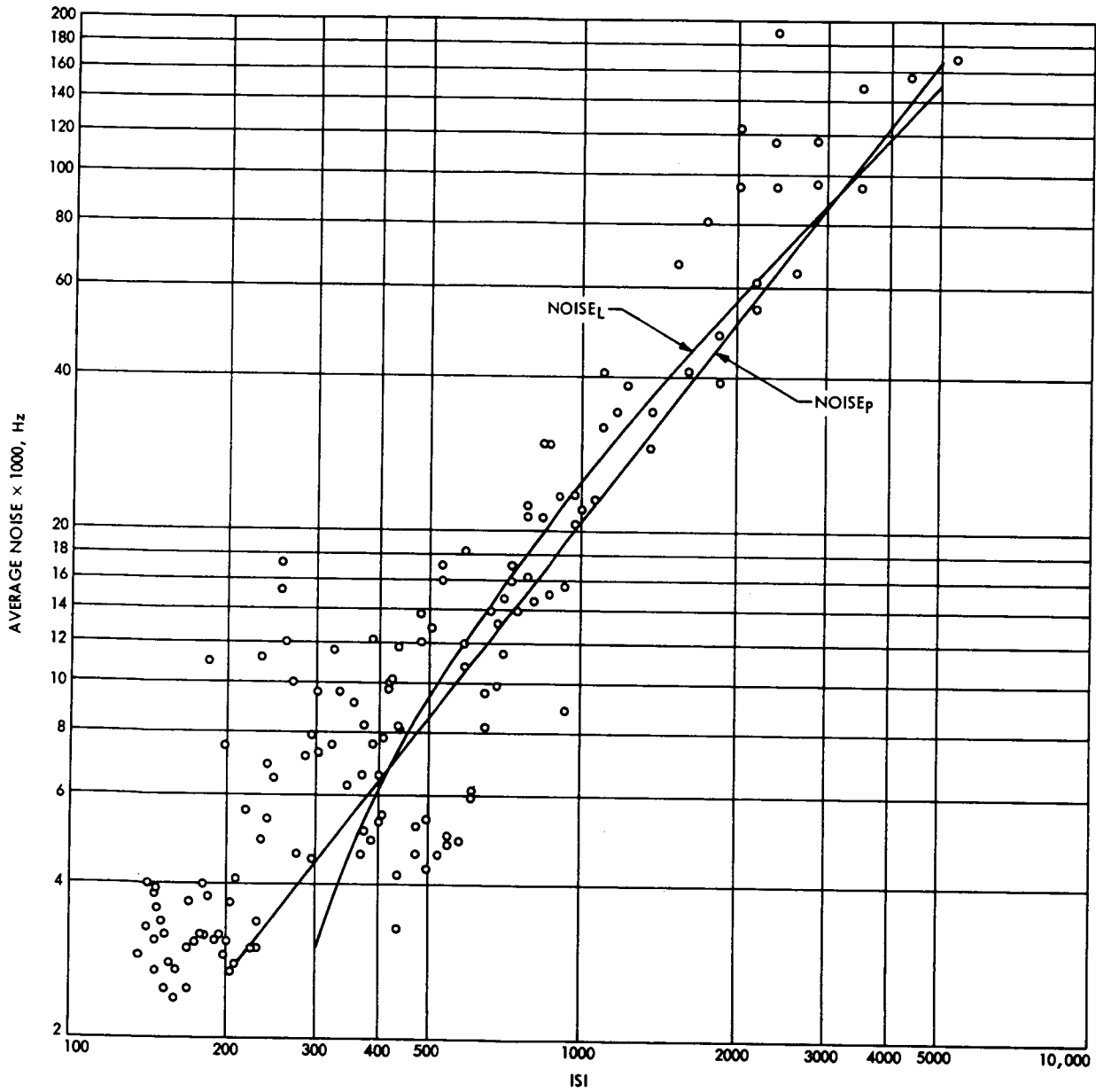


Fig. 8. Pioneer 10 average noise vs ISI

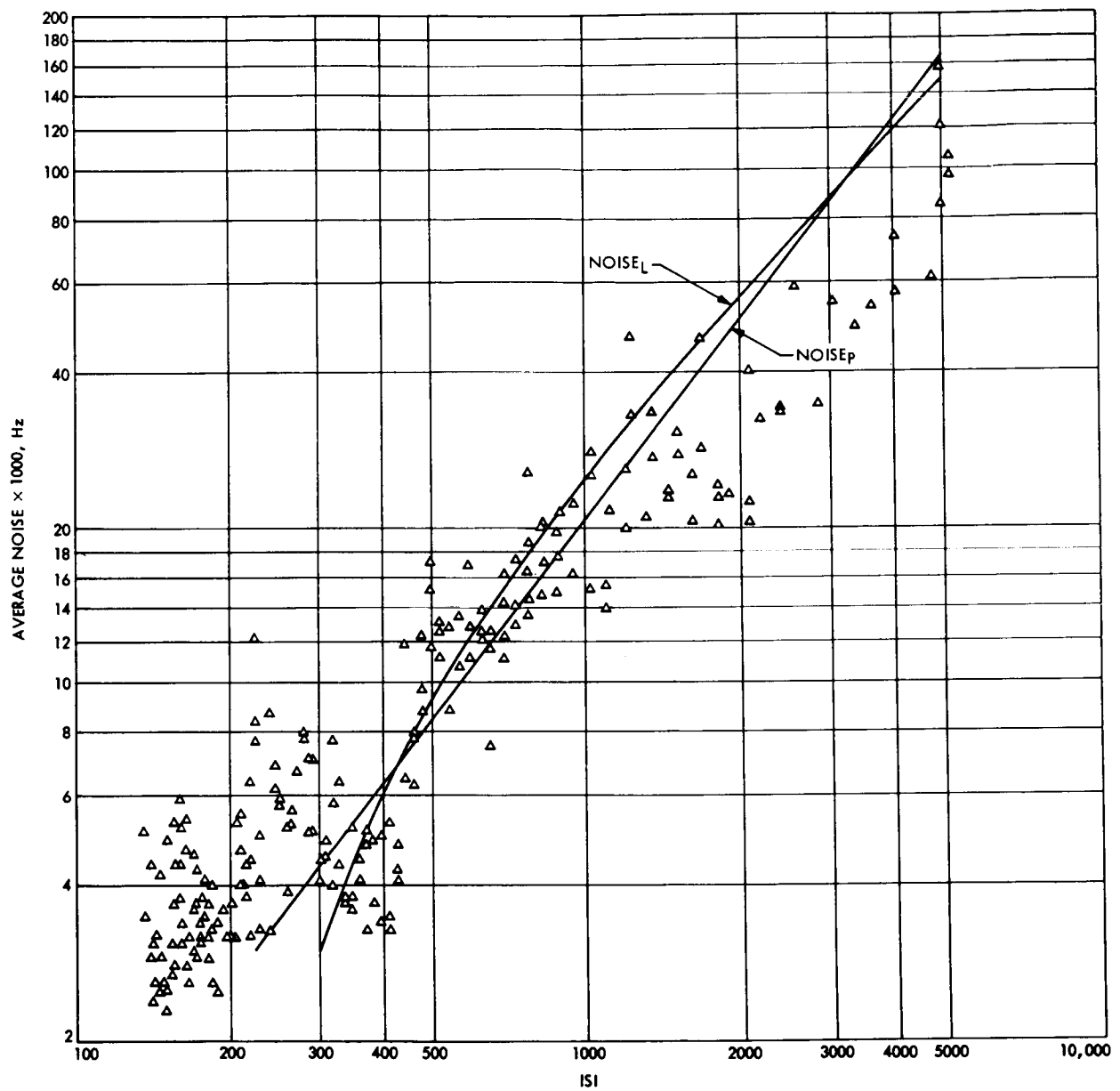


Fig. 9. Pioneer 11 average noise vs ISI

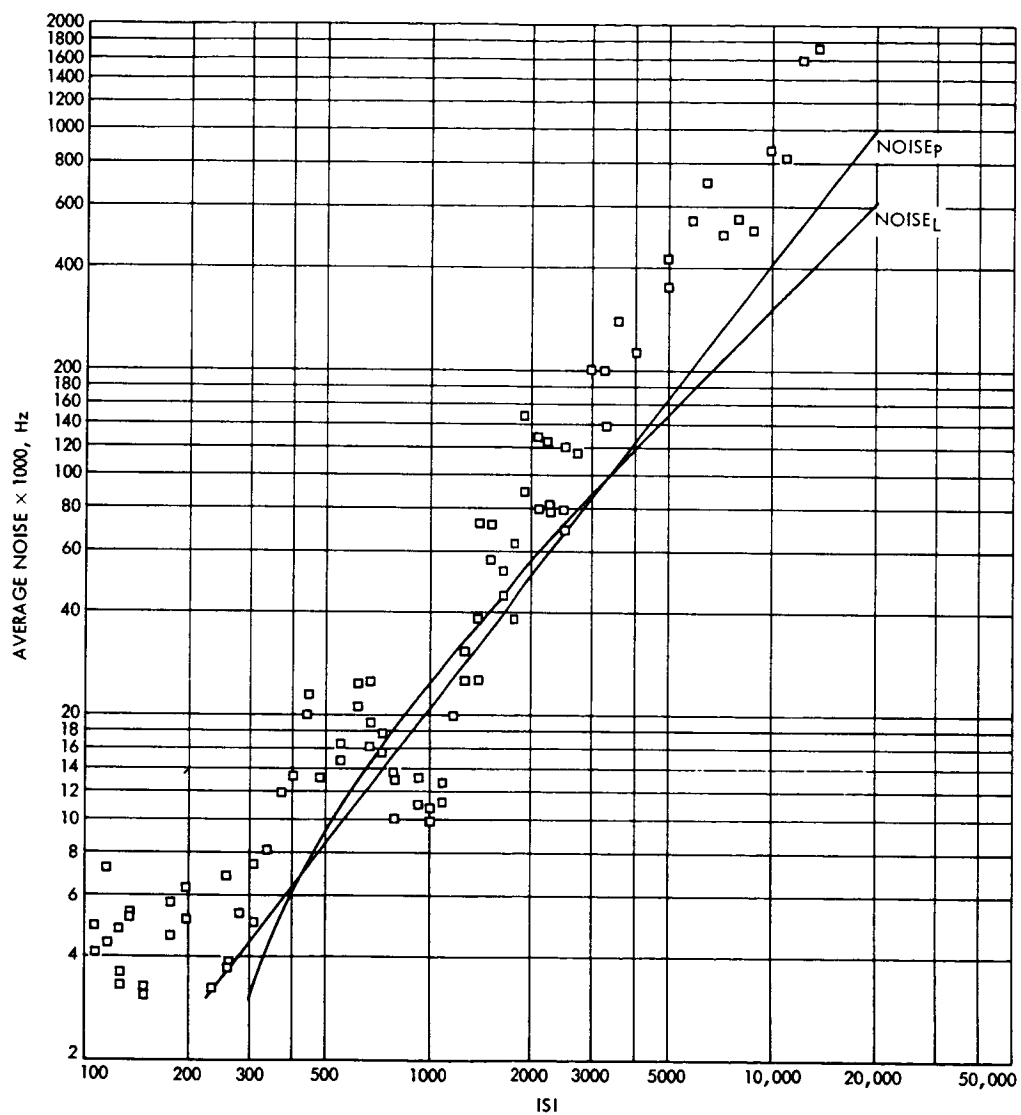


Fig. 10. Helios 1 average noise vs ISI

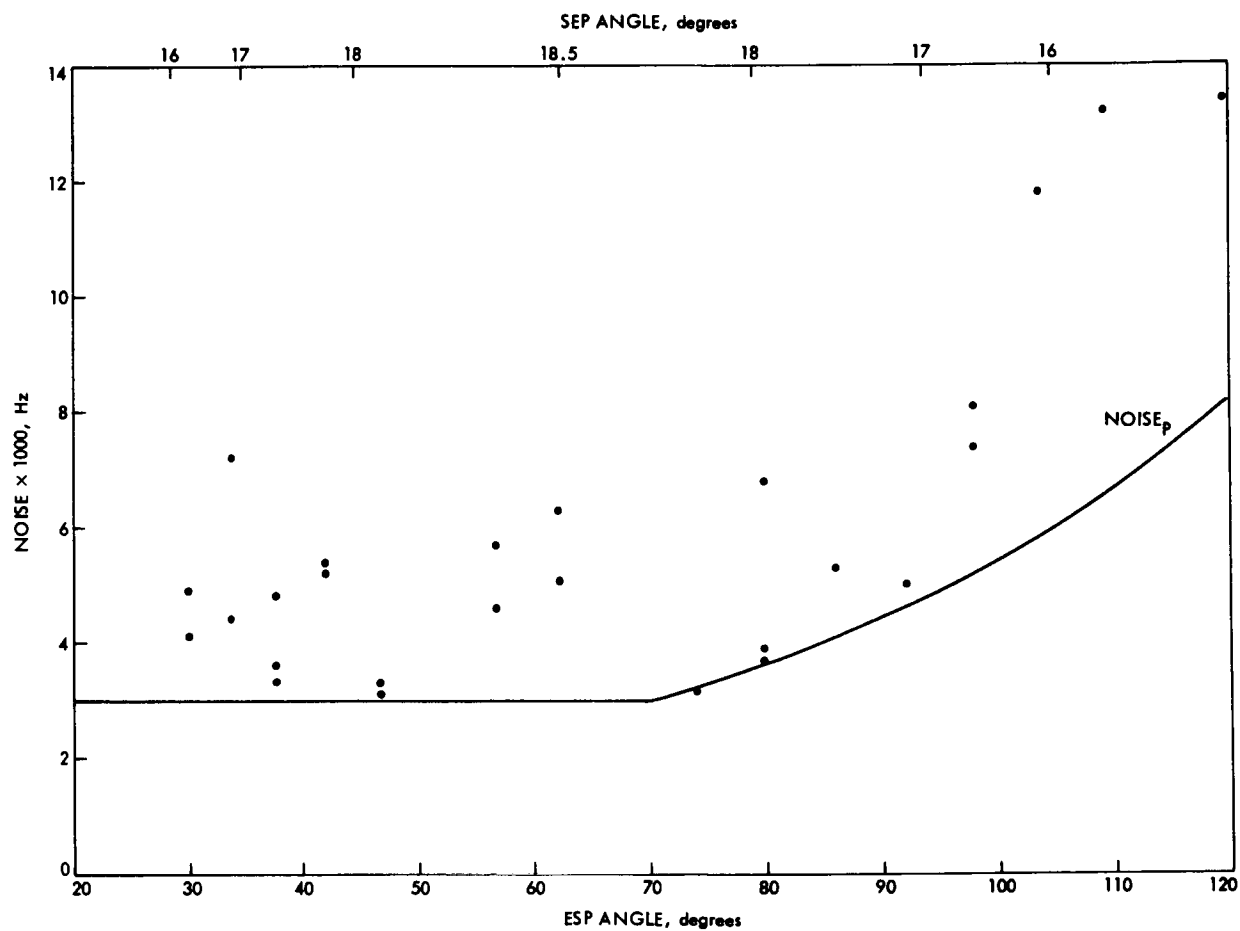


Fig. 11. Helios 1 perihelion: ESP vs average noise

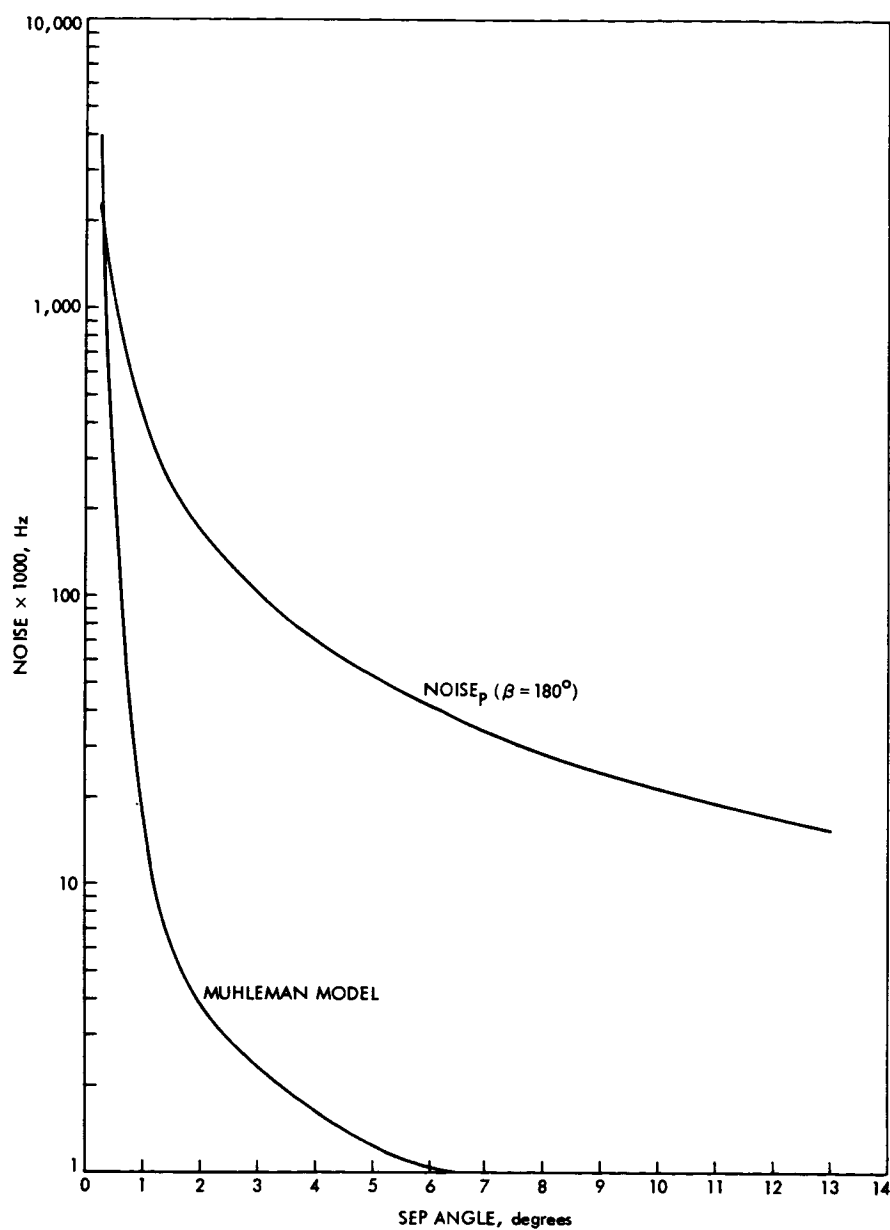


Fig. 12. Model comparison: average noise vs SEP angle

CH
N 76 - 15 2 1 0

Correlation of Doppler Noise During Solar Conjunctions With Fluctuations in Solar Activity

A. L. Berman and S. T. Rockwell
Network Operations Office

In a previous report, a geometric model to predict doppler noise during solar conjunctions was developed. In this report, deviations between observed doppler noise and the noise model are analyzed. Based on the analysis, it is tentatively concluded that deviations between the observed noise and the model are due to short-term fluctuations in solar activity as seen along the signal path, and not to solar/antenna structure effects or system noise temperature.

I. Introduction

In the preceding report (Ref. 1), the authors, after considering doppler noise estimates accumulated during the 1975 solar conjunctions of Pioneer 10, Pioneer 11, and Helios 1, developed a geometric solar noise model for 2-way, 60-second-sample-rate doppler data as follows:

$$NOISE_P \text{ (Hz)} = \begin{cases} 0.003, & ISI \leq 223 \\ K_1 (ISI)^{1+K_2}, & ISI > 223 \end{cases}$$

where

$$K_1 = 2.8 \times 10^{-6}$$

$$K_2 = 2.9 \times 10^{-1}$$

$$ISI = \frac{\beta}{\sin \alpha}$$

α = Sun-Earth-probe angle, degrees

β = Earth-Sun-probe angle, degrees

In this report, residuals between the observed doppler noise and the predicted doppler noise, in percent deviation from predicted,¹ are formed as follows:

$$\text{Residual} = \frac{\text{observed noise} - \text{predicted noise}}{\text{predicted noise}} \times 100$$

where

Residual = residual in percent

Observed noise = observed noise (DOY)

Predicted noise = $NOISE_P (\alpha(\text{DOY}), \beta(\text{DOY}))$

DOY = day of year

These residuals are herein analyzed, and, from this analysis, the authors draw the tentative conclusion that

¹The residuals are put in this form because the data span almost three orders of magnitude.

the deviations in the observed data from the $NOISE_p$ model are for the most part due to short-term fluctuations in solar activity as seen along the signal path.

II. Doppler Noise due to Solar/Antenna Structure Effects and System Noise Temperature

During previous solar conjunctions, it was observed that there existed periods when the doppler noise rose dramatically and then receded back to follow a course of more orderly progression with the Sun-Earth-probe (SEP) angle. It was conjectured at the time that these "spikes" were due to solar/antenna structure effects. Additionally, it was hypothesized by some observers that part of the increase in observed doppler noise could be accounted for by the increase in system noise temperature. If either of the above were significant, one might expect to see a systematic deviation of the doppler noise residuals when plotted collectively as a function of SEP (since both effects would only be functions of SEP while the noise model is a function of both Earth-Sun-probe (ESP) angle and SEP). Such a graph is seen as Fig. 1, and one would certainly be hard pressed to detect any significant systematic trends in the figure. It thus seems reasonable to assume that neither solar/antenna structure effects nor system noise temperature are significant factors in the high doppler noise during solar conjunctions.

III. Multimission Correlation of Doppler Noise Residuals

Two of the assumptions made in the original derivation of the $NOISE_p$ solar noise model were:

- (1) Constant solar radiation and emission of charged particles.
- (2) Solar radial symmetry (as opposed to radial asymmetry and rotation!).

These assumptions were useful in deriving an "average" geometric model; however, both assumptions ignore a time-dependent component of solar radiation and charged-particle density. Therefore, one might expect to gain some insight by examining the residuals as a function of time (i.e., DOY). If the residuals display well-defined trends as a function of time, one might think that time-dependent fluctuations in solar activity along the signal

path were the cause; in particular, the argument would be additionally strengthened if the same trends were seen in more than one mission (and hence at different SEPs for the same DOY). Figure 2 presents Pioneer 10, Pioneer 11, and Helios 1 residuals as a function of time (DOY 82 to DOY 132); in this figure a very strong similarity is seen in the Pioneer 10 and 11 signatures, while a much weaker similarity is seen between the Pioneer 11 and Helios 1 signatures. Figure 3 presents Pioneer 10 and 11 residuals for an earlier period (DOY 64 and 84), and, once again, a similarity in residual signatures is observed for both spacecraft. Noting the strong evidence of multi-mission correlation of doppler noise with time as presented in Figs. 2 and 3, it seems reasonable to look to fluctuations in solar activity as the predominant cause of deviations in observed doppler noise from the $NOISE_p$ model.

IV. Correlation of Doppler Noise Residuals With Fluctuations in Solar Activity

The major fluctuation in solar activity as seen at Earth is an approximate 4-week cycle, which is due to solar radial asymmetry and a solar rotation rate of slightly less than 4 weeks. A secondary effect within this cycle is the intrinsic variation of solar activity with time of any given area on the solar surface. All common indices of solar activity, such as number of sunspots, solar flare index, solar energy flux, move (roughly) in unison with the basic cycle. To observe if any correlation exists between doppler noise residuals and the solar rotation cycle, the daily solar energy flux (Ottawa, 2800 MHz; see Ref. 2) was chosen for convenience as a representative index. Figure 4 presents the Pioneer 10, Pioneer 11, and Helios 1 noise residuals as compared to observed solar energy flux, with both as functions of DOY. The residuals and the solar flux obviously seem to bear some similarity to each other in terms of a basic several-week cycle, although in some regions the residuals seem to be in phase with the flux and, in other regions, out of phase. A possible explanation for a "variable lag" between Earth-observed solar activity and observed doppler noise residuals is the rapidly changing orientation of the signal path to the (rotating) Sun. A situation which would alleviate the complexity of a changing signal path with respect to the (rotating) Sun would be a spacecraft with a near static Earth-Sun-spacecraft geometry over some period of time. For this situation, one might expect the "phase difference" between doppler noise residuals and Earth-observed solar activity to be nearly a constant. Helios 1 exhibited just

this type of geometry after the first superior solar conjunction; during an appropriate two-month period, the ESP and SEP varied only slightly. Figure 5 presents the Helios 1 doppler noise residuals during this period² as compared to observed solar flux which has been advanced to a later date by 10 days, and the correlation seems uncanny. Although the above embodies a great deal of guesswork, it seems reasonable to assume the following:

- (1) The $NOISE_p$ model is a good geometric representation for "average" solar activity.
- (2) Deviations from the $NOISE_p$ model are primarily due to fluctuations in solar activity as seen along the signal path; these fluctuations are a result of:
 - (a) Radial asymmetry of solar activity combined with solar rotation.
 - (b) Variation with time of solar activity for any region of the solar surface.

As a final consideration, the Sun is currently near the bottom of a long-term (several year) cycle and presumably the $NOISE_p$ (or any other) model would have to be updated from time to time to reflect long-term changes in "average" solar activity.

²The data after DOY 203 were not part of the original data base, but were abstracted from the monthly tracking reports.

V. Summary

In a previous report, the authors developed a geometric model for solar-induced doppler noise. This report analyzes the signatures left in the observed doppler noise after subtracting the noise model. From this analysis, the following observations are made:

- (1) Multimission noise residuals do not appear to correlate with the SEP angle.
- (2) Multimission noise residuals do correlate as a function of DOY.
- (3) Multimission noise residuals appear to correlate in some fashion with short-term fluctuations in solar activity.

from which the following tentative inferences are drawn:

- (1) Deviations from the $NOISE_p$ model are not related to solar/antenna structure effects or system noise temperature.
- (2) Deviations from the $NOISE_p$ model are predominantly related to short-term fluctuations in solar activity as seen along the signal path, these fluctuations in turn resulting from:
 - (a) Radial asymmetry of solar activity, combined with solar rotation.
 - (b) Variation with time of solar activity for any region of the solar surface.

References

1. Berman, A. L., and Rockwell, S. T., "Analysis and Prediction of Doppler Noise During Solar Conjunctions," in *The Deep Space Network Progress Report 42-30* (this volume), Jet Propulsion Laboratory, Pasadena, Calif., Dec. 15, 1975.
2. *Solar-Geophysical Data*, Prompt Reports 367-1, 368-1, 369-1, 370-1, and 373-1, National Oceanic and Atmospheric Administration, Department of Commerce, Ashville, N. C., 1975.

Bibliography

- Brandt, J. C., *Introduction to the Solar Wind*, W. H. Freeman and Co., San Francisco, 1970.
- Motz, L., and Duveen, A., *Essentials of Astronomy*, Wadsworth Publishing Co., Inc., Belmont, Calif., 1966.
- Sonett, C. P., Coleman, P. J., Jr., and Wilcox, J. M., *Solar Wind*, Ames Research Center, National Aeronautics and Space Administration, Washington, D. C., 1972.

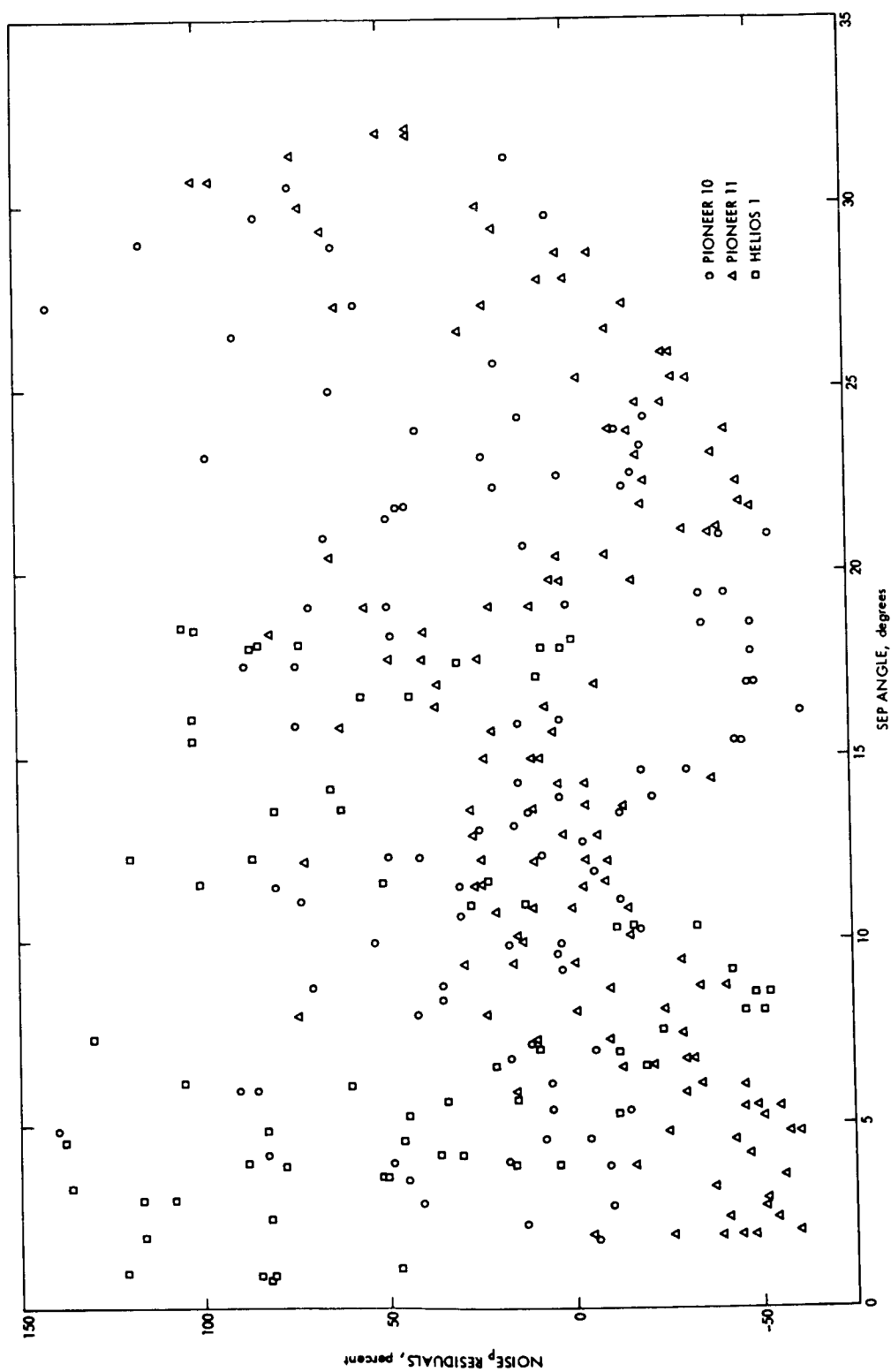


Fig. 1. Multimission $NOISE_r$ residuals vs Sun-Earth-probe angle

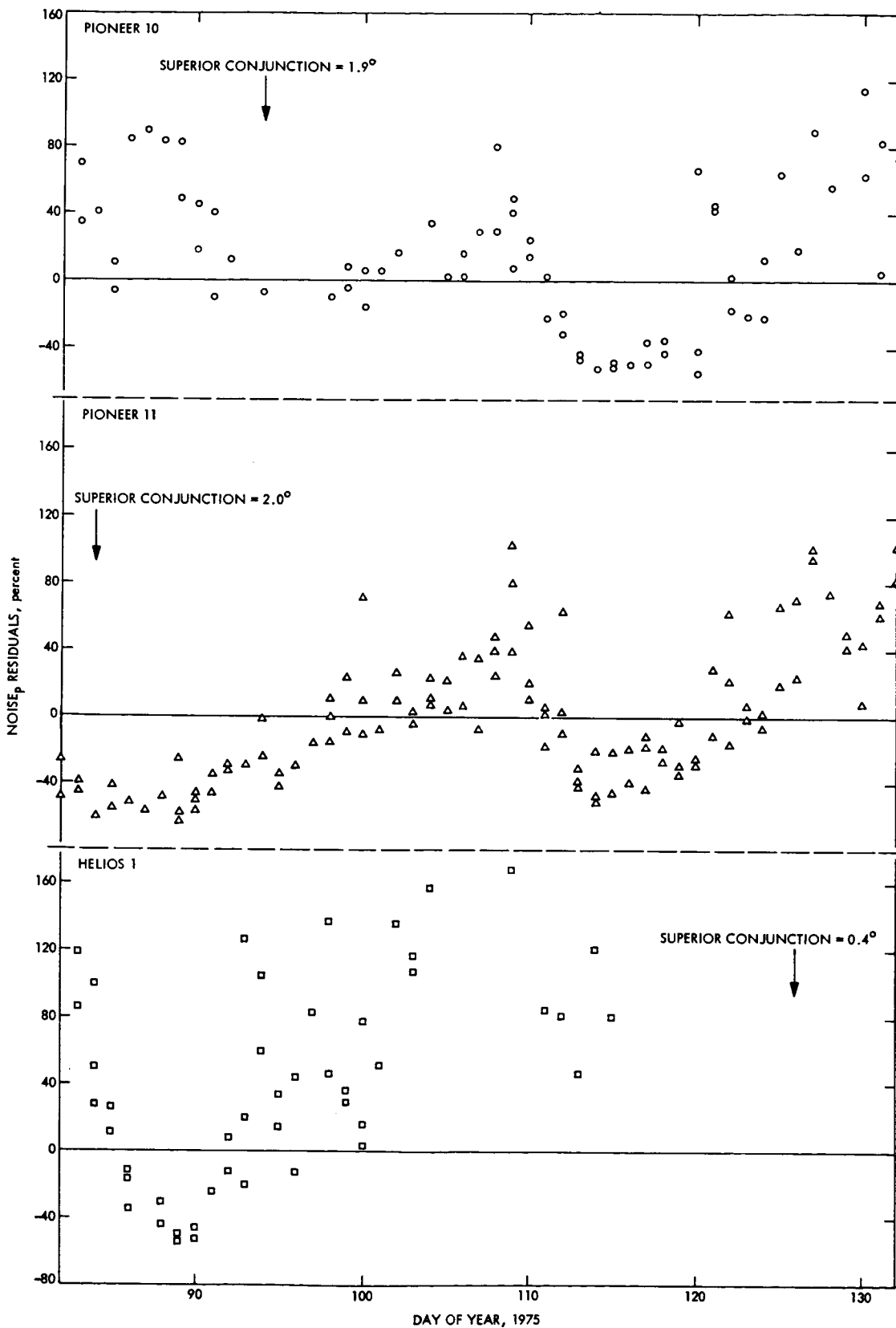


Fig. 2. Separate mission $NOISE_p$ residuals vs day of year

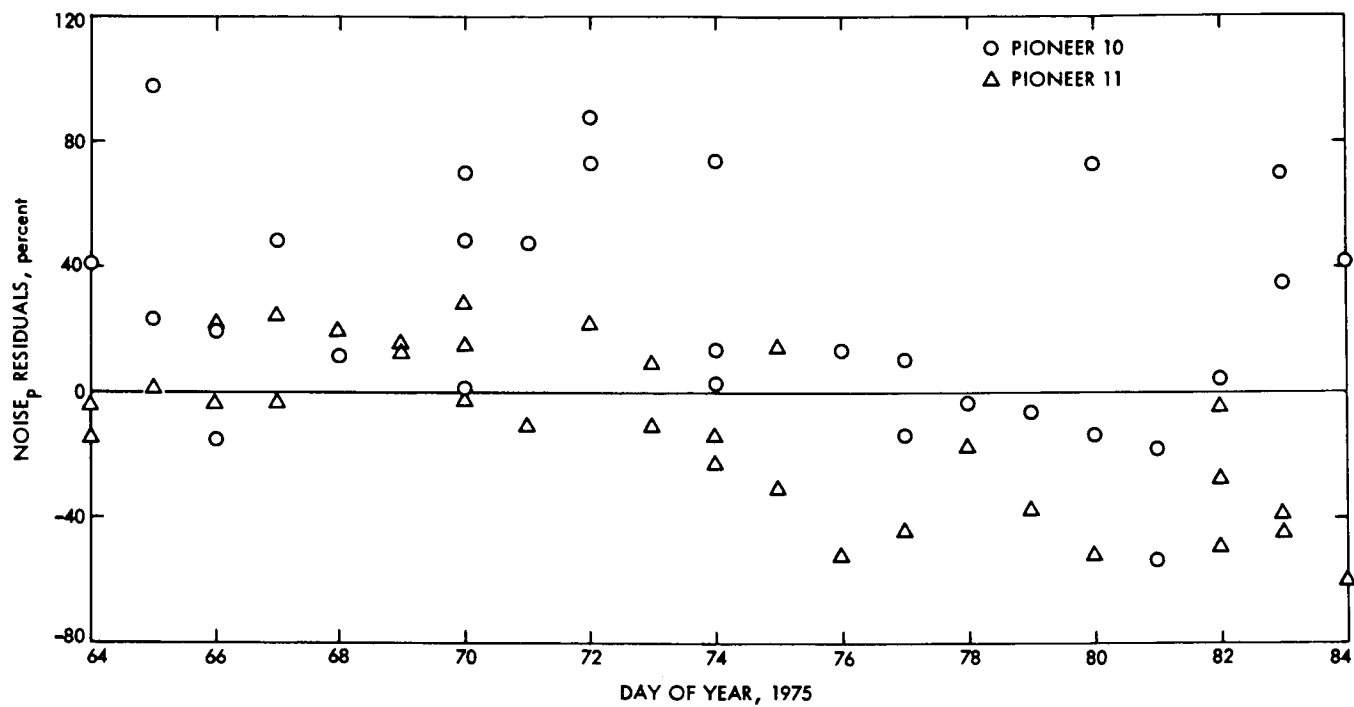


Fig. 3. Pioneer 10 and 11 NOISE_p residuals vs day of year

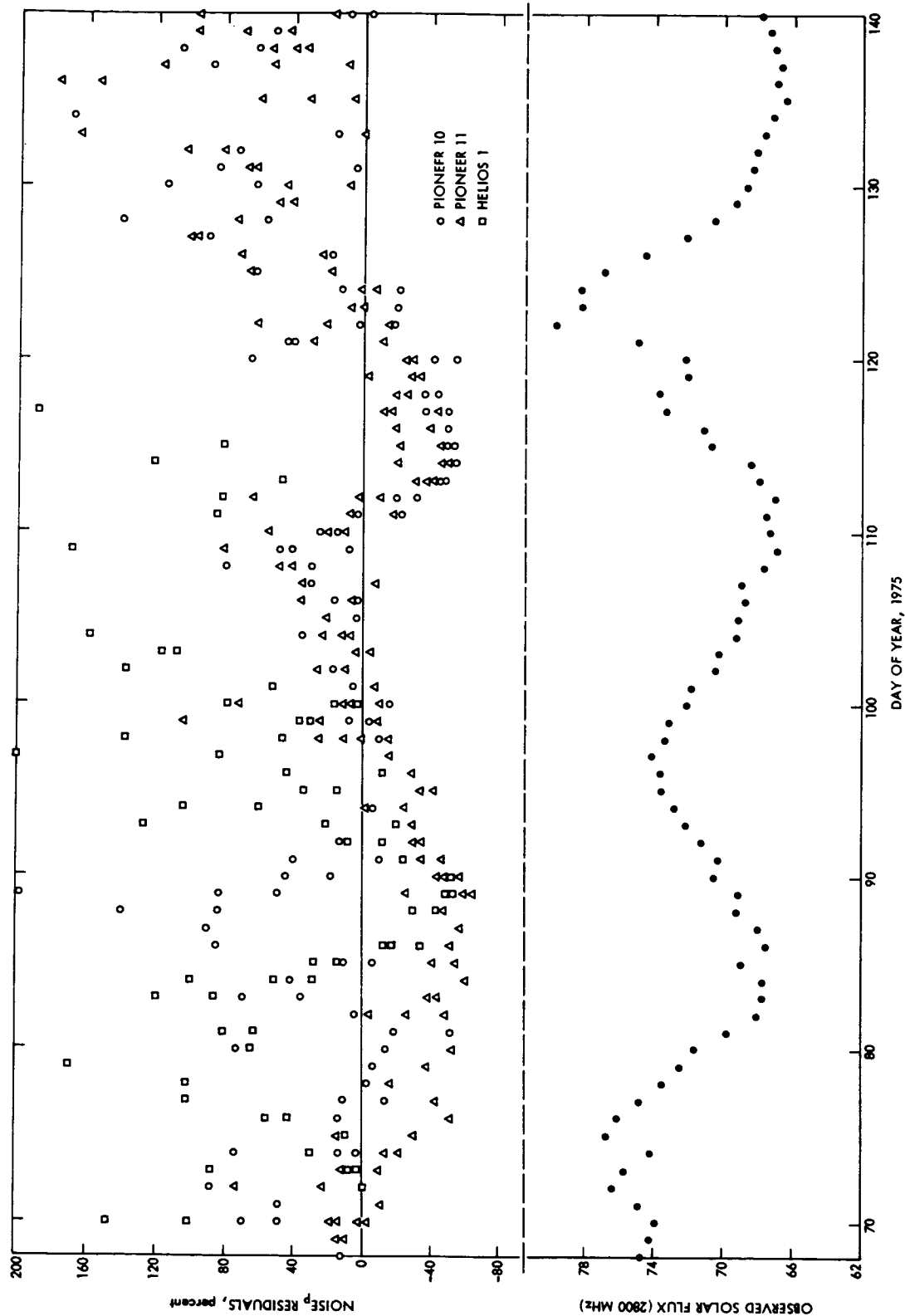


Fig. 4. Multimission NOISE_p residuals/observed solar flux vs day of year

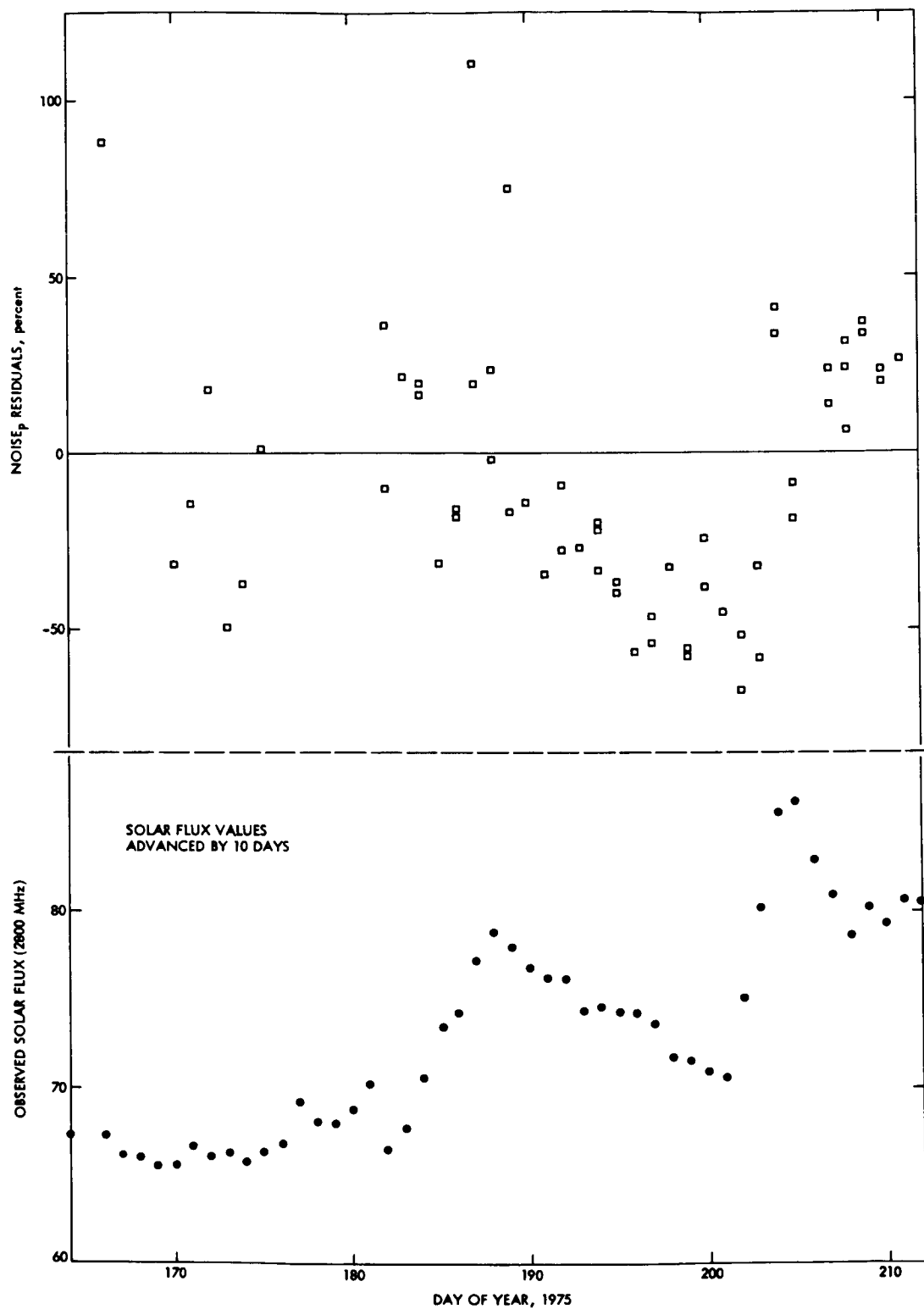


Fig. 5. Helios 1 NOISE_p residuals/solar flux vs day of year

N76-15211

Tracking Operations During the Viking 1 Launch Phase

A. L. Berman and J. A. Wackley
Network Operations Office

Viking 1 launch phase tracking operational procedures were intensively considered and conservatively designed to accommodate even the most unfavorable of launch possibilities. These procedures were successfully implemented and strongly contributed to the highly successful launch of Viking 1. This report details the prelaunch planning for and subsequent analysis of tracking operations during the Viking 1 launch phase.

I. Introduction

The Viking 1 spacecraft was launched from the Air Force Eastern Test Range (AFETR) on August 20, 1975, at 21:22:00.632 Greenwich Mean Time (GMT), and at a launch azimuth of 96.57 degrees. The purpose of the Viking 1 mission is to study the planet Mars via direct measurements in its atmosphere, on its surface, and in orbit about it. To accomplish this goal, the Viking 1 spacecraft was lofted into a trans-Mars, heliocentric orbit by a combination Titan III-E/Centaur D-1T launch vehicle in the parking orbit ascent mode. Trans-Mars orbital injection occurred over southern Africa, and the resulting near-Earth portion of the orbit was such that within the Deep Space Network (DSN), the Australian complex was the first to view the spacecraft post-injection. The Deep

Space Station (DSS) selected to perform the initial acquisition was DSS 42 (Weemala, Australia) with DSS 44 (Honeysuckle Creek, Australia) as backup.

In the following sections, the prelaunch tracking operations planning and the subsequent analysis of launch phase tracking operations at these stations will be detailed.

II. Viking 1 Trajectory Considerations

The open window Viking 1 launch trajectory for August 20 resulted in angle and frequency rates which were quite small, even when compared to previous (but otherwise similar) mission parking orbit ascent type launch trajectories over Australian stations. Maximum

angular and frequency rates were as follows:

$$\frac{d}{dt} \{D2\} \approx 80 \text{ Hz/s (S-band)}$$

$$\frac{d}{dt} \{XA\} \approx 0.4 \text{ Hz/s (VCO level)}$$

$$\frac{d}{dt} \{HA\} \approx 0.04 \text{ deg/s}$$

where

$D2$ = two-way doppler frequency

XA = spacecraft receiver best lock, with doppler accounted for

HA = local (station) hour angle

Figure 1 stereographically illustrates the Viking 1 launch pass over DSS 42, while Fig. 2 details the elevation angle versus time and Fig. 3 the XA frequency versus time. Additionally, Fig. 2 serves as a time line for the important tracking events at DSS 42. The pass was approximately 5 hours 15 minutes long, with the retrograde point, defined by

$$\frac{d}{dt} \{HA\} = 0$$

occurring at approximately 23:16:00 GMT and at an HA of

$$HA \approx 47.7 \text{ deg}$$

A facet of information necessary to the determination of the initial acquisition strategy for the Viking 1 launch was the expected uncertainties in tracking observables as translated from the expected uncertainties in the launch vehicle performance. The Viking Flight Path Analysis Group (FPAG) provided a typical 3σ perturbed trajectory and the corresponding nominal trajectory. Tracking observable predictions were then generated from both trajectories and, when differenced, yielded the following maximum 3σ uncertainties in tracking parameters for DSS 42:

$$\Delta HA \approx 0.002 \text{ deg}$$

$$\Delta D2 \approx 10 \text{ Hz (S-band)}$$

$$\Delta XA \approx 0.05 \text{ Hz (VCO)}$$

These numbers are miniscule and are, in fact, smaller by orders of magnitude than assumed trajectory uncertainties for previous mission launch phases. For instance,

the equivalent numbers for the Helios 1 launch (see Ref. 1) were:

$$\Delta HA \approx 1.15 \text{ deg}$$

$$\Delta D2 \approx 3500 \text{ Hz (S-band)}$$

$$\Delta XA \approx 17 \text{ Hz (VCO)}$$

The impact of the above numbers on the initial acquisition strategy, as well as the results of the actual launch trajectory, will be discussed in later sections.

III. Launch Tracking Predictions

A. New Prediction System

The Network Operations Control Team (NOCT) generates a variety of predict sets¹ during the launch phase which reflect spacecraft frequency updates, different possible trajectories, different remote site uses, etc. Prior to May 15, 1975, predictions were generated via a Probe Ephemeris Tape (PET) produced by the Flight Path Analysis Group (FPAG) on the Univac 1108 computer, in combination with prediction software ("PREDIX") on the IBM 360 computer. Subsequent to May 15, 1975, predictions were and are currently generated via a Polynomial Coefficient Tape (PCT) produced by the FPAG on the Univac 1108 computer, in combination with prediction software ("PREDIK") on the Network Data Processing XDS Sigma-5 computer. Viking 1 thus became the first launch phase to be executed under the PCT/PREDIK system. The major concern with the new system was the throughput time (here defined as the time interval from initiation of a PCT to start of predict transmission to the DSS). The most optimistic forecast of the throughput time for launch predicts was initially:

$$\Delta t \approx 41 \text{ min}$$

Since rise at DSS 42 occurred at approximately L plus 48 minutes, the chances of getting predictions initiated shortly after liftoff and based on the actual liftoff time to DSS 42 prior to rise appeared only marginal. The prediction generation sequence was exercised repeatedly during launch simulations in the months prior to launch, such that at the conclusion of the Operational Readiness Test (ORT) the predict generation process appeared to be optimized and the final throughput time minimized, thereby greatly increasing confidence in the ability to

¹ Additionally, predictions are also generated at AFETR by the Real Time Computing System (RTCS).

transmit actual liftoff predictions to DSS 42 well ahead of rise. Some partial test results are presented below:

Test/date	PCT generation	PREDIK generation	Total
Forecast	20 M	21 M	41 M
VT1B	—	17 M	—
6-25-75	25 M	16 M	41 M
	—	13 M	—
	—	22 M	—
DT-1	—	21 M	—
7-25-75	18 M	20 M	38 M
	18 M	27 M	45 M
	—	16 M	—
ORT-1	—	14 M	—
8-6-75	16 M	10 M	26 M
	19 M	13 M	32 M
	—	12 M	—
	—	10 M	—

B. Launch Predicts Identification System

During a typical launch phase, numerous predict sets are necessitated due to changes in spacecraft frequencies, trajectories, etc. To allow for immediate recognition of the differing sets of predicts by users within the Network Operations Control Team and at the DSS, a new more informative and systematic code was developed for the four-character alpha-numeric predict identifier. The code is described as follows:

WXYZ = 4-character alpha-numeric predict identifier with

W = spacecraft identifier: A for Viking 1, and B for Viking 2

XY = launch date/test identifier. For actual launches, XY is the day of the month of the launch, while for launch tests X = T, and Y indicates the particular type of test.

Z = origin or usage of predicts. Z denotes the basis for the data used to generate the predicts, such as nominal open window predicts, actual liftoff predicts, etc., or the intended usage of predicts, such as drive tape predicts, frequency update (text) predicts, etc. A description of the various types of predicts denoted by Z is seen in Table 1.

C. Polynomial Coefficient Tape Generation

The optimum set of (preflight) nominal predicts would be those based on the nominal trajectory corresponding to the actual liftoff time. However, since the actual liftoff time usually varies within a second or two of the scheduled (or rescheduled) liftoff, and, in consideration of the tracking observable errors induced in the predicts as a function of a Δt offset, it was decided that a reasonable goal would be to strive for the generation of a PCT based on a liftoff time within 2 seconds of the actual liftoff time. The Viking FPAG developed a scheme to maximize the possibility of rapidly producing such a PCT, and this scheme is seen in Fig. 4. The PCT numbers in Fig. 4 are identified with the various predict sets as follows:

PCT number	Predict identifier (Z)
1	D, F
2	E
3	E
4	A

IV. Angle Drive Strategy at DSS 42

The relevant considerations, in attempting to formulate the angle drive strategy at DSS 42 for the Viking launch phase were as follows:

- (1) Desire to acquire the uplink shortly after rise (at about rise plus 3 minutes).
- (2) Requirement for being on Antenna Pointing Subsystem (APS) drive tape during the uplink sweep so as not to drive the antenna off point (in autotrack) when the one-way/two-way downlink switch causes the receivers to drop lock.
- (3) High probability (but not certainty) of accurate angle predictions (APS drive tape).
- (4) Desire for early acquisition of autotrack data.
- (5) Desire to lock the S-band cassegrain monopulse (SCM) feed cone as well as the acquisition aid antenna (SAA) prior to initiation of the uplink sweep.

One obviously achieves the highest probability of being on the spacecraft (and, hence, initially acquiring the one-way downlink) by driving the antenna to the best (drive tape) predictions. However, it was clear from items (1) and (2), above, that there would be insufficient time to acquire one-way on APS drive tape, go to autotrack, and

then return to APS drive tape prior to rise plus 3 minutes. Thus the simplest scheme with a high probability of success in meeting the goals delineated above would be to stay on APS drive tape throughout the two-way acquisition, and then shortly thereafter proceed to autotrack. To facilitate the details of this strategy, two phases were defined:

- (1) Phase I: Rise to 2-way acquisition.
- (2) Phase II: Post 2-way acquisition.

The hierarchy of preference or required action for each phase, which was heavily dependent on the availability of differing sets of predicts, is presented below:

(1) Phase I—Rise to 2-way acquisition

- (a) Prior to rise, the antenna to be positioned at the rise point of the prime (as defined) prediction set.
- (b) angle drive mode subsequent to predicted rise (in order of preference).
 - (i) Applicable condition: launch occurs within 2 seconds of the open window launch time.

Angle drive mode: a verified drive tape in GMT and based on preflight nominal open window predictions (predict code XXXD; see Section III).

- (ii) Applicable condition: launch does not occur at the open window, but a verified drive tape based on the actual launch time is available at DSS 42 prior to rise.

Angle drive mode: a verified drive tape in GMT and based on the actual launch time (codes XXXE, XXXA).

- (iii) Applicable condition: launch does not occur at the open window, an actual launch time drive tape is not available before rise, but actual launch time page print (fixed point) predicts are available.

Angle drive mode: a preflight nominal verified drive tape in time from launch (TFL) with a Δt offset equal to the actual launch time in GMT (predict codes XXXO, XXXM, XXXC). Angle offsets to be calculated and applied to correct the antenna position to the actual launch time page print predictions.

- (iv) Applicable condition: launch does not occur at open window, and neither actual

launch time page print (fixed point) nor APS drive tape predicts (binary) are available at DSS 42 prior to rise.

Angle drive mode: a preflight nominal verified drive tape in TFL with a Δt offset equal to the launch time in GMT (codes XXXO, XXXM, XXXC). Angle biases to be provided to DSS 42.

(2) Phase II—Post 2-way acquisition

- (a) Acquire and verify receiver lock on the acquisition aid antenna.
- (b) Antenna to autotrack on the acquisition aid antenna.
- (c) Acquire and verify receiver lock on the S-band cassegrain monopulse.
- (d) Antenna to autotrack on S-band cassegrain monopulse.

V. Uplink Acquisition Strategy at DSS 42

The Viking two-way initial acquisition study team, meeting in May/June 1975, formulated two desired guidelines for the initial two-way acquisition:

- (1) Start the uplink acquisition at approximately rise plus 3 minutes.
- (2) Perform the uplink acquisition on the S-band cassegrain monopulse instead of the more usual acquisition aid antenna.

However, it was subsequently reassessed that item (2), above, might be undesirable for the following reasons:

- (1) Because of the slowness of the new PCT/PREDIK prediction system, DSS 42 might not have the correct (and necessary) verified APS drive tape available prior to rise.
- (2) Even if item (1), above, were satisfied, the APS drive tape might not be accurate enough for the SCM for any "non-nominal" modes of launch vehicle performance.
- (3) Use of the SCM would require transmitter operation and calibration in a region (50 watts) for which it was not designed and where it has only infrequently been used.
- (4) Finally, there is (at least theoretically) no perceptible degradation in doppler quality (signature and

noise) when transmitting on the acquisition aid antenna versus the S-band cassegrain monopulse.

In light of the above, the uplink acquisition was planned to be performed on the acquisition aid antenna. The following uncertainty information, as pertained to the uplink, was provided by the Viking Project (all frequencies at S-band):

3σ XA trajectory ~ 5 Hz (from Section II)

3σ XA S/C receiver ~ 1500 Hz

3σ XA S/C "random walk" ~ 750 Hz

3σ XA S/C temperature $\sim 10^\circ\text{F}$ (5.6°C)

$$\frac{\partial XA}{\partial T} \approx 500 \text{ Hz}/^\circ\text{F} \text{ or } 900 \text{ Hz}/^\circ\text{C}$$

Combining the above, one has for a total 3σ uncertainty:

$$3\sigma \text{ XA total} \sim 5300 \text{ Hz}$$

To be extremely conservative, the above 3σ XA uncertainty was doubled, thus resulting in an uplink acquisition search of approximately $XA \pm 11,000$ Hz.

The Viking spacecraft receiver characteristics indicated an acquisition sweep region bounded by:

$$70 \text{ Hz/s} < \text{frequency rate} < 800 \text{ Hz/s}$$

under conditions of strong signal strength, as would be expected to apply in the initial acquisition. Therefore, a sweep rate of $+300$ Hz/s was selected because:

- (1) It was felt that 300 Hz/s was close to the limit at which the site would no longer be able to accurately (manually) tune the exciter.
- (2) A rate of $+300$ Hz/s would result in an effective rate at the spacecraft of about $+250$ Hz/s, which is very close to the geometric mean of the upper and lower sweep limits (237 Hz/s).

Finally, the sweep was chosen to be in the direction of XA change so that the end of the sweep would become TSF for the remainder of the pass. This would be advantageous in that no additional tuning (to TSF) would be required, and the spacecraft static phase error (SPE) for the rest of the pass would be reasonably small. Incorporating the above characteristics, the uplink acquisition procedure was planned as follows:

- (1) Transmitter to be connected to the acquisition aid antenna and set to radiate at an initial power level of 10 kW.
- (2) Transmitter on at (defined) start of uplink sweep minus 20 seconds.
- (3) Station to throw 2-way doppler data switch at start of uplink sweep minus 10 seconds (this so that the NOCT can immediately know when (and if) two-way lock is achieved, and if lock is on the main carrier or a sideband).
- (4) The uplink sweep to begin at approximately rise plus 3 minutes.
- (5) The sweep to cover at least $XA \pm 11,000$ Hz.
- (6) The sweep rate to be $+180$ Hz/min (VCO level), which would result in a rate of approximately 250 Hz/s at the spacecraft (receiver rate = sweep rate minus spacecraft rate).
- (7) The sweep duration to be 90 seconds.

For the actual launch on August 20, 1975, the uplink acquisition sweep selected according to the above guidelines was as follows:

Sweep start time = $22:14:00$ GMT

Start frequency = 21.996130 MHz (VCO)

Frequency rate = 180 Hz/min (VCO)

Sweep end time = $22:15:30$ GMT

End frequency = 21.996400 MHz (VCO)

This uplink sweep pattern is seen in Fig. 5.

If the first sweep was not successful, it was planned to execute a second contingency sweep. This sweep would be at the same rate as the prime sweep, but would cover a region approximately 50% greater ($XA \pm 16,500$ Hz). It would start 3 minutes 30 seconds after the end of the first sweep, and would include a downleg, an upleg, and then a downleg back to TSF. The station would be given the parameters of the contingency sweep considerably prior to rise so that they would have sufficient time to plan for and implement it if necessary.

VI. Post-Flight Analysis of the Viking 1 Launch Phase

A. Tracking Predictions

1. New PCT/PREDIK system. The PCT/PREDIK predicts generation system functioned smoothly during

the launch of Viking 1. Following the PCT generation scheme shown in Fig. 4, the Viking FPAG delivered PCT No. 1 at launch minus 4 hours 25 minutes. The stations were therefore able to receive the predicts necessary for generating a drive tape (predicts set A20D) well ahead of schedule. Additionally, since no changes were made to the frequencies provided by the Orbiter Performance Analysis Group (OPAG), it was decided not to generate the planned frequency predicts (predicts set A20F).

All remaining possible predict generation throughput time problems were alleviated when the launch occurred within a fraction of a second of the expected time.

Only one set of predicts (predicts set A20E) had to be generated between launch and spacecraft rise; this set was to give the station predicts with a GMT time field. (All previous text predicts were generated in time from launch.) Thus, while the PCT/PREDIK generation scheme had been carefully planned to handle any launch situation, the optimum situation (i.e., nominal countdown and launch) occurred, alleviating the problem of getting actual liftoff predicts to DSS 42 prior to spacecraft rise.

2. Prediction accuracy. During the early portion of the DSS 42 launch pass, the radio metric data, when differenced with the preflight nominal predict set A20E by the Network Operations Control Center (NOCC) pseudo-residual program, produced the following residuals:

$$\begin{aligned}\Delta HA &\sim -0.07 \text{ deg} \\ \Delta D2 &\sim 10 \text{ Hz (S-band)} \\ \Delta XA &\sim -0.3 \text{ Hz (VCO)}\end{aligned}$$

These can be compared to the 3σ uncertainties presented in Section II:

$$\begin{aligned}\Delta HA &\sim 0.002 \text{ deg} \\ \Delta D2 &\sim 10 \text{ Hz (S-band)} \\ \Delta XA &\sim 55 \text{ Hz (VCO; total frequency/trajectory uncertainty)}\end{aligned}$$

The residuals were generally within the 3σ uncertainties. While it substantially exceeded the 3σ uncertainty, the hour-angle residual caused no impact on the acquisition of the downlink and no degradation of the received signal level. Additionally, from a historical perspective, this was perhaps the smallest early launch

pass hour-angle residual yet achieved. The two-way doppler residuals (Fig. 6) started quite large (approximately -70 Hz) but gradually decreased to approximately the 3σ value of 10 Hz as the apparent motion of the spacecraft approached sidereal rate.

Considering the many possible sources of error, both in frequency and in trajectory, the miniscule difference between the measured and predicted best lock frequencies, ΔXA , indicates that the reference frequency supplied by the OPAG was highly accurate. Additionally, since the difference between predicted and measured best lock frequencies was smaller than the 3σ uncertainty supplied by OPAG by more than two orders of magnitude, one must consider that perhaps the 3σ frequency uncertainty calculations were overly pessimistic.

B. One-Way Acquisition at DSS 42

The Viking 1 one-way downlink was acquired by DSS 42 at 22:10:05 GMT, 33 seconds before the predicted 22:10:38 GMT spacecraft rise time. Subsequent stereographic plots of the spacecraft trajectory indicate a possible 1.5-degree hour-angle error in the horizon mask used in the predicts software. Considering the rate of change of hour angle that occurred during this period (approximately 0.04 degree per second), this error would seem to account for the discrepancy in the rise time.

The downlink acquisition is depicted in Fig. 7. As can be seen in this plot, the receiver appears to have been drifting in the region around a one-way doppler frequency of 1047000 Hz prior to expected acquisition time. The signal was apparently detected at 22:09:51 GMT with receivers reported in lock at 22:10:05 GMT, though both monitor and tracking data indicate possible continuous receiver lock as early as 22:09:53 GMT.

C. Two-Way Acquisition at DSS 42

DSS 42 was instructed by means of the acquisition message shown in Fig. 8 to perform the following uplink acquisition sweep:

Transmitter on:	22:13:40 GMT
Start sweep:	22:14:00 GMT
Starting frequency:	21.996130 MHz (VCO)
Sweep rate:	3 Hz/s (VCO)
End sweep:	22:15:30 GMT
Ending frequency:	21.996400 MHz (VCO)
Sweep duration:	90 seconds

A comparison of the instructed sweep and the sweep as actually performed can be seen in Fig. 5. As can be seen, the uplink sweep began approximately 8 seconds later than planned. The switch to the two-way, coherent mode occurred at 22:14:49 GMT, within 5 seconds of the expected time. After an extensive search that included momentarily (~4 seconds) locking onto the telemetry subcarrier (see Table 2), the two-way downlink was acquired at 22:15:19 GMT. Even after the late start, the station was able to complete the uplink sweep within one second of the planned 22:15:30 time. The tuning rate averaged a commendable 3.2 Hz/s.

D. Angle Tracking

In adherence to the angle drive strategy as outlined in Section IV, the antenna at DSS 42 was initially computer-driven, using the preflight nominal predict set A20D, generated at launch minus two hours.

The drive mode was successfully changed to autotrack at 22:15:40 GMT, 9 seconds after completion of the uplink acquisition sweep.

In preparation for an uplink transfer from DSS 42 to DSS 44, the drive mode was changed to computer mode at 23:00:00 GMT. At 23:07:50 GMT, after maser No. 1 had been switched into the Antenna Microwave Subsystem and the uplink transferred back to DSS 42, autotracking was resumed at DSS 42.

E. Ranging

Commencing at 01:10:02 GMT (August 21), DSS 42 began the acquisition of ranging data via the Planetary Ranging Assembly (PRA). Using the newly developed "Pseudo-DRVID" PRA ranging validation technique (see Ref. 2), it was rapidly apparent to the Network Operations Analysis Group, Tracking (NOAG TRK), that the PRA data were suspect, and this information was disseminated. Several hours later, after the FPAG had fit the PRA data, the problem (symptom) was identified—the T_0 s (acquisition times) were approximately 0.9 second early. This symptom could have been identified by the NOCT far more quickly via additional analysis of Pseudo-DRVID output; unfortunately due to the newness of the technique, not all of the Pseudo-DRVID analysis capabilities were known. As regards a constant error in T_0 , one can easily derive a relationship between the time offset and the Pseudo-DRVID output. Using the notation from Ref. 2 and additionally defining the following:

$$\text{Pseudo-DRVID}' = \Delta PRA' - \Delta DOP$$

$$\Delta PRA' = \Delta PRA(t'_b, t'_a)$$

$$t'_b = t_b + \Delta t$$

$$t'_a = t_a + \Delta t$$

one gets

$$\begin{aligned} \text{Pseudo-DRVID}' &= \Delta PRA' - \Delta DOP \\ &= \Delta PRA(t'_b, t'_a) - \Delta DOP(t_b, t_a) \end{aligned}$$

and

$$\begin{aligned} \Delta PRA(t'_b, t'_a) &= \Delta PRA(t_b + \Delta t, t_a + \Delta t) \\ &= \frac{c}{48(TSF)} \{PRTR(t_b + \Delta t) \\ &\quad - PRTR(t_a + \Delta t) + Y\} \end{aligned}$$

Now

$$\begin{aligned} PRTR(t_b + \Delta t) &= PRTR(t_b) + \{PRTR(t_b + \Delta t) \\ &\quad - PRTR(t_b)\} \end{aligned}$$

and

$$\begin{aligned} PRTR(t_a + \Delta t) &= PRTR(t_a) + \{PRTR(t_a + \Delta t) \\ &\quad - PRTR(t_a)\} \end{aligned}$$

so that

$$\begin{aligned} \Delta PRA(t'_b, t'_a) &= \frac{c}{48(TSF)} [PRTR(t_b) \\ &\quad - PRTR(t_a) + Y \\ &\quad + (\{PRTR(t_b + \Delta t) - PRTR(t_b)\} \\ &\quad - \{PRTR(t_a + \Delta t) - PRTR(t_a)\})] \\ &= \Delta PRA(t_b, t_a) \\ &\quad + \frac{c}{48(TSF)} (\{PRTR(t_b + \Delta t) \\ &\quad - PRTR(t_b)\} \\ &\quad - \{PRTR(t_a + \Delta t) - PRTR(t_a)\}) \end{aligned}$$

and

$$\begin{aligned} \text{Pseudo-DRVID}' &= \Delta PRA(t_b, t_a) - \Delta DOP(t_b, t_a) \\ &\quad + \frac{c}{48(TSF)} (\{PRTR(t_b + \Delta t) \\ &\quad - PRTR(t_b)\} \\ &\quad - \{PRTR(t_a + \Delta t) - PRTR(t_a)\}) \end{aligned}$$

= Pseudo-DRVID

$$+ \frac{c}{48(TSF)} \{ (PRTR(t_b + \Delta t) - PRTR(t_b)) - (PRTR(t_a + \Delta t) - PRTR(t_a)) \}$$

Since

$$\frac{c}{48(TSF)} PRTR(t) = RTR(t)$$

and using the definition of a derivative

$$\frac{f(x + \Delta x) - f(x)}{\Delta x} \cong \frac{df}{dx}$$

one has

$$\begin{aligned} & \frac{c}{48(TSF)} \{ (PRTR(t_b + \Delta t) - PRTR(t_b)) - (PRTR(t_a + \Delta t) - PRTR(t_a)) \} \\ &= \{ RTR(t_b + \Delta t) - RTR(t_b) \} - \{ RTR(t_a + \Delta t) - RTR(t_a) \} \\ &\cong \left(\frac{dRTR}{dt} \right)_{t_b} \Delta t - \left(\frac{dRTR}{dt} \right)_{t_a} \Delta t \\ &\cong \Delta t \left\{ \left(\frac{dRTR}{dt} \right)_{t_b} - \left(\frac{dRTR}{dt} \right)_{t_a} \right\} \end{aligned}$$

Now

$$\begin{aligned} D2 &= 96 \frac{240}{221} TSF \left(\frac{2\dot{r}}{c} \right) + 10^6 \quad (\text{Block III Receiver}) \\ &= 96 \frac{240}{221} TSF \left(\frac{1}{c} \left[\frac{dRTR}{dt} \right] \right) + 10^6 \end{aligned}$$

or

$$\frac{dRTR}{dt} = \frac{c(D2 - 10^6)}{96 \frac{240}{221} TSF}$$

so that

$$\begin{aligned} & \Delta t \left\{ \left(\frac{dRTR}{dt} \right)_{t_b} - \left(\frac{dRTR}{dt} \right)_{t_a} \right\} \\ &\cong \Delta t \frac{c}{96 \frac{240}{221} TSF} \{ [(D2)_{t_b} - 10^6] - [(D2)_{t_a} - 10^6] \} \end{aligned}$$

$$\cong \frac{c \Delta t}{96 \frac{240}{221} TSF} \{ (D2)_{t_b} - (D2)_{t_a} \}$$

which is to say, finally,

$$\text{Pseudo-DRVID}' \cong \text{Pseudo-DRVID}$$

$$+ \frac{c \Delta t}{96 \frac{240}{221} TSF} \{ (D2)_{t_b} - (D2)_{t_a} \}$$

If one ignores Pseudo-DRVID (i.e., considers it small compared to any timing error contribution), one would have:

$$\Delta t \approx 96 \frac{240}{221} \left(\frac{TSF}{c} \right) \{ \text{Pseudo-DRVID}' \}$$

Below are presented the Pseudo-DRVID results from the DSS 42 launch pass, and calculations of Δt offsets using the above equation:

Acquisitions	Pseudo-DRVID, RU	Δt , seconds
1/2	188	-0.92
2/3	161	-0.87
3/4	174	-1.00
4/5	136	-0.82
5/6	138	-0.89
6/7	132	-0.90

The above results clearly demonstrate the ability of the Pseudo-DRVID technique to detect PRA "timing" errors in the near-real-time operations environment.

The malfunction which resulted in the -0.9-second error in T0 was not identified until several days later. At that time, it was found that the receiver coder in the Ranging Logic Assembly was being synchronized onto the trailing edge of the 10% duty cycle 1 pps, rather than the leading edge as it should properly have been. The problem was cleared by readjusting the threshold level of an isolation amplifier in the Frequency and Timing Subsystem (FTS), which supplies the 1 pps to the PRA.

VII. Summary of Tracking Operations During the Viking 1 Launch Phase

Viking 1 launch phase tracking operational procedures, and in particular the DSN initial acquisition procedures,

were very intensively considered and conservatively designed to accommodate even the most unfavorable of launch possibilities. These procedures were successfully implemented, and strongly contributed to the highly successful launch phase of the Viking 1 mission.

Acknowledgment

The authors would like to acknowledge L. E. Bright for the provision of the PRA data, and M. F. Cates and C. Darling for the fine graphical illustrations.

References

1. Berman, A. L., and Bright, L. E., "Tracking Operations During the Helios 1 Launch Phase," in *The Deep Space Network Progress Report 42-28*, pp. 83-94, Jet Propulsion Laboratory, Pasadena, Calif., Aug. 15, 1975.
2. Berman, A. L., "Pseudo-DRVID: A New Technique for Near-Real-Time Validation of Ranging System Data," in *The Deep Space Network Progress Report 42-29*, pp. 180-187, Jet Propulsion Laboratory, Pasadena, Calif., Oct. 15, 1975.

Table 1. Description of predicts denoted by Z

Z	Description	PCT generated
O	Open window predicts	$L - 7 \text{ days}^a$
M	Mid window predicts	$L - 7 \text{ days}^a$
C	Close window predicts	$L - 7 \text{ days}^a$
P	Parking orbit predicts	$L - 7 \text{ days}^a$
F	Frequency update predicts	$L - 165 \text{ min}$
D	Drive tape predicts	$L - 165 \text{ min}$
E	Estimated launch time predicts	$L - 10 \text{ min}$
A	Actual launch time predicts	$L + 5 \text{ min}$
B	Burn (TMI) estimate predicts	$L + 20 \text{ min}$
N	No TMI burn predicts	$L + 25 \text{ min}$
I	Injection estimate predicts	$L + 50 \text{ min}$

^aTo be regenerated at $L - 24 \text{ hours}$ if launch slips.

Table 2. Doppler residuals

GMT	Residual	Comments
22:13:30	34.416	Final one-way residual
22:14:00	-9420.715	Tuning—one-way doppler flagged two-way
22:14:10	-9163.489	Tuning
22:14:20	-6156.806	Tuning
22:14:30	-3037.731	Tuning
22:14:40	222.214	Tuning
22:14:49	-2280.683	Receiver out of lock—switch to coherent mode
22:15:00	-24066.756	Receiver locked on telemetry subcarrier
22:15:02	-24065.680	Receiver locked on telemetry subcarrier
22:15:19	-68.254	Receiver locked on carrier— good two-way
22:16:00	-66.052	Good two-way residual
22:18:00	-50.027	Good two-way residual
22:20:00	-37.420	Good two-way residual

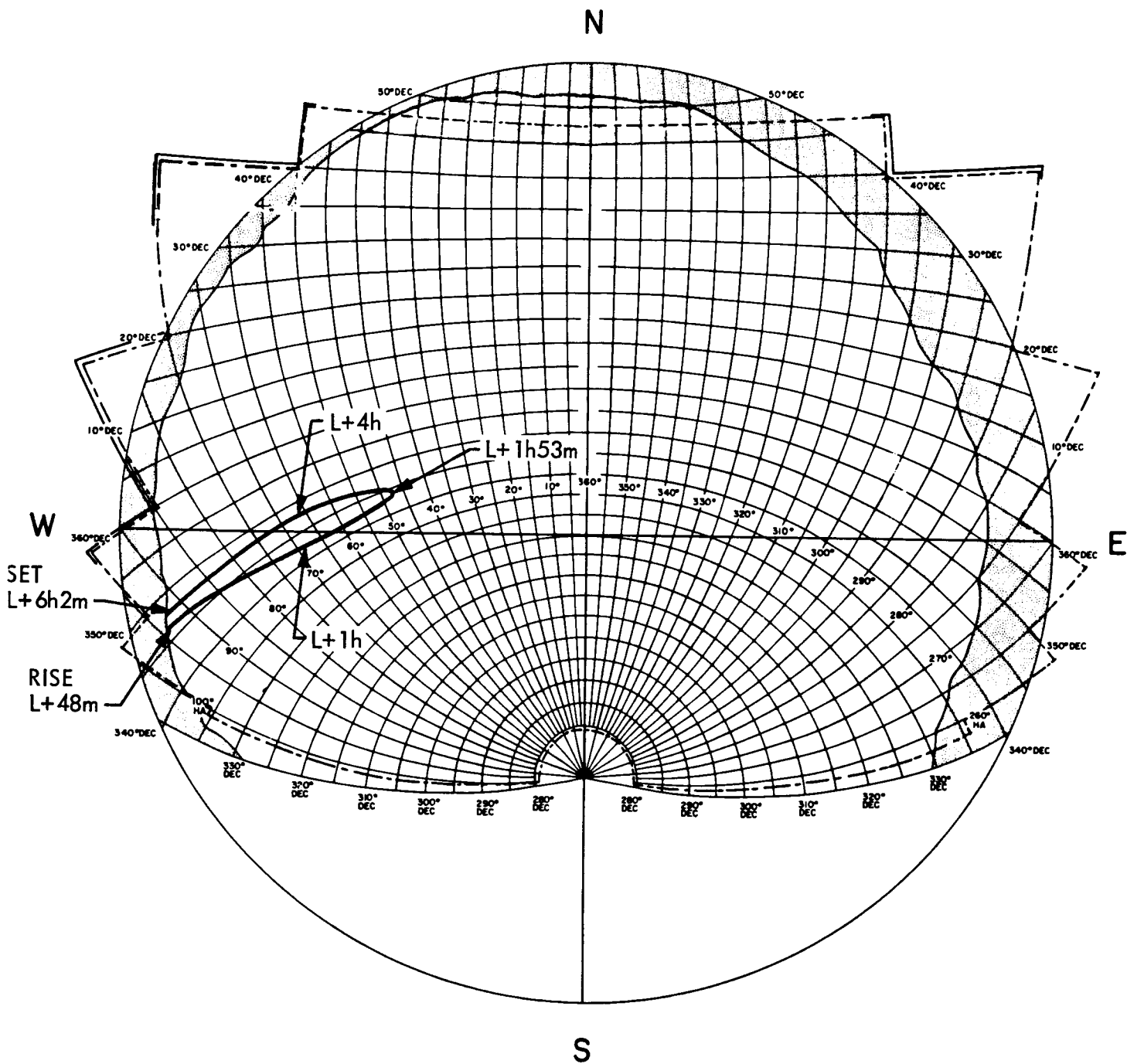


Fig. 1. DSS 42 Viking 1 launch, August 20, 1975

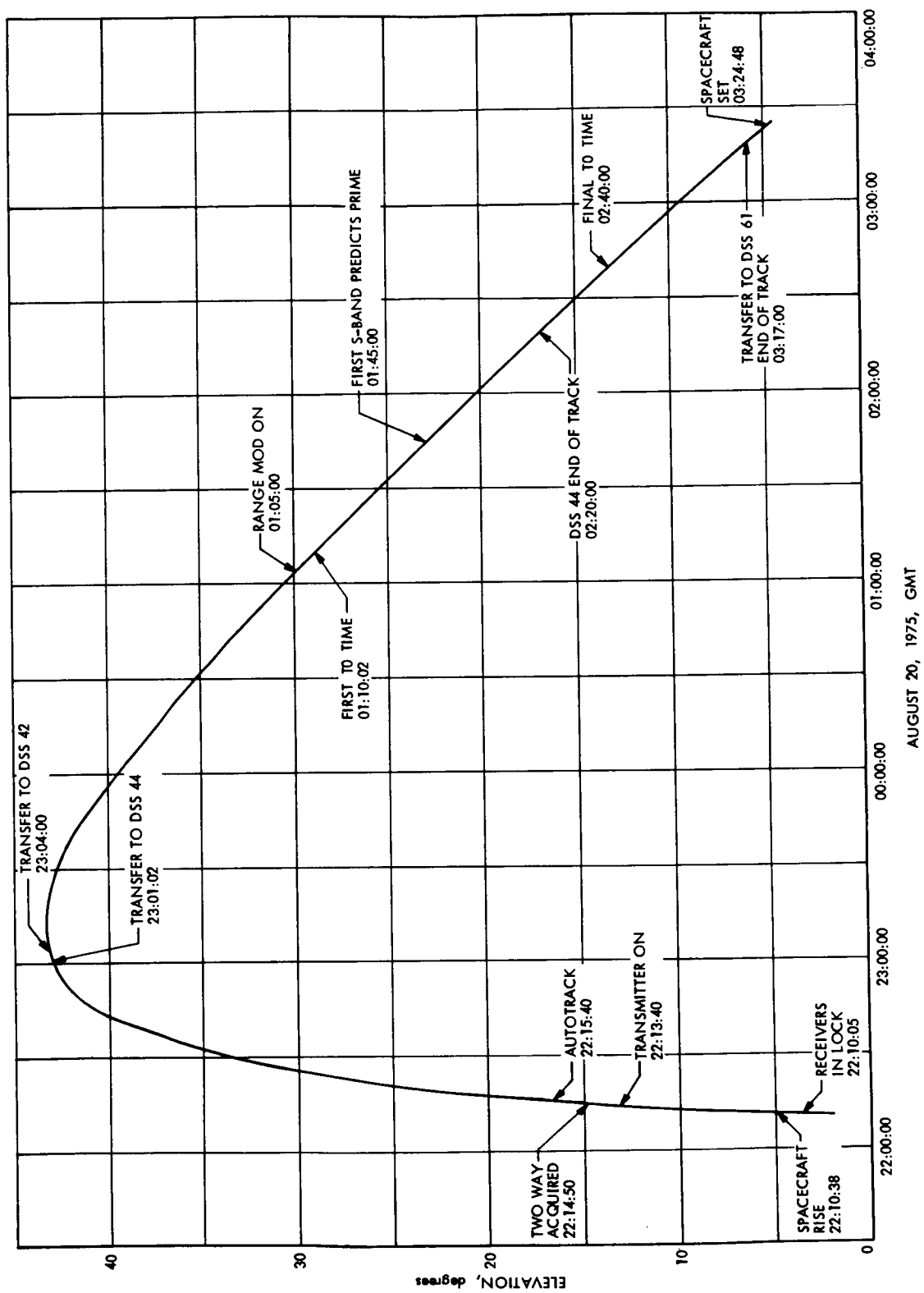


Fig. 2. Spacecraft elevation at DSS 42 Viking 1 launch

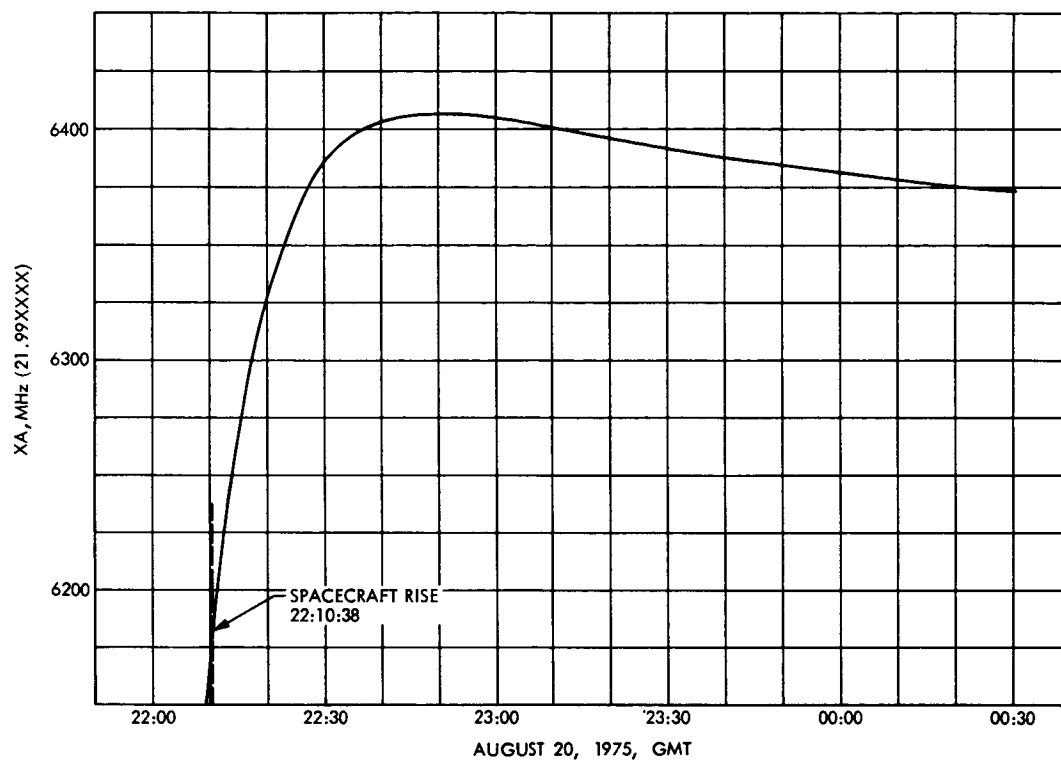


Fig. 3. Best-lock frequency at DSS 42 Viking 1 launch

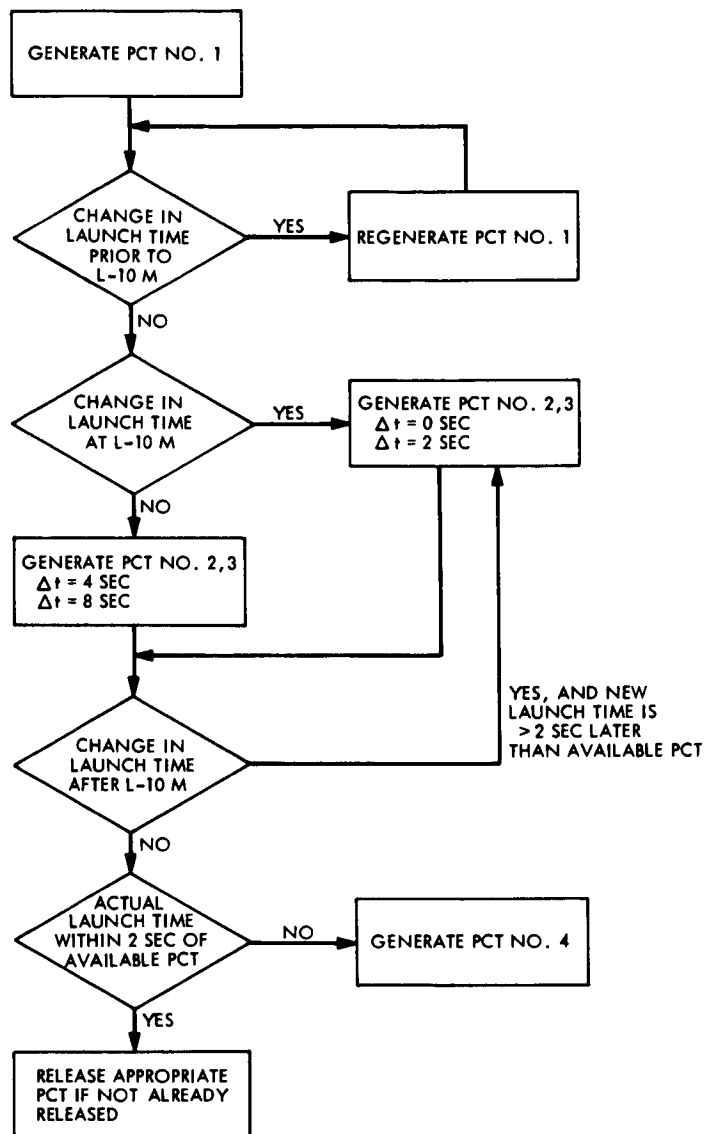


Fig. 4. PCT generation scheme

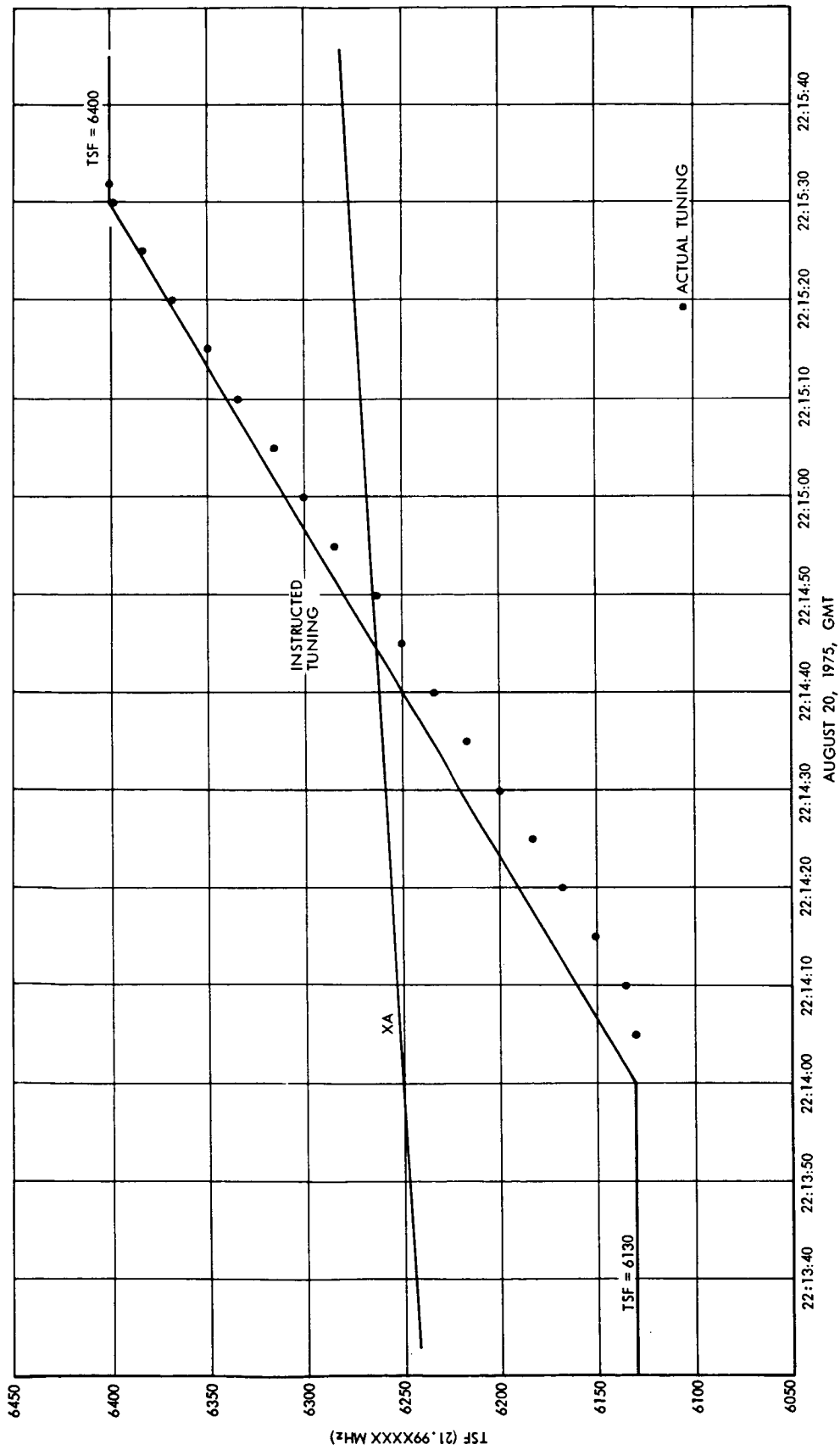


Fig. 5. Comparison of actual tuning to instructed tuning at DSS 42 Viking 1 launch

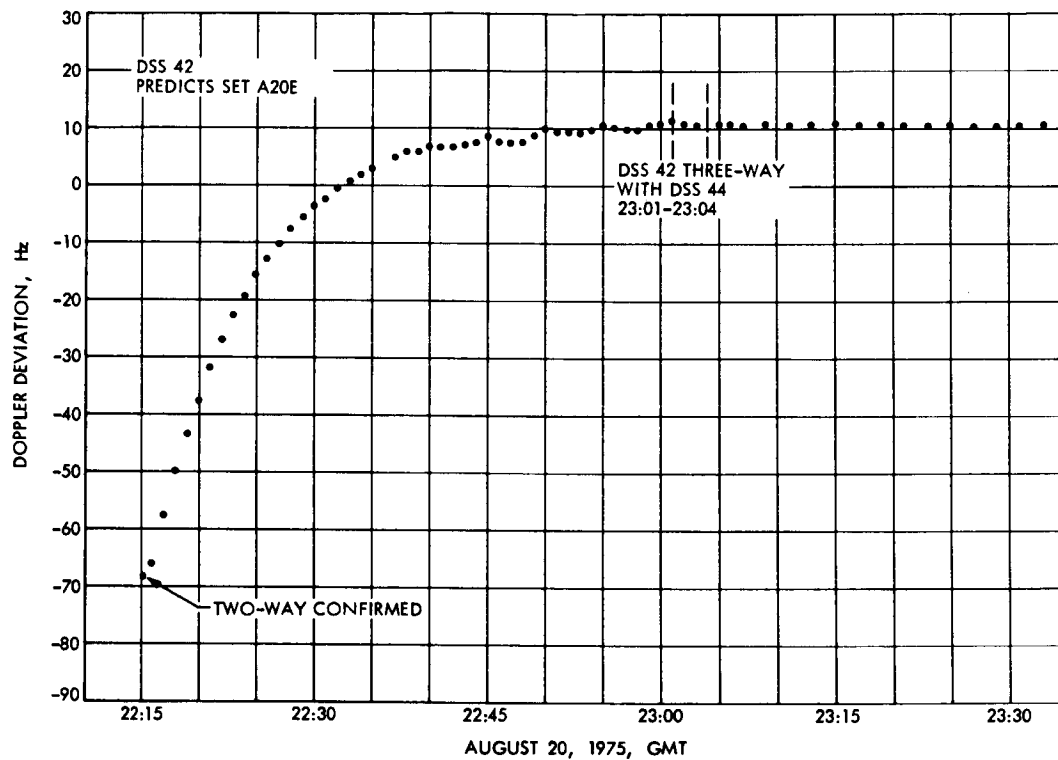


Fig. 6. Doppler deviation from preflight nominal predicts

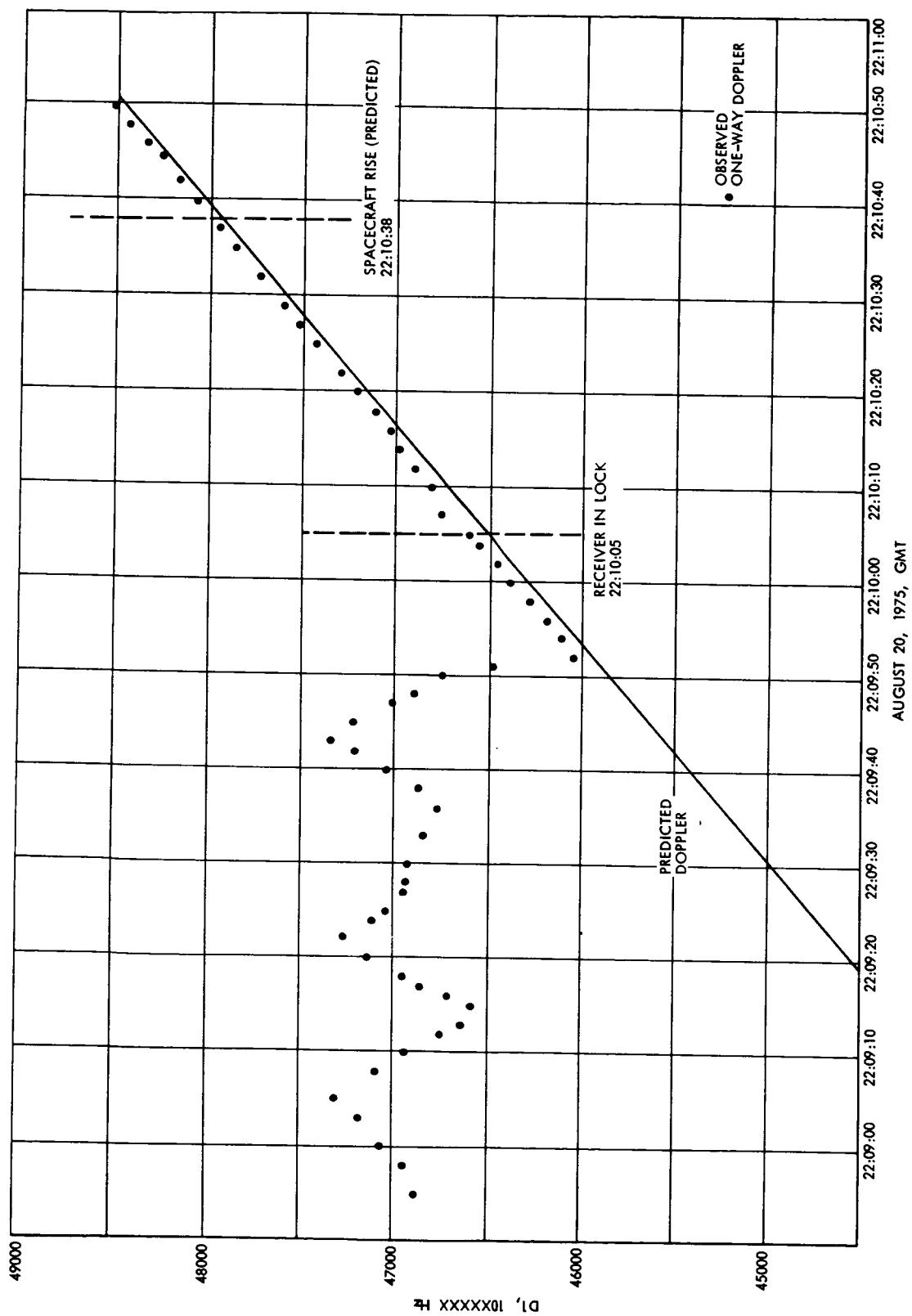


Fig. 7. Initial downlink acquisition at DSS 42 Viking 1 launch

A. PREDICTS		
1. TEXT	A20E	IS PRIME
2. DRIVE TAPE	A20D	IS PRIME
3. HA/X BIAS	—	DEG
4. DEC/Y BIAS	—	DEG
5. APS TIME BIAS	—	GMT
B. INITIAL UPLINK ACQUISITION SWEEP		
6. TXR ON	22:13:40	GMT
7. TXR POWER	10	KW
8. FREQUENCY	21.996130	MHZ
9. START TUNING	22:14:00	GMT
10. TUNING RATE	180	HZ/MIN(VCO)
11. TRACK SYN FREQ	21.996400	MHZ
12. CMD MOD ON	—	GMT
C. CONTINGENCY SWEEP: EXECUTE ONLY IF DIRECTED		
13. START TUNING	22:19:00	GMT
14. TUNING RATE	180	HZ/MIN(VCO)
15. SWEEP DOWN TO	21.996160	MHZ
16. SWEEP UP TO	21.996510	MHZ
17. SWEEP DOWN TO TSF	21.996400	MHZ
18. CMD MOD ON	—	GMT

SPECIAL INSTRUCTIONS:

Fig. 8. Actual Viking 1 acquisition message

N76-15212

A Relational Data Base Implemented Using MBASIC

R. M. Smith
DSN Facility Operations Office

The implementation of a relational data base in MBASIC is described. Five relational operations are implemented, and their use on two data bases is described.

I. Introduction

The relational model of data is presently state-of-the-art in data base technology. The relational approach offers a simply understood, generalized data model that allows a relatively easy attainment of security, integrity, and privacy controls as well as implementation of the usual query and update transaction capability. The model also allows relatively easy expansion and reorganization. For these reasons, the relational model is an attractive candidate for the DSN Facility Operations data base. This article describes initial efforts at exploring the features of the relational model. Included in the scope of this effort was the construction of a demonstration relational data base and the implementation in MBASIC of several relational data base manipulation operations. The capability

to manipulate the data base with the operations was demonstrated.

II. Relational Structure

In the relational model, data are organized into arrays (called relations) with fields (called domains), so that each record entry (called a tuple) is essentially a set of attributes describing one or more characteristics of a real-world entity. For instance, the relation "equipment identification" might be described by the following set of domain names:

CONTROL NUMBER	MANUFACTURER CODE	MODEL	USAGE CATEGORY	PROPERTY NUMBER
-------------------	----------------------	-------	-------------------	--------------------

Adding domain values would record the identification of equipment:

CONTROL NUMBER	MANUFACTURER CODE	MODEL	USAGE CATEGORY	PROPERTY NUMBER
AA1A23	HEA	5245L	Ø3	J270(F)12345
AB5CØ1	TEA	547	Ø7	LA546785
AA2B47	EPI	100	Ø2	NONE

Other relations may be constructed to describe other relationships such as equipment location, service history, etc.

III. Relational Operations

There are several specific relational operations (described in Refs. 1 -3) that are used to manipulate data in the data model:

- (1) Join
- (2) Restriction
- (3) Division
- (4) Projection
- (5) Permutation

The reader may refer to the references for detailed descriptions of the relational operations; the following brief description may suffice for this reading:

- (1) *Join*. Two relations that have at least one domain in common may be combined in a way that preserves all the information in both relations but does not repeat the duplicate domain values in the resultant tuples. The join is equivalent in action to a union of sets.
- (2) *Restriction*. Tuples may be selected from a relation by testing each tuple for the presence of a specified attribute.
- (3) *Division*. Tuples may be selected from a relation by testing each tuple for the presence of a specified constant value. Tuples so selected are listed or stored, minus the domain containing the constant value, as though the selected tuples were remainders in a division process.
- (4) *Projection*. Specific domains in a relation may be selected (striking out the others) and duplicate tuples removed. The resultant array is a projection of the original relation.

- (5) *Permutation*. Domain positions in a relation may be interchanged, resulting in a permutation of the relation.

IV. Examples of the Relational Operations

Figures 1, 2 and 3 use flow charts derived from MBASIC programs described in this article (see *MBASIC, Vol. 1: Fundamentals*, and *MBASIC, Vol. 2: Appendices*, Jet Propulsion Laboratory, 1973) to illustrate the relational operations: join, restriction, and division. The projection operation is inherent in each of the relational operations when either "PRINT" or "WRITE ON" is used. Permutation is not illustrated separately but occurs in the program 'REFERENCE' when the record domains are reordered in the "PRINT" operation.

V. Description of the Data Base

The data base consists of two parts. The first part is purely for demonstration and consists of five MBASIC files containing equipment data to be manipulated and one file that serves as a directory. There is one program that may be used to demonstrate relational operations on the files. Figure 4 illustrates the domain assignments for each demonstration relation. Figure 5 contains a flow diagram of the demonstration program 'RELATIONAL'. Figure 6 illustrates the domain assignment for the directory relation.

The program 'RELATIONAL' performs a relational operation using relations, domains, and domain values selected by the user. In performing the selected operation, the program uses the relational operators as intermediate steps in manipulating the selected relations and domains.

The second part is a working data base that records a collection of technical articles and the subjects and key words contained in the articles. There are three MBASIC programs written especially for using the data base:

- (1) 'REFERENCE': Locates and prints the author and title of all articles that reference a subject or key word selected by the user.
- (2) 'INPUTREF': Maps into storage new articles and subjects or key words.
- (3) 'TERNARY': Prints a list of subjects and key words without printing duplications.

Figure 7 illustrates the domain assignment for the working part of the data base. Figures 8, 9, and 10 are flow charts for the special MBASIC programs.

VI. Details of the Implementation and Functions

There are several "traits" that are desirable in a relational data base, and the following were specifically chosen for inclusion in the described data base:

- (1) Record order independence. Application programs should generally not be dependent upon stored order of the records.
- (2) Use of domain names rather than domain positions. The user should not have to know the positions of domains.
- (3) Deletion and addition of relations. These should not affect application programs.

For this implementation, no effort was made to produce a data sublanguage (Ref. 3); therefore, all transactions are carried on in a full prompting mode, and the user deals with individual programs.

Figures 11 and 12 contain, respectively, the content of the demonstration files and the content of the working

files. Figure 13 illustrates a session at a terminal using the demonstration program 'RELATIONAL' to produce the join of two relations over a common domain and the restriction of a relation. Figure 14 illustrates a session at a terminal using the working program 'REFERENCE' to produce a list of articles on a selected subject.

VII. Conclusions

The capability for exclusive use of domain names was fully realized in the program entitled 'RELATIONAL'. Record order independence is observed in all relations but one: 'SUBJECTS'. For practical reasons, it was decided to store 'SUBJECTS' in a particular, sorted order rather than to write a program containing a sort routine. The ability to add and delete relations was fully realized in the demonstration program ('RELATIONAL') and associated directory file ('RREL'). All of the previously listed relational operations take place during the operation of the special MBASIC programs referenced in this article and are annotated on the 'RELATIONAL' flow diagram.

References

1. Codd, E. F., "A Relational Model of Data for Large Shared Data Banks," *Communications of ACM*, Vol. 13, No. 6, June 1970.
2. Codd, E. F., "Normalized Data Base Structure: A Brief Tutorial," *Proceedings of 1971 ACM SIGFIDET Workshop on Data Description, Access and Control*, ACM, New York, 1971.
3. Date, C. J., *An Introduction to Database Systems*, Addison-Wesley, 1975.

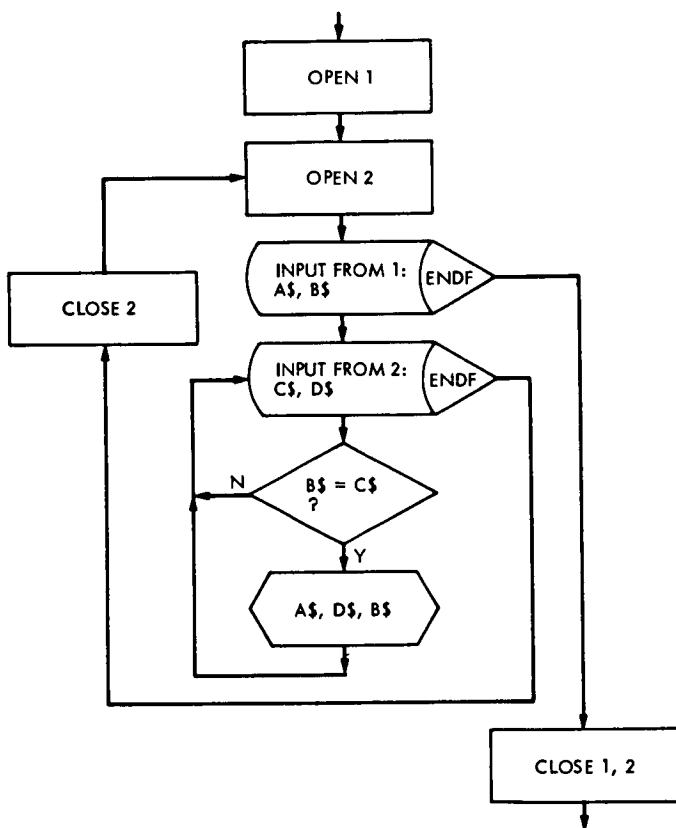


Fig. 1. Flow chart for the relational operation "Join"

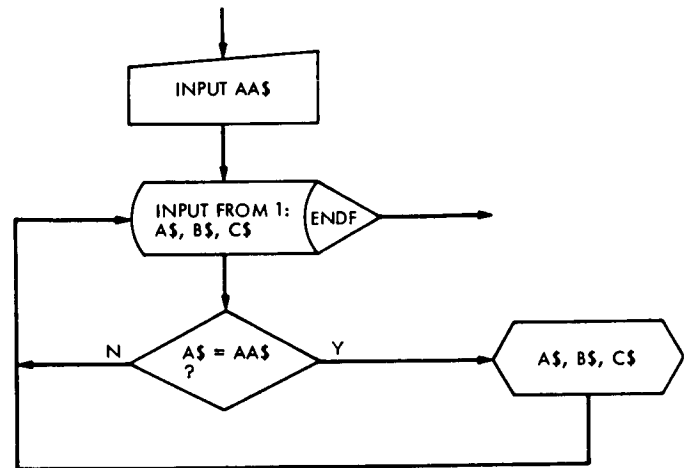


Fig. 2. Flow chart for the relational operation "Restriction"

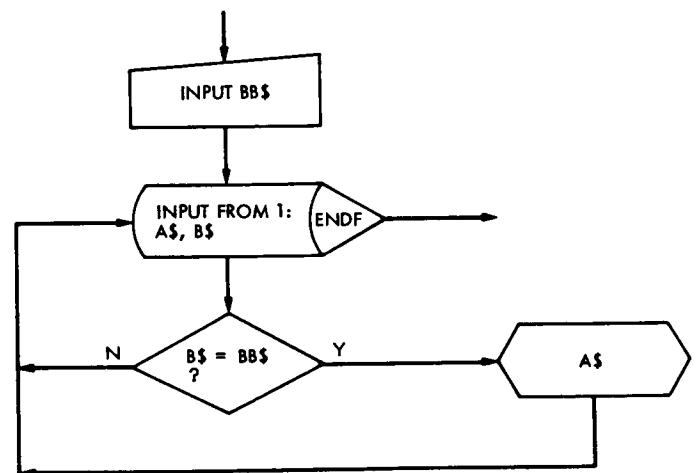
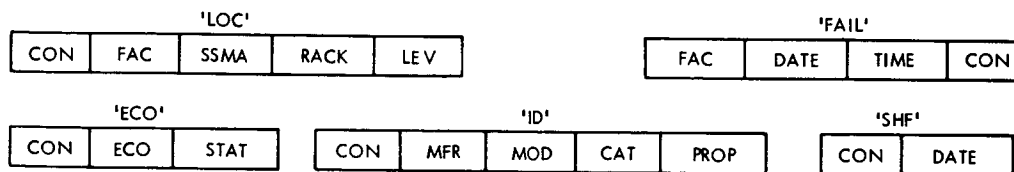


Fig. 3. Flow chart for the relational operation "Division"



CON = DSN CONTROL NUMBER
 FAC = FACILITY
 SSMA = SUBSYSTEM AND MAJOR ASSEMBLY
 RACK = RACK
 LEV = LEVEL
 ECO = ENGINEERING CHANGE ORDER
 STAT = STATUS
 DATE = DATE
 TIME = TIME
 MFR = MANUFACTURER THREE LETTER CODE
 MOD = MODEL
 CAT = CATEGORY
 PROP = PROPERTY NUMBER

'LOC': EQUIPMENT LOCATION DATA
 'FAIL': EQUIPMENT FAILURE HISTORY DATA
 'ECO': EQUIPMENT DESIGN DATA
 'ID': EQUIPMENT IDENTIFICATION DATA
 'SHF': EQUIPMENT SERVICE HISTORY DATA

Fig. 4. Demonstration relations and domains

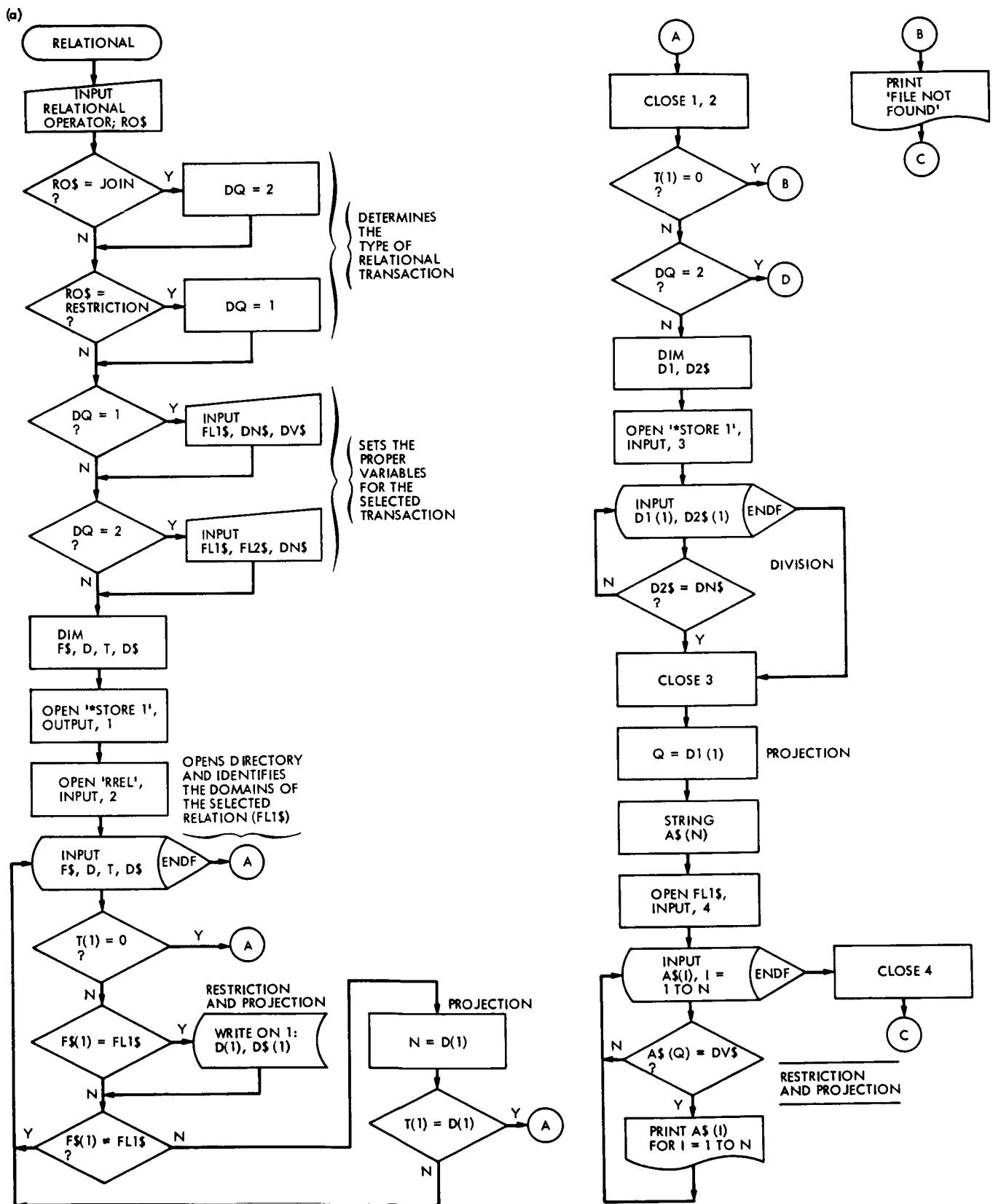


Fig. 5. Flow diagram for the MBASIC demonstration program 'RELATIONAL'

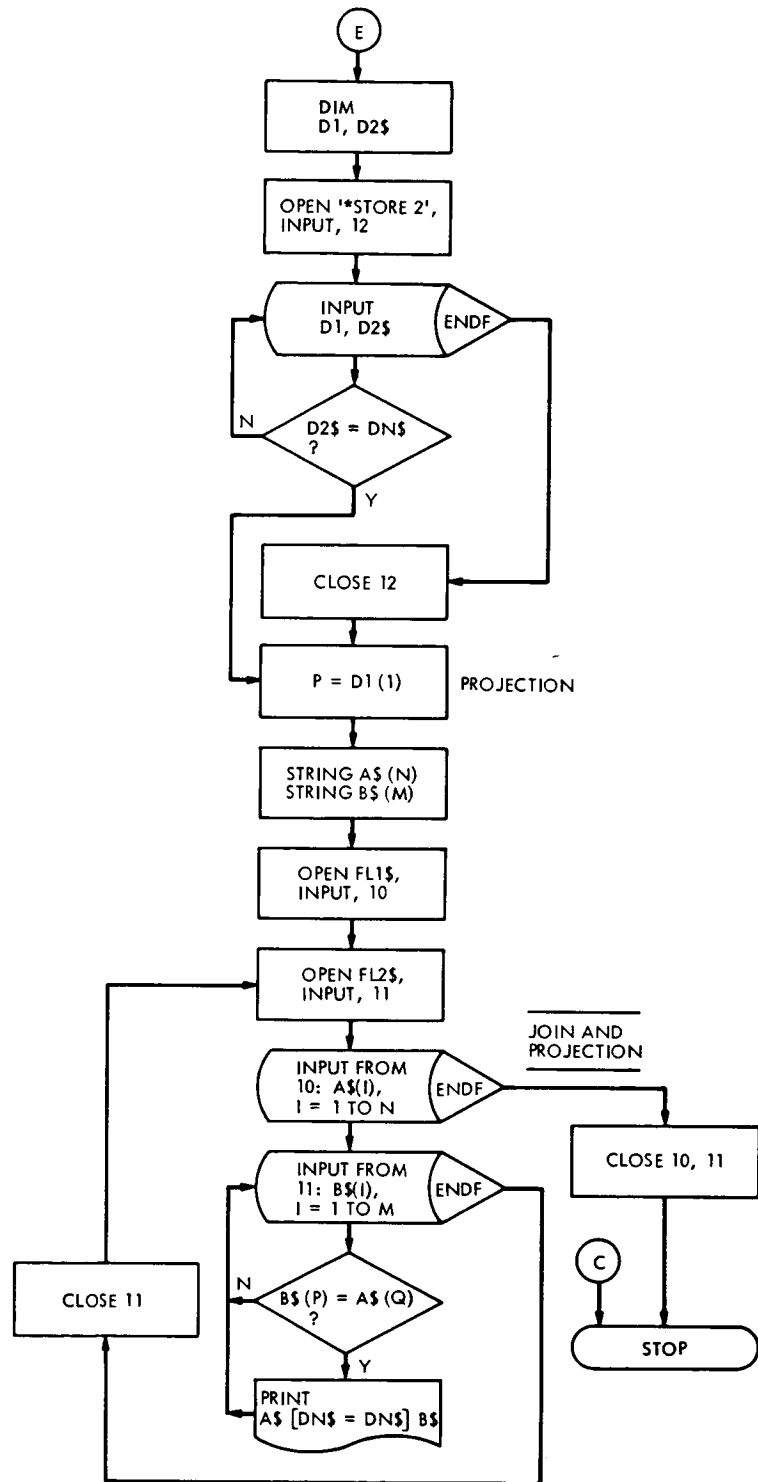
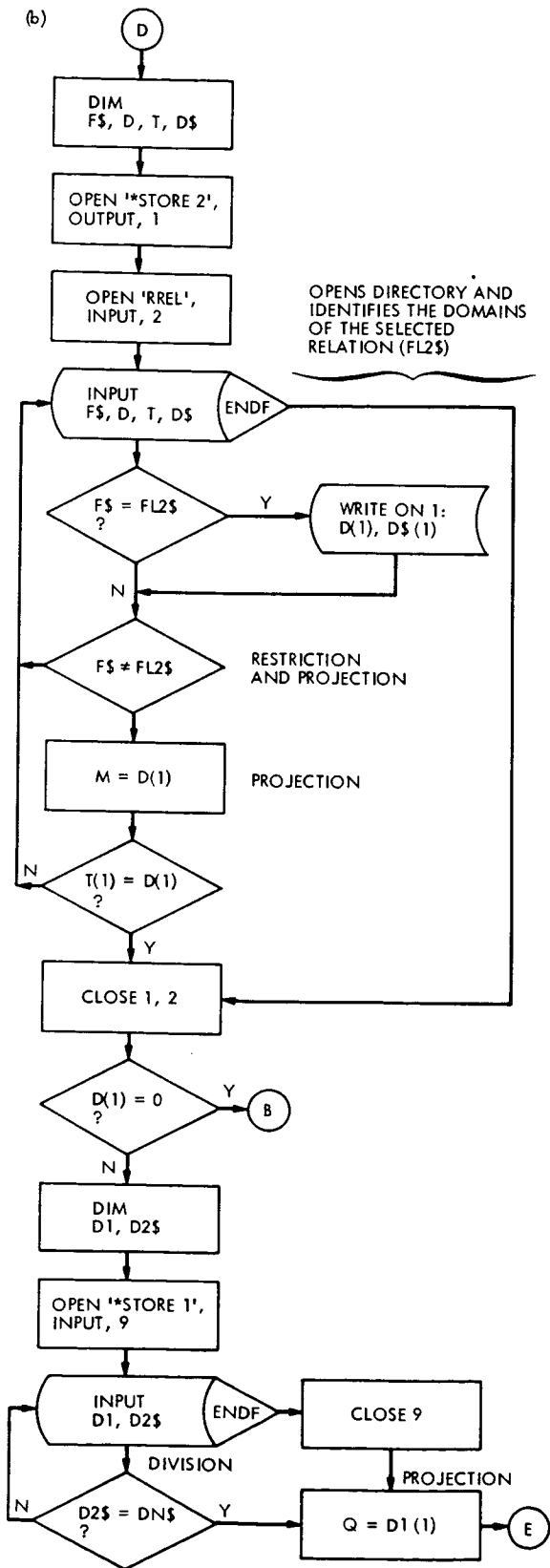


Fig. 5. (contd)

'RREL'			
FILENAME	DOMAIN NUMBER	QUANTITY OF DOMAINS	DOMAIN NAME

FILENAME = MBASIC NAME OF A RELATION FILE
 DOMAIN NUMBER = THE DOMAIN POSITION IN THE RELATION
 QUANTITY OF DOMAINS = TOTAL QUANTITY OF DOMAINS IN THE RELATION
 DOMAIN NAME = THE NAME ASSIGNED TO THE SPECIFIC DOMAIN

Fig. 6. Domain assignment for the directory relation 'RREL'

'SUBJECTS'	
REF #	SUBJECTS

'ARTICLES'		
REF #	TITLE	AUTHOR

REF # = A UNIQUE FILE NUMBER ASSIGNED TO AN ARTICLE
 SUBJECT = A SUBJECT NAME OR A KEY WORD
 TITLE = THE TITLE OF AN ARTICLE
 AUTHOR = THE NAME OF THE ARTICLE'S AUTHOR

Fig. 7. Working relations and domains

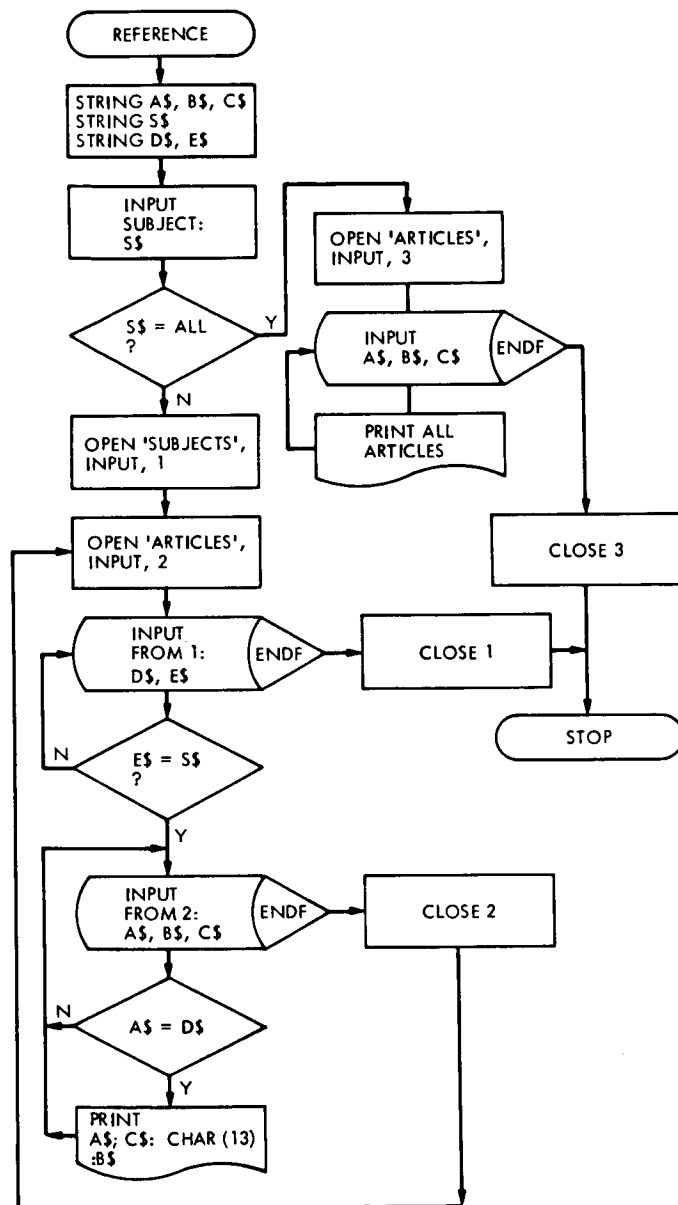


Fig. 8. Flow diagram for the MBASIC working program 'REFERENCE'



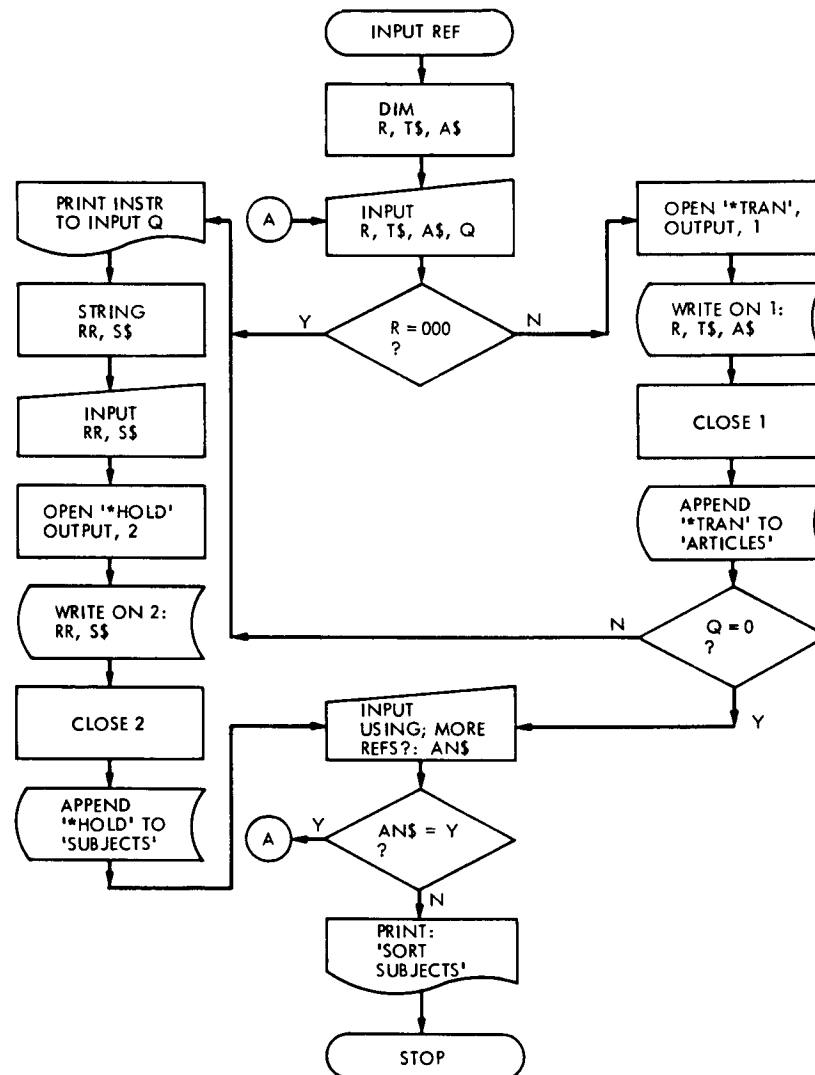


Fig. 10. Flow diagram for the MBASIC working program 'INPUTREF'

<p>COPY 'FAIL' TO TERMINAL</p> <p>14,2355,2215,AA30AA 14,2585,1612,AA30AA 41,2215,1525,AL32BA 11,2015,0032,AA01FG 11,2105,1512,AA32AP 21,0055,0722,AA30AA 44,1505,1220,AB21BA 12,1705,0117,AA32AS 20,0015,1515,AA30AA 14,1225,0711,AB21UG 12,0155,1010,AA50AB 14,3025,1706,AB56AA ></p> <p>COPY 'ID' TO TERMINAL</p> <p>AA30AA,HEA,1405,3,J270(F) AA32AP,JPL,9454233,7,NONE AA32AS,TEA,547,6,J270(F) AB21UG,LXA,1234,7,J270(F) AA01FG,JPL,10053231,7,NONE AA50AB,TEA,M,3,J270(F) AB56AA,LEA,1453R,3,J270(F) AA450W,XYZ,2122,6,J270(F) AZ34RT,JPL,9443207,7,J270(F) AV66YH,HEA,5303,2,J270(F) AX44RF,ABC,M165,7,J270(F) AD78UU,TXF,1A55,7,J270(F) ></p> <p>COPY 'ECO' TO TERMINAL</p> <p>AA32AS,74.001,1 AA450W,75.123,2 AB56AA,74.001,1 AZ34RT,75.001,1 AA50AB,74.001,2 AV66YH,74.001,3 AA01FG,75.123,3 AX44RF,73.010,4 AB21UG,74.246,1 AD78UU,73.378,3 AA32AP,73.854,2 AB56AA,71.132,3 AB21UG,73.229,4 AB21RE,75.424,2 AB56AA,75.444,1 AA32AS,71.105,1 ></p>	<p>COPY 'LOC' TO TERMINAL</p> <p>AA30AA,14,3301,125,2A2 AA32AP,11,3105,221,1A5 AA32AS,12,3702,003,1A1 AB21UG,14,3912,002,1A3 AA01FG,11,3606,010,1A6 AA50AB,12,3102,005,1A6 AB56AA,14,3510,003,1B5 AZ34RT,11,3105,067,1D4 ></p> <p>COPY 'SHF' TO TERMINAL</p> <p>AA32AS,1705 AA30AA,2005 AA32AP,1705 AB21UG,2005 AA01FG,1705 AA50AB,2355 ></p> <p>COPY 'RREL' TO TERMINAL</p> <p>SUBJECTS,1,2,REF# SUBJECTS,2,2,SUBJECT ARTICLES,1,3,REF# ARTICLES,2,3,TITLE ARTICLES,3,3,AUTHOR LOC,1,5,CON LOC,2,5,FAC LOC,3,5,SSMA LOC,4,5,RACK LOC,5,5,LEV ECO,1,3,CON ECO,2,3,ECO ECO,3,3,STAT FAIL,1,4,FAC FAIL,2,4,DATE FAIL,3,4,TIME FAIL,4,4,CON SHF,1,2,CON SHF,2,2,DATE ID,1,5,CON ID,2,5,MFR ID,3,5,MOD ID,4,5,CAT ID,5,5,PROP LAST,0,0,ITEM ></p>
--	---

Fig. 11. Content of demonstration relations

```

COPY 'SUBJECTS' TO TERMINAL
004, ADABAS
068, AUDIT
047, AUTOMATED PROGRAMMING
058, AUTOMATED PROGRAMMING
003, COMPOSITION
003, CONSISTENCY
069, CONSISTENCY
071, CONSISTENCY
068, CONSISTENCY
071, DATA DEFINITION LANGUAGE
081, DATA DEFINITION LANGUAGE
075, DATA DEFINITION LANGUAGE
001, DATA DEFINITION LANGUAGE
002, DATA DESCRIPTION
071, DATA VALIDATION
023, DATA VALIDATION
005, DATABASE
058, DATABASE
083, DATABASE
067, DATABASE
063, RELATIONAL
069, RELATIONAL
052, RELATIONAL
049, RELATIONAL
050, RELATIONAL
071, RELATIONAL
065, RELATIONAL
066, RELATIONAL
023, RELATIONAL
053, RELATIONAL
077, RELATIONAL
072, RELATIONAL IMPLEMENTATIONS
003, RESTRICTION
066, RESTRICTION
077, SECURITY
072, SECURITY
074, SECURITY
003, SECURITY
075, SECURITY
080, SECURITY
004, SYSTEM 2000
080, SYSTEM 2000
005, SYSTEM 2000
069, USER VIEW
>

```

Fig. 12. Content of working relations

REPRODUCIBILITY OF THE
ORIGINAL PAGE IS POOR

COPY 'ARTICLES' TO TERMINAL

001, A LANGUAGE FOR A RELATIONAL DATA BASE MGMT SYSTEM, BRACCHI/FEDELI/PAOLINI

002, ANOTHER LOOK AT DATA, MEALY

003, A RELATIONAL MODEL OF DATA FOR LARGE SHARED DATA BANKS, CODD

004, NEW SOFTWARE FOR DATA BASE MGMT: PART 2, EDP IN-DEPTH REPORT

005, THE CURRENT STATUS OF DATA MGMT, EDP ANALYZER

006, THE DATA BASE ADMINISTRATOR: PART 2, EDP IN-DEPTH REPORT

007, NETWORKS HIERARCHIES AND RELATIONS IN DBM SYSTEMS, STONEBRAKER/HELD

013, IMPLEMENTING PRODUCTION SYSTEMS WITH RELATIONAL SYSTEMS, JORDAN

023, INTEGRITY CONTROL IN A RELATIONAL DATA DESCRIPTION LANGUAGE, GRAVES

027, A COBOL DATA BASE FACILITY FOR THE RELATIONAL MODEL, WESTGAARD

032, DATA BASE ADMINISTRATION, SECREST

045, IMPLEMENTATION OF A STRUCTURED ENGLISH QUERY LANGUAGE, ASTRAHAN/CHAMBERLIN

046, COMPUTING JOINS OF RELATIONS, GOTLIEB

047, OPTIMIZING THE PERFORMANCE OF A RELATIONAL ALGEBRA DATABASE, SMITH/CHANG

048, IMPLEMENTATION OF INTEGRITY CONSTRAINTS AND VIEWS BY QUERY MODIFICATIONS,
STONEBRAKER

049, PERFORMING INFERENCES OVER RELATIONAL DATABASES, MINKER

050, INFORMATION RETRIEVAL IN FILES DESCRIBED USING SETS, WELCH/GRAHAM

052, A HIGH LEVEL TRANSL DEFINITION LANG FOR DATA CONVERSION, SHU/HOUSEL/LUM

053, A LOGICAL-LEVEL APPROACH TO DATABASE CONVERSION, SHOSHANI

054, INVESTIGATION INTO THE APPL OF THE RELAT MODEL TO DATA TRANS, NAVATHE/MERTEN

058, A PRELIM SYST FOR THE DESIGN OF DBTG DATA STRUCTURES, GERRITSON

062, FINDING CANDIDATE KEYS FOR RELATIONAL DATABASES, FORSYTH/FADOUS

063, ON THE SEMANTICS OF THE RELATIONAL MODEL, SCHMID/SWENSON

065, A UNIFIED APPROACH TO FUNCTIONAL DEPENDENCIES AND RELATIONS, &
BERNSTEIN/SWENSON/TSICHRITZIS

066, RELATIONAL COMPLETENESS OF DATA BASE SUBLANGUAGES, CODD

067, FURTHER NORMALIZATION OF THE DATABASE RELATIONAL MODEL, CODD

068, CONSISTENCY AUDITING OF DATABASES, FLORENTIN

069, USING A STRUCTURED ENGLISH QUERY LANGUAGE AS A DATA DEFINITIONS
FACILITY, BOYCE/CHAMBERLIN

070, COMPUTER FRAUD AND EMBEZZLEMENT, EDP ANALYZER SEPT 1973

071, AN INTRODUCTION TO DATABASE SYSTEMS, DATE

072, AFIPS CONFERENCE PROCEEDINGS 1975, AFIPS

073, THE ROLE OF THE DATABASE ADMINISTRATOR, LYON

074, SYSTEM IMPLICATIONS OF INFORMATION PRIVACY, PETERSEN/TURN

075, DATABASE TASK GROUP REPORT 1971, CODASYL

076, THE PROGRAMMER AS NAVIGATOR, BACHMAN

077, HIGH LEV INTEGRITY ASSURANCE IN RELATIONAL DATABASE MGMT SYST, STONEBRAKER

078, AVOIDING DEADLOCK IN MULTITASKING SYSTEMS, HAVENDER

079, SYSTEM DEADLOCKS, COFFMAN/ELPHIC/SHOSHANI

080, NEW SOFTWARE FOR DATABASE MGMT: PART 1, EDP IN-DEPTH REPORT

081, GENERALIZED DATABASE MGMT SYST DATA STRUCTURES, TAYLOR

082, RELATIONAL DATABASE SYSTEMS: A TUTORIAL, DATE

083, A SURVEY OF GENERALIZED DATABASE MGMT SYST, CODASYL

>

Fig. 12. (contd)

```

LOAD 'RELATIONAL'
>RUN
ENTER RELATIONAL OPERATION: RESTRICTION
ENTER FILENAME, DOMAIN NAME AND DOMAIN VALUE: ID, MFR, HEA
AA30AA HEA 1405 3 J270(F)
AV66YH HEA 5303 2 J270(F)

      END
>RUN
ENTER RELATIONAL OPERATION: JOIN
ENTER TWO FILENAMES AND DOMAIN NAME:          LOC, FAIL, CON
AA30AA 14 3301 125 2A2 14 2555 2215
AA30AA 14 3301 125 2A2 14 2585 1612
AA30AA 14 3301 125 2A2 21 0055 0722
AA30AA 14 3301 125 2A2 20 0015 1515
AA32AP 11 3105 221 1A5 11 2105 1512
AA32AS 12 3702 003 1A1 12 1705 0117
AB21UG 14 3912 002 1A3 14 1225 0711
AA01FG 11 3606 010 1A6 11 2015 0032
AA50AB 12 3102 005 1A6 12 0155 1010
AB56AA 14 3510 003 1B5 14 3025 1706

      END
>

```

Fig. 13. A session at a terminal using the MBASIC program 'RELATIONAL'

```

LOAD 'REFERENCE'
>RUN
ENTER SUBJECT: SECURITY
077  STONEBRAKER
    HIGH LEV INTEGRITY ASSURANCE IN RELATIONAL DATABASE MGMT SYST

072  AFIPS
    AFIPS CONFERENCE PROCEEDINGS 1975

074  PETERSEN/TURN
    SYSTEM IMPLICATIONS OF INFORMATION PRIVACY

003  CODD
    A RELATIONAL MODEL OF DATA FOR LARGE SHARED DATA BANKS

075  CODASYL
    DATABASE TASK GROUP REPORT 1971

080  EDP IN-DEPTH REPORT
    NEW SOFTWARE FOR DATABASE MGMT:PART 1

    END
>

```

Fig. 14. A session at a terminal using the MBASIC program 'REFERENCE'